Rotordynamic Instability Problems
in High-Performance Turbomachinery

Proceedings of a workshop
held at Texas A&M University
College Station, Texas
May 12-14, 1980

NASA

NASA Conference Publication 2133

Rotordynamic Instability Problems in High-Performance Turbomachinery

NASA

National Aeronautics
and Space Administration

Scientific and Technical
Information Branch

1980

Page intentionally left blank

PREFACE

In the past decade researchers in rotordynamics have met with considerable success in modeling the structural dynamics of flexible rotors and in developing analysis techniques for the bearings that support these rotors. Parallel advances have been made in the development of effective balancing techniques for flexible rotors. As a result of these advances rotor critical speeds and synchronous response amplitudes due to rotor imbalance can be predicted with a reasonable degree of confidence. Further the utilization of tilting-pad bearings eliminates hydrodynamic bearings as a mechanism for rotor instability. Partially as a result of these substantial technical advances, new high-performance turbomachinery has been designed, developed, and put into service that operates at higher speeds and higher energy-density levels. Many of these units, including the HPFTP (high-pressure fuel turbopump) of the SSME (Space Shuttle main engine) and various multistage centrifugal compressors, have experienced severe development and operational problems as a result of subsynchronous instabilities. Incidents of rotordynamic instability have stimulated the development and refinement of squeeze-film dampers for stability control, but the crisis circumstances accompanying these incidents have generally precluded the development of any basic understanding of the underlying mechanisms that are responsible for the instability. Hence, although techniques have been developed to cope with units that prove to be unstable, the degree of understanding is completely inadequate to design stable high-performance turbomachinery. Stated differently, the stability of a new or upgraded design can only be demonstrated by full-load operation in place.

This workshop was organized to address the general problem of rotordynamic instability by gathering those persons with immediate interest, experience, and knowledge for a discussion and review of both past stability problems and present research and development efforts. The intent of the workshop organizers and sponsors is that the discussions within the workshop and the proceedings that documents these discussions provide an initial catalyst for the systematic resolution of these problems.

Chairmen:

Dara W. Childs
Texas A&M University

Robert C. Hendricks
NASA Lewis Research Center

John M. Vance
Texas A&M University

iii

Page intentionally left blank

DEDICATION
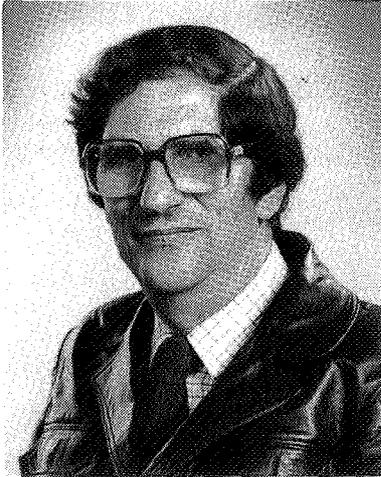
The proceedings of this workshop is respectfully
dedicated to the memory of Professor Henry F. Black,
MSc, DSc, MIMechE, of Heriot-Watt University,
Edinburgh, Scotland. Henry was born in 1928 and died
on 17 January 1980. He is survived by his widow and
daughter.

It is difficult to briefly summarize Henry's
technical contributions to rotordynamics. He had
extensive first-hand industrial experience with rotat-
ing machinery and was in demand as a consultant on
rotordynamics problems. His recommendations and con-
tributions as a consultant to NASA and Rocketdyne
Division of Rockwell International were fundamental
to the resolution of rotordynamic instability prob-
lems with the Space Shuttle main engine.

Henry published numerous journal articles over a comparatively wide range
of topics during his professional lifetime. His papers were rarely "easy"
reading, requiring (and meriting) careful study and rereading. The standards
he applied to his published work were stringent, requiring in his judgment that
the results be worthwhile and of continuing interest as well as original. In
fact, conversations with Henry frequently turned up technical "gems" and re-
sults that he felt to be obvious and had declined to submit for publication.
Listed below are Henry's major contributions to the field of rotordynamics.
The breadth and quality of his work provide a continuing legacy and inspiration
to those of us who continue to work in this area.

Analysis of Turbulent Seals in Pumps

Henry pioneered the analysis and testing of liquid seals in pumps. His
publications alone, and in conjunction with Jensen and Cochrane, defined the
forces developed by neck-ring and interstage seals of pumps. He also defined
dynamic seal coefficients for linear rotordynamic analysis, demonstrating the
vital dependency of pump rotordynamic behavior on seal characteristics.

Clearance Effects Between Rotors and Stators

Henry's 1968 paper in the Journal of Mechanical Engineering Science de-
fined the necessary conditions for response interaction between a rotor and
stator across a radial clearance. The results apply for any multidegree-of-
freedom linear rotor and stator models, being restricted only by assumptions of
circumferential symmetry. This is a difficult paper to digest but remains the
definitive analysis of the phenomenon of rotor-stator motion across a clearance.

Optimum Bearing Damping for Flexible Rotors

The 1976 ASME Journal of Engineering for Industry paper demonstrated the
retrospectively obvious result that an optimum value for damping at bearings

exists. In other words this paper's message is that too much damping can be provided at the bearings of flexible rotors.

Parametric Excitation of Flexible Rotors Due to Stiffness Orthotropy

Henry's contribution in a 1969 Journal of Mechanical Engineering Science paper is remarkable in that one would be pessimistic that any significant contribution in this "mined-out" technical area would be possible. However, Henry demonstrated the potential for adjacent mode interaction, yielding new and to date definitive results.

Lubrication

Henry's contribution to the field of lubrication were twofold. First, he presented bulk-flow turbulent lubrication theories in two 1970 papers in the Journal of Mechanical Engineering Science. Second, he originated methods for "fast" solutions to the Reynolds equation to be used in conjunction with transient rotordynamic analyses. Work in this latter sector continues by his colleague R. David Brown of Heriot-Watt University.

Impeller-Diffuser Interactions

In the 1974 International Union of Theoretical and Applied Mechanics rotordynamics proceedings, Henry proposed an impeller-diffuser interaction mechanism for rotordynamic instability. Typically, this work relies heavily on physical insight and intuition. Its eventual validity remains to be demonstrated by more complete analysis and hopefully by experimental programs presently under development. The paper will remain, however, the initial direct attempt at resolving this problem.

Henry had planned to attend the workshop and coauthored a paper with Dave Brown of his university. He was a personal friend and professional colleague of many of the workshop participants, having worked and published in the area of rotordynamics for many years. Although it is regularly stated that no man is irreplaceable, Henry's absence is keenly felt by those who had come to rely on his extraordinary physical insight and analytical capabilities. His personal qualities of humor, integrity, consideration, and perceptiveness make his personal absence even more regrettable.

Dara Childs
Texas A&M University
June 1980

CONTENTS

SESSION I

FIELD EXPERIENCE WITH UNSTABLE TURBOMACHINERY

Edward Saibel, U.S. Army Research Office
Chairman

Page intentionally left blank

FIELD EXPERIENCES WITH ROTORDYNAMIC INSTABILITY
IN HIGH-PERFORMANCE TURBOMACHINERY

H. E. Doyle
Phillips Petroleum Company Europe-Africa
London, England

Instability in centrifugal compressors is a very serious problem and one that has caused the Phillips Petroleum Co., and our partners, considerable consternation and eventually resulted in lost production, extended construction periods and costs, and heavy maintenance expenditures.

Phillips Petroleum has been involved in two major incidents relative to rotordynamic instability of centrifugal compressors. Both incidents have resulted in serious problems for all parties concerned. In one instance we sustained a substantial loss of revenue on crude oil sales since we had no method of disposing of the gas which is associated with oil production. In the second instance we faced a possible shortfall in delivery of gas to meet contractual commitments. Fortunately, with the combined efforts of the manufacturer and our own people we were able to avert a major shortfall in gas delivery.

EKOFISK OIL FIELD PROBLEM

The Ekofisk oil field in the Norwegian Sector of the North Sea was developed by the Phillips Petroleum Norway Group (1) on the premise that early delivery of some of the crude oil would be possible by temporarily reinjecting all of the gas produced. This type of installation would allow production of a part of the oil prior to completion of the gas pipeline to shore. Accordingly, process and compression facilities were installed offshore to separate oil from gas and to compress the gas to approximately 625-bar pressure for injection into the formation. This arrangement would permit producing oil to the equivalent gas capacity of the injection compressors. Although this represented only a portion of the ultimate capacity of the field, nevertheless it was very important to the principals involved since it was the beginning of a return on a very large investment.

The reinjection compressors receive gas from the separator area at 68-bar pressure and boost it through two parallel trains to 625-bar pressure. Each train consists of two 15 000-kW units in series, with the first unit discharging at 240-bar pressure and the second unit at 625 bars. Each casing contains 8-stage rotors with back-to-back impeller construction. The flow was from the suction through the first four impellers in series out the center of the casing to an interstage cooler and then return to the opposite end of the compressor with flow through the final four impellers and discharge from the center of casing. This arrangement necessitated a long labyrinth in the center to break down discharge pressure from 625 bars to 440 bars.

An attempt was made in March 1974 to commission the reinjection compressors. By June it was evident that we were not going to be able to operate them in

3

their existing state and further that we had a full-grown rotordynamic instability problem with no immediate solution in sight. What followed was a long period of testing which, for the most part, yielded negative results and which has become characteristic of similar situations. First the manufacturer tried the relatively simple changes such as adjusting seal clearances, seal lockup, adding seal grooves, adjusting lube oil temperatures, and numerous bearing configurations.

All these many changes required that we operate the compressors to determine their effectiveness. At the conclusion of this period, several months had elapsed with no solution in sight. At this time it was decided by the manufacturer to design a squeeze film bearing that in a subsequent test proved to be successful and was adopted as an interim solution. On Christmas Eve 1974 we started gas injection into the formation, and shortly thereafter we commenced producing crude oil close to the anticipated design rate for that period.

Concurrently with the design and manufacture of the new squeeze film bearings the compressor manufacturer started work on a new rotor design incorporating a larger diameter shaft and a slightly shorter bearing span. At about the same time we decided to hedge our position and secure new compressors for the final stage of each string which incorporated a change in design by using two compressor bodies rather than one. Each set of compressors, which were manufactured by different firms, was designed, built, and full-load tested at actual operating conditions in approximately 1 year, a very laudable accomplishment. It is interesting to note that the calculated payout of these new compressors was somewhat less than 1 week in terms of lost crude oil production.

We were able to operate the compressors successfully with the squeeze film bearings and continued injecting gas and producing crude oil until the summer of 1975, when the new design rotors were installed. The machines have operated successfully since. They operate at reduced head now since the formation pressure is much lower. They are actually only needed when the gas pipeline is out of service for some reason or when it is operating at restricted capacity.

HEWETT GAS PLANT PROBLEM

The Hewett Partners (2) operate a gas plant on the East coast of England that furnishes natural gas for use in Britain. The gas comes from wells located approximately 17 miles offshore. All compression equipment is located on shore. During the initial operation of the plant no compression was necessary but, as the field pressure declines, compressors must be added to deliver gas at a constant 68-bar pressure. Three identical 3000-kW centrifugal compressor units were installed in 1973, two additional identical units in 1976, and finally one additional identical unit in 1979.

The compressors are divided between two parallel trains. There are other compressors of different sizes in each train, but they have no bearing on the problem under discussion. The compressors in question are fitted with single-stage, back-to-back, parallel-flow impellers. They operate at 13 750 rpm. Bearings are the 5-lobe, pressure-pad type.

Events concerned with this problem can best be presented in a chronological order as this gives a much better feel of the time frame required to identify and solve this type of problem.

Chronological History

June 1973: Units 1, 2, and 3 were installed. Unit 3 compressor rotor was removed during commissioning, and the original spare rotor was installed. The rotor has remained on this unit through current date.

January 1975: Unit 1 rotor was damaged by foreign object in compressor. Unit 1 rotor was removed and replaced with original unit 3 rotor.

January 1976: Unit 6 compressor was commissioned.

April 1976: Unit 7 compressor was commissioned.

November 1976: Unit 6 was shut down because of high vibration, presumably caused by foreign object damage, and replaced with the rotor removed from unit 1 in January 1975. The compressor has experienced numerous intermittent tripouts from that time to present date. Numerous attempts were made to correct the problem: Alignment was checked, and even the gearbox and coupling were changed in an effort to determine the cause of the problem.

At this stage no one thought that the problem could have been instability, particularly since many hours of running time had been logged on this and similar compressors without difficulty. In retrospect, it would appear that this was the beginning of our instability problems, although on this compressor we have never had our diagnostic instruments connected during a tripout to confirm this. A check somewhat later than the onset of tripouts indicated a 0.4-mil amplitude at 2/3-running-speed frequency. On this particular compressor the instability has always remained bounded when instruments were in place, but there is certainly no reason to believe now that the many tripouts were anything other than instability.

November 1978: Unit 7 started to experience random intermittent tripouts similar to those experienced on unit 6. In late November the unit would not go back on line because of constant high-vibration tripouts. Unit 7 rotor was removed, and unit 6 rotor was installed.

2 December 1978: Unit 7 continued to experience tripouts. Unit 6 rotor was pulled and rebalanced, a new coupling assembly was fitted, and the rotor was reinstalled.

19 December 1978: With little or no improvement in operation of the compressor of unit 7, unit 6 rotor was removed and unit 7 rotor, which had been repaired and rebalanced, was installed.

22 December 1978: There being no improvement in the operation of unit 7 and with high-vibration tripouts continuing, the unit 7 rotor was pulled, rebalanced, and reinstalled. The unit was operable, and once again on-line operation was established at reduced speed and head.

11 January 1979: Frequent tripouts in unit 7 again required a shutdown. Unit 6 rotor was installed, and an acceptable level of operation was finally established although at something less than normal head.

5 February to 7 March 1979: During this period numerous attempts were made to commission the unit 8 compressor, but we were unable to do so because of high vibration and the resulting tripouts. Because of damage from foreign objects and frequent tripouts, it was necessary to rebuild the compressor rotor. On 7 March a short run was attempted with the rebuilt rotor in position, but this ended with a severe tripout because of high vibration on both bearings.

12 March 1979: For the first time a run was attempted with unit 8 with diagnostic instruments in place, and the results clearly showed a subsynchronous vibration at 2/3 running speed. The compressor tripped at 13 200 rpm as a result of this subsynchronous vibration. It was a typical example of an instability trip accompanied by a slow buildup of the 2/3-running-speed component, which then suddenly became unbounded and reached several mils amplitude.

Figure 1 is a plot of speed versus amplitude of vibration for the unit 8 inboard horizontal bearing probe. This figure shows the first indication on instruments of the presence of instability. Instability is building up slowly around 8000 to 9000 cycles per minute, and at this point the amplitude is quite low, only about 0.25 mil. Figure 2 is a plot of speed versus amplitude of vibration for the inboard horizontal bearing probe and shows the instability tripout that occurred immediately following the plot in figure 1. Tripout occurred at a frequency of 9300 cycles per minute and an amplitude of 12.5 mils.

This was the first clear indication of the reason for our inability to commission unit 8, and in all probability was the cause of all the troubles on the other units, particularly unit 7. Six months had elapsed since the beginning of serious troubles on unit 7, and two months since starting to commission the unit 8 compressor. As an example of the amount of work encountered on this problem, rotors were changed eight times during this interval.

15 March 1979: Unit 2 had been operating since commissioning in June 1973 with the original rotor and during this period displayed no problem with tripouts from high vibration. It was decided to remove this rotor to make minor repairs of a nature not related to the instability problem. Unit 7 compressor rotor was installed, and immediately upon startup the compressor began experiencing high-vibration tripouts. Examination with diagnostic instruments in place a few days later revealed a strong subsynchronous component at 2/3 running speed. However, the compressor was able to operate continuously at heads somewhat below design.

Where operation is possible but limited by instability, as was the case with this compressor as well as others, an area of the performance curve between the surge line and the design point and extending roughly from 80 percent speed to 100 percent speed was observed to be particularly sensitive to instability. As a general rule, but certainly not in all cases, operation was feasible in the section well to the right of this area. This permitted the plant to operate but at much lower head than always needed. An upset on another compressor in

the same train would often force the unit to operate in or near the sensitive area and result in an instability trip.

21 March 1979: Continued high vibration of the unit 6 rotor in the unit 7 compressor required a shutdown to remove, rebalance, and reinstall it. On starting up after shutdown with instruments in place, the machine tripped at a running speed of 13 000 rpm. Once again instability was present, and an unbounded component at 2/3 running speed was observed.

9 April to 14 May 1979: During this period four rotor changes were made in the unit 7 compressor in an effort to obtain some level of acceptable operation. Numerous tripouts were experienced, many of them as a result of coupling unbalance. However, at the end of this period unit 7 was still exhibiting instability and was unable to operate for any length of time, and then only at reduced head.

Figure 3 is a plot of speed versus vibration for the unit 7 inboard bearing probe. This plot shows an instability tripout that reached 4 mils.

Mid-year 1979 summary: By this time it was recognized that we had a serious instability problem with no solution in sight. With regard to the six identical units the following conditions existed at this time:

(1) Units 1 and 3 never experienced any difficulties with instability, and a check with a frequency analyzer showed only a very small pip at 2/3 running speed. These compressors continued to run satisfactorily the entire time.

(2) Units 2 and 6 had some instability at all times. For the most part these units had operated satisfactorily but at a reduced head for the preceding 6 months.

(3) The instability experienced on unit 8 has prevented this unit from operating since its commissioning on 5 February 1979. Unit 7 had operated for only brief periods since the beginning of its serious problems in November 1978, which were later identified as instability.

(4) The manufacturer had been actively involved in arriving at a satisfactory solution and had undertaken the following:

(a) Performed a complete rotor stability analysis

(b) Arranged for a consultant to study and conduct field tests to determine if a problem existed external to the compressors. No problem external to the compressors was identified.

(c) Collected and analyzed a large accumulation of data from various field tests to determine a solution. This included several bearing and seal configurations and even impeller changes. Each of these changes required a run to determine results.

(d) Made an exhaustive study to determine any differences between the six units which would explain why some units did not experience instability whereas others did. Nothing of any significance was determined.

13 July 1979: A complete new rotor had been manufactured and was installed in unit 8. There were no changes in this rotor over previous ones; however, because of the large number of tripouts, rubs, and foreign object damage experienced on Units 7 and 8, it was believed prudent to obtain a new one. The initial run on this rotor was very similar to previous runs, with a strong instability indicated at 2/3 running speed. Thus it was necessary to operate at low speed. After having operated at low speed for several hours an instability tripout occurred. Upon restarting unit 8, a major lessening of instability was detected; and it was possible, at least for a period, to operate unit 8 at full speed and load. The machine was dismantled and completely inspected and careful measurements made of all clearances and fits to try to determine what change had occurred during the tripout which could account for the improvement, but no reasons could be found.

The compressor was rebuilt and started up once again. At first it operated satisfactorily, but its performance gradually deteriorated and it suffered a number of instability tripouts during August. Finally, it was observed to be in much the same condition as on previous runs.

18 September 1979: The manufacturer fabricated a new bundle for unit 8 with two major changes. The shrink fit of impellers was reduced in areas by shortening the length of the fit. To do this it was necessary to key impellers to the shaft. The diaphragm wall was extended into the area between the backs of the two impellers and gas was introduced by two holes to induce a laminar flow along the back plates. Although there were several high-vibration tripouts upon startup, enough data were collected to indicate a change in instability frequency in that instability no longer tracked running speed but remained at one frequency regardless of running speed. The instability frequency appeared to be locking on the critical frequency of the shaft. Figure 4 is a plot of vibration for the outboard vertical probe made just before a tripout. Note that instability is not tracking running-speed frequency. Figure 5 is a plot for the the inboard vertical bearing probe at tripout. Tripout amplitude was 8.2 mils at 8300 cycles per minute.

The bundle was rebuilt with the same diaphragm arrangement as previously but by reverting to the original rotor design by eliminating the keyed impeller and the reduced shrink fit. The combination proved successful and on Oct. 10, 1979, the unit was placed on the line with the instability completely bounded. Even after a violent surge the instability remained bounded. The compressor continues to run to date in this manner with no instability difficulties. Figure 6 is a plot of the inboard and outboard vertical and horizontal probe vibration representing unit 8 as finally modified. Maximum instability is only 0.1 mil.

Units 2 and 7 have been fitted with the new diaphragm arrangement. Unit 7 has operated satisfactorily without instability since this change. However, unit 2 still has had some vibration tripouts but at present is operating satis-

8

factorily. Some instability appears to be present, but it remains bounded. Unit 6 will be modified as soon as plant schedules permit.

From our standpoint it would appear that the combination of the new diaphragm arrangement, whereby laminar flow was induced on the impeller back plates, along with better than normal rotor balance results in successful operation with the 2/3-running-speed component remaining bounded. The plant is now operating smoothly, although you can understand that after having gone through the experiences of the past 18 months everyone is not convinced that similar problems will not recur. Only successful operation over a long period will provide the final proof.

FIELD SOLUTION OF INSTABILITY PROBLEMS

My purpose in leading you through this rather detailed description of a major instability problem is to point out forcefully to all concerned - designers, manufacturers, consultants, contractors, and users alike - the very serious consequences of an instability problem.

Field solution of instability problems may be characterized as follows:

(1) Difficulties are encountered and time is lost in properly identifying the problem. A clearer understanding of the phenomenon surrounding instability by users, along with more widespread use of diagnostic instruments, will undoubtedly help this situation. I strongly advocate users owning or at least having ready access to such equipment along with trained personnel to operate and interpret results. Signature analysis and good records of operation and maintenance are also very important.

(2) Ineffective methods are used and excessive time is required in determining the cause of instability. Far too much time is consumed in making minor changes and operating the compressors to determine results. Endless combinations of bearing designs, preloads, etc., along with seal configurations, clearances, grooves, etc., can require weeks if not months to check out. Bear in mind that this is even before we have encountered the heavy-artillery-like effects of hysteresis at the impeller shaft mating surface, new diaphragms, larger diameter shafts, reducing bearing span, squeeze film bearings, and others. Add to this the time required to determine if the cause of the instability is external or internal to the compressor and you may have encompassed a very long costly period of time. More effective means of making analytical determinations of the results of various modifications is needed in order to reduce the time required to obtain a satisfactory solution.

Finally, I believe there is a great need for better methods of identifying potential instability problems in the design stage. Maybe closer cooperation between all parties will eventually lead to this. Conferences such as this will help. Better specifications by users and contractors in defining all aspects of service in which the compressor will be used will also help. Wider use of rotordynamic analysis by designers will be an aid. I am certain that many improvements have been made, but there is need for many more. I hope that such improvements will be forthcoming because the need is great and the potential penalty very high.

(1) The Phillips Norway Group consists of the following companies:

Phillips Petroleum Company Norway (Operator)   36.960%
American Petrofina Exploration Company Norway 30.000%
Norsk Agip A/S   13.040%
Elf Aquitaine Norge A/S   8.094%
Norsk Hydro A/S   6.700%
Total Marine Norsk A/S   4.047%
Eurafrep Norge A/S   0.456%
Coparex Norge A/S   0.399%
Cofranord A/S   0.304%

(2) The Hewett Group consists of the following companies:

Phillips Petroleum Company (Operator)   18.97%
American Petrofina Exploration Company   16.26%
Agip (UK) Ltd.   8.13%
Century Power & Light Ltd.   3.91324%
Plascom Ltd.   2.30892%
Halkyn District United Mines Ltd.   2.30892%
Oil Exploration Ltd.   2.30892%
ARCO British Ltd.   4.58%
ARCO Oil Producing Inc.   15.26667%
Canadian Superior Oil (UK) Ltd.   1.52666%
North Sea Exploration & Research Co. Ltd.   4.58%
North Sea Sun Oil Co. Ltd.   10.68667%
Superior Overseas Development Co. Ltd.   9.16%

PHILLIPS PETROLEUM COMPANY— ENGINEERING AND SERVICES

8.1   J.R.ADAMS

| ☑ VIBRATION DATA mils/div | ☐ STRAIN DATA μ-in./in.div |
| ☐ PULSATION DATA psi/div | ☐ NOISE DATA dB/div |

Test Point___INBOARD H___ Plant___BACTON___
Unit Speed___12950___rpm Unit_____
Vert. Scale_1.4 VOLTS__14 MILL Time_____
Horiz. Scale O-_30000 R.P.M.__Hz Date___12 MARCH 1979___

RUNNING SPEED

X1000 R.P.M.

INSTABILITY

VOLTS

X1000 R.P.M.
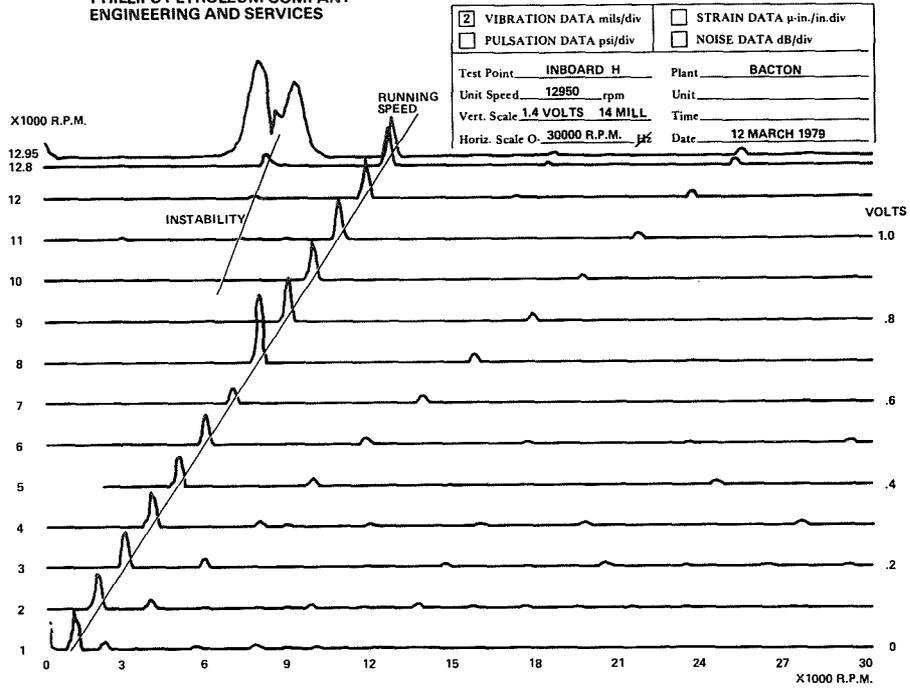
FIGURE 1

PHILLIPS PETROLEUM COMPANY— ENGINEERING AND SERVICES

8.2   J.R.ADAMS

| ☑ VIBRATION DATA mils/div | ☐ STRAIN DATA μ-in./in.div |
| ☐ PULSATION DATA psi/div | ☐ NOISE DATA dB/div |

Test Point___INBOARD H___ Plant___BACTON___
Unit Speed___12950___rpm Unit___No.8___
Vert. Scale_1.4 VOLTS__14 MILL Time_____
Horiz. Scale O-_30000 R.P.M.__Hz Date___12 MARCH 1979___

VOLTS

1.2

1.0   10 MILL

0.8

0.6

0.4

0.2

9.3

8.3

12.95 R.P.M.

X1000 R.P.M.
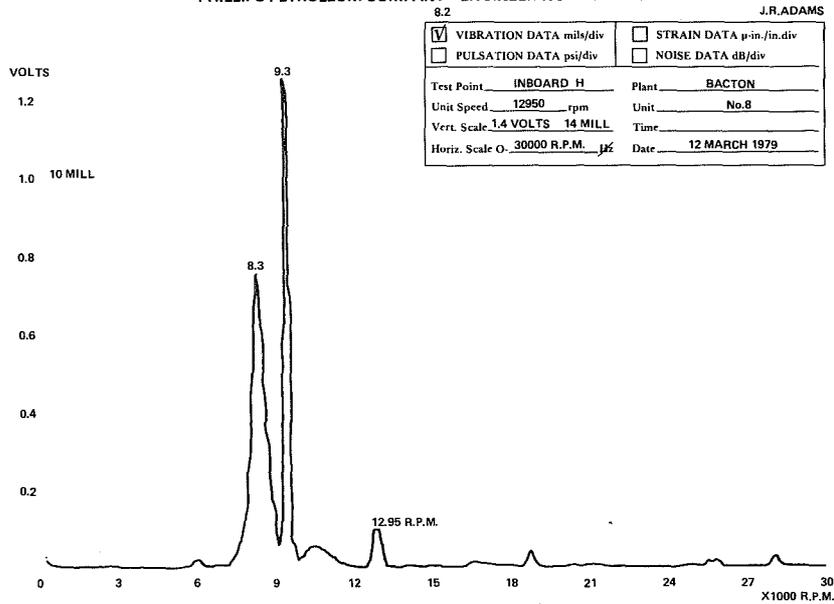
FIGURE 2

PHILLIPS PETROLEUM COMPANY—ENGINEERING AND SERVICES

7.1   J.R.ADAMS

| ☑ VIBRATION DATA mils/div | ☐ STRAIN DATA μ-in./in.div |
| ☐ PULSATION DATA psi/div | ☐ NOISE DATA dB/div |

Test Point____INBOARD____   Plant____BACTON____
Unit Speed____12960____rpm   Unit____No.7____
Vert. Scale____   Time____
Horiz. Scale O-_30000 R.P.M._Hz   Date____10 APRIL 1979____

TRIP FREQUENCY

3 1 2

RUNNING SPEED

R.P.M.X1000

12.96

12.95

12.9

12.8

12.6

12.4

12.2

12

0   3   6   9   12   15   18   21   24   27   30

X1000 C.P.M.

FIGURE 3

79 MV
@ 7900 C.P.M.

PHILLIPS PETROLEUM COMPANY—ENGINEERING AND SERVICES

8.9   J.R.ADAMS

| ☑ VIBRATION DATA mils/div | ☐ STRAIN DATA μ-in./in.div |
| ☐ PULSATION DATA psi/div | ☐ NOISE DATA dB/div |

Test Point____O.B.V.____   Plant____BACTON____
Unit Speed____rpm   Unit____
Vert. Scale____100 MV/MILL____ Time____
Horiz. Scale O-_30000 R.P.M._Hz   Date____18 SEP 1979____

X100 R.P.M.

12.8

12.5

12

11

10

0   3   6   9   12   15   18   21   24   27   30

X1000 R.P.M.

FIGURE 4

12

FIGURE 5

PHILLIPS PETROLEUM COMPANY – ENGINEERING AND SERVICES

8.10   J.R. ADAMS

☑ VIBRATION DATA mils/div	☐ STRAIN DATA μ-in./in.div
☐ PULSATION DATA psi/div	☐ NOISE DATA dB/div

Test Point _____ I.B.V. _____   Plant _____ BACTON _____
Unit Speed _____ 12900 _____ rpm   Unit _____
Vert. Scale _____ 1″:- 2 MILL _____   Time _____ 1231 HRS. _____
Horiz. Scale O- 30000 R.P.M. μ⁄   Date _____ 18 SEP 1979 _____
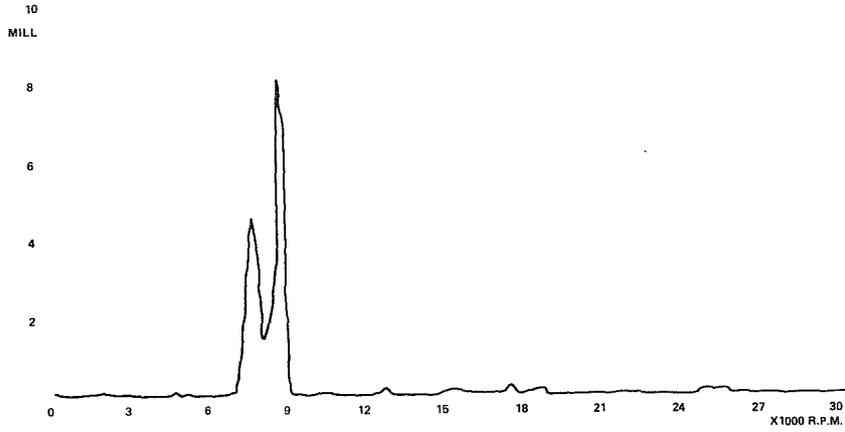
FIGURE 5

FIGURE 6

PHILLIPS PETROLEUM COMPANY – ENGINEERING AND SERVICES

8.19   J.R. ADAMS

☑ VIBRATION DATA mils/div	☐ STRAIN DATA μ-in./in.div
☐ PULSATION DATA psi/div	☐ NOISE DATA dB/div

Test Point _____   Plant _____ BACTON _____
Unit Speed _____ 14000 _____ rpm   Unit _____
Vert. Scale _____ 1″:- 0.2 MILL _____   Time _____ 1056 HRS. _____
Horiz. Scale O- 30000 C.P.M. μ⁄   Date _____ 18 OCT 1979 _____

8300 C.P.M.

OUTBOARD H.

OUTBOARD V.

INBOARD H.

INBOARD V.

X1000 C.P.M.

FIGURE 6

13
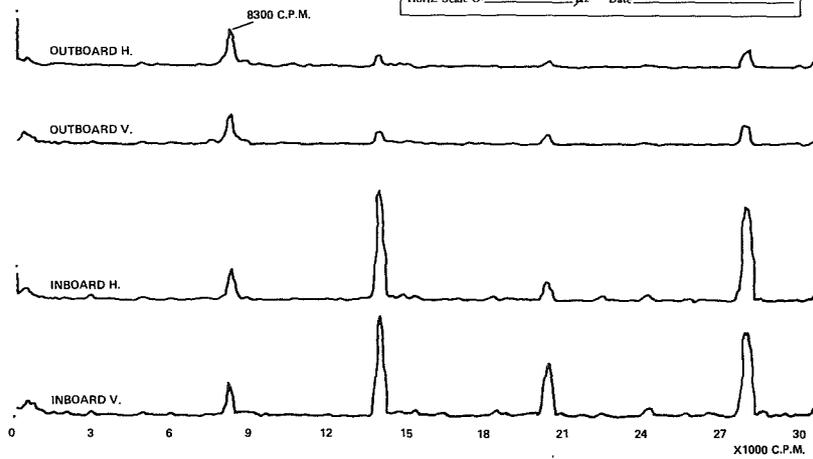
Page intentionally left blank

FIELD VERIFICATION OF LATERAL-TORSIONAL COUPLING
EFFECTS ON ROTOR INSTABILITIES
IN CENTRIFUGAL COMPRESSORS

J. C. Wachel and F. R. Szenasi
Southwest Research Institute
San Antonio, Texas 78284

SUMMARY

Lateral and torsional vibration data were obtained on a centrifugal compressor train which had shaft instabilities and gear failures. The field data verifies that the stability of centrifugal compressors can be adversely affected by coincidence of torsional natural frequencies with lateral instability frequencies. The data also indicates that excitation energy from gearboxes can reduce stability margins if energy is transmitted either laterally or torsionally to the compressors. The lateral and torsional coupling mechanisms of shaft systems have been investigated both in theory and in laboratory models by other investigators. This paper documents these coupling mechanisms in a large industrial compressor train and demonstrates the potential effect on rotor stability. Guidelines are set forth to eliminate these potential problems by minimizing the interaction of torsional and lateral responses and their effect on rotor stability.

INTRODUCTION

Rotor instability vibrations in compressors and turbines have occurred more frequently in recent years and have caused severe failures and costly downtime for several large projects. Rotor instabilities can occur in flexible shaft units which operate above their first critical speed. The whirling instability frequency is usually near one of the shaft critical speeds and can be caused by many factors, including hydrodynamic bearings, seals, internal friction, aerodynamic cross coupling, and torsional coupling. The whirling motion can be subsynchronous or supersynchronous, and may be forward or backward precession; however, most serious problems are subsynchronous and have forward whirl (refs. 1, 2, 3, 4).

In the past few years, vibration data has been collected on several compressors that have experienced severe instabilities. These compressors differed in manufacture, shaft diameter, weight, bearing span, critical speeds, and running speed. Using modern instrumentation, the instantaneous spectral characteristics of shaft vibrations were observed in real time as the compressors approached the onset of instability, i.e., before the machine experienced the high level vibrations normally associated with full scale instability. Real time analysis of the vibration data has shown that on most units that have instability problems, a trace of vibration at some instability frequency

15

normally exists at all times; however, it is not possible to verify the severity of the instability from vibration measurements at one operating condition. The threshold of instability can be fully defined only from testing over the full performance range of the machine, and even this approach is not always completely adequate. Units have run satisfactorily for several years before serious instability trip-outs occurred. After one year of satisfactory operation, one compressor failed eight times in the next three years from instabilities caused by unexpected transients. Because the stability margin on some units is so delicately balanced, its characteristics can be drastically changed whenever small changes are made in factors such as pressure ratio, flow, bearing clearance, oil temperature, unbalance, alignment, etc., or upsets in the process such as liquid slugs, surge transients, or electrical trip-outs.

It follows, therefore, that the threshold of stability can likewise be improved by small changes in these same parameters, but the exact improvement required to make an unstable system stable is sometimes difficult to predict.

There are several mechanisms which have been observed to contribute to rotor instabilities. The most sensitive elements which influence rotor stability include the following:

(1) hydrodynamic cross coupling in fluid film bearings
(2) seals and labyrinths
(3) aerodynamic cross coupling forces
(4) hysteretic or internal friction damping
(5) pulsations
(6) pulsating torque and axial loads
(7) asymmetric shafting
(8) fluid trapped in rotor
(9) stick-slip rubs and chatter
(10) dry friction whip.

To properly calculate the stability margin of a rotor, the mathematical model must be able to simulate all possible destabilizing components. The logarithmic decrement evaluation of rotor system damping as presented by Lund (ref. 4) is useful for predicting rotor stability. Field experience shows that while this technique provides proper direction in designing for stability, uncertainty still exists in quantitatively predicting the onset of instability and defining the contribution of individual influencing parameters.

When instability vibrations occur in installed machinery, better estimates of the possible effects of system changes can be made if measured field data is available for normalization of the mathematical model. The normalization procedures compensate for unknown dimensional variations which affect bearing and seal properties and adjust for actual aerodynamic loading. This paper will present measured field data on several compressors which exhibited instabilities. Data analysis techniques presented can define rotor stability thresholds and the effects of modifications to seals, bearings, shafts, and process variations.

Comprehensive experimental data can be invaluable in defining critical elements in the computer simulation of rotor instability, and can aid in improving their modeling.

ANALYSIS OF ROTOR INSTABILITY VIBRATION DATA

Capturing rapid instability transients and presenting a maximum of readily understandable information requires specialized instrumentation to develop Campbell diagrams, spectral time histories, and order tracking plots. Field instrumentation used to document compressor instabilities, including a real time analyzer, oscilloscope, X-Y recorder, FM tape recorders, proximity probe instrumentation, transducer amplifiers for pulsation and accelerometer measurements, trim balance analyzer, spectral time history generator, order tracking instrumentation, tachometers, switch boxes, and signal cables, are shown in figure 1.

A clearer understanding of the sequence of events during instabilities can be obtained by the development of spectral time histories than by viewing events on a strip chart recorder or oscilloscope. The complex waves (amplitude versus time) of two shaft vibration probes during a compressor instability trip-out are given in figure 2. Although this method of presentation is important in obtaining the total peak-to-peak vibration amplitude as a basis for identifying damage to bearings, seals, and labyrinths, etc., due to touch-off or high vibration, it is difficult to define the system running speed from strip chart records, since the initiation of instability will completely mask other vibration components.

The spectral time histories, or rasters, of vibration data are generated using a real time analyzer, and can be taken either off the machine directly or from FM tape or using digital FFT computer techniques (waterfall diagrams). By making sequential frequency analyses and incrementing the analysis vertically on a storage oscilloscope, a frequency analysis versus time record can be conveniently generated and effectively displayed and photographed. Compare the spectral time history (figure 3) of the same compressor rotor instability shown in figure 2. The time intervals marked on the strip chart correspond to the numbers on the analysis.

By using a fiber optics strip chart recorder, the complex wave can be displayed alongside the frequency analyses, allowing a direct comparison of overall peak-to-peak amplitudes with amplitudes of each spectral component (figure 4).

The authors have found these data acquisition techniques to be particularly useful in the solution of instability problems in large industrial compressor units.

17

INSTABILITY OF SYN GAS COMPRESSOR

The spectral time history of the compressor instability presented in figure 3 was for a 13000 horsepower, 10600 rpm, 8 stage compressor with back-to-back impellers. The compressor had a 163 cm (64 inch) bearing span with a critical speed of 3800 cpm and a rigid bearing critical of 4300 cpm. The suction pressure was 10.3 bars (150 psi) and the discharge pressure 34.5 bars (500 psi). The complex wave (figure 2) shows that the instability component at 4300 cpm increased from 25.4 μm to 101 μm (1 mil to 4 mils) over about a 1 second interval, and then sharply increased to 406 μm (16 mils) in approximately 0.2 seconds. The vibrations then shifted to 6000 cpm and then locked in on 4300 cpm (406 μm, or 16 mils) until the compressor speed was below 4000 rpm. The inboard vertical probe had slightly different characteristics, emphasizing the need for full instrumentation. This compressor failed eight times due to these nonsynchronous vibrations. The seals and labyrinths were wiped in an increasing bow pattern such that the inner labyrinths had approximately 2.5 mm (0.10 inches) of material removed. The vibration orbit was so circular that the pieces appeared to have been turned in a lathe.

Several modifications were required to improve the machine's stability characteristics. The impeller hubs were undercut to reduce the hysteresis effects at the mating surfaces. The clearances in the seals and labyrinths were increased. The five-shoe tilted pad bearings were modified by reducing the pad areas on the side and by increasing the radial clearance to force the rotor to vibrate in a horizontal elliptical orbit. In this compressor the installed recommended changes were sufficient; and the machine has run for several years without further nonsynchronous vibrations.

TORSIONAL-LATERAL COUPLING EFFECTS ON STABILITY

A recent study involving a complex centrifugal compressor train reveals considerable evidence that the torsional natural frequency of the system coincided with an unstable vibration mode of the fourth stage compressor and contributed to the failures encountered. Others have discussed this problem, but little experimental data is available on large industrial units (refs. 5, 6, and 7).

The high speed compressor (17000 rpm) could not be operated above 70 percent load because the lateral vibrations would suddenly increase to destructive levels whenever the load increased. Vibrations as high as 101-127 μm (4-5 mils) occurred when the instability was excited, resulting in seal wipes, bearing failures, and shaft scoring.

In addition to the high lateral shaft vibrations on the fourth stage compressor, several gear failures were experienced in the intermediate and pinion gears. A complete investigation of the system, requiring extensive testing, was made to determine the cause of the problem and to evaluate the modifications. The data obtained illustrates the influence of the torsional natural

frequency upon compressor instabilities and lateral vibrations in the gearbox. In addition, the influence of the lateral vibrations of the shafts in the gearbox upon compressor vibrations will be documented.

The system consists of a gas turbine, steam turbine, two gearboxes, and five centrifugal compressors (figure 5). The gas turbine gearbox has a bull gear, two intermediate (idler) gears, and two pinions. One pinion drives the first and second stage compressors in a back-to-back arrangement on opposite sides of the pinion. The other pinion drives the third, fourth, and fifth stage compressors; the third stage compressor is on one side and the fourth and fifth stage on the other side. Directly in line with the bull gear is another gearbox with an auxiliary steam turbine. This system is rigidly coupled between the pinions and compressors as opposed to having gear couplings, which caused lateral vibrations to be transmitted throughout the entire system.

The compressors were instrumented with proximity probes; however, to completely evaluate the instabilities in the fourth stage compressor and gear tooth failures, additional proximity probes were installed in the gearbox to measure lateral vibrations. In addition, three FM torsiographs were installed in the gearbox (figure 6), one monitoring the bull gear and one on each of the pinions. The FM torsiograph measures torsional vibrations by monitoring the gear tooth passing frequency signal from a magnetic pickup or proximity probe and demodulates this signal using a frequency-to-voltage converter. The resulting demodulated signal can be frequency analyzed to obtain the torsional velocity vibrations in the system.

The unstable lateral vibration characteristics of the compressor can be seen in figure 7 which gives the outboard horizontal vibrations in a raster plot or Campbell diagram presentation. This Campbell diagram was made directly in the field with a real time analyzer and appropriate electronic instrumentation. The instability vibrations at 4800 cpm are only about 13 μm (0.5 mil); however, the gas turbine speed had been lowered to 3460 rpm (compressor speed of 16400 rpm) to keep the instability amplitude from tripping the unit. It can be seen that the amplitude of the instability near 4800 cpm reduces as the speed is lowered. Both reduction in speed and reduction in load caused the instability amplitude to decrease. Vibrations at the same frequency (4800 cpm) as measured in the fourth stage compressor also occurred in other compressors in the train even though no apparent excitation source exists in the train at that frequency. The horizontal vibration of the third stage compressor (figure 8) shows vibrations at 4800 rpm which was the instability frequency that was tripping out the fourth stage compressor.

The torsional natural frequencies of the train can be seen from the Campbell diagram generated from the bull gear torsiograph signal (figure 9). The first three torsional critical speeds occurred at 1155 cpm, 1590 cpm, and 4760 cpm. One interesting phenomenon to note is that the first and second torsional critical speeds are always present, and modulate with fairly high amplitudes. Note that the third torsional natural frequency at 4800 cpm corresponds with the lateral instability frequency of the fourth stage compressor.

The maximum amplitude measured over the entire running speed range is recorded by the peak store envelope (figure 10). Figure 11 illustrates the correlation of the natural frequencies measured from the pinion gear torsiograph. The torsiograph on the pinion gives the same frequency information and also shows modulation of the first and second torsional critical speeds.

The fourth stage compressor originally had pressure pad bearings. At this high speed of 17000 rpm, it was suspected that a change to tilted pad bearings would be sufficient to solve the instability problem; however, to ensure that the system would still operate satisfactorily under design loading conditions, stability calculations were made for the original system and the system with tilted pad bearings. Also the effect of the change to tilted pad bearings upon the lateral critical speed response was investigated. The critical speed map was generated and forced vibration analyses were performed to verify that the location of the new critical speeds would be acceptable. The critical speed map in figure 12 has the presure pad and tilted pad bearing curves superimposed. The new bearings were four-shoe, load-between-pad bearings. The new system critical speeds are near the horizontal critical speeds for the original system. The compressor running speed is above the fourth critical speed; therefore, the change to tilted pad bearings would not definitely solve the problem since there are many systems which have tilted pad bearings and still have instabilities.

It has been found that to determine if proposed bearing modifications will be satisfactory from a stability standpoint, it is necessary to analyze the system for the fluid or aerodynamic loading that the compressor will be experiencing. To ensure that an adequate range of loading is covered, normally the log decrement versus effective aerodynamic loading is evaluated as plotted in figure 13. The lowest calculated instability forward mode near 4600 cpm agreed with the 4800 cpm which was actually measured (figure 7). The compressor stability is lowered as the effective aerodynamic cross coupling loading increases. With the new bearings, significant improvement in the log decrement is apparent and the tendency toward instability as a function of load is not evident. This calculated stability data indicates that the unit should be stable. The field data supports this analytical prediction, as can be seen from figure 14 which shows that as the gas turbine speed increases above 3000 rpm, no instabilities were found. Under maximum operating conditions, maximum pressure, and rated flow, vibrations in the low frequency range were carefully examined for all types of incipient instabilities and none was found. Therefore, from a stability standpoint, the changes made in the unit were satisfactory.

One interesting phenomenon that occurred on startup was the excitation of lateral vibrations in the fourth stage compressor due to the idler gear frequency excitation as it passed through the compressor shaft critical speeds. In figure 15 (the peak-store plot of the compressor shaft vibrations, as compressor speed went from 5700 rpm to 13300 rpm), the excitation of the shaft criticals at 3000-4450 cpm can be seen. These measured critical speeds match those determined from the critical speed map. On this initial startup, the high amplitude, low frequency vibrations measured on the fourth stage compressor were unexpected due to the predicted improvement in the stability

20

characteristics for the rotor with the tilted pad bearings. When the experimental Campbell diagram of the vibrations was displayed, it was found that the instability was not the classical type of instability. The low frequency vibrations were a result of the idler gear frequency exciting the lateral critical speeds of the fourth stage compressor. The cause of the excitation was the lack of steady-state loading on the gears in the gearbox. Subsequent runs were made with higher suction pressures which significantly reduced the idler gear excitation. These characteristics were shown in figure 14 for increased suction pressure. These data show that in closely coupled systems the lateral energy can be transmitted throughout the train.

COUPLING OF TORSIONAL VIBRATIONS INTO LATERAL VIBRATIONS

The following data illustrates the coupling of torsional vibrations into lateral vibrations throughout the compressor train. While it is felt that the rigid couplings greatly influence the magnitude of the coupled torsional to lateral amplitudes, the mechanism which causes the increased lateral vibration at torsional natural frequencies is the same for all rotating equipment. The important factor to be stressed is that the coupling of the torsional vibrations into the entire system can also serve as an instigator of instability. Therefore, it is vitally important to design systems which are free from gear excitation which might coincide with the torsional natural frequency of the system or the instability frequencies of individual shafts in the system. The interaction that occurred between the torsional and lateral vibrations for this system is discussed below.

For the pinion driving the fourth stage compressor, the Campbell diagram in figure 16 shows that whenever one of the excitation sources matches a torsional natural frequency, the lateral vibrations drastically increase. The energy from the idlers can couple directly into compressor shaft lateral vibrations; therefore, it can be surmised that any time the idler gear, bull gear, or one of the excitation sources is coincident with the torsional natural frequency, increased lateral vibration would occur and this could be transmitted to the compressors.

In addition to presenting the data in the form of the Campbell diagram, order tracking was performed to separate the vibration components in the pinion vibration. Figure 17 gives the lateral vibrations at the bull gear, the pinion, and the idler gear frequencies present on the pinion over the speed range. Notice that whenever the idler gear frequency matches the torsional natural frequency at 4800 cpm, there is a sharp increase in the amplitude. The two idler gears had slightly different frequencies; therefore, there was a modulation of the amplitude of the lateral vibrations on the high speed pinion when tracking this frequency. This amplitude increase can be directly transmitted to the fourth stage compressor and serve as an instigator for the instability frequency.

The Campbell diagram for the other pinion lateral vibrations (figure 18) shows that the torsional energy is transferred laterally throughout the train. Again there are similar characteristics on the pinion with large responses at the first and the third torsional critical speeds, indicating that this excitation can cause large lateral vibrations.

The effect on the idler gear horizontal vibration is shown in figure 19. This is a time raster rather than a Campbell diagram. The increase in lateral vibration can be seen when the idler gear frequency approaches 4800 cpm. This data is pertinent relative to the two problems experienced: the instability and the gear tooth failures. Notice that every time one of the excitation frequencies is coincident with the torsional natural frequency, the torsional vibrations and the lateral vibrations increase. This energy is transmitted through the shafts to the first and second stage compressors, as can be seen in figure 20 which gives the second stage compressor inboard vibrations. There were large vibrations excited even on the second stage compressor; however, this compressor also had a lateral critical speed near 4800 rpm which may have caused some amplification. This data shows that if a compressor had a potential instability, it would be easy for the torsional resonances to act as perpetrators for instabilities.

For this system with the new tilted pad bearings, the stability was significantly improved. The new instability mode frequency was out of the range of the idler gear and bull gear excitations; therefore, this system was completely stable over the range of operations.

CONCLUSIONS

These field investigations have served to provide insight into potential destabilizing instigators and sensitive operating conditions for high speed rotor systems. Several useful guidelines have been set forth for evaluating new designs of high speed rotor systems as well as existing systems with chronic stability problems.

(1) Torsional vibrations in a system can serve as an instigator for an instability; therefore, it would be important in designing systems not to have the torsional natural frequency of the system coincide with potential unstable vibrating modes of a centrifugal compressor.

(2) In rigidly coupled systems, excitation sources in the gearbox should not match potential instability natural frequencies since this could serve as an exciting mechanism for the instability.

(3) In systems where an instability mode could occur near a torsional natural frequency of the system, a potential exists for coupling of the vibrations into the gearbox to increase the dynamic loads on the gears and in some cases can cause gear tooth failures.

22

(4) If gear failures are experienced in a gearbox, it is standard procedure to check for torsional natural frequencies in the system which can amplify the dynamic loads. The system should also be checked for unstable vibrations on one or more of the compressors which may be causing increased dynamic loads through the torsional-lateral coupling mechanisms as demonstrated in this example.

REFERENCES

1. Wachel, J. C.: Nonsynchronous Instability of Centrifugal Compressors, ASME Paper 75-PET-22.

2. Sparks, Cecil R., and Wachel, J. C.: Quantitative Signature Analysis for On-Stream Diagnosis of Machine Response, Materials Evaluation, vol. XXXI, no. 4, April 1973.

3. Gunter, E.: Rotor Bearing Instability, 1972 Turbomachinery Conference Proceedings, Texas A&M University.

4. Lund, J.: Stability and Damped Critical Speeds of a Flexible Rotor in Fluid-Film Bearings, ASME Paper 73-DET-103.

5. Eshleman, R. L.: Torque-Induced Lateral Vibrations in Rotating Machinery, Vibration Institute Seminar, Machinery Vibrations III,, September 1979.

6. Vance, J. M.: Torquewhirl - A Theory to Explain Nonsynchronous Whirling Failures of Rotors with High-Load Torque, Journal of Engineer for Power, April 1978, vol. 100, pp. 235-240.

7. Szenasi, F. R., and Blodgett, L. E.: Isolation of Torsional Vibrations in Rotating Machinery, National Conference on Power Transmission, October 21-23, 1975.

FIELD INSTRUMENTATION
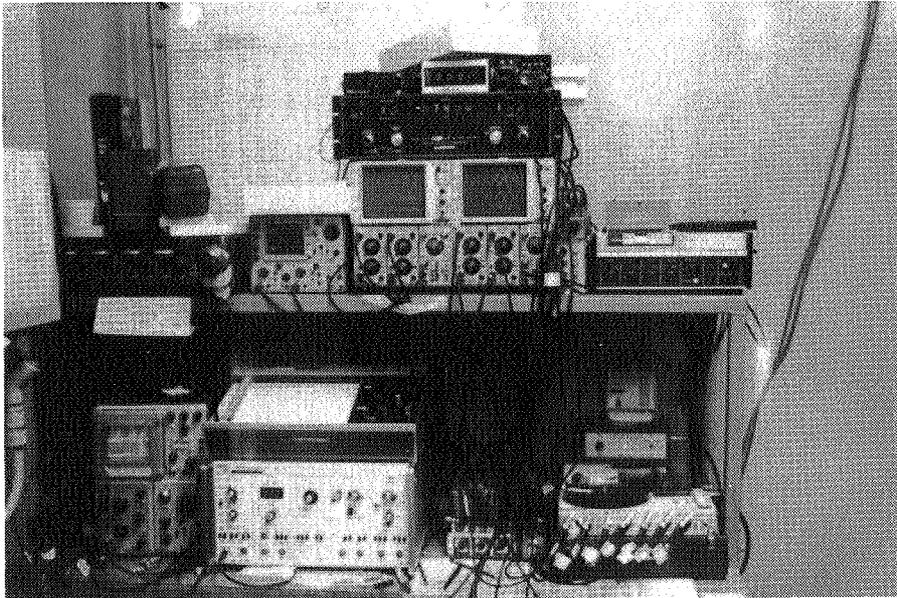
Figure 1

COMPLEX WAVE PRESENTATION OF COMPRESSOR INSTABILITY
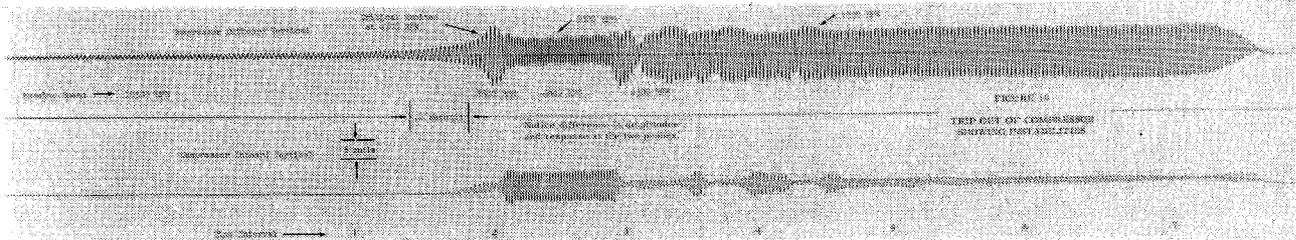
Figure 2

SPECTRAL TIME HISTORY OF COMPRESSOR
TRIPOUT SHOWING INSTABILITIES

254 μm/div (10 mils/div), 0.16 sec/line
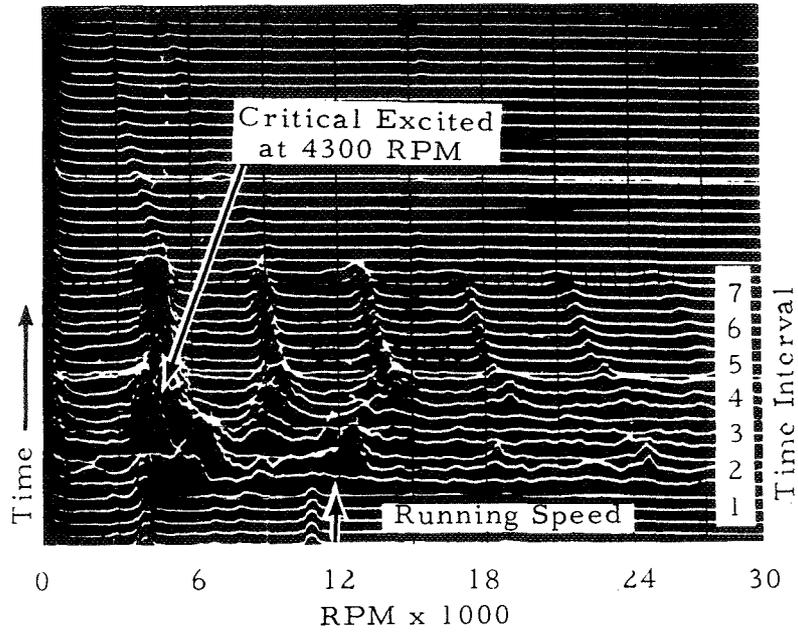
Figure 3

SPECTRAL TIME HISTORY GENERATED
BY FIBER OPTICS RECORDER
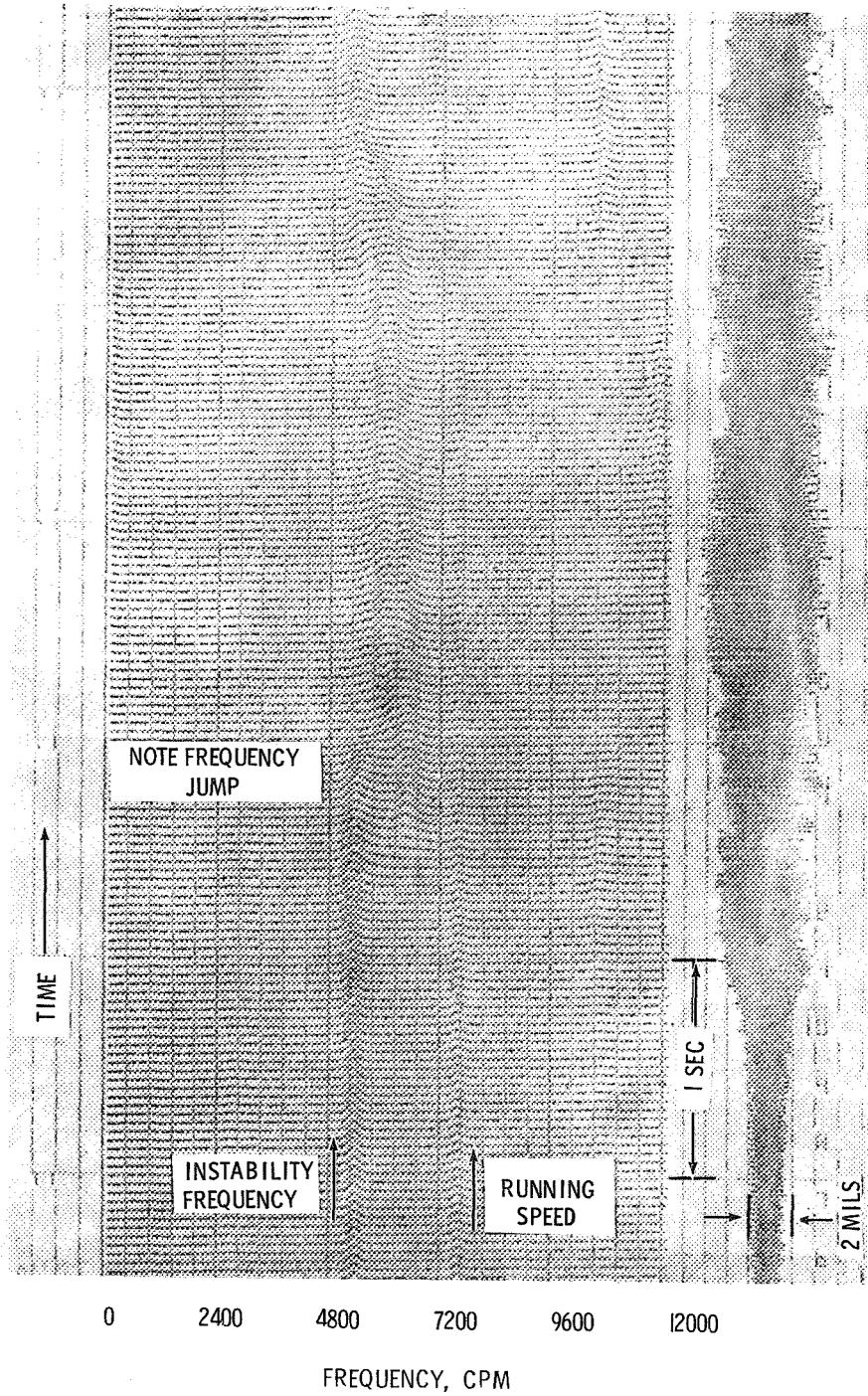
Figure 4

SCHEMATIC OF COMPRESSOR TRAIN
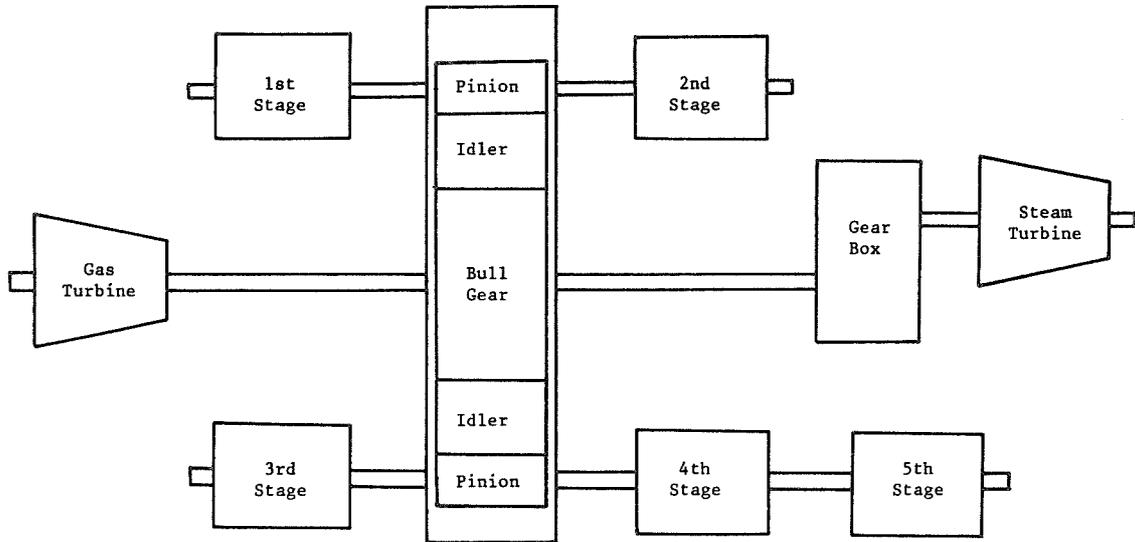
Figure 5
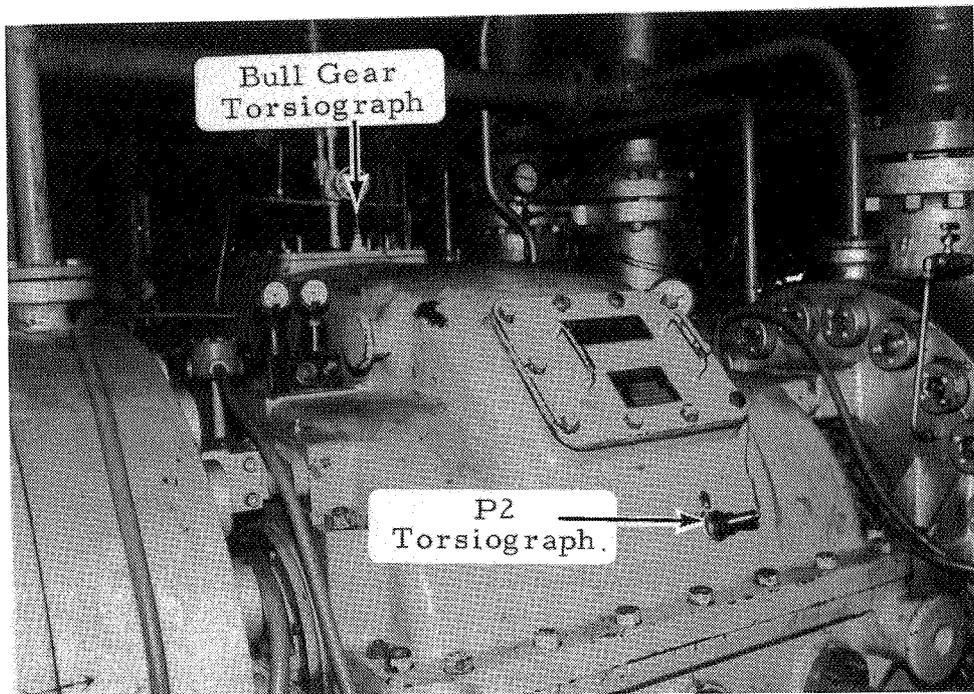
Figure 6

CAMPBELL DIAGRAM
OF FOURTH STAGE COMPRESSOR VIBRATIONS SHOWING INSTABILITIES
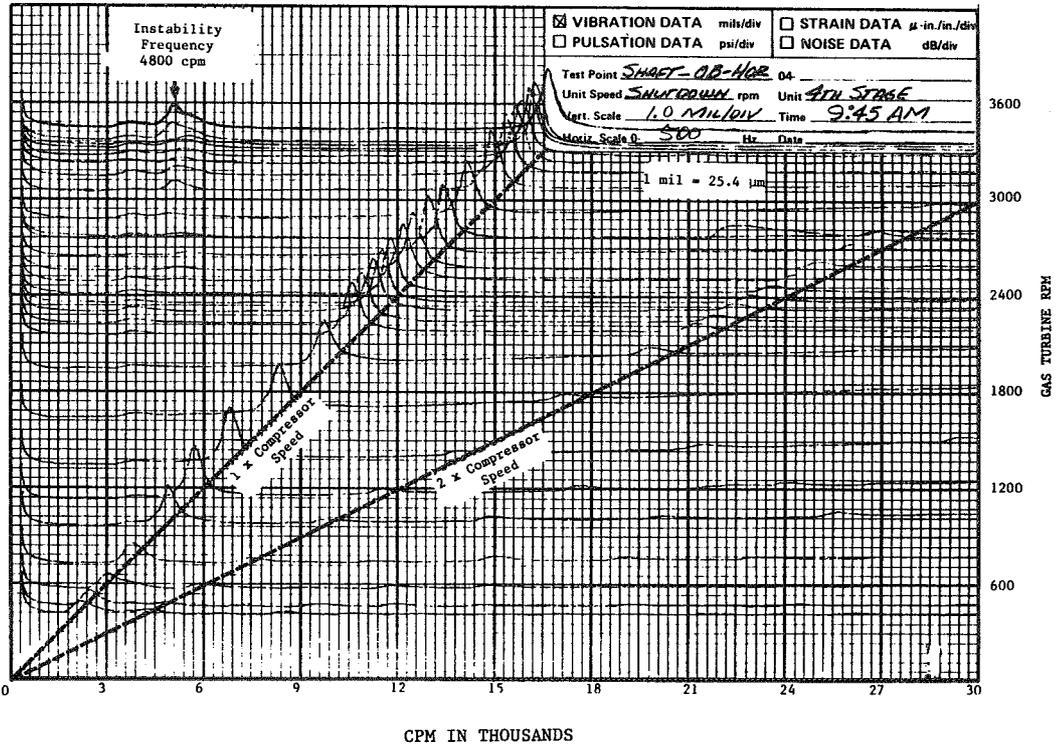
Figure 7

LATERAL VIBRATIONS OF THIRD STAGE COMPRESSOR
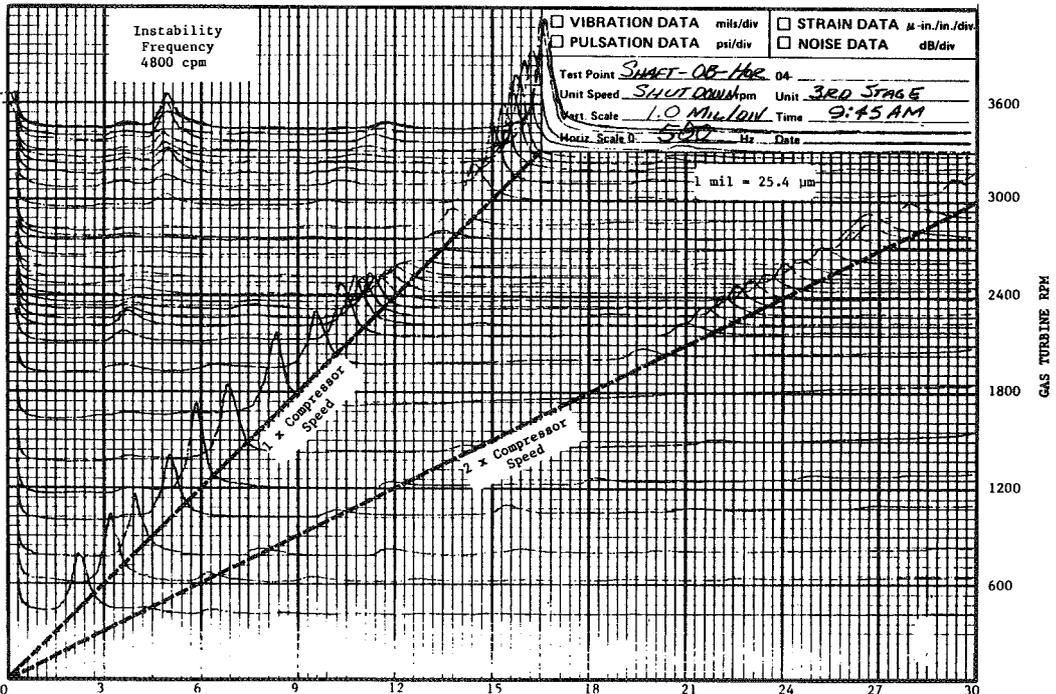
Figure 8

BULL GEAR TORSIONAL VIBRATIONS

SOUTHWEST RESEARCH INSTITUTE—APPLIED PHYSICS DIVISION
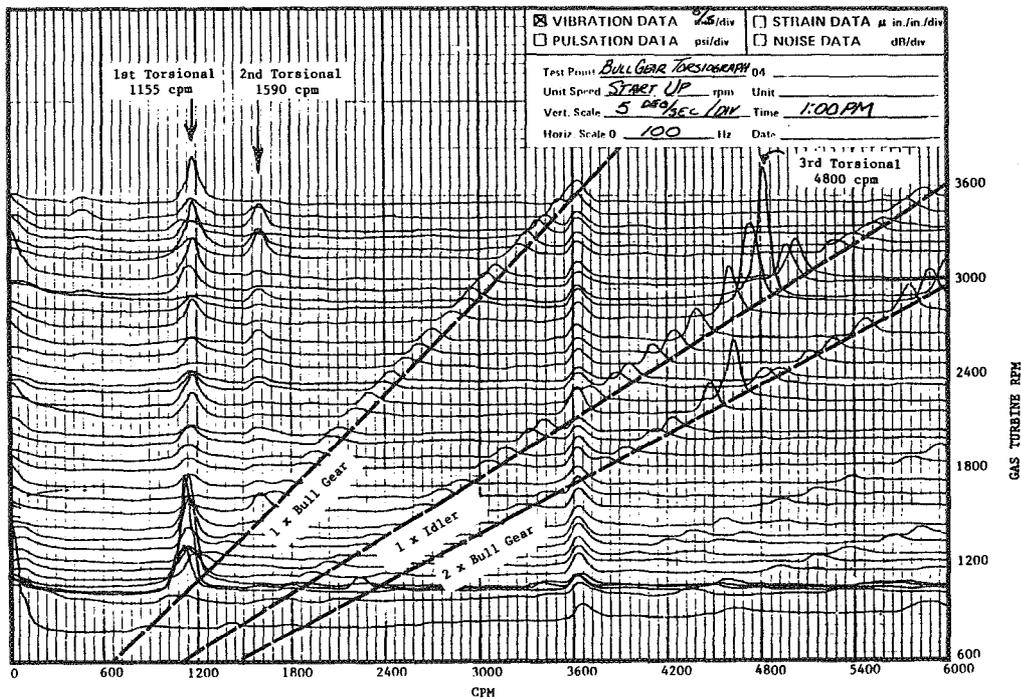
Figure 9

PEAK-STORE BULL GEAR TORSIONAL VIBRATIONS

SOUTHWEST RESEARCH INSTITUTE—APPLIED PHYSICS DIVISION

Figure 10

29
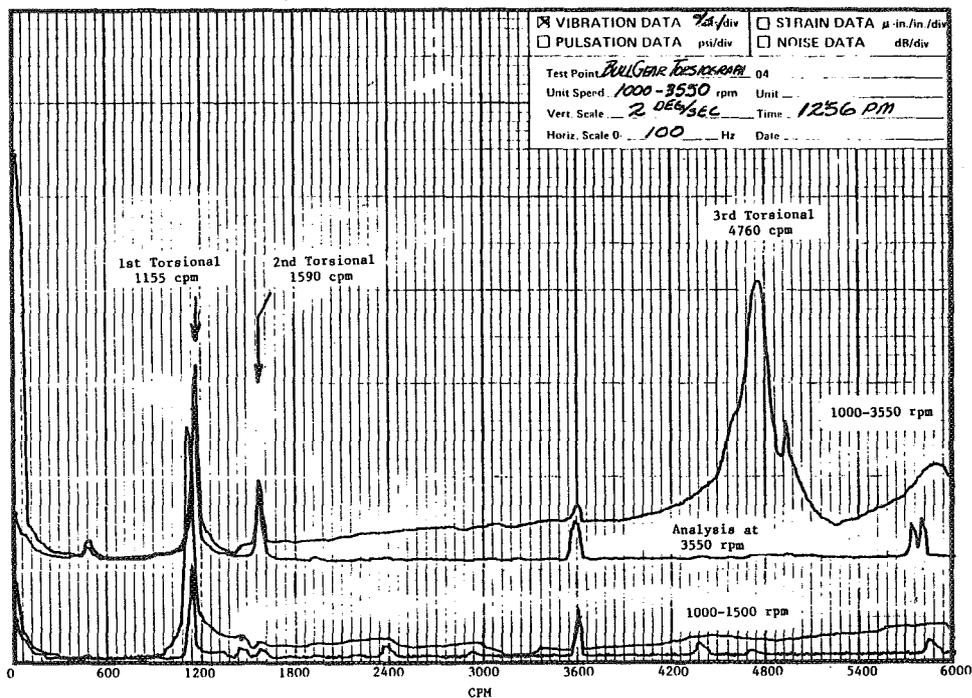
TORSIONAL VIBRATIONS MEASURED ON PINION

SOUTHWEST RESEARCH INSTITUTE—APPLIED PHYSICS DIVISION
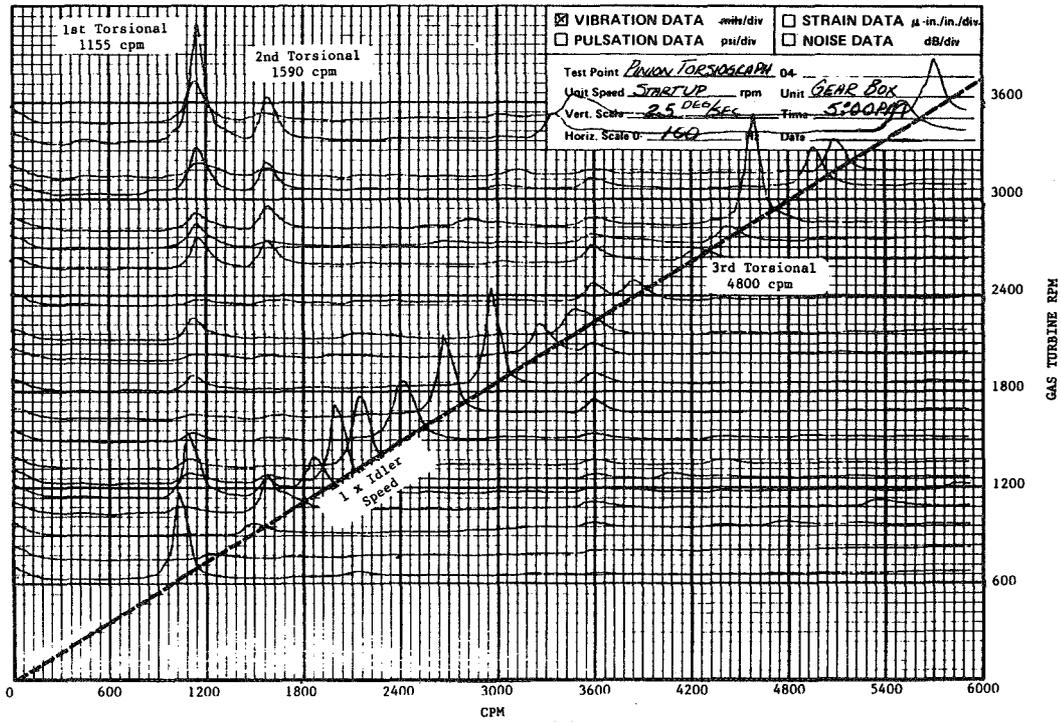
Figure 11

CRITICAL SPEED MAP
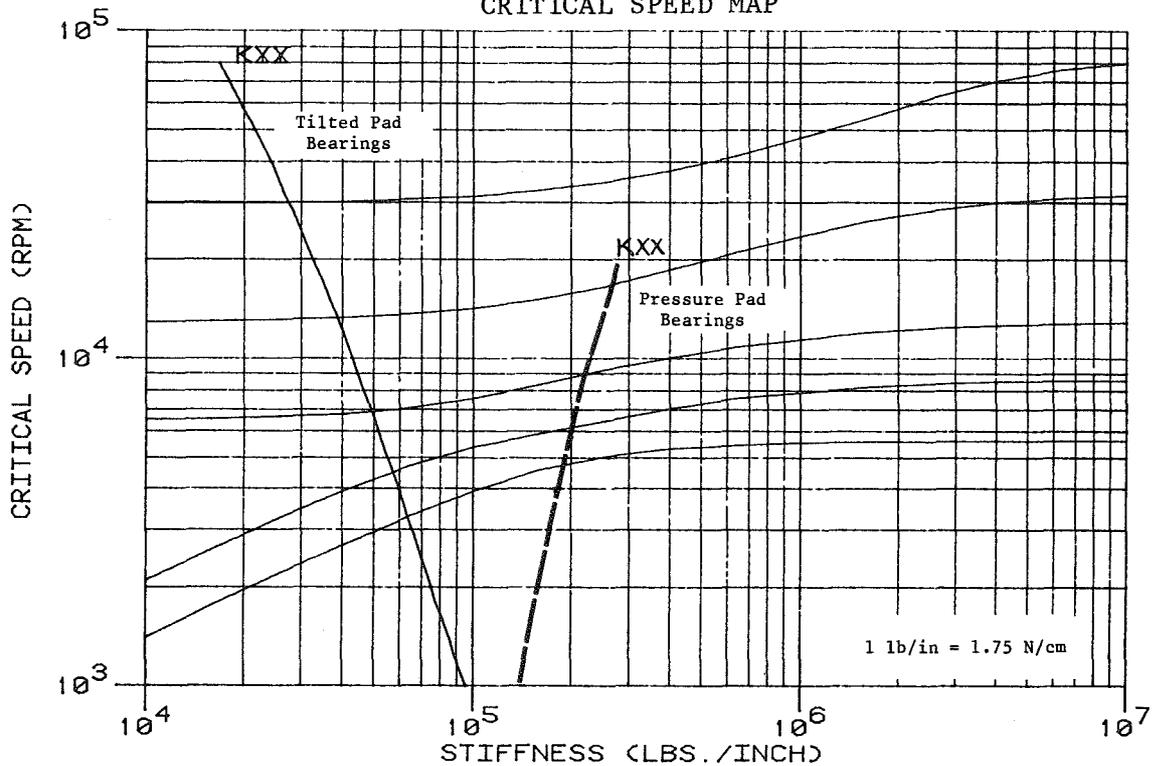
Figure 12

EFFECT OF AERODYNAMIC
CROSS COUPLING ON STABILITY
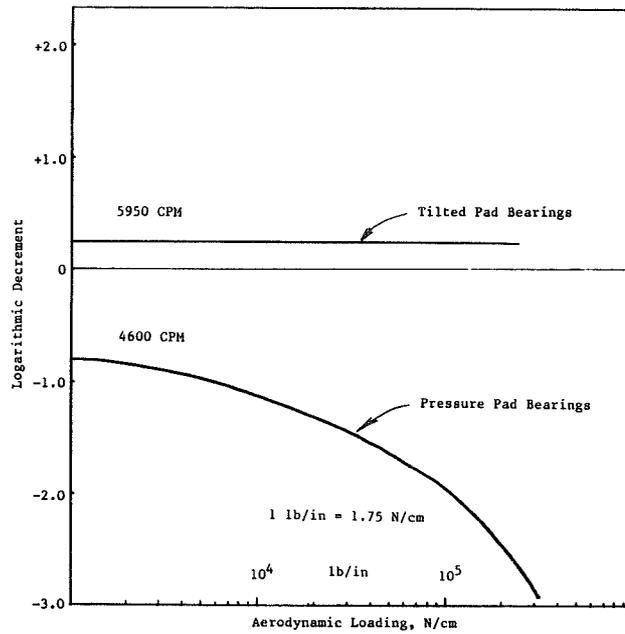
Figure 13

FOURTH STAGE COMPRESSOR VIBRATIONS
WITH TILTED PAD BEARINGS
SOUTHWEST RESEARCH INSTITUTE – APPLIED PHYSICS DIVISION
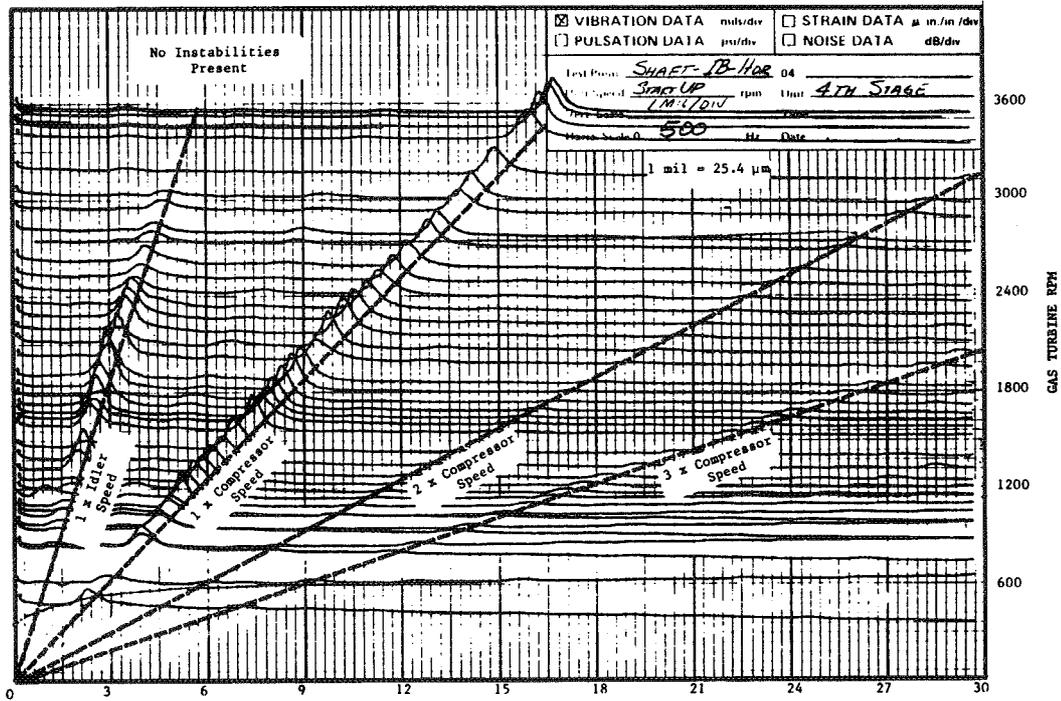
CPM IN THOUSANDS

Figure 14

31

COMPRESSOR SUBSYNCHRONOUS VIBRATIONS
EXCITED BY IDLER GEARS
SOUTHWEST RESEARCH INSTITUTE — APPLIED PHYSICS DIVISION

CPM IN THOUSANDS
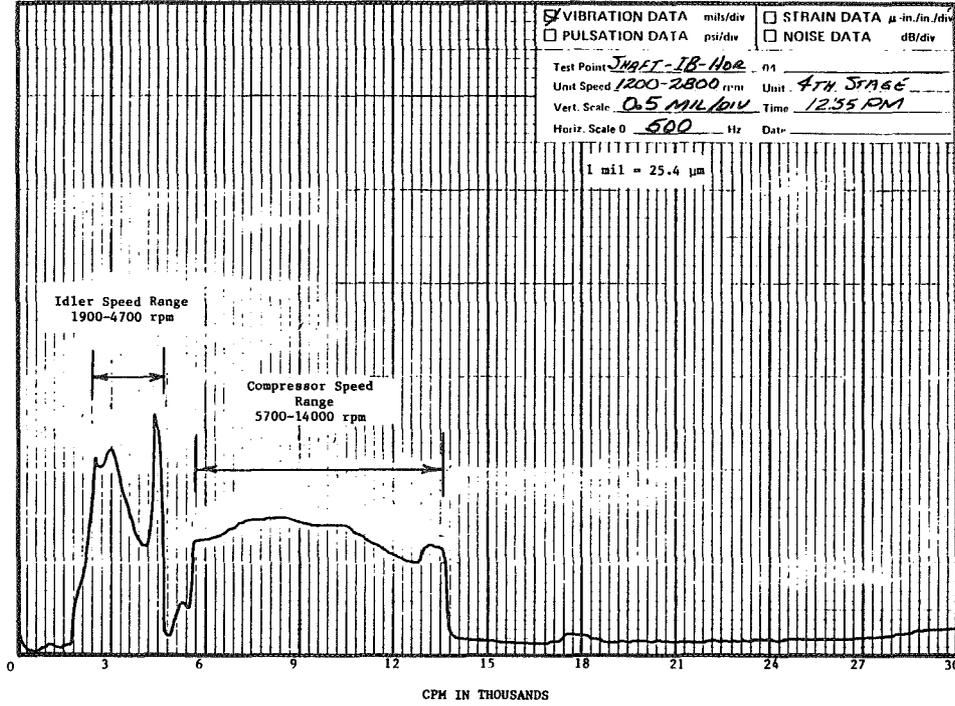
Figure 15

PINION LATERAL VIBRATIONS
CAUSED BY TORSIONAL-LATERAL COUPLING
SOUTHWEST RESEARCH INSTITUTE — APPLIED PHYSICS DIVISION

CPM IN THOUSANDS

Figure 16

32
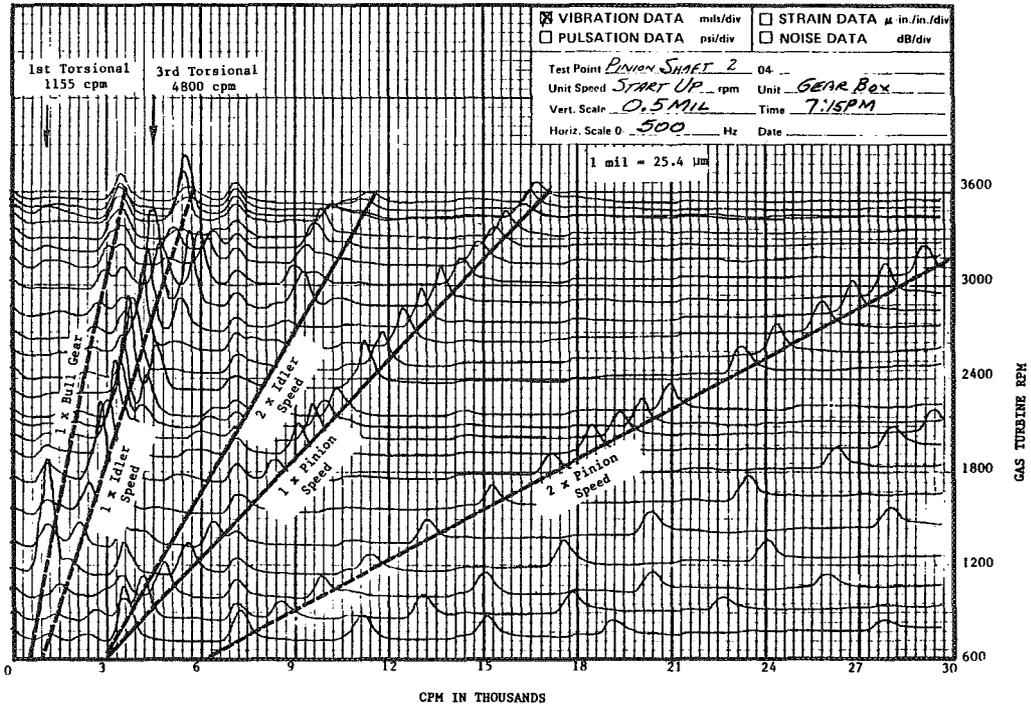
ORDER TRACKING OF PINION VIBRATIONS

Lateral vibrations increase when
idler speed matches third tor-
sional natural frequency at 4800
cpm.

1.61 x (Idler Speed) →

Modulation of amplitude occurs
due to beating effect of two
idler gears.

4.9 x (Pinion)

1 x (Bull Gear)

Vibration, mils p-p (1 mil = 25.4 μm)

Gas Turbine Speed, rpm
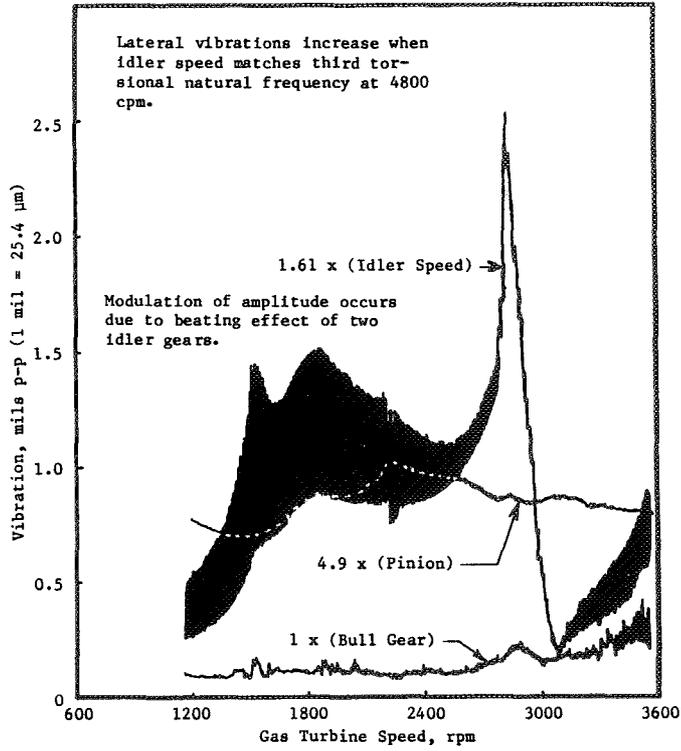
Figure 17

FIRST STAGE PINION LATERAL VIBRATIONS

SOUTHWEST RESEARCH INSTITUTE – APPLIED PHYSICS DIVISION

☒ VIBRATION DATA mils/div ☐ STRAIN DATA μ in./in./div
☐ PULSATION DATA p-i/div ☐ NOISE DATA dB/div

Test Point _PINION SHAFT_ |04 _____
Unit Speed _START UP_ rpm Unit _GEAR BOX_ _____
Vert Scale _0.5 MIL/DIV_ Time _____
Horiz. Scale 0 _500_ Hz Date _____

1 mil ≈ 25.4 μm

Torsional
Criticals

Bull Gear

1 x Idler

2 x Idler Speed

1 x Pinion Speed

2 x Pinion Speed

GAS TURBINE RPM
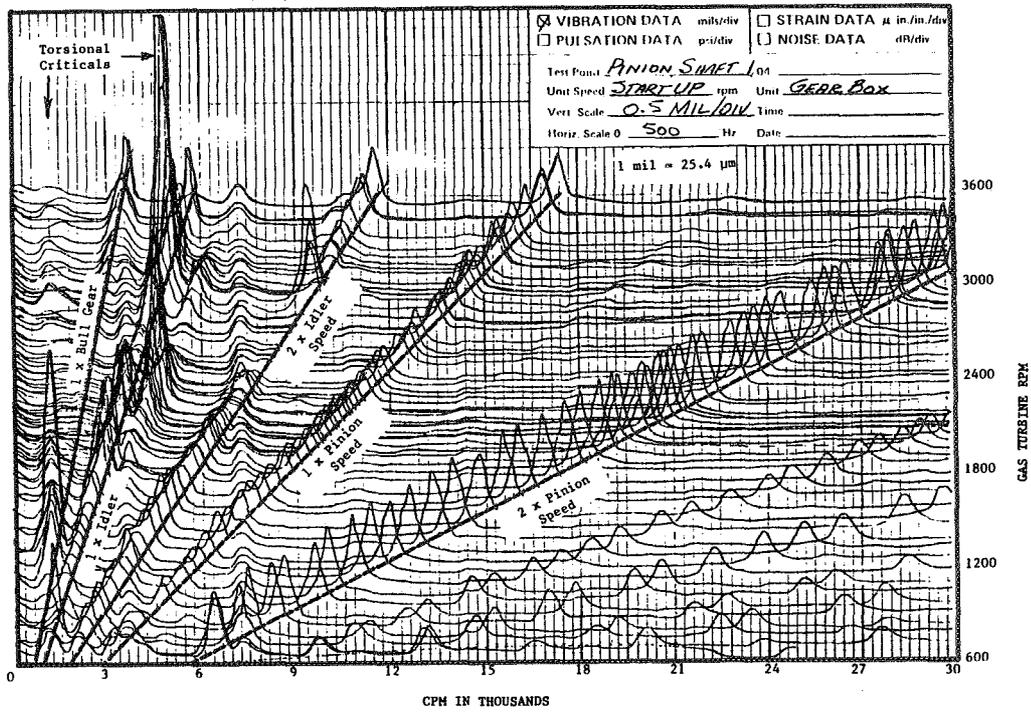
CPM IN THOUSANDS

Figure 18

IDLER GEAR LATERAL VIBRATIONS

SOUTHWEST RESEARCH INSTITUTE—APPLIED PHYSICS DIVISION
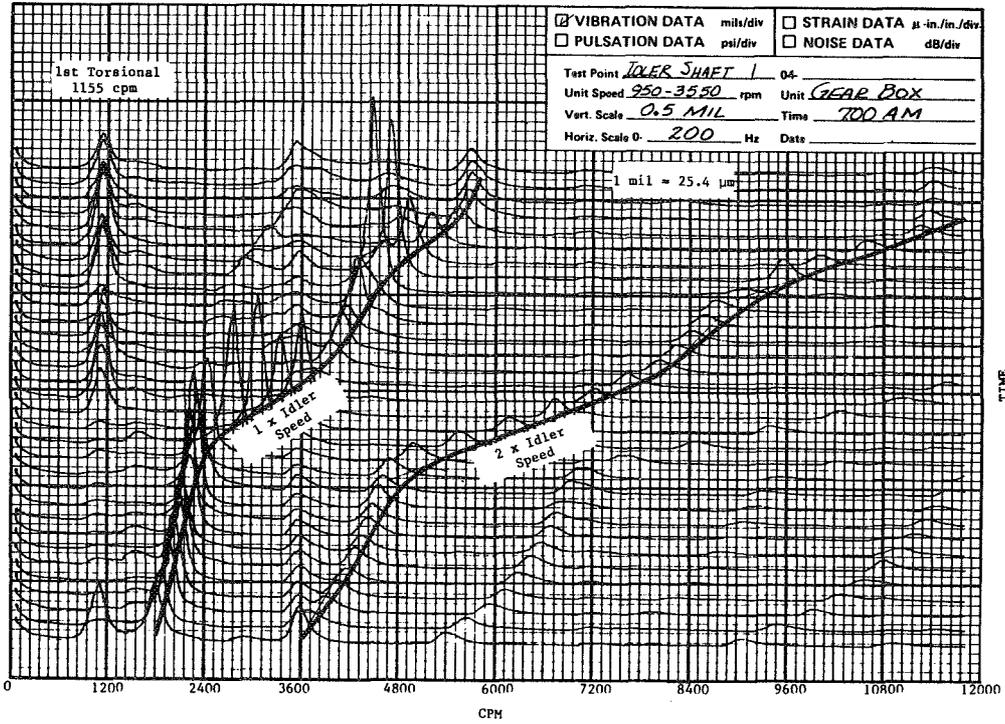
Figure 19

SECOND STAGE COMPRESSOR VIBRATIONS

SOUTHWEST RESEARCH INSTITUTE—APPLIED PHYSICS DIVISION
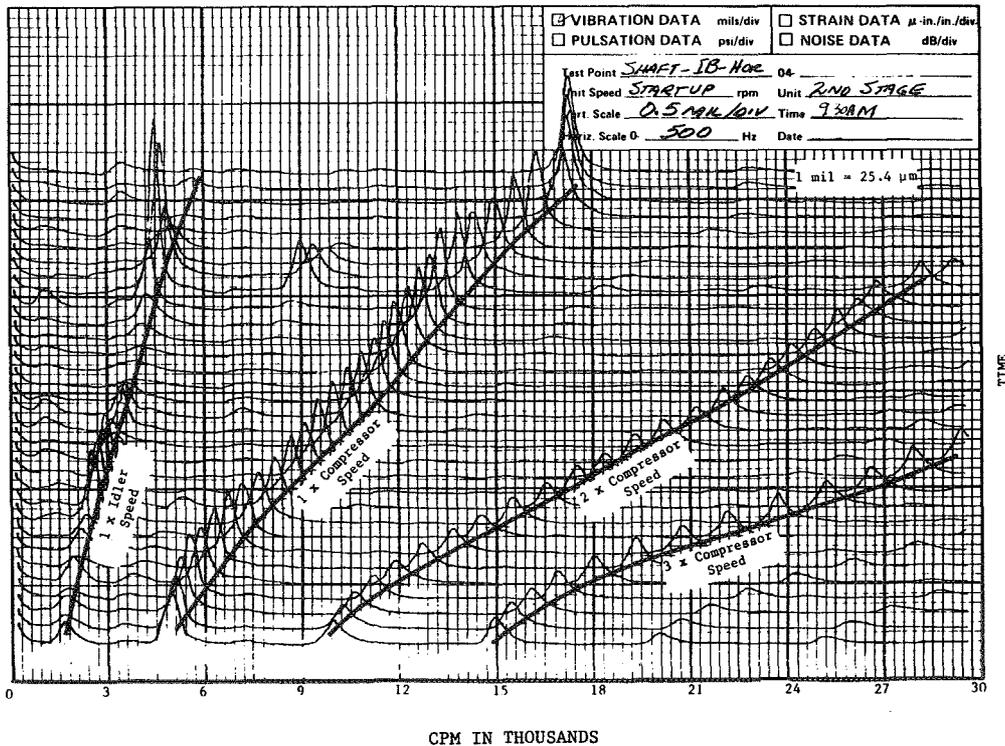
CPM IN THOUSANDS

Figure 20

34

PRACTICAL EXPERIENCE WITH UNSTABLE COMPRESSORS

Stan B. Malanoski
Mechanical Technology Incorporated
Latham, New York 12100

SUMMARY

High and low pressure compressors which operate well above their fundamental rotor-bearing lateral natural frequencies can suffer from destructive subsynchronous vibration. Usually the elements in the system design which contribute to this vibration, other than the shafting and the bearings, are the seals (both gas labyrinth and oil breakdown bushings) and the aerodynamic components.

Using analytical mathematical modeling techniques for the system components, an attempt is made to gauge the destabilizing effects in a number of compressor designs.

Recommendations are made, based on experiences with stable and unstable compressors, which can be used as guides in future designs.

INTRODUCTION

During the past ten years, the author had the experience of analyzing new designs or "trouble-shooting" existing machines suffering from high vibration. The practical experience gained is the main subject of this paper.

Over 200 single-stage, custom designed, overhung, high-speed compressors have been shipped by the author's firm. These machines compress such gases as air, nitrogen, oxygen, hydrogen, ammonia, natural gas, carbon dioxide, carbon monoxide, and freon. All have been analyzed before manufacture and have functioned well in the field. The methodology used in the rotor-bearing design analysis is referenced herein.

Over 50 compressors of predominately the "straddle-mount" design have been analyzed to determine the causes for high vibration and to propose subsequent corrective actions. A number of these compressors have been selected as representative examples of subsynchronous vibration and are discussed herein.

Before getting into the detailed discussion of these experiences, a review of the literature on the subject of subsynchronous vibration in turbomachinery is given.

It should be noted that a complete list of references with discussions on the subject of rotor-bearing dynamics emphasizing subsynchronous instabilities could be the subject of another paper since there have been numerous important contributions in this area during the past seven years. The reference list provided herein cites publications which are familiar to this author and are related

to the theme of the present paper. By no means is this list meant to be complete.

DISCUSSION OF REFERENCES

In 1973, Reference 1, which should be considered a classic in rotor dynamics, was presented at an ASME conference. This paper offered a method for calculating the damped critical speeds of a general flexible rotor in fluid-film bearings. The recommended procedures for preparing the mathematical model for the rotor, bearings, seals, and fluid dynamic forces and the gauging of the rotor-bearing system sensitivity to vibration in terms of a system logarithmic decrement have been followed by the author's firm. The extensive use of this methodology over this past time period has provided the author with the experience reported herein.

Procedures for rotor-bearing dynamic analysis have been recommended in References 2, 3, 4, and 5, and it would behoove the manufacturers and users of rotating mechanical equipment to be aware of the content of these papers.

Lack of confidence was previously stated in the use of these analytical methods in References 6 and 7 as a substitute for full-load testing. However, actual tests (Reference 8) and experiences have provided a better understanding such that confidence has been regained — at least in this author's viewpoint.

Practical experiences with high pressure compressor vibration instabilities, with which this author is intimately familiar, are reported in References 9, 10, 11, and 12.

Various important contributions that have been made which should aid in the preparation of the mathematical models of the bearings, seals, and fluid dynamic components are included in the reference section. In the bearing area, References 3, 13, 14, 15, and 16 are cited. In the squeeze-film, damper bearing area, References 17, 18, 19, and 20 are cited. In the oil breakdown bushing seal area, References 21 and 22 are useful. In the labyrinth seal area, including the balance piston, References 12, 23, 24, and 25 should be referred to. In the area of aerodynamics or fluid dynamic excitation, References 23, 26, 27, and 28 form an excellent foundation.

As mentioned above, confidence in available analysis techniques, such as Reference 1, has grown. Presently, manufacturers of compressors are analyzing, designing, and manufacturing compressors without troublesome subsynchronous vibrations (References 29 and 30).

An excellent discussion on mechanisms causing unstable whirl in rotating machinery is presented in Reference 31. One message obtained from this reference is that liquids can either provide significant benefits or problems depending on how they act with the rotor.

It is the author's opinion that considerable knowledge has been accumulated over the last ten years in the area of vibrations in rotating machinery in general and in subsynchronous whirl in particular.

A serious problem in compressor design and/or trouble-shooting with regard to rotor dynamics and vibration sensitivity is the inability to prepare the proper mathematical model of the contributing members and to police the design, manufacture, and assembly procedures such that the model agrees with the machine and vice versa.

In the following, a discussion is given on a number of case histories where subsynchronous instability was a predominant vibration problem. Where possible, a gauging of the damping or lack of damping is given in terms of system log decrement (References 1 and 2). Also, practical problems which reflect upon the analytical model versus the actual machine are discussed.

DISCUSSION OF EXPERIENCES

The following discussion is divided into two sections where first the overhung (or cantilevered) compressor design is addressed and, second, the straddle-mounted (or simply supported) compressor design is addressed.

Overhung Designs

In Reference 20, reference is made to two particular three-stage overhung design, low pressure compressors that were completely stabilized by employing squeeze-film damper bearings. The rotors are supported on tilt-pad bearings and only labyrinth seals are used.

In one of these designs which compresses air and operates at 52,000 rpm, well above its first rotor-bearing natural frequency (approximately 12,000 cpm), the base rotor-bearing log decrement varies from 0.05 to 0.25. This range is a function of the clearance tolerance in the tilt-pad bearings. The machine was marginally stable; however, it did run stably after modifications were made to the wheel-to-shaft fits and the oil distribution within the bearing pad clearances. This is a case where the machine did not represent the mathematical model. In overhung designs, which operate at high speed, gyroscopic stiffening is important and can be present only if the wheel-to-shaft fits are retained at operating speed. Furthermore, in gear-driven units, the gear loads on the bearings have a variable load direction with speed which must be accounted for. A good design for this application is to have each tilt-pad in the bearing serviced by an individual inlet restrictor.

In a second three-stage overhung design which operated at 33,000 rpm, and also well above its first rotor-bearing natural frequency of approximately 9000 cpm, the rotor-bearing log decrement was calculated to range from 0.08 to 0.15 because of clearance tolerances in the tilt-pad bearings. This machine had proper wheel-to-shaft fits and properly lubricated bearings and ran stably in air. However, when compressing CO_2, the machine was unstable in a subsynchronous mode. Because rotor modifications were impractical, a squeeze-film damper bearing was employed to achieve a log decrement well above 0.5 and a stable running machine. This machine provides a gauge on the stability of machines with gases with molecular weights of 29 and 44. (Note that compressor dynamic stability is affected by gas density and mass flow levels. However, for machines operating with similar temperatures and pressures the gas molecular weight becomes a convenient gauging parameter.)

Lessons that can be learned from these experiences are as follows:

- Wheel-to-shaft fits must be retained at all speeds.

- Tilt-pad bearings must have the proper oil distribution in order to achieve the calculated stiffness and damping.

- Higher molecular weight gases do provide larger fluid dynamic forces, thus necessitating a higher base system log decrement.

In Reference 29, the state-of-the-art of single-stage, high-speed, overhung compressor design is discussed. This author had the opportunity to make rotor-bearing dynamic analyses on over 200 compressors of this design. None of these compressors is suffering from subsynchronous vibrations. The basic elements that comprise the dynamic mathematical modeling of this machine are a flexible, overhung rotor, tilt-pad bearings possessing stiffness and damping, and fluid dynamic forces at the wheel and/or gas labyrinths seals. These rotor-bearing systems are operating above the first natural frequency and below the second.

A gauge that has been followed for this machine design is the minimum allowable system base, log decrement versus gas molecular weight (MW). For example, the following is a list of system log decrement versus gas molecular weights for machines that have run stably above their first damped natural frequency and are free from subsynchronous vibrations:

Gas	MW	Minimum Log Decrement	Ratio of Operating Speed to First Damped Natural Frequency
Ammonia, Oxygen	17, 32	0.32 to 0.45	3 to 2
Carbon Dioxide	44	0.42 to 0.52	~2
Freon-Air Mixture	94	0.62 to 0.75	2 to 1.5

These values have been used to provide machines with stable operation and are not to be misconstrued as threshold values.

The key parameters for achieving high stability (high log decrement) for these compressors are

- Minimum overhang length

- Minimum wheel weight and inertia

- Maximum shaft diameter between overhang and inboard bearing centerline

- Bearings with a nominal machined clearance ratio of 3 mm/m, a nominal geometric preload of 0.15, and usually load orientation on a pad.*

---

* It should be noted that changing the load orientation of the tilt-pad bearing is an effective means of gaining stability in marginal machines.

"Straddle-Mount" Designs

An excellent discussion is given in Reference 30 on the design and full-load testing of a high pressure natural gas compressor with this mounting type. The particular 13,000 horsepower compressor, reported in this reference, operates at 6500 rpm and compresses natural gas (molecular weight of approximately 20) to pressures over 2.76×10^7 Pa (4000 psig). The base rotor-bearing log decrement of this machine was reported at 0.44 with a damped natural frequency of 3900 cpm. The breakdown oil seals were designed to be ineffective as destabilizing elements. An aerodynamic cross-coupling stiffness was used at each impeller to represent the fluid dynamic excitation. The value of 1.15×10^6 N/m (6570 lb/in.) per impeller brought the theoretical log decrement down to 0.19. The machine ran stably under full-load test.

This author has performed analyses on other similar compressors and some of the experiences are reported in the following paragraphs.

Reports on a very high pressure natural gas compressor are given in References 10 and 11. This particular eight-stage compressor is presently operating at 8500 rpm ($\sim$20,000 horsepower) with a discharge pressure approaching 6.2×10^7 Pa (9000 psig). At various stages in this compressor development, calculations were made to assess the rotor dynamic stability of the machine. The first design had a base rotor-bearing log decrement of 0.21 with a damped natural frequency of 3500 cpm. However, it was determined that, if the oil breakdown seals were active dynamically, they could short circuit the effect of the bearing damping and reduce the log decrement to a low value of 0.030 with a damped natural frequency of 4300 cpm.

By tuning the mathematical model to the machine performance, it was further determined that a fluid dynamic excitation, in terms of radial cross-coupling stiffness, was present at approximately 2.98×10^5 N/m (1700 lb/in.) per impeller. By deactivating the seals (pressure balancing) and incorporating a squeeze-film damper bearing, stable operation was realized. A log decrement value of 1.0^+ was achieved with the damper design. In the final machine design stage, a rotor with a larger shaft diameter was employed. This machine has a base rotor-bearing log decrement of approximately 0.6 with a damped natural frequency of approximately 4800 cpm and proved very insensitive to seal and aerodynamic excitations.

From the above, it would appear that, for natural gas injection compressors, an aerodynamic excitation cross-coupling stiffness of say 3.5×10^5 N/m (2000 lb/in.) per wheel is a reasonable design value. A rotor-bearing system capable of retaining a positive log decrement with this excitation should be stable in the field. This statement is made based on the assumption that the oil breakdown seals are not locked or are deactivated dynamically.

A simple breakdown seal can have an axial force as high as $\pi/2$ Dt Δp. For a seal with Δp = 1000 psi, a diameter, D = 6.5 in., a face of t = 1/4 inch, the axial locking force is approximately 2500 pounds.* For three seals and assuming

---

* In SI units, this would correspond to a pressure of 6.89×10^6 Pa, a seal diameter and face width of 0.165 m and 6.35×10^{-3} m, respectively, and locking and radial forces of 1.11×10^4 N and 3.34×10^3 N, respectively.

a coefficient of friction of 0.1, the radial load capacity could be as high as 750 pounds, or a value equal to a typical bearing load. It is easy to see that, unless a special pressure balanced seal is employed in medium-weight rotor, high pressure machines, the bearings and seals will interact as rotor supports. In heavy rotor, lower pressure machines this interaction is less likely.

Thus, the high pressure can indirectly cause instability in otherwise stable machines by influencing the gas density and, therefore, the fluid dynamic excitation levels, and by locking oil breakdown seals axially such as to cause interaction with the stable rotor tilt-pad bearing system.

Many natural gas reinjection compressors have been analyzed because of instability problems experienced at the oil field sites. The primary problems associated with these machines have been tilt-pad bearings with too high a stiffness and locked, oil buffered seals.

The analytical results for a representative machine are discussed in the following paragraphs.

This particular compressor was operating above 13,000 rpm with a damped natural frequency of approximately 5500 cpm. The base rotor-bearing log decrement was calculated to be 0.29. With a representative aerodynamic cross-coupling stiffness, the base log decrement was reduced from 0.29 to 0.11. However, with locked oil buffered seals, the base log decrement was reduced from 0.29 to -0.01. A softer, low geometric preload bearing provided more damping and increased the basic log decrement from 0.29 to 0.46. With the new bearing design and typical aerodynamic and oil seal destabilizing forces acting together, the base log decrement was reduced from 0.46 to 0.08 (still greater than zero). With circumferential grooved oil seals, the rotor-bearing, aero, seal log decrement was increased to 0.25.

Success was achieved at the site by incorporating the new bearing and seal designs.

Other recurring practical problems are worth mentioning because they have caused considerable loss of production and much grief between the analyst and the operating personnel.

In the bearing area, improper clearances, too small an axial length pad, and insufficient oil flow or improper oil flow distribution have caused problems.

In the damper bearing area, damper bottoming out, or hang-up, and too low an oil supply pressure have prevented effective damper performance.

Shafts which are too small in diameter or have improper wheel fits (too loose, too tight, or too long) are poor in mechanical design integrity and can be the main causes of high vibrations.

Finally, oil-buffered seals should be designed to act as sealing elements only and should not be part of the dynamic system of rotor and bearings. Thus, a pressure balanced seal should be a design requirement, and means for causing seal lock-up should be eliminated from the compressor design.

RECOMMENDATIONS

1. Prepare a complete and accurate mathematical model of the dynamic system and then perform a dynamic analysis as suggested in Reference 1.

2. Police the design, manufacture, and assembly procedures such that the mathematical model agrees with the actual machine and vice versa. See discussion for details.

3. Design for a base rotor-bearing log decrement of 0.5 if possible as suggested in Reference 2. This appears to be representative of practical, stable systems.

4. Higher molecular weight gases require higher base log decrements. See discussion herein and design accordingly.

5. Beware of high pressure compressors because they can have inherent destabilizing effects from not only fluid dynamic forces at the impellers and in the labyrinth seal areas (including the balance piston), but from locked, high pressure oil breakdown seals.

6. Tilt-pad bearings with looser clearances (lighter geometric preloads) in conjunction with stiffer shafts usually yield higher system log decrements. Design with these facts in mind.

REFERENCES

1. Lund, J. W., "Stability and Damped Critical Speeds of a Flexible Rotor in Fluid-Film Bearings," _Trans. ASME_, Journal of Engineering for Industry, Vol. 96, No. 2, May 1974, pp. 509-517.

2. Malanoski, S. B., "Rotor-Bearing System Design Audit," Proceedings - 4th Turbomachinery Symposium, Gas Turbine Laboratories, Texas A & M, October 1975, pp. 65-70.

3. Smalley, A. J. and Malanoski, S. B., "The Use of the Computer in the Design of Rotor-Bearing Systems," ASME Publication: _Computer-Aided Design of Bearings and Seals_, LCCC #76-028853, 1976.

4. Kirk, R. G., "The Impact of Rotor Dynamics Analysis on Advanced Turbo-Compressor Design," Vibrations in Rotating Machinery, I Mech E Conf, Pub. 1976-9, Mech. Eng. Pub. Limited for the Inst. of Mech. Eng., London and New York, 1977, pp. 139-150.

5. Shapiro, W. and Colsher, R., "Rotor Whirl in Turbomachinery: Mechanisms, Analysis, and Solution Approaches," ASME Publication: _Turbomachinery Developments in Steam and Gas Turbines_, Presented at Atlanta, Georgia, November-December 1977, pp. 89-98.

6. Fowlie, D. W. and Miles, D. D., "Vibration Problems with High Pressure Centrifugal Compressors," ASME Paper 75-Pet-28, Presented at the Petroleum Mechanical Engineering Conference, Tulsa, Oklahoma, September 1975.

7. Wachel, J. C., "Nonsynchronous Instability of Centrifugal Compressors,"
    ASME Paper 75-Pet-22, Presented at the Petroleum Mechanical Engineering
    Conference, Tulsa, Oklahoma, September 1975.

8. Ferrara, P. L., "Vibrations in Very High Pressure Centrifugal Compressors,
    ASME Miscellaneous Paper, Paper No. 77-DET-15, Presented at the ASME
    Design Eng. Tech. Conf., Chicago, Illinois, September 1977.

9. Smith, K. J., "An Operation History of Fractional Frequency Whirl," Pro-
    ceedings - 4th Turbomachinery Symposium, Gas Turbine Laboratories, Texas
    A & M, October 1975, pp. 115-126.

10. Geary, Jr., C. H. and Damratowski, L. P., "Evolution of High Pressure Gas-
    Injection Centrifugal Compressors," Journal of Petroleum Technology, June
    1977, pp. 630-638.

11. Cochrane, W. W., "New Generation Compressors Injecting Gas at Ekofisk,"
    The Oil and Gas Journal, May 10, 1976, pp. 63-70.

12. Criqui, A. F. and Wendt, P. G., "Design and Closed Loop Testing of High
    Pressure Centrifugal Gas Compressors for the Suppression of Subsynchronous
    Vibration," Trans. ASME, Journal of Engineering for Power, Paper No.
    79GT86, 1979, pp. 1-5.

13. Lund, J. W., "Spring and Damping Coefficients for the Tilting Pad Journal
    Bearings," ASLE Trans. No. 7, 1964, pp. 342-352.

14. Nicholas, J. C., et al., "Stiffness and Damping Coefficients for the Five-
    Pad Tilting Pad Bearing," ASLE Trans., Vol. 22, No. 2, April 1979,
    pp. 113-124.

15. Nicholas, J. C. and Kirk, R. G., "Selection and Design of Tilting Pad and
    Fixed Lobe Journal Bearings for Optimum Turborotor Dynamics," Proceedings -
    8th Turbomachinery Symposium, Gas Turbine Laboratories, Texas A & M,
    December 1979, pp. 43-57.

16. Barrett, L. E., et al., "Optimum Bearing and Support Damping for Unbalance
    Response and Stability of Rotating Machinery," Trans. ASME, Journal of
    Engineering for Power, January 1978, Vol. 100, pp. 89-94.

17. Lund, J. W., "The Stability of an Elastic Rotor in Journal Bearings with
    Flexible Damped Supports," Trans. ASME, Journal of Applied Mechanics,
    Vol. 87, 1965, pp. 911-920.

18. Tonnesen, J., "Experimental Parametric Study of a Squeeze-Film Bearing,"
    Trans. ASME, Journal of Lubrication Technology, Vol. 98, No. 2, April
    1976, pp. 206-213.

19. Gunter, E. J., "Stabilization of Turbomachinery with Squeeze-Film Dampers -
    Theory and Applications," Vibrations in Rotating Machinery, I Mech. E
    Conference Publication 1976-9, Mech. Eng. Pub. Limited for the Inst. of
    Mech. Eng., London and New York, 1977, pp. 291-300.

20. Malanoski, S. B., "Case Histories in Which Subsynchronous or Synchronous Vibration Amplitudes Have Been Minimized After Employing Custom Designed Damper Bearings," Presented at the Workshop on The Stability and Dynamic Response of Rotors with Squeeze-Film Bearings, Sponsored by the U.S. Army Research Office, University of Virginia, May 8-10, 1979.

21. Lund, J.W. and Saibel, E., "Oil Whip Whirl Orbits of a Rotor in Sleeve Bearings," Trans. ASME, Journal of Engineering for Industry, November 1967, pp. 813-823.

22. Kirk, R. G. and Miller, W. H., "The Influence of High Pressure Oil Seals on Turborotor Stability," ASLE Trans., Vol. 22, No. 1, January 1979, pp. 14-24.

23. Alford, J. S., "Protecting Turbomachinery from Self-Excited Rotor Whirl," Trans. ASME, Journal of Engineering for Power, Vol. 87, No. 4, October 1965, pp. 333-344.

24. Kostyuk, A. G., "A Theoretical Analysis of the Aerodynamic Forces in the Labyrinth Glands of Turbomachines," Moscow Power Inst., Teploenergetika, 1972, Vol. 19, No. 11, pp. 29-33.

25. Benckert, H. and Wachter, J., "Studies on Vibrations Stimulated by Lateral Forces in Sealing Gaps," In German, Institut für Thermische Strömungsmaschinen, Unwersität Stuttgart.

26. Warner, R. E. and Soler, A. I., "Stability of Rotor-Bearing Systems with Generalized Support Flexibility and Damping and Aerodynamic Cross-Coupling," Trans. ASME, Journal of Lubrication Technology, Vol. 97, No. 3, July 1975, pp. 461-471.

27. Thompson, W. E., "Fluid Dynamic Excitation of Centrifugal Compressor Rotor Vibrations," Trans. ASME, Journal of Fluids Engineering, Vol. 100, March 1978, pp. 73-78.

28. Black, H. F., "Effects of Fluid-Filled Clearance Spaces on Centrifugal Pump and Submerged Motor Vibrations," Proceedings - 8th Turbomachinery Symposium, Gas Turbine Laboratories, Texas A & M, December 1979, pp. 29-34.

29. Pennink, H., "The State-of-the-Art of High Speed Overhung Centrifugal Compressors for the Process Industry," Proceedings - 7th Turbomachinery Symposium, Gas Turbine Laboratories, Texas A & M, December 1978, pp. 35-46.

30. Sood, V. K., "Design and Full Load Testing of a High Pressure Centrifugal Natural Gas Injection Compressor," Proceedings - 8th Turbomachinery Symposium, Gas Turbine Laboratories, Texas A & M, December 1979, pp. 35-42.

31. Lund, J. W., "Some Unstable Whirl Phenomena in Rotating Machinery," The Shock and Vibration Digest, Vol. 7, No. 6, June 1975, pp. 5-12.

Page intentionally left blank

ANALYSIS AND IDENTIFICATION OF SUBSYNCHRONOUS VIBRATION
FOR A HIGH PRESSURE PARALLEL FLOW CENTRIFUGAL COMPRESSOR

R.G. Kirk, J.C. Nicholas, G.H. Donald, and R.C. Murphy
Ingersoll Rand Company
Easton, Pennsylvania 18042

SUMMARY

The evaluation of turbomachinery designs prior to actual hardware test and field installation is now the rule rather than the exception for rotating machinery manufacturers. This requires the verification of the current state of the art analytical techniques for rotor-bearing-seal dynamics by development testing and/or controlled test stand or field vibration studies. This paper presents the summary of a complete analytical design evaluation of an existing parallel flow compressor and reviews a recent field vibration problem that manifested itself as a subsynchronous vibration that tracked at approximately 2/3 of compressor speed. The comparison of predicted and observed peak response speeds, frequency spectrum content, and the performance of the bearing-seal systems are presented as the events of the field problem are reviewed. Conclusions and recommendations are made as to the degree of accuracy of the analytical techniques used to evaluate the compressor design.

INTRODUCTION

The design of dependable turbomachinery has always been of utmost importance in natural gas pipeline and petro-chemical installations. To meet this challenge it is necessary for the designer of the turbomachinery to utilize state of the art aerodynamic and mechanical vibration analytical prediction capabilities. Tremendous advances have been made in the past ten years in these areas (ref. 1-8). Improved data retrieval and data reduction equipment make it possible for mechanical vibration and aerodynamic pressure levels to be monitored to assist in test stand design verification and/or the solution of field problems in the event that they should occur (ref. 9-12). The correlation of predicted to actual system behavior has been less than desirable in the area of rotor-bearing system stability. This is especially true in regards to the prediction of levels of destabilizing forces and the self-excited whirl frequencies. It has generally been the rule that actual whirl frequencies are higher than predicted frequencies for turbocompressors. Further complications arise when the exact source or characteristic of an excitation cannot be categorized relative to prior operating behavior of turbocompressors.

The following paper will document such an occurrence for a particular design configuration of a single-stage, parallel flow compressor in a gas transmission facility. The summary of the compressor rotor dynamics analysis will be presented in addition to selected field data taken to characterize the vibration before and after a successful field redesign to eliminate the source of the nonsynchronous excitation.

NOMENCLATURE

Values are given in both SI and U.S. Customary Units. The measurements and calculations were made in U.S. Customary Units.

C_B	$R_V - R$, tilt pad bearing assembled radial clearance in line with a pivot (L)
C_P	$R_p - R$, pad radial clearance (L)
C_S	seal radial clearance (L)
C_{xx}, C_{xy}, C_{yx}, C_{yy}	bearing or seal damping coefficients (FTL^{-1})
D	journal diameter (L)
K_{xx}, K_{xy}, K_{yx}, K_{yy}	bearing or seal stiffness coefficients (FL^{-1})
L	bearing axial length (L)
L_B	bearing span (L)
M	$1-(C_B/C_P)$, tilt pad bearing preload
N	shaft rotational speed (RPM)
N_{CR}^1	compressor first critical speed (RPM)
P_S	seal ring supply pressure (FL^{-2})
Q	aerodynamic cross-coupling (FL^{-1})
R_V	radius from bearing center to pad surface in line with a pivot (L)
R_p	pad radius of curvature (L)
U	imbalance (FL)
W_R	total rotor weight (F)
X,Y	horizontal, vertical fixed coordinates

OPERATING HISTORY OF COMPRESSORS

The compressors that are the basis for this paper are similar to over 80 units in operation throughout the world with the same basic shaft and bearing configuration. The compressors are driven through a flexible gear coupling by an Ingersoll-Rand GT-22 power turbine which is rated at up to 4250 H.P. at a max speed of 14,500 RPM. The units under discussion consist of 6 separate compressors that may be operated either in series or isolated for closed loop evaluation. The compressor configuration is shown in fig. 1 for parallel flow operation. The rotor is supported on preloaded 5-shoe tilting pad bearings with high pressure oil seal rings just inboard of the bearings as shown in fig. 2. The bearings are fed from the discharge of the outer seal ring and hence the seals and bearings have a common lube oil system. All six units are designed for purge gas injection for sour gas service while only three are typically utilized for this service. The bearing and seal housings are close tolerance double cartridge design to facilitate assembly and disassembly. The high pressure loading locks the cartridge with several tons of axial loading and thus assures a rigid interface to the compressor casing. The compressor rotor stage configuration is indicated in fig. 3 where the parallel flow stages are shown with the vaneless diffuser in cross-section. The stages are balanced aerodynamically at inlet and discharge as a result of system symmetry about the center diffuser ring.

Three of the compressors have been in service since 1973 with no major vibration problem encountered prior to the spring of 1979. Tripout due to surge related phenomena had occurred but the units were always capable of restart without incident. Two additional units were shipped in late 1974 and the sixth in mid-1978. The units will be denoted as 1-6. Unit Number 5 experienced vibration problems at high speed and load which necessitated several rebuilds, from December 1978 through May 1979, associated with coupling adjustments, impeller fits, and bowed rotor induced imbalance. The rotor was locked in a 13 mil bow on one occasion which came straight upon disassembly. Rubs were noted on the latter runs of this unit.

Compressor Number 6 had been damaged on commissioning via foreign object ingestion resulting in excessive vibration and rubbing on the impeller rims.

Compressor Number 2 had sustained damage in the seal area due to a lack of cleanliness during reassembly which required that the shaft be built up by chrome deposition in the seal area. Upon retrofit this unit began experiencing vibration tripouts at high speed and load, but was capable of restart. As of May 1979 two of the units, Nos. 1 and 3, were capable of continuous operation without limitation, one of which had not been disassembled since shipment in 1973. Two units, Nos. 2 and 5, were experiencing tripouts but could be restarted. The remaining units, Nos. 4 and 6, would vibrate such that restart was questionable. This fact, being unsatisfactory to the customer and Ingersoll-Rand, prompted action including analytical studies of the existing design using latest analytical techniques, documentation of vibration and pulsation data on site by both IR and consultants, and the examination of potential retrofit designs for the rotor-bearing-seal system.

Vibration data had been taken and reduced in March of 1979 that revealed a 2/3 rotative speed component of vibration that tracked with speed and came into coincidence with another fixed frequency component at a frequency of approximately 140 Hz. This is shown in fig. 4 where the 2/3 component is noted to appear above 200 Hz (12,000 cpm) rotor speed. The distinct frequencies are shown more clearly in fig. 5 where the 2/3 component is coming into coincidence to the fixed frequency. This figure does not have the line frequency (50 Hz) and 3X line frequency interference as noted on the earlier data given in fig. 4.

The forced response for the same No. 6 Unit is given in fig. 6 for the coupling and thrust end probe locations. This startup had a sequenced pressurization and fast accel through the critical of approximately 124-129 Hz. The units were typically started under full pressure which raised the peak response frequency to 130-140 Hz as a result of the increased stiffness and damping from the seal rings. This influence is indicated by the traces given in fig. 7 plotted for a portion of the accel. It is noted that the scales of figs. 6 and 7 are not all the same but the values of peak amplitude and frequency noted on the traces were read from an RTA and give an accurate indication of the peak response frequencies and amplitudes.*

SUMMARY OF ROTOR DYNAMICS ANALYSIS

The vibration problem as described in the previous section had not been documented by any reference that was available to the knowledge of Ingersoll-Rand or numerous consultants contacted concerning the nature of the field problem (ref. 14-20). The obvious potential sources - motors, pumps, power takeoffs gas generator, etc., were investigated without a valid mechanical element in the overall system design that could give the 2/3 x compressor speed forcing function. The thrust of the initial analytical investigation was therefore to conclude what could be modified in the bearing-seal system to improve the response and stability of the compressor. This procedure was less desirable than eliminating the source of the excitation, but at that time the source was unknown.

The compressor was analyzed by in-house computer programs for bearing analysis (ref. 5), seal dynamics (ref. 4), rotor response (ref. 13), and system dynamic stability (ref. 7). The compressor shaft was initially modeled neglecting the impeller shrink fits, which is in general the most conservative design technique since added stiffness typically improves stability.

The undamped critical speed map for the 160 lb. rotor is given in fig. 8 including and neglecting the potential impeller fit stiffness. The fits were more likely to add stiffness since the design was keyless and the fit was necessary to transmit the horsepower. Fig. 8 indicates that the first critical can be raised as much as 17 Hz (~ 1000 cpm) by the impeller fit since the midspan position of the fits have a large influence on the first mode. Overplotted on this map are the bearing characteristics for the minimum and approximate maximum clearance for the current bearing design to be referred to as the new design.

---

* All experimental data presented in this report was very capably taken and reduced by Mr. Terry Mitchell of Ingersoll-Rand, Wythenshawe, England.

The original units were shipped with a shorter pad and are referred to as the old design. The properties of these designs are given in table 1 for reference. Three compressors had the old design and three the new, but no correlation existed between bearing type and severity of vibration. The unit with the longest trouble-free operation had the old design bearings. However, another unit, No. 5, exhibited strong instability with the old design. The results of the analysis indicated the old design to be less desirable for stability. Since all current units utilize the new design, the analytical results herein are for the new bearing design.

The rotor system was modeled including the influence of the oil ring seals under design pressure and temperature conditions. For example, table II gives the characteristics for the outer seal at N=208 Hz (12,500 RPM) for a suction pressure of 1000 psi.

Compressors having covered stages are considered to have little or no destabilizing aerodynamic cross-coupling. The compressor stability or growth factor is plotted in fig. 9 and indicates that a total level of over 10,000 lb/in could be tolerated for nominal design conditions without excessive excitation. The basic design has proven very stable in applications having more stages and hence higher design to 1st peak response speed ratios. Classical aerodynamic excitation is not known to be characterized by a tracking component.

Figure 10 presents the stability of the compressor as a function of bearing preload. The solid curve is the new design and the preload range of 0.55 to 0.7 is indicated to be acceptable. It should be noted that when the bearings were designed the capability to predict stability was not available and hence the judgement indicates good design practice. The dashed line has a better optimum stability and a preload range of 0.24 to 0.52 will result in the optimum bearing configuration. This design is referred to as the redesign bearing (see table I).

The response of the coupling end bearing is plotted in fig. 11 for a range of bearing clearances showing that the compressor can experience a peak response, ranging from 108 Hz (6500 RPM) to 137 Hz (8200 RPM) depending on the actual build clearances in the compressors.

The influence of the seals on the response is indicated in fig. 12. For centered seals a single peak response at 112 Hz (6700 RPM) is indicated whereas the more likely response would appear as a double peak with peaks occurring in the range of 115 Hz-145 Hz (6900 RPM-8700 RPM) without any account of impeller stiffness.

The influence of the seals' eccentricity on system damped natural frequencies and stability is shown in fig. 13. The eccentric seal is noted to split the 1st mode from 2.8 Hz (168 cpm) to 26 Hz (1567 cpm) for maximum pressure at startup. The frequencies vary as a function of speed as indicated in fig. 14. It is noted that one damped critical tracks with little change in frequency at near 130 Hz (7800 cpm) while the lower damped critical also remains reasonably fixed in frequency but becomes less stable at higher speeds. While the higher frequency mode is indicated to be backward, the response study of fig. 15 clearly illustrates that both these modes are excited by a forward

rotating excitation for bearing and seal characteristics fixed at values for N=225 Hz (13,500 RPM) whereas on runup the only mode excited is the higher (backward) mode.

A summary of the bearing optimization study is presented in figs. 16 and 17 for the new and redesign bearings (reference table I). The forward modes are noted to optimize for the nominal redesign bearings with a seal ring groove, whereas the new bearing design is best for the condition of no seal ring groove. Further, while the redesign bearings can be optimized, the potential oversize clearance condition is indicated to be more severe for the redesign bearings.

The results of a stability study, wherein the rotor system was artificially stiffened to match the forward mode to the 140 Hz frequency are presented in figs. 18 and 19 for the new and redesign, nominal bearing conditions. The plots are given as growth factor versus aerodynamic excitation with the conclusion being that the redesign nominal condition is far superior to the new bearing design. The stabilizing influence of the seals on system stability is also indicated by these plots. This is characteristic of rotors operating below 2.2 times the rotor first peak response frequency (ref. 4).

Consideration was given, following recommendations from the customer, to possibly overboring the impeller and retrofitting a larger diameter shaft in an attempt to improve the overall system rotor dynamics. The compressor design is now and was always considered to be acceptable for normal levels of aerodynamic excitation. The present design is noted to be at a N/N_{cr} ratio of less than 1.7 which puts this compressor out of the class of the original Kaybob ($N/N_{cr} \sim 2.8$) and Ekofisk ($N/N_{cr} \sim 2.2$) designs (see refs. 9 and 11). It is noted that the Ekofisk redesign shaft moved the critical from 48% to 66% of rated speed. The present design places the critical at 60% of design speed.

With this background the concept of a stiffer shaft for the compressor seems inconsistent with past experience. An improvement in stability is predicted as would be expected but the once-per response levels and minimum speed range would be greatly influenced as noted by the response results of fig. 20. These response levels may be scaled linearly to approximately 2.0 mils for increased levels of imbalance. It is evident that the once-per response level at 13,000 rpm will be increased by 255% for nominal bearing clearances with the peak response speed occurring as high as 11,000 rpm.

With the above facts indicating a very possible degradation of design speed response and only a marginal improvement in stability, the concept of the stiffer shaft was considered as an absolute last resort redesign consideration.

The following section will summarize the redesign steps and results that paralleled the analytical studies briefly reviewed in this section.

SUMMARY OF FIELD MODIFICATIONS AND CONCLUSIONS OF OUTSIDE CONSULTANTS

The analytical study summarized in the previous section was paralleled with field modifications and discussions with major turbomachinery consultants. The basic conclusion of the consultants was that the analytical studies were state of the art and only selected checks were run on the basic model to confirm the results. In addition, no occurrence of the 2/3 tracking phenomena was known to any of the consultants engaged.

Initial field variations in hardware consisted of changing out rotors and impellers to assure that an impeller blade rework to remove a casting problem on the leading edge blades of the original compressor stages was not responsible for the superior response of the original units. No correlation was found to this small difference and the severe tripouts.

As mentioned previously, the original units were fitted with shorter, lower preload bearings but no correlation could be made relative to bearing type and the sensitivity to the nonsynchronous excitation.

The analysis indicated that removing the circumferential groove from the outer seal ring would improve the dynamic performance. This was tried and the result was affirmative but not sufficient to control the nonsynchronous forcing mechanism.

Prior test stand experience indicated light rubs could reexcite the first critical on this type compressor. For this reason, and since deep grooving was noted in the buffer gas laby babbitted surface, the laby clearance was increased to assure that no rub was occurring before tripout. After the laby clearance was increased, the compressor spectrum was noted to be substantially cleaner but the 2/3 component was still present and the units were speed limited.

As mentioned earlier, the stages were not keyed but relied on the shrink fit for torque transmission. Some concern existed for a possible internal friction mechanism at the impeller-shaft interface since these fits were at midspan, the most sensitive position for reexcitation of the 1st critical. Also of concern, but without any analytical grounds for verification, was the stage spacing and the design of the center ring diffuser (see fig. 3). These concerns were overshadowed by possible excitation from reflected pressure pulsation from either inlet or discharge (see fig. 1) and the potential for a rotating stall cell in the inlet or rotating stall in the vaneless diffuser.

The latter concerns were proven to be of no consequence by dynamic pressure pulsation data taken in the piping, the inlet area of the stages, and the diffuser. No evidence of pulsations that tracked or correlated to the vibration was detected in the No. 5 compressor instrumented with internal dynamic pressure transducers. Additional piping pressure pulsation data were taken on other units without any correlation to the forcing frequency.

At the same time an order was placed for the redesign bearing, the No. 6 compressor was modified to a keyed shaft with reduced fits, and the center diffuser inside diameter was dropped to improve stage isolation. Additionally,

the cavity was pressurized to force flow radially up the back sides of the stages. The result of this modification was the elimination of the 2/3 forcing frequency. Upon replacement with an original impeller shaft configuration the 2/3 component was still absent.

At this time the redesign bearings were tried in compressor No. 5 in addition to another trial of the old style bearings. The critical was noted to drop in speed from 135 Hz (8100 RPM) to 122 Hz (7350 RPM) after a shutdown and immediate restart. As much as 0.25 mil subsynchronous was still present at a frequency of 130 Hz (7800 cpm).

RESULTS OF FINAL DESIGN MODIFICATIONS

The events of the field retrofits and analysis resulted in a decision to use the original, keyless shaft with the new bearing design and grooveless seal rather than the redesign bearings and grooved seal. In addition, the diffuser was dropped and the center cavity pressurized to discharge pressure. This configuration was installed in two other compressors in addition to No. 6 (No. 2 and No. 5) with the result being the elimination of the 2/3 component and only a very small level of fixed frequency sub-synchronous vibration (0.05 mil max. typical). The No. 2 compressor was speed limited due to balance, initially. When this was corrected, the speed limit was removed. All units were then capable of going the full speed range without encountering sub-synchronous vibration levels in excess of acceptable or tolerable levels. The compressors with the modified diffusers have no 2/3 component while the unmodified compressors are not speed limited, but do have a small 2/3 component that is detectable but remains bounded.

The frequency spectrum before and after the final design modification for compressor No. 5 is given in figs. 21 and 22, respectively. The improved low level of fixed frequency is acceptable to both Ingersoll-Rand and the customer.

CONCLUSIONS

The following conclusions have been reached from a critical review of the design evaluation and field vibration performance of the six single-stage, parallel flow compressors discussed in this report:

1. Complex turbomachinery can be modeled to the necessary accuracy to study response sensitivity if all impeller fits, bearing clearances, seal clearances, and balance levels are known.
2. It is practical to do a design optimization to study design variation trends without achieving exact agreement between predicted and actual measured levels for damped frequencies.
3. Achieving bearing optimization in production bearings requiring less than 1/2 mil total variation in radial clearance at assembly is impractical and impossible to achieve in reality.

4. Compressors having oil seals and tilting pad bearings should have the bearing designed with a minimum preload value greater than about 30% for the best stability characteristics.

5. Zero or low preload tilting shoe bearings used in compressors having oil seals are more susceptible to oil seal or aerodynamic excited shaft whip than higher preload designs.

6. High pressure compressors utilizing oil seals and operating below 2.2 - 2.5 x N_{cr}^1 can have increased stability and improved forced response sensitivity with eccentric seals as compared to centered seals.

7. Oil seals can alter the peak response speed of compressors by as much as 30 Hz with likely variation during startups on the order of 10 Hz.

8. Both forward and backward analytically predicted damped natural modes can be excited by forward rotative forcing mechanisms.

9. Compressors operating below 1.8 x N_{cr}^1 cannot have substantial improvements in overall dynamic sensitivity by increasing the rotor shaft stiffness. This is especially true when a speed range is desirable from 80-100% design speed, for instance.

10. A forcing function mechanism has been proven to occur in parallel flow compressors due to the spacing and flow of high pressure gas in the space and on the back sides of the double flow stages. The detected mechanism produced a 2/3 x compressor speed excitation that can produce large level subsynchronous vibration when this frequency of excitation coincides with a system natural frequency.

11. A successful solution to the 2/3 x speed forcing component was arrived at by combined field tests, analytical work, and engineering judgement.

REFERENCES

1. Lund, J.W., "Stability and Damped Critical Speeds of a Flexible Rotor in Fluid-Film Bearings", Journal of Engineering for Industry, Trans. ASME, Series B, Vol. 96, No. 2, May 1974, pp. 509-517.

2. Lennemann, E., and Howard, J.H.G., "Unsteady Flow Phenomena in Rotating Centrifugal Impeller Passages", Journal of Engineering for Power, Trans. ASME, January, 1970, pp. 65-72.

3. Dussourd, J.L., et al, "An Experimental Investigation of the Control of Surge in Radial Compressors Using Close Coupled Resistances", Journal of Fluids Engineering, Trans. ASME, March, 1977, pp. 64-75.

4. Kirk, R.G., and Miller, W.H., "The Influence of High Pressure Oil Seals on Turbo-Rotor Stability," ASLE Trans., Vol.22, No.1, Jan. 1979, pp. 14-24.

5. Nicholas, J.C., Gunter, E.J., and Barrett, L.E., "The Influence of Tilting Pad Bearing Characteristics on the Stability of High Speed Rotor-Bearing Systems," Topics in Fluid Film Bearing and Rotor Bearing System Design and Optimization, an ASME special publication, April 1978, pp. 55-78.

6. Lund, J.W., "Modal Response of a Flexible Rotor in Fluid-Film Bearings", Journal of Engineering for Industry, Trans. ASME, Series B, Vol. 96, No. 2, May 1974, pp. 525-533.

7. Kirk, R.G., "Stability and Damped Critical Speed - How to Calculate and Interpret the Results", CAGI, Technical Digest, Vol. 12, No. 2.

8. Nicholas, J.C., and Kirk, R.G., "Selection and Design of Tilting-Pad and Fixed Lobe Journal Bearings for Optimum Turborotor Dynamics", Proceedings of the 8th Turbomachinery Symposium, Texas A & M University, College Station, Texas, 1979, pp. 43-57.

9. Smith, K.J., "An Operation History of Fractional Frequency Whirl," Proceedings of the Fourth Turbomachinery Symposium, Texas A & M University, College Station, Texas, 1975, pp. 115-125.

10. Wachel, J.C., "Nonsynchronous Instability of Centrifugal Compressors", ASME Paper 75-Pet-22, Presented at Petroleum Mechanical Engineering Conference, Tulsa, Oklahoma, Sept. 21-25, 1975.

11. Booth, D., "Phillips' Landmark Injection Project", Petroleum Engineer, Oct. 1975, pp. 105-109.

12. Sparks, C.R., and Wachel, J.C., "Pulsations in Liquid Pumps and Piping Systems", Proceedings of the 5th Turbomachinery Symposium, Texas A & M University, College Station, Texas, 1976, pp. 55-61.

13. Lund, J.W., "Rotor Bearing Dynamics Design Technology, Part V", AFAPL-TR-65-45, Aero Propulsion Laboratory, Wright-Patterson Air Force Base, Ohio, May 1965.

14. Jansen, W., "Steady Fluid Flow in a Radial Vaneless Diffuser", Journal of Basic Engineering, Trans. ASME, Series D, Vol. 86, 1964, pp. 607-619.

15. Jansen, W., "Rotating Stall in a Radial Vaneless Diffuser", Journal of Basic Engineering, Trans. ASME, Series D, Vol. 86, 1964, pp. 750-758.

16. Alford, J.J., "Protecting Turbomachinery from Self-Excited Rotor Whirl", Journal of Engineering for Power, Trans. ASME, Series A, Vol. 87, Oct. 1965, pp. 333-344.

17. Nicholas, J.C., Gunter, E.J., and Allaire, P.E., "Stiffness and Damping Coefficients for the Five-Pad Tilting-Pad Bearing", ASLE Trans., Vol. 22, No. 2, April 1979, pp. 113-124.

18. Black, H.F., "The Stabilizing Capacity of Bearings for Flexible Rotors with Hysteresis," Journal of Engineering for Industry, Trans. ASME, Feb. 1976, pp. 87-91.

19. Kirk, R.G., and Gunter, E.J., "Non-Linear Transient Analysis of Multi-Mass Flexible Rotors - Theory and Application", NASA CR-2300, Sept. 1973.

20. Ferrara, P.L., "Vibrations in Very High Pressure Centrifugal Compressors", ASME Preprint 77-DET-15, Presented at Design Engineering Technical Conference, Chicago, Illinois, Sept. 26-30, 1977.

Bearing	L in (cm)	C_B mils (mm x 10^{-2})	M	K_{xx} x 10^{-5} lb/in (N/cm)	K_{yy} x 10^{-5} lb/in (N/cm)	C_{xx} lb-s/in (N-s/cm)	C_{yy} lb-s/in (N-s/cm)
				N = 12,500 RPM			
New	1.375 (3.49)	1.400(3.36) Min 1.775(4.51) Nom 2.150(5.46) Max	.70 .62 .55	7.86 (13.76) 4.31 (7.55) 2.57 (4.50)	7.96 (13.94) 4.43 (7.76) 2.68 (4.69)	433 (758) 291 (510) 205 (359)	436 (764) 295 (517) 209 (366)
Old	1.000 (2.54)	2.000(5.08) Min 2.375(6.03) Nom 2.750(6.99) Max	.52 .40 .27	1.63 (2.85) .887 (1.55) .499 (0.87)	1.88 (3.29) 1.20 (2.10) .90 (1.58)	131 (229) 98 (172) 76 (133)	142 (249) 114 (200) 99 (174)
Redesign	1.375 (3.49)	1.900(4.83) Min 2.275(5.78) Nom 2.650(6.73) Max	.52 .38 .24	3.14 (5.50) 1.62 (2.84) .785 (1.37)	3.27 (5.73) 1.76 (3.08) .979 (1.71)	277 (485) 204 (357) 159 (278)	283 (496) 212 (371) 172 (301)

D   =   2.75 in (6.985 cm)   L/D   =   1/2 (New, Redesign)

W_R =   160 lbs (711.7 N) L_B =   33 in (83.82 cm)

Table I   Geometry and dynamic characteristics for old, new, and redesign five shoe tilting-pad bearings

Seal	K_{xy} x 10^{-5} lb/in (N/cm)	K_{yx} x 10^{-5} lb/in (N/cm)	C_{xx} (lb-s/in) (N-s/cm)	C_{yy} (lb-s/in) (N-s/cm)	Lock-up Eccentricity
w/groove	7.86 (13.76)	-1.12 (-1.96)	171 (299)	1460 (2557)	.84
w/o groove	4.85 (8.49)	-2.03 (-3.55)	310 (543)	717 (1256)	.55

$K_{xx} = K_{yy} = C_{xy} = C_{yx} = 0$ P_S = 1000 psi (689.4 N/cm^2)

C_S = 4.0 mils radial (.1016 mm)   N   = 12,500 RPM

Table II   Oil ring seal characteristics for outer ring with and without circumferential groove

Figure 1 Top view of a single stage parallel flow compressor configuration similar to the units discussed in the text

Figure 2 Cross-section of bearing-seal cartridge including the buffer labyrinth
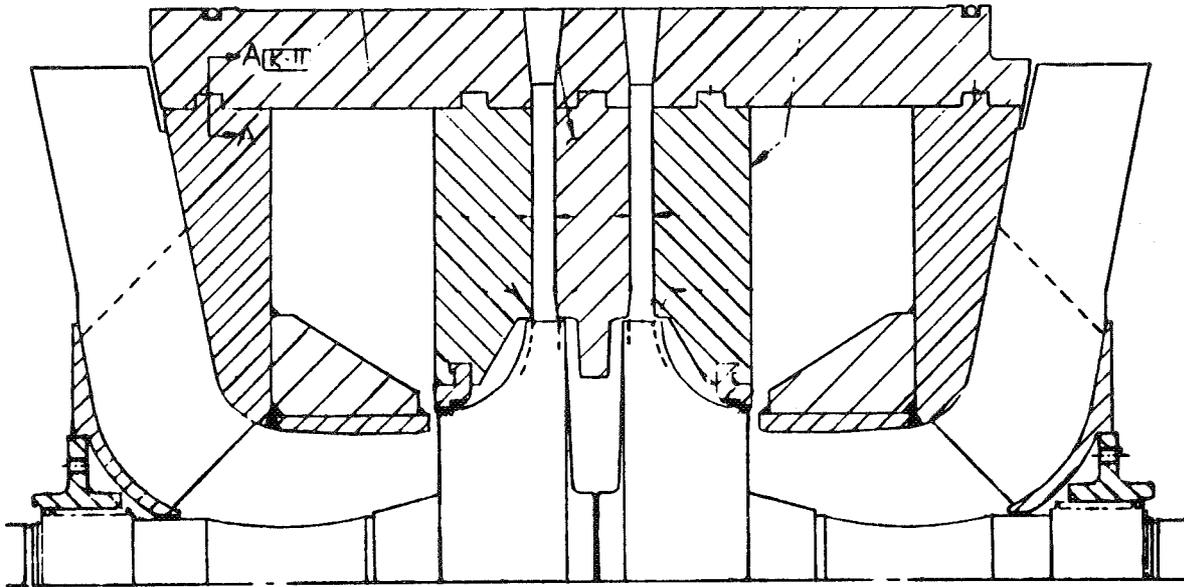
Figure 3   Rotor mid-section showing diffuser elements in cross-section
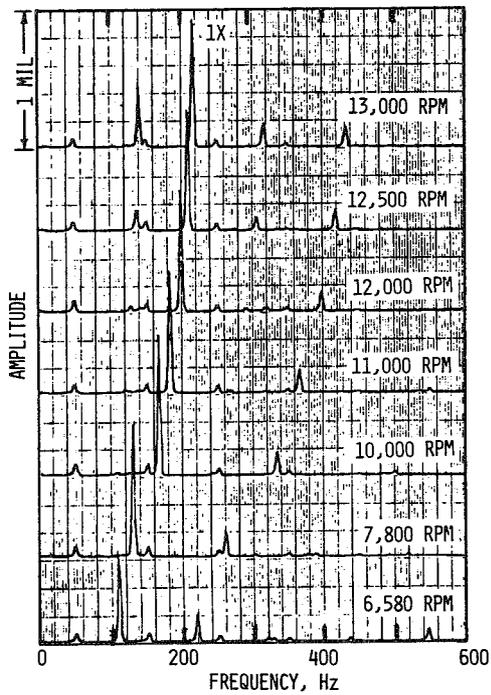
Figure 4   Field data for compressor No. 6 showing non-synchronous vibration increasing above 200 Hz rotor speed
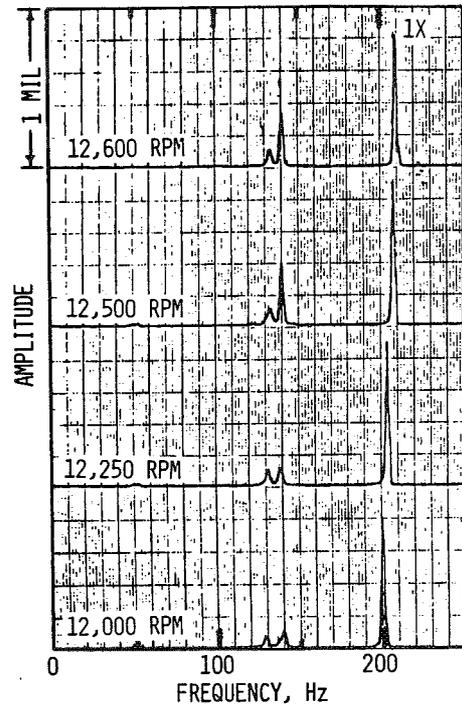
Figure 5   Detail spectrum for compressor No. 6 showing 2/3 tracking component moving into fixed 140 Hz component as rotor speed is increased above 200 Hz
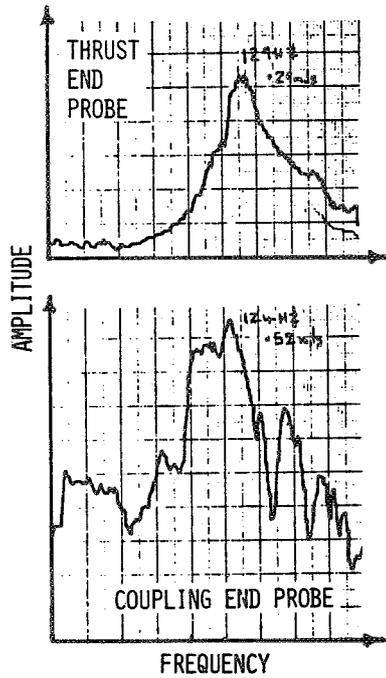
Figure 6 Peak hold response for accel under step pressurization from 95 psi showing peak response frequencies of 124 and 129 Hz
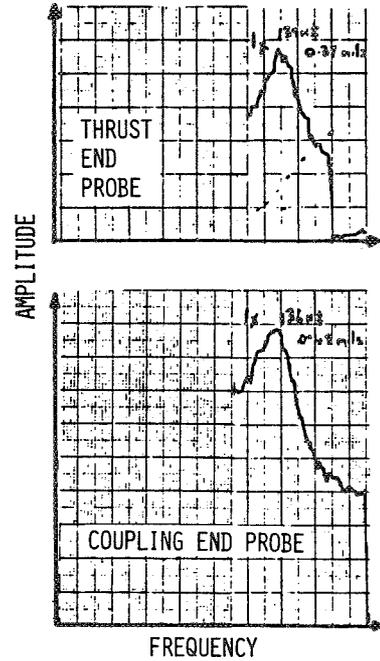
Figure 7 Peak hold response for normal accel under full pressure (800 psi) showing increased peak response frequencies of 136 and 139 Hz
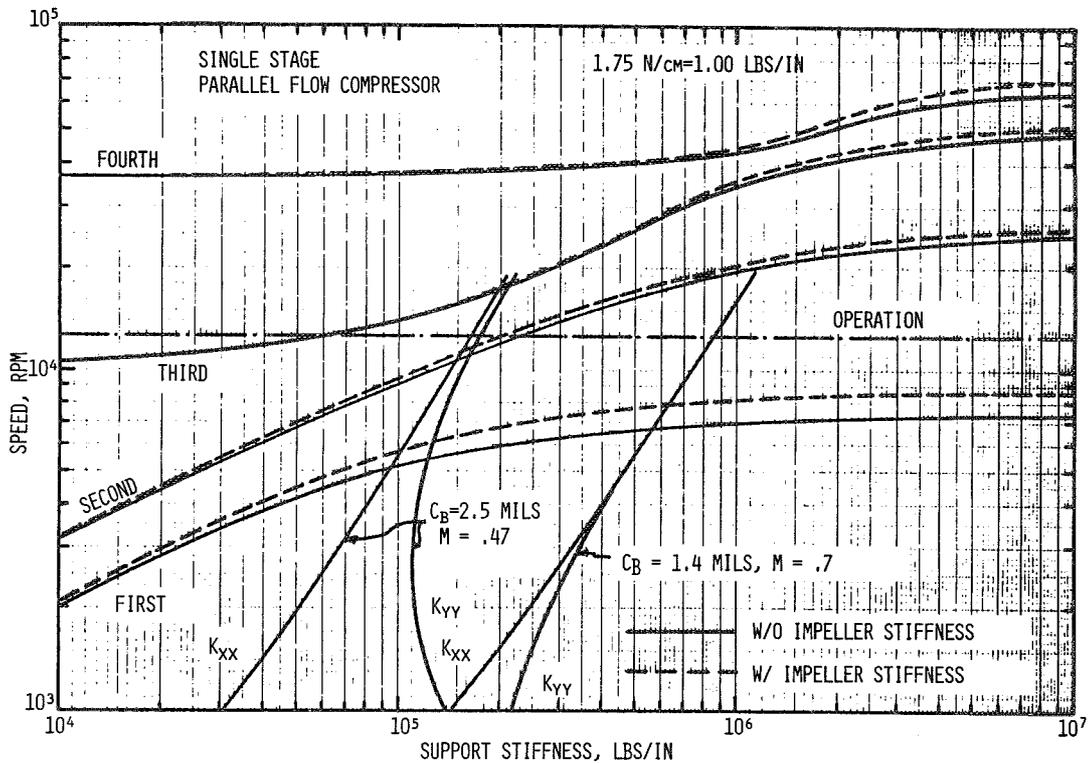
Figure 8 Undamped critical speed map with and without impeller stiffness with new bearing characteristics overplotted

58
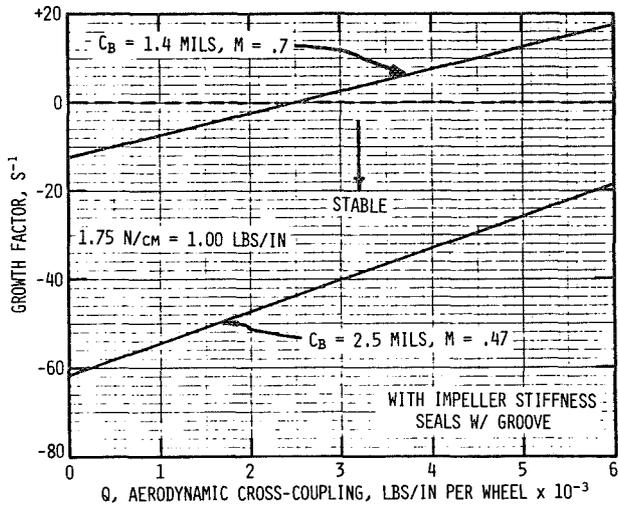
Figure 9 Stability map for standard design new bearings showing growth factor as a function of aerodynamic cross-coupling per stage
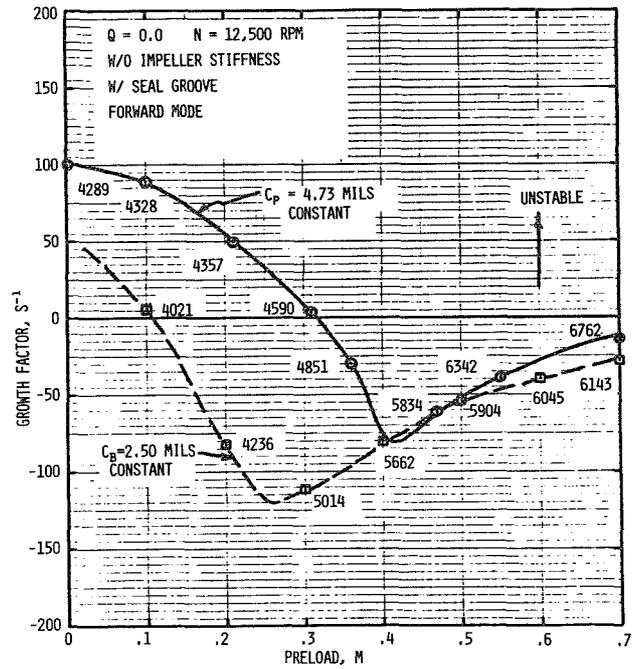
Figure 10 Stability map for bearing design variations on preload showing optimum for new design (C_p = 4.73 mils) and redesign bearings (C_B = 2.5 mils)
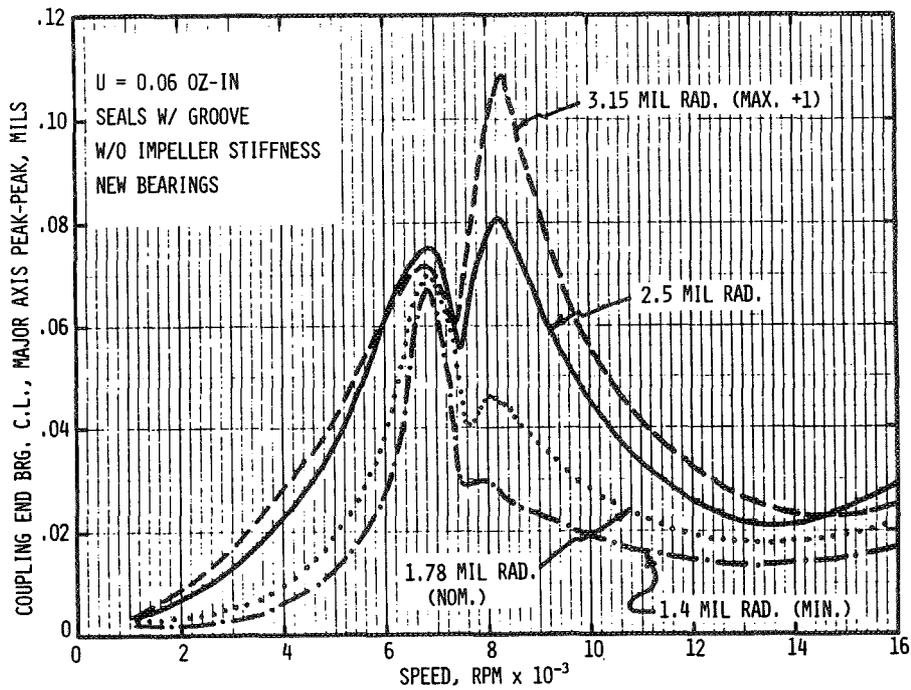
Figure 11 Coupling end response versus rotor speed for numerous bearing clearance values showing response levels increasing above 8000 RPM for increased clearances

59
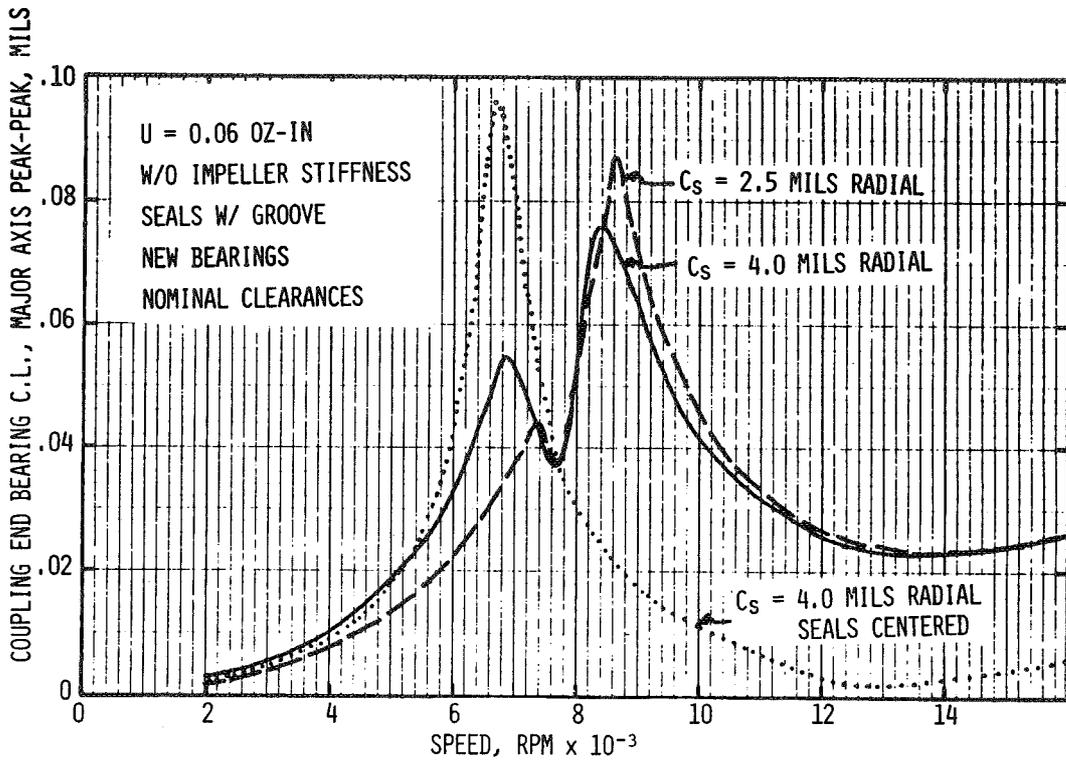
Figure 12 Coupling end response versus rotor speed for numerous seal clearances and operating eccentricity ratios
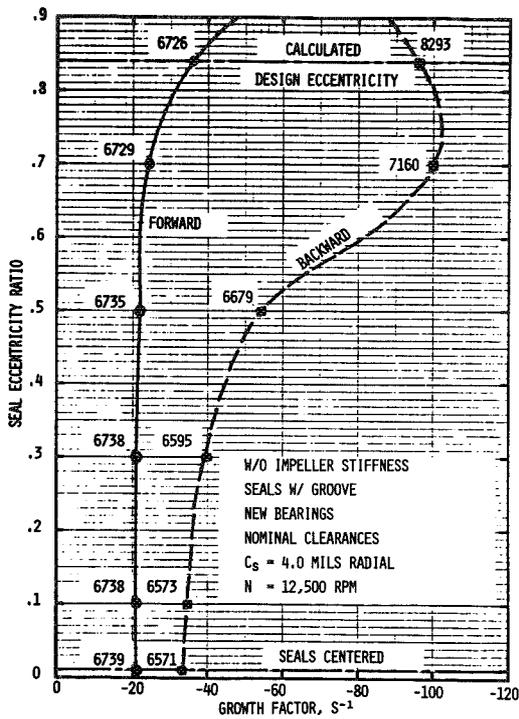
Figure 13 Rotor system stability versus seal eccentricity ratio for new bearing showing improved stability for increased seal eccentricity
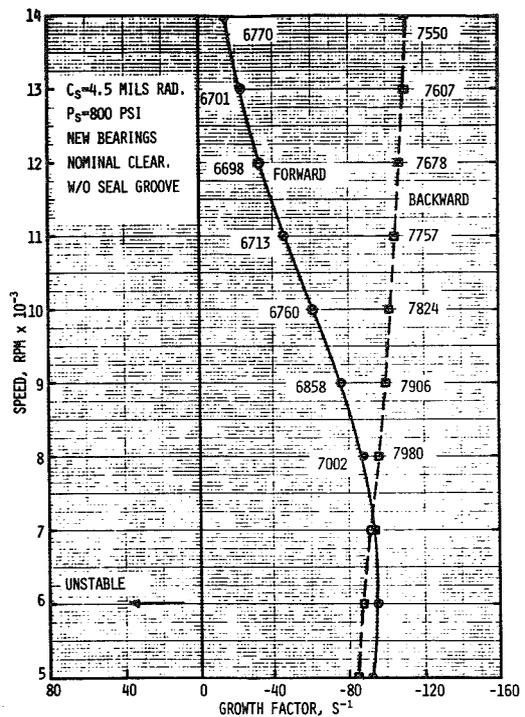
Figure 14 Rotor system stability versus rotor speed for new bearings and seals without circumferential groove showing nearly fixed damped natural frequencies

60
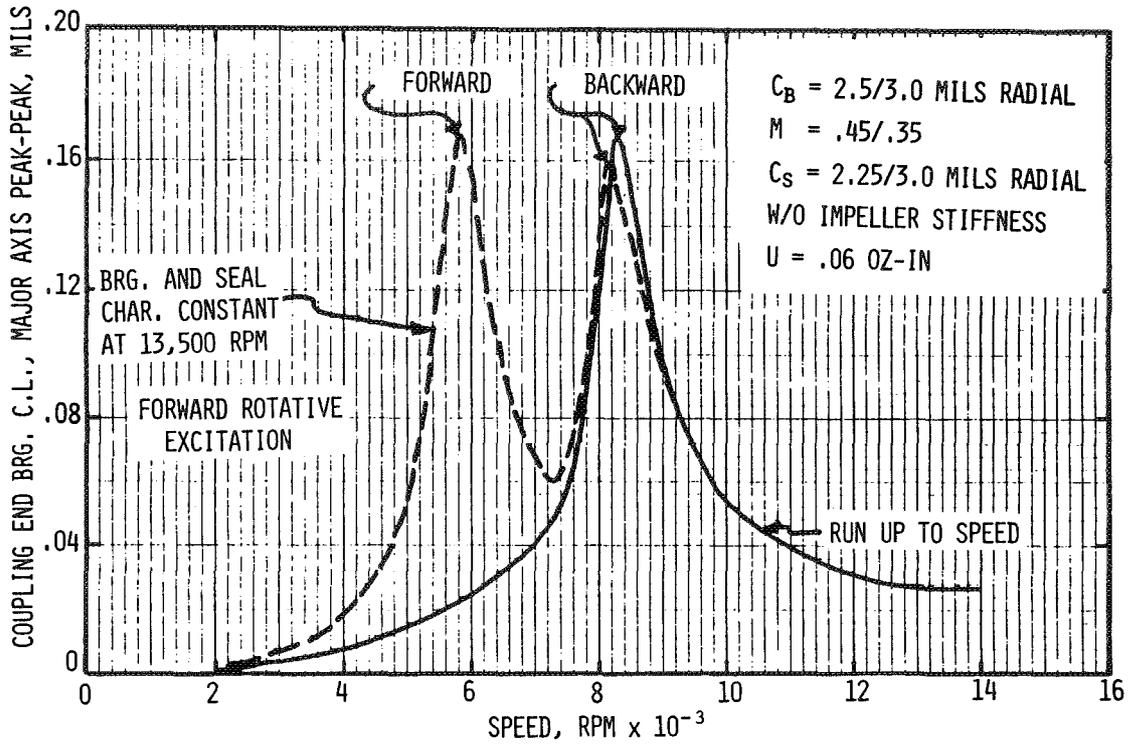
Figure 15 Response study showing that both the forward and backward modes may be excited by a forward rotative forcing function when the bearing and seal characteristics are fixed at values for N = 13,500 RPM
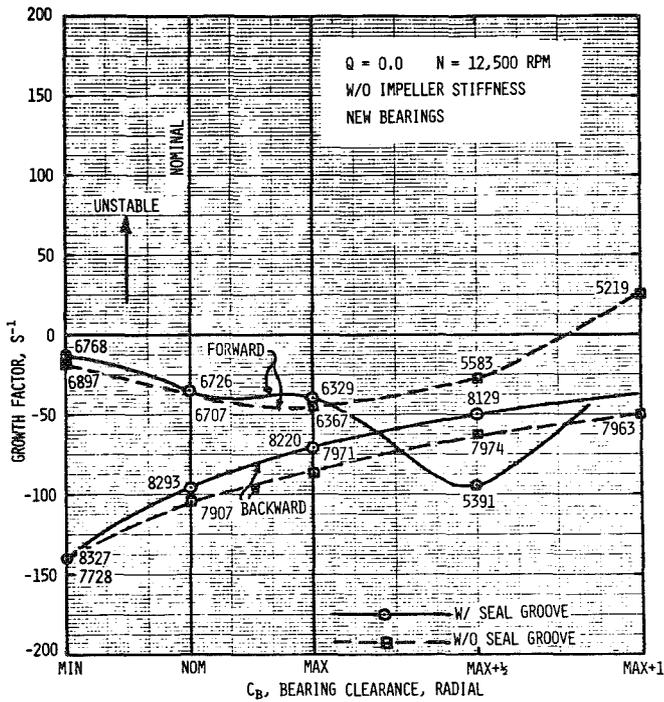
Figure 16 Stability plot showing design optimization study for the new bearings
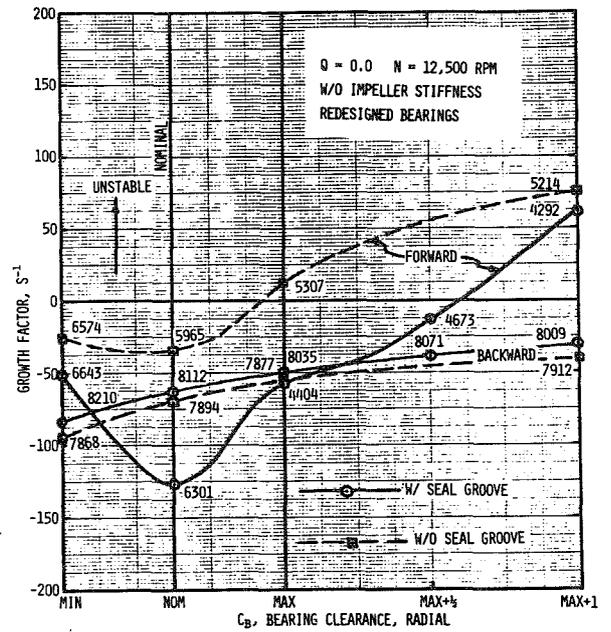
Figure 17 Stability plot showing design optimization study for the redesign bearings
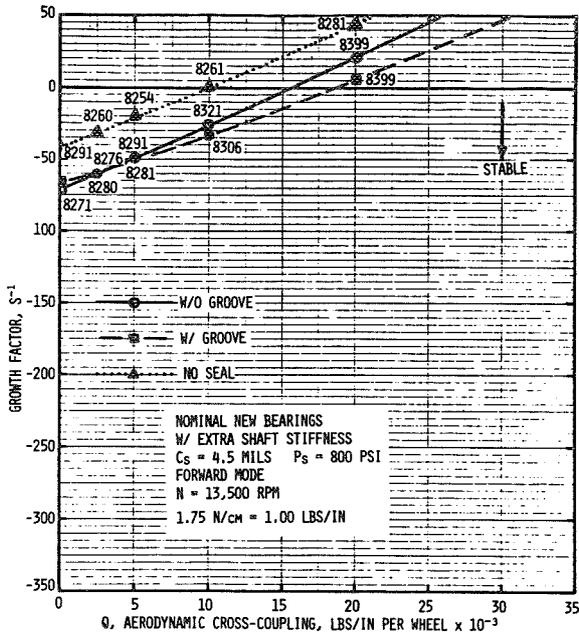
Figure 18 Stability versus aerodynamic cross-coupling for the stiffened rotor system to give the forward mode at 140 Hz for the nominal new bearing for various oil seal conditions
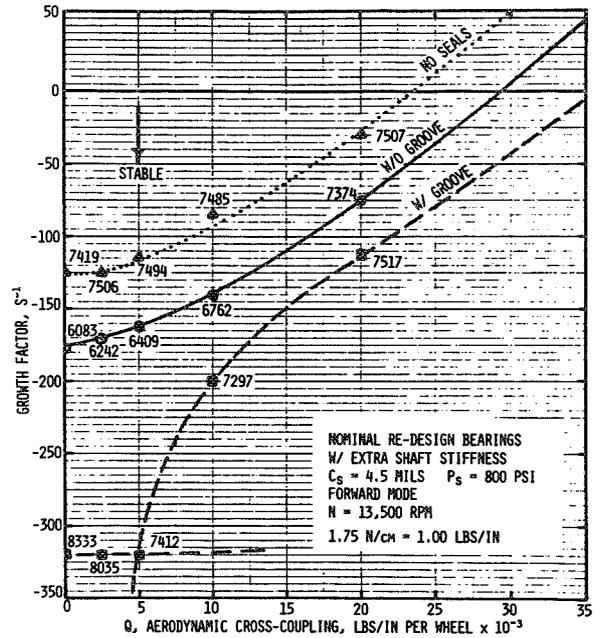
Figure 19 Stability versus aerodynamic cross-coupling for the stiffened rotor system for the forward mode and redesign bearings for various seal conditions
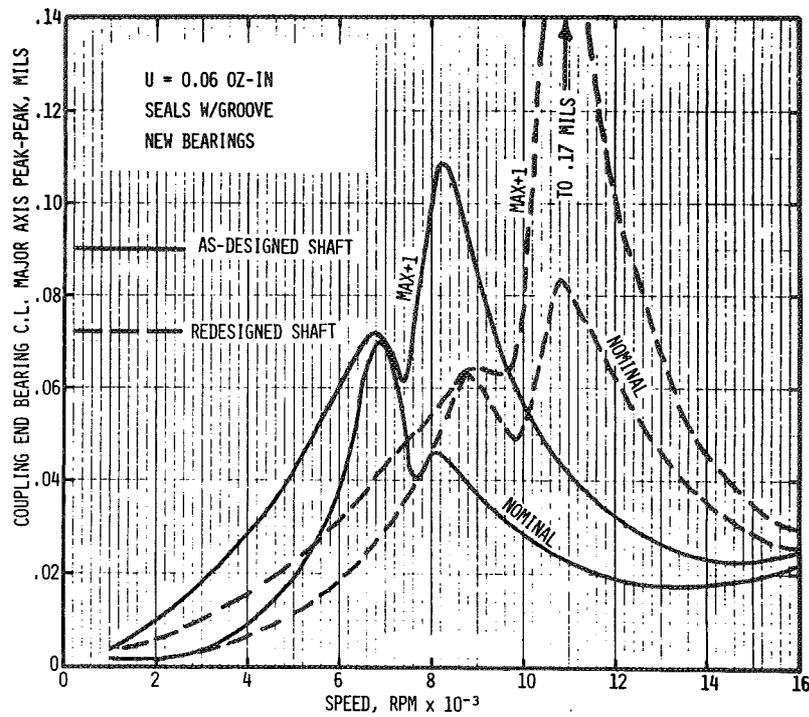
Figure 20 Coupling end response versus rotor speed for the current and over-bored impeller, over size rotor shaft showing greatly increased response sensitivity between 166 and 266 Hz

62
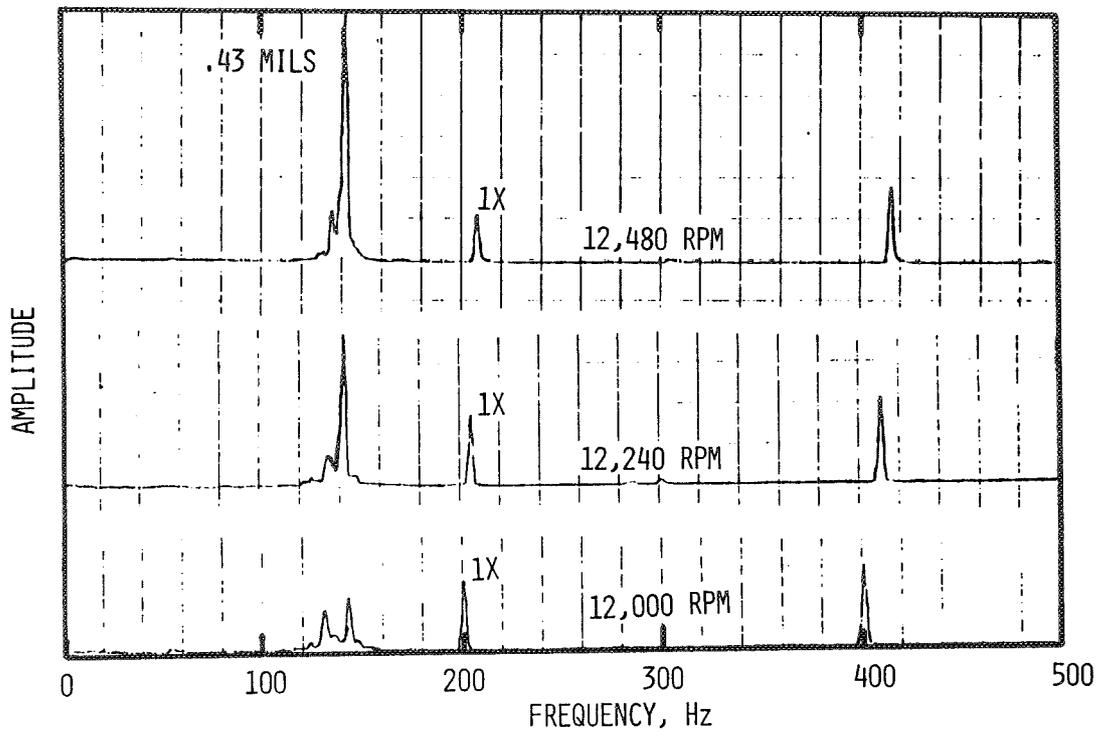
Figure 21 Spectrum for compressor No. 5 before the final design for eliminating the 2/3 tracking component showing rapidly increasing sub-synchronous vibration at 140 Hz
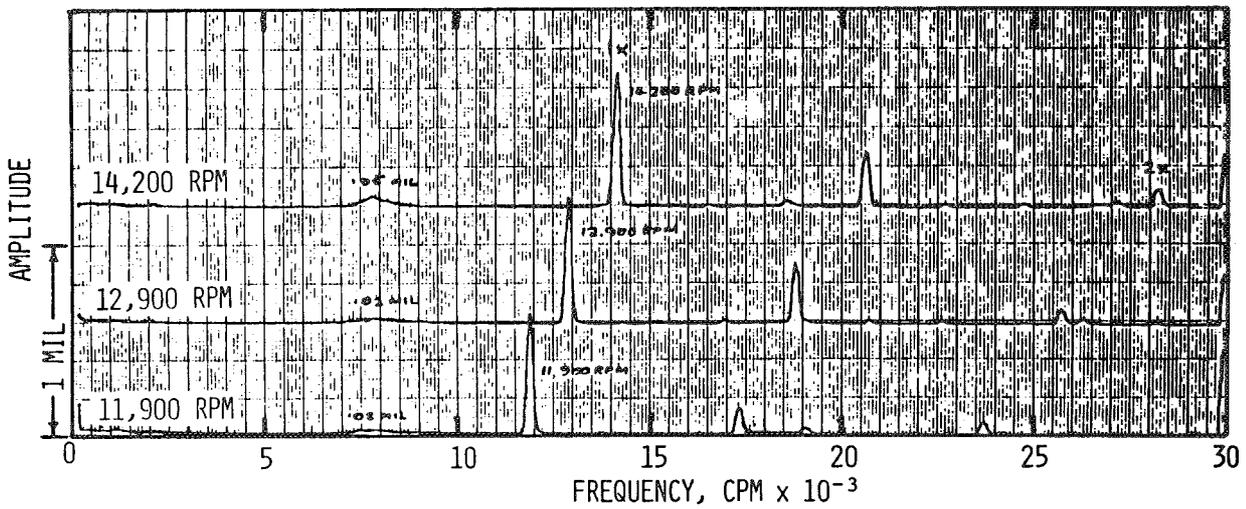
Figure 22 Spectrum for compressor No. 5 after final design for diffuser showing the total absence of the 2/3 component and a maximum sub-synchronous component of 0.05 mils at fixed frequency

Page intentionally left blank

SESSION II

ADDITIONAL FIELD EXPERIENCE WITH UNSTABLE MACHINERY, DIAGNOSIS, AND DATA ANALYSIS

Albert Kascak, NASA Lewis Research Center
Chairman

Page intentionally left blank

SUBSYNCHRONOUS INSTABILITY OF A GEARED CENTRIFUGAL
COMPRESSOR OF OVERHUNG DESIGN

J. H. Hudson and L. J. Wittman
Allis-Chalmers Corp.
Milwaukee, Wisconsin 53201

INTRODUCTION

This paper presents the original design analysis and shop test data which
were obtained for this compressor. Also included are field test data, sub-
sequent rotor dynamics analysis, modifications, and final rotor behavior.

BASIC COMPRESSOR CHARACTERISTICS

The subject unit is a three-stage (poster) air compressor, with impellers
mounted on the extensions of a twin pinion gear, driven by an 8000-hp synchro-
nous motor. The motor speed is 1200 rpm, with speeds of 8057 rpm on the low-
speed pinion and 9400 rpm on the high-speed pinion. The compressor is rated at
approximately 40 000 acfm and an approximate discharge pressure of 100 psia
under normal summer conditions of temperature and humidity. Operation of the
process plant is basically constant weight flow at constant pressure.

At the time of design the compressor represented the highest horsepower
and largest volume for a three-poster design that had been built by Allis-
Chalmers. Four-poster designs had been built for higher horsepower levels using
the same frame size.

SUMMARY OF ORIGINAL ROTOR DESIGN METHODS

According to usual practice for a compressor of this type the aerodynamic
requirements were defined initially, thus establishing minimum pinion center
distances to allow for casing clearance. The gear vendor then designed the
gearing to satisfy power and ratio requirements in accordance with Allis-
Chalmers' specifications, which included data on pinion extension details.
After the pinion was designed to satisfy gearing and bearing loading require-
ments a rotor response evaluation of the pinions was performed.

At the time this compressor was designed, rotor analysis was limited to
undamped critical speed and synchronous unbalance response analysis, both as-
suming a circular orbit (isotropic bearing properties).

Details of speeds, horsepower, bearing types, and loading, as well as the
lubricant, are given in table 1.

Figure 1 is a pseudo-undamped critical speed map for the low-speed pinion.
Because of unequal bearing properties the usual intersect point on this curve
is not appropriate. The stiffness for the bearings range from 5×10^5 to
4×10^6 lb/in. A similar pseudo-mode shape plot is also presented in figure 2

for a stiffness of 1×10^6 lb/in. Figure 3 is a synchronous unbalance response plot assuming unequal but constant bearing loadings with unbalance distribution to excite the first mode. Assumption of constant bearing loading and direction is not correct, as can be seen from figure 4; however, the program at that time could not accommodate variations of this type.

Figure 5 is an undamped critical speed map of the high-speed pinion with part- and full-load bearing stiffnesses superimposed. Figures 6 and 7 are mode shapes of the rotor at 1×10^6- and 1×10^7-lb/in bearing stiffnesses. This range encompasses the actual bearing stiffness. Figure 8 is a synchronous unbalance response plot with combined unbalance to excite the first and second modes. Based on the rotor dynamics analysis the compressor design was deemed acceptable and proceeded through manufacture.

SHOP TESTING

The compressor was mechanically and aerodynamically tested. The first stage was tested at atmospheric discharge conditions; therefore the low-speed pinion was loaded to approximately 45% of design horsepower. The high-speed pinion was tested with atmospheric inlet conditions and was loaded to approximately 35% of its rated load.

The compressor was equipped with radial proximity probes in the vertical direction only. Vibration was monitored by using a digital vector filter and real-time analyzer. The vibration spectrum for the low-speed pinion contained synchronous and low-level two-per-revolution signals at 0.65 and 0.1 mil, respectively, for the impeller end probe and 0.3 and 0.1 mil, respectively, for the thrust bearing end probe. The vibration spectrum for the high-speed pinion showed a synchronous component of 0.2 mil at both pinion probes and was virtually free of all nonsynchronous components. The vibration signals were tape recorded for quality assurance documentation. The compressor met mechanical and aerodynamic requirements and was shipped.

FIELD PERFORMANCE

Shortly after startup the compressor exhibited overall vibration levels of 1.0 to 1.5 mils. It was observed that nearly 0.75 mil existed at slow roll. Test tape recordings revaled that about 0.3 mil existed as electrical and mechanical runout when the unit was tested at the factory. The additional electrical runout was attributed to magnetic fields induced by welding cables that slung over the casing during installation.

During the early commissioning of the compressor the customer reported sporadic vibration behavior of the low-speed rotor. At periods the overall vibration level was around 1.5 mils and occasionally levels of 3 mils and greater were reported. Figure 9 reveals operating points where moderate and high vibration conditions existed. A test was conducted with the compressor guide vane fixed at $0°$ prewhirl. Test points were taken at flows from beyond the rated point to close to the surge limit of the compressor. The high flow points showed very little subsynchronous vibration (<0.1 mil); however, as the flow was decreased the subsynchronous component continued to increase until the subsynchronous component was approximately 1.5 mils, or 3 times the synchronous

level of vibration. A point of interest is that two levels of subsynchronous frequency appeared. Refer to figures 10 to 13, which depict the changing subsynchronous spectrum. It was apparent that a bounded subsynchronous instability existed in the rotor.

ANALYSIS OF FIELD DATA

Between the time when the compressor design was originally analyzed and the time of the field tests in which subsynchronous vibration was found, considerable improvements were made to Allis-Chalmers rotor dynamic analysis capabilities (refs. 1 and 2). This finite-element method of analysis enabled us to calculate undamped critical speeds with unequal bearing forces. Input of bearing forces to reflect external loading, such as gear reactions, was an added capability. Synchronous unbalance response was upgraded to account for possible bearing asymmetry. Rotor stability calculations were improved and made more convenient and less expensive. A pad assembly program was developed which enabled the development of a full matrix to represent bearing stiffness and damping for the stability analysis with a minimum of effort. Refer to figures 16 and 17, which reflect mode shape and response plots for the subject rotor with these capabilities.

The low-speed pinion was modeled by using these programs to gain insight into its base log decrement at operating conditions and subsequently to evaluate proposed modifications. The rotor model included the added weight of shrunk-on parts without any additional stiffening effect of these parts. The effective stiffness of the center section of the rotor, where significant difference in shaft diameters exists, was based on data presented in reference 5. A horsepower level was chosen for analysis based on aerodynamic data for a test point represented by figure 13. Bearing and gear manufacturer's quality records were procured. They revealed that the actual bearing diametral clearance ranged from 0.0075 to 0.0093 inch with preload between 0.2 and 0.4, respectively.

The modeled original configuration was analyzed without any calculated destabilizing force at the impeller. No attempt was made to make allowances for labyrinth seal effects or nebulous factors such as internal friction. This analysis resulted in a relatively sizable value of log decrement (table 2 and fig. 14). The frequency and mode shape were in good agreement with probe data from field tests. Several other cases were analyzed and are summarized here.

Destabilizing Forces

It was assumed that the primary cause of instability in the rotor was associated with aerodynamic destabilizing forces. Several levels were analyzed until a log decrement of 0.0 was obtained (fig. 18). As a point of reference the destabilizing force was calculated according to references 4 and 8 per the equation

$$Kxy = -Kyx = \frac{T}{2rh}$$

where

Kxy,Kyx   aerodynamic destabilizing force represented as cross-coupled bear-
           ing stiffness, lb/in

T   torque input to stage, in-lb

r   impeller mean radius, in.

h   blade height, in.

The computed value of the 0° guide vane instability (fig. 13) test point is
742.5 lb/in. The destabilizing value calculated to create a log decrement of
0.0 is approximately 16 000 lb/in, or 21.5 times the calculated value.

As a basic of comparison it was decided to use 16 000 lb/in for the re-
mainder of the analysis.

Rotation of Existing Bearings

It was decided to determine the effects of rotating the journal bearings
based on data presented in reference 6. An analysis was made for loading
directly into the pivot and directly centered between the pivots. It was deter-
mined that rotation would be of little benefit. Refer to table 2 for summary
details.

Increased Bearing Width

The effect of increased bearing width (1.0 L/D) was analyzed to establish
if improvements in the log decrement could be made. Several combinations of
diametral clearances and preload were evaluated for loading into the pivot. It
was found that a lower preload (normally 0.2) and bearing clearances toward the
upper range of the clearance range defined in table 2 would produce the best im-
provement in log decrement. The relative increase in log decrement for a bear-
ing preload of 0.2 and an average diametral clearance of 0.0085 inch is pre-
sented in figure 18. Details are tabulated in table 2.

A run using the above preload and clearance (0.2 and 0.0085 in., respec-
tively) was performed for load between pivots. A decrease in log decrement was
found (table 2).

Reduction of Impeller Overhang

An analysis was performed of the bearings as designed and installed and the
pinion as designed except for removing 2 inches from the shaft between the im-
peller and the impeller end bearing. The effect on the log decrement was a con-
siderable improvement, as detailed in table 2.

Increase in Shaft Section Modulus

An analysis was made of the compressor rotor as designed except for increas-
ing the pinion bearing diameter to 4.5 inches. The bearing L/D was maintained
at 0.75 with an average preload of 0.2 and a clearance of 0.0095 inch. Again a
considerable improvement was found in the log decrement, nearly equal to that
for reducing the overhang. Details are listed in table 2.

70

Oil Viscosity Effects

A higher viscosity was used in the compressor to favor gear lubrication. The effects of viscosity changes were analyzed for the case of a bearing L/D equal to 1 with load into the pivot. As can be seen from the data in table 2 further increase in oil viscosity would either raise or lower the log decrement for this rotor.

ACTUAL FIELD MODIFICATIONS AND FIELD RETESTING

As a result of this analysis it was apparent that the most expedient modification to improve rotor stability is a bearing modification. A wider bearing (L/D = 1.0) with a nominal preload of 0.2 and clearance range of 0.0075 to 0.0095 inch was specified. Bearings were oriented such that each bearing would be loaded into the pivot at rated power, even though load angles were different for each bearing.

The compressor was modified and retested. The retesting at previous test points and other operating and nonoperating points revealed only synchronous frequencies. All signs of subsynchronous frequencies were removed.

DISCUSSION

There are two areas for further investigation as a result of this problem and subsequent analysis. First is the observation of two distinct subsynchronous frequencies. Allis-Chalmers' analysis predicted the higher frequency of approximately 3100 cpm quite well; however, the frequency of major amplitude occurred at approximately 2700 cpm. Allis-Chalmers had not seen this type of double subsynchronous frequency previously on a conventional midspan compressor rotor. It is assumed to have been generated as a result of unequal bearing loadings compounded by the magnitude of levels of subsynchronous vibration. A point of interest is that the lower frequency agrees reasonably well with a peak on the synchronous response curve (fig. 17).

Second, and most disconcerting, is the fact that subsynchronous instabilities did develop despite the substantial values of the log decrement. Even if one were to increase the destabilizing force four times, a log decrement of approximately 0.3 would still exist. There are many conventional midspan rotors with log decrements much lower than this value with equal or higher destabilizing force values that have a history of successful operation. It is postulated that some not-yet-defined level of excitation exists on this type of rotor. There are several possibilities:

(1) Gear error effects - No attempt has been made to add any destabilizing force as a result of gear inaccuracies or torsional-lateral coupling.

(2) Effects of open impellers - The impeller on this pinion was of an uncovered design. It is physically impossible to assure operation of this type of impeller with uniform circumferential and axial clearances. Perhaps the nonuniform clearances along with the turbulent bypass effects from blade to blade are generating much higher destabilizing forces than normally associated with a

closed impeller. In addition, other aerodynamic factors such as flow separation and stall have not been quantified as to their destabilizing influence.

It is worth noting that our experiences are in reasonable agreement with data presented in reference 7.

CONCLUSIONS

1. A subsynchronous instability existed on a geared, overhung rotor. State-of-the-art rotor dynamics analysis techniques provided a reasonable analytical model of the rotor. A bearing modification, arrived at analytically, was made to the compressor and eliminated the instability.

2. Further research is required to more accurately define the mechanism and to quantify the forces which cause the instability.

REFERENCES

1. Rouch, K. E.; and Kao, J. S.: Reduction in Rotor Dynamics by the Finite Element Method. ASME Paper 79-DET-70, 1979.

2. Rouch, K. E.; and Kao, J. S.: A Tapered Beam Finite Element for Rotor Dynamic Analysis. J. Sound Vibr., 1979, vol. 66, no. 1, pp. 119-140.

3. Wittman, L. J.: Compressor Division Engineering Report 16-ER-416. November 13, 1978.

4. Alford, J. S.: Protecting Turbomachinery from Self-Excited Rotor Whirl. J. Eng. Power, Trans. ASME Series A, vol. 87, October 1965, pp. 333-334.

5. Brown, J. M: Lateral and Torsional Stiffness of Shafts of Varying Diameter. Doctoral thesis, Purdue University, 1952.

6. Jones, G. J.; and Martin, F. A.: Geometry Effects in Tilt Pad Journal Bearings, Paper AT449/80, Glacier Publication.

7. Pennink, Hans: The State of the Art of High Speed Overhung Centrifugal Compressors for the Process Industry. Proceedings of 7th Turbomachinery Symposium.

8. Lund, J. W.: Stability and Damped Critical Speeds of a Flexible Rotor in Fluid Film Bearings. ASME Paper 73-DET-103, 1973.

TABLE 1

	LOW SPEED	HIGH SPEED
SPEED (RPM)	8057	9400
HORSEPOWER (BHP)	3774	4226
BEARING LOADS (POUNDS$_{FORCE}$)	1114 DOWNWARD 1ST STAGE	432 DOWNWARD 2ND STAGE
STATIC (WEIGHT)	242 UPWARD THRUST BRG.	352 DOWNWARD 3RD STAGE
TOTAL (WEIGHT AND GEAR REACTIONS)	1782 ⤢ 17° 1ST STAGE	3560 ⤢ 10.5° 2ND STAGE
	3487 ⤢ 28° THRUST BRG.	3936 ⤢ 27° 3RD STAGE
JOURNAL DIAMETER (IN.)	4.0	4.0
LENGTH (IN.)	3.0	3.0
DIAMETRAL CLEARANCE INCLUDING JOURNAL TOLERANCE (IN.)	.007/.010	.007/.010
m (BEARING PRELOAD)	.33	.33
BEARING TYPE	5 PAD TILT PAD CENTRAL PIVOT	5 PAD TILT PAD CENTRAL PIVOT
LUBRICANT	215 SSU @ 100°F VI = 95	

TABLE 2

Case #	Description	BEARING - 1ST STAGE				BEARING - BLIND SIDE				Aero Q(Lb/In)	Freq. (CPM)	Prec.	Log Dec	Comments
		Dia. (In.)	L/D	Dia. Clr.(In.)	Load Dir.	Dia. (In.)	L/D	Dia. Clr.(In.)	Load Dir.					
1	Original Configuration	4.0	.75	.0084	18° Off. Pivot	4.0	.75	.0084	8° Off. Pivot	0	3151	Fwd.	.3666	m = .285
2	Org.Configuration	4.0	.75	.0084	18° Off. Pivot	4.0	.75	.0084	8° Off. Pivot	10,000.	3185	Fwd.	.136	m = .285
3	Org.Configuration	4.0	.75	.0084	18° Off. Pivot	4.0	.75	.0084	8° Off. Pivot	16,000.	3195	Fwd.	.0004	m = .285
4	Rotated Brg. Load Into Pivot	4.0	.75	.0084	Into Pivot	4.0	.75	.0084	Into Pivot	16,000.	3014	Fwd.	.0071	m = .285
5	Rotated Brg. Load Between Pivot	4.0	.75	.0084	Between Pivot	4.0	.75	.0084	Between Pivot	16,000.	3288	Fwd.	.0026	m = .285
6	2" Shorter Overhang	4.0	.75	.0084	18° Off. Pivot	4.0	.75	.0084	8° Off. Pivot	16,000.	3596	Fwd.	.184	m = .285
7	Final Fix w/ L/D = 1 Brg.	4.0	1.0	.0085	Into Pivot	4.0	1.0	.0085	Into Pivot	16,000.	3086	Fwd.	.082	m = .2
8	Alternate Arrangemt. w/ L/D = 1 Brg.	4.0	1.0	.0085	Between Pivot	4.0	1.0	.0085	Between Pivot	16,000	3261	Fwd.	.054	m = .2
9	Stiffer Shaft 4.5 Brg & Shaft	4.5	.75	.0095	18° Off. Pivot	4.5	.75	.0095	8° Off. Pivot	16,000	3275	Fwd.	.181	m = .2
10	Stiffer Shaft 4.5 Brg & Shaft	4.5	.75	.0095	Into Pivot	4.5	.75	.0095	Into Pivot	16,000	3189	Fwd.	.168	m = .2
11	Case 7 w/reduced Oil Temp. 140°	4.0	1.0	.0085	Into Pivot	4.0	1.0	.0085	Into Pivot	16,000	3151.4	Fwd.	.1161	m = .2
12	Case 7 w/reduced Oil Temp. 120°	4.0	1.0	.0085	Into Pivot	4.0	1.0	.0085	Into Pivot	16,000	3328	Fwd.	.0764	m = .2

For L/D = .75 orientation makes essentially no difference. (bracketing cases 3, 4, 5)

CRITICAL SPEED MAP
12 JUN 75
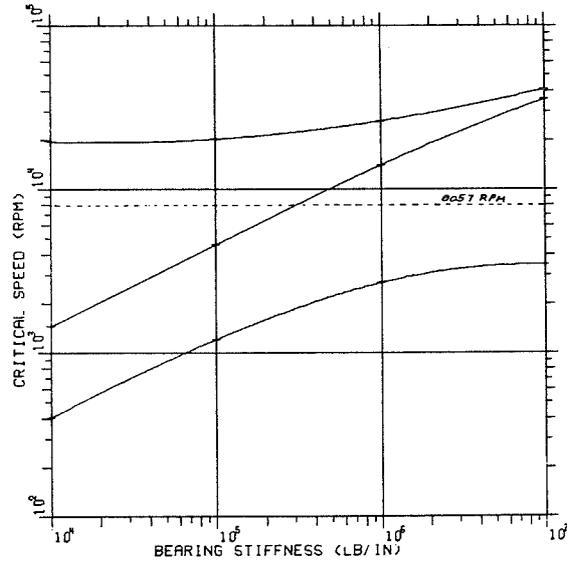
LOW SPEED PINION

ASSUMES EQUAL STIFFNESS

Figure 1

ROTOR MODE SHAPE AT CRITICAL SPEED
PROGRAM 8166-001

DATE
12 JUN 75

BRG   BRG
NO.   STIFF
1   1X10⁶
2   1X10⁶

CRITICAL SPEED
1   2687   RPM
2   14029 RPM
3   26044 RPM

LOW SPEED PINION

Figure 2

CIRCULAR ORBIT ROTOR UNBALANCE RESPONSE
PROGRAM 8166-002
12 DEC 75
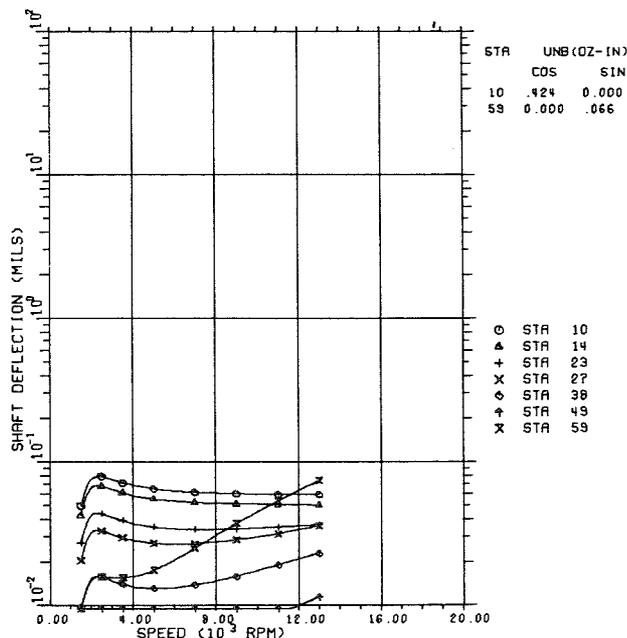
L.S. PINION
Figure 3
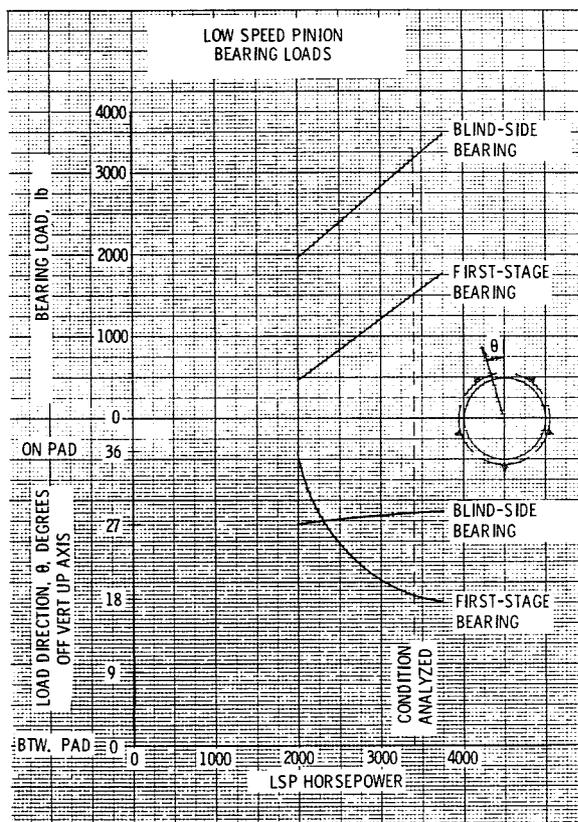
Figure 4

CRITICAL SPEED MAP
12 JUN 75

BEARING STIFFNESS (LB/IN)
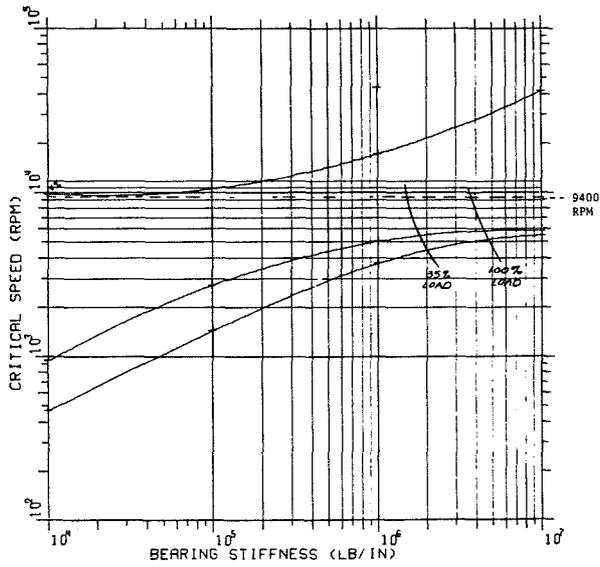
HIGH SPEED PINION

Figure 5

ROTOR MODE SHAPE AT CRITICAL SPEED
PROGRAM 8166-001
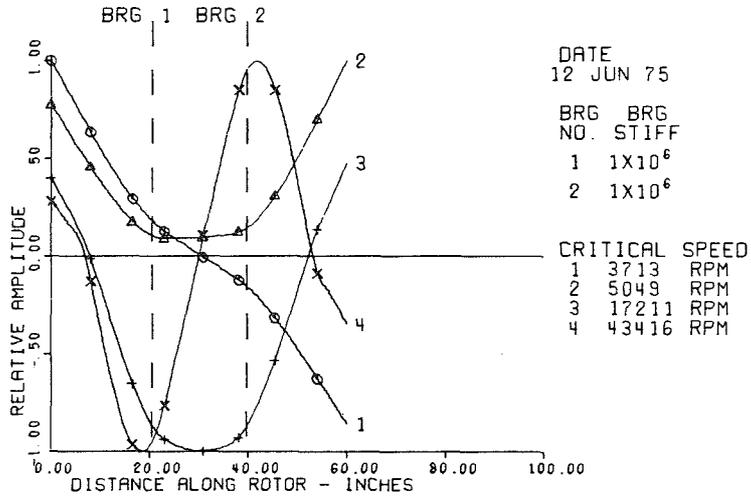
BRG 1   BRG 2

DISTANCE ALONG ROTOR - INCHES

DATE
12 JUN 75

BRG   BRG
NO.   STIFF
1   1×10^6
2   1×10^6

CRITICAL SPEED
1   3713   RPM
2   5049   RPM
3   17211 RPM
4   43416 RPM

HIGH SPEED PINION

Figure 6

77

ROTOR MODE SHAPE AT CRITICAL SPEED
PROGRAM 8166-001

BRG 1   BRG 2

DATE
12 JUN 75

BRG   BRG
NO   STIFF

1   1X10⁷

2   1X10⁷

CRITICAL SPEED
1   5474   RPM
2   5810   RPM
3   41743 RPM
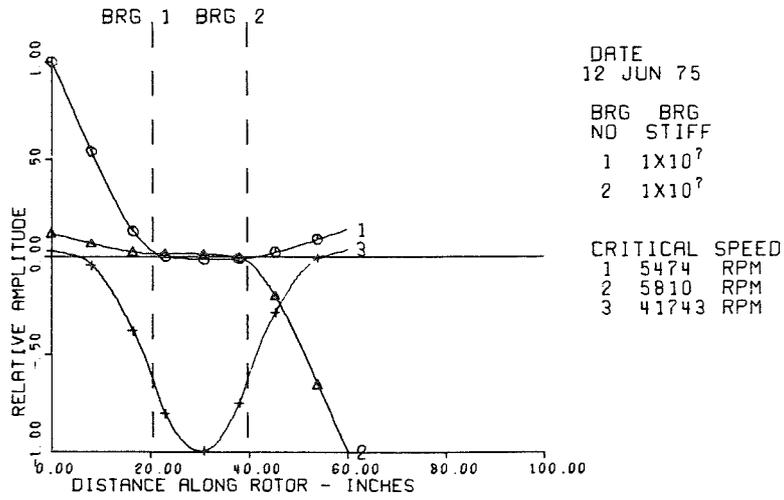
HIGH SPEED PINION

Figure 7

CIRCULAR ORBIT ROTOR UNBALANCE RESPONSE
PROGRAM 8166-002
27 JUN 75

STA   UNB(OZ-IN)
       COS   SIN

6   .192   .192
21   0.000   0.000
43   0.000   0.000
58   .157   -.157

⊙ STA   6 IMP CG
△ STA   9 SEAL
+ STA 21 BRG
X STA 32 CENTER
◇ STA 43 BRG
✦ STA 54 SEAL
X STA 58 IMP CG
Z STA 16 PROBE
Y STA 48 PROBE

HIGH SPEED PINION

Figure 8

78

Figure 9

Figure 10

3075 RPM
0.48 MILS

6065 RPM
0.64 MILS

Figure 11

6040 RPM
0.50 MILS

3120 RPM
0.41 MILS

2850 RPM
0.16 MILS

Figure 12

2670 RPM
1.56 MILS

3090 RPM
0.62 MILS

6040 RPM
0.56 MILS

Figure 13

LOW SPEED PINION
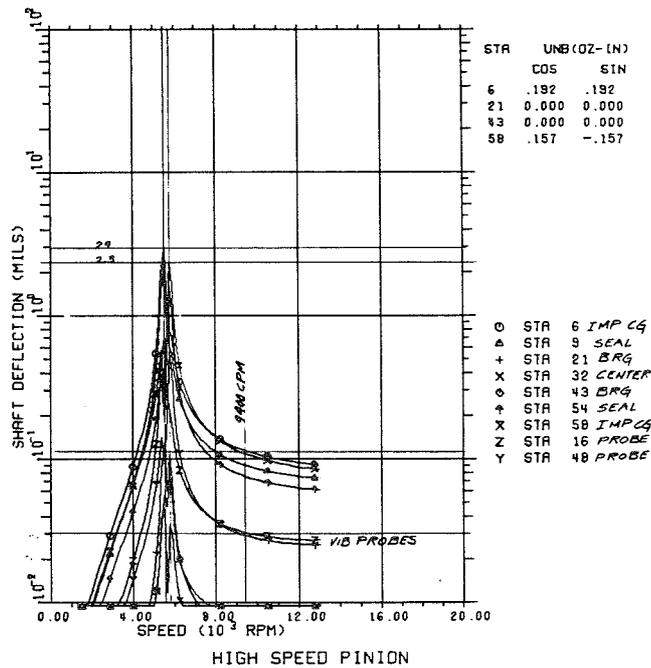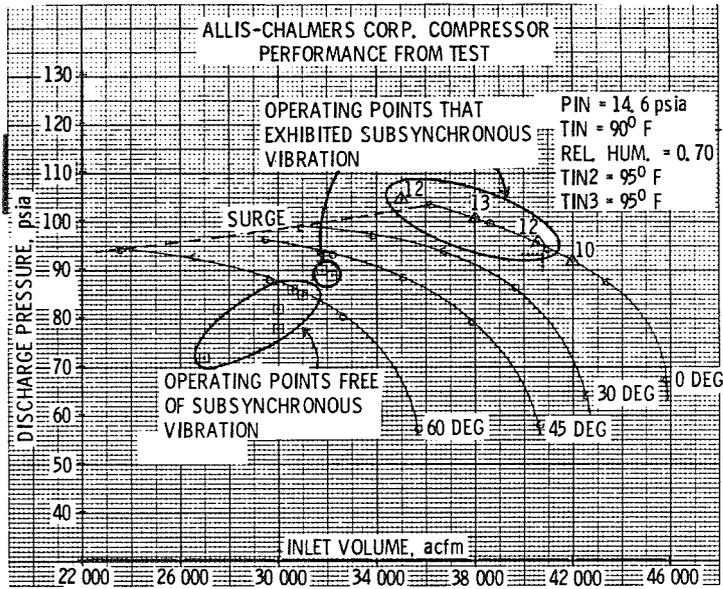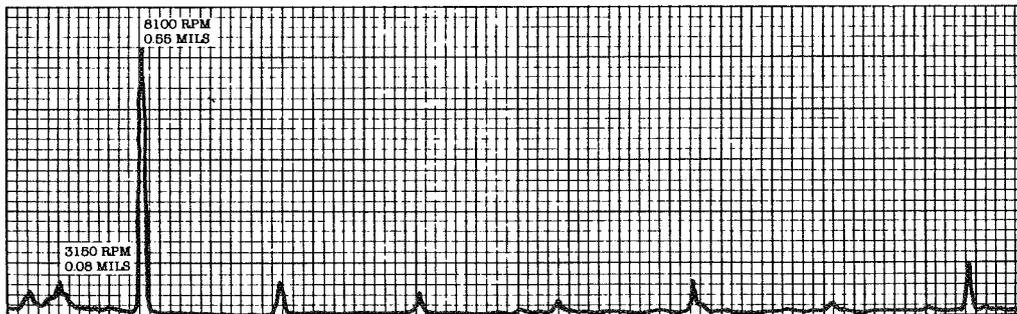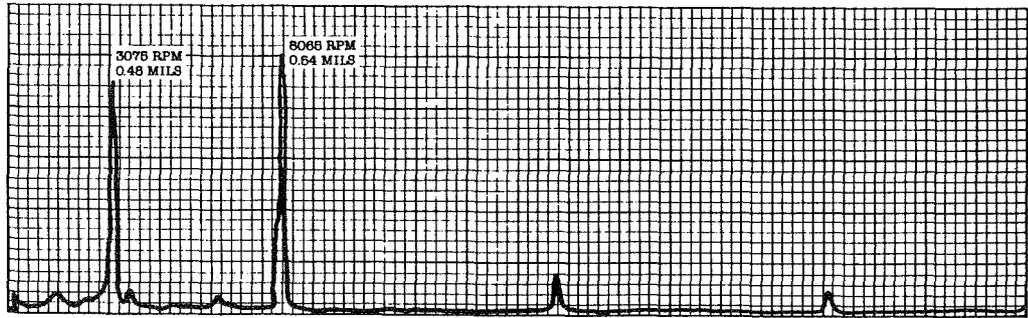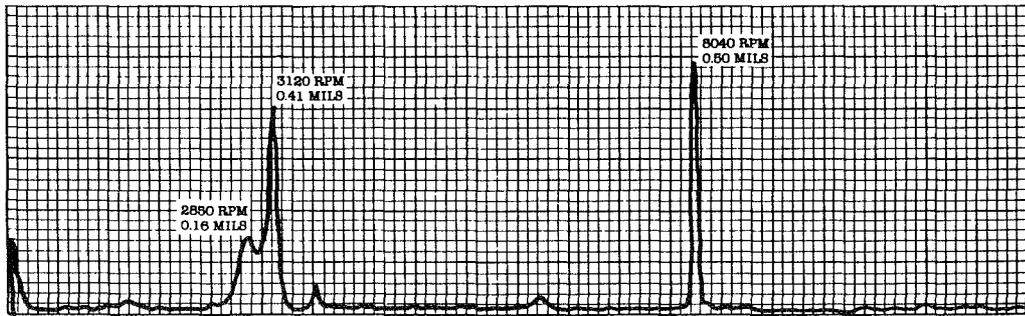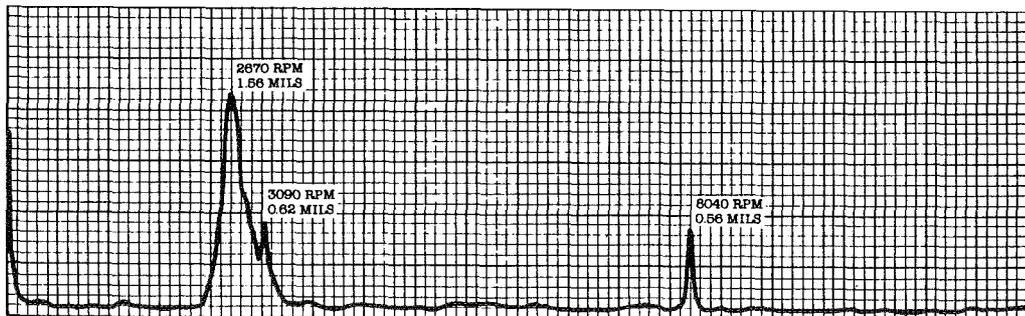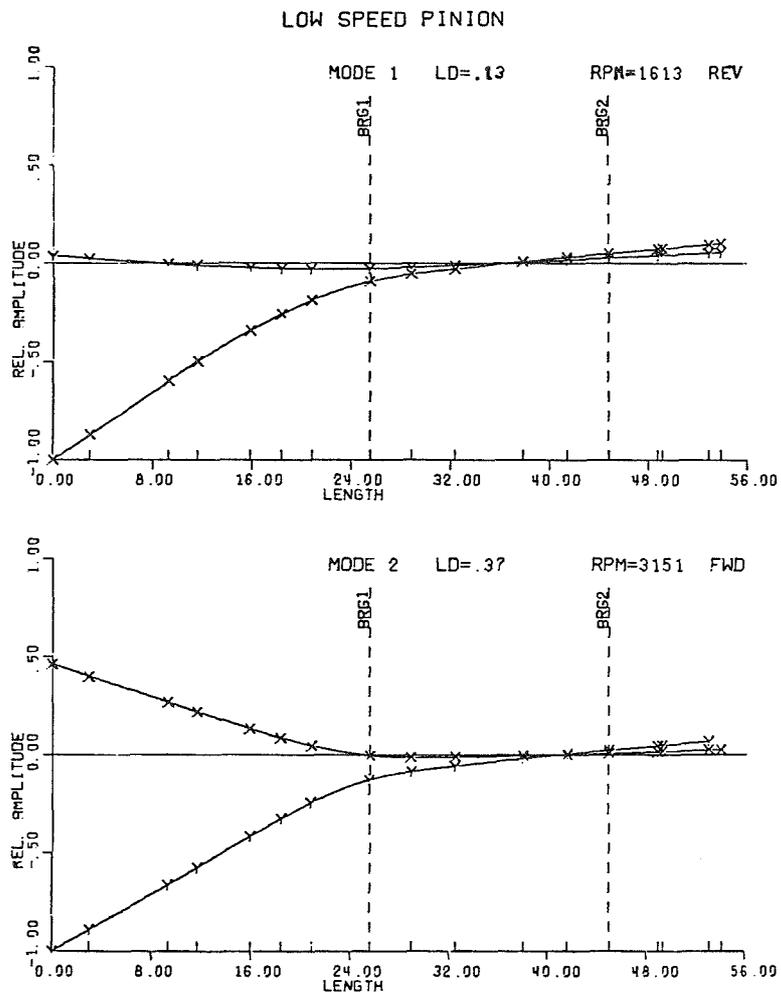
Figure 14

FIRST-STAGE BEARING
LOAD DIRECTION

BLIND-SIDE BEARING
LOAD DIRECTION
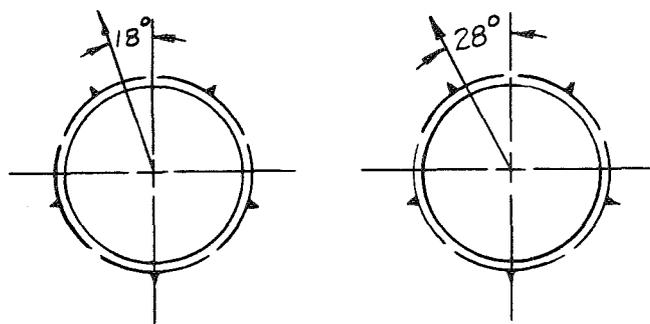
Figure 15

OVERHUNG GEAR COMPRESSOR — UNDAMPED
VERTICAL CRITICAL SPEEDS

CRITICAL SPEED SEARCH

CRITICAL #	BRG #1 STIFFNESS LB/IN	BRG #2 STIFFNESS LB/IN
1	968,170.	463,540.
2	714,580.	2,525,200.

ROTOR MODE SHAPE AT CRITICAL SPEED

CRITICAL SPEED
1   2582   RPM ⊙
2   10470 RPM △
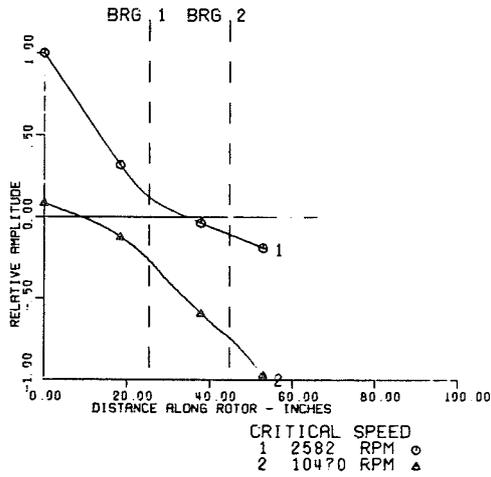
Figure 16

OVERHUNG GEAR COMPRESSOR
SYNCH. RESPONSE AT IMPELLER
(UNBALANCE BASED ON 10% OF ROTOR WEIGHT)
EXTERNAL FORCES DUE TO GEAR INCLUDED.

STA UNBAL ANG
IN.OZ
3   424   0.
⊙ IMPELLER

Figure 17

82

OVERHUNG GEAR COMPRESSOR - LOG DECREMENT VS. AERODYNAMIC DESTABILIZING
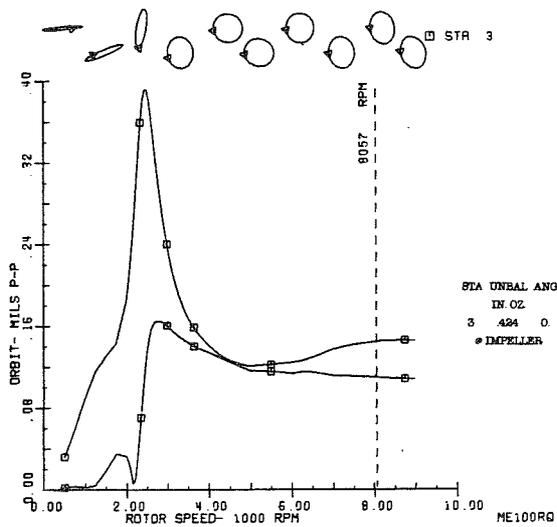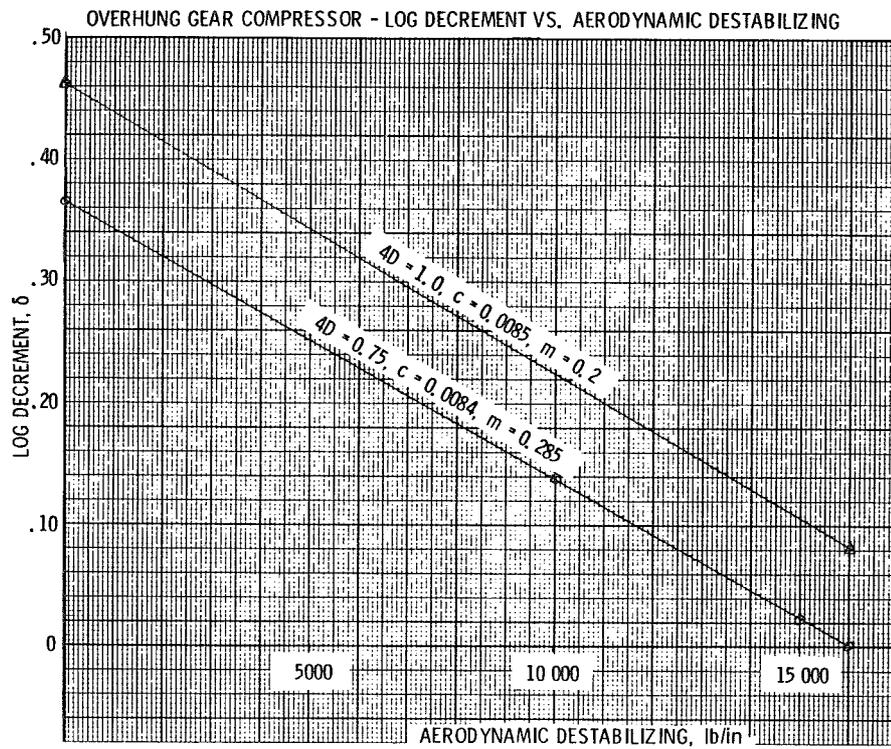
Figure 18

Page intentionally left blank

Aero-induced Vibrations in Centrifugal Compressors

Full load tests carried out on high pressure
centrifugal compressors confirmed the
presence of asynchronous vibrations due to
aerodynamic forces, mainly at flows nearing
surge. Analysis of the behavior of the rotors
would seem to suggest that there could be
aerodynamic excitation on the final stage.
The vibration analysis results are discussed
in light of this hypothesis.

L. BONCIANI*
P. L. FERRARA*
A. TIMORI*

Over the last few years, the use of centrifugal-compressors for high density gas compression services, such as injection of natural gas at high pressures, has become increasingly widespread (1) (2).

However, the early experiences on these machines revealed the occurrence of asynchronous vibrations, which at times had the result of limiting their range of applications (3) (4) (5).

In September 1975, a very high pressure (700 bar- 10,000 psi) compressor was tested at full load with natural gas. The test results are described in a previous paper (6).

Between the end of 1979 and the beginning of 1980, four different injection compressors were tested at full load with natural gas. Throughout testing, special attention was paid to investigating the vibrations along the compressor performance range, including surge. The performance of the four machines was qualitatively similar.

A detailed analysis of the results obtained on two of these machines follows. The first, designated compressor A, had the highest delivery pressure of those tested, the second, designated compressor B, handled gas having the highest molecular weight (ethane injection).

The first compressor, to be driven by a variable-speed gas turbine on-site, was tested with natural gas according to the ASME PTC 10, Class I, and at speeds between 74 and 112% of design. The second, to be driven by an electric motor on-site, was tested with natural gas according to the ASME PTC 10, Class I, with carbon dioxide (ASME PTC 10, Class III) and nitrogen (in completely off-design conditions). In all cases, asynchronous vibrations occurred when approaching surge. Analysis of the two rotors would seem to suggest that there could be aerodynamic excitation on the final stage. The vibration analysis results will be discussed in light of this hypothesis.

Characteristics of compressor A

The design features of compressor A are summerized in Table. I.

A cross-section of the five-stage compressor of in-line design is shown in fig. 1.

Fig. 2 shows the rotor responses for synchronous excitations (e. g. unbalancing) located in the middle and at both ends of the rotor. The amplitudes were calculated at the vibration probe locations.

Fig. 3 shows the damped natural lateral frequencies of the rotor (with logarithmic decrements) (7).

Fig. 4 shows the frequency response of the system to an asynchronous excitation. Amplitudes were again calculated at the vibration probe locations.

COMPRESSOR A (TYPE BCL 400/C)
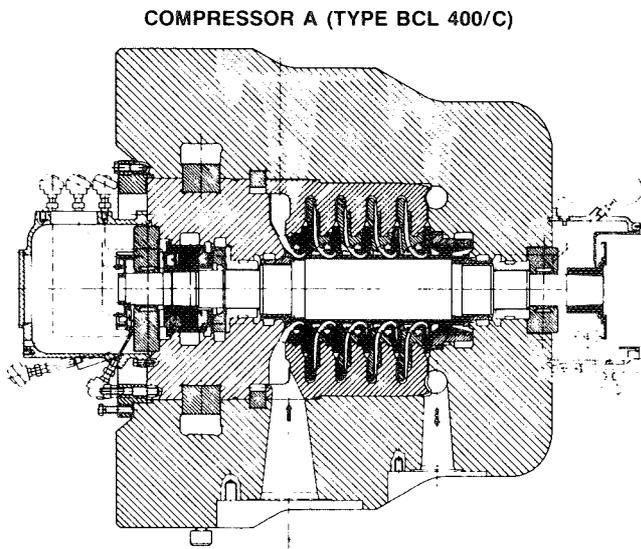
Fig. 1

TABLE I. - DESIGN FEATURES OF COMPRESSOR A

— suction pressure bar (psia)	171.7	(2490)
— suction temperature °C (°F)	48.9	(120)
— discharge pressure bar (psia)	394	(5715)
— design speed RPM	10,300	
— max continuous speed RPM	11,450	
— gas handled	natural gas	
— specific gravity	0.717	
— bearing type	tilting pad	
— driver	27,500 hp (ISO) gas turbine	
— coupling	diaphragm type	

This type of diagram, to which we will refer again later, has been developed to check the sensitivity to asynchronous excitations of these compressors, since experience of previous tests (6) demonstrated that such excitations could occur as a result of aerodynamic effects. Calculations were carried out for the complete operating speed range, assuming that an excitation force be applied to the final impeller, whose position was believed most critical from an aerodynamic standpoint. The diagram (fig. 4) indi-

COMPRESSOR A - SYNCHRONOUS RESPONSE
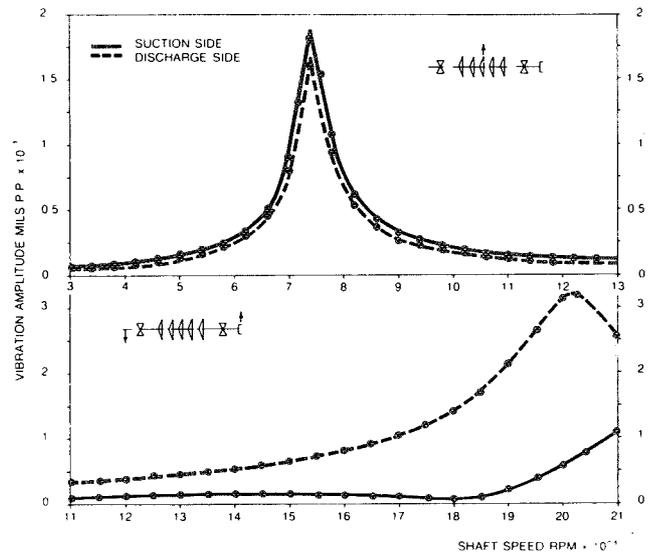
Fig. 2

COMPRESSOR A - DAMPED NATURAL FREQUENCIES
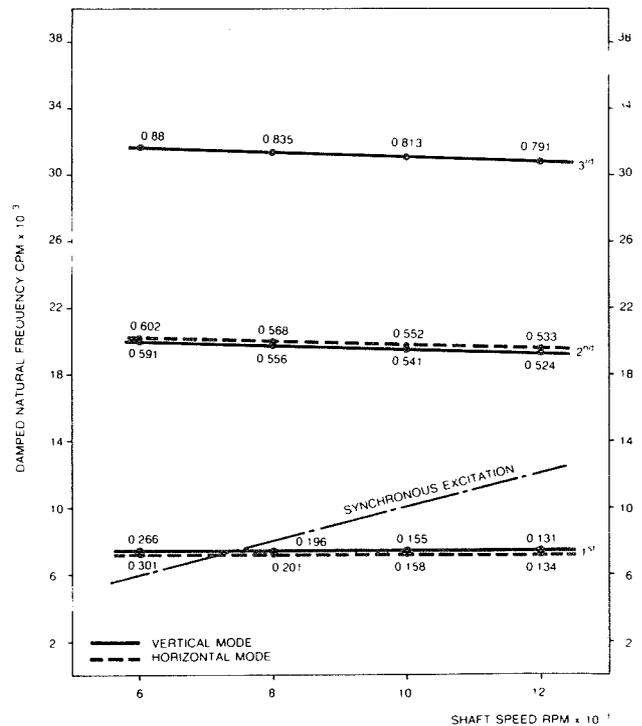
Fig. 3

COMPRESSOR A - ASYNCHRONOUS RESPONSE
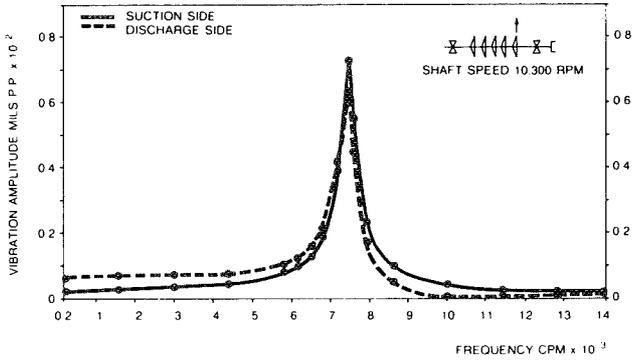
Fig. 4

COMPRESSOR A - DISCHARGE SIDE VIBRATION SPECTRUM AND SHAFT ORBIT AT 10,300 RPM
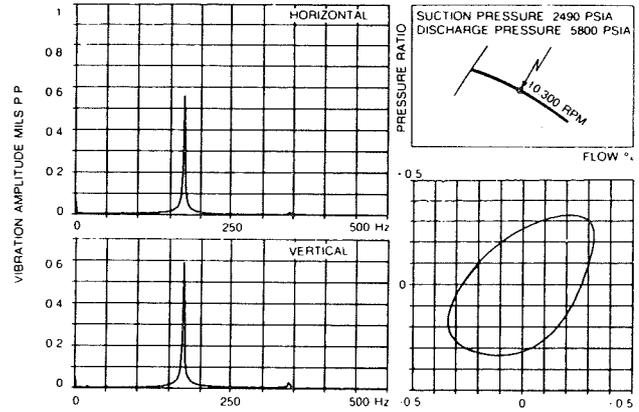
Fig. 6

COMPRESSOR A - TESTED PERFORMANCE CURVES
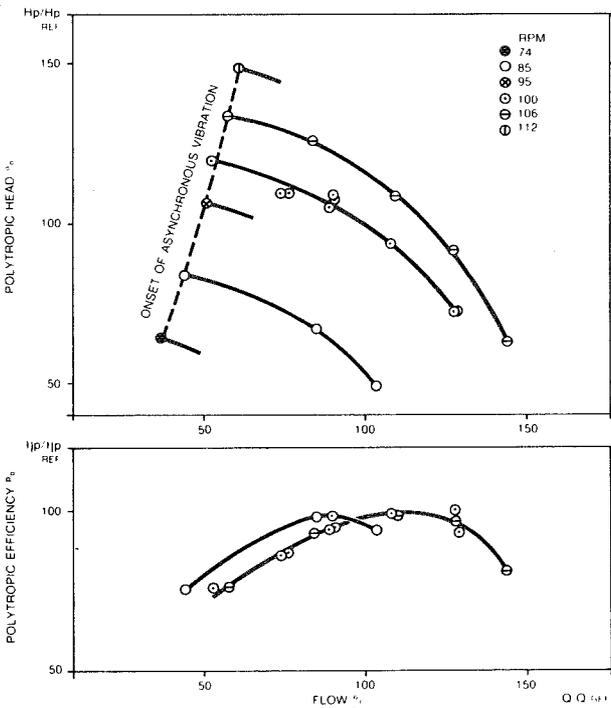
Fig. 5

cates the behavior at the design speed of 10,300 RPM. Similar behavior was been found for all speeds of the operating range.

Test results of compressor A

Upon succesful completion of the mechanical test, the compressor was installed on the outdoor facilities for full load testing. A two-shaft 35,000 hp (ISO) gas turbine was used to drive the compressor through the job step-up gear box. The gas was circulated in a loop provided with an air cooler. The gas system was completed by a throttling valve on the final delivery line, a blow-off valve, and a pressurizing station using reciprocating compressors to boost the inlet pressure to the desired value. All mechanical and thermodynamic data were processed during the test through a data acquisition system. Shaft vibrations were detected by two no-contact probes at 90° on each bearing. Two axial probes were also provided, one to monitor the shaft axial movement, the other to monitor the phase angle.

The compressor was tested according to ASME PTC 10, Class I, using natural gas. Tests were also carried out at speeds between 74 and 112% of design with a maximum discharge pressure of 7100 psi. During the tests, the gas composition was constantly checked, while suction pressure and temperature were maintained within 1% of design value.

Fig. 5 shows the polytropic head and efficiency curves versus flow as percentages of the reference values at design speed. The compressor exhibited an extremely wide operating range with 20% increase in polytropic head between reference and minimum flow at constant speed. It is worthwhile noting that none of the tested points at minimum flow corresponded to surge on the test loop, but rather to the onset of a well-defined asynchronous vibration.

At design point, and, in general, for flows other than minimum, the compressor presented an extremely clearcut vibration spectrum (fig. 6). As can be seen, the vibrations were practically wholly synchronous, and there were no other frequencies worthy of note.

When delivery pressure was increased at a constant speed in the area right by surge (corresponding to approximately 50% of reference flow at design speed), a low frequency vibration with amplitude comparable to the synchronous one and often exceeding it, invariably appeared. The occurrence of this asynchronous component was sudden, as is re-vealed by the time histories presented (fig. 7, 8).

The remarks that can be made concerning the experimental data are:

— the asynchronous vibration frequencies were in an approximately constant ratio to the RPM
— the asynchronous component of the vibrations usually increased as rotating speed increased
— the basic frequency at which excitation occurred corresponded to approximately 8% of RPM
— for flows slightly exceeding those characterizing the occurrence of excitation at 8% RPM, excitation at approximately 27% RPM often occurred. This disturbance was usually of slight importance and did not seem to be appreciably modified by the appearance of excitation at the lower frequency.

Characteristics of compressor B

The design features of compressor B are summarized in Table II.

COMPRESSOR A - TIME HISTORIES AT 10,300 RPM
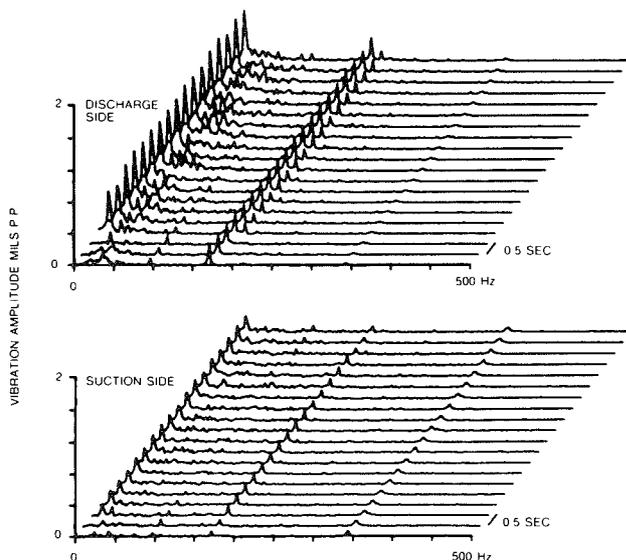
Fig. 7

COMPRESSOR A - TIME HISTORIES AT 10,900 RPM
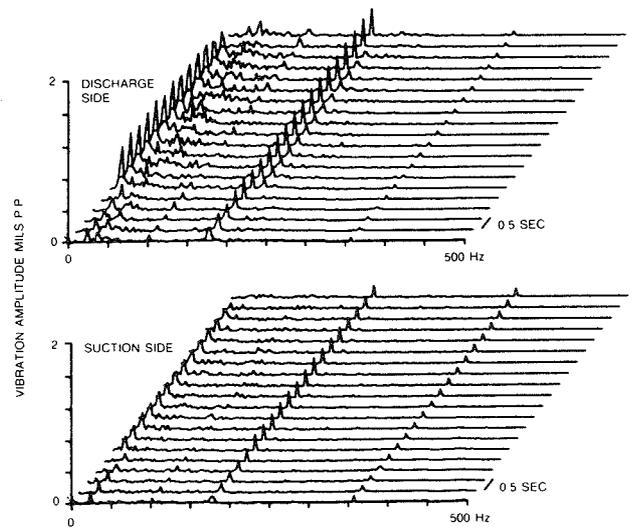
Fig. 8

COMPRESSOR B (TYPE BCL 400/B)

Fig. 9

A cross-section of the six-stage compressor of in-line design is shown in fig. 9.

Fig. 10 shows the rotor responses for synchronous excitations (e.g. unbalancing) located in the middle and at both ends of the rotor. The amplitudes were calculated at the vibration probe locations.

Fig. 11 shows the damped natural lateral frequencies of the rotor (with logarithmic decrements) (7).

Fig. 12 shows the frequency response of the system for asynchronous excitation, as described for compressor A. The diagram indicates the response to an excitation force applied on the final impeller, with the compressor running at the design speed of 9,220 RPM.

It should be noted that compressor B exhibited a greater sensitivity to asynchronous excitation than compressor A, in particular for frequencies not higher than the first lateral mode. Compressor B, being driven by an electric motor, required clearances on journal bearings higher than those on compressor A, which was gas-turbine driven. In addition, compressor B featured a higher number of stages of smaller diameter.

TABLE II. - DESIGN FEATURES OF COMPRESSOR B

— suction pressure bar (psia)	69.5	(1008)
— suction temperature °C (°F)	88	(190)
— discharge pressure bar (psia)	220	(3190)
— design speed	9,220 RPM	
— gas handled	ethane	
— specific gravity	1.049	
— bearing type	tilting pad	
— driver	10,000 hp electric motor	
— coupling	diaphragm type	

COMPRESSOR B - SYNCHRONOUS RESPONSE

Fig. 10

COMPRESSOR B - DAMPED NATURAL FREQUENCIES
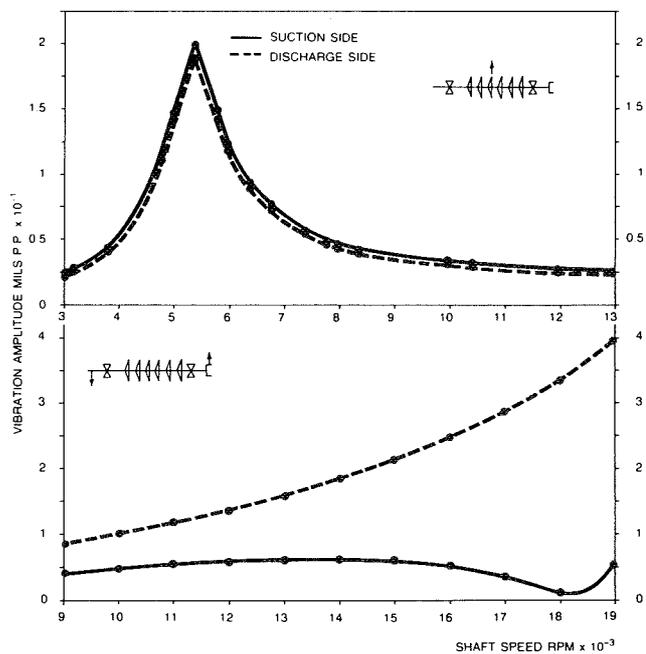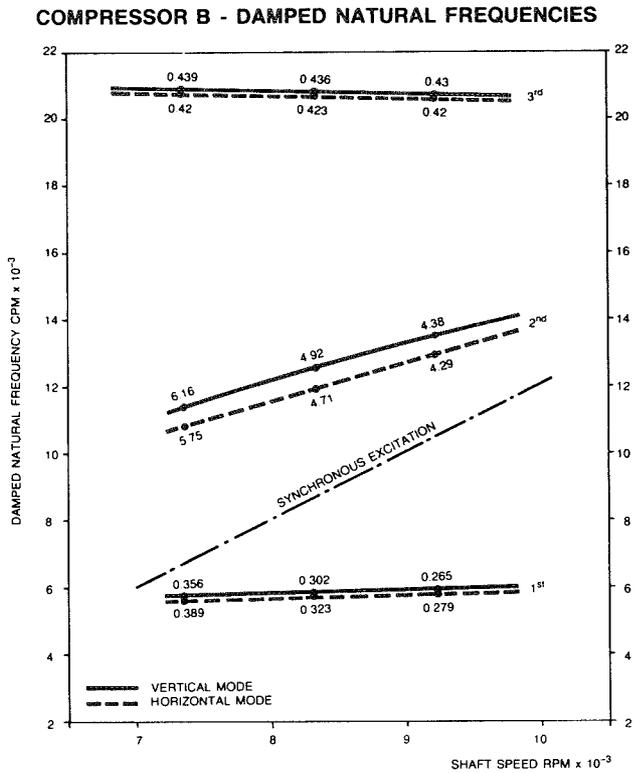
Fig. 11

COMPRESSOR B - TESTED PERFORMANCE CURVES
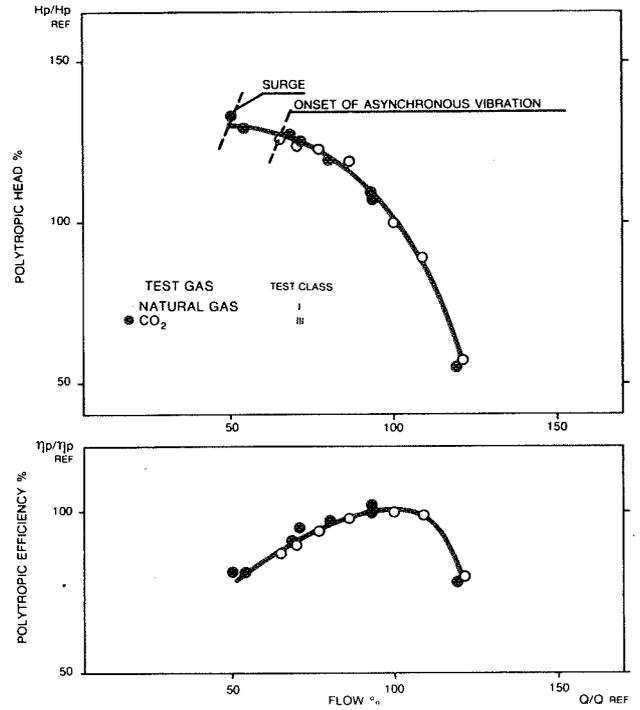
Fig. 13

COMPRESSOR B - ASYNCHRONOUS RESPONSE
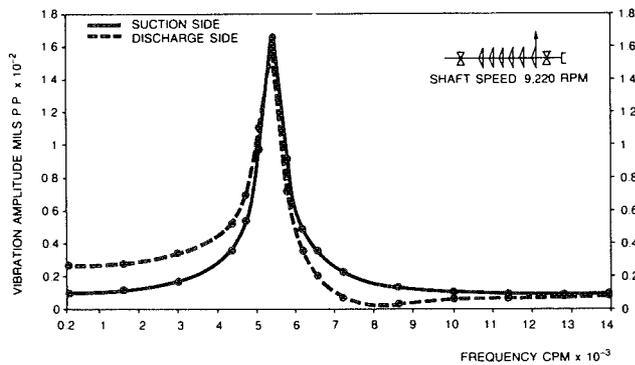
Fig. 12

Test results of compressor B

Upon successful completion of the mechanical test, the compressor was installed on the second outdoor facility for full load testing. A two-shaft 14,600 hp (ISO) gas turbine was used to drive the compressor through a shop step-up gear box. The gas was circulated in a loop similar to the one described for compressor A. Data processing, vibration read-out, and analyses were also handled in a similar way. The compressor was tested, according to ASME PTC 10 in Class I, with natural gas at design speed, and in Class III, with carbon dioxide at 8,250 RPM.

An additional test with nitrogen in completely off-design conditions was also carried out at 10,500 RPM and normal suction pressure.

Fig. 13 shows the polytropic head and efficiency versus flow for both natural gas and carbon dioxide tests.

The compressor exhibited a satisfactory operating range, with an increase in polytropic head of 25%

between maximum efficiency and minimum flow at constant speed.

As previously noted for compressor A, the spectrum of the vibrations was practically wholly synchronous at the design point and, in general, for flows other than minimum (fig. 14). When the compressor flow was decreased below 65% of maximum efficiency flow, asynchronous vibrations, with characteristics similar to those occurring on compressor A, appeared. The time histories (fig. 15, 16, 17) show a sudden onset of asynchronous vibrations, as for compressor A. We note that, on suction side, vibration readings were affected by a run-out disturbance.

The following remarks can be made concerning experimental data:

— the asynchronous vibration frequencies were in an approximately constant ratio to the RPM
— the asynchronous component of the vibration increased when increasing the speed from 8,250 RPM (test with carbon dioxide) to 9,220 RPM (test with natural gas), while decreased when increasing the speed from 9,220 RPM (test with natural gas) to 10,500 RPM (test with nitrogen).
— the basic frequency at which excitation occurred corresponded to approximately 15% of RPM
— no significant asynchronous components were found other than 15% of RPM.

COMPRESSOR B - TIME HISTORIES AT 9,220 RPM

Fig. 15

COMPRESSOR B - DISCHARGE SIDE VIBRATION SPECTRUM AND SHAFT ORBIT AT 9,220 RPM

Fig. 14
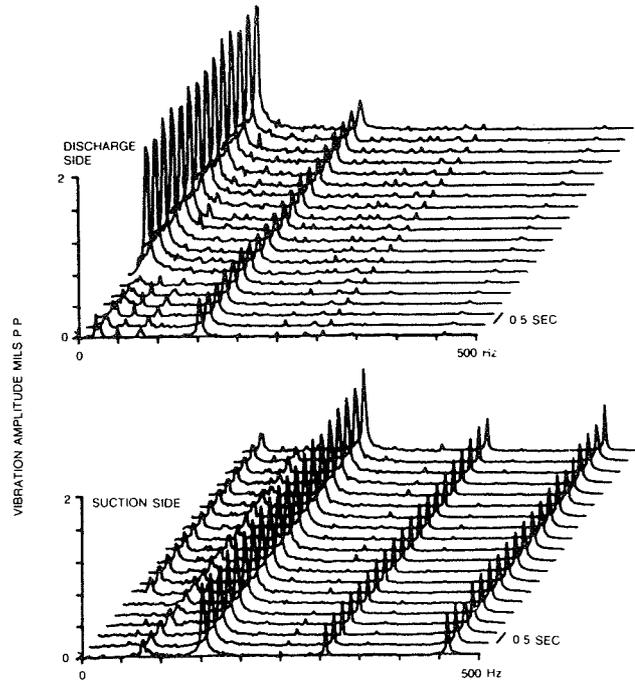
An attempt to correlate test data

Let us assume, as a working hypothesis, that the situation occurring is due to an aerodynamic excitation on the final stage. In such case, the following conditions should be verified:

a) Ranging the Mach numbers during the tests in a region where no appreciable variation of the stage characteristics occurs, the phenomenon should appear for the same value of the flow coefficient of the last stage. This may be considered valid whether the aerodynamic disturbances derive from the impeller itself or from the statoric components. Considering the test conditions, it could be demonstrated that the inlet flow coefficient of the last stage may be represented by the inlet flow coefficient of the compressor (φ) times the ratio between the discharge (v_2) and suction (v_1) specific volumes. In accordance with this hypothesis, the phenomenon should thus appear

91

for an almost constant value of φ (v_2/v_1).

b) As aerodynamic conditions are similar, it is reasonable to assume that the amplitude of the stall cell is nearly the same. Considering the discharge density representative of the mean density on the final stage, the excitation force should be proportional to the product of the discharge density (γ_2) and the impeller tip speed (U_2) squared:

$$F = \text{const. } \gamma_2 \, U_2^2.$$

As a consequence, M_D and M_S respectively being asynchronous vibration on the discharge and suction side amplitudes at pick-up location when a unit force is applied on the last impeller, the tested amplitudes versus speed should be:

$$A_D = \text{const. } M_D \, \gamma_2 \, U_2^2$$
$$A_S = \text{const. } M_S \, \gamma_2 \, U_2^2$$

c) If the theory regarding the location of the excitation (last stage of each rotor) is valid, higher asynchronous vibrations should occur at the discharge side.

The ratio between the amplitudes at both ends can be theoretically estimated from the asynchronous frequency response of the rotors (fig. 4, 12).

d) Most of the theories on rotating stall and relevant experimental data (8) (9) (10) indicate constant ratio between stall frequency and rotating speed, so that it is reasonable to expect asynchronous vibration frequencies proportional to RPM.

Fig. 18 shows, for both compressors, the discharge flow coefficient φ (v_2/v_1) versus the suction flow coefficient φ. It should be noted that the onset of the asynchronous vibrations occurred for a constant value of the discharge flow coefficient. This would also appear valid for compressor B, even running it with nitrogen in a complete off-design condition. Point a) is, therefore, verified.

COMPRESSOR B - TIME HISTORIES AT 8,250 RPM
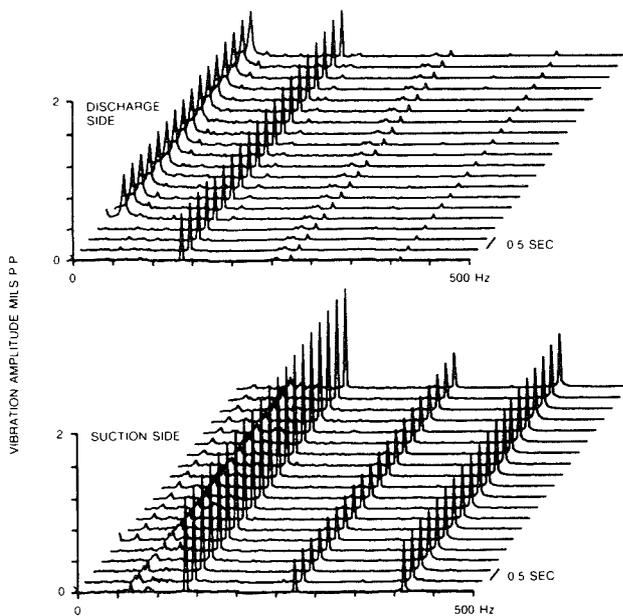
Fig. 16

COMPRESSOR B - TIME HISTORIES AT 10,500 RPM
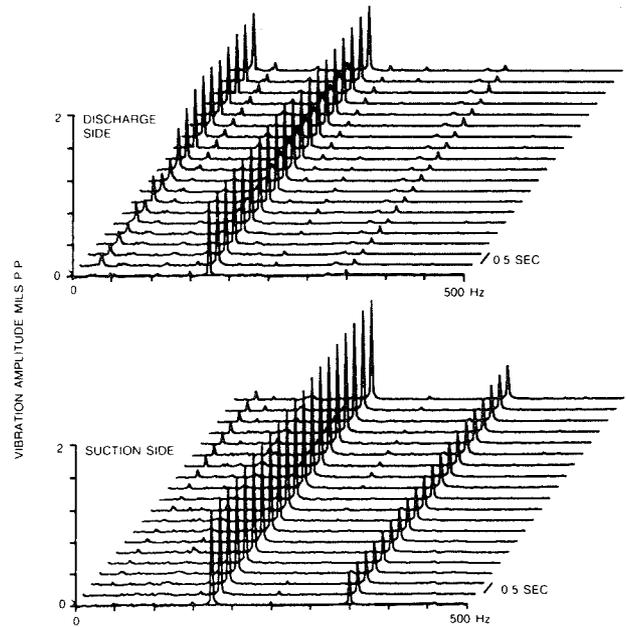
Fig. 17

Analysis of the asynchronous vibration component of the discharge and suction sides (fig. 7, 8, 15, 16, 17) shows that the amplitude of vibration on the discharge side was always higher than on the suction side, as theoretically predicted (fig. 4, 12). This would appear to verify point c).

As already pointed out in the preceding paragraphs, an analysis of the vibration carried out with a real time spectrum analyzer clearly showed that the frequency of the asynchronous component was in an approximately constant ratio with the rotating speed. This ratio is .08 for compressor A and .15 for compressor B. This seems to verify point d).

Let us now attempt to verify point b).

Assuming the onset of asynchronous vibrations at 10,300 RPM as a reference situation for compressor A and that of asynchronous vibrations at 9,220 RPM as a reference situation for compressor B, fig. 19 shows, as a function of RPM:

EXPERIMENTAL VERSUS EXPECTED VIBRATION AMPLITUDES

COMPRESSOR A

COMPRESSOR B
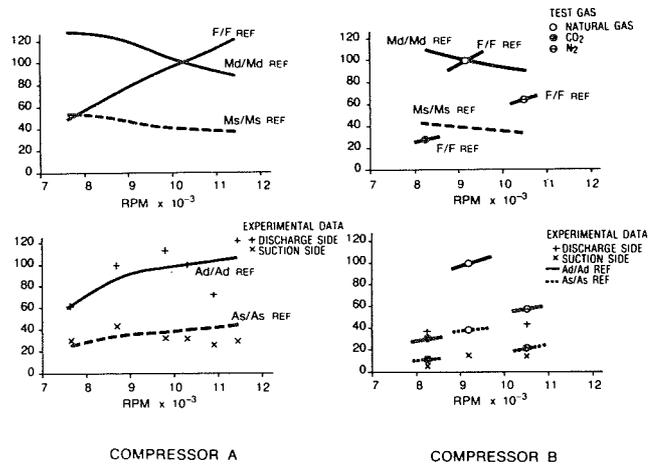
Fig. 19

ONSET OF ASYNCHRONOUS VIBRATION VERSUS FLOW COEFFICIENT
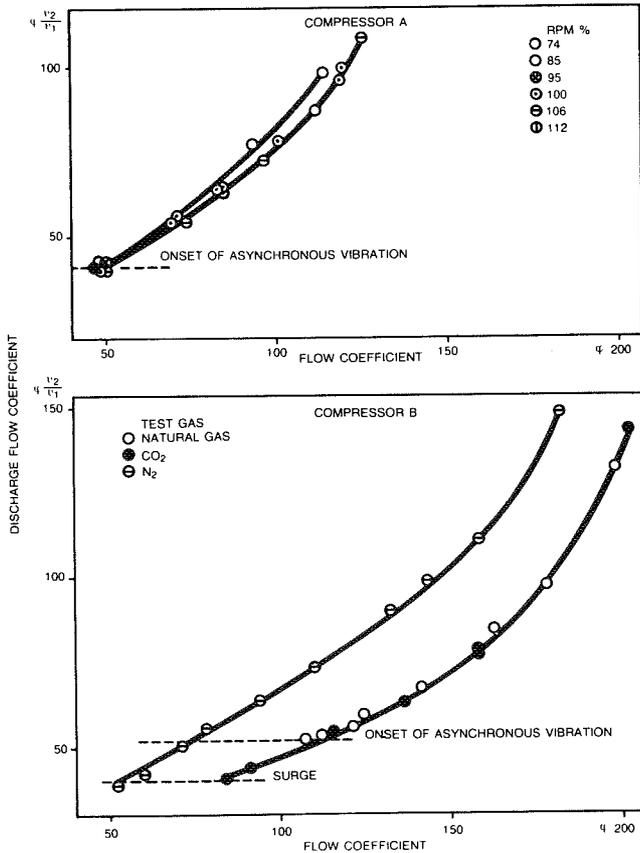
Fig. 18

— the relative amplitude of the calculated asynchronous vibration at the discharge and suction sides for a constant excitation force acting on the last impeller $(M/M_{R1.1})$

— the relative amplitudes of the excitation force (F/F_{REF})

— the relative amplitude of the asynchronous component of the vibration at the discharge and suction sides (A/A_{REF}) compared with experimental data. (Of course, $A/A_{REF} = M/M_{REF}\ F/F_{REF}$.)

It should be noted that specific delivery volume (evaluated using the Benedict, Webb, Rubin equation generalized by Starling) progresses in such a way as to almost exactly balance the tip speed squared. As a result, F is plotted practically as a straight line. A similar procedure was followed for compressor B, for which data exists at three different rotation speeds, each of which corresponds to one of three different gases (fig. 19).

Despite the fact that the discrepancies are hardly negligible, the agreement may be termed fairly satisfactory, considering the type of measurements. In particular, it can be noted that even in the test using nitrogen at 10,500 RPM (114% of the design speed) performed on compressor B, the asynchronous vibration amplitude recorded is in satisfactory agreement with the predicted one.

These considerations, of course limited by the small amount of available data, would seem to indicate that shaft asynchronous vibrations are excited by aerodynamic forces which are not of a self-excited nature.

COMPRESSOR A - DISCHARGE SIDE AT 11,450 RPM
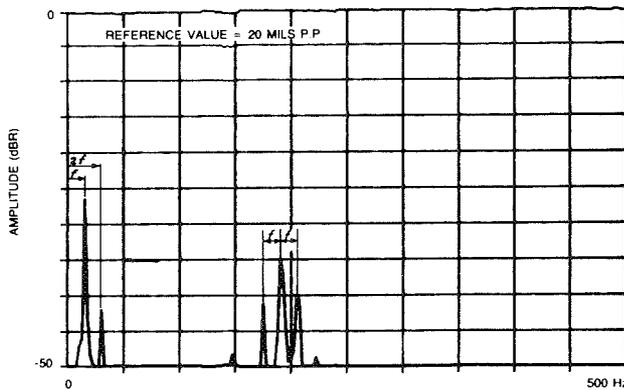
Additional remarks

The analysis of these two cases ends on a curious note.

Examining the vibration spectrum on a logarithmic scale, as for example in fig. 20, it can be seen that, when the low frequency component (f) appeared, small components at 2f and $1 \times RPM \pm f$ always appeared as well.

Their amplitude usually became more pronounced as the amplitude of vibration at frequency f increased. The phenomenon appeared on both compressors and, moreover, has been observed in other compressors approaching surge. A possible explanation of the phenomenon most likely lies in a nonlinear response of the bearing system. In effect, if the forces on the bearings are represented by a series development truncated at the 2nd order in the shaft displacement (instead of at the 1st as is normal in a linear analysis) and assuming that the excitation consists of a sinusoidal disurbance of frequency $1 \times RPM$ and another sinusoidal disturbance of frequency f, a small perturbation method makes it easy to find additional components at $2 \times RPM$, $2 f$ and $1 RPM \pm f$ (modulation of the low frequency signal with carrier $1 \times RPM$).

Further investigation is needed to ascertain the validity of the explanation proposed.

Conclusions

Two compressors handling high density gas were investigated.

In both cases, disturbances were observed in the zone nearing surge, which could be explained by aerodynamic excitations on the last stage.

The vibrations observed do not appear to be of a self-excited nature.

As a consequence, artificial introduction in the log decrement calculation of destabilizing forces proportional to rotor displacement and normal to it, would not seem to be a satisfactory approach.

Proper evaluation of the stability of this type of rotor can be made by asynchronous excitation frequency response. As a consequence, theoretical-experimental investigations into single stages are required in order to determine amplitude and frequency of the excitation forces.

BIBLIOGRAPHY

(1) A. MEOZZI: *Natural Gas Reinjection Stations with Turbocompressor Unit.* GE, ESOA Lisbon, May 1972.

(2) C. H. GEARY, JR, L. P. DAMRATOWSKI, C. SEYER: *Design and Operation of the World's Highest Pressure Gas Injection Centrifugal Compressors.* Paper no. O.T.C. 2485 presented at the *Offshore Technology Conference*, Houston, Texas, May 1976.

(3) K. J. SMITH: *An Operation History of Fractional Frequency Whirl. 4th Turbomachinery Symposium*, Gas Turbine Laboratories, Texas A & M University, October 1975, pp. 115-125.

(4) D. D. MILES, D. W. FOWLIE: *Vibration Problems with High Pressure Centrifugal Compressors*, presented at *ASME Petroleum Group Conference*, Tulsa, Oklahoma, September 21, 1975.

(5) J. C. WACHEL: *Nonsynchronous Instability of Centrifugal Compressors*, ASME paper No. 75-PET-22.

(6) P. L. FERRARA: *Vibrations in Very High Pressure Centrifugal Compressors*, ASME paper No. 77-DET-15.

(7) J. W. LUND: *Stability and Damped Critical Speeds of a Flexible Rotor in Fluid-Film Bearings*, ASME paper No. 73-DET-103.

(8) O. ACTON: *Studio sperimentale e teorico dello stallo in un compressore centrifugo*, Atti dell'Accademia delle Scienze di Torino Vol. 95, 1960-61.

(9) A. ANTONINI, A. D. MARTEGANI: *Sui fenomeni di instabilità fluido-dinamica in una soffiante centrifuga*, La Termotecnica Vol. XXXI n. 4 - 1977.

(10) A. N. ABDELHAMID, N. H. COLWILL, J. F. BARROWS: *Experimental Investigation of Unsteady Phenomena in Vaneless Radial Diffusers*, ASME Journal of Engineering for Power, Vol. 101, January 1979, pp. 52-60.

THE PARAMETERS AND MEASUREMENTS OF THE DESTABILIZING
ACTIONS OF ROTATING MACHINES, AND THE
ASSUMPTIONS OF THE 1950'S

Donald E. Bently
Bently Nevada Corporation
Minden, Nevada 89423

SUMMARY

Employing a rotor built to produce one of the forward circular self-excited category malfunctions known as "gas whip", "steam whip", or "aerodynamic whip", it is possible to show the results of deliberate perturbation while the rotor is still in stable operation. This test indicates that the destabilizing actions are not mystical or unmeasurable and that the mathematical modeling done today can be more realistic than the models assumed in the 1950s and which still exist essentially unchanged more than 25 years later. The continued use of the original modeling is unfortunate in that it has led to the use of inappropriate words to express what is happening and a lack of full understanding of the category of forward circular whip instability mechanisms. It is hoped that this work, although incomplete, will be followed by better mathematical theory and better experimental tests to help clarify the mysteries of rotating machinery stability.

SYMBOLS

The measurements and calculations are expressed in both SI and English units.

Q   Amplification factor (dimensionless), as specified for lateral and angular position, and for synchronous or balance resonance speed

ζ (Zeta) damping factor (dimensionless) $= 1/2Q = D/2\sqrt{KM}$

ω (Omega) angular velocity (radians/sec)

K   Spring coefficient (lb/in)

M   Mass (lb sec^2/in)

D   Damping coefficient (lb sec/in)

SYSTEM DESCRIPTION

The test rotor kit for this study used a slightly tapered aluminum wheel 3.2 inches long and 4.25 inches in diameter mounted at the mid-point of the span on a 0.375-inch diameter rotor shaft. The tapered wheel was fitted into an

equally tapered seal housing mounted to the base of the rotor kit. The seal housing was designed for adjustment in the axial direction thereby permitting selection of a desired radial clearance from the aluminum tapered wheel. A diametral clearance of 30 mils was employed for all of these tests. An antifriction bearing was employed on the driver end of the rotor system and a bronze OIL-LITE bearing was used on the free end of the system. The total bearing span was 23.25 inches.

Dynamic motion measurments were taken adjacent to the seal housing with Proximity transducers mounted in an X-Y orientation. The data from the transducers was conditioned via a Bently Nevada Digital Vector Filter (DVF 2) and an HP 3582A Spectrum Analyzer and displayed on a Tektronix oscilloscope. The digitized data from these instruments was then acquired through the Bently Nevada ADRE Computer System and reduced into polar, Bode, and spectrum cascade graphical formats.

TEST PROCEDURE

The rotor system speed was increased from 0 to 10,000 rpm; however, the acceleration rate was very slow to provide accurate identification of the translational and pivotal balance resonance speeds. The first balance resonance was observed at 1550 rpm. The test procedure was as follows:

ROTATIVE SPEED TESTING

The rotor system was slowly accelerated and the location of the first balance resonance was plotted and defined.

The rotor system was then accelerated to the rotative speed at which the onset of instability occurred.

The nature and frequency of the instability were then described.

The system was then accelerated until the shaft deflection initiated a rub between the tapered wheel and the seal housing.

This data base was then presented in polar, Bode, and spectrum cascade formats.

PERTURBATION TESTING

A free-spinner perturbation device was attached to the rotor system adjacent to the seal housing.

With the rotor system held stationary, the free spinner was accelerated to 8000 rpm. This procedure documents the location of the first balance resonance.

The rotor system was then operated at a constant speed (approximately 4000 rpm). The free spinner perturbation device was operated in the forward mode (rotating in the same direction as the rotor system) and also in the reverse mode (opposite rotation of the rotor system).

STEADY STATE ATTITUDE ANGLE TEST

A spring scale was attached to the perturbation spinner keeping it from rotating but allowing application of a known soft unidirectional preload (like gravity) in order to determine the steady-state attitude angle of this rotor system at various speeds.

RESPONSE OF THE TEST ROTOR SYSTEM

Using a gap setting of 30 mils diametral clearance, it was observed that with forward circular whip at the self-balance resonance speed ("first critical") of 1550 rpm the rotor became unstable at about 6000 rpm. This is shown in the "There it is; darned if it isn't " cascade plot of figure 1. The polar plots and Bode´ plots of the rotor system response with deliberate unbalance shown in figures 2, 3, and 4 confirm the self-balance resonance rpm to be centered at 1550 rpm.

A further test was run with the stator removed to confirm that contributions from other forward circular whip categories, especially internal friction, were not making large contributions to the action. It is the nature of rotor systems that this category is distinctly mutually aiding and abetting (in fact it is only the lagging attitude angle mechanisms of dry, semi-dry, and lubricated rubs that provide a limit cycle of these instabilities). The rotor exhibited about a 5 degree synchronous leading attitude angle through 10,000 rpm; thus, it was concluded for this fairly basic test that the other contributions were negligible.

The synchronous amplification factor Q (from figure 3) is approximately 6.6, so the damping factor ζ is about 0.075.

Next, the free spinner was run in the forward direction with just sufficient unbalance to drive the system without rubbing at the resonant peaks shown in figure 8. Obviously, the translational self-balance resonance damping factor is reduced virtually to zero, due to the existence of the destabilizing aerodynamic whirl forces. Figures 5, 6, 7 and 8 show this action.

The next test was run in exactly the same manner except that the perturbation from the free spinner is the reverse of shaft rotation. The cascade, polar and Bode´ plots are shown in figures 9, 10, 11, and 12. The evidence that the aerodynamic forces are providing a net force adding to the damping to the reverse perturbation may be observed. The reverse resonance amplification factor is approximately Q = 2, yielding a reverse resonance damping factor of ζ = 0.25.

It may be observed from figure 1 that the resonance increases from 1580 rpm with rotative speed of 3800 rpm to 1980 rpm at a rotative speed of 6800 rpm. Since this system has very little gyroscopic action for the translational balance resonance, and is not yet rubbing at 6800 rpm, it must be concluded that an additional direct spring is being added by the gas bearing. A calculation by the point transfer matrix method shows that for the resonance to increase by that amount, the gas bearing has an added 30 lb/in stiffness at its lateral location at the rotative speed of 6800 rpm. This effect seems to increase linearly with rotative speed.

The seal in the cartoon (figure 13) demonstrates the delicate balancing act that any bearing or bearing-like area always has in either a liquid, gas, or mixed medium. With the vertical input force shown, the shaft is moved over with just enough positive attitude angle to allow the lubrication wedge to balance the load exactly. In the situation of oil whip, steam whip, pumping whip, internal friction whip and all the rest of the forward circular self-excited instability mechanisms except oil whirl, it is easy to see that if a force were set up which acted counter to the system damping such as to nullify the effect of the damping, then the shaft is restrained only by the $(K-\omega^2 M)$ term. Below a self-balance resonance region the spring constant K predominates, above a resonance the $\omega^2 M$ term predominates. However, exactly at resonance, shaft orbit energy is exchanged between kinetic and potential energy (evenly between spring and mass). The limit size of the shaft orbital whipping is determined by additional drag-type damping from dry, semi-dry, and lubricated rubbing at seals and bearings.

While the steady-state attitude angle apparently can be any value (for this particular forward circular instability mechanism), high positive attitude angle (in the direction of rotation) is an indicator of a tendency toward instability. This test rotor, however, exhibited only 20 degrees positive steady-state attitude angle at 5000 rpm.

The situation of the very commonplace oil whirl forward circular instability is a most unusual type of instability mechanism. Rather than determining its frequency from spring and mass, it is reliant on the average speed of lubricant around the bearing and sets up oscillation by a difference equation which acts like a second order differential equation but is frequency dependent on rotative speed. Further, pure oil whirl will occur only when the steady-state attitude angle reaches and attempts to exceed 90 degrees.

In figures 2, 3, and 4 a small structural resonance at approximately 1600 rpm, caused by local variations in amplitude and phase on the Bodé plots may be observed, and also a pivotal balance response at 7800 rpm, but both of these may be ignored in this study.

For 30 years many experimenters have noted that these forward circular self-excited mechanisms have a tendency to get locked into 1/2, 1/3, 4/9, etc., of rotative speed. This author spent many hours puzzling about that tendency until he observed that it was simply a separate, resultive Mathieu

effect from the nonlinearities of the partial rub. The mechanism of the Mathieu, Hill, Meissner, Duffing equation as applied to rotating machinery was described and documented by this author six years ago in an ASME paper, and recently further studied by D. Childs and by M. Adams. Any integer fraction of rotative speed may be latched onto by way of the Mathieu action, but this effect has very little to do with the prime action. It does, however, cause upward frequency shift in the "There It Is Again" cascade plots shown in figure 1.

On the general subject of rotor instability, it should be noted that there is a Mathieu effect that is a full reverse circular self-excited action, but it requires such poor damping to reverse orbiting action that this malfunction category remains a laboratory curiosity, and does not seem to appear in operating machinery.

FREQUENCY OF OCCURRENCE OF THE FORWARD CIRCULAR WHIRL AND WHIP SELF-EXCITED MECHANISMS RELATIVE TO ROTATIVE SPEED AND TO SELF-BALANCE RESONANCE SPEEDS

Oil Whirl: This mechanism occurs at an average rate of lubricant travel around the bearing, from 15% of rotative speed on a lightly loaded starved bearing to 48% of rotative speed (usually in the 40 to 48% speed range), and is governed by the relative roughness of shaft and bearing. It can be pulled to 50% or a little higher with a smooth bearing and rough shaft, but this is rarely a consideration. It can also be locked to any integral fraction of rotative speed by a resultive Mathieu action and must have 360 degree lubrication, except for the lightly loaded starved case. The 360 degree lubricant may be pure liquid, pure gas, or a mixed flow. The bearing with stable void islands in the high clearance area exhibits a classical Half Sommerfeld Curve and never can oil whirl as long as that is maintained. Pure oil whirl, like internal friction, must exhibit very high positive attitude angle.

Oil Whip, Radial and Thrust: This mechanism occurs at the self-balance resonance nearest the 40 to 48% rotative speed. With poor system damping it may occur from 15 to 85% of rotative speed, but occurrences are usually at 37 to 47%. It can also be locked to integer fractions of rotative speed by Mathieu action. This mechanism frequently occurs with 360 degree liquid, gas, or mixed flow lubrication but may also occur on the Half Sommerfeld Curve, with a small attitude angle. Thrust oil whip is a laboratory curiosity as thrust bearings are always segmented. However thrust bearing-like surfaces of impellers are fully subject to this action, whether handling gas or liquid.

Internal Friction: This mechanism occurs at the self-balance resonance speed that allows the greatest shaft deflection. Rotative speed must be any speed above that resonance speed. This action is also subject to locking at an integral fraction of running speed by Mathieu action and must exhibit a high positive attitude angle as in the case of oil whip.

Steam Whip, Pumping Whip, Aerodynamic Cross-Coupling, Alford Whip, etc.:
This mechanism occurs at any self-balance resonance which allows major
deflection of the shaft by bowing or by eccentricity in the bearings. In
several instances of poor damping after seals have been opened by a prior
malfunction, this excitation has occurred above running speed, but it most
often occurs below running speed and at the translational self-balance
resonance. On these compressors, the synchronous amplification factor to
translational self-balance resonance had increased to Q > 6, so not only has
the natural damping degraded, but the shaft is easily deflectable due to the
excessive seal clearance. It may also experience locking by Mathieu action.

Vortexing, Helmholz, and Near Surge: While these are oscillations which may
be separate from the rotor action as reported by P. Ferrara in an ASME paper
two years ago and observed by this author, they are often highly mobile in
frequency, and if they succeed in getting close to the self-balance reso-
nance rotor rpm, will tend to latch onto that resonance, strongly exciting
the instability. Their occurrence frequently has been observed from 10% to
over 200% of rotative speed.

Entrained Bubbles in Pumps: While this is a forced category action, its
symptoms are the same as the forward circular self-excited category. The
bubbles amount to a lack of fluid mass and therefore provide the imbalance.
The frequency is just below rotative speed down to 80% of rotative speed. A
self-balance resonance in this range may be strongly excited by this cir-
culating imbalance.

Conclusions: Some Notes on the Studies of Rotating Machinery Instabilities.

Even though a rotor is a simple structure that goes around in a circle and
the compressible or incompressible fluids in bearings and seals between
rotor and stator also go around, the rotor system tends to do more tricks
than a monkey on a 100 meter rope. In every rotating machine, velocity-to-
displacement is sinusoidal in timing, and therefore if the shaft is orbit-
ing, the velocity vector is 90 degrees ahead of the displacement vector.
Every rotating machine therefore has cross-coupled tendencies, allowing
forces to be set up which may act against the damping forces. The more
easily deflectable the shaft, the easier it is for these forces which act
against damping to occur.

Add to this the complexity of the Navier-Stokes equation and suddenly a
simple object becomes difficult to describe mathematically. Furthermore
some unfortunate assumptions and misused expressions have come into
existence and continue to be used. The use of the word "criticals" to
express the rotor self-balancing speed regions is one example. Another is
the use of the expression "unbalance sensitivity." This should be properly
stated as an "imbalance response."

Another pitfall expression is "influence coefficient." The expressions
"kelley constant" or "finagle factor" are equally inappropriate. When a
calibration weight is added to a machine to unbalance it, there is a direct

response observed at the lateral plane where the weight is added, and a transfer response at each other plane. It is a vector quantity, not a scalar, and it has dimensions. Typically, an unbalance weight of 1 gram installed at 8 cm balance hole diameter at 0 degrees, yielding a direct response of 4 p/p (peak-to-peak) mils at 172 degrees and a transfer response to an adjacent lateral place of 2 p/p mils at 355 degrees, yields at a specific speed:

Direct response

$$\frac{4 \text{ p/p mils } \angle 172°}{8 \text{ gm cm}} = \frac{0.5 \text{ p/p mils } \angle 172°}{\text{gm cm}}$$

Transfer response

$$\frac{2 \text{ p/p mils } \angle 355°}{8 \text{ gm cm}} = \frac{0.25 \text{ p/p mils } \angle 355°}{\text{gm cm}}$$

The use of the expression "log decrement" is also unfortunate. Log decrement is applicable where there are responses to unit or step impulses, as in diving boards. Amplification factor Q, damping factor ζ and attitude angle are directly applicable to the study of rotor instability. Often the expression "negative log decrement" is used to express instability. Of course it does, but the expression does not pass the "so what" test. Once the log decrement and damping factor become negative the rotor system is unstable by definition.

Perhaps the most misleading expressions, however, are the references to "cross springs" and "cross dampers." When these originated in the 1950s they were probably adequate for the original experiments, plus they have the misfortune of fitting into point matrix equations very neatly; too neatly. If these cross-coefficents are to be used, they must first be proven. Once proven, they may be acceptable provided that they are not a function of the term that they are multiplied by. For example, in the force term KxyY, if Kxy is a function of Y itself, then no differentiation or integration can be done on the term treating Kxy as a constant and still retain much relationship to reality. The term, however, could be a function of anything else.

It is most interesting that the strength of aerodynamic forces are often referred to in terms of lbs/in or newtons/meter instead of pounds, or newtons, or, if treated as moments, should be ft-lbs or newton-meters. A typical statement is, "This machine has an aerodynamic cross-coupling of 40,000 lb/in."

It would seem logical to go back to the basics and re-examine the fluid mechanics by both careful experiment and by sophisticated computer studies of fluidics finite elements and also by observing the results of iterative solutions to bearing and seals where the computer is given very few assumptions and is working on the Navier-Stokes equation with inertial effects included.

It should be more widely recognized that there are clearly two different mechanisms of instability in fluid film bearings. They are (1) the widely accepted stability rules of Half Sommerfeld assumed lubrication and (2) the largely neglected 1956 works of Cole and Hughes. The transparent bearing clearly shows that when a bearing can mix flow it can change suddenly to a 360 degree bearing and become unstable.

In addition to further experiments and mathematics to clarify the forward circular instability mechanisms of rotors, the following general rules should be applied for better control of harmful actions:

1. Provide more passive damping to the rotor system (this has limits if damping must be at the bearing as pointed out by E. Gunter).

2. Provide active damping by way of force balance active bearings (noting the limitation above).

3. Control the machine design, such as limiting the soft unidirectional preloading by gasses and liquids as well as limiting the introduction of the aerodynamic forces which act against the damping force.

4. Deliberately introduce reverse circular whirl mechanisms to the rotor system such as the propeller whirl shown by Chen and by J. Vance to neutralize the forward instability tendency of virtually all rotating machinery.

FIGURE 1

RESONANCE SHIFT DUE TO ROTOR CONTACT WITH STATOR

TBR   0.5x   1x

MACHINE SPEED (RPM x 1000)

2x

3x

FREQUENCY (EVENTS/MIN x 1000)

AMP SCALE = 3 Mils,Pk-Pk PER POINT

FIGURE 2

RUN 1A   0

ROTN

VERTICAL

270   90

9718
1769
1695
1454
1517
1566
1621

180

* 15 MIL CLEARANCE
* NO FREE SPINNER
* SYNCHRONOUS ROTOR RESPONSE

FULL SCALE AMP = 40 MILS, PK-PK   AMP PER DIV = 2 MILS, PK-PK

FIGURE 3

RUN 1A   270

ROTN

HORIZONTAL

180   0

1745
1695
1668
1435
1517
1536
1566
1621   1595

90

* 15 MIL CLEARANCE
* NO FREE SPINNER
* SYNCHRONOUS ROTOR RESPONSE

FULL SCALE AMP = 40 MILS, PK-PK   AMP PER DIV = 2 MILS, PK-PK

FIGURE 4

RUN 1A 0

PHASE, DEGREES

-180

-360

PIVOT   VERTICAL ————
HORIZONTAL-------

-540

TBR

40

32

24

16

8

0

* 15 MIL CLEARANCE
* NO FREE SPINNER
* SYNCHRONOUS ROTOR RESPONSE

MILS, PK-PK

SPEED, RPM x 1000

103

FIGURE 5

FIGURE 6

FIGURE 7

FIGURE 8

104

RUN 6

REVERSE
PERTURBATION
SPEED   ROTOR SPEED

0.5X   1X   2X

3X

TBR

MACHINE SPEED (RPM × 1000)

3

2.5

2

1.5

1

.5

0

0   1   2   3   4   5   6   7   8

15 MIL CLEARANCE
ROTOR AT 5000 rpm
REVERSE SPINNER

FREQUENCY (EVENTS/MIN × 1000)

AMP SCALE = 5 Mils,Pk-Pk PER POINT

FIGURE 9

RUN 6   270

ROTN   HORIZONTAL

180   0

90

15 MIL CLEARANCE
ROTOR AT 5000 rpm
REVERSE SPINNER

FULL SCALE AMP = 40 MILS, Pk-Pk   AMP PER DIV = 2 MILS, Pk-Pk

FIGURE 10

RUN 6   0

ROTN   VERTICAL

270   90

180

15 MIL CLEARANCE
ROTOR AT 5000 rpm
REVERSE SPINNER

FULL SCALE AMP = 40 MILS, Pk-Pk   AMP PER DIV = 2 MILS, Pk-Pk

FIGURE 11

RUN 6   0   TBR

PHASE, DEGREES

-180   HORIZONTAL

-360   VERTICAL

-540

15 MIL CLEARANCE
ROTOR AT 5000 rpm
REVERSE SPINNER

MILS, Pk-Pk

40

32

24

16

8

0

0   .6   1.2   1.8   2.4   3

SPEED, RPM × 1000

FIGURE 12

105

FIGURE 13

COMMENTS AND PERSPECTIVES OF RECENT ADVANCES IN
DESIGN FEATURES FOR TURBOMACHINERY

Joseph Alford
Retired, General Electric Company
Cincinnati, Ohio   45215

SUMMARY

Mr. Alford repeated the major conclusions of his landmark paper, "Protecting Turbomachinery From Self-Excited Rotor Whirl", which was published in the ASME Journal of Engineering for Power, October 1965, pp. 333-344. The abstract of that paper was as follows:

"Aerodynamic exciting forces have caused severe rotor whirl of axial compressors and turbines. One disturbing force investigated is due to circumferential variation of static pressure acting on the cylindrical surface of rotor, particularly within labyrinth seals. Another aerodynamic disturbing force is due to eccentricity of rotor causing circumferential variation of blade-tip clearance, and a corresponding variation of local efficiency and unbalanced torque. Seal deflection criteria and torque deflection criteria are presented as design guides for stable rotor systems. These criteria, the form of which comes from analysis of rotor dynamics, correlate design parameters of four examples of unstable rotor systems which exhibited whirl."

Page intentionally left blank

ASYNCHRONOUS VIBRATION PROBLEM

OF CENTRIFUGAL COMPRESSOR

Takeshi Fujikawa, Naotsugi Ishiguro and Mitsuhiko Ito
Kobe Steel, Ltd.
Kobe, Japan

INTRODUCTION

Unstable asynchronous vibration problem in high pressure centrifugal compressor were reported by J.C. Wachel(ref.1), K.J. Smith(ref.2), D.W. Fowlie (ref.3), etc. This paper describes the similar problem we have experienced and the remedial actions against it.

GENERAL CONFIGURATION

A schematic of compressor train system is shown in Fig.1. 5000kW moter drives L.P. (low pressure) and H.P. (high pressure) compressors through the speed up gear. Asynchronous vibration was observed in H.P. compressor. Fig. 2 shows the cross sectional view of the H.P. compressor. The rotor has 6 shrink fitted impellers and one balance piston which is integrated with the shaft. The rotor is supported by tilting pad journal bearing characteristics of which are described in table 1. The Kingsbury type thrust bearing is used. The compressor has 1703 mm bearing span length with the rigid critical speed of 3894 rpm in the original design. L.P. and H.P. compressor are connected with a diaphragm type flexible coupling.

OBSERVED VIBRATION

Asynchronous vibration of H.P. compressor took place when the discharge pressure Pd was increased by controlling the valve, after the rotor was already at full speed. Fig. 3 shows the typical spectral data of the shaft vibration while Pd is increased. As the pressure Pd increases, pre-unstable vibration appears and becomes larger, and large unstable asynchronous vibration occurs suddenly at Pd = 5.49MPa in this case, as shown in Fig. 3 (d), (e).

Fig. 4 is the spectral time history of the shaft vibration in the condition like Fig. 3 (c). The amplitude of pre-unstable vibration fluctuates at some levels. A typical relationship between vibration amplitude and Pd is shown in Fig. 5. Fig. 6 shows the shaft orbit just before the vibration growing up large.

REMEDIAL ACTIONS AND SOLUTION

In order to prevent the above vibration, various kinds of remedial actions are tried based on the results of the complex-eigenvalue analysis mentioned later. Remedial actions adopted and their results are summerized in table 2

and Fig. 8, where

Case ① : The original design

Case ② : The width of pads of journal bearings is reduced to 2/3 of case ①.

Case ③ : The bearing span is shortened from 1703 mm to 1553 mm to increase the shaft stiffness.
Rigid critical speed increased from 3894 rpm to 4560 rpm.

Case ④ : Bearing width is put back to original one and 0.5 pre-load journal bearings are used.

Case ⑤ : Lubricating oil is changed from #90 (viscosity of 34 cSt at 38 degrees C) to #140 (50 cSt at 38 degrees C) in order to increase the damping effect.

Case ⑥ : 0.1 pre-load journal bearings are used.

After all, the full load operation is successfully carried out in the condition of case ⑥.

ANALYSIS

The computer program is used to analyze the rotor stability problem in order to help the remedial plans. The program calculates the logarithmic decrement and the damped natural frequency of the rotor bearing systems. The procedure of the program is as follows. Using a finite element method, the equation of motion of rotor bearing system is given by :

$$[M]\ddot{x} + [C]\dot{x} + [K]x = 0 \qquad (1)$$

where   [M] : mass matrix

[C] : damping matrix

[K] : stiffness matrix

The mass matrix consists of the concentrated mass of the rotor sections. The impeller has the mass effect and the gyroscopic effect. The stiffness matrix of rotor is obtained based on the beam theory. The bearing characteristics and the destabilizing factors are dealt with as the concentrated added damping and spring coefficients in the program. The destabilizing force Q is estimated by eq. (2) based on Lund (ref.4).

$$Q = \beta \frac{T}{2rh} \qquad (2)$$

where β : destabilizing force coefficient

110

T   :   torque

r   :   nominal radius of impeller

h   :   nominal width of impeller

In order to get the eigenvalues, eq. (1) is transformed into the canonical form and QR method is applied. The example of calculation model and results are shown in Fig. 7(a), (b).

DISCUSSION

Since there are many obscure points in the destabilizing forces (aero cross coupling forces), the six cases of remedial actions were prepared and carried out in order to be able to operate at full pressure load.

Fig. 8 shows the calculated results of log-decrement δ and the maximum pressure Pd attained without large vibration for the six cases in the field test.

Fig. 9 shows the change of stability due to oil temperature. Lower oil temperature gives better δ . In calculation of δ, the nondimensional factor β is estimated to 5 including the labyrinth effect. It is seen that the increasing of the rotor stiffness and the oil viscosity are effective to improve the stability of the system. The high preload bearing is not good. The system became to be operated in almost full load in case ⑤. However, the pre-unstable vibration level was not small, so the case ⑥ was carried out.

The comparison between the results of calculation and field data is shown in Fig. 10 . The bearing was selected in order that the limit β and δ of case ⑥ be larger than those of case ⑤. The stability of case ⑥ was improved and the pre-unstable vibration was suppressed sufficiently small in the field test.

CONCLUSION

(1) The high speed and high pressure compressor has inherently the possibility of the occurrence of unstable vibration. The stability analysis of δ is effective in the design stage of the rotor bearing system and in the remedial actions in order to prevent the unstable vibration. Details of the mechanism of destabilizing force is not clarified, so it seems better to consider the cross coupling force and the negative damping into the stability analysis.

(2) As the remedial actions, it is effective to increase the shaft stiffness and to select the appropriate bearings in order to increase the system damping.

REFERENCES

(1) Wachel, J. C. : Nonsynchronous Instability of Centrifugal Compressors.
    ASME Paper No. 75-Pet-22

(2) Smith, K. J. : An Operation History of Fractional Frequency Whirl.
    Proc. 4th Turbomachinery Symposium, Gas Turbine Laboratories,
    Texas A & M University, Oct. 1975

(3) Fowlie, D. W. and Miles, D. D. : Vibration Problems with High Pressure
    Centrifugal Compressors.
    ASME Paper No. 75-Pet-28

(4) Lund, J. W. : Stability and Damped Critical Speeds of a Flexible Rotor in
    Fluid-Film Bearings.
    Journal of Engineering for Industry, Trans. ASME, May 1974, pp. 509-517

Table 1 Tilting pad journal bearing

Diameter	76.2 mm
Width	31.8 mm
Number of pads	5
Arrangement	Load on pad

Table 2 Remedial actions

	Bearing span length mm	Width of bearing pad mm	Bearing diametral clearance 2 c/D	Bearing preload	Lubricating oil
CASE ①	1703	31.8	2.5/1000	0	#90
②	"	21.2	"	0	"
③	1553	"	"	0	"
④	"	31.8	"	0.5	"
⑤	"	"	"	0.5	#140
⑥	"	"	"	0.1	"
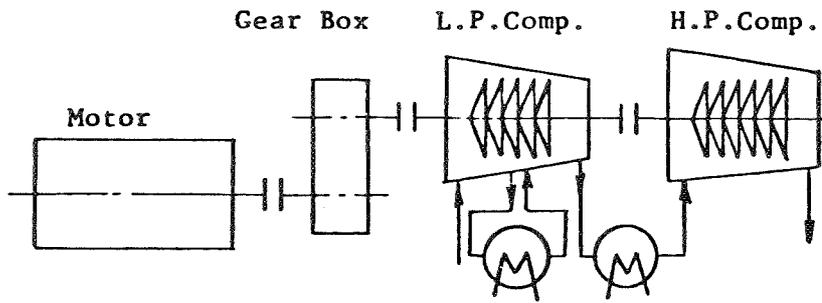
Specifications of H.P. compressor

Suction pressure	1.912 MPa
Discharge pressure	6.865 MPa
Shaft horse power	2980 kW
Shaft speed	10400 rpm
Fluid	N_2 gas

Fig.1 Schematic of compressor train
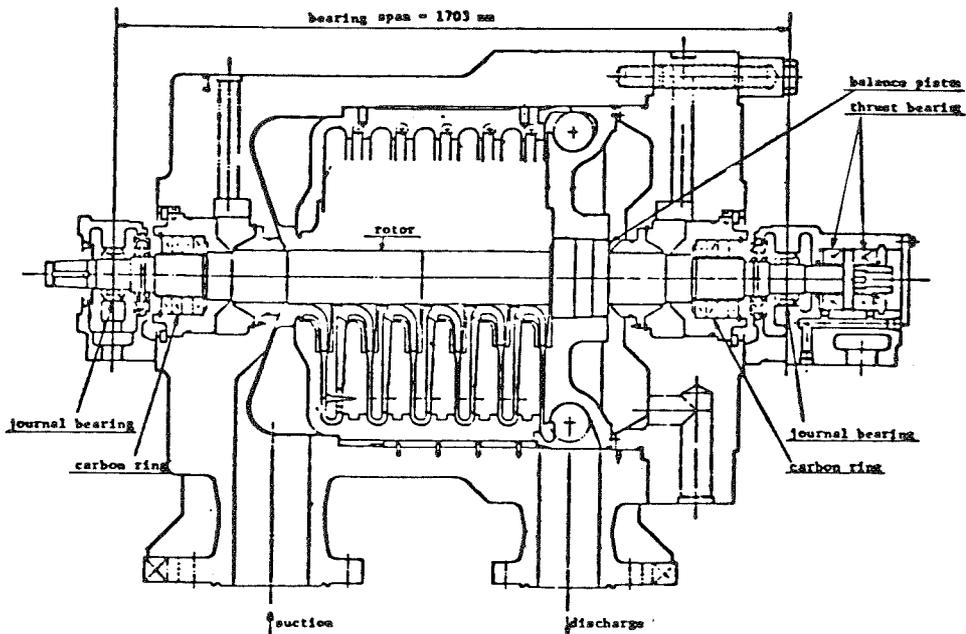
Fig.2 Cross-sectional view of H.P. compressor
(Original design)
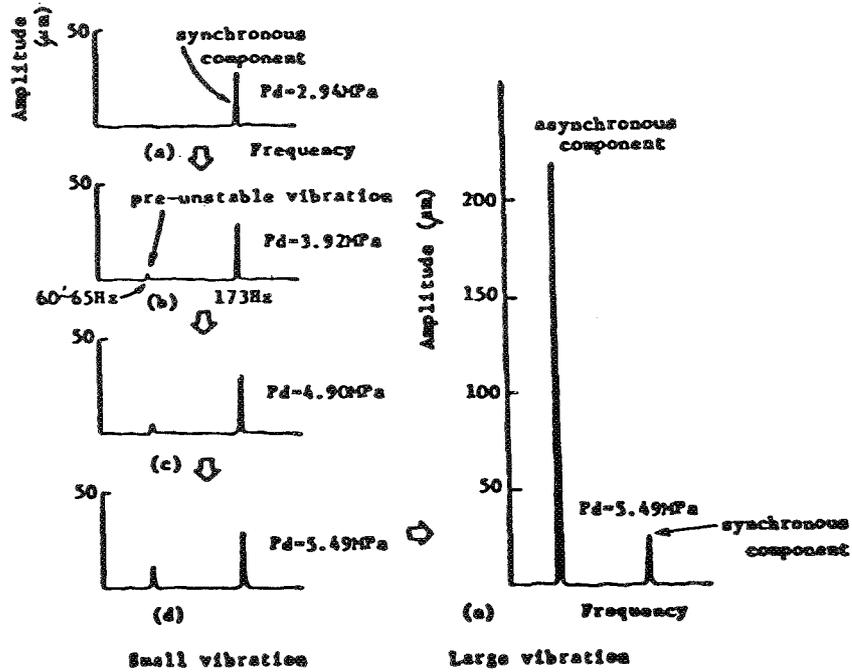
Fig.3 Variation of spectral rotor vibration with discharge pressure
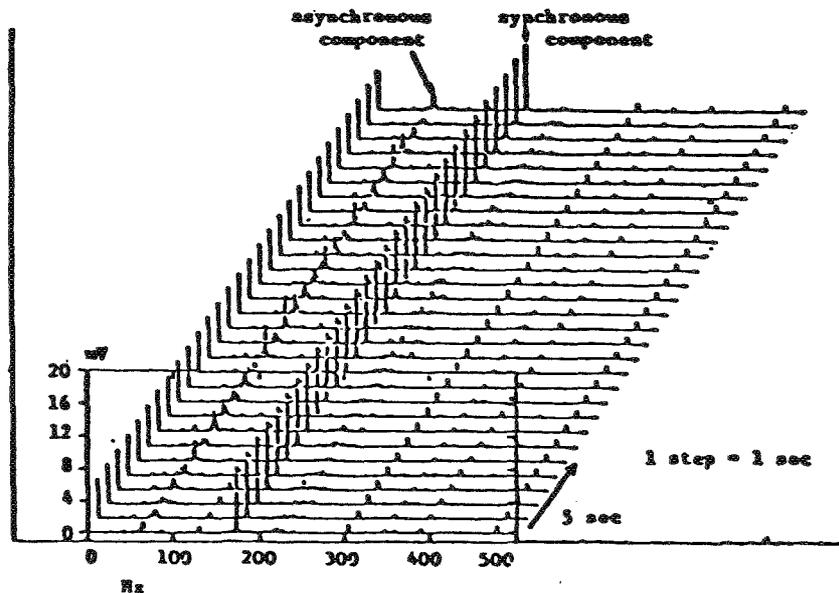
Fig.4 Spectral time history of asynchronous small vibration
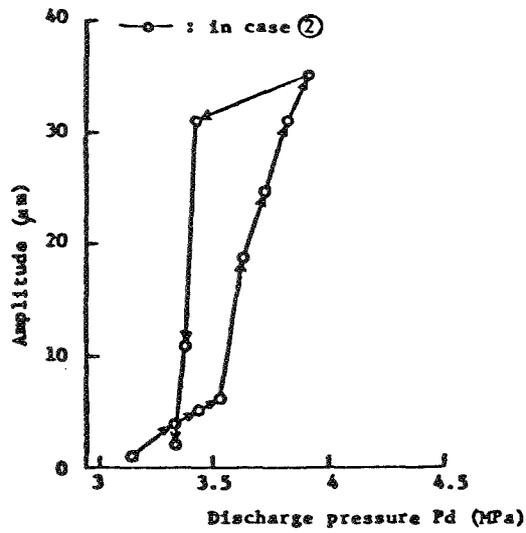
Fig.5 Variation of rotor vibration with discharge pressure Pd
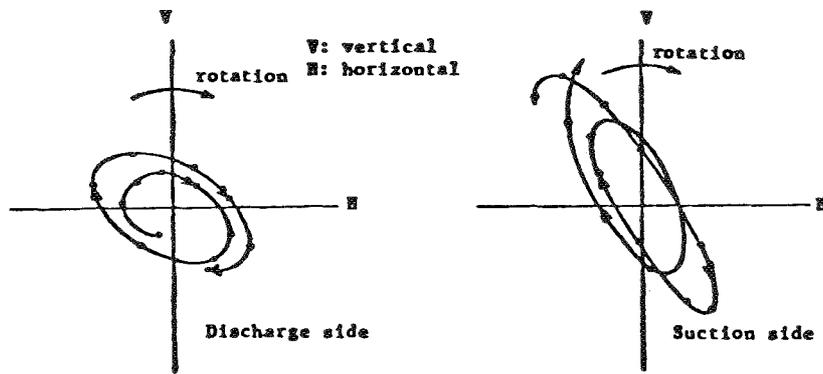
Fig.6 Whirl orbit of asynchronous vibration

impeller

shaft lumped mass

bearing

bearing

(a) Model

Mode = 2

Log-decrement = -0.01

Frequency = 3596.87 rpm

(59.95 Hz)

Ratation speed
N=10400.00 rpm
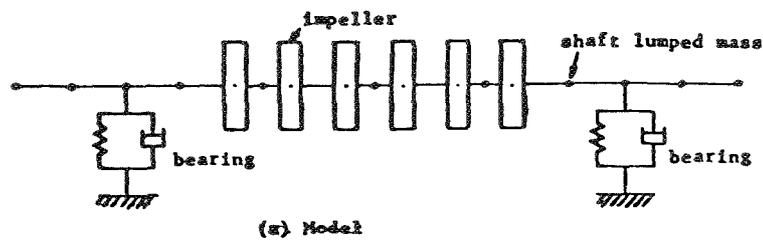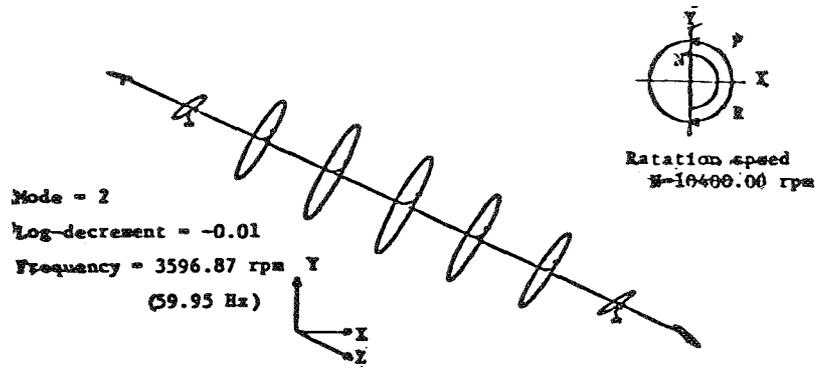
(b) Results

Fig.7 Calculation model and results

max. pressure Pd without vibration (MPa)

calculated Log-decrement δ

origianl design

full load

final condition
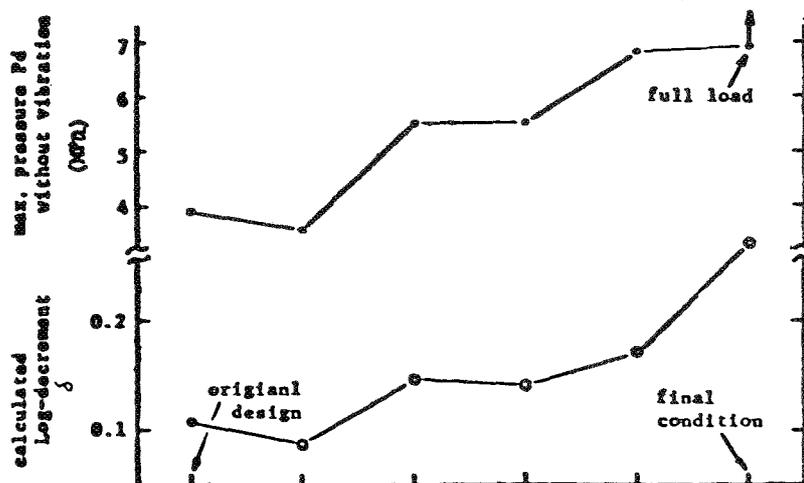
Case No.	①	②	③	④	⑤	⑥
bearing span (mm)	1703	1703	1553	1553	1553	1553
bearing width (mm)	31.8	21.2	21.2	31.8	31.8	31.8
diametral clearance $\frac{2c}{D}$	$\frac{2.5}{1000}$	$\frac{2.5}{1000}$	$\frac{2.5}{1000}$	$\frac{2.5}{1000}$	$\frac{2.5}{1000}$	$\frac{2.5}{1000}$
pre-load	0	0	0	0.5	0.5	0.1
oil	#90	#90	#90	#90	#140	#140

Fig. 8 System damping and maximum discharge pressure attained
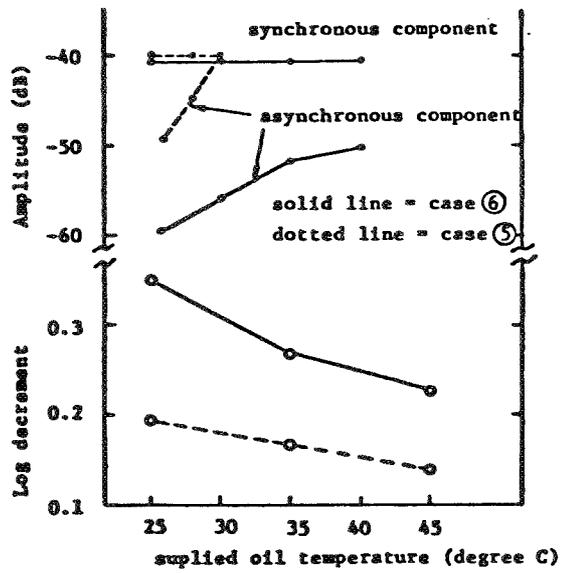
Fig.9 Variation of stability due to oil temperature
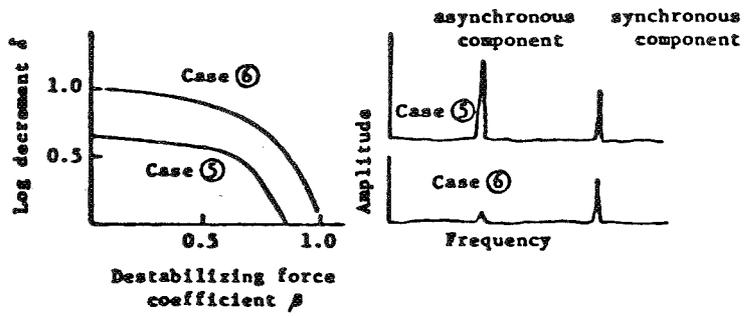
Fig.10 Comparison between calculated δ and field data
(relative representation)

SESSION III

SEAL FORCES IN TURBOMACHINERY

Robert C. Hendricks, NASA Lewis Research Center
Chairman

119

Page intentionally left blank

TESTING OF TURBULENT SEALS FOR ROTORDYNAMIC COEFFICIENTS*

Dara W. Childs and John B. Dressman
Mechanical Engineering Dept.
The University of Louisville
Louisville, Kentucky 40208

S. Bart Childs
Industrial Engineering Dept.
Texas A&M University
College Station, Texas 77840

SUMMARY

A facility has been developed for dynamic testing of straight and convergent-tapered seals, with the capability of separately determining both direct and cross-coupled stiffness, damping, and added mass coefficients. The test apparatus causes the seal journal to execute small-eccentricity centered circular orbits within its bearings. Dynamic measurements are made and recorded of the seal-displacement-vector components, and of the pressure field. The pressure field is integrated to yield seal reaction-force components. The displacement and force vector components are analyzed via a generalized Newton-Raphson procedure to yield the desired seal dynamic coefficients. Representative test data are provided and discussed.

INTRODUCTION

Black [1, 2, 3, 4] in a series of publications incorporating theoretical and experimental results has demonstrated that the rotordynamic behavior of pumps is critically dependent on forces developed by neck-rings and interstage seals illustrated in figure 1. Subsequent experience [5] has demonstrated that the stability of cryogenic turbopumps is comparably dependent on seal forces. The test program discussed here was stimulated by stability difficulties encountered in developing the turbopump of [5], and has the objective of separately identifying stiffness, damping, and inertia coefficients for turbulent seals.

The contents of this section are provided to briefly review theoretical models and prior experimental results and procedures for seals. Also, since the seals of figure 1 are geometrically similar to plain journal bearings, applicable prior test programs to identify journal bearing coefficients are also reviewed.

Seal Analysis: Leakage and Dynamic Coefficients

Black [1, 2, 3, 4] is largely responsible for developing currently employed dynamic seal models. Black's analysis yields a definition of the force acting on a rotor due to its motion at a seal location, and is based on the following leakage relationship from Yamada [6] for flow between concentric rotating cylinders.

$$\Delta P = (1 + \xi + 2\sigma)\rho V^2/2 \tag{1}$$

where ξ is a constant entry-loss coefficient, ρ is the fluid density, V is the average fluid velocity, and σ is a friction-loss coefficient defined by

$$\sigma = \bar{\lambda}L/C \tag{2}$$

In the above, L is the seal length, C is the radial clearance, and $\bar{\lambda}$ has been defined by Yamada to be the following function of the axial and radial Reynolds numbers (R_a, R_r)

$$\bar{\lambda} = 0.079 \, R_a^{-1/4}[1 + (\frac{7R_r}{8R_a})^2]^{3/8} \; ; \; R_a = 2VC/\nu, \; R_r = R\omega C/\nu \tag{3}$$

where ν is the fluid's kinematic viscosity, R is the seal radius, and ω is the rotor's rotational speed. The friction law definition of Eq. (3), Yamada's definition for $\bar{\lambda}$, is based on an assumed 1/7 power velocity distribution, and fits the Blasius equation for pipe friction.

Black's analysis for a plain non-serrated seal yields a motion/reaction-force definition of the form

$$- \frac{\bar{\lambda}}{R\pi\Delta P} \begin{Bmatrix} R_X \\ R_Y \end{Bmatrix} = \begin{bmatrix} \tilde{K} & \tilde{k} \\ -\tilde{k} & \tilde{K} \end{bmatrix} \begin{Bmatrix} r_X \\ r_Y \end{Bmatrix} + \begin{bmatrix} \tilde{C} & \tilde{c} \\ -\tilde{c} & \tilde{C} \end{bmatrix} \begin{Bmatrix} \dot{r}_X \\ \dot{r}_Y \end{Bmatrix} + \begin{bmatrix} \tilde{m} & \tilde{o} \\ \tilde{o} & \tilde{m} \end{bmatrix} \begin{Bmatrix} \ddot{r}_X \\ \ddot{r}_Y \end{Bmatrix} \tag{4}$$

where

$$\tilde{K} = \bar{\mu}_0 - \bar{\mu}_2\omega^2T^2/4, \; \tilde{k} = \bar{\mu}_1\omega T/2, \; \tilde{C} = \bar{\mu}_1 T, \; \tilde{c} = \bar{\mu}_2\omega T^2, \; \tilde{m} = \bar{\mu}_2 T^2, \; T = L/V \tag{5}$$

In Black's original analysis [1], the coefficients $\bar{\mu}_0$, $\bar{\mu}_1$, $\bar{\mu}_2$ were developed for short seals for which, "circumferential pressure-induced flows are negligible compared with axial flows". Black subsequently [2] examined

122

the effect of circumferential pressure-induced flow for finite-length seals, and developed the following formulae to account for finite (L/R) ratios

$$
\left.
\begin{array}{l}
\mu_0(\tfrac{L}{R}) = \bar{\mu}_0\{1 + 0.28(L/R)^2\}^{-1} \\[2mm]
\mu_1(\tfrac{L}{R}) = \bar{\mu}_1\{1 + 0.23(L/R)^2\}^{-1} \\[2mm]
\mu_2(\tfrac{L}{R}) = \bar{\mu}_2\{1 + 0.06(L/R)^2\}^{-1}
\end{array}
\right\}
\qquad (6)
$$

Black's second refinement of the original development [3] was the definition of $\bar{\mu}_0$, $\bar{\mu}_1$, $\bar{\mu}_2$ in terms of the following additional parameter

$$
\beta = (\frac{7R_r}{8R_a})^2 / \{1 + (\frac{7R_r}{8R_a})^2\}
\qquad (7)
$$

which accounts for a circumferential variation in $\bar{\lambda}$ due to a radial displacement perturbation from a centered position. Plots of $\bar{\mu}_0$, $\bar{\mu}_1$, and $\bar{\mu}_2$ are provided in figure 2 as a function of β and σ for $\xi = 0.5$. These coefficients are comparatively insensitive to anticipated variations of the entrance loss factor ξ.

Finally, Black [4] examined the influence of inlet swirl on seal coefficients. Specifically, in previous analyses, a fluid element entering a seal was assumed to instantaneously achieve the half-speed tangential velocity $R\omega/2$. Black in [4] demonstrates that a fluid element must travel a substantial distance axially along the seal before asymptotically approaching this limiting velocity. The practical consequence of this swirl effect is that predictions for the cross-coupling terms $\tilde{k}$, $\tilde{c}$ may be substantially reduced.

One of the authors [7] has recently completed a seal analysis based on Hirs turbulent lubrication model [8,9], which largely repeats Black's developments (which were based on various ad hoc models). The results resemble, but do not coincide with Black's results. They also do not include the finite-length correction of Eq. (6).

Prior Seal Testing Procedures and Results

The pertinent data which must be measured to confirm the seal leakage model of Eqs. (1) - (3) are ΔP, V (from flow rate), ω, and the axial pressure gradient within the seal. This latter measurement yields σ which in turn yields $\bar{\lambda}$. Yamada's model for the friction factor was based on testing for these variables over the Reynolds number range ($200 \leq R_a \leq 40,000$; $0 \leq R_r \leq 40,000$) and clearance to radius ratios of ($.0106 \leq C/R \leq .0129$).

Various approaches can be taken to the measurement of seal dynamic properties as defined by Eqs. (4) and (5). For example, if the journal segment

of the seal is stationary (i.e., $\dot{r}_X = \dot{r}_Y = \ddot{r}_X = \ddot{r}_Y = 0$), Eq. (4) can be inverted to obtain

$$\left\{ \begin{matrix} r_X \\ r_Y \end{matrix} \right\} = - \frac{\bar{\lambda}}{R\pi PK_e^2} \begin{bmatrix} \tilde{K} & -\tilde{k} \\ \tilde{k} & \tilde{K} \end{bmatrix} \left\{ \begin{matrix} R_X \\ R_Y \end{matrix} \right\}, \quad K_e^2 = \tilde{K}^2 + \tilde{k}^2$$

Hence by applying the static load definition ($F_X = F_s$, $F_Y = 0$), and measuring the displacement components r_X, r_Y, one obtains a combined measure of the direct and cross-coupled stiffness coefficients. This is predominantly the type of testing performed by Black, who cites results in the form of "receptance magnitudes", i.e.,

$$|r|/F_s = \bar{\lambda}\{\tilde{K}^2 + \tilde{k}^2\}^{1/2}/R\pi\Delta P$$

From Black's model, the relative magnitudes of the direct $\tilde{K}$ and cross-coupled $\tilde{k}$ stiffness coefficients depend on the relative magnitudes of the axial and radial Reynolds numbers. Specifically, at zero running speeds $\tilde{k}$ is zero, but increases with R_r, and can exceed $\tilde{K}$.

For softly supported rotors, the direct stiffness of a non-serrated seal represented by $\tilde{K}$ may significantly influence the location of a critical speed. However, the stability of a flexible rotor is less sensitive to the direct stiffness term, depending primarily on the cross-coupled stiffness coefficient $\tilde{k}$, and direct damping coefficient $\tilde{C}$. For <u>most</u> rotors, the cross-coupled damping coefficients $\tilde{c}$, and inertia terms $\bar{m}$ have no appreciable influence on rotor stability or response.

Most of Black's testing [2, 3, 10, 11] has been of the static nature cited above. The second type of test cited consists of analytically modeling a test rotor including the theoretically predicted seal dynamics, and comparing the dynamic characteristics of the model with test data. For example, in [2] the test rotor was rapped and a correlation was made with the observed logarithmic decrement on the decay curve. In [3], known imbalances were applied to the test rotor, and a comparison was made with synchronous amplitudes and phase, critical-speed location, and onset speed of instability. Comparisons between rotor model results and tests, of this nature, are helpful in deciding whether the general seal model is reasonable. However, this type of test-correlation does not yield specific information about the individual dynamic coefficients. Further, discrepancies between predictions and results can be the result of either an inadequate rotor model or an inadequate seal model. For example, in [3], Black indicates that discrepancies in synchronous amplitude and phase results could result from an inadequate initial balance.

A summary of the test results of references [2, 3, 10, 11] is provided in Table 1. The correlation in these tests ranges from "good" to "fair". The nature and results of the test support the following general conclusions

concerning the adequacy of Black's dynamic seal model:

(a) Over the Reynolds number range tested, the prediction of the direct
stiffness coefficient $\tilde{K}$ is adequate for plain and serrated seals,
although less accurate for serrated seals. Black's test results
indicate a divergence between tests and theory for the direct damp-
ing coefficient $\tilde{C}$ as the axial Reynolds number is increased.

(b) Although the data cited generally supports Black's dynamic seal
model over the Reynolds number range considered, it is inadequate
to specifically verify the proposed relationships [Eq. (5)] for the
dynamic coefficients as functions of the axial and radial Reynolds
numbers.

Identification of the dynamic coefficients of seals in a centered position as
functions of the axial and radial Reynolds numbers is the objective of the
current test program.

Prior Journal-Bearing Coefficient Identification Approaches

The seals of figure 1 are geometrically similar to plain journal bearings
but have larger C/R ratios on the order of 0.01 as compared to bearings for
which C/R is on the order of 0.001. Seals customarily operate in the turbulent
regime, both axially and circumferentially, and have a substantial direct
stiffness at a centered zero eccentricity position. Further, seals are
nominally designed to operate in a centered position, while the operating
eccentricities of journal bearings vary with running speed and load. Hence,
dynamic bearing-identification work has generally had the objective of validat-
ing dynamic coefficients versus eccentricity relationships. The general
similarities between bearings and seals are such that procedures developed
for bearing-coefficient-identification may also apply for seals and are
briefly reviewed below.

On the basis of various analyses, the motion/reaction-force relationship
for a hydrodynamic bearing is defined, for small motion about an equilibrium
position, by the equation

$$
\begin{bmatrix} C_{xx} & C_{xy} \\ C_{yx} & C_{yy} \end{bmatrix}
\begin{Bmatrix} \dot{r}_X \\ \dot{r}_Y \end{Bmatrix}
+
\begin{bmatrix} K_{xx} & K_{xy} \\ K_{yx} & K_{yy} \end{bmatrix}
\begin{Bmatrix} r_X \\ r_Y \end{Bmatrix}
= -
\begin{Bmatrix} R_X \\ R_Y \end{Bmatrix}
\tag{8}
$$

The equations of motion of a rigid rotor of mass 2M supported symmetrically by
two identical bearings can then be stated

$$
\begin{bmatrix} M & 0 \\ 0 & M \end{bmatrix}
\begin{Bmatrix} \ddot{r}_x \\ \ddot{r}_y \end{Bmatrix}
+
\begin{bmatrix} C_{xx} & C_{xy} \\ C_{yx} & C_{yy} \end{bmatrix}
\begin{Bmatrix} \dot{r}_x \\ \dot{r}_y \end{Bmatrix}
+
\begin{bmatrix} K_{xx} & K_{xy} \\ K_{yx} & K_{yy} \end{bmatrix}
\begin{Bmatrix} r_x \\ r_y \end{Bmatrix}
= M\omega^2 a
\begin{Bmatrix} \cos(\omega t) \\ \sin(\omega t) \end{Bmatrix}
+
\begin{Bmatrix} F_X \\ F_Y \end{Bmatrix}
\tag{9}
$$

Where F_x, F_y are the components of the external force vector, a is the imbalance vector magnitude and ω is the constant rotor spin speed.

Published work related to the identification of the stiffness and damping coefficients of Eq. (9) date from Gleinecke [12] who excited the bearing segment of a 120 mm model bearing in two mutually orthogonal directions while measuring the amplitude and phase of the relative motion between the bearing and journal. The stiffness and damping coefficients are calculated from the frequency-domain equations. Morton [13] adopted this test procedure on a full-scale 308 mm (20 in.) industrial bearing, to calculate bearing stiffness and damping coefficients, and subsequently [14] developed a technique for introducing a step input into a full-scale operating turbine bearing, thereby defining the bearing transfer function. Burrows and Stanway [15] have proposed the use of a pseudo-random-binary sequency (pros) excitation force with a multiple-regression analysis for estimating the coefficients. Their estimation procedure consists of the following steps:

(a) The governing differential equations of motion (2) are expressed in state-variable format, i.e., as a system of first-order differential equations.

(b) The first-order differential equations are replaced by first-order difference equations.

(c) The unknown coefficients are calculated based on a minimum error-squared criterion from measurements of the state variables and the pros input signal.

They also applied the method to the estimation of squeeze-film damper coefficients [16].

THE UNIVERSITY OF LOUISVILLE DYNAMIC SEAL TEST PROGRAM

Test Section Design

Figure 3 illustrates the test-section design employed in the current seal test program. Water enters the center of the section and flows axially across the two rotating test seals exiting at the bottom of the test section. The seal journals (L = 4 in = 10.16 cm, D = 2 in = 5.08 cm) are mounted eccentrically on the shaft with a constant eccentricity e_s = .005 in = 1.27 x 10^{-4}m. The nominal seal clearance is C = .02 in = 5.08 mm, which yields C/R = .01. Accordingly, shaft rotation causes the seal journals to execute circular centered orbits at the nominal eccentricity ratio ε = 0.25. Axial and radial Reynolds numbers may be specified over the range $R_a \varepsilon$[5000, 30,000] $R_r \varepsilon$[0, 11,000] by varying the shaft rotational speed (0 - 4,000 rpm) and flowrate. Shaft-speed is measured by a once-per-revolution counter, while turbine flowmeters separately measure flowrate through each seal.

The rotor of figure 3 is supported in Torrington hollow roller

bearings [1] [17]. These precision bearings are preloaded radially, have zero internal clearances, and an accurately predictable radial stiffness. When supported in these bearings, the stiff rotor design of figure 3 yields a first critical speed of approximately 12,500 rpm. The end thrust bearing is provided to react the small axial load developed by the opposed test-seal design.

Instrumentation and Data Analysis

The dynamic instrumentation illustrated in figures 3 and 4 consists, for each seal, of Bently eddy-current motion transducers and five piezo-electric pressure transducers which are distributed both axially and circumferentially along and around the seal. The circumferential "clocking" of the pressure transducers is provided primarily as a matter of convenience, since the transducers are provided exclusively to define the time history of the axial pressure distribution. Since the seal journal is forced to execute a closed circular orbit at constant speed ω within its journal, the steady-state pressure distribution is constant with respect to an observer fixed to the shaft, and the circumferential pressure distribution at time $\bar{t}$, $p(z,\theta)$ is definable in terms of either past or future time measurements $p(z,t)$ at a fixed value of θ.

The direct extraction of circumferential pressure distributions from pressure time histories also permits the "reconstruction" of a pressure time history at a given circumferential location (e.g., $\theta = 0$), despite the fact that the transducers are distributed circumferentially around the seal as illustrated in figure 4. Specifically, given the measurements $p_1(t)$, $p_2(t)$, ... $p_5(t)$, the corresponding pressure signals for $\theta = 0$ are

$$\left.\begin{array}{l} p_1^*(t) = p_1(t) \\[10pt] p_2^*(t) = p_2(t + \bar{\beta}/\omega) \\[10pt] \cdots\cdots\cdots\cdots\cdots \\[10pt] p_5^*(t) = p_5(t + 4\bar{\beta}/\omega) \end{array}\right\} \tag{10}$$

where ω is again the shaft rotational speed. In words, the pressure measurements $p_i^*(\bar{t})$ define the axial pressure distribution at time $t = \bar{t}$ for $\theta = 0$.

The seal reaction forces at a given time $t = \bar{t}$ are defined by the integrals

---

$$R_x(\bar{t}) = - \int_0^{2\pi} \int_0^L p(\theta,z)\, \sin\theta\, Rd\theta\, dz$$

$$\tag{11}$$

$$R_y(\bar{t}) = - \int_0^{2\pi} \int_0^L p(\theta,z)\, \cos\theta\, Rd\theta\, dz$$

with θ as illustrated in figure 4. These integrals may also be stated as

$$\left.\begin{array}{l}
R_X(\bar{t}) = -RL \int_0^{2\pi} \sin\theta\, \bar{p}(\theta)d = -R\omega L \int_0^{\frac{2\pi}{\omega}} \sin\omega\tau\, \bar{p}(\tau)d\tau \\[4mm]
R_Y(\bar{t}) = -RL \int_0^{2\pi} \cos\theta\, \bar{p}(\theta)d\theta = -R\omega L \int_0^{\frac{2\pi}{\omega}} \cos\omega\tau\, \bar{p}(\tau)d\tau
\end{array}\right\}$$

$$\tag{12}$$

where $\bar{p}$ is the average axial pressure defined by

$$\bar{p}(\theta) = \frac{1}{L} \int_0^L p(\theta,z)dz \;,\quad \bar{p}(t) = \frac{1}{L} \int_0^L p(t,z)dz$$

$$\tag{13}$$

The integral of Eq. (13) is evaluated numerically from the pressure time histories $p_i^*(t)$. The axial spacing of the pressure transducers has been chosen from Gauss-Legendre quadrature formulas [18] to minimize the error involved in evaluating this integral, and yields the following simple formula for the integration with respect to z

$$\bar{p}(t) = \frac{1}{2}\{A_1 p_1^*(t) + A_2 p_2^*(t) + A_3 p_3^*(t) + A_2 p_4^*(t) + A_1 p_5^*(t)\}$$

where

$$A_1 = 0.23693, \quad A_2 = 0.47862, \quad A_3 = 0.56889$$

The time integrals in Eq. (12) are executed with a simple Simpson's-rule-based algorithm. Note that a pressure time-history is required over the interval $[\bar{t}, \bar{t} + 2\pi/\omega]$ to obtain $R_X(\bar{t})$, $R_Y(\bar{t})$. Hence, pressure time histories $p_i^*(t)$ over a total time period ΔT will yield force histories $R_X(t)$, $R_Y(t)$ over the reduced interval $[\Delta T - 2\pi/\omega]$. However, since the signals are periodic, an

adequate sampling rate[2] yields sufficient output ($r_X(t)$, $r_Y(t)$, $R_X(t)$, $R_Y(t)$) from a limited number of data cycles to identify the dynamic seal coefficients K, k, C, c, m of the following dimensional verion of Eq. (4)

$$\begin{bmatrix} m & 0 \\ 0 & m \end{bmatrix} \begin{Bmatrix} \ddot{r}_X \\ \ddot{r}_Y \end{Bmatrix} + \begin{bmatrix} C & c \\ -c & C \end{bmatrix} \begin{Bmatrix} \dot{r}_X \\ \dot{r}_Y \end{Bmatrix} + \begin{bmatrix} K & k \\ -k & k \end{bmatrix} \begin{Bmatrix} r_X \\ r_Y \end{Bmatrix} = -\begin{Bmatrix} R_X \\ R_Y \end{Bmatrix} \qquad (14)$$

Note that m in this equation is the seal added fluid mass, and has nothing to do with the actual mass of the test rotor. Eq. (14) is solely the seal governing equation, and the test procedure which yields $r_X(t)$, $r_Y(t)$, $R_X(t)$, $R_Y(t)$ is not influenced by dynamics of the test-section rotor.

Identification Procedure

A generalized NR (Newton-Raphson) procedure [19], [20], [21] is employed for parameter identification. This procedure can be visualized as fitting the solution of Eqs. (14) to the observed data, in much the same manner regression analysis does with algebraic models. These solutions are obtained by numerical integration of the ordinary differential Eqs. (14). Note that this procedure operates on the differential Eq. (14), and is not a frequency-response or transfer-function approach. In fact, a frequency-response approach can provide only a restricted amount of information from the circular-orbit data of this program. This statement is illustrated by substituting the assumed solution

$$r_X = A \cos\omega t \ , \quad r_Y = A \sin\omega t$$

into Eq. (14), solving for (R_X, R_Y), and forming the dot and cross products

$$\frac{|r \times R|}{A^2} = k - C\omega \ , \quad \frac{r \cdot R}{A^2} = m\omega^2 - c\omega - K$$

For a given speed ω, a frequency-response approach yields the sums on the right hand side of these expressions; however, the N-R procedure can separately identify the coefficients.

The N-R procedure as applied to Eq. (14) requires the following first-order restatement

---

[2] Biomation data acquisition units are employed with a sampling rate per channel of 100,000 Hz to digitally record $r_X(t)$, $r_Y(t)$ and $p_i(t)$.

$$\dot{y}_1 = y_3$$

$$\dot{y}_2 = y_4$$

$$\dot{y}_3 = -y_5 \, y_3 - y_6 \, y_4 - y_7 \, y_1 - y_8 \, y_2 + y_9 \, f_1(t) \tag{15}$$

$$\dot{y}_4 = +y_6 \, y_3 - y_5 \, y_4 + y_8 \, y_1 - y_7 \, y_2 + y_9 \, f_2(t)$$

$$\dot{y}_5 = \dot{y}_6 = \dot{y}_7 = \dot{y}_8 = \dot{y}_9 = 0$$

The identities relating Eqs. (14) and (15) are $y_1 = \dot{r}_X$, $y_2 = \dot{r}_Y$, $y_3 = r_X$, $y_4 = r_Y$, $y_5 = C/m$, $y_6 = c/m$, $y_7 = K/m$, $y_8 = k/m$, and $y_9 = 1/m$. Note that the original differential equations have been augmented by the trivial differential equations, $\dot{m} = 0$, $\dot{K} = 0$, etc., to enforce the time invariance of these seal coefficients. The identification procedure minimizes, in a least-square sense, the errors between the solution to Eq. (15) and the test data.

Unfortunately, this procedure involves the solution of a multipoint-boundary value problem for which existence and uniqueness theorems are simply not available. Hence, the procedure was validated [21] by generating fake data with simulated noise and theoretically predicted seal coefficients, and then analyzing the data to "identify" the coefficients. Even with severely degraded data, the procedure yields errors less than 8%.

TEST RESULTS AND DISCUSSION

Experimental Results

The beginning phase of testing has consisted of marginal advances followed by precipitous retreats. Tests were conducted on straight seals (D = 4 in, L/D = 0.5, C/R = 0.01) in June and October 1979. Because of data transfer problems, the bulk of the dynamic data taken in June was unusable; however, test results for three good R_a, R_r sets are provided in the first three rows of Table 2. These data sets indicate that experimental estimates of m, C, c, k are smaller than predicted, while K is substantially larger. Figure 5(a) illustrates the theoretical [7] and experimental pressure distributions for case 1 of Table 2, demonstrating that the experimental pressure amplitudes are smaller than predicted. The oscillation observable in P_3 of this figure is exactly 18 times rotational speed (3660 rpm), and is at present unexplained. However, as illustrated in figure 6(a), the integration which yields the force components eliminates this and all other fourier components, leaving only the fundamental component of running speed. The displacement vector components are illustrated in figure 6(b). The "notch" in the lower portion of these signals is the result of damage to the seal journal extension caused by rubbing of the displacement transducer probe during start up.

Tests in October 1979 were repeated in the straight seal configuration; however, the measured pressure fields were noisy and erratic, and one of the pressure transducers failed. When the test unit was disassembled, chemical deposits were found on the seal bearing and journal. These deposits apparently formed when the test section was drained following the June test series. The deposits were irregular, and substantially increased the surface roughness of the seals. The results of two tests from this series are provided in the last two rows of Table 2, demonstrating the same basic trend as the June tests. Note, however, that the added mass term is now larger than predicted.

The leakage $-\Delta P$ data for a large number of tests has consistently deviated from Black's and Yamada's results in that the leakage is consistently (by 5 to 8%) smaller than predicted.

Discussion of Results

Generally speaking, an inadequate amount of data has been taken to support any conclusions about the adequacy of the theory. The differences between the tests in June and October are consistent with the theory in that an increase in surface roughness would increase σ. Over the range of σ anticipated, the coefficient μ_2 is much more sensitive to σ than μ_0, μ_1. Hence, a relatively sharper increase in the added mass m is anticipated with increasing surface roughness.

The reduced leakage results obtained in the tests as compared to Yamada's and Black's predictions are at present unexplained. It is possible that the oscillating entry clearance accounts for this result.

Additional Planned Testing

Tests were conducted on a seal with a convergent tapered sleeve segment during April 1980, and the dynamic data related to this test are currently being processed and analyzed. The taper angle for the seal tested is less than optimal [22] from a direct stiffness viewpoint. Tests will also be conducted on both an optimal taper seal and a seal with a taper angle approximately 25% larger than optimal.

Tests will be repeated in June of 1980 on the straight seal over a wide Reynolds number range. The straight seal will then be modified by rounding the sleeve inlet.

Strain-gauge pressure transducers are on order to replace and/or complement the piezo-electric transducers presently employed. With these new transducers, we should get a better idea of the dynamic entry loss, and dynamic pressure gradient.

REFERENCES

1. Black, H. F., "Effects of Hydraulic Forces in Annular Pressure Seals on
    the Vibrations of Centrifugal Pump Rotors," J. M.Eng. Sci., Vol. 11,
    No. 2, pp. 206-213, 1969.

2. Black, H. F. and Jensen, D. N., "Dynamic Hybrid Properties of Annular
    Pressure Seals," Proc. J. Mech. Engin., Vol. 184, pp. 92-100, 1970.

3. Black, H. F. and Jensen, D. N., "Effects of High Pressure Ring Seals on
    Pump Rotor Vibrations," ASME Paper No. 71-WA/FF-38, 1971.

4. Black, H. F., "The Effect of Inlet Flow Swirl on the Dynamic Coefficients
    of High-Pressure Annular Clearance Seals," unpublished analyses per-
    formed at the University of Virginia, Charlottesville, Va., August 1977.

5. Childs, D., "The Space Shuttle Main Engine High-Pressure Fuel Turbopump
    Rotordynamic Instability Problem," ASME Transactions for Power, pp.
    48-57, January 1978.

6. Yamada, Y., "Resistance of Flow through Annulus with an Inner Rotating
    Cylinder," Bul. J.S.M.E., Vol. 5, No. 18, pp. 302-310, 1962.

7. Childs, D. W., "Dynamic Analysis of Turbulent Annular Seals Based on
    Hirs' Lubrication Equation," submitted to ASME Trans., J. of Lubrica-
    tion Technology.

8. Hirs, G. G., "Fundamentals of a Bulk-Flow Theory for Turbulent Lubricant
    Films," Doctoral Thesis, Delft Technical University, Delft, The
    Netherlands, June 1970.

9. Hirs, G. G., "A Bulk-Flow Theory for Turbulence in Lubricant Films,"
    ASME J. Lubrication Technology, pp. 137-146, April 1973.

10. Black, H. F., "Empirical Treatment of Hydrodynamic Journal Bearing Per-
    formance in the Superlaminar Regime," J. Mech. Engin. Sci., Vol. 12,
    No. 2, pp. 116-122, 1970.

11. Black, H. F. and Cochrane, E. A., "Leakage and Hybrid Bearing Properties
    of Serrated Seals in Centrifugal Pumps," Paper G5, 6th International
    Conference on Fluid Sealing, February 27 - March 2, 1973, Munich,
    German Federal Republic.

12. Glienecke, J., "Experimental Investigation of the Stiffness and Damping
    Coefficients of Turbine Bearings and Their Application to Instability
    Prediction," Proceedings of the Institute of Mechanical Engineers,
    Vol. 181, Series 88, p. 116, 1966-67.

13. Morton, P. G., "Measurement of the Dynamic Characteristics of a Large
    Sleeve Bearing," ASME Trams., Journal of Lubrication Technology,
    pp. 143-150, January 1971.

14. Morton, P. G., "The Derivation of Bearing Characteristics by Means of Transient Excitation Applied Directly to a Rotating Shaft," G.E.C. Journal of Science and Technology, Vol. 42, pp. 43-47, 1975.

15. Burrows, C. R. and Stanway, R., "Identification of Journal Bearing Characteristics," ASME Trans., Journal of Dynamic Systems, Measurement and Control, pp. 167-173, September 1977.

16. Stanway, R., Burrows, C. R., and Holmes, R., "Parametric Excitation of a Squeeze-Film Bearing," 5th IFAC Symposium on Identification and Parameter Estimation, September 24-28, 1979.

17. Bowen, W. L. and Bhateja, "The Hollow Roller Bearing," ASME Paper No. 79-Lub-15, ASME-ASLE Lubrication Conference, Dayton, Ohio, October 16-18, 1979.

18. Fröberg, Introduction to Numerical Analysis, Second Edition, Addision Wesley, 1969.

19. Childs, B., Luckinbill, D., Bryan, J., and Boyd, J., "Numerical Solution of Multipoint Boundary Value Problems in Linear Systems," Int. J. Systems Science, pp. 49-57, 2(1971).

20. Childs, B., Doiron, H., and Holloway, C., "Numerical Solution of Multi-point Boundary Value Problems in Nonlinear Systems," Int. J. Systems Science, pp. 53-66, 2(1971).

21. Childs, B., Childs, D., and Dressman, J., "Estimation of Seal Stiffness and Damping Parameters from Experimental Data," accepted for presentation at the 2nd International Conference on Vibrations in Rotating Machinery, Cambridge, England, September 2-4, 1980.

22. Fleming, D. P., "High-Stiffness Seals for Rotor Critical-Speed Control," ASME Paper No. 77-DE7-10, Design Engineering Technical Conference, Chicago, Illinois, 26-30 September 1977.

Ref.	R_a	R_r	L/D	(C/R) x 10	Seal Type	Cited Results
[2]	[6,000, 14,000]	[0, 3,500]	.25 , .5, 1.	10.5 , 12.9	plain	a, b, c
[3]	[3,000, 20,000]	[0, 6,000]	.5, 1.	7.23, 10.3	plain	d, e
[10]	10,000	[0, 8,000]	1.	10.7	plain	f
[11]	[3,000, 12,000]	[0, 6,000]	.232, .5, 1.	7.1	Serrated	d

a. Static force-deflection curves for $0 \leq \varepsilon \leq 0.8$.

b. Resultant stiffness F_s/r for centered position and $\omega = 0$.

c. Rotordynamic modeling to correlate with test data on the direct damping coefficient $\bar{C}$.

d. Receptance magnitudes for centered position.

e. Rotordynamic modeling to correlate with synchronous test results. Correlation includes amplitude, phase, critical speed, and onset speed of instability.

f. Receptance magnitude and phase at centered position.

TABLE 1. PRIOR DYNAMIC SEAL TESTS

			C	c	K	k	m
1.	$R_a = 18,317$	Theory	47.	14.	9712	3585	0.06
	$R_r = 10,079$	Estimated	21.	2.5	14170	2700	0.013
2.	$R_a = 11,997$	Theory	31.	14.	4592	3046	0.06
	$R_r = 10,410$	Estimated	22.	0.33	8859	3204	0.017
3.	$R_a = 20,814$	Theory	53.4	14.	12203	3879	0.06
	$R_r = 10,079$	Estimated	25.9	2.89	16972	2556	0.013
4.	$R_a = 17,834$	Theory	50.2	4.0	9106	855	0.07
	$R_r = 2,644$	Estimated	13.2	14.3	9662	655	0.098
5.	$R_a = 19,022$	Theory	54.0	8.9	10739	2096	0.07
	$R_r = 5,783$	Estimated	18.6	1.33	14759	2200	0.113

Table 2. Test Results for June 1979 (Rows 1, 2, 3) and
October 1979 (Columns 4, 5) versus Theory [7]
(in-lb-sec units)

134
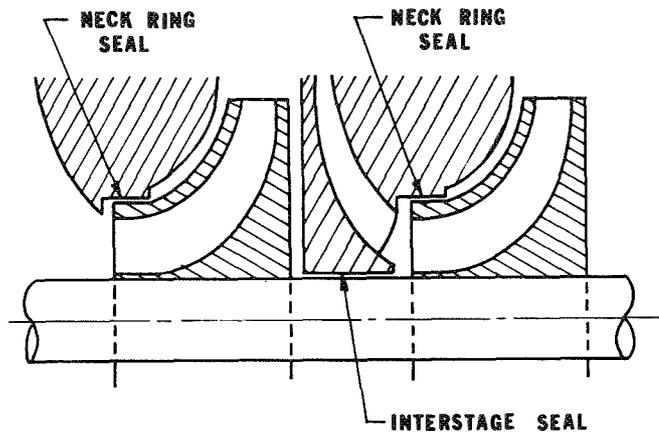
Figure 1. Seals in multistage centrifugal pumps
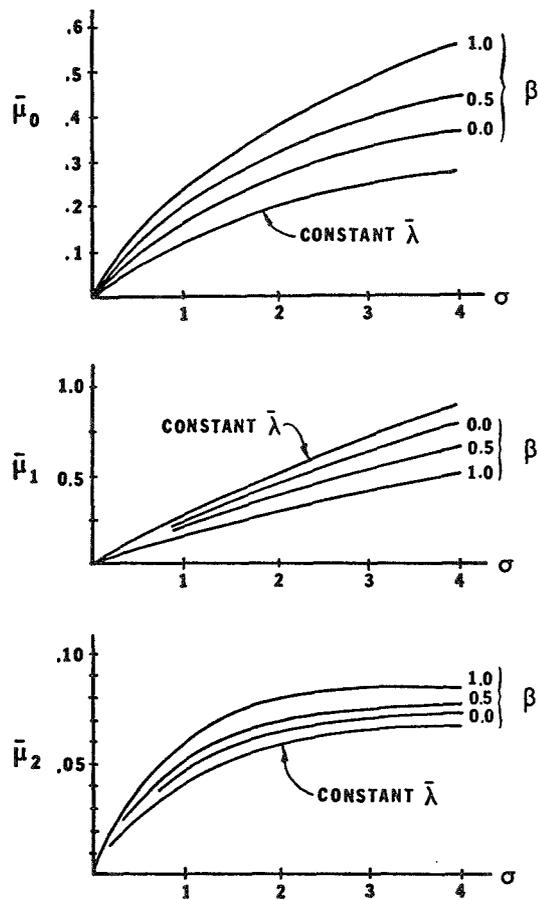
Figure 2. Dimensionless dynamic seal coefficients $\bar{\mu}_0$, $\bar{\mu}_1$, $\bar{\mu}_2$ versus σ and β for $\xi = 0.5$
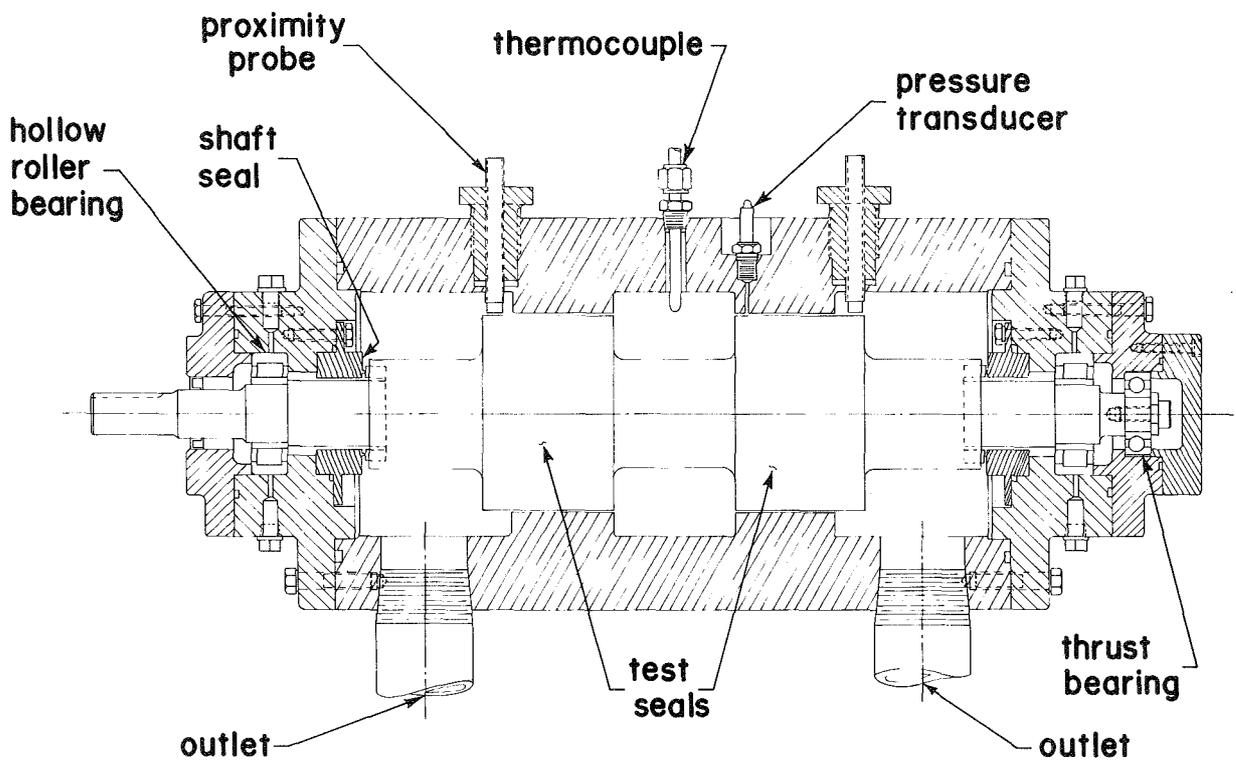
Figure 3.   University of Louisville test section assembly
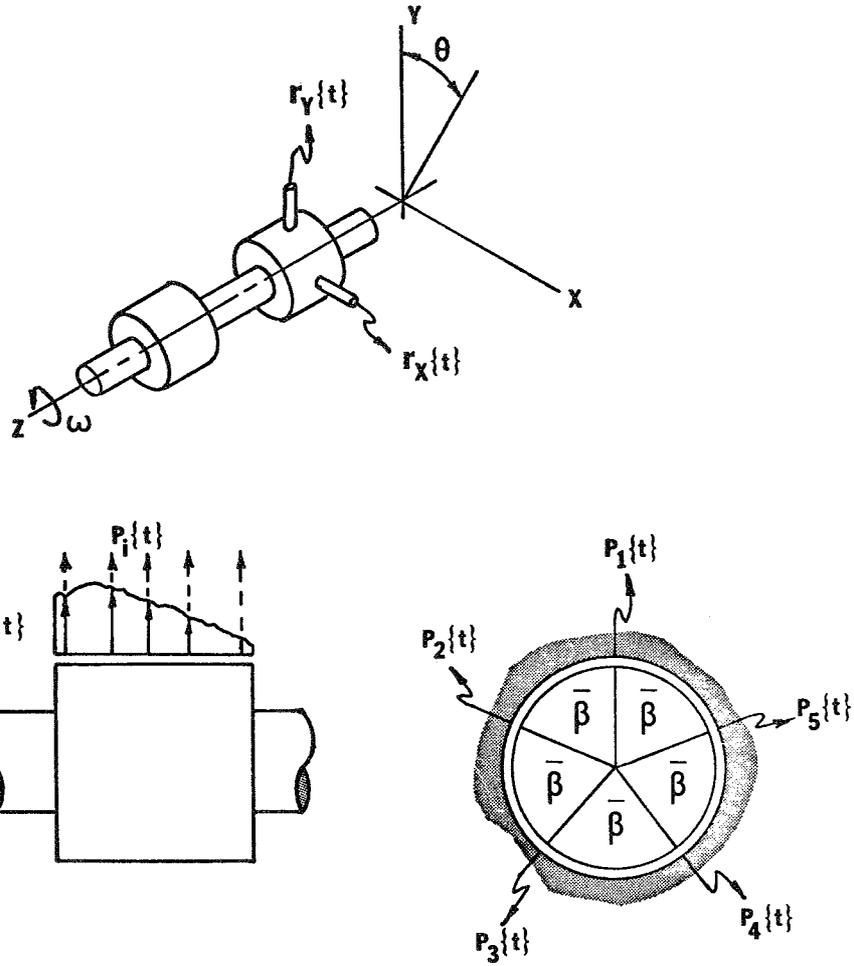
Figure 4. Instrumentation for the University of Louisville
dynamic-seal test program
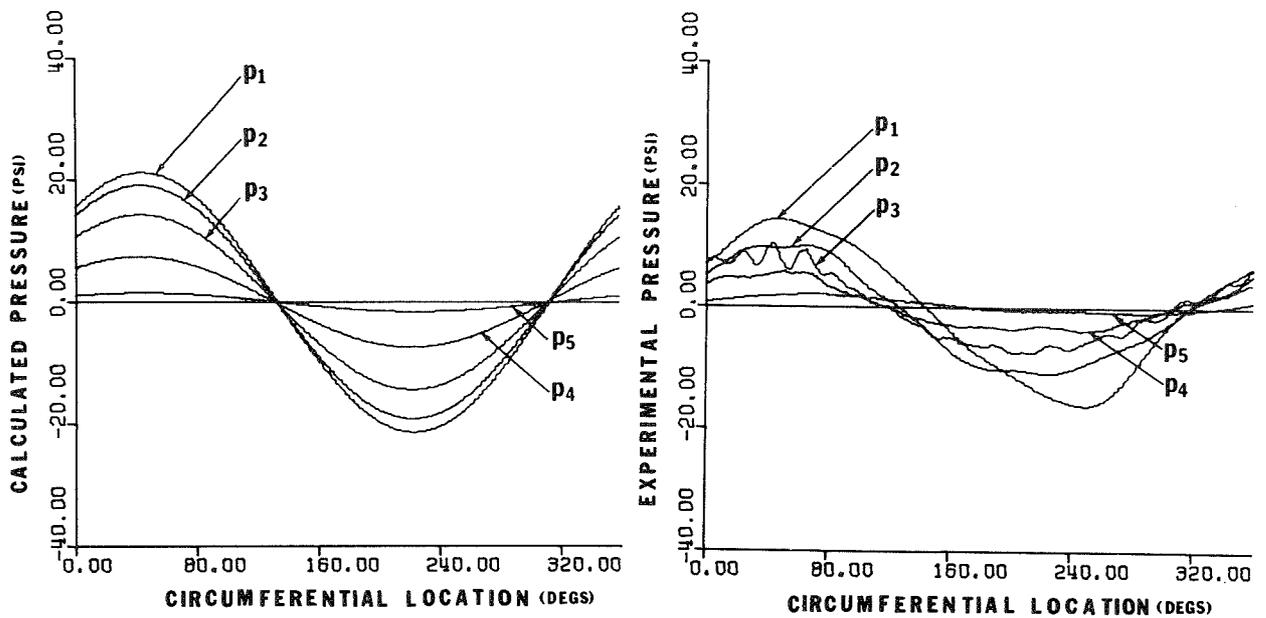
Figure 5. Theoretical and experimental pressure distributions for case 1 of Table 2
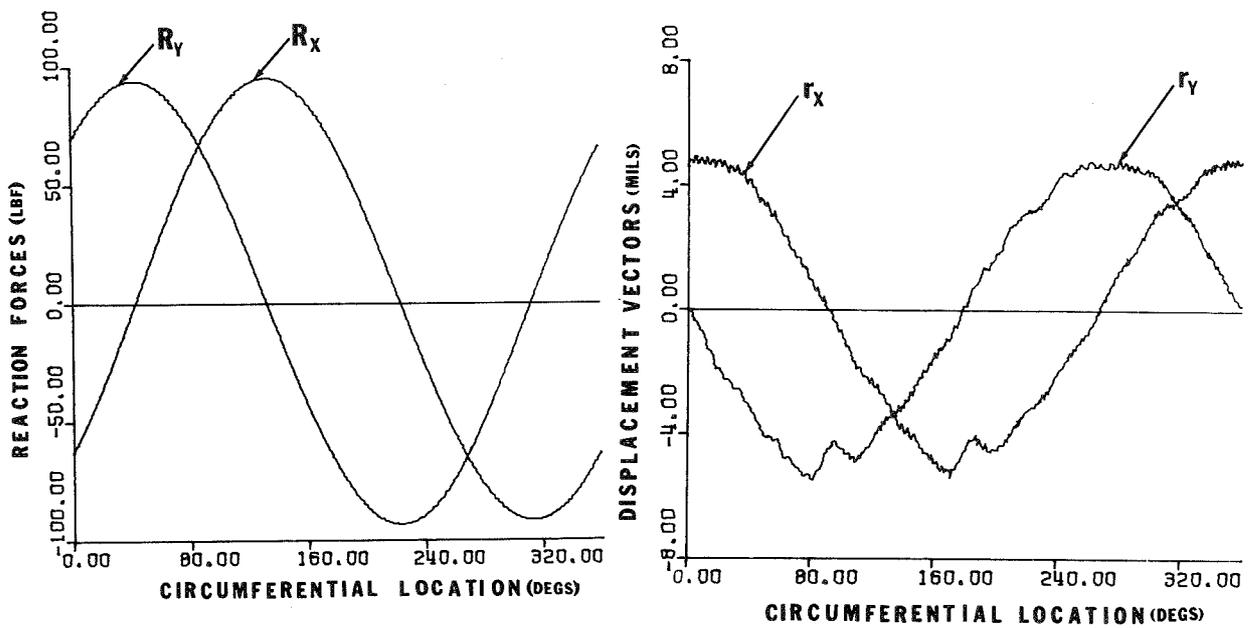
Figure 6. Measured reaction force and displacement components

EVALUATION OF INSTABILITY FORCES OF LABYRINTH
SEALS IN TURBINES OR COMPRESSORS

Takuzo Iwatsubo
Faculty of Engineering, Kobe University,
Rokko, Nada, Kobe, 657 Japan

SUMMARY

This work investigates the effects of a force induced by the labyrinth seal on the stability of rotor systems and the factors of the seal which affect the stability. In the analysis, it is assumed that the fluid in the seal is steady and that the rotor is set vertically in order to avoid the effects of gravity force. The force induced by the seal is expressed in terms proportional to the velocity and displacement of the rotor and is deduced to that expression for the oil-film force in journal bearings. That force is taken into account in the equations of motion; then the stability of the system is discussed by energy concept.

The force induced by the labyrinth seal always makes the rotor system unstable, and the tendency is remarkable when seal leakages are small. The resonance point of the rotor system is also affected by the labyrinth seal; that is, the resonance point of the rotor system is removed by the seal leakages. The flow pattern in the labyrinth seal was investigated experimentally, and the force induced by the labyrinth seal was measured by using a water-tunnel experimental system which was designed to measure the labyrinth seal force by using the similarity between gas and liquid flow theory.

INTRODUCTION

After the oil shock, high-performance turbines and compressors are required in order to save energy. For this purpose, designers would like to minimize leakage from labyrinth seals, so they design the clearances of the labyrinth seal to be small. However, if the clearances are small, self-excited rotor vibrations are caused by the flow forces of the working fluid. The origins of the exciting forces are at present only partially known as a steam whirl excitation. So it is not enough to evaluate these forces in order to design the labyrinth seals for compressors and turbines. Thus the analysis of labyrinth seals and the materials for design are strongly required by the designer of turbines and compressors. This paper is devoted to a basic analysis of the fluid force due to labyrinth seals.

First, the fundamental equation proposed by Kostyuk (refs. 1,2) is extended in order to consider the effect of the variation of gland cross section. For the analysis, the fundamental equation is rewritten to ordinary differential equations by using the finite difference method. Then spring and damping coefficients of the labyrinth seals are calculated for selected models from the fundamental equation and perturbation from the steady state. The flow rate and pressure, etc., in the steady state are also calculated. Then the stability of

139

the rotor system is discussed in terms of these coefficients by using the concept of energy. Furthermore, experiments were executed to observe the flow pattern in the gland and to study the characteristics of the flow-induced forces in the labyrinth seals.

FUNDAMENTAL EQUATION FOR GAS FLOW IN LABYRINTH SEAL

For the derivation of the equations, the following conditions are assumed;

(1) Fluid in the labyrinth seal is assumed to be gas, and its behavior is assumed to be ideal.

(2) Temperature of the fluid in the labyrinth seal is assumed to be constant.

(3) Cross-sectional area of the seal gland is assumed to be constant in spite of the deflection of rotor, and only the time derivative of the cross-sectional area is considered.

(4) Change of flow state in the gland is assumed to be isentropic.

Thus from the illustrations of figure 1 the fundamental equations with respect to the flow rate and pressure are as follows;

$$\frac{\partial(\rho_i f_i)}{\partial t} + f_i \frac{\partial(\rho_i C_i)}{\partial w} + (g_{i+1} - g_i) = 0 \tag{1}$$

$$f_i \frac{\partial(\rho_i C_i^2)}{\partial w} + \frac{\partial(\rho_i f_i C_i)}{\partial t} + (g_{i+1} C_i - g_i C_{i-1}) + \tau' U' - \tau'' U'' = -f_i \frac{\partial P_i}{\partial w} \tag{2}$$

$$\tau' = \frac{1}{2} \chi' \rho_i C_i^2 \tag{3}$$

$$\tau'' = \frac{1}{2} \chi'' \rho_i (u - C_i)^2 \tag{4}$$

$$P_{i-1}^2 - P_i^2 = \frac{g_i^2 RT}{\mu_i^2 \delta_i^2} \tag{5}$$

$$P_i = \rho_i g RT \tag{6}$$

$$Re = \frac{C\varepsilon}{\nu} \tag{7}$$

Equations (1) to (7) are nonlinear partial differential equations; so for the analysis they must be rewritten to linear partial differential equations by using the perturbation terms from the steady state. Therefore, pressure, axial flow rate, and peripheral velocity in the steady state should be obtained.

ANALYSIS OF FLOW IN STEADY STATE

As the flow in the seal is steady, all state variables are constant; therefore time derivatives and space derivatives of the state variables are zero. Thus the fundamental equations become as follows:

$$g_{i+1} - g_i = 0 \tag{8}$$

$$g_{i+1} C_i - g_i C_{i-1} + \tau' U' - \tau'' U'' = 0 \tag{9}$$

From these equations, state variables in the equilibrium condition are obtained by using the iterative method as shown in figure 2. For this calculation, the pressure recovery factor η_p is

$$\eta_p = \frac{2A}{1+A}$$

where

$$A = \frac{(\delta/\ell) C_c}{(\delta/\ell) + \tan\Theta} \tag{10}$$

and H is the angle between the rotating axis and the flow direction passing through the seal strip.

The steady-state flow rate is given as

$$g_{\ast i} = \alpha_i \delta_{\ast i} g \sqrt{\frac{2\varkappa}{\varkappa-1} \cdot p'_{\ast i-1} \cdot \rho'_{\ast i-1} \left[\left(\frac{p_{\ast i}}{p'_{\ast i-1}} \right)^{2/\varkappa} - \left(\frac{p_{\ast i}}{p'_{\ast i-1}} \right)^{\varkappa+1/\varkappa} \right]} \tag{11}$$

LINEARIZATION OF FUNDAMENTAL EQUATION

For the linearization of the fundamental equation, the perturbations of pressure, peripheral velocity, and flow rate from those of the steady state are introduced as

$$p_i = p_{\ast i} (1 + \xi_i) \tag{12}$$

141

$$C_i = C_{*i}(1 + \eta_i) \tag{13}$$

$$q_i = q_{*i}(1 + \zeta_i) \tag{14}$$

where P_{*i}, C_{*i}, and q_{*i} are pressure, peripheral velocity, and axial flow rate of steady state in the ith gland and ξ_i, η_i, and ζ_i are the nondimensional perturbation terms of pressure, peripheral velocity, and axial flow rate.

The cross-sectional area in the ith gland is represented as

$$f_i = \ell(h_i + \delta_i) \tag{15}$$

where h_i and δ_i are the height of the gland and the radial labyrinth clearance.

By denoting the displacement of the center of the rotor (x,y) as

$$x = r_1 \cos \Omega t$$
$$y = r_2 \sin \Omega t \tag{16}$$

the area of the ith chamber section is obtained as

$$f_i = \ell(h_i + \delta_{*i} - \delta_{*i} r_1 \cos \Omega t \cos \psi - \delta_{*i} r_2 \sin \Omega t \sin \psi) \tag{17}$$

Because the change of state in the gland is isentropic change, the following relation is obtained:

$$\frac{P_{*i}}{\rho_{*i}^{\chi}} = \frac{P_i}{\rho_i^{\chi}} = const$$

Therefore

$$\frac{\partial P_i}{\partial t} = \chi \frac{P_i}{\rho_i} \frac{\partial \rho_i}{\partial t} \tag{18}$$

From the above equations, the following linear equations are obtained:

$$\frac{\ell}{\varkappa}(h_i + \delta_{*i})\dot{\xi}_i + \frac{C_{*i}\ell}{\varkappa R_s}(h_i + \delta_{*i})\xi'_i + \frac{C_{*i}\ell}{R_s}(h_i + \delta_{*i})\eta'_i$$

$$- \frac{gRT\mu^2 \delta^2_{*i+1} P^2_{*i+1}}{P_{*i}\,g_*}\,\xi_{i+1} + \frac{gRT\mu^2 P_{*i}}{g_*}(\delta^2_{*i+1} + \delta^2_{*i})\xi_i$$

$$\dot{=} \frac{gRT\mu^2 \delta^2_{*i} P^2_{*i-1}}{P_{*i}\,g_*}\,\xi_{i-1} + \frac{gRT\mu^2 \delta^2_{*i+1}}{2P_{*i}\,g_*}(P^2_{*i} - P^2_{*i+1})$$

$$- \frac{gRT\mu^2 \delta^2_{*i}}{2P_{*i}\,g_*}(P^2_{*i-1} - P^2_{*i}) = \frac{gRT\mu^2}{P_{*i}\,g_*}\Big\{\delta_{*i+1}(P^2_{*i} - P^2_{*i+1})$$

$$+ \delta_{*i}(P^2_{*i} - P^2_{*i-1})\Big\}(r_1 \cos\Omega t \cos\psi + r_2 \sin\Omega t \sin\psi)$$

$$+ \ell(-r_1 \Omega \sin\Omega t \cos\psi + r_2 \Omega \cos\Omega t \sin\psi) \tag{19}$$

$$\frac{\ell}{\varkappa}(h_i + \delta_{*i})\dot{\xi}_i + \ell(h_i + \delta_{*i})\dot{\eta}_i + \frac{\ell(h_i + \delta_{*i})}{R_s}\left(\frac{C_*}{\varkappa} + \frac{gRT}{C_*}\right)\xi'_i$$

$$+ \frac{2C_*\ell}{R_s}(h_i + \delta_{*i})\eta'_i - \frac{gRT\mu^2 \delta^2_{*i+1} P^2_{*i+1}}{P_{*i}\,g_*}\,\xi_{i+1} + \left(\frac{\varkappa' U'_i C_*}{2} + \frac{gRT\mu^2 \delta^2_{*i+1} P_{*i}}{g_*}\right.$$

$$\left.+ \frac{gRT\mu^2 \delta^2_{*i} P_{*i}}{g_*} - \frac{\varkappa'' U''_i (u - C_*)^2}{2C_*}\right)\xi_i - \frac{gRT\mu^2 \delta^2_{*i} P^2_{*i-1}}{P_{*i}\,g_*}\,\xi_{i-1}$$

$$+ \left(\varkappa' U'_i C_* - \varkappa'' U''_i (C_* - u) + \frac{gRT\,g_*}{P_{*i}}\right)\eta_i - \frac{gRT\,g_*}{P_{*i}}\,\eta_{i-1}$$

$$+ \frac{\varkappa' U'_i C_*}{2} - \frac{\varkappa'' U''_i (u - C_*)^2}{2C_*} + \frac{gRT\mu^2}{2g_*}\left(\delta^2_{*i+1} P_{*i} - \delta^2_{*i+1}\frac{P^2_{*i+1}}{P_{*i}} - \delta^2_{*i}\frac{P^2_{*i-1}}{P_{*i}}\right.$$

$$\left.+ \delta^2_{*i} P_{*i}\right) = \frac{gRT\mu^2}{g_*}\left(\delta_{*i+1} P_{*i} - \delta_{*i+1}\frac{P^2_{*i+1}}{P_{*i}} - \delta_{*i}\frac{P^2_{*i-1}}{P_{*i}} + \delta_{*i} P_{*i}\right)$$

$$\times (r_1 \cos\Omega t \cos\psi + r_2 \sin\Omega t \sin\psi)$$

$$+ \ell(-r_1 \Omega \sin\Omega t \cos\psi + r_2 \Omega \cos\Omega t \sin\psi) \tag{20}$$

where

$$(\overset{\bullet}{\bullet}) = \frac{\partial(\bullet)}{\partial t} \quad , \quad (\bullet)' = \frac{\partial(\bullet)}{\partial \varphi}$$

Equations (19) and (20) are rewritten in the matrix form as

$$T\dot{u} + Vu' + Bu = f\left(r_1 \cos\Omega t \cos\varphi + r_2 \sin\Omega t \sin\varphi\right)$$
$$+ g\left(r_1 \sin\Omega t \cos\varphi - r_2 \cos\Omega t \sin\varphi\right) \quad (21)$$

where T, V, and B are (2k - 1) × (2k - 1) matrix and u, f and g are (2k - 1) row vectors and u is represented as

$$u^T = \lfloor \xi_1 , \eta_1, \xi_2, \eta_2, \text{----}, \xi_{k-1}, \eta_{k-1}, \rfloor$$

ANALYSIS BY FINITE DIFFERENCE METHOD

Multiplying equation (21) by T^{-1} yields

$$I\dot{u} + Du' + Qu = s\left(r_1 \cos\Omega t \cos\varphi + r_2 \sin\Omega t \sin\varphi\right)$$
$$+ r\left(r_1 \sin\Omega t \cos\varphi - r_2 \cos\Omega t \sin\varphi\right) \quad (22)$$

where

$$D = T^{-1}V \quad , \quad Q = T^{-1}B$$
$$s = T^{-1}f \quad , \quad r = T^{-1}g$$
$$I = \text{unit matrix}$$

By dividing the circumferential space of the rotor into n elements as shown in figure 3, the following finite difference equation is obtained about the jth element:

$$I\dot{u}_j + P(u_{j+1} - u_{j-1}) + Qu_j = a_j \cos\Omega t + b_j \sin\Omega t$$
$$+ c_j \sin\Omega t - d_j \cos\Omega t \quad (23)$$

where

144

$$\mathbb{P} = \mathbb{D}/2\Delta \ , \quad a_j = \$ \, r_1 \cos \varphi_j \ , \quad b_j = \$ \, r_2 \sin \varphi_j$$

$$\mathbb{C}_j = \mathbb{r} \, r_1 \cos \varphi_j \ , \quad d_j = \mathbb{r} \, r_2 \sin \varphi_j \ ,$$

$$\mathbb{U}_j^T = \llcorner u_{1j}, u_{2j}, \text{-----}, u_{ij}, \text{----}, u_{k-1\,j}, 1 \lrcorner$$

$$\mathbb{a}_j^T = \llcorner a_{1j}, a_{2j}, \text{-----}, a_{ij}, \text{-----}, a_{k-1\,j}, 0 \lrcorner$$

$$\mathbb{b}_j^T = \llcorner b_{1j}, b_{2j}, \text{-----}, b_{ij}, \text{-----}, b_{k-1\,j}, 0 \lrcorner$$

$$\mathbb{C}_j^T = \llcorner c_{1j}, c_{2j}, \text{-----}, c_{ij}, \text{-----}, c_{k-1\,j}, 0 \lrcorner$$

$$\mathbb{d}_j^T = \llcorner d_{1j}, d_{2j}, \text{-----}, d_{ij}, \text{-----}, d_{k-1\,j}, 0 \lrcorner$$

When the boundary conditions are set as $u_j(\phi_j, t) = u_j(\phi_j + 2\pi, t)$, equation (23) is reduced for the overall system to

$$\mathbb{I} \dot{\mathbb{X}} + \mathbb{A} \mathbb{X} = a \cos \Omega t + \mathbb{b} \sin \Omega t + \mathbb{c} \sin \Omega t - \mathbb{d} \cos \Omega t \qquad (24)$$

where x, a, b, c, d are n(2k − 1) row vectors and A is n(2k − 1) × n(2k − 1) matrix

The solution of equation (24) is obtained in matrix form as

$$\mathbb{X} = e^{-\mathbb{A}t} e + \int_0^t e^{-(t-s)\mathbb{A}} a \cos \Omega s\, ds + \int_0^t e^{-(t-s)\mathbb{A}} \mathbb{b} \sin \Omega s\, ds$$

$$+ \int_0^t e^{-(t-s)\mathbb{A}} \mathbb{c} \sin \Omega s\, ds - \int_0^t e^{-(t-s)\mathbb{A}} \mathbb{d} \cos \Omega s\, ds \qquad (25)$$

If the rotor is rotating at the steady state, the perturbation terms are equal to zero; so the initial condition for analysis becomes

$$\mathbb{e} = 0 \qquad (26)$$

By using this condition, equation (25) becomes

$$\mathbb{X} = \mathbb{E} \, r_1 \cos \Omega t + \mathbb{F} \, r_2 \sin \Omega t + \mathbb{G} (-r_1 \Omega \sin \Omega t)$$

$$+ \mathbb{H} \, r_2 \Omega \cos \Omega t \qquad (27)$$

where

$$E = \frac{1}{r_1}\left\{ \frac{1}{\Omega^2}\left(I + \frac{A^2}{\Omega^2}\right)^{-1} A\, a - \frac{1}{\Omega}\left(I + \frac{A^2}{\Omega^2}\right)^{-1} b \right\}$$

$$F = \frac{1}{r_2}\left\{ \frac{1}{\Omega^2}\left(I + \frac{A^2}{\Omega^2}\right)^{-1} A\, b + \frac{1}{\Omega}\left(I + \frac{A^2}{\Omega^2}\right)^{-1} a \right\}$$

$$G = \frac{1}{r_1\Omega}\left\{ \frac{1}{\Omega}\left(I + \frac{A^2}{\Omega^2}\right)^{-1} d - \frac{1}{\Omega^2}\left(I + \frac{A^2}{\Omega^2}\right)^{-1} A\, c \right\}$$

$$H = \frac{1}{r_2\Omega}\left\{ -\frac{1}{\Omega}\left(I + \frac{A^2}{\Omega^2}\right)^{-1} c - \frac{1}{\Omega^2}\left(I + \frac{A^2}{\Omega^2}\right)^{-1} A\, d \right\}$$

By using the nondimensional variable of pressure, fluid forces acting on the rotor are given as

$$F_x = -R_s \sum_{i=1}^{k-1} \int_0^{2\pi} P_{*i}\, \xi_i\, \ell \cos\psi\, d\psi$$
$$\doteqdot -\frac{2\pi R_s \ell}{n} \sum_{i=1}^{k-1} P_{*i} \sum_{j=1}^{n} \xi_{ij} \cos\left(\frac{2\pi}{n}(j-1)\right)$$

$$F_y = -R_s \sum_{i=1}^{k-1} \int_0^{2\pi} P_{*i}\, \xi_i\, \ell \sin\psi\, d\psi$$
$$\doteqdot -\frac{2\pi R_s \ell}{n} \sum_{i=1}^{k-1} P_{*i} \sum_{j=1}^{n} \xi_{ij} \sin\left(\frac{2\pi}{n}(j-1)\right) \tag{28}$$

where ξ_{ij} is nondimensional variable of the ith gland and the jth element. By applying the relation

$$r_1 \cos\Omega t = x \quad , \quad r_2 \sin\Omega t = y$$
$$-r_1\Omega \sin\Omega t = \dot{x} \quad , \quad r_2\Omega \cos\Omega t = \dot{y} \tag{29}$$

to equation (28), the flow-induced force due to the labyrinth seal is obtained as

$$F_x = k_{xx} x + k_{xy} y + C_{xx} \dot{x} + C_{xy} \dot{y}$$
$$F_y = k_{yx} x + k_{yy} y + C_{yx} \dot{x} + C_{yy} \dot{y} \tag{30}$$

where

146

$$k_{xx} = -\frac{2\pi R_s \ell}{n} \sum_{i=1}^{k-1} P_{*i} \sum_{j=1}^{n} \mathbb{E}_{\xi_{ij}} \cos\left(\frac{2\pi}{n}(j-1)\right)$$

(31)

$$k_{xy} = -\frac{2\pi R_s \ell}{n} \sum_{i=1}^{k-1} P_{*i} \sum_{j=1}^{n} \mathbb{F}_{\xi_{ij}} \cos\left(\frac{2\pi}{n}(j-1)\right)$$

$$C_{xx} = -\frac{2\pi R_s \ell}{n} \sum_{i=1}^{k-1} P_{*i} \sum_{j=1}^{n} \mathbb{G}_{\xi_{ij}} \cos\left(\frac{2\pi}{n}(j-1)\right)$$

(32)

$$C_{xy} = -\frac{2\pi R_s \ell}{n} \sum_{i=1}^{k-1} P_{*i} \sum_{j=1}^{n} \mathbb{H}_{\xi_{ij}} \cos\left(\frac{2\pi}{n}(j-1)\right)$$

$$k_{yx} = -\frac{2\pi R_s \ell}{n} \sum_{i=1}^{k-1} P_{*i} \sum_{j=1}^{n} \mathbb{E}_{\xi_{ij}} \sin\left(\frac{2\pi}{n}(j-1)\right)$$

(33)

$$k_{yy} = -\frac{2\pi R_s \ell}{n} \sum_{i=1}^{k-1} P_{*i} \sum_{j=1}^{n} \mathbb{F}_{\xi_{ij}} \sin\left(\frac{2\pi}{n}(j-1)\right)$$

$$C_{yx} = -\frac{2\pi R_s \ell}{n} \sum_{i=1}^{k-1} P_{*i} \sum_{j=1}^{n} \mathbb{G}_{\xi_{ij}} \sin\left(\frac{2\pi}{n}(j-1)\right)$$

(34)

$$C_{yy} = -\frac{2\pi R_s \ell}{n} \sum_{i=1}^{k-1} P_{*i} \sum_{j=1}^{n} \mathbb{H}_{\xi_{ij}} \sin\left(\frac{2\pi}{n}(j-1)\right)$$

These coefficients are the spring constants and damping coefficients for the gas flow through the labyrinth seal when the rotor moves parallel to the casing axis.

NUMERICAL EXAMPLE

The labyrinth seal having three teeth is used as a numerical model, and the seal is divided into 24 elements for the finite difference method. Details of the labyrinth seal, the rotor, and the fluid are shown in tables 1 to 3. In table 1, models A to C investigate the effect of seal clearance, models D to F investigate the effect of precession, and models G and H investigate the effect of divergence and convergence seals.

For the calculation, the following values are used:

Flow coefficient = 0.7

λ = 64/Re for Re < 1200

λ = 0.3164Re$^{-0.25}$ for Re $\geq$ 1200

where   Re   is Reynolds number.

Table 4 shows the pressure and flow rate in the steady state. Figures 4 to 6 show the spring constants and damping coefficients for each model. Because the rotor axis is coincident with the casing axis for the calculation, the following relations are obtained:

$$Kxx = Kyy, \qquad Kxy = -Kxy$$

$$Cxx = Cyy, \qquad Cxy = -Cyx$$

(35)

Figure 4 shows the spring constants and damping constants for models A, B, and C in order to investigate the effect of clearance. From figure 4(b), principal diagonal terms of the damping coefficients are constant for the variation of rotating speed; on the other hand, the cross terms of the damping coefficient vary with rotating speed. Decreasing the clearance makes the coefficients large. Figure 5 shows the effect of precession, from which it is known that the diagonal terms of both the spring and damping coefficients are constant for the variation of rotating speed but that the cross terms of both the spring and damping coefficients are strongly dependent on rotating speed. Figure 6 shows the different effects of convergence and divergence seals. From these figures it becomes clear that the cross terms of the spring coefficients and the damping coefficients are quantitatively different.

ENERGETIC APPROACH TO STABILITY

In this section, the energy, eigenvalue, and phase difference between two modes are derived for a two-degree-of-freedom system, and the result is applied to the stability analysis of a rotor having a labyrinth seal. The general equation of motion is represented in matrix form as

$$M \ddot{x} + B \dot{x} + K x = 0 \tag{36}$$

where

$$x = \begin{Bmatrix} x_1 \\ x_2 \end{Bmatrix}, \quad M = \begin{bmatrix} m_{11} & 0 \\ 0 & m_{22} \end{bmatrix}, \quad B = \begin{bmatrix} b_{11} & b_{12} \\ b_{21} & b_{22} \end{bmatrix}, \quad K = \begin{bmatrix} k_{11} & k_{12} \\ k_{21} & k_{22} \end{bmatrix}$$

As equation (36) has two eigenvalues, we consider the energy for each mode by assuming the periodical vibrational mode, that is, by neglecting the real part of the eigenvalue. Then the vibrational energy for one cycle for each mode is written as

$$E = \int \dot{x}^T M \ddot{x} \, dt + \int \dot{x}^T B \dot{x} \, dt + \int \dot{x}^T K x \, dt \tag{37}$$

The first term of expression (37) is kinetic energy, the second is dissipative energy, and the third is potential energy. The energies of each term for one cycle (one period = τ) are obtained as

$$\int_0^\tau \dot{x}^T M \ddot{x} \, dt = 0 \tag{38}$$

$$\int_0^\tau \dot{x}^T B \dot{x} \, dt = \int_0^\tau (b_{11} \dot{x}_1^2 + b_{22} \dot{x}_2^2 + 2\bar{b} \dot{x}_1 \dot{x}_2) \, dt \equiv E_1 + E_2 \tag{39}$$

where

$$\bar{b} = \frac{1}{2} (b_{12} + b_{21})$$

$$\int_0^\tau \dot{x}^T K x \, dt = \int_0^\tau \Delta k (\dot{x}_1 x_2 - x_1 \dot{x}_2) \, dt \equiv E_3 \tag{40}$$

where

$$\Delta k = \frac{1}{2} (k_{12} - k_{21})$$

Therefore the total energy of the system for one cycle becomes

$$E = E_1 + E_2 + E_3 \quad , \tag{41}$$

where

$$E_1 = \frac{\omega_j}{\omega} (b_{11} u_1^2 + b_{22} u_2^2) \, ,$$

$$E_2 = \frac{\omega_j}{\omega} \cdot 2\bar{b} \, u_1 u_2 \cos(\phi_1 - \phi_2) \, , \tag{42}$$

$$E_3 = -2 \Delta k \, u_1 u_2 \sin(\phi_1 - \phi_2) \, ,$$

u_i is the eigenvector and $(\phi_1 - \phi_2)$ is the phase angle between the first and second modes. By using this result, the stability of the system may be stated from the energy point of view as follows:

149

(1) If $E > 0$, the energy of the system is absorbed, and thus the system is stable.

(2) If $E < 0$, the energy of the system is dissipative, and thus the system is unstable.

In expression (42), E_i is the energy obtained by diagonal elements of the damping coefficient. It is always positive; so if the damping coefficient is positive, this term always makes the system stable. Also E_2 is the energy obtained by cross elements of the damping coefficient, and its sign is dependent on the phase angle between ϕ_1 and ϕ_2. Finally E_3 is the energy obtained by cross elements of $(k_{12} - k_{21})$ and the phase angle between ϕ_1 and ϕ_2.

From the above discussion, cross elements of the stiffness and the diagonal elements of the damping make the system unstable, and the cross elements of the damping do not affect the stability in this case.

EXPERIMENTS

The experimental apparatus shown in figure 7 was used to observe the flow pattern in the labyrinth seal and to investigate the dynamic behavior of the labyrinth seal. The rotor is driven by a variable-speed motor system, and its bearing (with eccentricity) is also driven by another variable-speed motor in order to obtain an arbitrary whirling speed and spinning speed. A two-stage labyrinth seal (straight type) is set up at the rotor, whose depth of gland, pitch, and mean clearance are 18.2, 30.0, and 1.8 millimeters, respectively. Rotating speed of the rotor and shaft for whirling drive are 84 337 and 93 460 rpm, respectively. The casing is made from polymethyl-meta-acrylate in order to show the flow state, and water is used for the working fluid.

Pressure in the shroud is measured by the semiconductor pressure gage, and its signal is analyzed by a real-time analyzer. Figure 8 shows the flow pattern in the shroud, where a continuous vortex in the circumferential direction occurs in the fluid flow. The form is like a sinusoidal wave which is rotating in the same direction as the rotor. Figures 9 and 10 show the dynamic pressure (perturbation term) of the gland and the phase angle between deflection and the pressure for forward and backward precession, respectively. From these figures it is known that the dynamic pressure of the both cases is increased in proportion to the increase of rotating speed but that the tendency of the phase angle of both cases is the reverse.

MOTION PICTURE SUPPLEMENT

The 8-mm film was taken in order to observe the flow pattern in the gland of the labyrinth seal, where a continuous vortex in circumferential direction occurs. The vortex form is like a sinusoidal wave which is rotating in the same direction as the rotor. Figure 11 shows the two different flow patterns. The left side shows a conventional mathematical model of the flow pattern in the gland. This model is usually used to derive the fundamental equation. The real flow pattern is not similar to the model. In the gland the flow is composed of vortex and expansion flow as shown by the right side of figure 11.

150

Thus the next subject we should approach is the mathematical derivation of the fundamental equation considering the vortex in the gland.

CONCLUSIONS

The force induced by the labyrinth seal is solved by using the finite difference method, expressed in proportional terms to the velocity and displacement of the rotor, and reduced to the expression of oil-film force of journal bearings. Then the effect of the coefficients of the induced force on the stability of the rotor system is discussed from the energy point of view. The force induced by the labyrinth seal always makes the rotor system unstable, and the tendency is remarkable when leakage of the seal is small. The flow pattern in the labyrinth seal was investigated experimentally, and it is known that a continuous vortex in the circumferential direction occurs in the fluid flow. The form is like a sinusoidal wave which is rotating in the same direction as the rotor.

EDITORIAL SUPPLEMENT

Reproduction of the film frame (fig. 8) was not very successful, so we introduce figures 12 and 13 in an attempt to demonstrate the film supplement. Figure 12 is a sketch of what appears in the film to be a spiral vortex. Figure 13 represents a possible sequence of motions of the vortex center resulting from the periodic behavior of the flow interface. One must also be aware of the possible disturbance caused by the air bubbles in the flow field.

These instabilities appear to be linked with those noted in unpublished work by Robert C. Hendricks and T. Trent Stetz of the NASA Lewis Research Center, where a flow visualization study was carried out on a water table to determine some characteristics of flows through sequential Borda-type inlets (no rotation and no centerbody). In figure 14(a) the four lucite Borda models were placed in such a way that they touched each other to form a continuous channel. The inlet water depth was similar to the passage width. The injected dye revealed that the flow through this configuration continued uninterrupted after passing the vena-contracta. The models were then placed with spacings of 1/3 of the channel passage width (fig. 14(b)). The flow still continued in an uninterrupted manner after the vena-contracta. The models were then placed with spacings of 3/2 of the channel passage (fig. 14(c)). At this separation distance part of the flow entered the cavities and slight oscillations were observed. At a separation distance of 2-1/4 channel passage widths a very strong oscillation was observed (fig. 14(d)): The exhaust of one passage would "fan" the flow across the inlet of the subsequent Borda passage. These oscillations weakened when the separation distance was increased to 4 channel passage widths (fig. 14(e)). A separation of 6 channel widths showed minor oscillations (fig. 14(f)). At distances beyond 16 channel widths the flow through each Borda passage appeared nearly independent of the preceding flow (fig. 14(g)).

REFERENCES

(1) Kostyuk, A. G.: A Theoretical Analysis of the Aerodynamic Forces in the Labyrinth Glands of Turbomachines. Teploenergetica, 1972, vol. 19, no. 11, pp. 29-33.

(2) Kostyuk, A. G.: Circulation Forces over the Shrouding and Their Influence
     on the Threshold Capacity of Large Turbine Unit." Teploenergetica, 1975,
     vol. 22, no. 3, pp. 41-46.

BIBLIOGRAPHY

Alford, J. S.: Protecting Turbomachinery from Self-Excited Rotor Whirl.
  Trans. ASME, J. Eng. Power, Oct. 1965, pp. 333-344.

Spurk, J. K. and Keiper, R.: Selbsterregte Schwingungen bei Turbomachinen
  infolge der Labyrinthströmung. Ingenieur-Archiv, vol. 43, 1974, pp. 127-135.

Thomas, H. J.: Zur Laufstabilität einfacher Turborotoren, besonders bei
  Spalterregung. Konstruktion, vol. 30, 1978, H.9, pp. 339-344.

Wright, D. V.: Air Model Tests of Labyrinth Seal Forces on a Whirling Rotor.
  Trans. ASME, J. Eng. Power, Oct. 1978, pp. 533-543.

TABLE 1. - CALCULATION MODELS OF LABYRINTH SEAL FORCE

MODEL	Rs(mm)	l(mm)	θ(rad)	δ(mm)	WHIRL DIREC.	WHIRL FREQ.
A	40	10	0	0.3	FORWARD	ω_n
B	40	10	0	0.45	FORWARD	ω_n
C	40	10	0	0.6	FORWARD	ω_n
D	40	10	0	0.3	FORWARD	$0.5\,\omega_n$
E	40	10	0	0.3	BACKWARD	ω_n
F	40	10	0	0.3	FORWARD	$2\,\omega_n$
G	40	10	0	0.2 0.3 0.4	FORWARD	ω_n
H	40	10	0	0.4 0.3 0.2	FORWARD	ω_n

TABLE 2. - DATA OF ROTOR

FOR CALCULATION

Rs	0.04	m
m	1.98	Kg
k	2503.6	Kg/m
ω_n	111.45	rad/sec

TABLE 3. - DATA OF GAS

FOR CALCULATION

T	573	K
R	29.23	Kg m/Kg K
α	0.7	
p_0	20000	Kg/m
p_z	10000	Kg/m

TABLE 4. - STEADY-STATE VALUES

MODEL	Q(Kg sec/m²)	P(1) (ata)	P(2) (ata)	P(3) (ata)	P(4) (ata)
A	0.5004×10^{-1}	2.0	1.7130	1.4377	1.0
B	0.7592×10^{-1}	2.0	1.7049	1.4335	1.0
C	0.1019	2.0	1.7002	1.4394	1.0
D	0.5004×10^{-1}	2.0	1.7130	1.4377	1.0
E	0.5004×10^{-1}	2.0	1.7130	1.4377	1.0
F	0.5004×10^{-1}	2.0	1.7130	1.4377	1.0
G	0.4373×10^{-1}	2.0	1.3711	1.1621	1.0
H	0.4375×10^{-1}	2.0	1.8546	1.6000	1.0

P(1): inlet pressure, P(2): first gland pressure

P(3): second gland pressure, P(4): outlet pressure
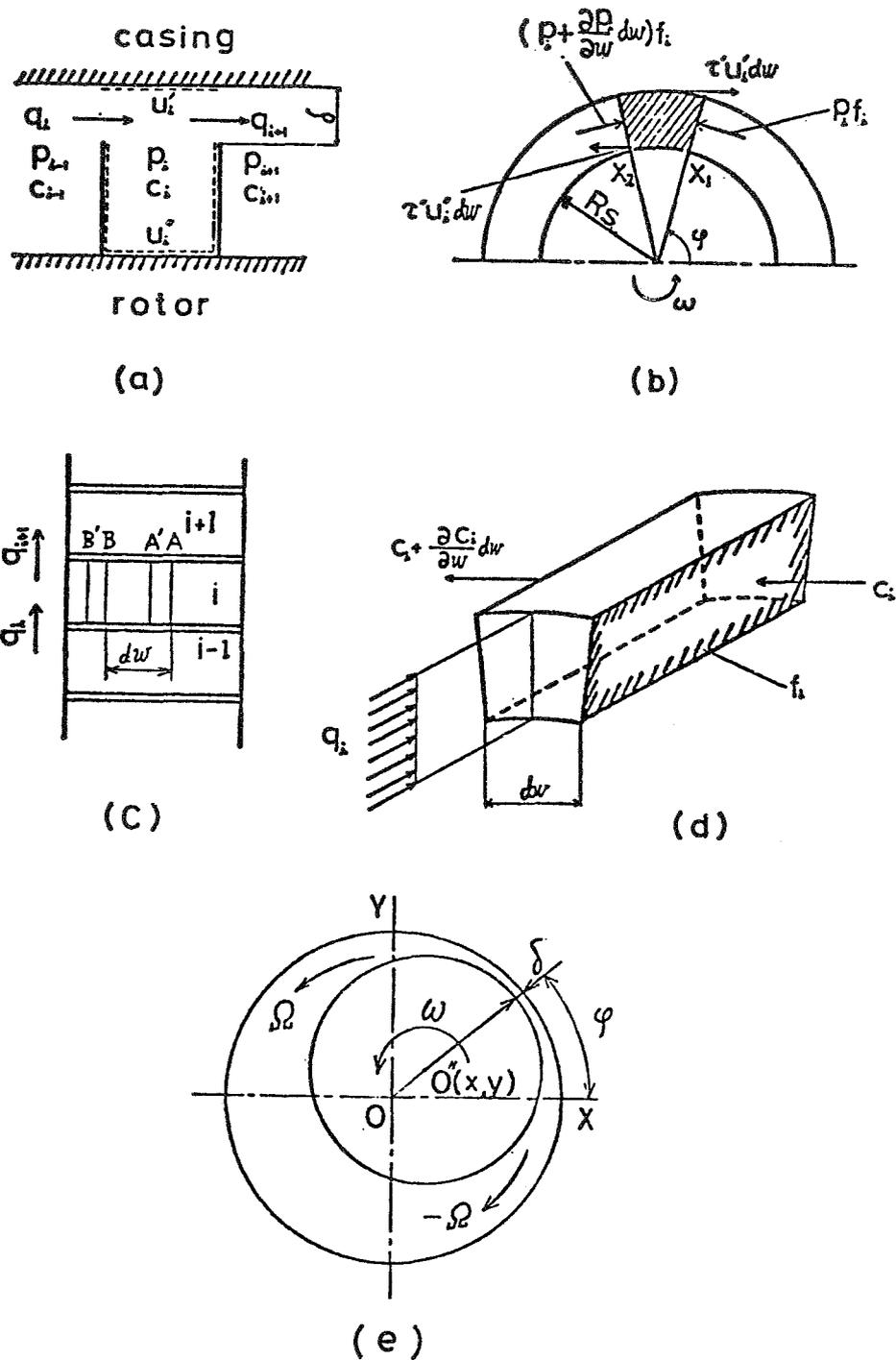
Figure 1. - Cross section of labyrinth seal and definition
    of coordinate.
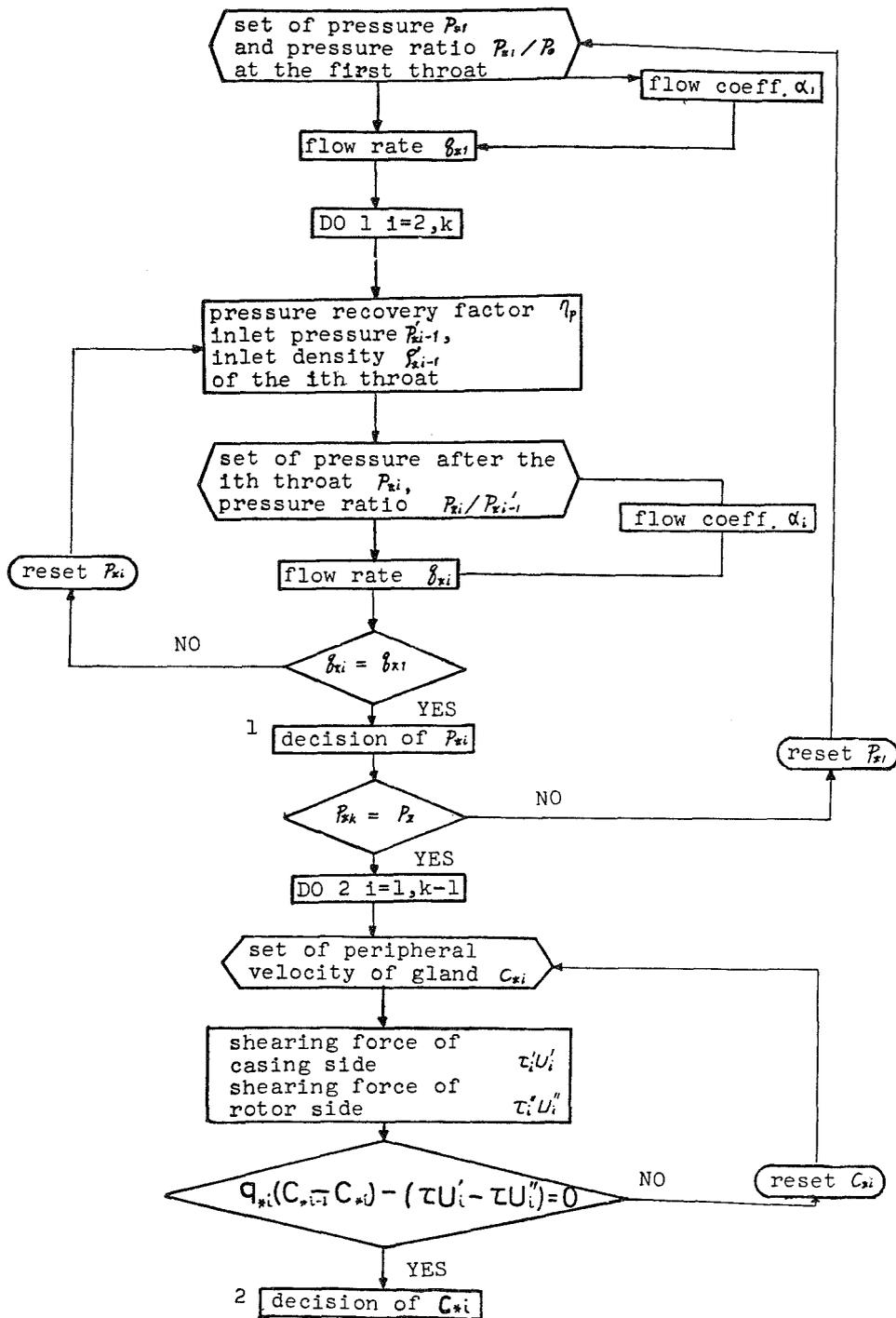
Figure 2. - Calculation procedure for steady state.
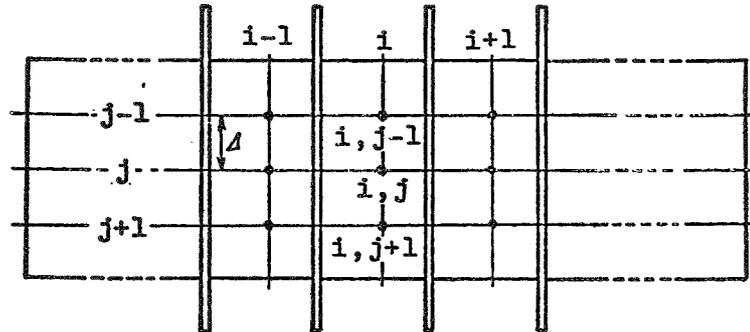
Figure 3. - Definition of mesh points for finite
difference method.
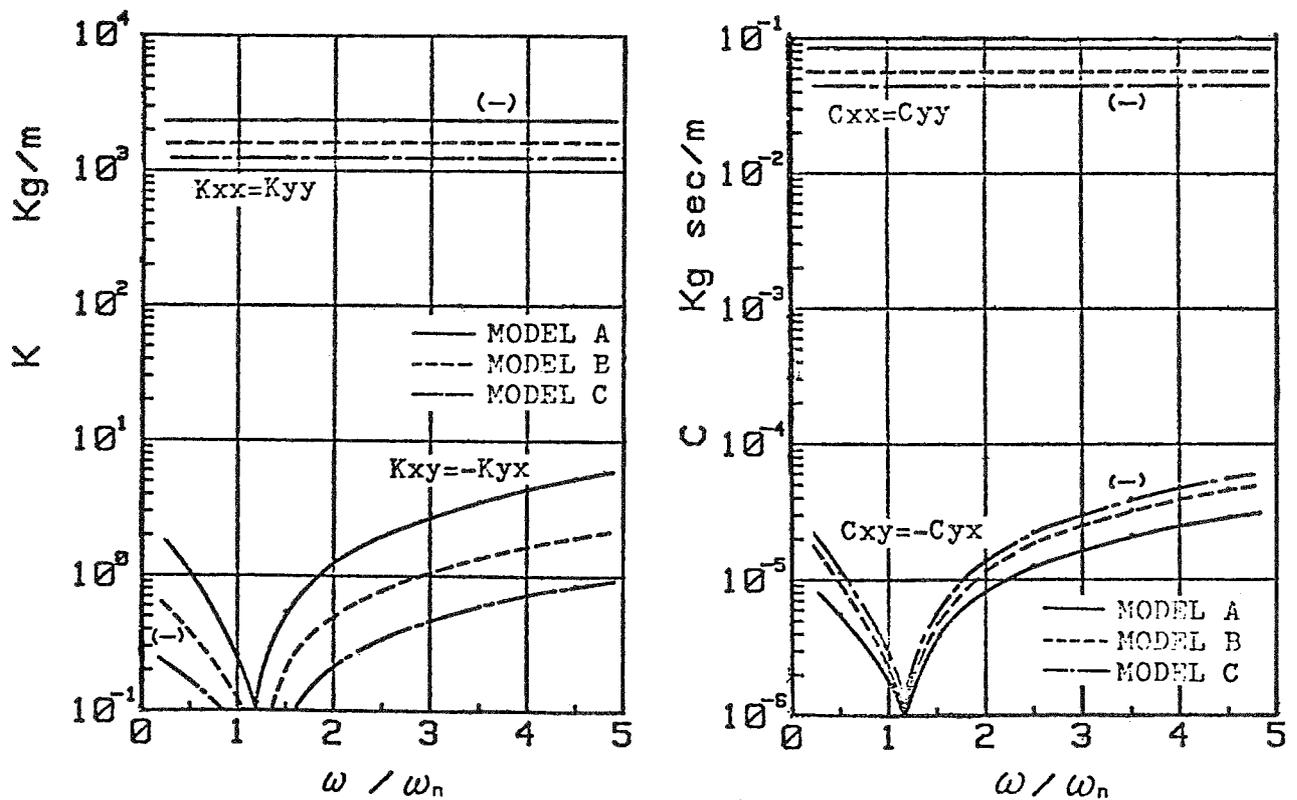
(a) Spring coefficients.

(b) Damping coefficients.

Figure 4. - Coefficients of flow-induced force for models A to C.
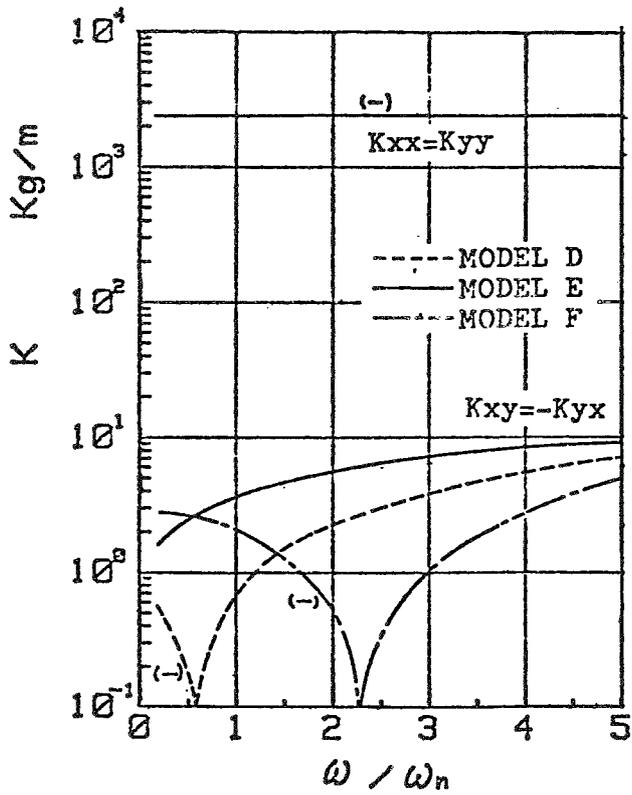
(a) Spring coefficients.
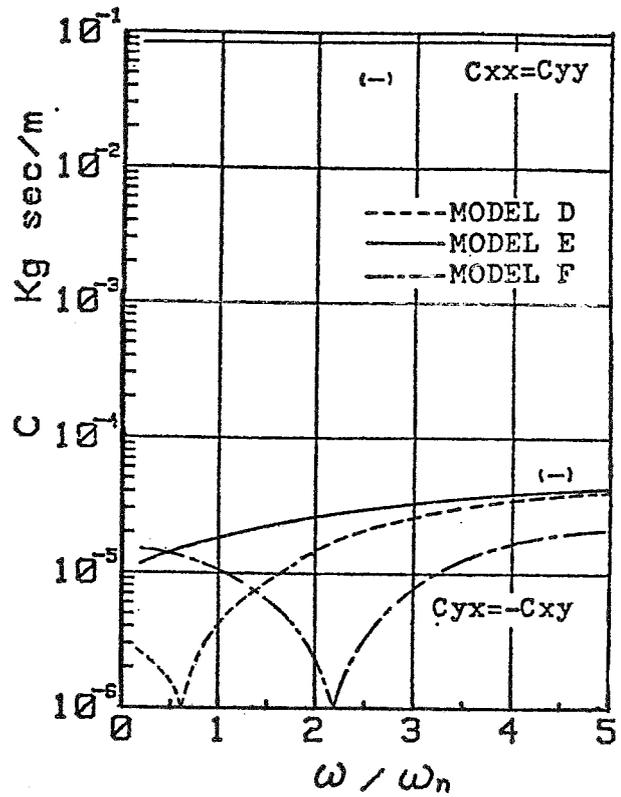
(b) Damping coefficients.

Figure 5. - Coefficients of flow-induced force for models D to F.
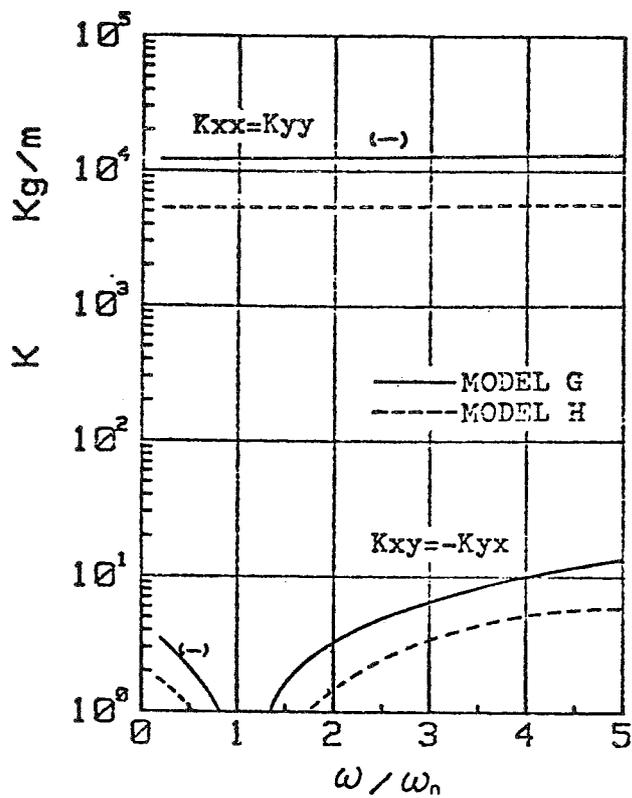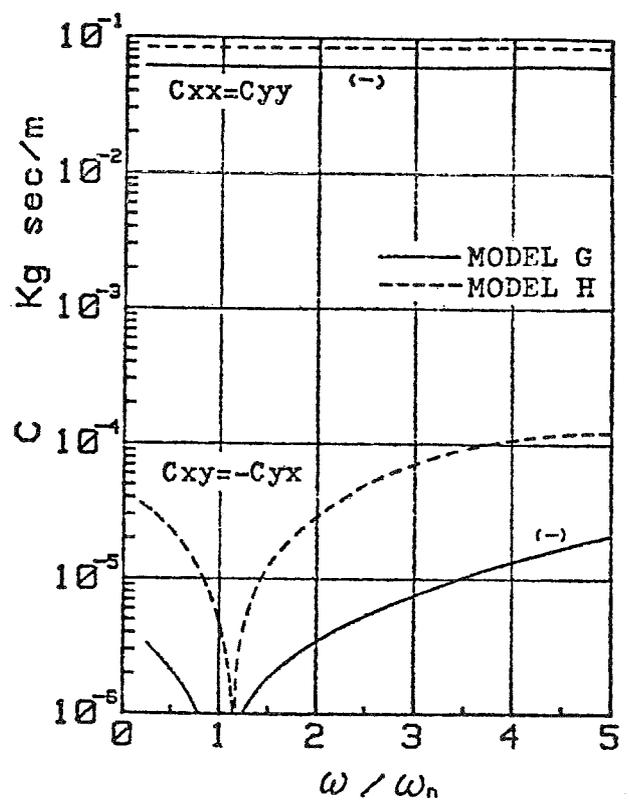
(a) Spring coefficients. (b) Damping coefficients.

Figure 6. - Coefficients of flow-induced force for models G and H.

Figure 7. – Testing facility for labyrinth.
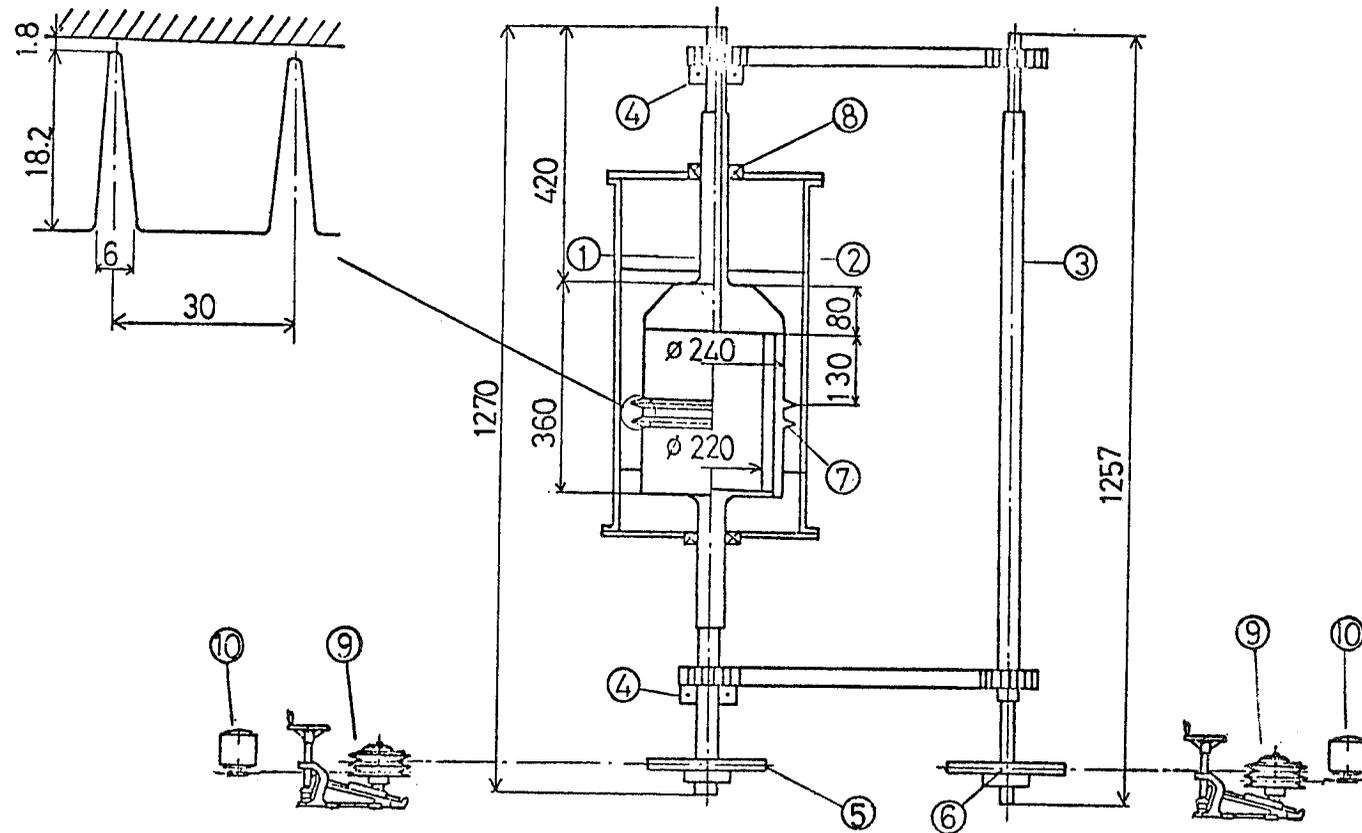
(1) rotor (2) casing (3) shaft for whirling drive (4) bearing with eccentricity (5) belt wheel for rotor spinning (6) belt wheel for whirling (7) test seal (8) diaphragm seal (9) transmission (10) motor
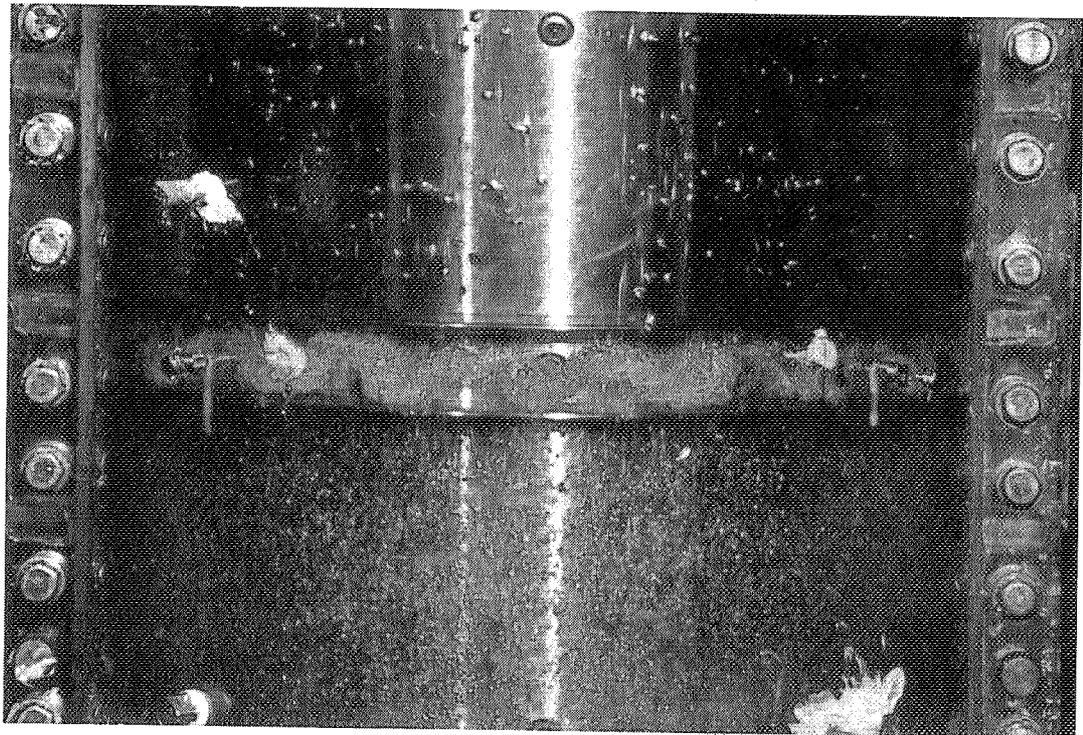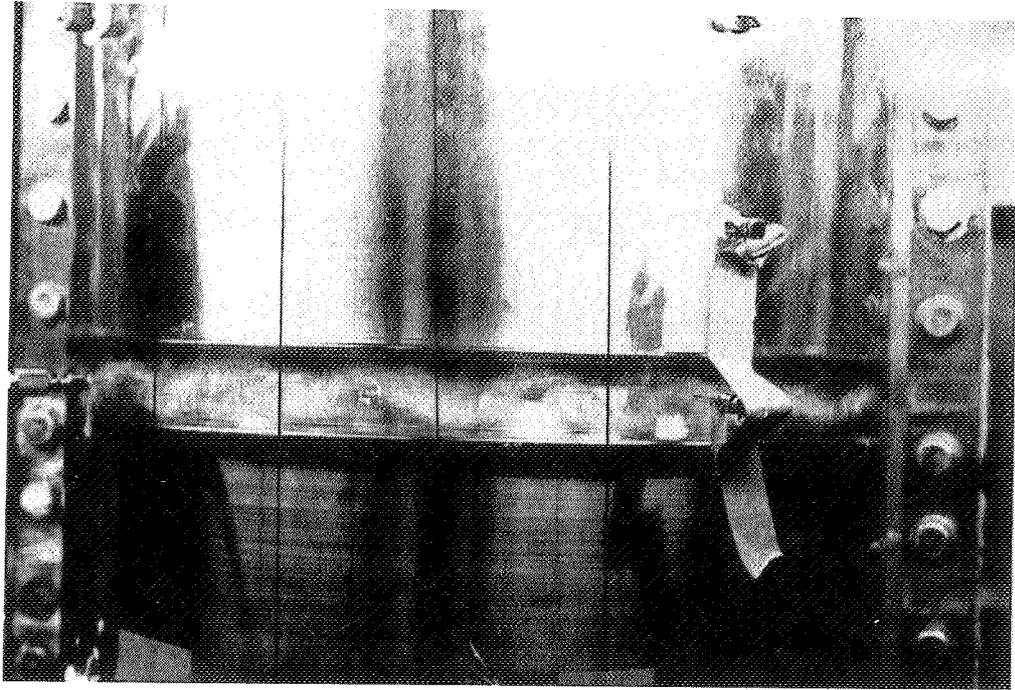
Figure 8. - Flow pattern in gland.

162
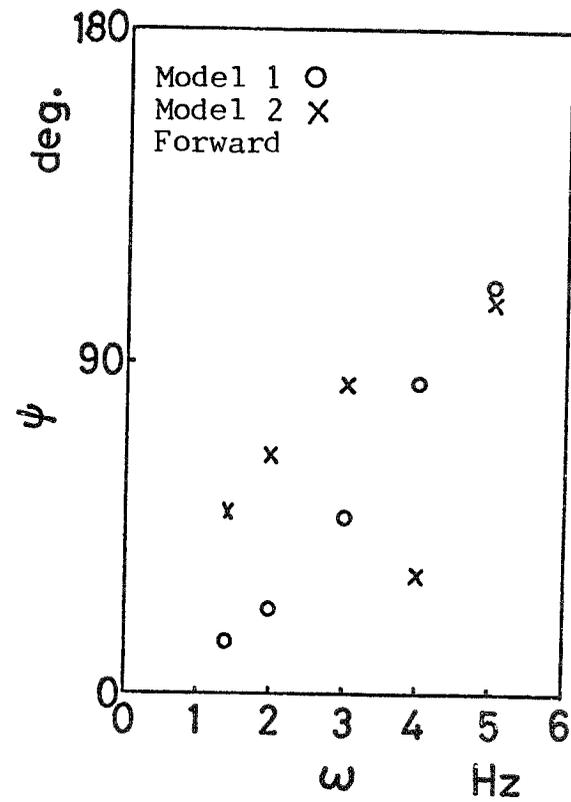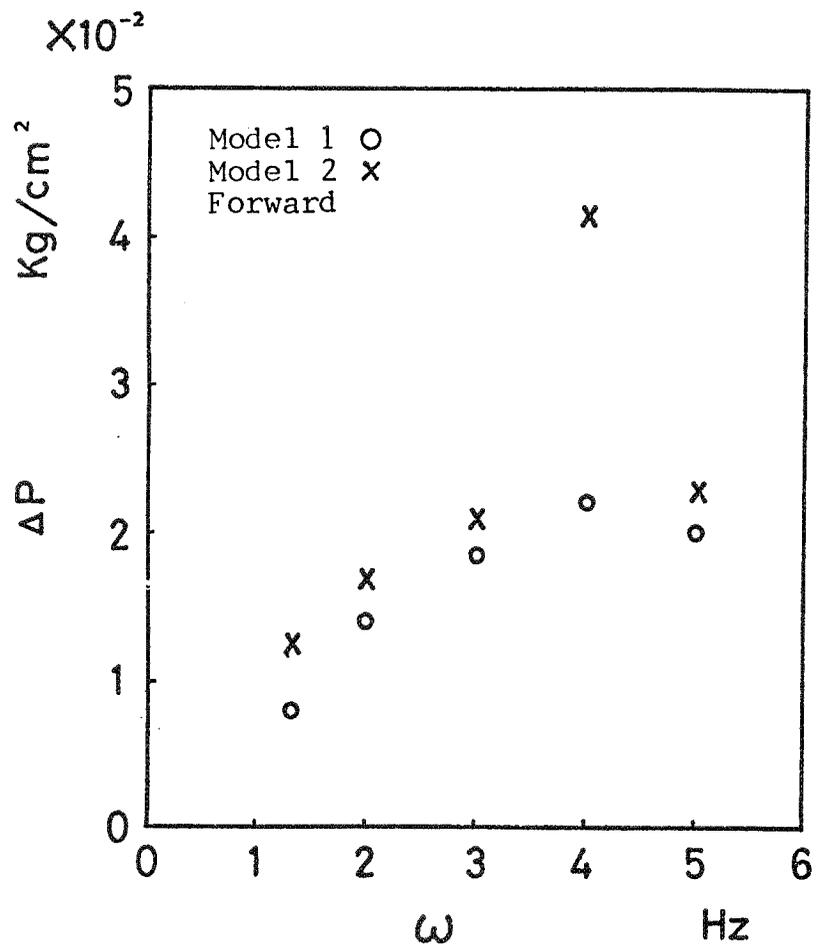
Figure 9. – Experimental results for forward precession.
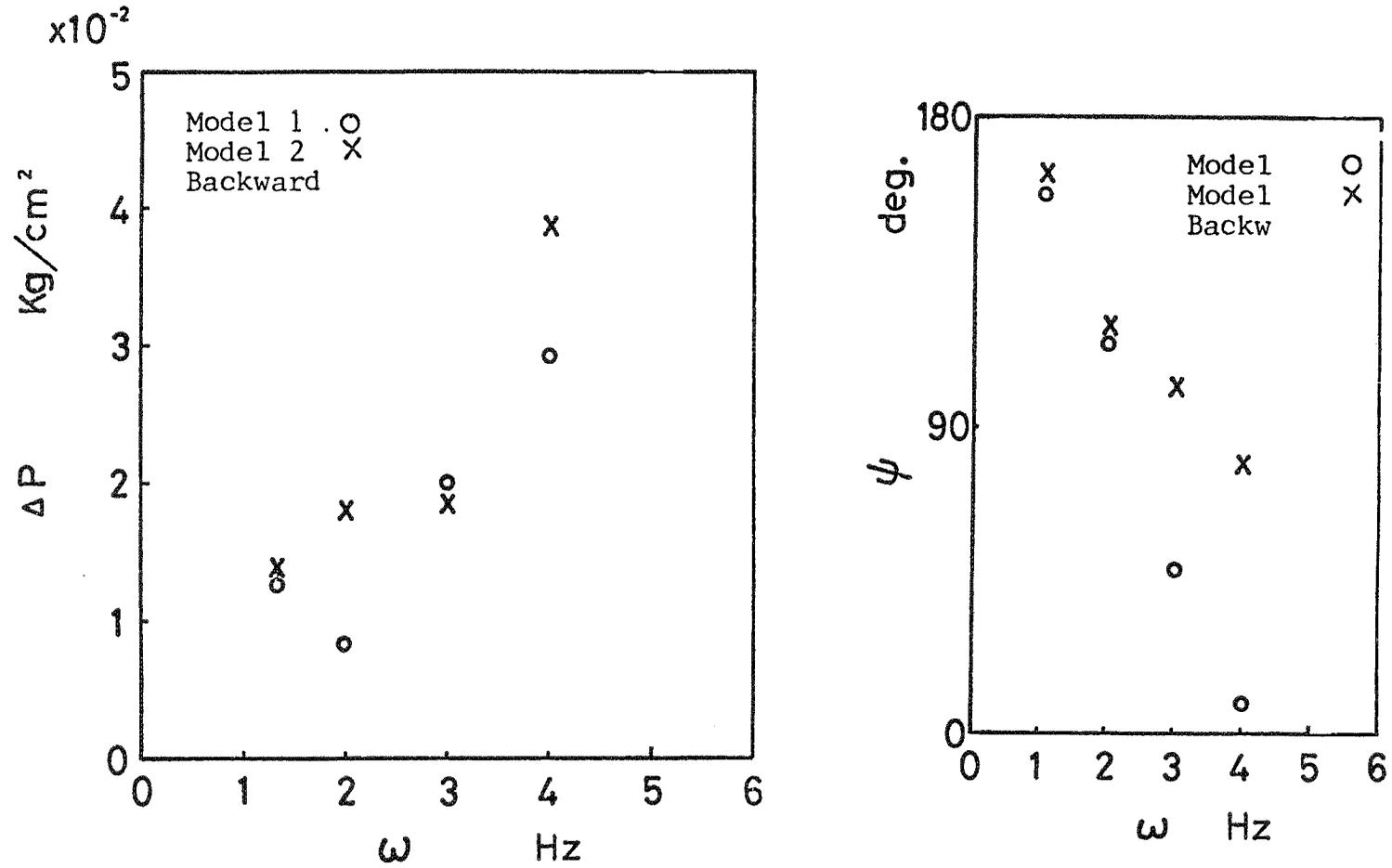
Figure 10. - Experimental results for backward precession.
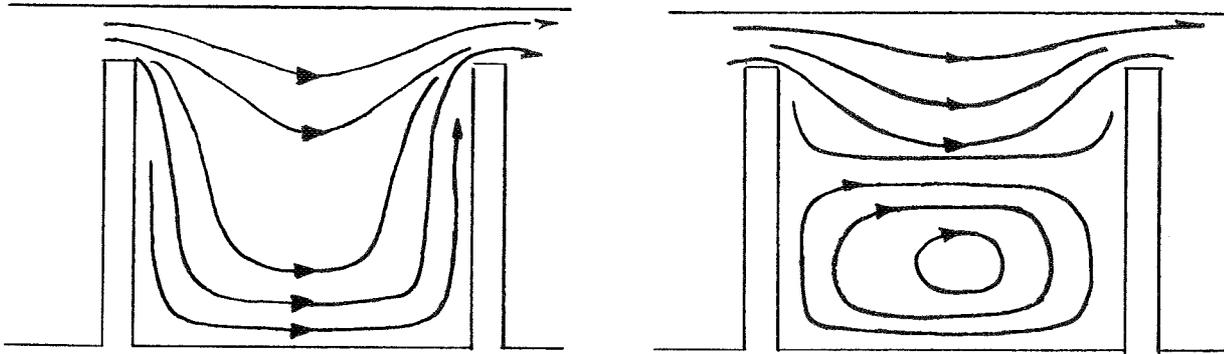
Conventional mathematical model　　　　Real flow pattern

Figure 11. - Sketch of flow patterns.
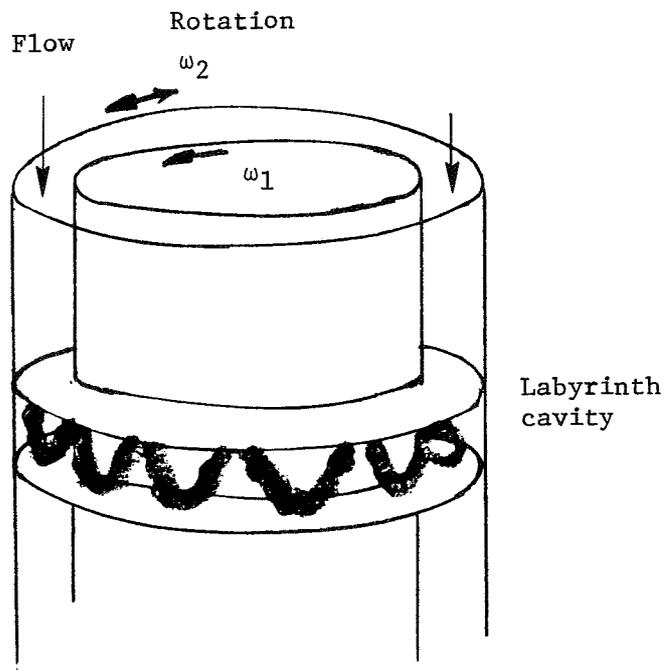
Figure 12. - Spiral vortex.
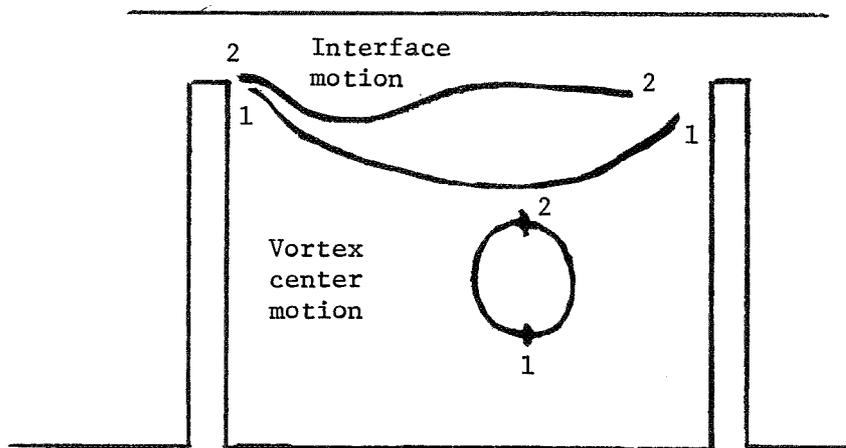
Figure 13. - Possible interface and vortex motions
leading to a "spiral vortex."

(a) Zero separation - jetting.

(b) D/3 Separation - jetting.

(c) 3D/2 Separation - oscillation.

(d) 9D/4 Separation, maximum-amplitude oscillation.

(e) 4D Separation, oscillation.

(f) 6D Separation, minor oscillations.

(g) 16D Separation, nearly independent of reservoir.
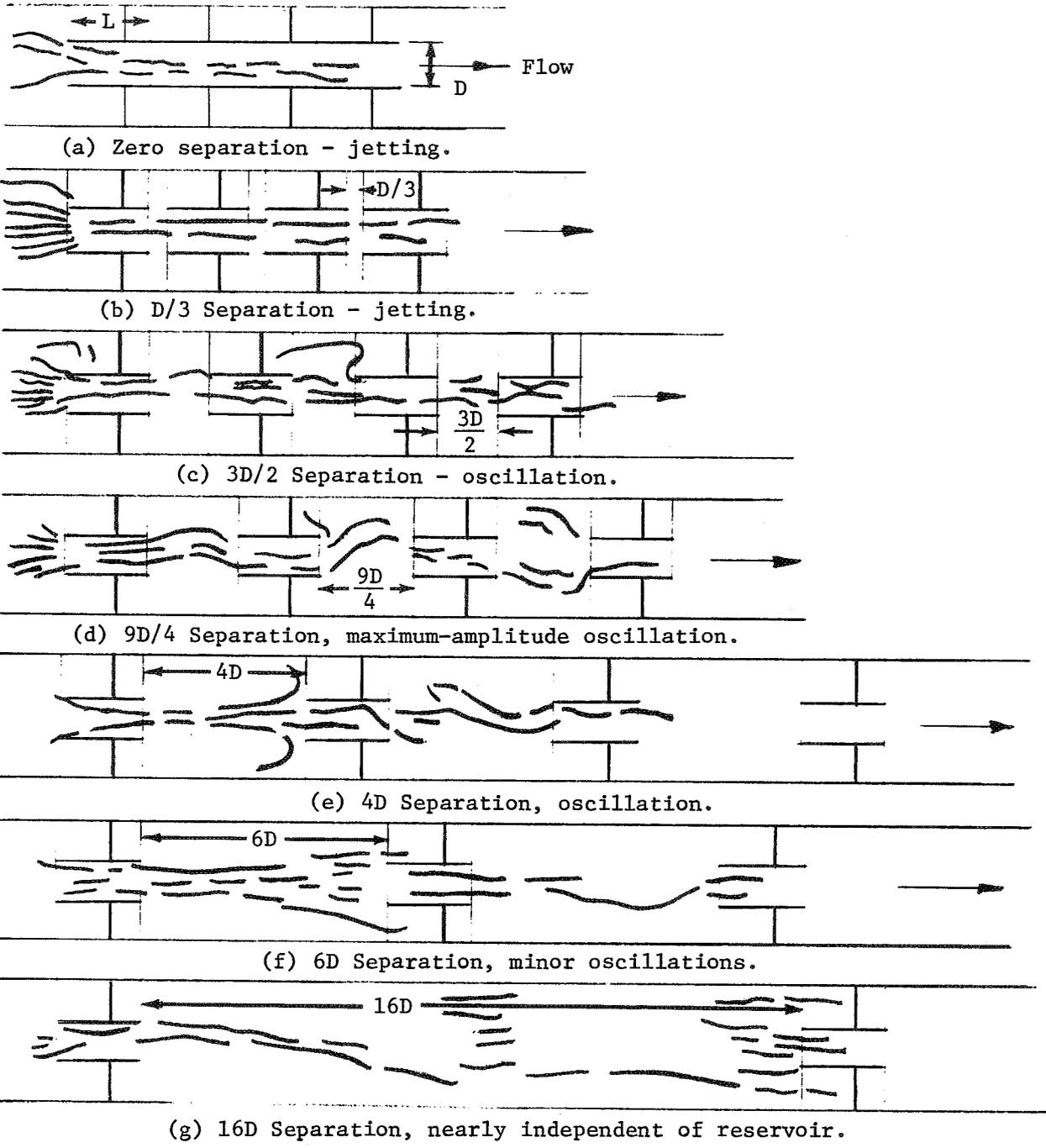
Figure 14. - Flow visualization of four sequential Borda-type inlets.

Page intentionally left blank

DAMPING IN RING SEALS FOR COMPRESSIBLE FLUIDS

David P. Fleming
National Aeronautics and Space Administration
Lewis Research Center
Cleveland, Ohio 44135

SUMMARY

An analysis is presented to calculate damping in ring seals for a compressible fluid. Results show that damping in tapered ring seals (optimized for stiffness) is less than that in straight bore ring seals for the same minimum clearance. Damping in ring seals can promote fractional frequency whirl and can, thus, be detrimental. Thus, tapered seals can benefit rotor and seal stability by having lower damping as well as higher stiffness. Use of incompressible results leads to large errors.

INTRODUCTION

Ring seals (annular seals) can have a considerable influence on the dynamic behavior of rotors. This is not surprising when one considers that such a seal has the appearance of a journal bearing, although with larger clearances than usual bearing practice. With a large pressure difference across the seal, most of the force generated is due to the high velocity throughflow of sealed fluid. In a series of papers (refs. 1 to 3) Black and coworkers calculated stiffness and damping in annular seals having constant clearance in the axial direction and sealing an incompressible fluid. In references 4 and 5, it was shown that stiffness could be considerably increased by tapering the seal bore so that clearance is greater at the inlet than at the exit. The higher stiffness can be beneficial in stabilizing rotors by shifting critical speeds; floating-ring seals can also benefit from higher stiffness with resulting longer life. Such a tapered bore configuration solved a wear problem in the hot gas seal of the Space Shuttle high pressure oxygen turbopump.

Damping, as well as stiffness, influences seal and rotor behavior. As previously mentioned, damping coefficients were calculated by Black, et al. (refs. 1 to 3), for constant-clearance seals and incompressible fluids. Reference 6 presented damping data for tapered ring seals with incompressible fluids. Heretofore no damping information has been available for seals passing compressible fluids. The purpose of this work is to provide such data for both constant-clearance and tapered seals.

169

SYMBOLS

B	damping coefficient
$\bar{B}$	dimensionless damping, $BC_2^3/RL^3\mu_0$
$\tilde{B}$	dimensionless damping, $\bar{B}L/Re_0C_2$
C	seal radial clearance
c_v	specific heat at constant volume
e	seal eccentricity
F	seal force
f	Fanning friction factor
g	seal force per unit of circumference, eq. (40)
H	clearance ratio, C_1/C_2
h	seal local film thickness
K	seal stiffness
$\bar{K}$	dimensionless stiffness, KC_2/p_0LD
k	entrance loss coefficient
L	seal length
M	Mach number, $u/\sqrt{\gamma\mathscr{R}T}$
P	pressure ratio, p_t/p_s
p	pressure
Q	M_s^2
q	heat flux
R	seal radius
Re_0	"sonic" Reynolds number, $2\rho_0C_2\sqrt{\gamma\mathscr{R}T_0}/\mu_0$
$\mathscr{R}$	gas constant
T	absolute temperature
t	time

170

U	velocity ratio, u_t/u_s
u	axial velocity
v	$\partial h/\partial t$
W	Mach number ratio, M_t/M_s
z	axial coordinate
α	seal taper angle
γ	specific heat ratio
ϵ	eccentricity ratio, e/C_2
η	$1 + k$
θ	circumferential coordinate
μ	dynamic viscosity
ρ	fluid density
σ	density ratio, ρ_t/ρ_s
φ	altitude angle, $\tan^{-1} (B\omega_r/K)$
ω_p	orbital frequency
ω_r	shaft rotational speed

Subscripts:

e	entrance
rad	radial
s	steady state
t	perturbed
tan	tangential
x	seal exit
0	upstream stagnation condition
1	seal entrance
2	seal exit
3	downstream reservoir condition

ANALYSIS

The configuration to be analyzed is that of a tapered bore ring seal whose clearance decreases in the flow direction (fig. 1). Around the circumference the clearance is given by

$$h(z,\theta) = C(z) + C_2 \epsilon \cos \theta \qquad (1)$$

where C is the clearance when the seal is concentric. The variation of C with axial coordinate z is

$$C(z) = C_1 - \alpha z \qquad (2)$$

The analysis is applicable to a straight seal by setting the taper angle α to 0.

When the seal has a velocity relative to the shaft in the radial direction, a damping force is generated. To determine this force, the pressure distribution within the seal will be calculated and integrated over the seal area. The following assumptions are employed:

(1) Eccentricity is small compared with the concentric clearance; that is, $\epsilon \ll 1$.

(2) The fluid behaves as a perfect gas.

(3) Rotational effects on the flow field are neglected; the flow is one-dimensional in the axial direction.

(4) The friction factor is constant everywhere within the seal.

(5) Time derivatives of the fluid properties and velocity are neglected; that is, the flow field is quasi-steady-state. Reference 6 examined this assumption for an incompressible fluid and concluded that acceptable accuracy results.

The analysis begins from the time-dependent equations of continuity, momentum, and energy as presented by Shapiro (ref. 7). For a channel, which the seal passage approximates, these are, respectively,

$$\frac{\partial}{\partial z}(\rho u h) + \frac{\partial}{\partial t}(\rho h) = 0 \qquad (3)$$

$$-\frac{\partial}{\partial z}(p h) + p\frac{\partial h}{\partial z} - f\rho u^2 = \frac{\partial}{\partial t}(\rho u h) + \frac{\partial}{\partial z}(\rho u^2 h) \qquad (4)$$

$$q = \frac{\partial}{\partial t}\left[\rho h\left(c_v T + \frac{u^2}{2}\right)\right] + \frac{\partial}{\partial z}\left[\rho u h\left(c_v T + \frac{p}{\rho} + \frac{u^2}{2}\right)\right] \qquad (5)$$

172

The momentum equation may be simplified by using the continuity equation. In turn, the energy equation may be simplified through use of the continuity and momentum equations. Additionally, for a perfect gas

$$\frac{p}{\rho} = \mathscr{R}T \tag{6}$$

and

$$c_v = \frac{\mathscr{R}}{\gamma - 1} \tag{7}$$

The seal taper angle is

$$\alpha \equiv \frac{\partial h}{\partial z} \tag{8}$$

Defining

$$v \equiv \frac{\partial h}{\partial t} \tag{9}$$

allows the continuity, momentum, and energy equations to be written as, respectively,

$$\frac{\partial \rho}{\partial t} + \frac{\rho v}{h} + u \frac{\partial \rho}{\partial z} + \rho \frac{\partial u}{\partial z} - \frac{\rho u \alpha}{h} = 0 \tag{10}$$

$$-\frac{\partial p}{\partial z} = \frac{f \rho u^2}{h} + \rho \frac{\partial u}{\partial t} + \rho u \frac{\partial u}{\partial z} \tag{11}$$

$$q/h + \frac{f \rho u^3}{h} + \frac{p v}{h} = \frac{1}{\gamma - 1} \left[\frac{\partial p}{\partial t} + u \frac{\partial p}{\partial z} - \frac{\gamma p}{\rho} \left(\frac{\partial \rho}{\partial t} + u \frac{\partial \rho}{\partial z} \right) \right] \tag{12}$$

The next step is to invoke the small perturbation assumptions and write the pressure, density, and velocity as the sum of a steady-state value plus a small perturbation

$$\left. \begin{aligned} p &= p_s + p_t \\ \rho &= \rho_s + \rho_t \\ u &= u_s + u_t \end{aligned} \right\} \tag{13}$$

The steady-state equations are

$$u_s \frac{d\rho_s}{dz} + \rho_s \frac{du_s}{dz} - \frac{\rho_s u_s \alpha}{h} = 0 \tag{14}$$

$$-\frac{dp_s}{dz} = \frac{f \rho_s u_s^2}{h} + \rho_s u_s \frac{du_s}{dz} \tag{15}$$

$$q_s/h + \frac{f\rho_s u_s^3}{h} = \frac{u_s}{\gamma - 1}\left(\frac{dp_s}{dz} - \frac{\gamma p_s}{\rho_s}\frac{d\rho_s}{dz}\right) \qquad (16)$$

The steady-state equations were solved (for $q = 0$) in reference 5 and will not be dealt with further. The perturbed equations of continuity, momentum, and energy are, respectively,

$$\frac{\partial \rho_t}{\partial t} + \frac{\rho_s v}{h} + \frac{\partial}{\partial z}(\rho_t u_s + \rho_s u_t) - \frac{\rho_s u_t \alpha}{h} - \frac{\rho_t u_s \alpha}{h} = 0 \qquad (17)$$

$$-\frac{\partial p_t}{\partial z} = \frac{f\rho_t u_s^2}{h} + \frac{2f\rho_s u_s u_t}{h} + \rho_s \frac{\partial u_t}{\partial t} + \rho_s u_s \frac{\partial u_t}{\partial z} + (\rho_s u_t + \rho_t u_s)\frac{\partial u_s}{\partial z} \qquad (18)$$

$$q_t/h + \frac{f\rho_t u_s^3}{h} + \frac{3f\rho_s u_t u_s^2}{h} + \frac{p_s v}{h}$$

$$= \frac{1}{\gamma - 1}\left[\frac{\partial p_t}{\partial t} + u_s\frac{\partial p_t}{\partial z} + u_t\frac{\partial p_s}{\partial z} - \frac{\gamma p_t u_s}{\rho_s}\frac{\partial \rho_s}{\partial z} + \frac{\gamma p_s \rho_t u_s}{\rho_s^2}\frac{\partial \rho_s}{\partial z}\right.$$

$$\left. - \frac{\gamma p_s}{\rho_s}\left(\frac{\partial \rho_t}{\partial t} + u_s\frac{\partial \rho_t}{\partial x} + u_t\frac{\partial \rho_s}{\partial z}\right)\right] \qquad (19)$$

In accordance with the assumptions, the time derivatives of p_t, ρ_t, and u_t are neglected, and the heat flow q is taken to be zero. Equations (17) to (19) then become ordinary differential equations which may conveniently be written in dimensionless variables

$$\left.\begin{array}{c} P = \dfrac{p_t}{p_s} \\[2ex] \sigma = \dfrac{\rho_t}{\rho_s} \\[2ex] U = \dfrac{u_t}{u_s} \end{array}\right\} \qquad (20)$$

Additionally, the Mach number is defined as

$$M = \sqrt{\frac{u}{\gamma \mathcal{R} T}} = u\sqrt{\frac{\rho}{\gamma p}} \qquad (21)$$

As with the other variables, the Mach number may be considered as the sum of a steady-state quantity and a small perturbation.

$$M = M_s + M_t \tag{22}$$

Defining

$$W = \frac{M_t}{M_s} \tag{23}$$

we find, from equation (21),

$$W = U + \frac{\sigma}{2} - \frac{P}{2} \tag{24}$$

After some algebraic manipulation, making use of equations (14) to (16), the perturbed continuity, momentum, and energy equations become, respectively,

$$\frac{d\sigma}{dz} + \frac{dU}{dz} + \frac{v}{u_s h} = 0 \tag{25}$$

$$\frac{dP}{dz} + \gamma Q \frac{dU}{dz} = \frac{2W}{P_s} \frac{dp_s}{dz} \tag{26}$$

$$\frac{dP}{dz} - \gamma \frac{d\sigma}{dz} = \frac{\gamma - 1}{h} \left(2QW\gamma f + \frac{v}{u_s} \right) \tag{27}$$

wherein

$$Q \equiv M_s^2 \tag{28}$$

Thus, we have three simultaneous, ordinary differential equations in four unknown variables P, σ, U, and W. A fourth equation needed to obtain a solution may be obtained by differentiating equation (24) with respect to z:

$$\frac{dW}{dz} = \frac{dU}{dz} + \frac{1}{2} \left(\frac{d\sigma}{dz} - \frac{dP}{dz} \right) \tag{29}$$

Equations (25) to (27) and (29) may now be solved simultaneously for the perturbed variables. As for the steady-state variables (ref. 7), the differential equations for the perturbed variables may be combined to yield a single differential equation in the perturbed Mach number W.

Reference 8 derives a differential equation for the steady-state pressure p_s, which may be written as

$$\frac{1}{P_s} \frac{dp_s}{dz} = - \frac{\gamma Q}{h(1 - Q)} [\alpha + f + f(\gamma - 1)Q] \tag{30}$$

With this, the equation for perturbed Mach number is

$$\frac{dW}{dz} = \frac{W}{h(1-Q)} \left\{ \frac{(\gamma+1)Q}{1-Q} \left[\alpha + f + f(\gamma-1)Q\right] \right.$$

$$\left. + (\gamma-1)fQ(\gamma Q + 1) \right\} - \frac{(\gamma+1)v}{2\gamma u_s h(1-Q)} \qquad (31)$$

From the steady-state solution (ref. 5), Q is a known function of z. Equation (31) will be easier to solve if we make the substitution (ref. 5, eq. (2))

$$\frac{dQ}{dz} = \frac{2Q\left(1 + \frac{\gamma-1}{2}Q\right)(\gamma fQ + \alpha)}{h(1-Q)} \qquad (32)$$

Also, u_s varies according to (ref. 8)

$$\frac{u_e}{u_s} = \frac{M_e}{M_s} \sqrt{\frac{1 + \frac{\gamma-1}{2}Q}{1 + \frac{\gamma-1}{2}Q_e}} \qquad (33)$$

where the subscript e denotes the steady-state value at $z = 0$. Equation (31) becomes

$$\frac{dW}{dQ} = \frac{W}{2\left(1 + \frac{\gamma-1}{2}Q\right)(\gamma fQ + \alpha)} \left[\frac{\gamma+1}{1-Q}\alpha + \gamma f\left(\frac{1+\gamma Q}{1-Q} + \gamma Q + 1 - Q\right)\right]$$

$$- \frac{(\gamma+1)vM_e}{4\gamma u_e Q^{3/2}(\gamma fQ + \alpha)\sqrt{\left(1 + \frac{\gamma-1}{2}Q\right)\left(1 + \frac{\gamma-1}{2}Q_e\right)}} \qquad (34)$$

The perturbed Mach number W may now be found by solving equation (34).

To determine the seal damping force, the perturbed pressure P must be known. Equations (25) to (27) may be combined to yield a differential equation for P. Making use also of equations (32) and (33) yields

$$\frac{dP}{dQ} = - \frac{\gamma W}{\left(1 + \frac{\gamma-1}{2}Q\right)(\gamma fQ + \alpha)} \left[\frac{\alpha + \gamma fQ}{1-Q} + f(1 + \gamma Q - Q)\right]$$

$$+ \frac{vM_e}{2u_e M_s(\gamma fQ + \alpha)\sqrt{\left(1 + \frac{\gamma-1}{2}Q\right)\left(1 + \frac{\gamma-1}{2}Q_e\right)}} \qquad (35)$$

Boundary conditions. - At the seal exit it is assumed that there is no change in the boundary conditions of the steady-state problem. Thus, for choked flow

$$M = 1 \left.\right\}$$
$$W = 0 \left.\right\} \tag{36}$$

For flow which is not choked

$$p = p_3 \left.\right\}$$
$$P = 0 \left.\right\} \tag{37}$$

At the seal entrance, the pressure and Mach number are related by (ref. 5)

$$\frac{p}{p_0} = \left(1 + \frac{\gamma - 1}{2} \eta Q\right)^{\gamma/(1-\gamma)} \tag{38}$$

The pressure and Mach number may be written as the sums of their steady-state and perturbed components and a binomial expansion performed on the right side of equation (38). After neglecting all powers of Q higher than unity and subtracting out the steady-state terms, there remains

$$P = - \frac{\gamma \eta Q_e W}{1 + \frac{\eta(\gamma - 1)}{2} Q_e} \tag{39}$$

Solution of equations. - The results presented herein were obtained through a numerical solution of the differential equations for W and P (eqs. (34) and (35)). For the case of choked flow, Q = 1 at the seal exit; it is not possible to integrate numerically to this limit because of the term 1 - Q in the denominator of equations (34) and (35). However, W and P may be determined as accurately as desired by taking the solution close to Q = 1 without reaching the limit. To ascertain the validity of this approach, equations (34) and (35) may be rewritten, in simplified form, for the case when Q → 1. The resulting equations may be solved analytically, yielding solutions for W and P which remain finite as Q → 1. Thus, the error is of the order $(1 - Q_{lim})P_{Q = 1}$ which can be made as small as desired by taking Q_{lim} arbitrarily close to 1.

Calculation of seal forces. - The seal force per unit of circumference due to the perturbed pressure p_t is given by

$$g = \int_0^L p_t \, dz = \int_{Q_e}^{Q_x} Pp_s \frac{dz}{dQ} \, dQ \tag{40}$$

where Q_x is the value of Q at z = L. The steady-state pressure p_s does not contribute to the total seal force because it is uniform around the circumference. From reference 8

$$\frac{P_s}{P_e} = \frac{h_e M_e}{h M_s} \sqrt{\frac{1 + \frac{\gamma - 1}{2} Q_e}{1 + \frac{\gamma - 1}{2} Q}} \tag{41}$$

Making use of this and equation (32) results in

$$g = \frac{1}{2} P_e h_e M_e \sqrt{1 + \frac{\gamma - 1}{2} Q_e} \int_{Q_e}^{Q_x} \frac{P(1 - Q)dQ}{Q^{3/2} \left(1 + \frac{\gamma - 1}{2} Q\right)^{3/2} (\gamma f Q + \alpha)} \tag{42}$$

The integral in equation (42) is easily evaluated numerically.

The total seal damping force in the direction $\theta = 0$ is

$$F = -\int_0^{2\pi} gR \cos \theta \, d\theta \tag{43}$$

For a seal velocity in the direction $\theta = 0$

$$v = v_0 \cos \theta \tag{44}$$

and, thus,

$$g = g_0 \cos \theta \tag{45}$$

where the subscript 0 now denotes the condition at $\theta = 0$. With this the integral in equation (43) may be evaluated, yielding

$$F = -\pi R g_0 \tag{46}$$

A damping coefficient is now defined:

$$B = \frac{F}{v_0} = -\frac{\pi R g_0}{v_0} \tag{47}$$

or

$$B = -\frac{\pi R}{2 v_0} P_e h_e M_e \sqrt{1 + \frac{\gamma - 1}{2} Q_e} \int_{Q_e}^{Q_x} \frac{P(1 - Q)dQ}{Q^{3/2} \left(1 + \frac{\gamma - 1}{2} Q\right)^{3/2} (\gamma f Q + \alpha)} \tag{48}$$

where it is understood that P is evaluated for $v = v_0$. The actual value of v_0 is immaterial. Since both W and P are directly proportional to v_0, it will cancel out of the expressions for the proper choice of dimensionless variables.

178

RESULTS

The analysis of the preceding section was implemented on a digital computer. The differential equations were solved using a fourth-order Runge-Kutta integrator with automatic error control. The computer programs made use of the results of reference 5.

Results are presented in figures 2 and 3 for choked flow and in figures 4 and 5 for a sealed pressure ratio of 2, for which the flow is not choked. The independent variable in all cases is $Re_0 C_2/L$ where Re_0 is the "sonic" Reynolds number $2C_2\rho_0\sqrt{\gamma \mathcal{R} T_0}/\mu_0$. This independent variable was chosen because laminar flow results are then independent of seal clearance-to-length ratio C_2/L. The specific heat ratio γ was 1.4 for all cases. Results are shown for straight seals and for tapered seals optimized for maximum stiffness-to-leakage ratio (ref. 5).

Figure 2 shows laminar flow results for small values of seal parameter $Re_0 C_2/L$. Damping is plotted in terms of the dimensionless variable

$$\overline{B} = \frac{BC_2^3}{RL^3\mu_0} \tag{49}$$

There is little variation for the range of seal parameter up to 10. Damping approaches a constant value as $Re_0 C_2/C \rightarrow 0$. Damping is higher in the straight seal than in the tapered design because of the lower average clearance (seals are compared on the basis of minimum clearance).

Figure 3 shows results for choked flow over the complete range of seal parameter for both laminar and turbulent flow. In this figure, damping is shown in terms of the dimensionless quantity

$$\widetilde{B} = \frac{\overline{B}L}{Re_0 C_2} = \frac{BC_2}{2RL^2\sqrt{\gamma P_0\rho_0}} \tag{50}$$

For this choice of variable, laminar flow damping varies strongly with seal parameter. In contrast, turbulent flow damping shows a much smaller variation. For turbulent flow, damping depends on clearance-to-length ratio C_2/L, appearing to reach a minimum for the middle values of C_2/L investigated, and rising for either higher or lower values. Overall, however, variation is small even for the extreme values of C_2/L considered; thus, for all other factors held constant, equation (50) indicates that damping is approximately proportional to the square of seal length.

The left end of the curves for turbulent flow corresponds to a Reynolds number in the seal passage of 3000; this is generally considered the lowest value for which one can be assured of turbulent flow. A Reynolds number of 2300 is usually taken as the upper limit for laminar flow. Points where Re = 2300 are shown for various C_2/L values on the laminar flow curves.

179

Damping for a pressure ratio of 2 is shown in figure 4 for small values of $Re_0 C_2/L$. For this pressure ratio the flow is not choked. In common with figure 2, damping does not vary greatly with seal parameter.

Results for a pressure ratio of 2 are shown in figure 5 for the complete range of seal parameter. As in figure 3, the damping is expressed as

$$\tilde{B} = \frac{BC_2}{2RL^2 \sqrt{\gamma p_0 \rho_0}}$$

For the straight seal, damping values are lower than for choked flow, as less mass passes through the seal when the flow is unchoked. For the tapered seal, damping for $p_0/p_3 = 2$ is higher than the choked case when the flow is laminar and somewhat lower when the flow is turbulent. This apparently anomalous behavior for laminar flow can be explained by observing that the optimum clearance ratio is lower for $p_0/p_3 = 2$ than for choked flow; thus, the average clearance is less than in the seal optimized for choked flow. Optimum clearance ratios $H = C_1/C_2$ appear in figures 6 and 7 (taken from ref. 5).

Example of seal calculation. - Calculate damping for the example seal of reference 5. Pertinent seal data are

$$L = 10 \text{ mm}$$
$$D = 50 \text{ mm}$$
$$C_2 = 0.05 \text{ mm}$$
$$p_0 = 100 \text{ bar}$$
$$p_3 = 4 \text{ bar}$$
$$T_0 = 800 \text{ K}$$
Fluid: Hydrogen gas

Thus, it was calculated in reference 5 that

$$\frac{C_2}{L} = 0.005$$

$$Re_0 = 37\ 100$$

$$Re_0 \frac{C_2}{L} = 186$$

The flow is choked; thus, damping data are taken from figure 3. For a straight seal

$$\tilde{B} = 0.89$$

yielding

$$B = 570 \text{ N sec/m}$$

180

For the tapered seal

$$\tilde{B} = 0.47$$

and

$$B = 300 \text{ N sec/m}$$

Effect of seal rotation. - The effect of rotation was examined in reference 6 for a seal passing incompressible fluid using an approximation derived by Black and Jenssen (ref. 2). For the analysis presented herein, fluid temporal derivatives were neglected; thus, the inertia terms calculated in reference 6 do not appear in the present results. The expression for seal forces then becomes

$$\begin{bmatrix} F_x \\ F_y \end{bmatrix} = - \begin{bmatrix} K & \frac{1}{2} B\omega_r \\ -\frac{1}{2} B\omega_r & K \end{bmatrix} \begin{bmatrix} x \\ y \end{bmatrix} - \begin{bmatrix} B & 0 \\ 0 & B \end{bmatrix} \begin{bmatrix} \dot{x} \\ \dot{y} \end{bmatrix} \tag{51}$$

In equation (51) ω_r is the shaft rotational speed.

In the usual case of seal motion, the seal journal describes some orbit within the seal clearance. We will consider the case of a centered circular orbit with orbital frequency ω_p. For this condition, it is easy to calculate the radial restoring force and the tangential (whirl direction) force. Similar to reference 6, we find

$$\left. \begin{aligned} F_{rad} &= -Ke \\ F_{tan} &= Be \left(\frac{1}{2} \omega_r - \omega_p \right) \end{aligned} \right\} \tag{52}$$

where e is the eccentricity of the seal (fig. 8). The radial force depends only on the eccentricity e (the minus sign appears because F_{rad} is defined as positive in the outward direction). The tangential force, however, depends on the relative magnitudes of the spin and whirl speeds. Equation (52) may be written in terms of radial and tangential stiffnesses:

$$\left. \begin{aligned} K_{rad} &= -\frac{F_{rad}}{e} = K \\ K_{tan} &= -\frac{F_{tan}}{e} = -B\omega_r \left(\frac{1}{2} - \frac{\omega_p}{\omega_r} \right) \end{aligned} \right\} \tag{53}$$

A positive value of K_{tan} will inhibit positive whirl; conversely, negative K_{tan} promotes positive whirl. Equation (53) for K_{tan} shows that a positive damping coefficient promotes forward whirl when $\omega_p/\omega_r < 1/2$ and inhibits whirl when $\omega_p/\omega_r > 1/2$. As pointed out in reference 6, this is remarkably similar to the behavior of a full circular journal bearing. The seal differs from a self-acting bearing (but is similar to an externally pressurized bearing) in

that the radial stiffness is independent of whirl speed. Equation (53) also shows that damping in a rotating seal is not entirely beneficial. Damping produces a tangential force which inhibits synchronous whirl but promotes whirl at half frequency or less.

Example of whirl forces. - Seal damping has been presented in dimensionless form, as were stiffness and leakage in reference 6. Also, damping force varies with rotor speed (eq. (53)). Thus, the relative size of the radial and tangential stiffness of equation (53) can only be compared for specific examples. The seal example above is similar to one of the hot-gas seals in the Space Shuttle high-pressure oxygen turbopump. This pump has a nominal operating speed of 31 000 rpm at full-power level. For this speed, table I compares the stiffness and damping for straight and tapered seals. Stiffness data are taken from reference 6. As table I shows, tapered seal stiffness is much higher than that for a straight seal, and damping lower. This means that for a tapered seal the force generated is more nearly in line with the displacement, a situation that is considered to promote stability.

Difference between compressible and incompressible results. - Before the availability of stiffness, damping, and leakage flow data for seals handling compressible fluids, some workers used incompressible data as the "best available." It is instructive to examine the difference in results using compressible and incompressible analyses. Table II compares results for the seal used in the example above. Compressible fluid stiffness and leakage flow are taken from reference 5. Incompressible data from references 4 and 6 are applied two ways: first using the upstream (stagnation) fluid density and second using fluid density as the mean of upstream and downstream densities.

The incompressible theory grossly overestimates seal stiffness, by an order of magnitude for the straight seal. There is little difference in using upstream or mean density. Damping is underestimated by the incompressible theory more severely when the mean density is used. Leakage flow is overestimated by incompressible theory, although not as much when a mean density is used.

One would not expect incompressible theory to yield accurate results because the nature of the flow is much different than with a compressible fluid. Fluid compressibility results in decreasing density and increasing velocity in the flow direction, and the flow becomes choked for large pressure ratios. The pressure gradient increases in the flow direction and, theoretically, becomes infinite at the seal exit for choked flow.

CONCLUDING REMARKS

An analysis has been performed to calculate the damping in straight and tapered seals for a compressible fluid. Results show that damping in optimized tapered seals is considerably less than in straight seals for the same minimum clearance. It was also pointed out that damping in rotating seals is not entirely beneficial as it can sometimes promote whirl. Thus, for rotor or seal

stabilization, tapered seals may confer a double benefit. Not only is tapered seal stiffness generally higher than that for straight seals, but damping is lower.

REFERENCES

1. Black, H. F.: Effects of Hydraulic Forces in Annular Pressure Seals on the Vibrations of Centrifugal Pump Rotors. J. Mech. Eng. Sci., vol. 11, no. 2, Apr. 1969, pp. 206-213.

2. Black, H. F.; and Jenssen, D. N.: Dynamic Hybrid Bearing Characteristics of Annular Controlled Leakage Seals. Proc. Inst. Mech. Eng., vol. 184, part 3N, 1969-70, pp. 92-100.

3. Black, H. F.; and Jenssen, D. N.: Effects of High Pressure Ring Seals on Pump Rotor Vibrations. ASME Paper 71-WA/FE-38, 1971.

4. Fleming, D. P.: High Stiffness Seals for Rotor Critical Speed Control. ASME Paper 71-DET-10, Sep. 1977.

5. Fleming, D. P.: Stiffness of Straight and Tapered Annular Gas Path Seals. J. Lubr. Technol., vol. 101, no. 3, July 1979, pp. 349-355.

6. Fleming, D. P.: Damping in Tapered Annular Seals for an Incompressible Fluid. NASA TP-1646, 1980.

7. Shapiro, A. H.: The Dynamics and Thermodynamics of Compressible Fluid Flow, Vol. II. Ronald Press Co., 1953.

8. Zuk, J.; and Smith, P. J.: Computer Program for Quasi-One-Dimensional Compressible Flow with Area Change and Friction - Application to Gas Film Seals. NASA TN D-7481, 1974.

TABLE I. - STIFFNESS AND DAMPING FOR HPOTP

STRAIGHT AND TAPERED SEALS

	Straight seal	Tapered seal
Dimensionless stiffness, $\overline{K}$	0.015	0.095
Stiffness, K, MN/m	1.5	9.5
Dimensionless damping, $\tilde{B}$	0.89	0.47
Damping, B, N sec/m	570	300
$B\omega_r$, MN/m	1.9	1.0
Attitude angle φ, deg	51	6

TABLE II. - COMPARISON OF COMPRESSIBLE AND INCOMPRESSIBLE RESULTS FOR

HPOTP STRAIGHT AND TAPERED SEALS

	Stiffness, K, MN/m		Damping, B, N sec/m		Leakage flow, g/sec	
	Straight seal	Tapered seal	Straight seal	Tapered seal	Straight seal	Tapered seal
Compressible theory	1.5	9.5	570	300	17	22
Incompressible theory, stagnation density	15.1	29.1	308	245	32	42
Incompressible theory, mean density	14.6	28.6	223	176	22	29
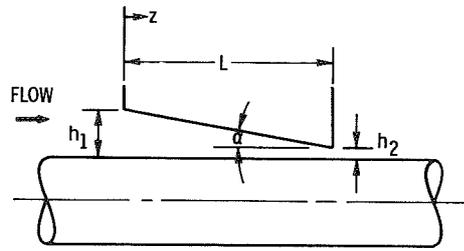
Figure 1. – Tapered ring seal.
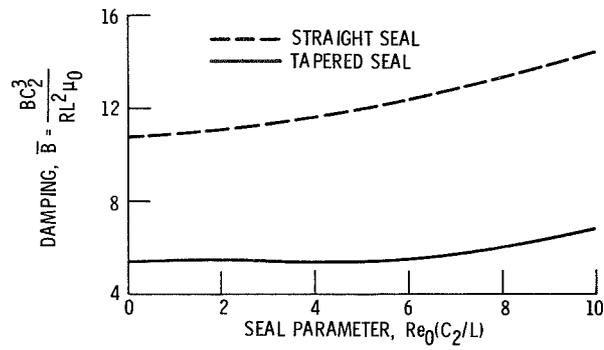
Figure 2. – Damping in ring seals; choked, laminar flow, small value of seal parameter.
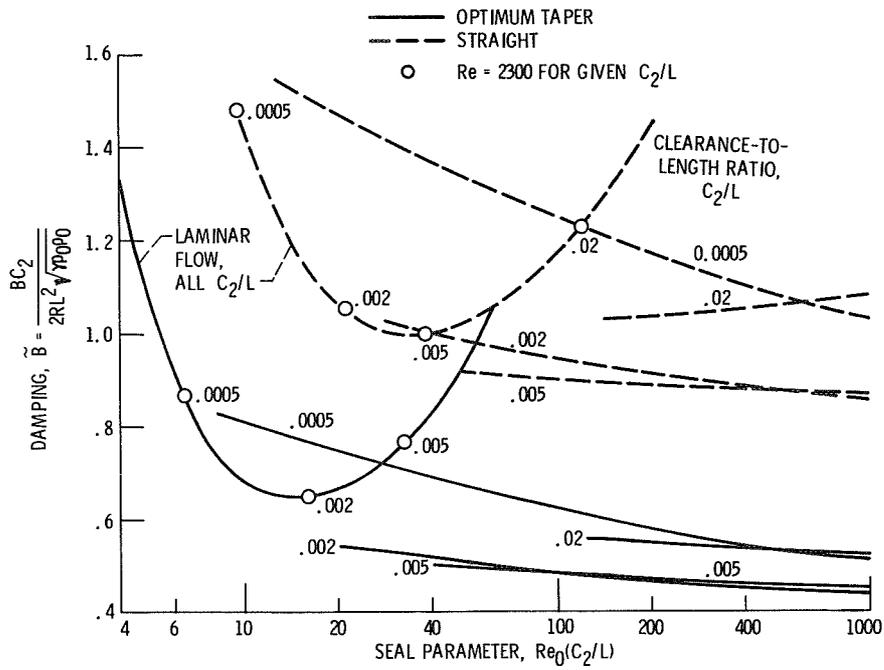
Figure 3. - Damping in ring seals; choked flow, laminar and turbulent.
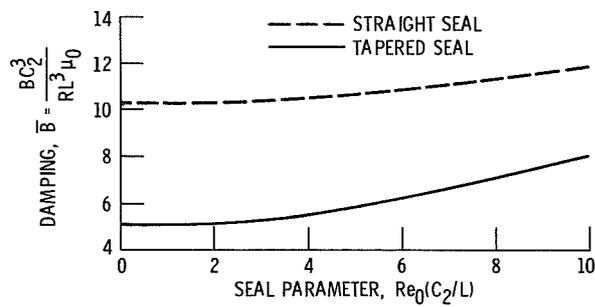
Figure 4. - Damping in ring seals; unchoked, $p_0/p_3 = 2$, laminar flow, small values of seal parameter.
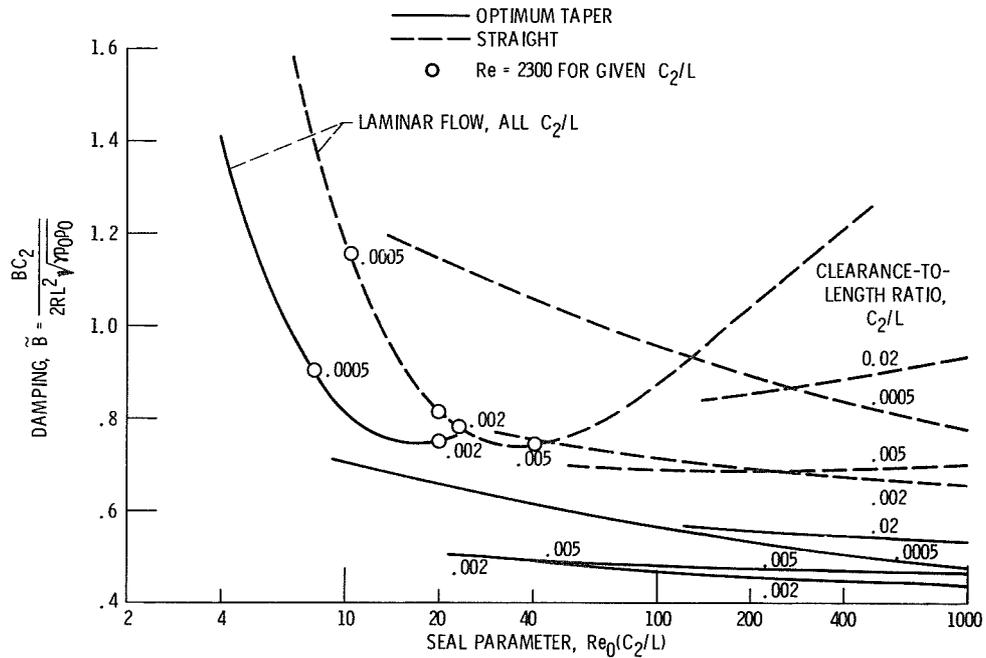
Figure 5. - Damping in ring seals; $p_0/p_3 = 2$, laminar and turbulent flow.
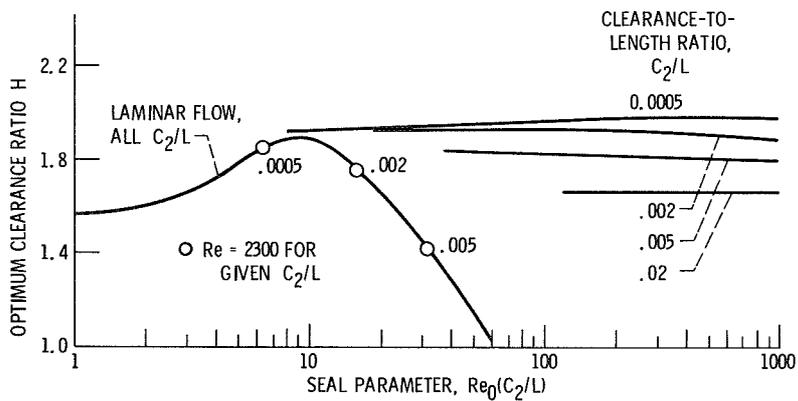
Figure 6. - Optimum clearance ratio of tapered seals, choked flow.
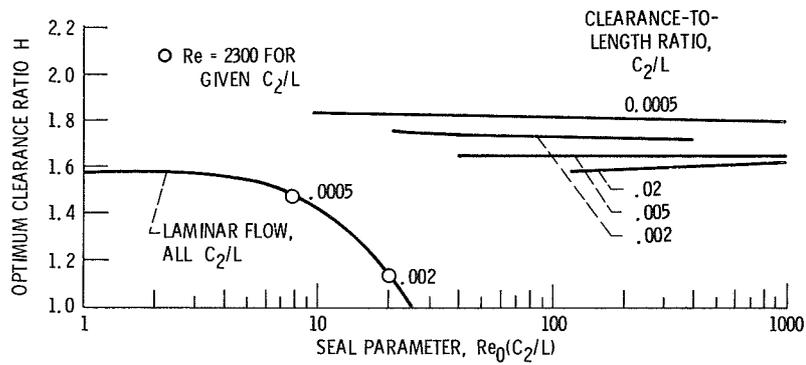
Figure 7. – Optimum clearance ratio of tapered seals, unchoked ($p_0/p_3 = 2$) flow.
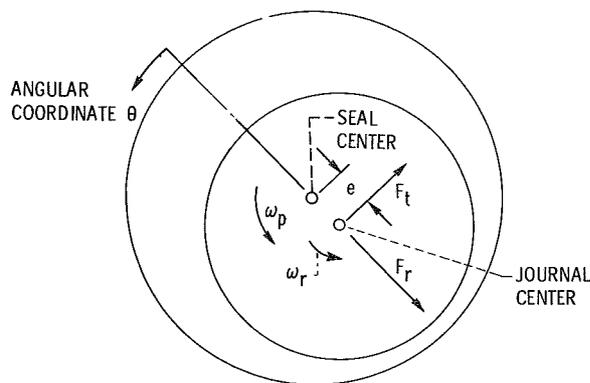
Figure 8. – Whirling seal.

FLOW INDUCED SPRING COEFFICIENTS OF LABYRINTH
SEALS FOR APPLICATION IN ROTOR DYNAMICS

H.Benckert and J.Wachter
Institut für Thermische Strömungsmaschinen
Universität Stuttgart
Stuttgart, Germany

SUMMARY

Self-excited rotor vibrations which are a function of output are being increa-
singly observed in high-performance turbo-machinery, in particular high-pressure
compressors. The labyrinth lateral force components of the rotor loadings, which
are related to the unequal pressure patterns over the circumference of the
contactless sealings by an eccentric shaft location, are one possible reason for
the self excitation.

The investigations presented in this paper deal with the flow induced aerodynamic
spring coefficients of labyrinth seals, with the restoring force in the deflec-
tion plane of the rotor and the lateral force acting perpendicularly to it. The
discussion includes the effects of operational conditions on the spring charac-
teristics of these components, such as differential pressure, speed, inlet flow
conditions and the geometry of the labyrinth seals.

Estimation formulas for the lateral forces due to shaft rotation and inlet swirl,
which are developped through experiments, are presented. The utilisation of the
investigations is explained and results of stability calculations, especially for
high pressure centrifugal compressors, are added. Remarks about possibilities to
avoid the exciting forces in labyrinths will finish this report.

INTRODUCTION

Non-contacting labyrinth-type seals are conventional design elements in turbo-
machinery which have proved their value for a considerable period of time. Until
today, investigations of labyrinth seals gave priority to the improvement of the
sealing effect. Labyrinth seals in these investigations have been considered as
a series of throttling points controlling leakage flow. A comprehensive equation
to determine mass flow through the labyrinth was published by "Stodola" (ref.1).

However, the user of a turbomachinery is not only affected by the economic value
of the labyrinths due to leakage losses, but also has to consider the limitation
of the operation range of the plant, because the rotor dynamics are influenced by
forces created in labyrinth seals. These forces result from the ununiform pres-
sure distributions on the circumference of the contact free seals, where the
clearance differ on the circumference of the shaft with the shaft in a out-of-
centre position. In the case of thermal turbomachinery of high energy density
– energy conversion in respect to rotor mass – the forces resulting from non-
symmetrical aerodynamics in the labyrinth gaps cannot be neglected in the rotor
dynamic evaluation, since the lateral force components of these forces acting

vertical to the rotor eccentricity plane can be the source of self excited
flexural vibrations of the shaft. Reference 2 is showing for the high pressure
part of a steam turbine, how suddenly the lateral forces can change the vibra-
tion pattern of the turbomachinery. The points of attack of the exciting lateral
forces are distributed over the length of the rotor, according to the positions
of the sealing gaps. The self exciting mechanism of contact free seals is com-
parable to the gap excitation of impellers (ref.3,4). The reason for both gaps
excitations is based on the aerodynamics of the fluid (aerodynamic excitation)
and tend to occur as a function of load at constant speed.

DEFINITION OF THE PROBLEM

The importance of the aerodynamic forces due to eccentric seal gaps in thermal
turbomachinery was underestimated until now, in respect to the effect on rotor
dynamics. It was assumed that a pressure difference in the individual laby-
rinth chambers would equalize itself rapidly. Basing on this assumption, it
would be possible to practically neglect this phenomena as a potential cause
acting on the rotor.

The excitation of the rotor by aerodynamic forces from labyrinth seals was
described in first time for a labyrinth seal with one sealing chamber by
"Alford" (ref.5). This work yields that vibrations of the shaft induce lateral
forces within the seal, which move the shaft asynchronously and therefore may
start instabilities. Important for this theory is the difference in gap width
between inlet and outlet labyrinth tip; circumferential flows in the chamber
are neglected. Another theoretical study (ref.6) also investigated the flow
through a labyrinth with one chamber and its effects on the dynamics of the
rotor. Here the influence of the drag effect by the rotating shaft on the flow
was not considered. Results of experiments of different labyrinths with one
sealing chamber are described in reference 7. The measurements are in respect
to the dynamic behavior of a whirling rotor due to the instationary forces in
the flow.

Besides lateral forces in the labyrinths caused by the dynamic behaviour of the
whirling rotor (Alford effect), pressure distributions also appear in the
sealing chambers, when the rotor has a stationary eccentricity. The resulting
lateral forces from these pressure distributions can have a destabilizing in-
fluence on the dynamic of the rotor. It could be proved that the existence of
a resulting lateral force from the pressure distribution in the labyrinth
chambers is related to circumferential velocities of the fluid in the seal.
Due to the action of the diffusors and the rotation of the rotor, flow through
the labyrinth seal is imparted a circumferential component in the direction of
rotation whereby the maximum pressure in the spaces between the sealing strips
is displaced in a direction opposite the direction of rotation at a point ahead
of the narrowest clearance.

"Kostyuk, 1972" (ref.8) presented a theoretical approach to determine the aero-
dynamic forces in the labyrinth seal with a shaft not parallel to the centerline.
According to this model the circumferential flows in the chambers are dependent
from the friction ratio between stator and rotor. Based on this friction ratio
a constant mean circumferential velocity can be calculated for each chamber.
"Rosenberg a.o." (ref.9) described the dominant effect of the spiral flow on
the gap flow forces. According to him, the spiral flow effect dominates the

friction effect within the seal. This model was used in ref. 10 to calculate the labyrinth gap flow induced forces on the rotor.

The pressent results of investigations (ref. 7,9,10), and also newer ones (ref.11), are limited however to very short labyrinth seals with 1 to 3 chambers, as they are commonly used in thermal turbomachinery for impeller sealing. The noted vibration problems at steam turbines (ref.2,12), give indication that besides the gap excitation due to ununiform energy conversion of blade cascade (ref.3) and the lateral forces due to the short impeller seals, the latter being considerably larger than the former (ref.13), also the other labyrinth seals of a turbomachinery influence the dynamic behavior of the rotor. Especially the multichamber designs of shaft end seals and balance piston seals earn attention in this respect. These problems were most pronounced in the case of high-pressure centrifugal compressors (ref.14). Because of the high density and the swirl components in such machines the labyrinths are entered with a considerable inlet swirl, while in longer seals the shaft rotation induces circumferential flows. Investigations of the dynamic behavior of such labyrinth assemblies with a large numbers of chambers, often also with a high pressure difference and considerable compressibility effect, have not been generally available for the user.

To get better know-how about the forces due to gap flow in labyrinth seals, the investigations at the "Institut für Thermische Strömungsmaschinen at the University of Stuttgart" are performed. This is done with the aim to point out the effects of operating parameters on the pressure distribution in the chambers, by investigating different non-contacting labyrinth seals. Integrating the pressure over the circumference of the chambers results in a total force, radial to the shaft, the two components of which - the restoring force opposite to the shaft displacement and the lateral force acting vertical to the shaft deflection plane - have to be investigated independently due to their different influence an the vibration behavior of the rotor. While the restoring force is of minor importance, because she does not induce self excitation, the lateral force components of the labyrinths may well be the cause for instabilities of turbomachines.

The investigations introduced in this paper result in labyrinth spring constants in relation to operational boundary conditions of the seal assemblies. In contrary to previous research work, a separate investigation was performed for multichamber labyrinths of different designs with static eccentricity of the rotor but without considering the rotor not to be parallel to the centerline. The achieved test results, first published, in part, already in 1978 (ref.15), shall contribute to a better understanding of the forces due to clearance flow in conventional labyrinth, to give a more differentiated view of the flow induced causes for self excitation in turbomachinery (ref.16).

EXPERIMENTAL SETUP

For the investigations, a test stand was needed, the design and fabrication of which was jointly done together with the manufacturers of turbomachines, engaged in these labyrinth studies. The test stand is shown in the cross section drawing of figure 1. Shown is a straight through labyrinth seal (half labyrinth) with plain shaft and mortised sealing tips in the casing. Each chamber of the labyrinth insert is equipped with twelve holes for static pressure measurements, which are arranged every 30 degrees over the circumference. The seal flow enters the test labyrinth from the top. Several inlet elements are available to vary the entry swirl at the inlet. The working fluid is air, which is expanded to the ambient conditions. The shaft circumferential speed is continously adjustable ($u_{w\ max}$=150 m/s). The rotor eccentricity can be arbitrarily selected within the mean gap width Δr.

The pressure measurement is done with range calibrated differential-pressure voltage-transformers. The measured values totalling 216, of which 188 are pressures, are collected by a data acquisition system. A central process computer controls the measuring system installed on the test stand and processes the digital measured values for pressure, temperature, leakage flow through the seal and rotor speed. The data output for test evaluation on the large capacity computer is selectable.

The influence of the following operation parameters on the pressure distribution in the chambers in circumferential and axial direction have been defined in the experimental investigations:

- pressure difference ratio p_a/p_o

- entry state of the first seal strip ρ_o, c_{uo}

- rotor excentricity ε

- geometry Δr, t, h and number m of chambers

- rotor circumferential speed $\pm u_w$

In this manner different labyrinth designs have been investigated. The mass flow throughput is additionally measured for every test point and was described in respect to the axial pressure distribution separably in reference 17. A detailed description of the test bed concept as well as a explanation of the measuring techniques and the testing procedures is given in reference 18.

EVALUATION

Based on the characteristic pressure distribution of figure 2, the interpretation method for the labyrinth investigation shall be explained. Characteristic pressure distributions for a labyrinth seal with two whirling chambers are shown in this diagram. The local pressure is related to the static pressure drop. Around the circumference of the seal, the static pressures of the chambers are measured in a distance of 30 degrees. The circumference angle $\phi = 0$ is the position of the widest gap. The centerline is parallel to the eccentric rotor. A non-parallel position of the rotor to the centerline can also be considered. The normal forces (Q and R), which act on the shaft, are the components of the force resulting from the pressure distribution. Since the pressure distributions in the chambers

$(p_i (\phi))$ are periodic phenomena around the rotor circumference, the evaluation by means of a Fourier development seems to be useful. The normal forces of a whirling chamber emerge as:

$$Q = r \cdot t \cdot \int_0^{2\pi} p_i (\phi) \sin \phi \, d\phi \qquad R = - r \cdot t \cdot \int_0^{2\pi} p_i (\phi) \cos \phi \, d\phi \qquad (1)$$

The utilized pressure integration method proved to be useful for the tests, since in this way also minimal changes of the basic vibrations have been graphed. The resulting normal forces emerge out of the summation of all chambers. For the systematic evaluation and presentation of the results however, a related representation of forces(related force: $F_B = r \cdot m \cdot t \cdot (p_o - p_a)$)for the lateral force $(\bar{Q}^*)$ and the restoring force $(\bar{R}^*)$ is recommendable. For different labyrinths, the force displacements curves for both forces have been graphed by varying the rotor excentricity (lateral force in fig.3). The gradients of the "Labyrinth spring characteristic curves" result in the "labyrinth spring constants" for the application in rotor dynamics, as defined in equation 2 for the related force spring constant.

$$\bar{K}_Q^* = d \bar{Q}^*/d\varepsilon \qquad (2)$$

The assumption of a linear relation between the forces and the rotor deflection is a supposition for the definition of the related force sensitivities. It could be proven that this is true for relative excentricity values of the lateral force component up to $\varepsilon = e/\Delta r = 0,6$ to $0,7$. The linearity of the restoring force deflection-curves is generally valid only for values $\varepsilon < 0,4$. The spring constants with dimensions of both components have to be calculated by means of the related force and the mean gap width. The lateral force exitation constant emerges as

$$K_Q = \bar{K}_Q^* \cdot F_B/\Delta r \qquad (3)$$

RESULTS

The exciting lateral forces are induced by the circumferential velocity components of the flow in the whirling chambers. In the labyrinths, two causes have to be considered responsible for this condition:

1. By the drag effect of the shaft a circumferential flow is caused in the chambers.

2. By an inlet condition with entry swirl at the first labyrinth tip a circumferential component is carried over into the labyrinth.

Both causes coexist with each other in a turbomachine. The separation of both effects could be achieved by separate investigations as part of this research. Whereas the speed related lateral forces exist primarily in longer labyrinths, the preswirl components dominate in short labyrinths with only few whirling chambers ($m < 5$), as used commonly as impeller seals.

Lateral forces due to shaft rotation

The effects of the lateral forces in a labyrinth seal induced by the drag effect of the shaft are dependent from the friction ratio between stator and rotor in the whirling chambers. Following equality conditions a mean circumferencial velocity develops in the chamber. For a labyrinth seal without axial pressure drop ($\Delta p_{st}=0$), this c_u-component is equal in each chamber and proportional to the circumferential speed of the shaft. The lateral and restoring forces resulting from the pressure distribution of the chambers are in a relationship of the square to the rotor velocity. The influence of speed is shown in figure 3 for a straight labyrinth without axial flow. Simultaneous this figure presents the influence of height of chamber. Along the rotor displacement the lateral forces are plotted. The slopes of these curves give the lateral force spring constants in the magnitude of K_Q = 5-50 N/mm. The listed measuring symbols are the average values of the pressure measurements from 17 whirling chambers out of two independent tests.

Similar results have been reached with investigations about the influence of shaft-rotation on the normal forces, when the seal had an axial flow due to an axial pressure difference (figure 4). For the circumferential component of the flow in the chambers a constant value for c_u along the whole length of the labyrinth cannot be assumed. Dependent on the mass flow, the conditions of the working fluid and the friction ratio in the seal, the circumferential flow will reach a constant velocity c_u at a certain chamber of the seal. The length of the seal, i.e. the number of chambers is therefore an important factor for the induction of lateral forces by rotation. Since the maximal number of chambers of the investigated labyrinths was 23, the results comprise the summation of all forces of the c_u-components - from starting up and the constant area of c_u. The direction of lateral force is dependent from rotation, whereas the restoring force is independent from rotation. This is further explained in the following. For the analysis of the rotation dependent lateral forces a related speed-flow value E_{ow}^* was defined (equation 4), in which the axial pressure drop entered with $\Delta p_{ges} = p_o - p_a + 0.5 \cdot \rho_o \cdot c_{ax}^2$.

$$E_{ow}^* = 0.25 \ (\rho_o + \rho_a) u_w^2 / \Delta p_{ges} \tag{4}$$

As a function of this value, figure 5 shows the characteristic curves of the related lateral force spring constants due to shaft rotation for two types of labyrinths. The listed symbols and the equation for K_{QW}^* are for the shown interlocking labyrinth design. For the investigated comb-and-groove seal, the short design (m=10 and 6) resulted in a low speed sensitivity. The factor k_A in the shown equation is the ratio between the propelling surfaces of the rotor and retarding surfaces of the stator. The value $k_{\Delta r} = \Delta r / 1mm$ includes the different gap width of the two labyrinth types. For sufficient long, i.e. multichamber labyrinth seals, the constant area of the circumference flow in the chambers is dominant, so that the relation between the speed u_w and the exciting lateral forces approach the limiting value:

$$K_{QW} \sim u_w^2 \tag{5}$$

Following from equation 4 this relation is equal to $K_{QW}^* \sim E_{ow}^*$ (fig.5).

194

Lateral forces due to entry swirl

The lateral forces due to entry swirl ($u_w=0$) are determined by the geometry and the flow boundary conditions at the seal entrance (figures 2 a. 6). The latter are covered by the relative admission energy E_o^* of the flow, which relates the volume-related swirl energy ahead of the first labyrinth tip to the existing total pressure drop:

$$E_o^* = 0,5 \cdot \rho_o \cdot c_u^2 / \Delta p_{ges} \qquad (6)$$

Without entry swirl ($E_o^*=0$) no lateral forces occur in an eccentric labyrinth seal with the shaft stationary.

The lateral force spring constants resulting from the lateral force/displacement curves are, in their related representation (equation 2) corresponding to the relationship "$\bar{K}_Q^* \sim \sqrt{E_o^*}$", depended on the magnitude of the related entry energy (fig.7). The proportionality factor is determined by the geometric parameters of the seal ($h, \Delta r, m, t$) and the flow coefficient μ. The calculation of the flow coefficient for the individual seals was carried out by means of the equation 7, since the mass flow was measured for each test point. Taking into account the

$$\dot{m} = \mu \cdot A \cdot \sqrt{(p_o^2 - p_a^2) / z \cdot p_o \cdot v_o} \qquad (7)$$

flow coefficient, the lateral forces due to preswirl can be calculated according to the equation in figure 8 for the different labyrinth designs. The mean height of the space between sealing strips covered by the equation is $h = 5-6$ mm with the factor $k_{\Delta r}$ indicating the effect of the clearance width in respect of $\Delta r=1$ mm. The dashed straight lines represent the scatter band of $\pm$ 8 % applying to the equation stated. The symbols entered result in each case from a lateral force/ displacement characteristic with 5-7 test points versus rotor eccentricity. As the height of the spaces between the sealing strips becomes less, the lateral forces tend to increase (fig.6). This geometry parameter can be included for the relative lateral force excitation constant in the relationship plotted in fig.9. In conjunction with further geometry variables, the following relation- ship has been estabilished for this parameter on the strength of tests made to date:

$$\bar{K}_Q^* \sim \Delta r \cdot \mu \cdot \sqrt{E_o^*} / m \cdot h \qquad (8)$$

Restoring forces of labyrinth seals

Depending on the labyrinth configuration, the restoring forces are widely dif- ferent. With seals having a number of spaces $m > 6-8$, restoring forces are mainly negative, i.e. decentering. In contrast with the lateral forces, they also tend to occur without entry swirl and shaft rotation (fig.10). The amount of negative restoring forces increases as the shaft circumferential velocity increases. In- dependent of the direction of rotor rotation, the force provides decentering action in the direction of the shaft displacement (fig.4). In the case of the interlocking labyrinth-type seal, the relative restoring force spring constants were found to be similar to the lateral force spring constants as a function of the speed-flow index E_{ow}^*. For multichamber labyrinths, the influence of the chamber circumferential flow by rotor rotation was confirmed, since the negative restoring forces increase considerably due to inertia conditions (fig.10).

Therefore, the chamber specific c_u-component is responsible for the decentering parts of the restoring forces along the chambers. Restoring forces centering the rotor could only be detected in the first whirling chamber of the individual labyrinth designs investigated. All further whirling chambers have been slightly decentering and therefore dominating in the summation of the total seal.

APPLICATION

A general impression of the effects of the flow parameter referred to on the dynamic behaviour of labyrinths can be seen in fig. 11 by the example of an interlocking labyrinth. Normaly in turbomachinery, a coexistance of lateral forces from entry swirl flow and from shaft rotation has to be accounted for. For a first evaluation of values, an addition of the swirl and speed related components can be done as an approximation. Figure 12 shows the influences of the most important values on the lateral force sensitivity for tests with shaft rotation and entry swirl. With increasing shaft circumferential speed - pressure ratio constant - the lateral force spring constants are growing. For the axial pressure drop, the following statement can be made: the inducing influence of the rotor speed on the related lateral force is growing with smaller pressure difference and therefore with smaller leakage flow while the other conditions are constant.

Makers of turbo-machinery participating in the research project are applying the results of the labyrinth studies for the stability analysis of their machines. The magnitudes of labyrinth excitation constants to be expected are widely different depending on the operational boundary conditions of the seal. The utilization of results from the investigations of this research on similar labyrinth designs is shown in the calculation of fig. 13. For short labyrinth designs with few whirling chambers, the preswirl related lateral forces dominate, whereas the speed influence cannot be neglected with growing labyrinth length.

Stability calculations have been performed for rotors with different damping characteristics (damping reserves) to receive statements about the influence of the lateral forces in seals on the vibration behavior of centrifugal compressors. The effect of the labyrinth forces on the vibration behaviour of centrifugal compressor is shown in figure 14. For demonstration purpose two different rotors (Rotor 1 and Rotor 2) have been investigated by "Mannesmann-DEMAG". They basically differ by their shaft stiffness. Compared with rotor 1, rotor 2 has two additional impellers, a larger bearing span and slightly smaller shaft diameters underneath the impeller hubs. Consequently the first "critical speed" of rotor 1 is considerably higher than of rotor 2. The operating speed is supposed to be 12 000 rpm for both rotors resulting in critical speed ratios $n_B/n_{K1} = 1.7$ for Rotor 1 and 2.7 for Rotor 2. For each rotor (1 and 2) two different impeller arrangements A ("in line") and B ("back to back") have been analysed in order to show the influence of the attack location (Pos.x) on the aerodynamic excitation. At version A the excitation acts close to the bearing, at version B in the middle of the rotor. The attack position x represents a long labyrinth taking a high differential pressure which is typical for a thrust balance drum. For simplification only at this location an aerodynamic lateral force has been taken into account whereby only the substantial Q-component was considered (R-component neglected). The influences of the different impeller seals, where large entry swirl components arise, are also neglected.

In fig. 14 the attenuation factor of the rotor-bearing system is plotted against the rotor speed. The solid lines represent the system damping without aerodynamic excitation. The dotted curves show the effect resulting from labyrinth forces with various intensities. The diminution of the system damping increases with increasing labyrinth force coefficients K_Q. In particular this is the case for the very flexible rotor 2 (version B, force acting in the middle), where the damping becomes "negative" before the operating speed range is reached. Below the threshold point ($u/\omega_K = 0$) the rotor runs strongly unstable, vibrating with large amplitudes and defined frequencies (not shown in fig.14) which are not synchronous with the rotor speed.

For rotor 1 the damping characteristics for a further eigenvalue (x-branch) of the rotor-bearing system have been plotted in addition to the determining y-branch. For this eigenvalue (which belongs to a motion dominantly directed in the x-plane) the damping factors become larger for increasing K_Q-values, but this has no effect on the stability, which is governed by the y-branches.

An important conclusion can be drawn from the examples given: The analytical results indicate that also with multistage hp-centrifugal compressors having a very flexible rotor, instability can be avoided if appropriate measures will be taken in order to minimize (or even eliminate) the trouble-some Q-forces in labyrinths.

Seeing that look-through labyrinths with few sealing strips are frequently used for impeller seals, it is possible to assume comparable lateral force spring constants in the range of 1 to 10 N/μm also in the interlocking labyrinths of a steam turbine. The calculations of a turbine maker for the high-pressure element of a 600 MW steam turbine plant has shown that the speed-related components of the dummy piston are responsible for a decrease in stability of the hp-rotor by about 3%. The negative restoring forces tend to reduce the natural frequencies of the individual sections of the turbo generator. Regarding the high-pressure section, the reduction in natural frequency for the two directions amounted to about 3.3-4.4%, whereas these effects were reduced for the IP section to about 1-2%.

CONCLUDING REMARKS

The presented labyrinth investigations confirm that the lateral force component resulting out of an unsymmetrical pressure distribution in eccentric gaps of labyrinth seals, acting at a right angle to the rotor deflection plane, represents a vibration exciting force, which has to be accounted for in rotor dynamics. The utilisation of the results shows the influences on the vibration behavior of high loaded turbomachines. A knowledge of the labyrinth spring constants permits a more accurate stability analysis. This makes it possible for any critical operational conditions to be detected already during the design stage of the machine.

To reduce the lateral force sensitivity of labyrinth seals, several possibilities are at hand. Their aim has to be to eliminate the circumferential flow in the chambers of the seal. Both effects - entry swirl and shaft rotation - induce circumferential components in the chambers and are therefore dangerous for the stability of the rotor. Two possibilities to avoid the exciting lateral forces shall be indicated. By a suitable change of the entry swirl of the flow ahead of the first seal tip in opposite direction of the sense of rotation of the shaft, a seal free of lateral forces can be achieved (figure 15, $u_W = -112$ m/s).

197

For short impeller seals, some swirl webs in front of the first fin at the periphery of the seal are sufficient to reduce the preswirl and therefore the lateral force sensitivity (fig.16). The influence of the speed related components of the lateral force, which will develop themselves within the seal, is minor with a small number of chambers.

LIST OF SYMBOLS

– International System of Units (SI) –

A	mean clearance area	μ	flow coefficient
c	flow velocity	ε	relative eccentricity ($\varepsilon = e/\Delta r$)
E	flow index	ρ	density
e	rotor eccentricity	ϕ	peripheral angle
F_B	reference force		
h	height of space between sealing strips		

Subscript

K	spring constant	o	in front of labyrinth
k	ratio factor	a	behind labyrinth
m	number of spaces between sealing strips	ax	axial direction
		ges	sum
$\dot{m}$	mass flow	i	labyrinth
p	pressure	Q	lateral force
Q	lateral force	R	restoring force
R	restoring force	u	peripheral direction
r	rotor radius	w	shaft rotation
Δr	mean clearance width		
t	labyrinth pitch		**Superscript**
u_w	peripheral velocity		
v	specific volume	*	related value
z	number of sealing strips	–	mean value

REFERENCES

1. Stodola, A.: Dampf- und Gasturbinen. Springer Verlag Berlin, 1924.

2. Greathead, S.H. and Bastow, P.: Investigations into Load Dependend Vibrations of the High Pressure Rotor on Large Turbo-Generators. Proc.Instn.Mech.Engrs., C 220/1976, pp. 279-285.

3. Thomas, H.J.: Unstable Oscillations of Turbine Rotors Due to Steam Leakage in the Clearances of the Sealing Glands and the Buckets. Bulletin Scientifique, A.J.M. 71, 1958, pp. 1039-1063.

4. Pollmann, E.: Stabilität einer in Gleitlagern rotierenden Welle mit Spalterregung. Fortschrittsbericht VDI-Z. Reihe 1, Nr. 15, 1969.

5. Alford, J.S.: Protecting Turbomachinery from Self-Exited Rotor Whirl. Transactions ASME, J. of Eng. f. Power, October 1965, pp. 333-344.

6. Spurk, J.H. and Keiper, R.: Selbsterregte Schwingungen bei Turbomaschinen infolge der Labyrinthströmung. Ingenieur-Archiv 43, 1974, pp. 127-135.

7. Wright, D.V: Air Model Test of Labyrinth Seal Forces on a Whirling Rotor. ASME Gas Turbine Div., Winter Annual Meeting 1977, pp. 61-73.

8. Kostyuk, A.G.: A Theoretical Analysis of the Aerodynamic Forces in the Labyrinth Glands of Turbomachines. Teploenergetika, 19(11) 1972, pp. 29-33.

9. Rosenberg, C.S., Orlik, W.G. and Marshenko, U.A.: Untersuchung aerodynamischer Querkräfte in den Labyrinthdichtungen bei Wellenexzentrizität. Energomashinostrojenie, No. 8, 1974, pp. 15-17.

10. Urlichs, K.: Durch Spaltströmungen hervorgerufene Querkräfte an den Läufern thermischer Turbomaschinen. Dissertation TU of Munich, 1975.

11. Kostyuk, A.G. and Kirjuchin, A.V.: Eigenschwingungen und Stabilität von Turbinenläufern in den Gleitlagern unter Berücksichtigung nichtkonservativer dynamischer Kräfte. Teploenergetika 25(9) 1978, pp. 14-19.

12. Linnemann, H. and Wettmann, K.: Laufstabilität thermischer Turbomaschinen. BBC-Nachrichten, Vol. 12, 1973 , pp. 396-401.

13. Thomas, H.J.: Zur Laufstabilität einfacher Rotoren, besonders bei Spalterregung. Konstruktion 30(9) 1978, pp. 339-344.

14. Aicher, W., Jenny, R. and Roduner, H.: Untersuchungen an Turbokompressoren: Rotorschwingungen, Schaufelschwingungen, Versuche mit schweren Gasen. Techn. Rundschau Sulzer, Vol. 60, Forsch. Heft 1978, pp. 11-18.

15. Benckert, H. and Wachter, J.: Studies on Vibrations Stimulated by Lateral Forces in Sealing Gaps. AGARD-CP-237, 1978, pp. 9.1-9.11.

16. Pollmann, E., Schwerdtfeger, H. and Termühlen, H.: Flow Excited Vibrations in High-Pressure Turbines (Steam Whirl). ASME Gas Turbine Div., Winter Annual Meeting 1977, pp. 75-87.

17. Benckert, H. and Wachter, J.: Investigations on the Mass Flow and the Flow Induced Forces in Contactless Seals of Turbomachines. Proceedings of the 6th Conference on Fluid Machinery, Budapest 1979, S. 57-66.

18. Benckert, H.: Spaltströmungen. Forschungsberichte Forschungsvereinigung Verbrennungskraftmaschinen Frankfurt/Main, H. 253, 1978.

APPENDIX

The appendix will give some informations about the studies on labyrinth seals furthermore done after writing the paper. The figures A1 - A9 are abridged from a publication of the institute (ref. 19).

The lateral forces due to the <u>swirl-type entry flow</u> of the labyrinth (rotor stationary, $u_w=0$) has been investigated separately for different look-through labyrinth configurations (fig. A1 and A2). In addition to the paper the influence of the labyrinth pitch could be proved also for this type of labyrinth. Figure A2 shows the results for the relative lateral force spring coefficients due to the entry swirl of the flow. The given geometry-factor k_G is related to the flow coefficient μ', which is defined especially for look-through labyrinths:

$$\mu' = \mu \ k_{\ddot{u}} \tag{9}$$

According to the paper, the factor μ in equation 7 and 8 corresponds for a look-through labyrinth to the product μ' (eq. 9). The factor $k_{\ddot{u}}$ describes the different behaviour of the mass flow for comparable look-through and inter-locking labyrinths. The effect of the radius of the shaft on the lateral forces differs nearly 30% from a quadratic relationship. In look-through labyrinths the "Spiral Flow Effect" is dominant for the exciting forces. The relationship for $\overline{K}_Q^*$ and the dimensioned lateral force spring coefficient K_Q are plotted in figure A2 ($\Delta p_{st} = p_0 - p_a \approx \Delta p_{ges}$). If the factor μ (in eq. 9) of the seal is not known, it is possible to estimate the lateral force spring coefficients for look-through labyrinths of usual design by using the following equation:

$$K_Q = k_G \ r^2 \ \sqrt{0,5 \ \varrho_o \ c_{uo}^2 \ \Delta p_{st}} \ / \ h \tag{10}$$

The lateral forces in labyrinths due to the <u>shaft rotation</u> are a function of the peripheral flow in the spaces between the sealing strips. In addition to the paper figure A3 shows in function of the entry swirl c_{uo} two areas for the circumferential velocities of the flow in the eddy chambers. The dominant influence of the constant c_{um}-area in long labyrinths can be demonstrated by figure A4. The lateral forces result mostly from the eddy chambers $m > 6$. Figure A5 was obtained evaluating the dimensionless force/displacement charac-teristics of the constant area for different running conditions. The stated function of the straight line in the figure A5 confirms equation 5. Independend from the number of eddy chambers (m = 17 and 23) the product "$\varrho_m \ c_{um}^2$" is a criterion for the lateral forces in multi-chamber labyrinth seals (subscript m: mean value in the constant area).

In addition to the experimental studies a <u>theoretical model</u> has been developed for the calculation of the speed induced forces in labyrinth seals (ref. 19). In the first step of the computation the peripheral velocity of the flow is calculated in each eddy chamber of the seal. Measured and calculated c_u-velocitie: have been compared and the accuracy of the model could be proved. Based on these results the flow induced forces of each chamber are calculated. Figure A6 shows

---

Reference 19: Benckert, H.: Strömungsbedingte Federkennwerte in Labyrinth-dichtungen. Mitteilung des Institutes für Thermische Strömungs-maschinen, Universität Stuttgart, Nr.8, 1980, 159 pages, 82 figur:

200

computed results, which are comparable with the experimental lateral spring constants shown in figure A4. The influence of the density of the fluid is demonstrated in figure A7 for the same type of labyrinth. Using the theoretical model for the constant area of the c_u-components of the flow in the labyrinth, the following relationship can be stated (m_n: number of eddy chambers in this area):

$$K_Q = \pi \ m_n \ r^2 \ \rho_m \left[\ (k_1 - k_2) \ c_{um}^2 + k_2 \ c_{um} \ u_w \right] / \ h^2 \qquad (11)$$

The factors $k_{1,2}$ correspond to the mean coefficients of friction of the stator (k_1) and the rotor (k_2) in the eddy chambers.

Additionally to the figures 15 and 16 of the paper the figures A8 and A9 should point out the problems in reducting speed-related lateral forces by using special constructions of labyrinth seals.
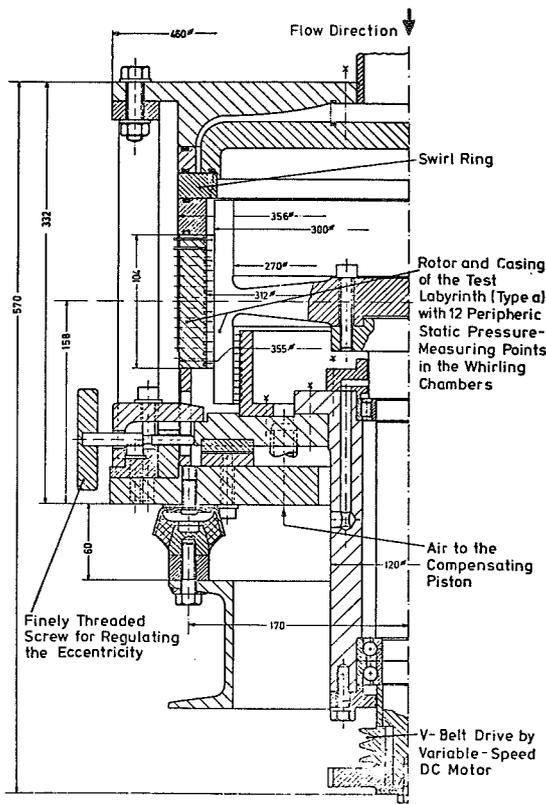
Fig. 1: Testing facility for labyrinths
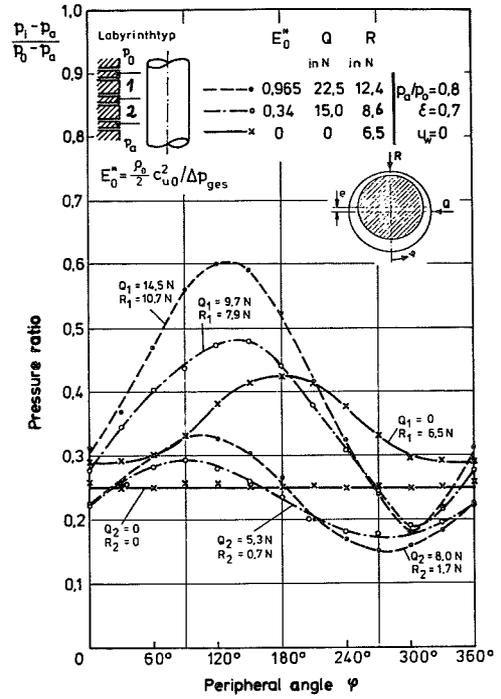
Fig. 2: Pressure distributions and forces in a half-labyrinth with eccentric rotor
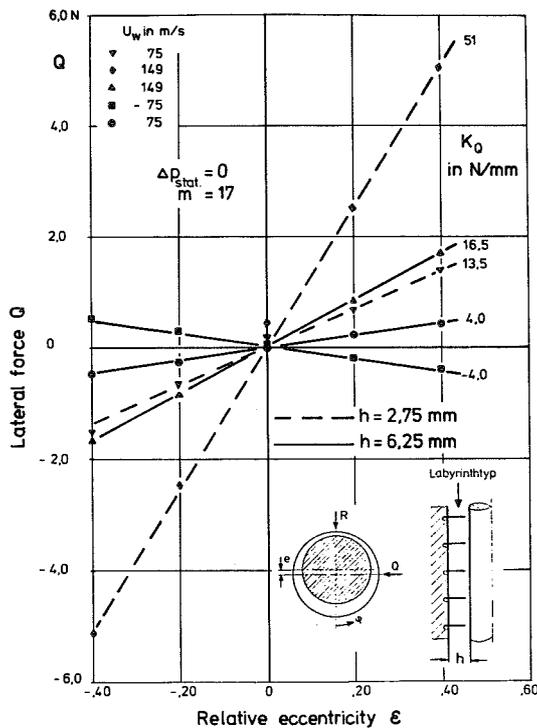
Fig. 3: Force characteristics due to height of chamber and shaft rotation without mass flow
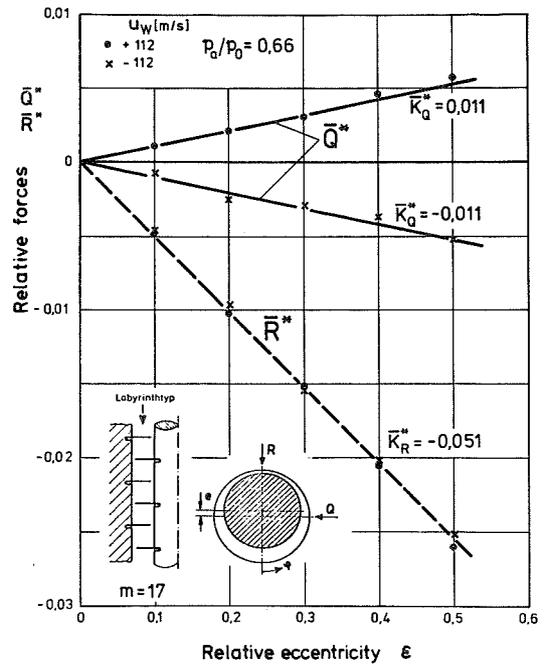
Fig. 4: Forces of an eccentric labyrinth due to reverse of shaft rotation

202
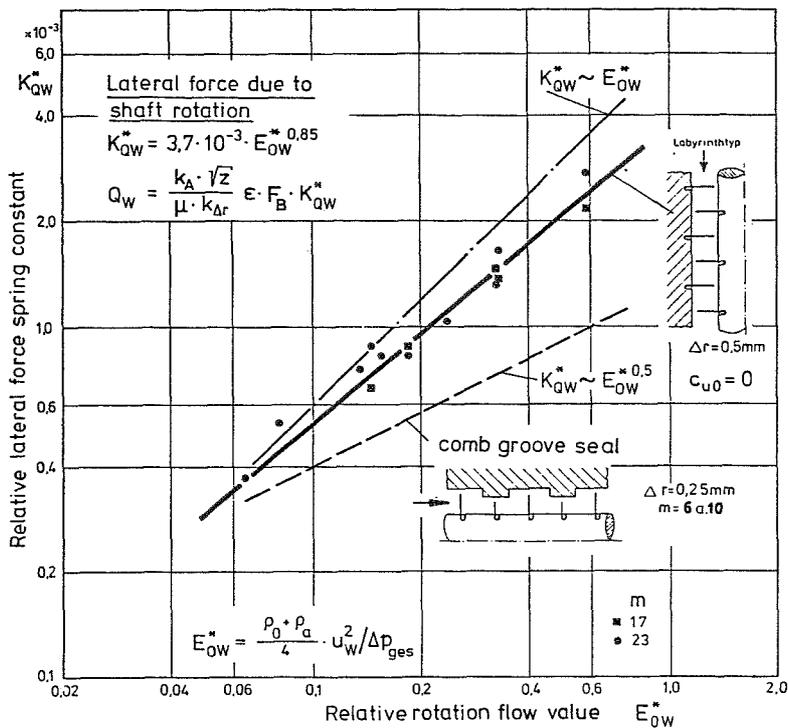
Fig. 5: Lateral force spring coefficients as function
of the relative rotation flow value
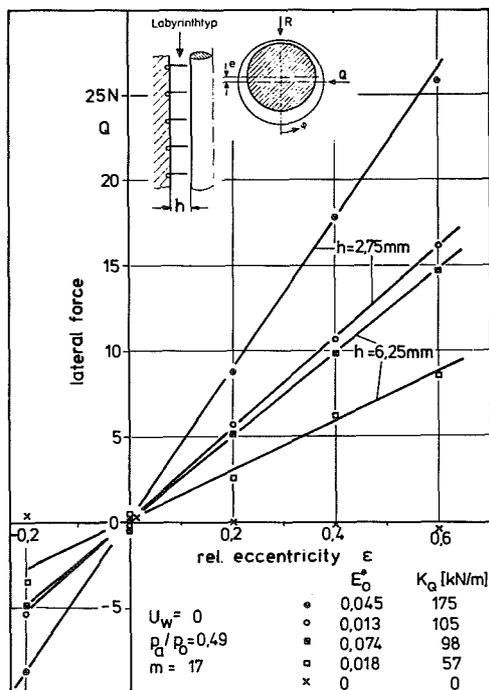
Fig. 6: Influence of height of chambers on the
lateral force due to entry swirl
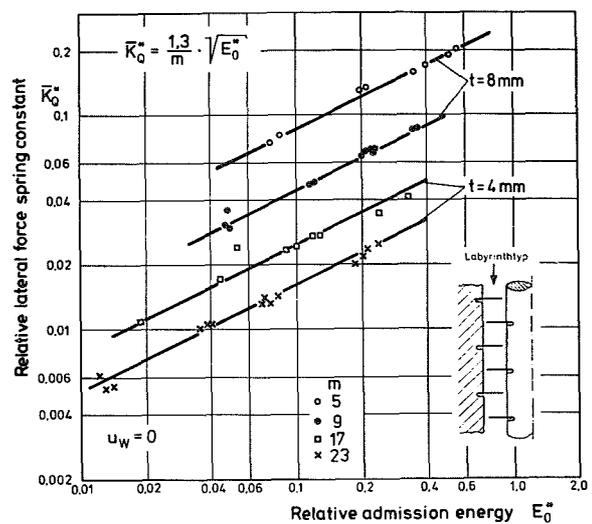
Fig. 7: Lateral force spring constants as function of
the relative admission energy of the flow
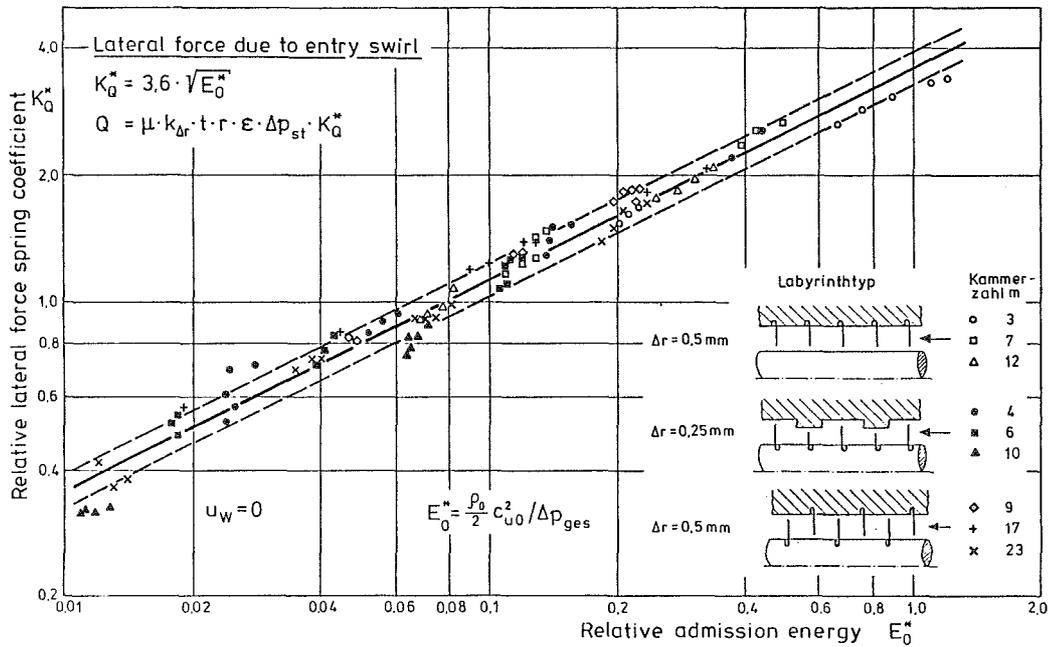
Fig. 8: Lateral force spring coefficients for different labyrinth
patterns as function of the relative admission energy of the flow
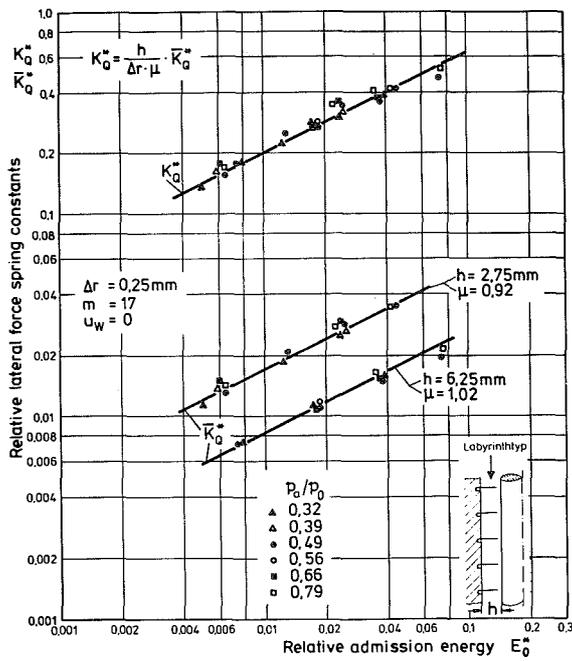
Fig. 9: Influence of height of chamber on the
lateral force spring coefficients
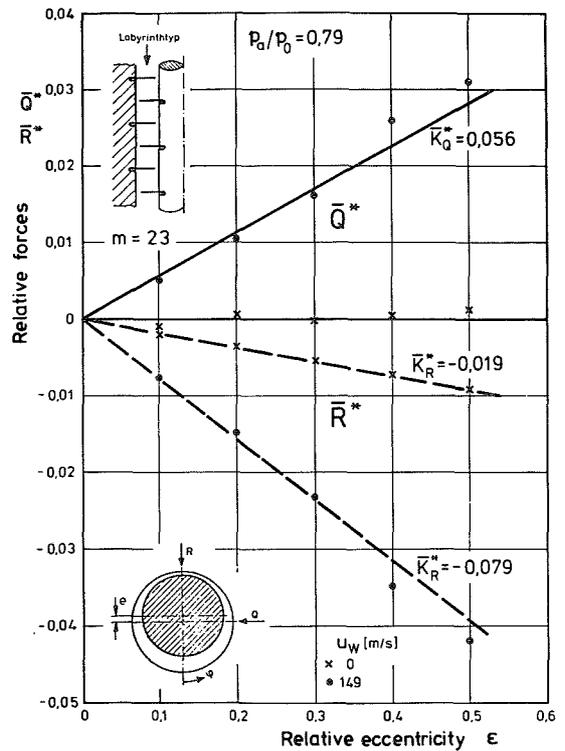
Fig. 10: Relative forces of an eccentric
labyrinth without entry swirl

204
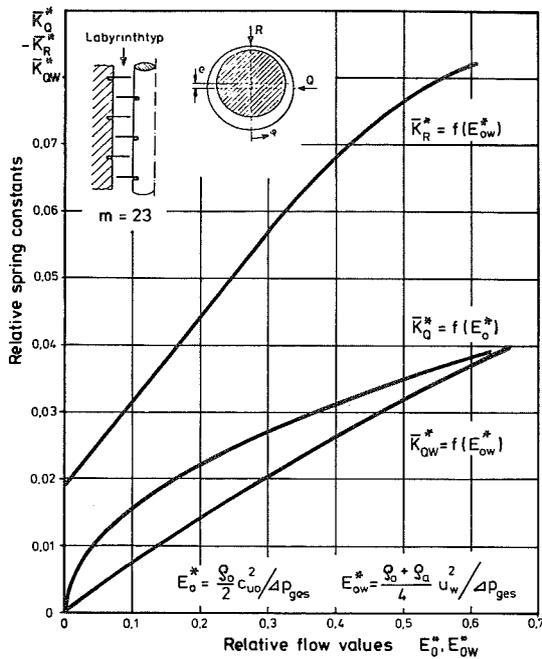
Fig. 11: Flow induced spring coefficients for the lateral and restoring force of a labyrinth as function of the relative characteristic flow values
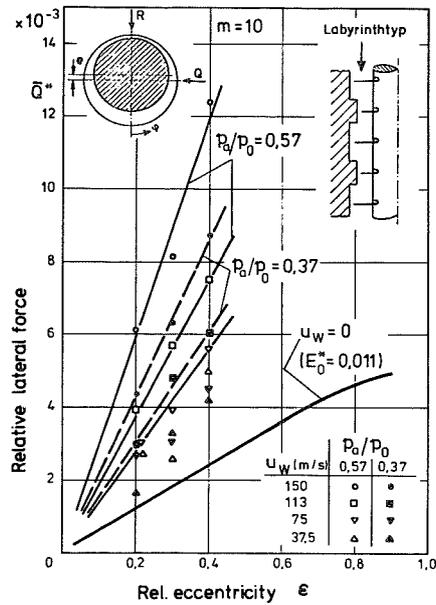
Fig. 12: Influence of rotor speed and pressure ratio on the lateral forces with entry swirl of the flow

Relevant equations from Fig. 11:

$$E_o^* = \frac{\varrho_o}{2} c_{uo}^2 / \Delta p_{ges} \qquad E_{ow}^* = \frac{\varrho_o + \varrho_a}{4} u_w^2 / \Delta p_{ges}$$

$\Delta r = 0{,}25$ mm $\quad$ h $= 6$ mm

r $= 150$ mm $\quad \mu = 0{,}98 \qquad$ $u_w = 188$ m/s $\quad c_{uo} = 150$ m/s

t $= 5$ mm $\quad k_A = 0{,}3 \qquad$ ($\hat{=}$ 12000 1/min) $\quad c_{axo} \approx 0$

Eccentricity of the rotor: $\quad$ e $= 0{,}1$ mm $\implies \varepsilon = 0{,}4$

Labyrinth type		Running conditions			
		p_o in bar	p_a in bar	E_o^*	E_{ow}^*
A:	short m $= 3$	200	160	0,67	0,95
B:	long m $= 30$	200	20	0,15	0,13

Lateral force due to	type A	type B
- entry swirl	0,9 kN	1,8 kN
- shaft rotation	~30 N	0,7 kN

Lateral force spring coefficients K_Q:

short version: 9 N/μm $\quad$ long version: 25 N/μm

Fig. 13: Estimation of lateral force constants for two labyrinths

205

Rotor 1

$\omega_{K1} = 739 \ 1/s$

$n_B / n_{K1} = 1.7$

$= A$

1400

$= B$

$\dfrac{-u}{\omega_{K1}}$

0,14
0,10
0,08
0,06
0,04
0,02
0

operating speed

$K_Q = 8 \ kN/mm$

$K_Q = 0$

$K_Q = 8 \ kN/mm$

x - branch

y - branch

B

A

A

B

4000   6000   8000   n [rpm]   12000   14000

0,5   0,75   1,0 n_B / n_{K1} 1,5   1,7   2,0

Rotor 2

$\omega_{K1} = 465 \ 1/s$

$n_B / n_{K1} = 2.7$

$= A$

1750

$= B$

$\dfrac{-u}{\omega_{K1}}$

0,10
0,06
0,04
0,02
0
-0,02
-0,04
-0,06

unstable

operating speed

$K_Q \left[\dfrac{kN}{mm}\right]$

0
4
6
8
4
6
8

A

B

4000   6000   8000   n [rpm]   12000   14000

0,75   1,0   1,25   1,5   2,0 n_B / n_{K1} 2,5   2,7   3,0
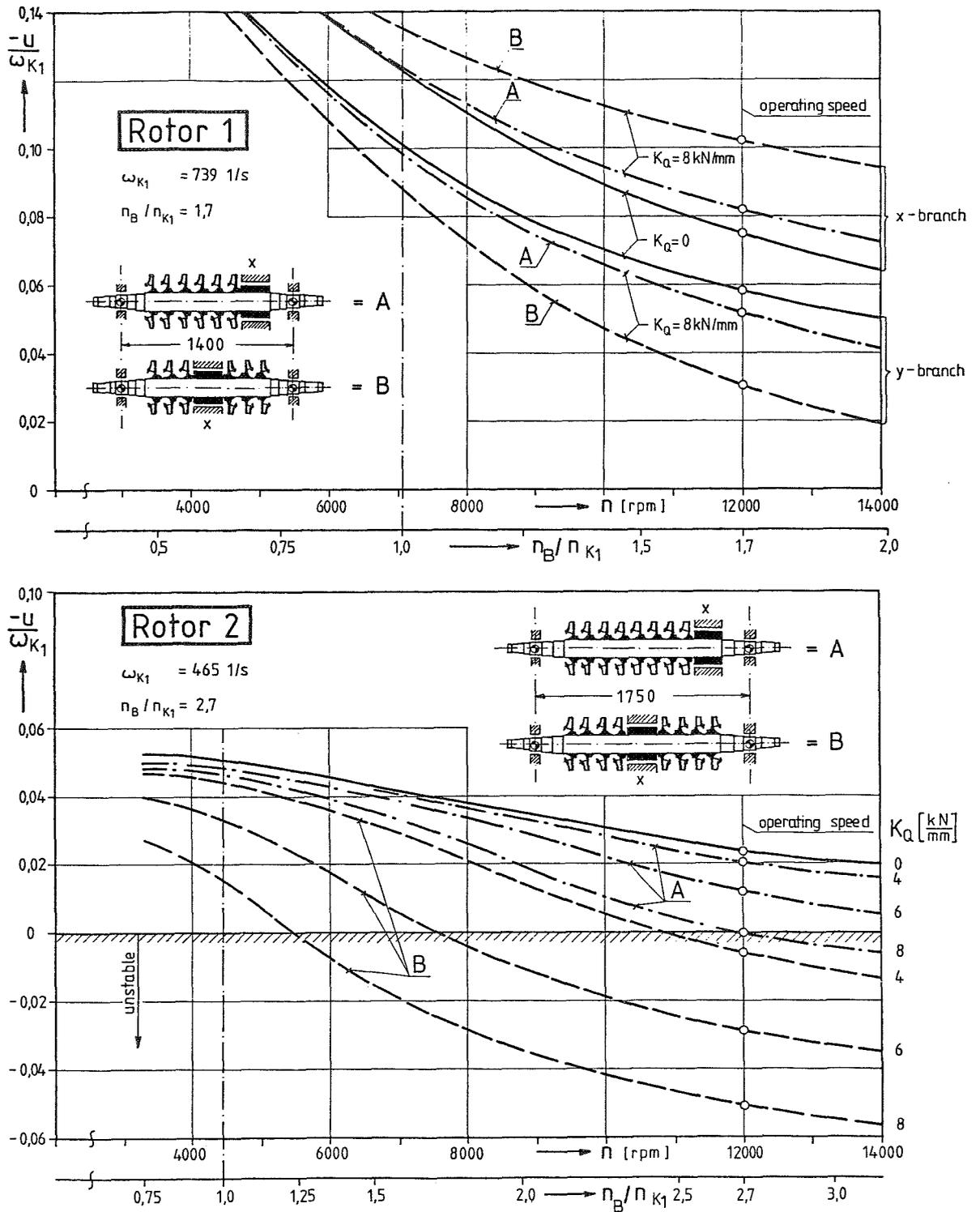
Fig. 14: Influence of lateral labyrinth forces on the damping
behaviour for two rotors with different shaft stiffness
(Bearings: tilting pad; n=5; B/D=0,5; m=2,5; Ψ=1,5·10^{-3})
- calculated by Mannesmann-DEMAG -

206
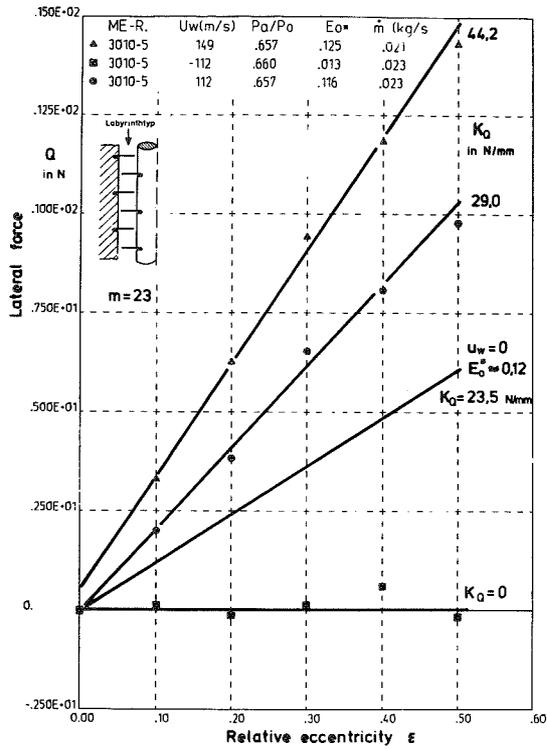
Fig. 15: Lateral force characteristics due to shaft rotation with entry swirl of the flow
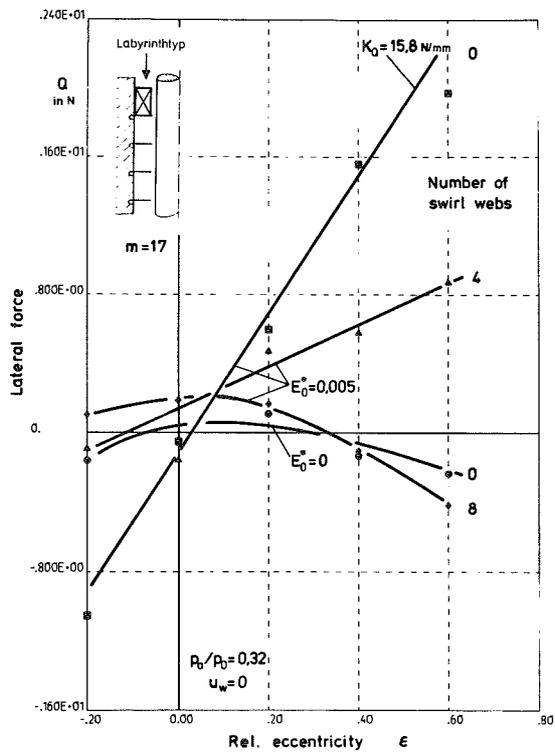
Fig. 16: Reduction of lateral forces by using swirl webs in front of the labyrinth

207
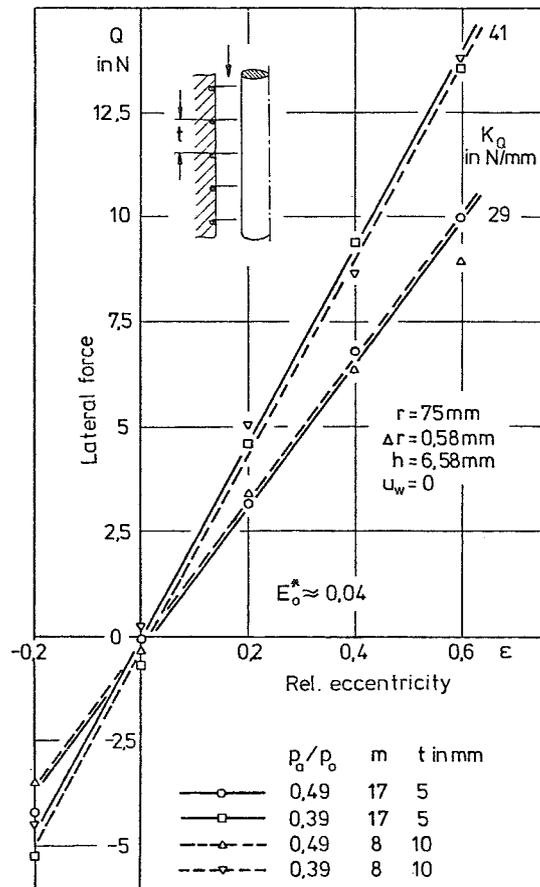
Fig. A1: Influence of the labyrinth-pitch
on the lateral forces due to flow
with entry swirl.
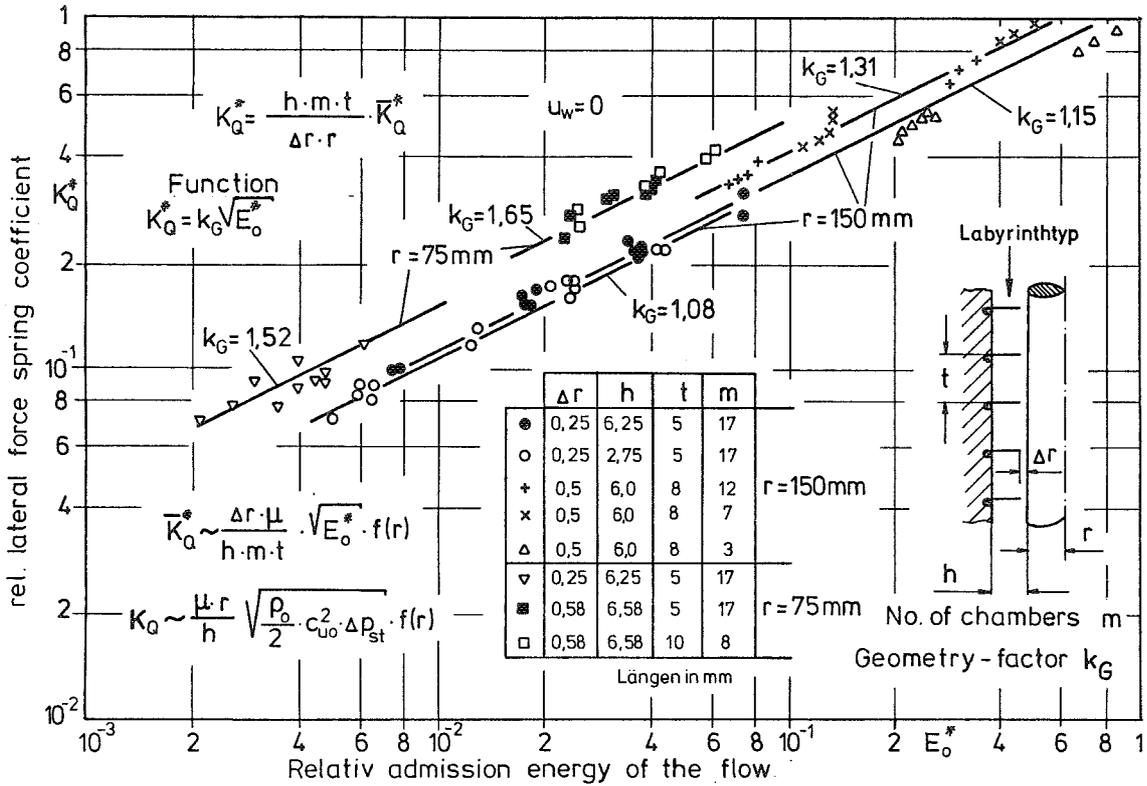
Fig. A2: Lateral force spring coefficients of look-through labyrinths with swirl type entry flow.
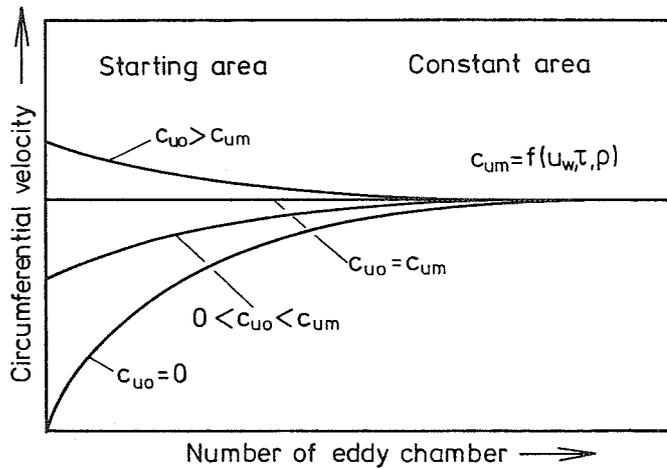
Fig. A3: Definition of two labyrinth areas for the circumferential velocity of the flow.
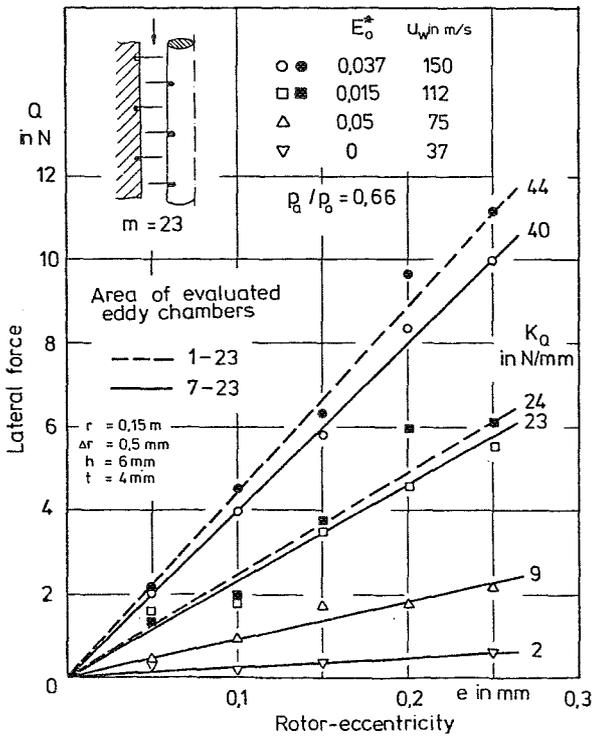
Fig. A4: Speed induced lateral forces of the total labyrinth and the area with constant peripheral flow components.
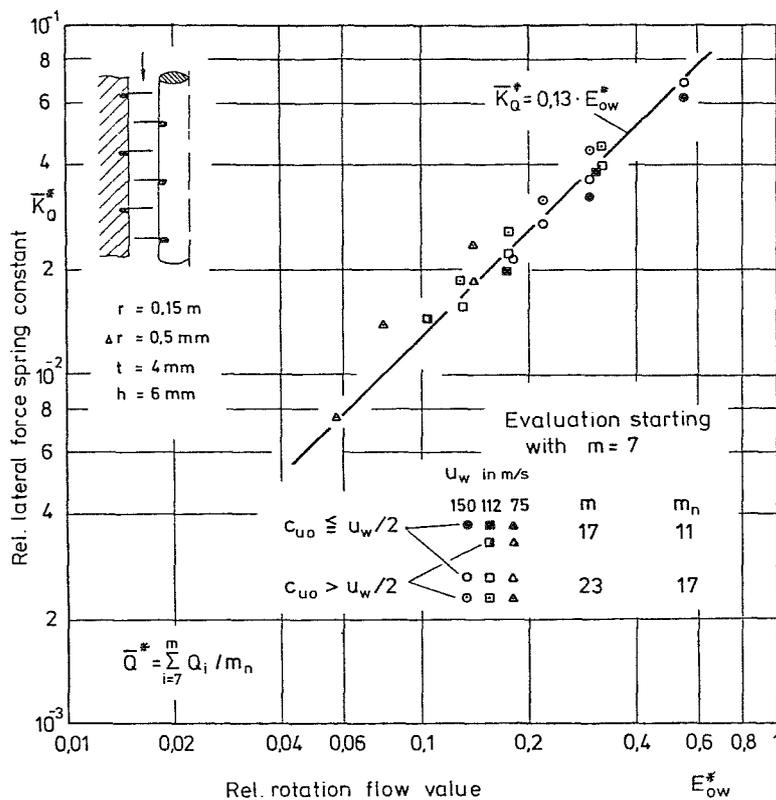
Fig. A5:

Lateral force spring coefficients without evaluation of the first six eddy chambers (shaft rotation and entry swirl).
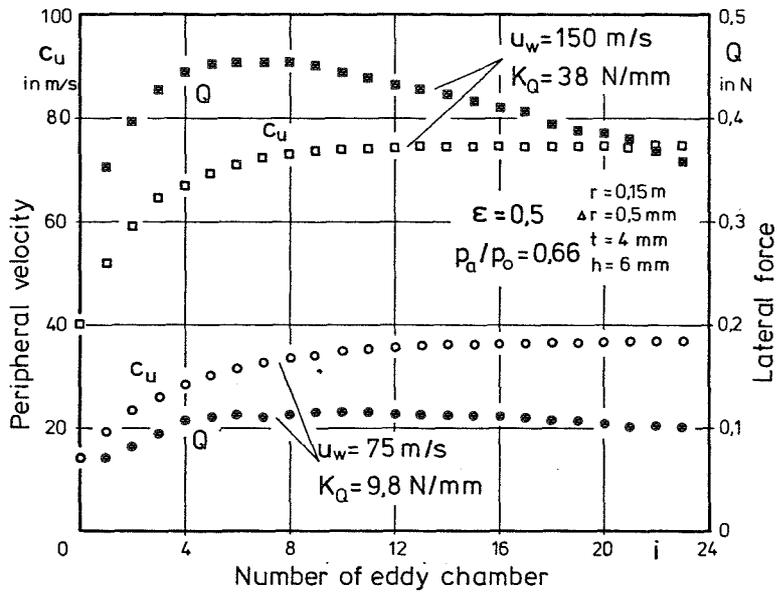
Fig. A6: Calculated distributions of the circumferential
velocity of the flow and the lateral forces due
to shaft rotation and entry swirl in an inter-
locking labyrinth seal.
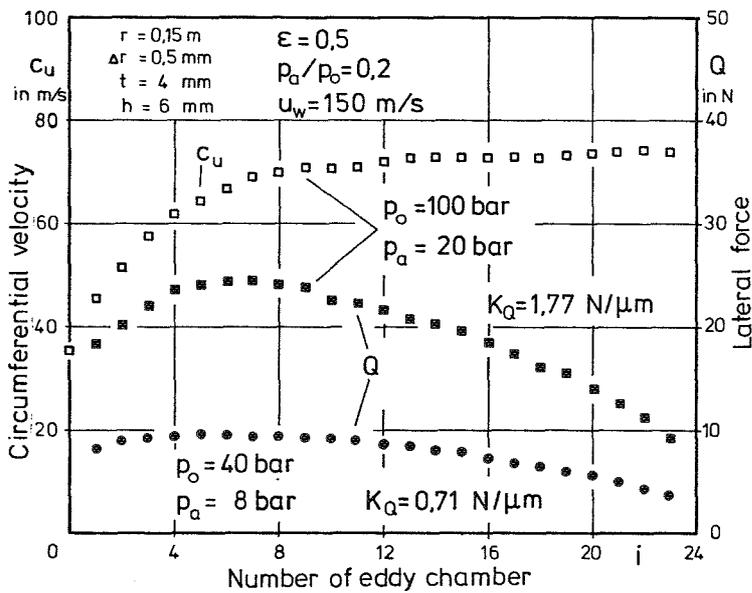
Fig. A7: Influence of density of the fluid on the peripheral
velocity of the flow and on the lateral forces in
an interlocking labyrinth (Calculation).
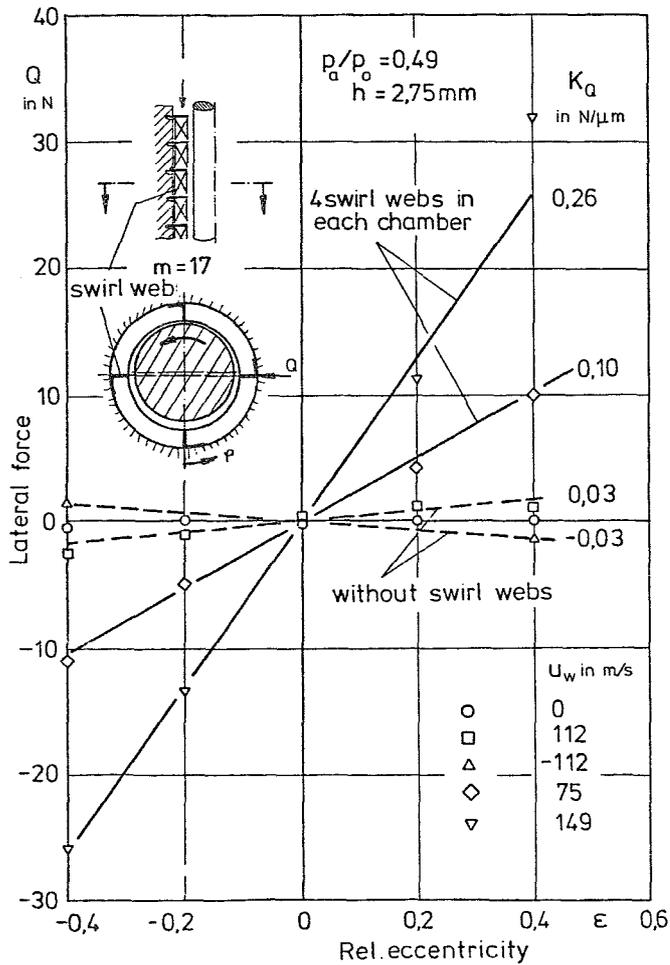
Fig. A8: Speed induced lateral forces by using swirl webs in each eddy chamber of the labyrinth.
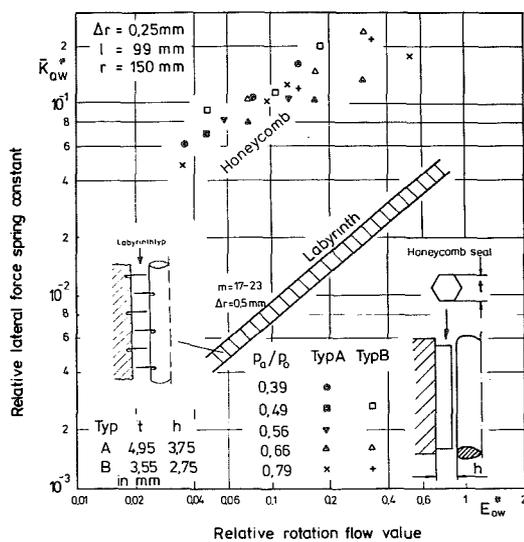
Fig. A9: Lateral force spring coefficients as function of the relative rotation flow value for two honeycomb seals.

212

HYDRAULIC FORCES CAUSED BY ANNULAR PRESSURE SEALS
IN CENTRIFUGAL PUMPS

T.Iino and H.Kaneko
Mechanical Engineering Research Laboratory, Hitachi,Ltd.
Tsuchiura, Japan

SUMMARY

An experimental study was performed with static and dynamic test appa-
ratus to investigate the hydraulic forces caused by annular pressure seals.
The measured inlet and exit loss coefficients of the flow through the seals
were much smaller than the conventional values, though the measured resistance
coefficients agreed well with the values calculated by the equations proposed
by Yamada and by Tao and Donovan. The results of the dynamic tests showed
that the damping coefficient and the inertia coefficient of the fluid film in
the seal were not affected much by the rotational speed or the eccentricity
of the rotor, though the stiffness coefficient seemed to be influenced by the
eccentricity.

INTRODUCTION

It has been reported that annular pressure seals in centrifugal pumps
have great influence on the lateral vibrations of the shaft systems (ref. 1
and 2). In order to analyze the dynamic properties of the fluid films in the
annular seals, it is necessary to know the boundary conditions of pressure
such as pressure at the both ends of the seal. It is also important to evalu-
ate properly the resistance coefficient of the flow in the seal both in the
axial and the circumferential directions. Unfortunately there are few data
available to evaluate those values, especially when the configuration of the
seal is complicated.

In this study two series of experiments, static tests and dynamic tests,
are carried out. In the static tests, pressure distributions in the eccentric
seals are measured under several conditions of the eccentricity, the axial
pressure difference and the speed of the rotor to investigate the inlet and
the exit loss coefficients and the resistance coefficients, which will help
the dynamic analysis.

Then the dynamic forces at the seals caused by a vibrating rotor are
measured. The dynamic properties of the fluid films in the seals are calcu-
lated from the test results.

NOMENCLATURE

The following nomenclature is used in the paper:

c   damping coefficient, N·s/m
d   seal diameter, m
e   eccentricity ratio ($=\delta/G$)
f   static force on an eccentric rotor, N
$\bar{f}$ non-dimensional force on the rotor ($=f/(0.5\rho\cdot v_m^2\cdot d\cdot 1)$)
F   dynamic force on the stator, N
G   seal clearance when concentric, m
k   stiffness coefficient, N/m
1   seal width, m
m   inertia coefficient, N·s^2/m
N   rotational speed, rps
p   pressure, N/m
$\bar{p}$ non-dimensional pressure ($=(p-p_6)/(p_1-p_6)$)
$\overline{\Delta p}_{max}$ non-dimensional maximum pressure difference in a section perpendicular
        to the axis ($=(p_{max}-p_{min})_{x=x}/(p_{max}-p_{min})_{x=0}$)
Q   leakage flow rate, m^3/s
R_a axial Reynolds number ($=v_m G/\nu$)
R_r rotational Reynolds number ($=\pi\cdot d\cdot N\cdot G/\nu$)
v   axial velocity component of the flow in the seal, m/s
v_m mean axial velocity ($=Q/(\pi\cdot d\cdot G)$), m/s
x   co-ordinate in the axial direction (x=0 at the inlet of the seal), m
X   rotor displacement in the vertical direction, m
Y   rotor displacement in the horizontal direction, m
δ eccentricity, m
θ co-ordinate in the circumferential direction (θ=0 at the top of the
        seal)
λ resistance coefficient ($dp=\lambda\cdot(dx/2G)\cdot(\rho\cdot v_m^2/2)$)
λ_0 resistance coefficient proposed by Yamada ($=0.26R_a^{-0.24}\{1+(7/8)^2\cdot(R_r/2R_a)^2\}^{0.38}$)
ν kinematic viscosity, m^2/s
ξ_{in} inlet loss coefficient ($=(p_1-p_2)/(0.5\rho\cdot v_m^2)-\lambda\cdot x_2/(2G)-1$)
ξ_{out} exit loss coefficient ($=1-(p_6-p_4)/(0.5\rho\cdot v_m^2)-\lambda\cdot(1-x_4)/(2G)$)
ρ density, kg/m
ω vibration angular velocity, rad/s

Subscripts:

0   amplitude at the frequency given by the vibrator
1-6   value at the measuring position 1-6
1-3   value corresponding to the vibration angular velocity $\omega_1-\omega_3$
X   component in the vertical direction
Y   component in the horizontal direction
XX, XY, YX, YY   used in the dynamic properties of the fluid film; The first
        subscript denotes the direction of the force. The second subscript
        denotes the direction of the displacement, velocity or acceleration.

STATIC TEST APPARATUS

The static test apparatus is shown in figure 1. Static pressure was measured at the pressure holes distributed at six axial positions and eight circumferential positions with pressure transducers of strain gauge type. The eccentricity of the rotor was measured with displacement sensors of eddy current type at two axial positions and two circumferential positions, 90 degree apart from each other. The radial load on the bearings in the both vertical and horizontal directions were also measured with load transducers of strain gauge type. The static pressure in the high and low pressure chambers were measured as well as the flow rate through the seals.

Tests were performed under conditions of the axial Reynolds number R_a between 1100 and 3500 and the rotational Reynolds number R_r between 0 and 4800.

TEST SEALS

The configurations of test seals are shown in figure 2. The seals have relatively small ratio of width to diameter. Figure 2 also shows the axial positions of the pressure holes 1 to 6 and the axial positions of the displacement sensors A and B.

TEST RESULTS

Figure 3 shows a typical pressure distribution measured in the test seal I. It is noted that the maximum pressue in a section perpendicular to the axis was measured near the circumferential position where the clearance was minimum throughout the whole width of the seal. It was the same regardless of the pressure difference or the rotor speed, provided that the ratio of the width to diameter of the seal was small and that the seal had grooves just like the seals I and III shown in figure 2.

It should also be noted that even at the position 5 behind the seal exit, considerable pressure difference in the circumferential direction still remained. This result implies that it is not appropriate to the analysis of the flow to assume that the pressure at the exit of the seal is uniform and equal to the pressure in the low pressure chamber.

Figure 4 shows the maximum pressure difference $\overline{\Delta p_{max}}$ in the section perpendicular to the axis. In the case of the flat seal (test seal II) $\overline{\Delta p_{max}}$ decreased linearly in the axial direction. On the other hand, in the case of the grooved seals (test seals I and III) $\overline{\Delta p_{max}}$ had the minimum value and then increased again.

Figure 5 shows the influence of the inclination between the axes of the rotor and the stator on the pressure distributions in the seal. The effect of the inclination can not be neglected, especially when the eccentricity is large.

Figures 6 and 7 show the inlet and the exit loss coefficients respectively calculated from the pressure distributions. The inlet loss coefficient ξ_{in} was much smaller than the conventional value, 0.5. The exit loss coefficient ξ_{out} was also considerably smaller than the conventional value, 1.0. Since the pressure at the exit is expressed by the equation

$$p(\theta)=p_{\ell} -(1-\xi_{out}) \cdot \rho \cdot v(\theta)^2 /2 \tag{1}$$

small ξ_{out} gives a reasonable explanation to the pressure distribution there. Acording to the experimental results by Stampa (ref. 3), inlet and exit loss coefficients are strongly affected by the axial and the rotational Reynolds numbers. Within the range of the Reynolds numbers of the experiments presented here, the rotational Reynolds number did not have much influence on the inlet loss coefficient, though it had some influence on the exit loss coefficient.

Figure 8 shows the resistance coefficient λ calculated from the pressure distribution. It was normalized by λ_0 , which was calculated by the equation proposed by Yamada for concentric flat seals (ref. 4). The experimental resistance coefficient λ for the flat seal agreed well with the coefficient calculated by Yamada's equation with consideration for the effect of eccentricity analyzed by Tao and Donovan (ref. 5).

Figure 9 shows the non-dimensional radial forces calculated from the measured pressure distributions. In the case of the test seals I and III, the radial forces did not depend much on the Reynolds numbers in these experiments. On the other hand in the case of the test seal II , the ratio of the rotational Reynolds number to the axial one had considerable influence on the forces. It is noted that the flow resistance in the circumferential direction is large in the flat seal and the rotor revolution has considerable effect on the flow in the eccentric flat seals.

DYNAMIC TEST APPARATUS

Figure 10 shows the dynamic test apparatus. The shaft was vibrated vertically by a hydraulic vibrator. Vertical and horizontal relative vibrations between the rotor and the stator of the test seal were measured at two axial positions with displacement sensors of eddy current type. Vertical and horizontal forces acting on the stator were measured at two axial positions with load sensors of strain gauge type.

TEST DATA PROCESSING

Test data were recorded on magnetic tapes and analyzed with a computer.

216

First the analogue signals were converted into digital signals with a high speed AD converter. Then the digital signals were processed by the digital filter method and the amplitudes and the phases at the frequency given by the vibrator were calculated. Vibration amplitudes at two axial positions were averaged to be used in the farther processing. Load amplitudes at two axial positions were added to each other to obtain the total values. The acceleration of the casing was also measured and was taken into account to correct the load amplitudes. The amplitudes and the phases were transformed into the real and the imaginary parts of complex expressions.

The relations between the dynamic properties of the fluid film and the hydraulic forces acting on the stator are expressed by the following equations.

$$m_{XX}\ddot{X} + m_{XY}\ddot{Y} + c_{XX}\dot{X} + c_{XY}\dot{Y} + k_{XX}X + k_{XY}Y = F_X$$
$$m_{YX}\ddot{X} + m_{YY}\ddot{Y} + c_{YX}\dot{X} + c_{YY}\dot{Y} + k_{YX}X + k_{YY}Y = F_Y$$

(2)

The vibrations of the rotor and the forces on the stator may be expressed in the complex number as follows.

$$X = X_0 e^{i\omega t} = \left\{ R_e(X_0) + iI_m(X_0) \right\} e^{i\omega t}$$
$$Y = Y_0 e^{i\omega t} = \left\{ R_e(Y_0) + iI_m(Y_0) \right\} e^{i\omega t}$$
$$F_X = F_{X0} e^{i\omega t} = \left\{ R_e(F_{X0}) + iI_m(F_{X0}) \right\} e^{i\omega t}$$
$$F_Y = F_{Y0} e^{i\omega t} = \left\{ R_e(F_{Y0}) + iI_m(F_{Y0}) \right\} e^{i\omega t}$$

(3)

Since only four equations are obtained for twelve unknowns m_{XX}, m_{XY}, m_{YX}, m_{YY}, c_{XX}, c_{XY}, c_{YX}, c_{YY}, k_{XX}, k_{XY}, k_{YX} and k_{YY} for each vibration frequency, three experiments at different vibration frequencies are necessary to obtain full equations. The final equations are expressed in the matrix form as follows.

$$
\begin{bmatrix}
R_e(X_{01}) & R_e(Y_{01}) & -\omega_1 I_m(X_{01}) & -\omega_1 I_m(Y_{01}) & -\omega_1^2 R_e(X_{01}) & -\omega_1^2 R_e(Y_{01}) \\
R_e(X_{02}) & R_e(Y_{02}) & -\omega_2 I_m(X_{02}) & -\omega_2 I_m(Y_{02}) & -\omega_2^2 R_e(X_{02}) & -\omega_2^2 R_e(Y_{02}) \\
R_e(X_{03}) & R_e(Y_{03}) & -\omega_3 I_m(X_{03}) & -\omega_3 I_m(Y_{03}) & -\omega_3^2 R_e(X_{03}) & -\omega_3^2 R_e(Y_{03}) \\
I_m(X_{01}) & I_m(Y_{01}) & \omega_1 R_e(X_{01}) & \omega_1 R_e(Y_{01}) & -\omega_1^2 I_m(X_{01}) & -\omega_1^2 I_m(Y_{01}) \\
I_m(X_{02}) & I_m(Y_{02}) & \omega_2 R_e(X_{02}) & \omega_2 R_e(Y_{02}) & -\omega_2^2 I_m(X_{02}) & -\omega_2^2 I_m(Y_{02}) \\
I_m(X_{03}) & I_m(Y_{03}) & \omega_3 R_e(X_{03}) & \omega_3 R_e(Y_{03}) & -\omega_3^2 I_m(X_{03}) & -\omega_3^2 I_m(Y_{03})
\end{bmatrix}
\begin{bmatrix}
k_{XX} \\ k_{XY} \\ c_{XX} \\ c_{XY} \\ m_{XX} \\ m_{XY}
\end{bmatrix}
=
\begin{bmatrix}
R_e(F_{X01}) \\ R_e(F_{X02}) \\ R_e(F_{X03}) \\ I_m(F_{X01}) \\ I_m(F_{X02}) \\ I_m(F_{X03})
\end{bmatrix}
$$

(4)

Only six equations for the equilibrium of the forces in the X direction are shown here. The equations in the Y direction are obtained by replacing the unknown vector and the vector in the right hand side.

TEST SEAL AND TEST RESULTS

A test seal similar to the test seal I in figure 2 was set in the apparatus and tested.

Figure 11 shows typical test data. Six vibration frequencies from 10 to

40 Hz were selected. The vibration amplitude $R_e(X_0)$ was set around 12 µm (7% of the seal clearance) and $I_m(X_0)$ and Y_0 were very small regardless of the vibration frequency.

$R_e(F_{x0})/R_e(X_0)$ decreased parabolically with the increase in the vibration frequency because in these experiments $R_e(F_{x0})/R_e(X_0) \doteq k_{xx} - \omega^2 \cdot m_{xx}$. On the other hand $I_m(F_{x0})/R_e(X_0)$ increased linearly with the vibration frequency because $I_m(F_{x0})/R_e(X_0) \doteq \omega \cdot c_{xx}$.

Figure 12 shows some results of dynamic properties of the fluid film in the seal. The pressure difference across the seal was maintained nearly constant. The time-averaged eccentricity of the rotor changed with the rotational speed. Damping coefficient c_{xx} and inertia coefficient m_{xx} did not change much with the speed or the eccentricity within the experimental range of the parameters. Stiffness coefficient k_{xx} changed considerably with the speed. From the results of the static test (fig. 9) this change in k_{xx} is considered to be the effect of the eccentricity rather than the effect of the speed.

CONCLUDING REMARKS

An experimental study was performed with static and dynamic test apparatus to investigate the hydraulic forces caused by annular pressure seals. The following conclusions are deduced.

1. The pressure at the exit of the seal had considerable variation in the circumferential direction.

2. The inclination between the axes of the rotor and the stator had much influence on the pressure distribution in the seal.

3. The inlet loss coefficient was much smaller than the conventional value, 0.5. It was affected by the axial Reynolds number.

4. The exit loss coefficient was smaller than the conventional value, 1.0. This result gives a reasonable explanation to the conclusion 1.

5. The experimental resistance coefficient for the flat seal agreed well with the coefficient calculated by Yamada's equation with consideration for the effect of eccentricity analyzed by Tao and Donovan.

6. The hydraulic forces caused by the eccentricity of the rotor had strong non-linearity to the eccentricity.

7. The results of the dynamic test showed that the damping coefficient c_{xx} and the inertia coefficient m_{xx} were not affected much by the rotational speed or the eccentricity of the rotor, though the stiffness coefficient k_{xx} seemed to be influenced by the eccentricity.

REFERENCES

1. Black, H.F. and Jenssen, D.N., "Effects of Pressure Ring Seals on Pump Rotor Vibration," ASME Paper, No.71-WA/FE-38, 1970.

2. Makay, E., "Eliminating Pump Stability Problems," Power, July 1970.

3. Stampa, B., "Experimentelle Untersuchungen an axial durchströmten Ringspalten," Ph.D. Thesis, Technischen Universität Carolo-Wilhelmina, Braunschweig, 1971.

4. Yamada, Y., "Resistance of a Flow through an Annulus with an Inner Rotating Cylinder," Bulletin of the Japan Society of Mechanical Engineers, Vol.5, No.18, May 1962.

5. Tao, L.N. and Donovan, W.F., "Through-Flow in Concentric and Eccentric Annuli of Fine Clearance with and without Relative Motion of the Boundaries," Trans. ASME, Vol.77, November 1955.
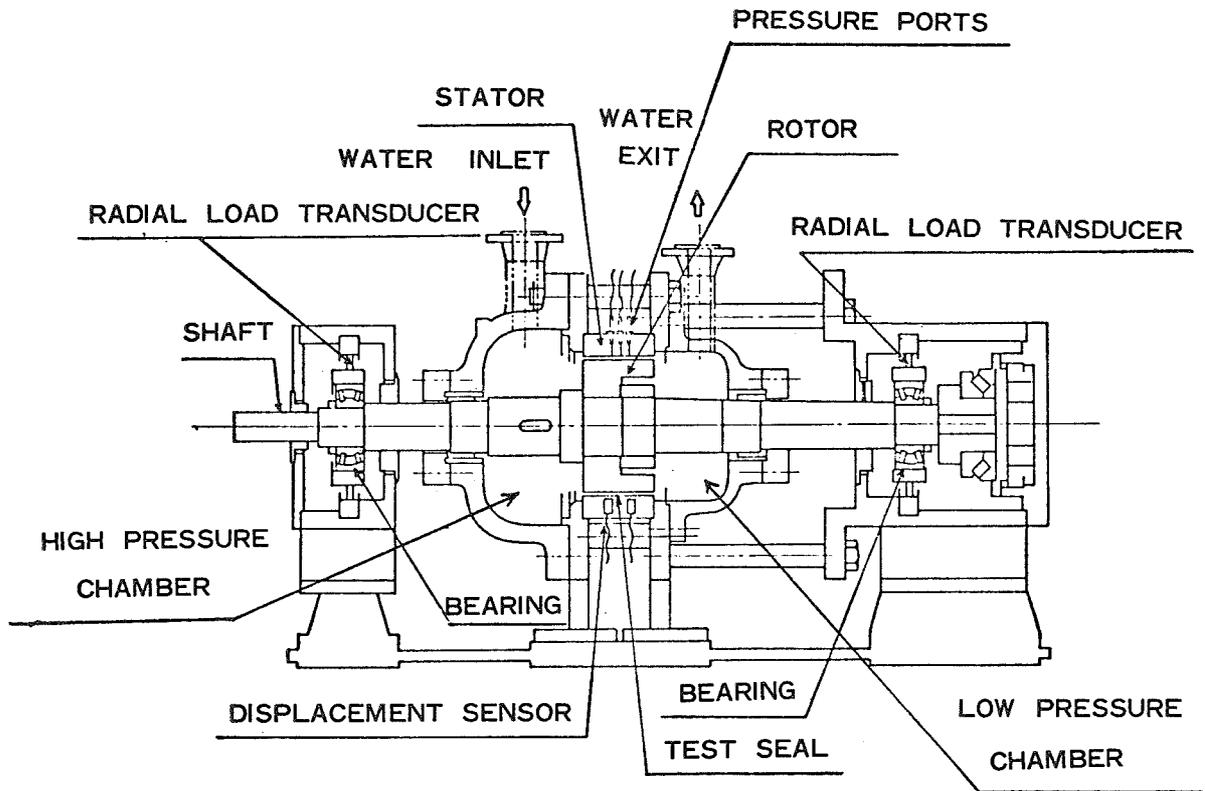
Figure 1. Static test apparatus

TEST SEAL I   TEST SEAL II   TEST SEAL III

UNIT IN mm

Figure 2. Test seals

TEST SEAL I

$$\bar{p} = \frac{p - p_6}{p_1 - p_6}$$

SYMBOLS	MEASURING POSITION
○	(1)
△	(2)
□	(3)
▽	(4)
◇	(5)
×	(6)

N = 33.3 rps

$p_1 - p_6 = 0.86$ MP$_a$

e = 0.63

θ = 0.05 rad :
at the minimum
clearance position

NON-DIMENSIONAL PRESSURE $\bar{p}$

CIRCUMFERENTIAL POSITION θ rad
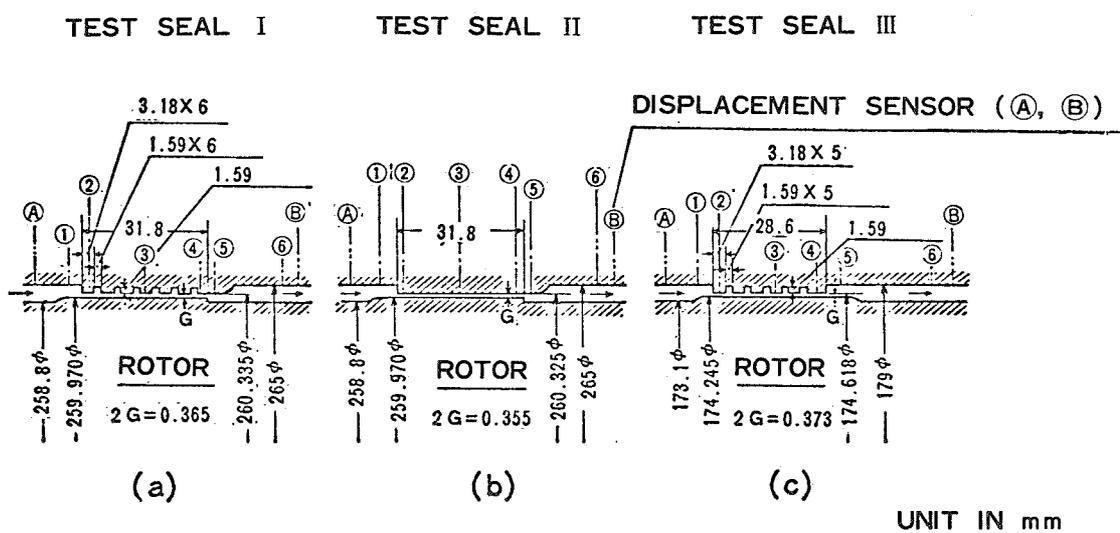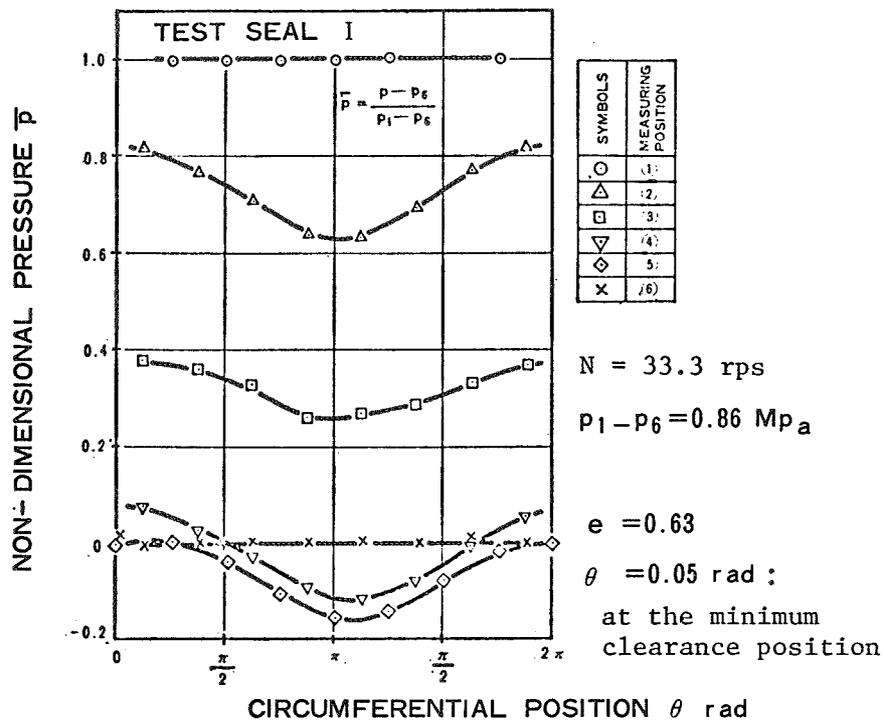
Figure 3. Pressure distribution in an eccentric seal

$$\Delta p_{max} = \frac{(p_{max} - p_{min})_{x=x}}{(p_{max} - p_{min})_{x=0}}$$

—	TEST SEAL I
--	TEST SEAL II
---	TEST SEAL III

N = 33.3 rps

$p_1 - p_6 \fallingdotseq 0.86$ MP$_a$

e $\fallingdotseq 0.3$

MAXIMUM PRESSURE DIFFERENCE Δp_{max}

AXIAL POSITION $\frac{x}{\ell}$
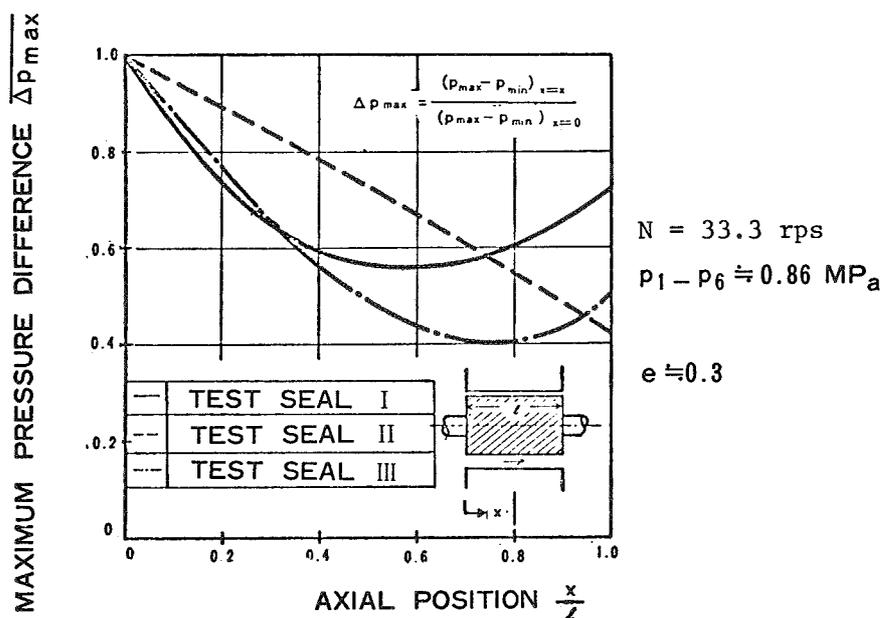
Figure 4. Change in circumferential pressure difference
in the axial direction
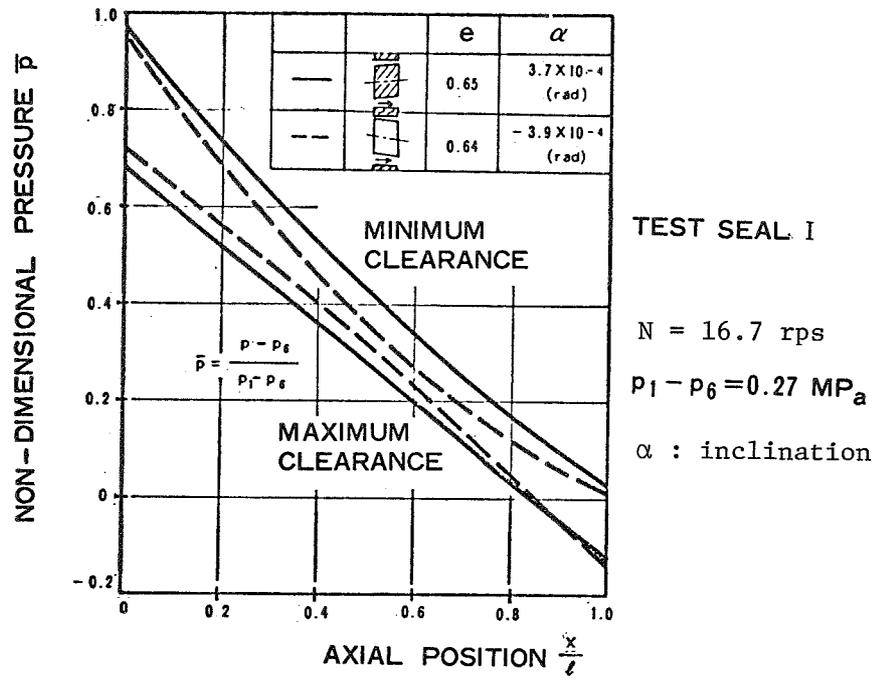
Figure 5. Pressure distribution in the axial direction
-Influence of inclination between rotor and stator axes
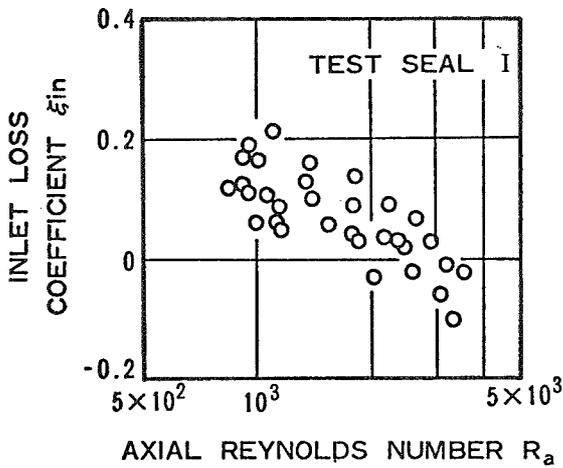
Figure 6. Inlet loss coefficient
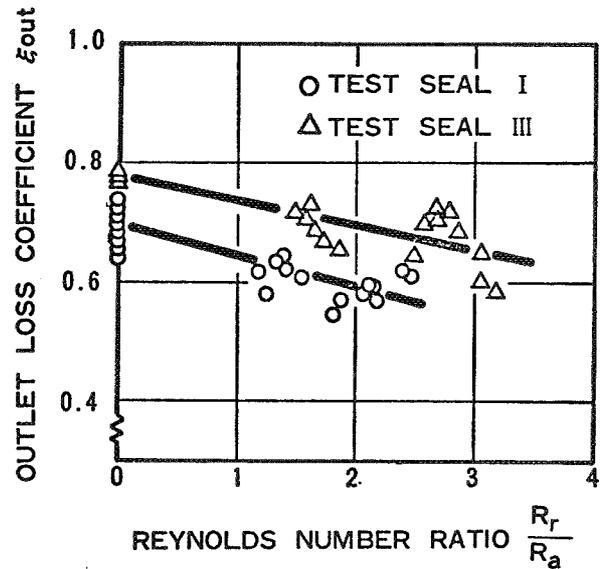
Figure 7.   Exit loss coefficient
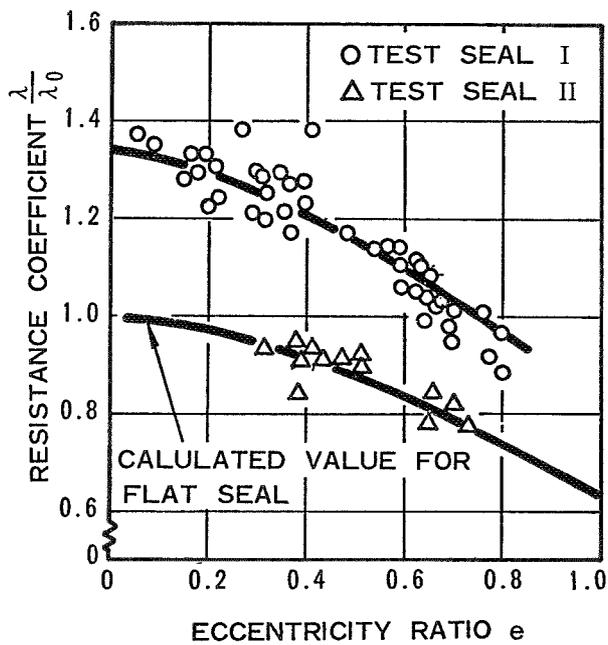
Figure 8. Resistance coefficient
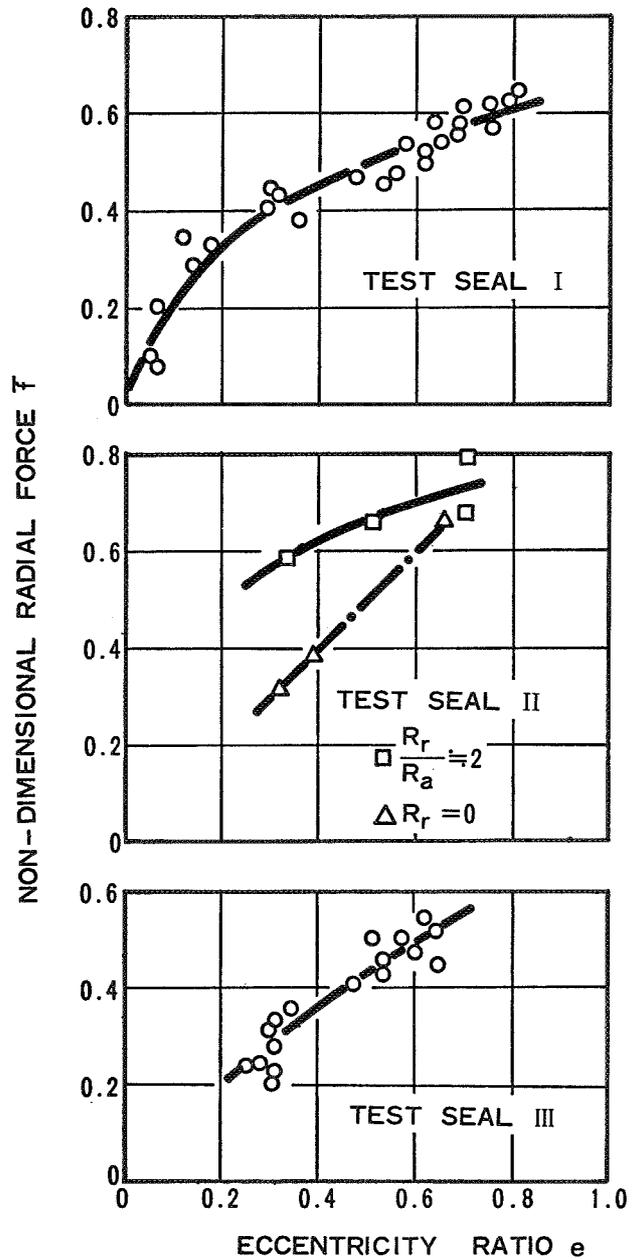
Figure 9. Radial force on the
eccentric rotor
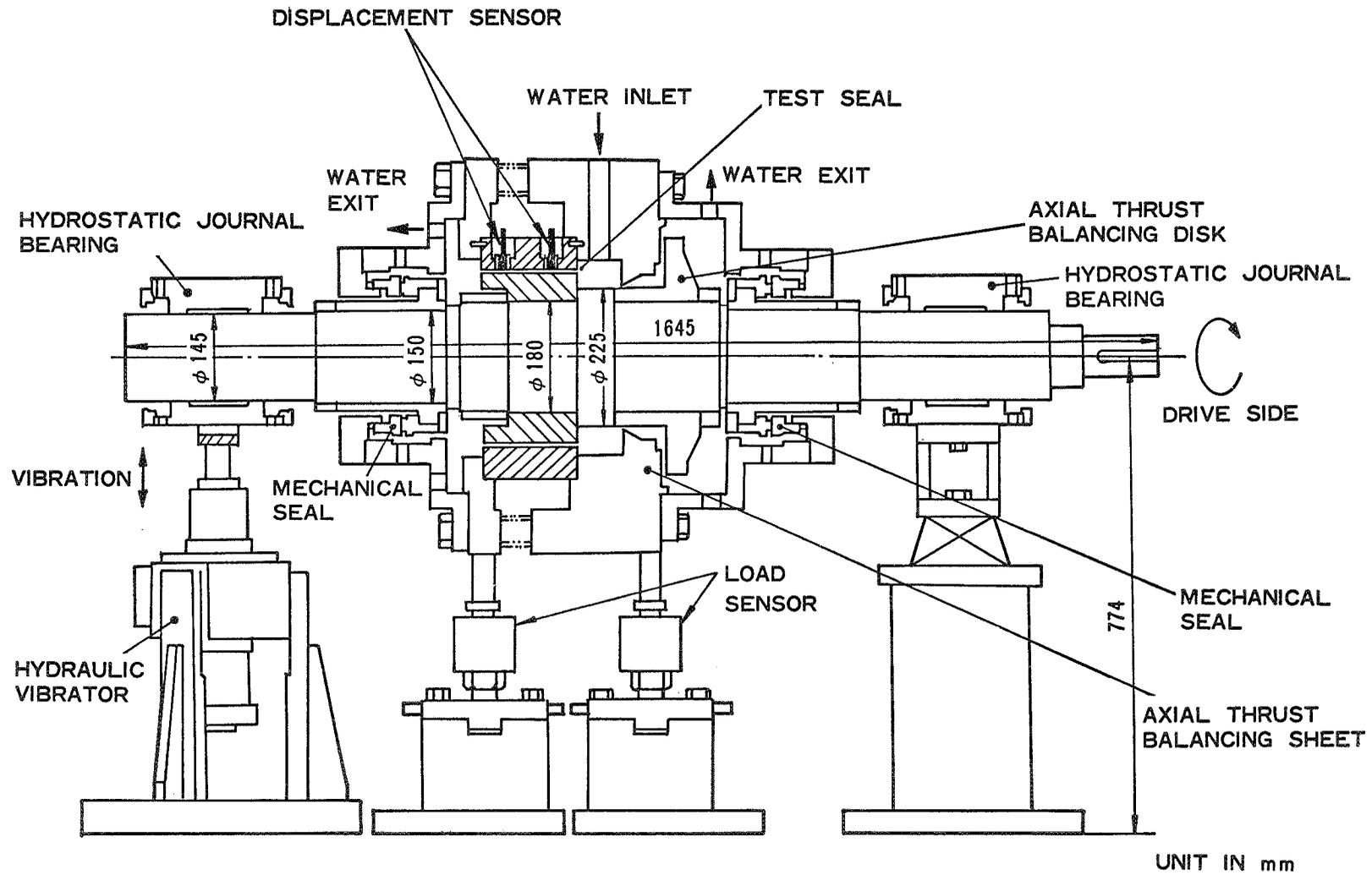
Figure 10. Experimental apparatus for annular seal dynamic properties

(a) Vibration amplitude

(b) Ratio of hydraulic force amplitude to vibration amplitude
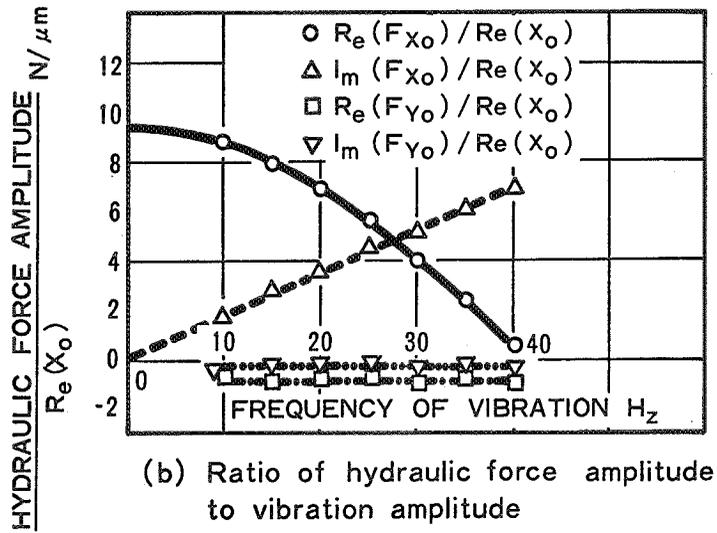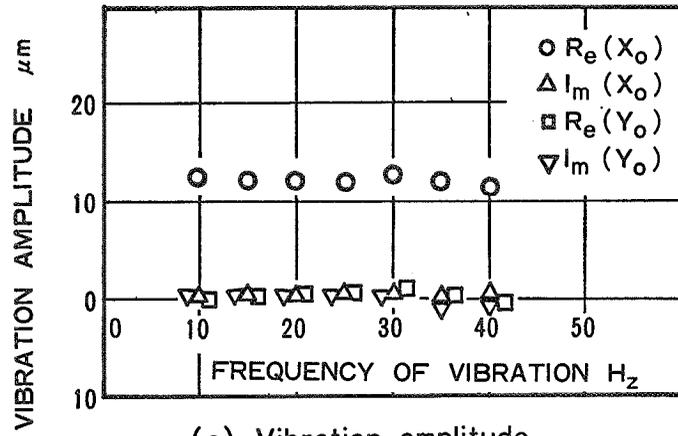
Figure 11.   An example of experimental data

Figure 12.   Test results of dynamic properties
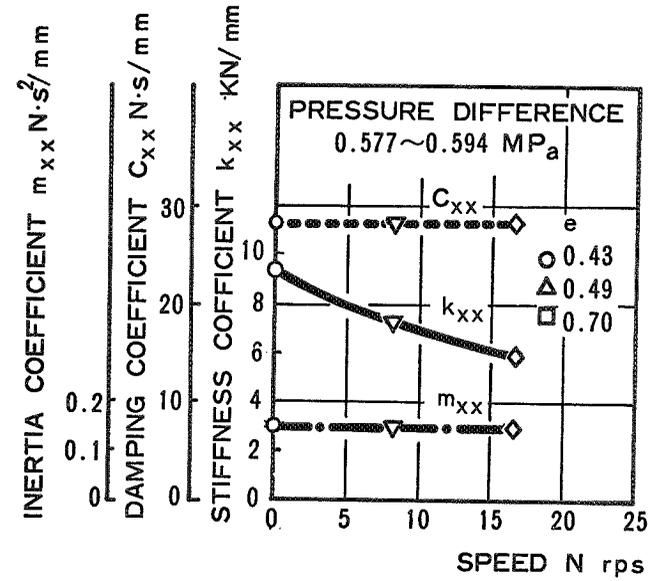
Page intentionally left blank

SESSION IV

WORK-FLUID DESTABILIZING FORCES

Carl Gerhold, Texas A&M University
Chairman

227

Page intentionally left blank

A TEST PROGRAM TO MEASURE FLUID MECHANICAL

WHIRL-EXCITATION FORCES IN CENTRIFUGAL PUMPS

C.E. Brennen, A.J. Acosta and T.K. Caughey
California Institute of Technology
Pasadena, California 91125

ABSTRACT

Much speculation has surrounded the possible unsteady hydrodynamic forces which could be responsible for the excitation of whirl instabilities in turbo-machines. However there exist very few measurements of these forces which would permit one to evaluate the merits of the existing fluid mechanical analyses. In keeping with the informal nature of this workshop we will present details of a proposed test program for the measurement of the unsteady forces on centrifugal impellers caused by either (i) azimuthal asymmetry in the volute geometry or (ii) an externally imposed whirl motion of the impeller. In the second case the forces resulting from the imposed whirl motions with frequencies ranging from zero to synchronous will be measured by means of a force balance upon which the impeller is mounted. This work is presently being carried out under contract with the NASA George Marshall Space Flight Center, Huntsville, Alabama (Contract NAS 8-33108).

INTRODUCTION

In recent years it has been increasingly recognized that hydrodynamic cross-coupling forces can cause serious rotor dynamic problems in high speed turbomachines. Such problems have been experienced not only in steam turbines (Refs.1,2), but also in large compressors (Refs. 3,4) and in high speed pumps (Ref. 5). Though other instability mechanisms such as internal damping or non-isotropic shaft stiffness rotor inertia can be fairly readily characterized the same cannot be said of the hydrodynamic cross-coupling forces. Various hydrodynamic flows have been identified as possible contributors to these de-stabilizing forces. Bearings and particularly seals can clearly play such a role as the papers in this volume attest. But much less is known about the potential for destabilizing forces arising from the flows associated with the impeller and diffuser of a compressor or pump; this brief paper will be con-fined to this issue.

The flow associated with the impeller/diffuser is significantly differ-ent from that in a seal or bearing in that the geometry of the volute can cause this flow to be significantly non-axisymmetric. The work of Domm and Hergt (Ref. 6) has shown that this could give rise to a lateral force on the impeller even in the absence of an orbiting motion of the shaft. They derived magnitudes for this stationary lateral force based on a source vortex model for the impeller. In an actual impeller this lateral force may also contain

an unsteady component at the blade passage frequency though the magnitude of this unsteady force and the role it might play in the rotor dynamics has not yet been determined. More realistic impeller models would be required for this purpose.

Recently Colding-Jorgensen (Ref. 7, see also this volume) has extended the work of Domm and Hergt. Imposing an orbiting motion on the source/vortex model of the impeller, he analyzed the resulting radial and tangential forces on the "impeller" and found that positive or whirl excitation tangential forces did indeed result from such an analysis and that the magnitudes of these forces were sufficient to have played a significant role in the Space Shuttle high pressure hydrogen pump instability (Ref. 5). However the main question here is the validity of the simple source/vortex model used for the impeller; further analyses with more realistic impeller models will be required in order to determine the limits of validity of such analyses. One useful intermediate model which is still fairly simple is the actuator disk which has been suggested by the work of Chamieh and Acosta (Ref. 8,9).

Other analyses have sought destabilizing tangential forces in the absence of volute asymmetries. Here we have two possible mechanisms which have been suggested. In an addenda to his paper on whirl-excitation forces in seals, Alford (1965) suggested that the same mechanism would occur in the tip clearance flows of steam turbines and others have further extrapolated this to the tip clearance flows in any turbomachine. The supposition is that a localized reduction in the tip clearance would cause a localized decrease in the torque shear stress with the reverse occurring on the other end of the diameter. This would lead to a positive or whirl-exciting tangential force.

Secondly, Thompson (Ref. 3) has posed the question of whether such a force would arise due to the perturbations imposed on the main flow through the impeller. Assuming quasi-static performance for each blade passage he used a detailed flow analysis program to assess the distribution of forces on the blades of an impeller performing whirling motions. Positive excitation did indeed occur with some impeller designs. It is not however clear whether the quasi-static assumption is valid in these circumstances.

Ultimately any review of the existing state of knowledge such as we have given above reveals a singular lack of hard experimental data with which to assess the merits of the various analyses. The primary purpose of this paper is to stress the fact that much remains to be done before the status of whirl-excitation forces on impellers can be put on a firm foundation. We are presently embarking on an experimental program whose intent is to measure these forces and the remainder of this paper is devoted to a brief description of this facility.

ROTOR FORCE TEST FACILITY

The objective of the facility is to impose known orbiting motions of frequency Ω on the basic rotary motion of a number of typical centrifugal pump impellers (rotating frequency, ω) and to measure the radial and tangential forces resulting from this motion. The core of the experiment is shown in

230
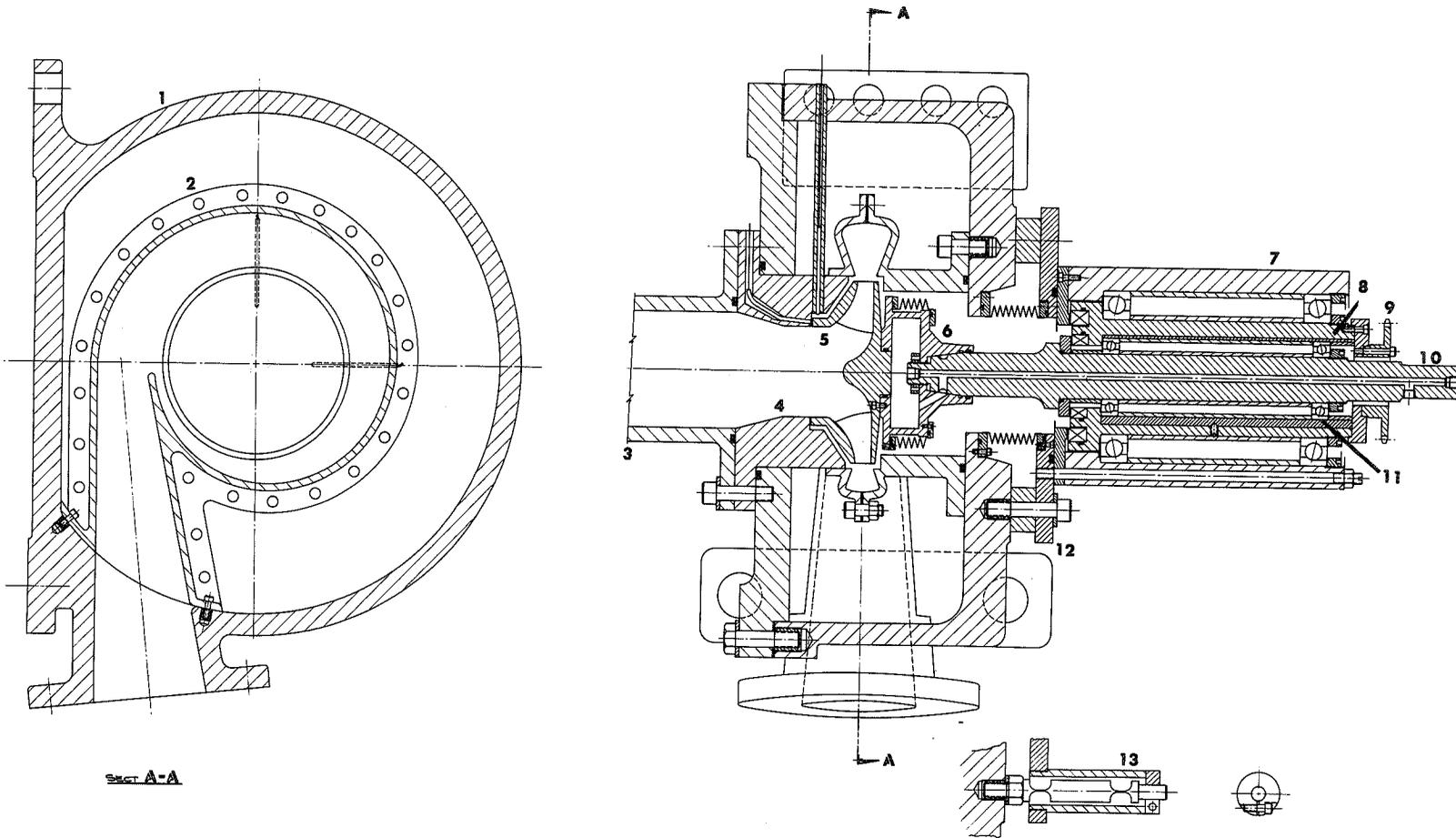
Figure 1. The impeller, volute, internal balance and eccentric drive of the Rotor
Force Test Facility

Fig.1.The flow enters the centrifugal impeller(6)from the inlet connection(3) and inlet bell(4). Volutes(2)of various geometries will be used in measurements of lateral force due to volute asymmetry; they are contained in the pump housing (1) so that they may be of lightweight construction. The impeller (5) is mounted directly on an internal force balance (6). The main shaft (10) rotates in a double bearing system (7,8,11) designed so that rotation of the sprocket (9) causes the orbiting motion. In addition to the rotating internal balance a back-up force measuring system(12,13)external to the eccentric drive system will also be used. Figure 2, an overall schematic of the mechanical system, shows the main drive system comprised of a 20HP variable speed motor, a gear box and a flexible shaft (necessary to accommodate the orbiting motion). This will be capable of speeds up to 35000 rpm ($\omega \rightarrow$ 60Hz.) Figure 2 also shows the eccentric drive motor (2HP) which can generate orbit frequencies, Ω, from 0 to 60 Hz.

Past experience with unsteady flow measurements has emphasized the need for rigorous dynamic control of the experiments. In the present facility a proximity probe senses the rotating frequency, ω; this signal is then used to produce digital signals with frequencies $M\omega/N$, ω/N, $(N-M)\omega/N$ and $(N+M)\omega/N$ where M and N are selected integers between 0 and 100 ($M \leq N$). The signal at $M\omega/N$ is then used to drive the eccentric motor such that $\Omega = M\omega/N$; a feedback control system fitted to this motor ensures accurate phase-locking. In this way measurements can be made over a wide range of Ω/ω from zero to unity.

Past experience has also indicated that the unsteady flow measurements can be quite noisy and that accurate results require cross-correlation of measurement and driving signal over many cycles. In the present case the measurements may include (i) six-components of force measurement from the internal balance or several components of force from the external balance (ii) axial and radial displacement of the impeller from four fibre-optic displacement probes (iii) pressure transducer measurements from locations both upstream and downstream of the impeller as well as within the impeller-volute flow (iv) unsteady flow rate measurement using existing laser doppler velocimeters or electro-magnetic flow meters. A sixteen channel digital signal processor is used for cross-correlation of these measurements with any of the basic frequencies (ω,$M\omega/N$,ω/N,$(N-M)\omega/N$ and $(N+M)\omega/N$) in order to extract the components of force at any of these fundamental frequencies or higher harmonics thereof; this cross-correlation can cover up to 10,000 cycles of the fundamental frequency.

The most critical component in the system is probably the internal balance and its design is as yet unproven. One must ensure high natural frequencies (>500Hz.) and yet maintain sufficient sensitivity. The present candidate design consists of four posts parallel with the axis which are monolithic with two solid end plates, one attached to the shaft and the other attached to the impeller. These posts are strain-gaged in such a way as to extract all six force components with sensitivities of the order of mV/lb.

The hydraulic system into which this mechanical system is being installed was previously utilized for measurements of the unsteady hydraulic performance of cavitating (and non-cavitating) axial flow pumps (see, for example Refs.
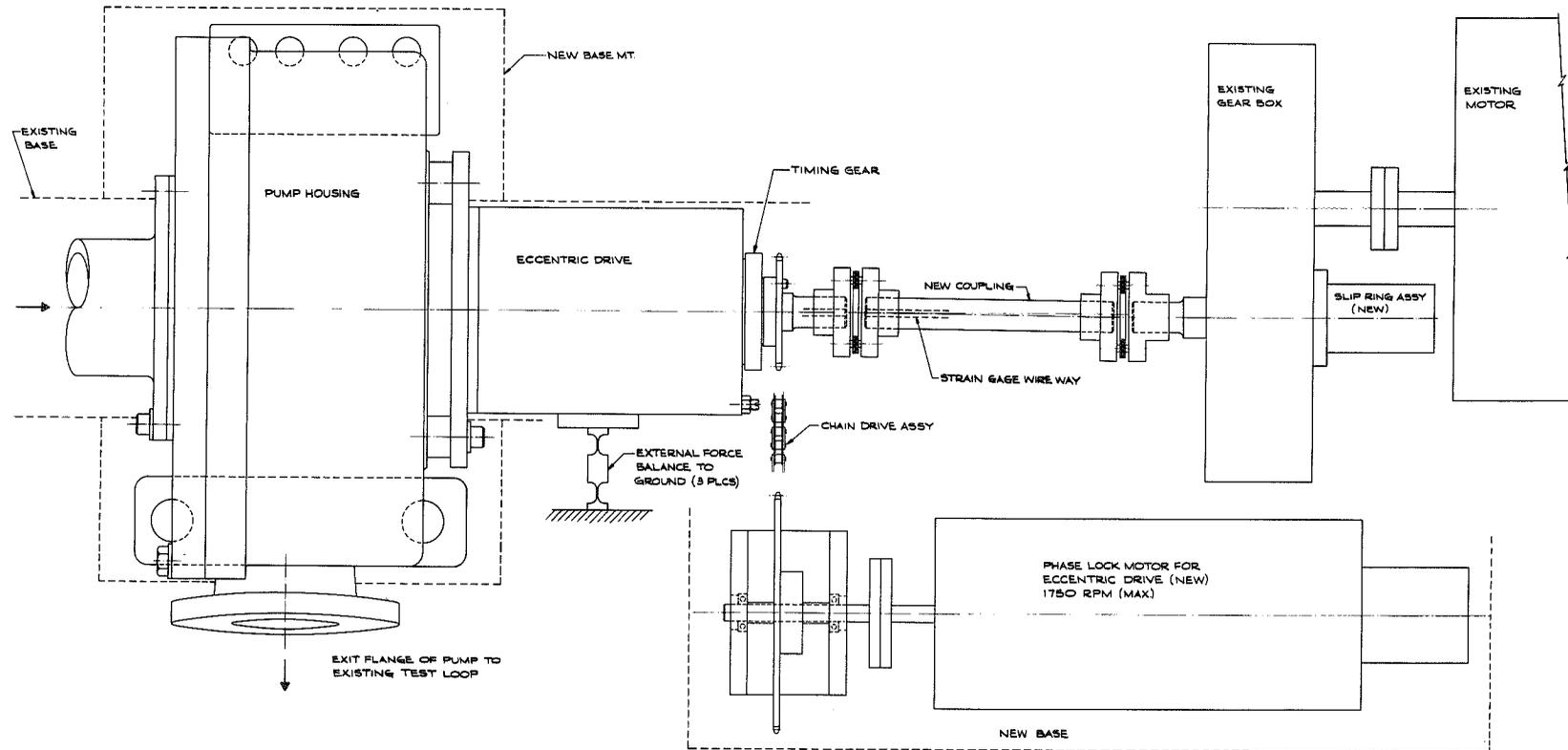
Figure 2.   Schematic planview of the mechanical layout of the Rotor Force Test Facility.

10,11). Specifically this involved finding the relations between the unsteady
pressures and flow rates at inlet and at discharge as a function of the fre-
quency of the unsteady components of the flow and of the mean flow conditions.
A schematic of this system, known as the Dynamic Pump Test Facility (DPTF), is
included as Fig. 3. The mechanical system of the Rotor Force Test Facility
(RFTF) described above is being installed in the lower left-hand corner in
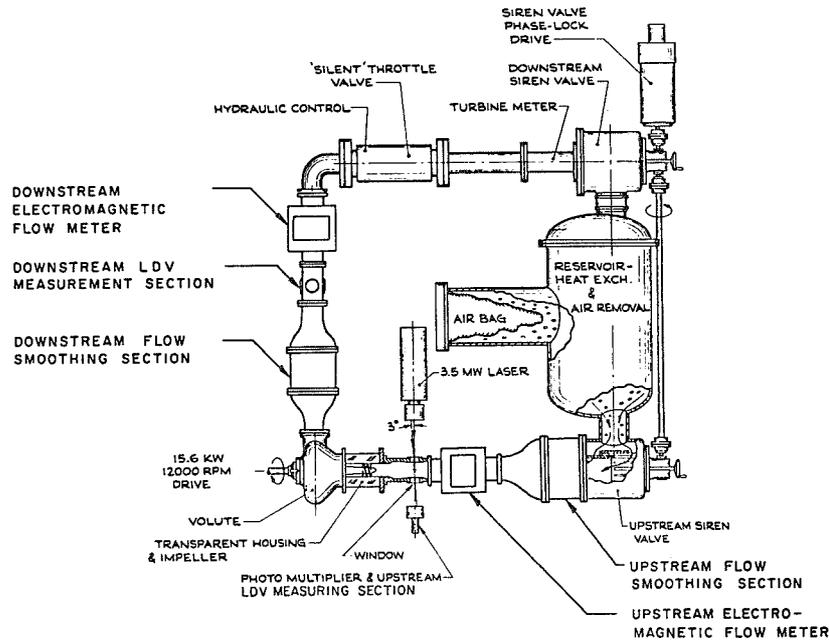
Figure 3. Schematic planview of the Dynamic Pump Test Facility

place of the impeller/volute system depicted in the Fig. 3. The DPTF included
two flow fluctuators (siren valves) with phase-lock drive systems similar to
that described above for the new eccentric drive system as well as instrumenta-
tion for measurement of the small oscillatory perturbations in pressure and
flow rate. In the context of the present experiment these will again be uti-
lized at a later stage to investigate whether flow fluctuations are associated
with impeller whirl or whether they can induce impeller whirl. From a global
dynamic point of view it is possible that the entire system of fluctuations
(mechanical and hydraulic) may have to be represented by a global transfer
function.

CONCLUDING REMARKS

Though bereft of results this paper is intended to highlight the lack of
experimental evidence for whirl-exciting fluid forces arising from the flow
through turbomachines. We hope that the experimental facility described
above will be valuable in providing such evidence.

REFERENCES

1. Alford J.S., 1965.. Protecting turbomachinery from self-excited rotor whirl. J. Eng. Power, Vol. 87A, pp. 333-344.

2. Pollman, E., Schwerdtfeger, H. and Termuehlen, H., 1978. Flow excited vibrations in high pressure turbines (steam whirl). J. Eng. Power, Vol. 100, pp. 219-228.

3. Thompson, W.E., 1978. Fluid dynamic excitation of centrifugal compressor rotor vibrations. J. Fluids Engineering, Vol. 100, No. 1, pp. 73-79.

4. Doyle, H.E., 1980. Problems with rotodynamic instabilities in high performance turbomachinery. Proc. Workshop on Rotordynamic Instability Problems in High Performance Turbomachinery, May 1980, Texas A & M Univ.

5. Ek, M.C., 1978. Solutions of the subsynchronous whirl problem in the high pressure hydrogen turbomachinery of the Space Shuttle Main Engine. AIAA/SAE 14th Joint Propulsion Conference, Las Vegas, July 1978.

6. Domm, H., and Hergt, P., 1970. Radial forces on impeller of volute casing pumps. Flow Research on Blading (L.S. Dzung, ed.), Elsevier, pp. 305-321.

7. Colding-Jorgensen, J., 1979. The effect of fluid forces on rotor stability of centrifugal compressors and pumps. Ph.D. Thesis, Technical Univ. of Denmark.

8. Chamieh, D. and Acosta, A.J., 1979. Dynamic forces on a whirling centrifugal rotor. Proc. 6th Conf. on Fluid Machinery, Akademiai Kiado, Budapest, Hungary.

9. Chamieh, D., Acosta, A.J., Brennen, C.E. and Caughey, T.K., 1980. A brief note on the interaction of an actuator cascade with a singularity. Unpublished manuscript.

10. Ng, S.L. and Brennen, C., 1978. Experiments on the dynamic behavior of cavitating pumps. J. Fluids Eng., Vol. 100, pp. 166-176.

11. Brennen, C.E., Meissner, C., Lo, E.Y. and Hoffman, G.W., 1980. Scale effects in the dynamic transfer functions for cavitating inducers. To be presented at ASME Winter Annual Meeting, Chicago, 1980.

Page intentionally left blank

A BRIEF NOTE ON THE INTERACTION OF AN
ACTUATOR CASCADE WITH A SINGULARITY[*]

Dimitri Chamieh, A.J. Acosta, C.E. Brennen, T.K. Caughey
California Institute of Technology
Pasadena, California 91125

Introduction

We have recently become concerned with making estimates of steady

forces that may be exerted between moving blade rows and stationary blade

rows or volutes. Our present interest is with time averaged forces for

estimation of shaft loads and flow asymmetry forces rather than with

transient processes. For this purpose we have adopted the well-known

"actuator" model for the blade row in which the flow leaving the row or

cascade is assumed to have a constant leaving angle. The disturbances

external to this row such as a volute may be represented by distributions

of vortex elements as was done for example by Domm and Hergt[1].

In the present case this singularity causes perturbations of the basic

one-dimensional flow through the actuator cascade which lead to overall

rotor forces and flow perturbations which are the subject of interest here.

The problem then is one of constructing a velocity field that includes the

disturbance (but adds no more) and satisfies the flow tangency condition

leaving the blade row. With reference to Fig. 1 this requires

$$\frac{v}{u} = \cos \beta \qquad\qquad (1)$$

at the row exit, $y = 0$, where v includes the disturbance velocity as

---

[*]Not presented at workshop.

well as added perturbations needed to satisfy Eq. (1). This is a partic-
ularly simple problem when the flow field leaving the actuator row is
irrotational. In the next paragraph we consider two such cases where this
assumption is valid.

The Actuator Cascade

Here we consider steady flow of constant total pressure through an
actuator cascade. The flow leaving this cascade has a given direction β_v
(see Fig. 1) as this is equivalent to the Kutta condition. We now consider
two situations: in the first, we may imagine that there are disturbances
downstream of the cascade. These disturbances may be due to the effect of
downstream diffuser vanes or a volute structure for example. In the second,
as a particularly simple example, we consider the effect of periodic changes
in the blade leaving angle β_v on the leaving flow without any downstream
disturbances.

(i) Downstream disturbances.

In the notation of Fig. 1, the trailing edge is situated on the real
z axis. The flow is assumed to be irrotational so that complex variable
methods may be used. Let us consider the problem of the interaction of the
cascade with a single disturbance located in the upper half plane at $z = z_0$.
This is denoted by

$$W_d(z-z_0) = u_d - iv_d \qquad (2a)$$

where (u,v) are the velocity components in the (x,y) directions respective-
ly. The effect of the disturbance gives rise to additional correction terms
$w_i(z)$ which cannot have any singularities in the upper half plane. The

238
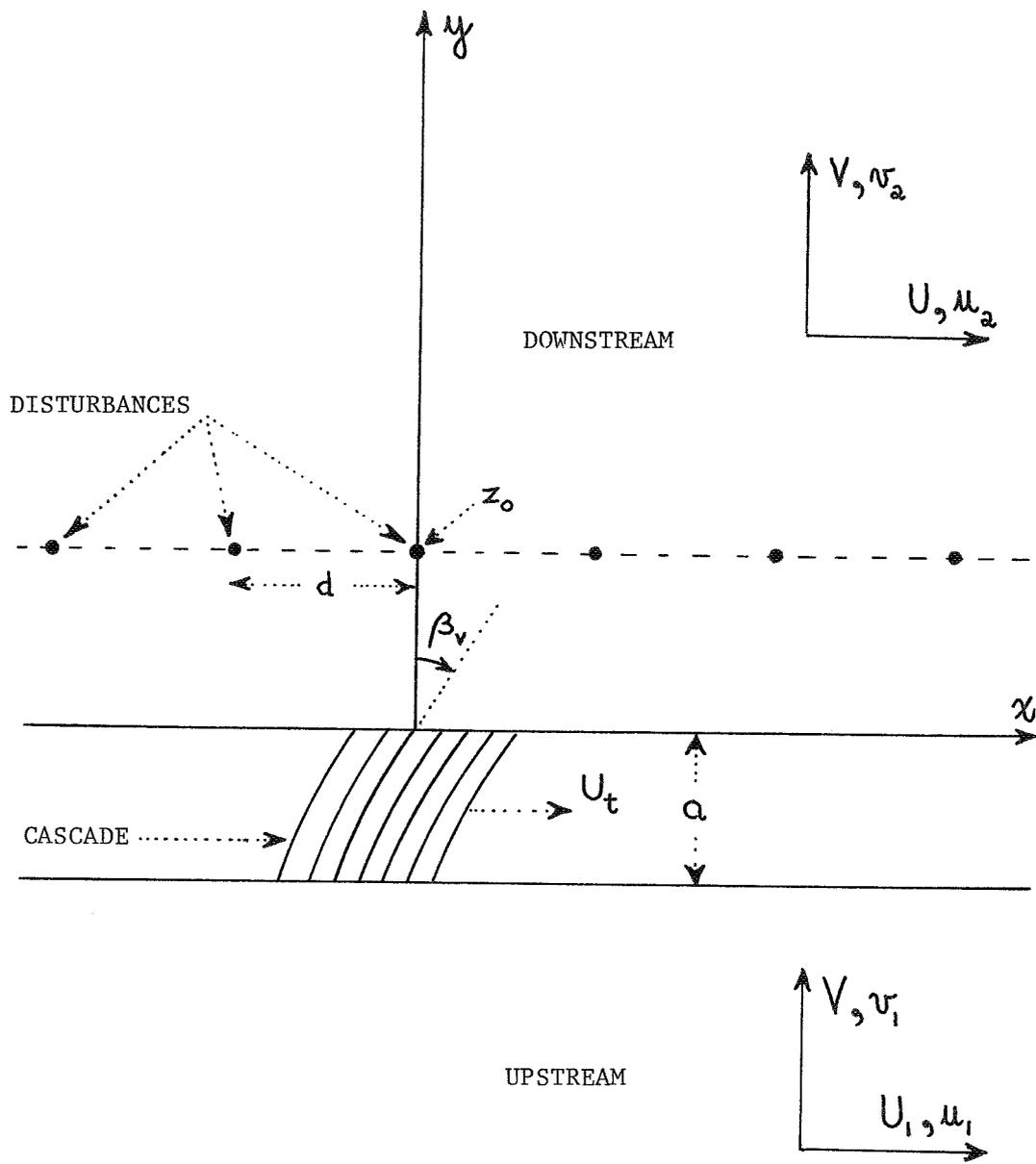
FIGURE 1.   SKETCH OF CASCADE ACTUATOR ROW
(z = x + iy)

sum

$$w_T \equiv w_d + w_i \qquad (2b)$$

must satisfy the flow angle leaving condition

$$\frac{v_d + v_i + V}{u_d + u_i + U} = \cot \beta_v \qquad (3)$$

where U, V are mean flow velocity components in the absence of any disturbance. Then on $y = 0$

$$v_d + v_i - (u_d + u_i) \cot \beta_v = 0 \qquad (4a)$$

since $V = U \cot \beta_v$. Here (v_d, u_d) are known. The induced disturbance w_i must result in the total velocity components satisfying (4a), i.e.,

$$a u_T + b v_T = 0 \qquad (4b)$$

(where here $a = 1$, $b = -\tan \beta_v$). Thus w_T has to satisfy a _mixed_ boundary condition on $y = 0$. This turns out to be neatly handled by the methods described by Cheng and Rott [2]. The induced disturbance w_i is

$$w_i = -\frac{a-ib}{a+ib} \, \overline{w}_d (z - \overline{z}_0) \qquad (5)$$

which is seen merely to be an "image" of w_d in the cascade exit plane. This is easy to show; let

$$H(z) = (a-ib) w_T \quad .$$

Then $\text{Re}\{H(z)\} = au + bv$ is required to be zero on the real axis. Now set

$$H(z) = (a+ib) w_d (z - z_0) - (a-ib) \overline{w}_d (z - \overline{z}_0) \quad , \qquad (6)$$

240

so that on $y = 0, H(x,0)$ is the difference of two complex conjugate functions and is therefore purely imaginary. As an example, consider the row of vortices of strength Γ and period d seen in Fig. 1. Then

$$w_d = -\frac{i\Gamma}{2\pi} \sum_{n=-\infty}^{\infty} \frac{1}{z-z_0-nd} \tag{7}$$

Then

$$w_i = -\frac{i\Gamma}{2\pi} e^{2i\beta_v} \sum_{n=-\infty}^{\infty} \frac{1}{z-\bar{z}_0-nd} \quad ,$$

and finally w_T has the well-known sum

$$w_T = \frac{\Gamma}{2d} \left\{ \cot \frac{\pi(z-z_0)}{d} + e^{2i\beta_v} \cot \frac{\pi(z-\bar{z}_0)}{d} \right\} . \tag{8}$$

We should point out here that this image system is almost the same as that used by Domm and Hergt to set up the interference problem for a volute in the presence of a point source-vortex. The principal difference is that here the leaving angle of the cascade is fully modelled instead of being approximated in the mean.

(ii) Leaving angle variation.

In the above it was assumed that the leaving angle β_v was constant. This is not essential as the following example shows. Suppose $\beta_v = \beta_v(x)$ and that $w_d = 0$. Then Eq. (3) becomes

$$\frac{v_i + V}{u_i + U} = \cot \beta_v$$

or

$$u_i - \tan \beta_v v_i = -(U - \tan \beta_v V) \quad .$$

Let's assume that

$$\beta_v(x) = \overline{\beta}_v + \Delta\beta(x)$$

where $\Delta\beta$ is a small change. Then w_i is proportional to $\Delta\beta$ and we have approximately

$$u_i - \tan\overline{\beta}_v v_i = \frac{V}{\cos^2\overline{\beta}_v}\,\Delta\beta_v(x) \quad , \tag{9a}$$

which is of the form

$$au_i + bv_i = c(x) \quad . \tag{9b}$$

Disturbance flows of this type may again be tackled by the methods of [2]; more complete formulations are given in the book by Carrier, Krook and Pearson [3]. Again we note that Eq. (9b) is equivalent to requiring that

$$\text{Re}\{(a+ib)w_i\} = c(x) \tag{9c}$$

on $y = 0$. A solution of this equation is

$$w_i = \frac{1}{a+ib}\,c(z) \tag{10}$$

provided $c(z)$ is chosen to have no singularities in the upper half plane. As a practical example we may imagine $c(x)$ is of the form

$$c(x) = \text{const. } \cos x$$

and then it is easily seen that

$$w_i = \frac{\text{const}}{a+ib}\,e^{iz}$$

is the required disturbance flow since w_i vanishes for $y \to \infty$.

Moving Cascades

The above examples were for irrotational, constant-energy flows. When the cascade moves in a tangential direction (parallel to the x axis) work is done on the fluid in accordance with the Euler formula. In what follows the absolute flow is assumed to be steady and the cascade moves at speed U_t parallel to the x axis. Assume also that the Bernoulli constant upstream of the cascade, B_1, is constant everywhere. Then it follows that the leaving Bernoulli constant B_2 is given by

$$B_2 = B_1 + U_t(u_2 - u_1) - \int_1^2 \frac{\partial w}{\partial t} \, ds$$

where w is the relative velocity parallel to the blades and ds is an increment of blade arc. The relative flow is unsteady since the absolute flow is steady. Thus

$$\frac{\partial}{\partial t} = U_t \frac{\partial}{\partial x} \quad .$$

With this and continuity we find

$$B_2 = B_1 + U_t \left\{ u_2 - u_1 - \frac{\partial v_2}{\partial x} \int_1^2 \frac{dy}{\cos^2 \beta_v} \right\} \qquad (11)$$

and here u_2, u_1 are tangential velocities immediately downstream of and upstream of corresponding points of the moving blade row. In general, B_2 is not constant at every point along the exit from the row and we therefore expect the leaving flow to be rotational through the relation

$$\nabla B = \underline{V} \times \underline{\omega}$$

243

from which we find the only component of $\underline{\omega}$ to be $\underline{k}\omega_z$ or simply

$$\omega(x,0) = \frac{U_t}{v(x,0)}\left\{\frac{\partial}{\partial x}(u_2(x,0)-u_1(x_c,-a)) + \frac{\partial^2 v(x,0)}{\partial x^2}L\right\} \qquad (11a)$$

From Fig. 1 the blade exit is at $y = 0$, the inlet is at $y = -a$ and L refers to the "length"

$$L \equiv \int_{-a}^{0}\frac{dy}{\cos^2\beta_v(y)} \quad .$$

We see that the downstream flow is then rotational. Progress is readily made now only if we assume the disturbances to the flow field are small compared to the mean velocity components (U,V). In that case it can be assumed that ω and B are constant* on mean flow streamlines given by

$$\frac{dy}{dx} = \frac{V}{U} = \tan\alpha \quad ,$$

thus

$$\omega(x,y) = \omega(x-y\cot\alpha)$$

and

$$B(x,y) = B(x-y\cot\alpha) \quad .$$

We now separate the unknown downstream and upstream flow field into components as follows

(i) downstream $(u,v)_2 = (U,V) + (u_d,v_d) + (u_i,v_i) + (u_r,v_r)$

(ii) upstream $(u,v)_1 = (U_1,V) + (u_1,v_1)$

where (U,V), (U_1V) are mean components, (u_d,v_d) is the downstream

_____
*i.e., we linearize the vorticity equations.

244

potential disturbance, (u_i, v_i) is a downstream irrotational flow

and (u_r, v_r) is a rotational (shear) flow which accounts for the vorticity

$$\omega = \frac{\partial v_r}{\partial x} - \frac{\partial u_r}{\partial y} \quad .$$

It follows that u_r, v_r are constant along lines of $x-y \cot \alpha = $ constant

and that $v_r = \tan \alpha \, u_r$. The upstream disturbance (u_1, v_1) is irrotational.

In this decomposition (u_d, v_d) are given disturbances. The problem

then is to find the three sets of components (u_r, v_r), (u_i, v_i) and (u_1, v_1).

One relation between these is given by Eq. (11a). Two more relations are

needed. One of these is given by continuity across the cascade, i.e.,

$$v_2(x,0) = v_1(x_c, -a) \tag{12}$$

(here $(x_c, -a)$ and $(x,0)$ are points corresponding to the same vane trace).

The other is by the flow tangency condition at $y = 0$, i.e.,

$$u_i + u_d + u_r = (v_i + v_d + v_r) \tan \beta_v \quad . \tag{13}$$

This is apparently a complicated system of relations to solve. To

sum up we have the initially unknown six velocity components (u_r, v_r), (u_i, v_i)

and (u_1, v_1). U_r and v_r are related to each other though the require-

ment that far downstream the mean flow angle is undisturbed. Both sets

(u_i, v_i) downstream and (u_1, v_1) upstream are conjugate (potential) func-

tions so that u and v are related. There are then only three unknown

functions left and we have the Eqns. (11a) (with the previous definition

of ω), (12) and (13) to relate them. Thus a closed system is obtained

from which solutions analogous to Eq. (8) can be found. Then in principle,

complete volute actuator impeller interactions can be worked out.

We should mention that the type of problem addressed in this section is not new except in its application to singular disturbances. Earlier Ehrich [4] studied the effect of inlet wakes passing through rotor and stator blade rows with a set of equations essentially identical to the present ones. Subsequently Katz [5] carried out a similar computation using the acceleration potential instead of the velocity components but with the inclusion of losses through the blade row. Again the matching problem across the blade row is essentially the same as the present one. The interaction flow fields in these works were determined by Fourier series expansion which is a suitable procedure when only a few terms are needed to represent the disturbance.

Discussion

We have used the singularities of Eq. (8) to study the interaction between a rotating actuator impeller and a volute (assuming, irrotational volute flow). The unknown vorticity distribution on the volute is expressed in a Glauert series the coefficients of which are then determined in the usual way to make the volute surface a streamline. With these, forces can be found. This task is nearly complete; we intend subsequently to include the rotational effects described in the previous section.

Acknowledgment

246

References

1. Domm, H. and Hergt, P. 1970. "Radial Forces on Impeller of Volute Casing Pumps". Flow Research on Blading, Dzung, L.S. (Ed.), Elsevier, pp. 305-321.

2. Chung, H.K., Rott, N. "Generalizations of the Inversion Formula of Thin Airfoil Theory". J. of Rational Mech. and Analysis, Vol. 3, No. 3, May 1954.

3. Carrier, G., Krook, M., Pearson, C., Functions of a Complex Variable, McGraw-Hill, 1966, Ch. 7.

4. Ehrich, F., "Circumferential Inlet Distortions in Axial Flow Turbo-machinery", J. Aero. Sci., 24, No. 6, p. 413, 1957.

5. Katz, R., "Performance of Axial Compressors with Asymmetric Inlet Flows". Calif. Inst. of Tech., Div. of Eng. & Appl. Sci., Jet Propulsion Center, 1953.

Page intentionally left blank

EFFECT OF FLUID FORCES ON ROTOR STABILITY OF
CENTRIFUGAL COMPRESSORS AND PUMPS

Jørgen Colding-Jørgensen
Technical University of Denmark

SUMMARY

In this paper a simple two-dimensional model for calculating the rotor-dynamic effects of the impeller force in centrifugal compressors and pumps is presented. It is based on potential flow theory with singularities. Equivalent stiffness and damping coefficients are calculated for a machine with a vaneless volute formed as a logarithmic spiral. It appears that for certain operating conditions, the impeller force has a destablizing effect on the rotor. The order of magnitude of this effect can be determined from the stiffness and damping coefficients calculated. The paper is a brief review of the author's thesis (ref. 14), where more details of the calculation can be found.

SYMBOLS

A_{ij}	induced velocity in normal direction in point i from singularity in point j
B	Busemann factor
B_{ij}	damping coefficient
b_{ij}	dimensionless damping coefficient
b_L	impeller width
b_0	diffuser width at inlet
b_2	diffuser width at outlet
c	absolute velocity of fluid at impeller outlet
c_i	induced velocity
D_L	impeller diameter
$\bar{e}$	eccentricity of rotor center
$\underline{F}_i$	impeller force
f_i	dimensionless impeller force
K_{ij}	stiffness coefficient
k_{ij}	dimensionless stiffness coefficient
N	number of elements
$\bar{n}$	normal vector
Q	total volume flow in impeller

Q_{opt} optimum volume flow

Q_{rel} total flow relative to optimum flow

r_L impeller radius

r_0 smallest radius of spiral

U tip velocity of impeller

$\underline{V}_\infty$ velocity from vortex source

α_0 angle between flow velocity and peripheral direction

β blade angle of impeller

Γ total circulation of impeller flow

γ vortex strength per unit length

ρ density of fluid

INTRODUCTION

The linearized governing equation for self-sustained lateral vibration of a rotor can be written

$$\underline{\underline{M}}\ddot{\underline{q}} + \underline{\underline{C}}\dot{\underline{q}} + \underline{\underline{K}}\underline{q} = \underline{0} \tag{1}$$

in the absence of external forces. The vector $\underline{q}$ represents the generalized coordinates of the system, $\underline{\underline{M}}$ is the mass matrix, $\underline{\underline{C}}$ the damping matrix, and $\underline{\underline{K}}$ the stiffness matrix. The stability of the system is determined by the solution to the equation

$$\det(\underline{\underline{M}}\lambda^2 + \underline{\underline{C}}\lambda + \underline{\underline{K}}) = 0 \tag{2}$$

where $\lambda = \alpha + i\beta$ and $\underline{q} = \underline{A}e^{\lambda t}$. If $\alpha > 0$, the system is unstable. Apart from elastic forces and inertia forces due to the deflection of the rotor itself, these matrices also depend on forces from bearings and seals. Furthermore in turbomachinery, forces from the working fluid acting on the rotor may affect the matrices and consequently alter the stability of the rotor (ref. 10).

In centrifugal pumps and compressors the working fluid exerts a force on the rotor caused by diffuser/impeller interaction, as shown experimentally and theoretically by different authors (refs. 1 to 9). As indicated by Domm and Hergt (ref. 2) and Hergt and Krieger (ref. 8), this force depends on the eccentricity of the rotor. In the literature this force is often called the radial force, but this term is a bit misleading in a rotordynamic sense since the force also has a tangential component. Therefore in this paper it will be called the impeller force.

In this paper a method is presented for calculating the impeller force, its dependency on the rotor eccentricity, and the force's associated stiffness coefficients. Furthermore it is shown that the impeller force also depends on the velocity of the rotor center. This gives rise to equivalent damping coefficients, which are also calculated. For simplicity the analysis is restricted to centrifugal pumps with a vaneless volute but can be extended to any

250

kind of diffuser, as long as neither losses associated with friction and three-dimensional flow nor compressibility seriously affects the pressure-distribution around the impeller. The calculated stiffness and damping coefficients represent the contribution to the stiffness and damping matrices $\underline{\underline{K}}$ and $\underline{\underline{C}}$ from the impeller force and thus permit one to determine the influence of the impeller force on rotor stability and synchronous response.

PHYSICAL MODEL

This model of a centrifugal pump or compressor stage with a vaneless volute is founded on the concept of Csanady (ref. 1). It is based on a two-dimensional representation of the diffuser and a representation of the impeller by an equivalent vortex source concentrated in a single point, as shown in figure 1.
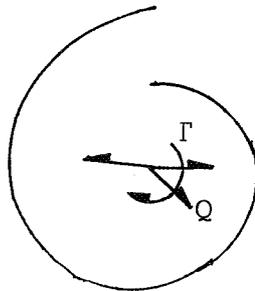
Figure 1

The flow is considered a potential flow field with the singularity Q, Γ.

The vortex-source point coincides with the rotor center, and it may have any eccentricity and velocity in a coordinate system fixed to the diffuser. The source strength and vortex strength Q and Γ are related to parameters of the impeller as shown later.

CALCULATION OF FLOW FIELD

The flow field is calculated by a singularity method, that is, a method based on the replacement of the diffuser contour by a distribution of vortices and/or sources. The method used was developed by Hess (ref. 11). The diffuser contour is considered as a series of small linear segments. Each segment is covered by a vortex distribution of uniform strength. The vortex strength varies from segment to segment. The normal component of the flow field on the contour must be zero. If we have N linear segments, we have N vortex strengths, and hence we can satisfy the condition in N points. These points are chosen as the N midpoints of the segments.

In a potential flow field with potential singularities the law of superposition is valid; that is, the velocity in any point is the sum of the velocities induced by all singularities in the field. Thus the kinematic conditions give

$$\sum_{j=1}^{N} A_{ij}\gamma_j = -\underline{V}_{\infty i}\underline{n}_i \tag{3}$$

where $\underline{V}_{\infty i}$ is the velocity at the midpoint at section i produced by the impeller flow (through the vortex source Γ,Q respresentation) with the impeller assigned some given eccentricity and velocity. The coefficients A_{ij} are evaluated as the normal velocity components induced in point i by a unit vortex strength along line segment j. The term γ_j is the unknown vortex strength per unit length of line segment j; $\underline{V}_{\infty i}$ is the velocity induced by the vortex source Γ,Q representing the impeller for a given eccentricity and velocity of the vortex source.

The solution of equation (3) gives the values of γ_j for all $j = 1,N$. After solution of equation (3), all the singularities in the flow field are determined, and thus the velocity in any point in the plane can be calculated. The development of the coefficients A_{ij} and $\underline{V}_{\infty i}\underline{n}_i$ is shown in appendix A for any rotor-center eccentricity and velocity. The method presented is valid for a vaneless volute with the rotor center coinciding with the spiral center for zero eccentricity. It could be developed for any diffuser geometry as long as the pressure distribution around the impeller is satisfactorily calculated by means of potential theory. Equation (3) will normally contain a large number of linear equations - from 100 to several hundreds - and the coefficients of the system are generally different from zero.

DETERMINATION OF Q AND Γ FROM MACHINE DATA

Figure 2 illustrates the velocity vectors of the flow at the exit of the impeller. With Csanady's nomenclature (ref. 1) the variables of this figure are defined as follows:

B   Busemann slip factor, tabulated by Wislicenus (ref. 12) for different impellers; depends on blade angle and number of blades

β blade angle of impeller

U   tip velocity of rotor

C   absolute velocity of fluid at outlet

The total volume flow is

$$Q = 2\pi r_L b_L \sin \alpha_0 C \tag{4}$$

where r_L and b_L are the radius and the width of the impeller, respectively. From figure 2

$$C(\cos \alpha_0 + \sin \alpha_0)\cot \beta = UB \tag{5}$$

Combining equations (4) and (5) yields

$$Q = UB2\pi r_L b_L/(\cot \alpha_0 + \cot \beta) \tag{6}$$

252
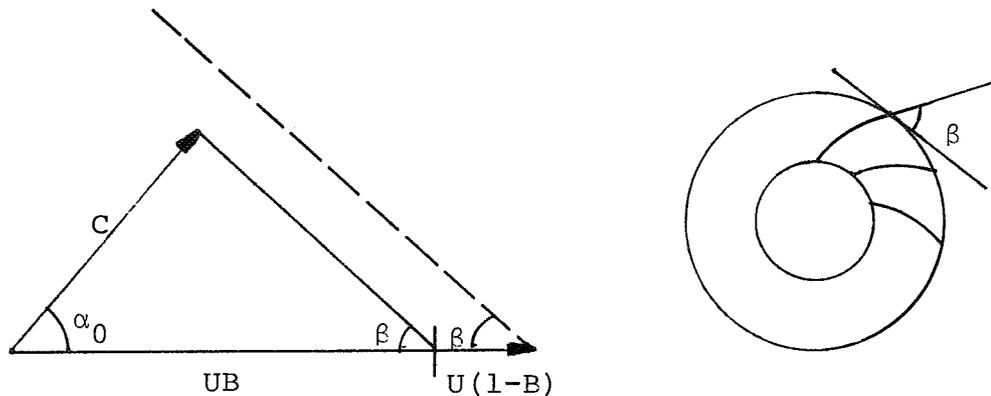
Figure 2

Furthermore

$$Q = \tan \alpha_0 \cdot \Gamma \qquad (7)$$

because α_0 is the angle between the flow and the peripheral direction at the outlet. The optimum efficiency with a spiral-formed volute with spiral angle λ is obtained when

$$90^\circ - \lambda = \alpha_0$$

at the volume flow Q_{opt}, according to Csanady (ref. 1). From equation (6) we obtain

$$Q_{rel} = Q/Q_{opt} = \frac{\tan \alpha_0 (\tan \beta \tan \lambda + 1)}{(\tan \beta + \tan \alpha_0)} \qquad (8)$$

CALCULATION OF IMPELLER FORCE

The force per unit width on a body with circulation Γ in the presence of a source Q in a parallel stream with the velocity $\underline{c}$ is, according to the theorems of Joukowski and Lagally (in ref. 13)

$$\underline{F} = \rho (\underline{c}Q + \underline{\hat{c}}\Gamma) \qquad (9)$$

where ρ is the density of the fluid. If we consider the velocity induced by the singularity distribution on the diffuser contour to be a parallel stream in the calculation of the impeller force, the impeller force is obtained by inserting equations (6) and (7) into equation (9) to yield

$$\underline{F}_i = \frac{UB2\pi r_L b_L}{1 + \tan \alpha_0/\tan \beta} (\underline{\hat{c}}_i + \tan \alpha_0 \underline{c}_i) \qquad (10)$$

253

In this equation, $\underline{c}_i$ is the velocity induced in the rotor center by the contour singularity distribution, as determined from equation (3). The solution procedure for $\underline{c}_i$ for any rotor-center eccentricity and velocity is carried out in appendix B for a vaneless volute formed as a logarithmic spiral, whose center coincides with the rotor center for zero eccentricity. The procedure requires the vortex distribution solution γ_j from equation (3). This could be done for any diffuser geometry.

CALCULATION OF EQUIVALENT STIFFNESS

AND DAMPING COEFFICIENTS

The impeller force can be calculated for any eccentricity and velocity of the rotor center as shown on the previous pages. The force is now calculated for different combinations of eccentricity and velocity of the rotor center in the x- and y-directions of figure 3.
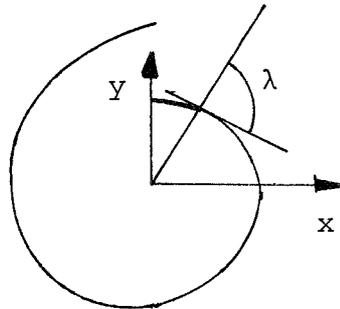
Figure 3

The values of the force can then be tabulated or stored in the computer, and the equivalent stiffness and damping coefficients are calculated as the following numerical derivations:

$$\left. \begin{array}{l} K_{ij} = -\Delta F_i / \Delta e_j \\[2mm] B_{ij} = -\Delta F_i / \Delta v_j \end{array} \right\} \quad (i=1,2; j=1,2) \tag{11}$$

where the index 1 corresponds to the x-direction, and the index 2 corresponds to the y-direction.

RESULTS

On the following pages some calculation results are shown for a given impeller with different volute-spiral angles. The force and stiffness and damping coefficients are presented in the following forms:

254

$$f_i = F_i / (U^2 \rho / 2b_L D_L)$$

$$b_{ij} = B_{ij} / (U\rho / 2b_L D_L) \qquad\qquad (12)$$

$$k_{ij} = K_{ij} / (U^2 \rho b_L)$$

with $D_L = 2r_L$. The impeller has $B = 0.8$, $\beta = 22.5^\circ$. Furthermore $b_0/b_2 = 0.7$ and $r_L/r_0 = 0.9$, where r_0 is the smallest radius of the spiral. The calculation is carried out for $\lambda = 83^\circ$, 86°, and 88°. The relative flow Q_{rel} is determined from equation (8).
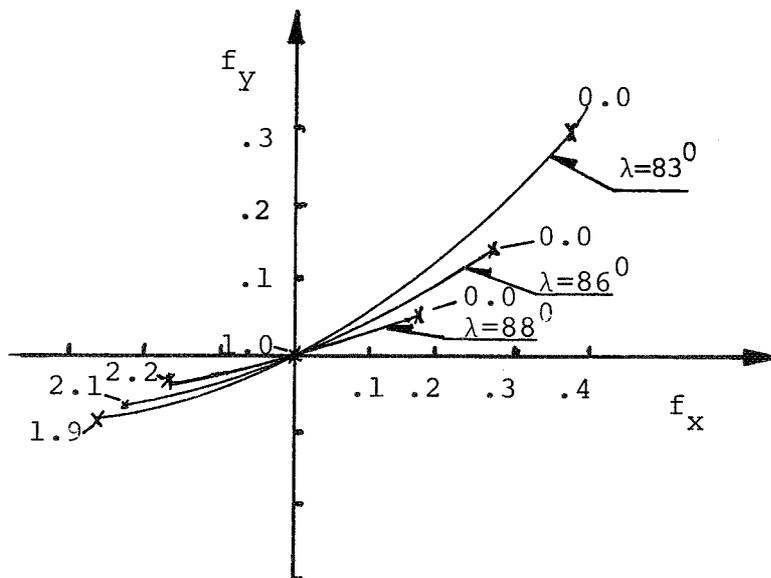
Figure 4
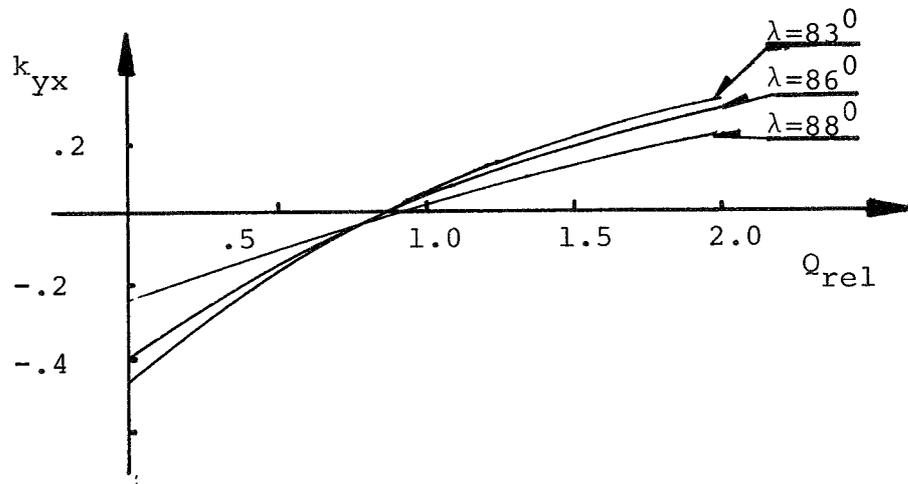
Figure 5
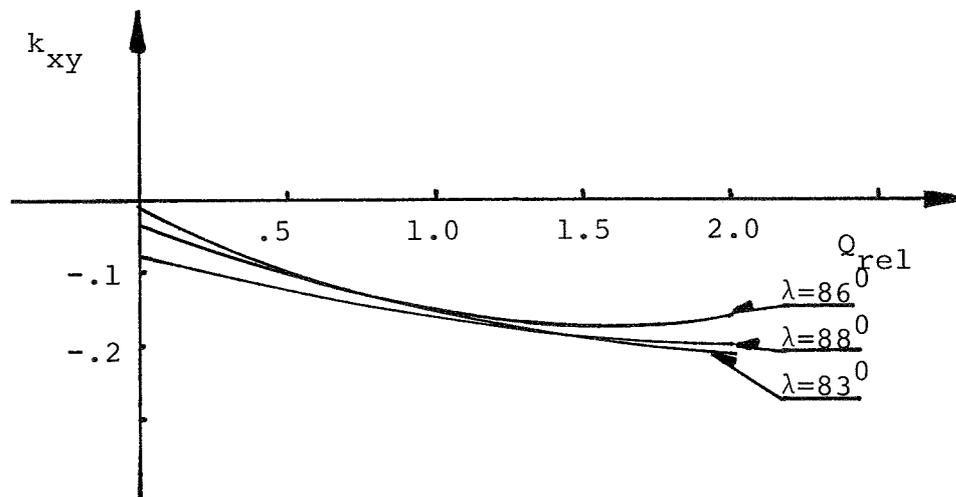
Figure 6
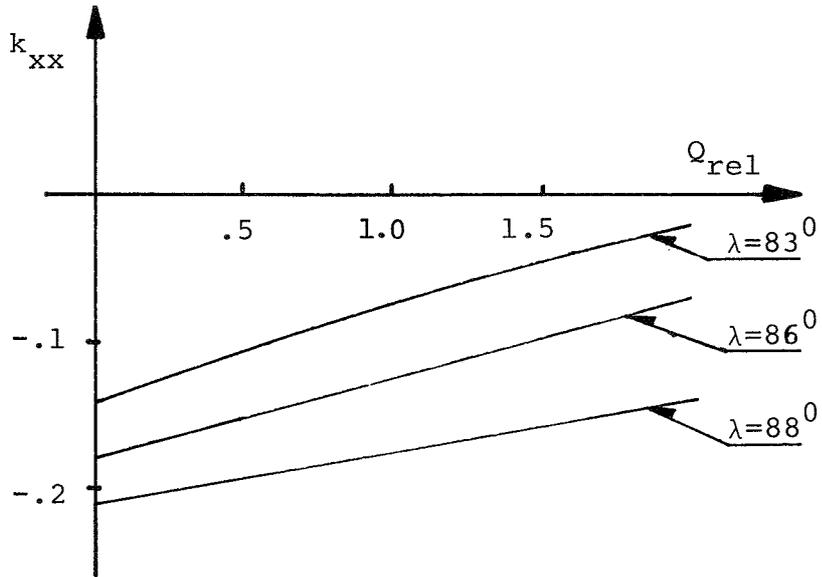
Figure 7
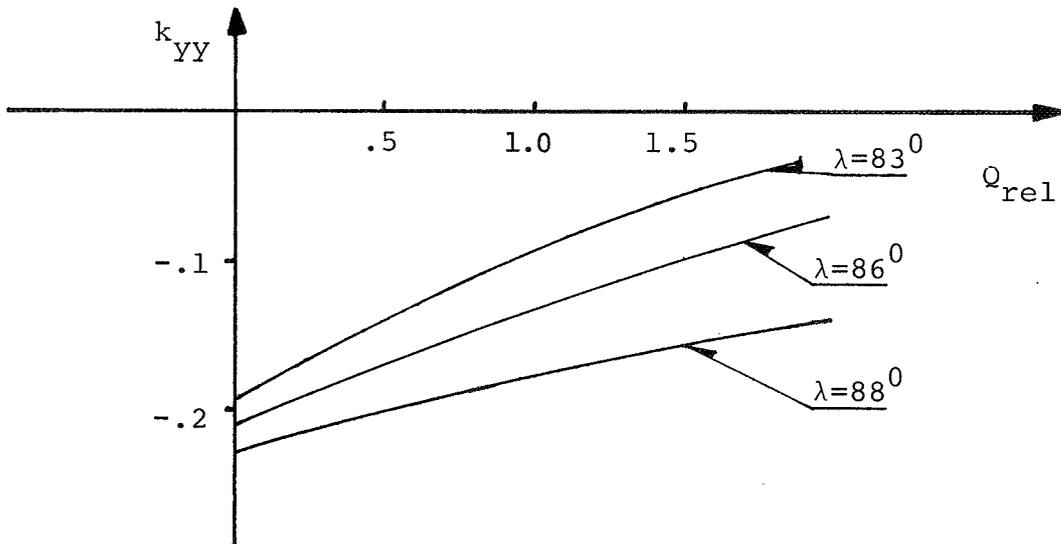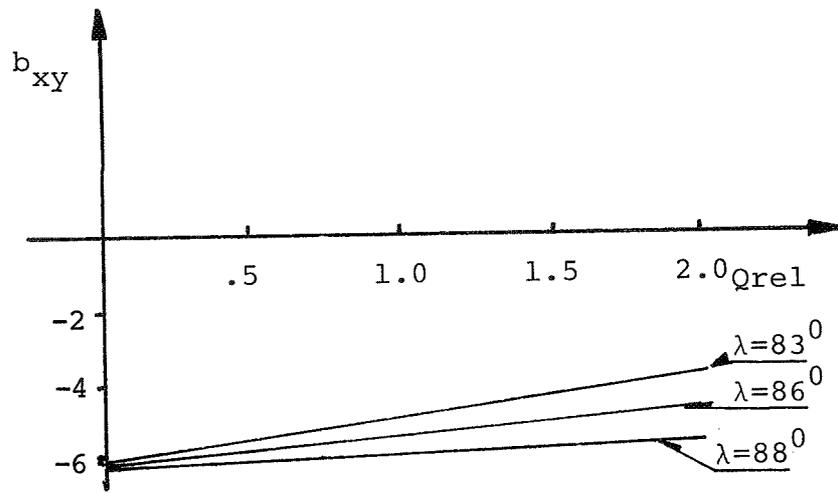
Figure 8

Figure 9
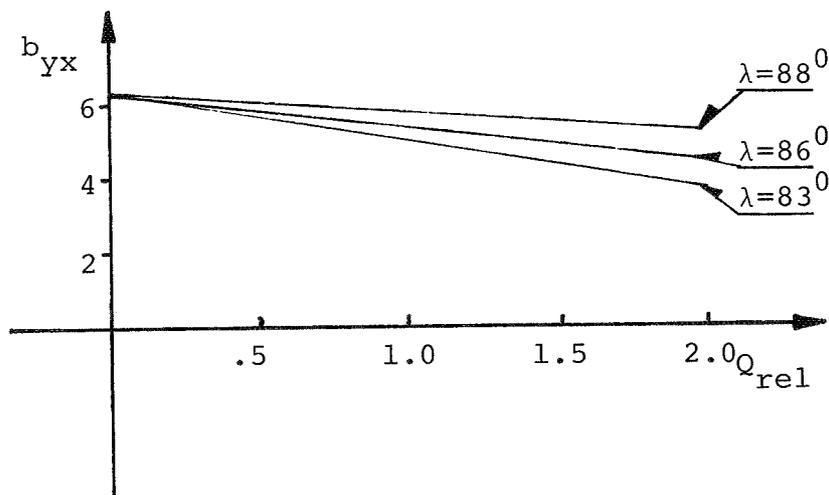
Figure 10
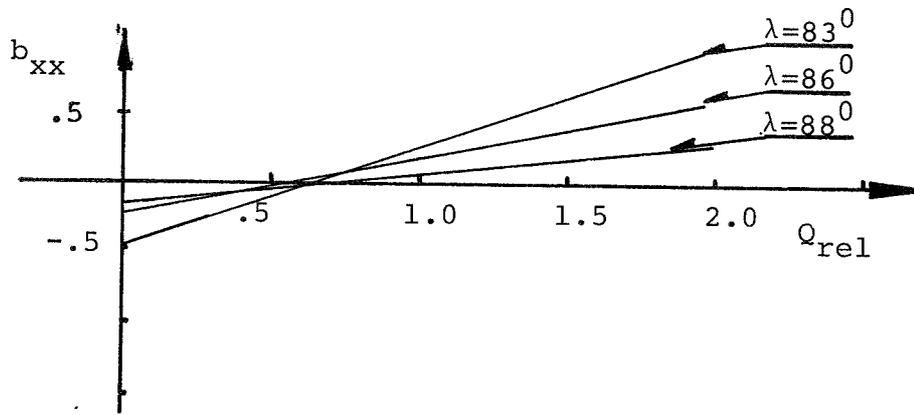
Figure 11
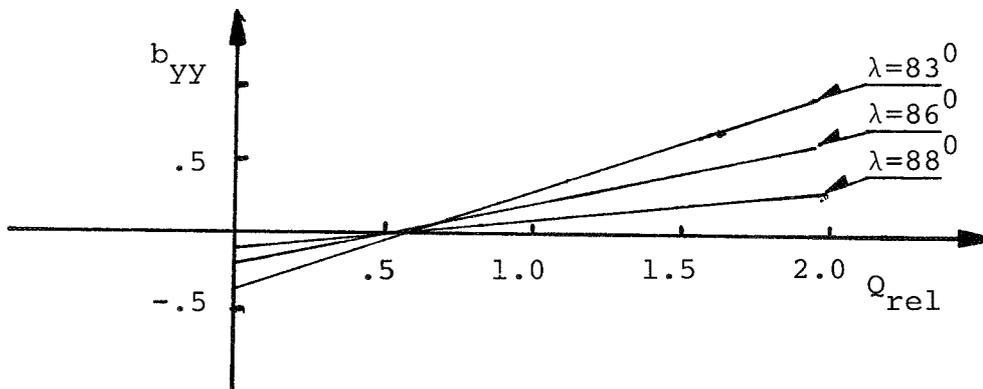
Figure 12

DISCUSSION

From figures 5 and 6 we see that for certain relative flows the cross-coupling stiffness coefficients KXY and KYX have opposite signs. This means that the impeller force has a destabilizing effect on the rotor. Furthermore the damping coefficients BXX and BYY become negative for certain values of the relative flows (figs. 11 and 12). This negative damping is highly destabilizing. For the cross-coupling damping coefficients BXY and BYX, we have almost exactly BXY = -BYX (figs. 9 and 10), and these coefficients are 4 to 10 times larger than BXX and BYY. This means that the rotor is subject to relatively large gyroscopic forces. These forces would tend to stabilize the rotor.

The spiral angle λ is a significant design parameter, as seen in figures 4 to 12. For increasing λ the impeller force decreases in magnitude, the stiffness coefficients increase in magnitude, BXX and BYY decrease in magnitude, and BYX and BXY increase in magnitude. The interval where the destabilizing effects are absent is moved to the right on the Q_{rel} -axis for increasing λ as seen from figures 5, 6, 9, and 10. The effects of impeller design parameters are not investigated in this paper. This effect could, if wished, be calculated by equation (8).

The only relevant measurements reported in the literature are those determining the impeller force as a function of the relative flow (refs. 2 to 5 and 9). There is qualitative agreement between the reported values of the magnitude of the impeller force and the present calculations. As for the direction of the force there is a large scatter in the results reported in the literature, and the results of this paper consequently only agree with some of these results. No direct measurements of stiffness and damping coefficients are reported in the literature. Experimental determination of stiffness and damping coefficients associated with the impeller force must be made before a comparision of calculated and measured values is possible.

APPENDIX A

CALCULATION OF INFLUENCE COEFFICIENTS A_{ij} AND $\underline{V}_{\infty i}\underline{n}_i$ FOR A

VANELESS VOLUTE FORMED AS LOGARITHMIC SPIRAL

For this purpose we have to use some basic formulas from potential-flow theory. The velocity induced in a point (x,y) by an infinately long line source in (0,0) is

$$\begin{pmatrix} u \\ v \end{pmatrix}_Q = Q/2 \; 1/(x^2 + y^2)\begin{pmatrix} x \\ y \end{pmatrix} \tag{13}$$

where Q is the source strength. For a vortex line of strength Γ, the corresponding velocity is

$$\begin{pmatrix} u \\ v \end{pmatrix} = \Gamma/2 \; 1/(x^2 + y^2)\begin{pmatrix} y \\ -x \end{pmatrix} \tag{14}$$

If we have a line segment placed as in figure 13, covered with a constant vortex strength of unity, an integration over the segment gives the following velocity induced by the line segment in point (x,y) (ref. 11):
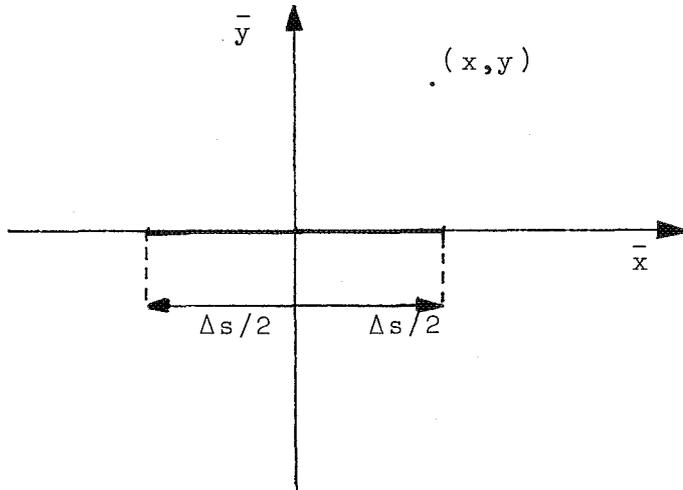
Figure 13

$$V_x = 1/2\pi \left[\arctan\left(\frac{x + \Delta s/2}{y}\right) - \arctan\left(\frac{x - \Delta s/2}{y}\right) \right]$$

$$V_y = -\ln\left[\frac{(x + \Delta s/2)^2 + y^2}{(x - \Delta s/2)^2 + y^2}\right]1/4\pi \tag{15}$$

where $V_y \to 0$ and $V_x \to 1/2$ for $x = 0$, $y \to 0$. Consider the logarithmic spiral of figure 14.
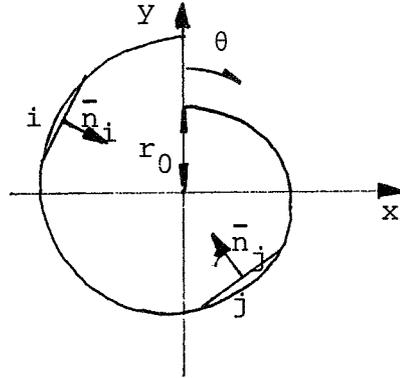
Figure 14

Take θ_i and θ_j as the values of the angle θ for the position vector of the midpoint of the line segment i and j. We have from figure 14

$$\underline{n}_i = \begin{bmatrix} \cos(\theta_i + \lambda) \\ -\sin(\theta_i + \lambda) \end{bmatrix} \tag{16}$$

$$\begin{pmatrix} x \\ y \end{pmatrix} = r_0 e^{\theta_j/\tan \lambda} \begin{pmatrix} \sin \theta_j \\ \cos \theta_j \end{pmatrix} + \begin{bmatrix} -\sin(\theta_j + \lambda) & \cos(\theta_j + \lambda) \\ -\cos(\theta_j + \lambda) & -\sin(\theta_j + \lambda) \end{bmatrix} \begin{pmatrix} x'_j \\ y'_j \end{pmatrix} \tag{17}$$

$$\begin{pmatrix} x'_j \\ y'_j \end{pmatrix} = \begin{bmatrix} -\sin(\theta_j + \lambda) & -\cos(\theta_j + \lambda) \\ \cos(\theta_j + \lambda) & -\sin(\theta_j + \lambda) \end{bmatrix} \begin{pmatrix} x - r_0 e^{\theta_j/\tan \lambda} \sin \theta_j \\ y - r_0 e^{\theta_j/\tan \lambda} \cos \theta_j \end{pmatrix} \tag{18}$$

These coordinate transformations are necessary for the calculation of the induced velocities from the vortex distribution. Furthermore we have for the induced velocities in the different coordinate systems

$$\begin{pmatrix} v_{xin} \\ v_{yin} \end{pmatrix} = \begin{bmatrix} -\sin(\theta_j + \lambda) & \cos(\theta_j + \lambda) \\ -\cos(\theta_j + \lambda) & -\sin(\theta_j + \lambda) \end{bmatrix} \begin{pmatrix} v_{x'_j in} \\ v_{y'_j in} \end{pmatrix} \tag{19}$$

If the point (x_i, y_i) is the midpoint of line segment i, we have

$$\begin{pmatrix} x_i \\ y_i \end{pmatrix} = r_0 e^{\theta_j/\tan \lambda} \begin{pmatrix} \sin \theta_i \\ \cos \theta_i \end{pmatrix} \tag{20}$$

Hence, by using the coordinate transformation (18), the coordinates of point (x_i, y_i) in reference system (x'_j, y'_j) are

$$
\begin{pmatrix} x'_{ij} \\ y'_{ij} \end{pmatrix} = r_0 \begin{bmatrix} -e^{\theta_i/\tan\lambda}\cos(\lambda + \theta_j - \theta_i) + e^{\theta_j/\tan\lambda}\cos\lambda \\ -e^{\theta_i/\tan\lambda}\sin(\lambda + \theta_j - \theta_i) + e^{\theta_j/\tan\lambda}\sin\lambda \end{bmatrix} \tag{21}
$$

From equations (16), (21) and (15), we get A_{ij}, the normal velocity induced in point i from line segment j

$$
A_{ij} = 0 \qquad\qquad \text{for } i = j
$$

$$
A_{ij} = \frac{1}{4\pi}\left\{ -\sin(\theta_i - \theta_j)2\left[\arctan\left(\frac{x'_{ij} + \Delta s/2}{y'_{ij}}\right) - \arctan\left(\frac{x'_{ij} - \Delta s/2}{y'_{ij}}\right)\right] \right.
$$

$$
\left. + \cos(\theta_i - \theta_j)\ln\left(\frac{(x'_{ij} + \Delta s/2)^2 + y'^2_{ij}}{(x'_{ij} - \Delta s/2)^2 + y'^2_{ij}}\right)\right\} \qquad \text{for } i \neq j \tag{22}
$$

In addition, from equations (13), (14), (7), and (20), we obtain

$$
\underline{n}_i \underline{V}_{\infty i} = \begin{bmatrix} -\cos(\theta_i + \lambda) \\ \sin(\theta_i + \lambda) \end{bmatrix}\left[\begin{pmatrix} v_x \\ v_y \end{pmatrix} + Q/2\pi\underline{r}_i^2(\underline{r}_i - \cot\alpha_0\hat{\underline{r}}_i)\right]
$$

$$
\text{with } \underline{r}_i = \begin{pmatrix} x_i \\ y_i \end{pmatrix} - \begin{pmatrix} e_x \\ e_y \end{pmatrix}
$$

This is the induced velocity in the normal direction in point i from the vortex source (Q,Γ) in the impeller center with eccentricity (e_x, e_y) and velocity (v_x, v_y). For this geometry a correction is required because the volute does not have a constant width. Domm and Hergt (ref. 2) use the correction factor b_0/b_2, where b_0 is the width at inlet and b_2 the width at outlet of the volute, so the final result is

$$
\underline{n}_i \underline{V}_{\infty i} = b_0/b_2 \begin{bmatrix} -\cos(\theta_i + \lambda) \\ \sin(\theta_i + \lambda) \end{bmatrix}\left[\begin{pmatrix} v_x \\ v_y \end{pmatrix} + Q/2\pi\underline{r}_i^2(\underline{r}_i - \cot\alpha_0\hat{\underline{r}}_i)\right] \tag{23}
$$

APPENDIX B

CALCULATION OF INDUCED VELOCITY IN ROTOR CENTER

From equations (15), (18), and (19), we can calculate the induced velocity contribution for each line segment in any point in the plane. If we calculate these contributions in the rotor center, the total induced velocity in the rotor center is the following sum from all N line segments of the volute contour:

$$\begin{pmatrix} V_x \\ V_y \end{pmatrix}_{center} = \sum_{j=1}^{N} \begin{pmatrix} V_{x_j} \\ V_{y_j} \end{pmatrix}_{center}$$

But the rotor center has the velocity (v_x, v_y), so the induced velocity is

$$\underline{c}_i = \sum_{j=1}^{N} \begin{pmatrix} V_{x_j} \\ V_{y_j} \end{pmatrix}_{center} - \begin{pmatrix} v_x \\ v_y \end{pmatrix} \tag{24}$$

REFERENCES

1. Csanady, G. T.:   Radial Forces in a Pump Impeller Caused by Volute Casing.
   J. Eng. Power, Oct. 1962, p. 337.

2. Domm, U.; and Hergt, P.:   Radial Forces on Impeller of Volute Casing Pumps,
   Flow Research on Blading.   L. S. Dzung, ed., Elsevier, 1971, p. 305.

3. Agnostelli, A.; Nobles, D.; and Mockridge, C. R.:   An Experimental Investi-
   gation of Radial Thrust in Centrifugal Pumps.   J. Eng. Power, April 1960,
   p. 120.

4. Biheller, H. J.:   Radial Force on the Impeller of Centrifugal Pumps with
   Volute, Semivolute, and Concentric Casings.   J. Eng. Power, July 1965,
   p. 319.

5. Iversen, H. W.; Rolling, R. E.; and Carlson, J. J.:   Volute Pressure Distri-
   bution, Radial Force on the Impeller, and Volute Mixing Losses of a Radial
   Flow Centrifugal Pump.   J. Eng. Power, April 1960, p. 136.

6. Black, H. F.:   Lateral Stability and Vibration of High Speed Centrifugal
   Pumps.   Symp. on Dynamics of Rotors, IUTAM, Dept. of Solid Mech., Tech.
   Univ. Denmark, 1974.

7. Grein, H., and Bachmann, P.:   Radial Forces on Hydraulic Turbomachinery,
   Part 1.   Sulzer Technical Review 1, 1975, p. 37.

8. Hergt, P.; and Krieger, P.:   Radial Forces in Centrifugal Pumps with Guide
   Vanes.   Proceedings of the Institution of Mechanical Engineers 1969-70,
   vol. 184, pt. 3N, p. 101.

9. Grotrian, J. Meir: Untersuchungen der Radialkraft auf das Laufrad einer
   Kreiselpumpe bei Verschiedenen Spiralgehäuse-formen, VDI-Bericht, no. 193,
   1973.

10. Black, H. F.:   Calculation of Forced Whirling and Stability of Centrifugal
    Pump Rotor Systems.   J. Eng. Industry, Aug. 1974, p. 107.

11. Hess, J. L.:   Numerical Solution of Inviscid Subsonic Flows, Von Karman
    Inst. for Fluid Dynamics, Lecture Series 34, March 1971.

12. Wislicenus, G. F.:   Fluid Mechanics of Turbomachinery, McGraw-Hill Book
    Co., Inc., New York, 1947.

13. Robertson, J. M.:   Hydrodynamics in Theory and Application, Prentice Hall,
    1965.

14. Colding-Jørgensen, J.:   Fluidkræfternes   Indvirkning på Stabiliteten af
    Centrifugalpumper og Kompressorer.   Dept. of Machine Design, Tech. Univ.
    Denmark, 1979.

Page intentionally left blank

NON-SYNCRHONOUS WHIRLING DUE TO FLUID-DYNAMIC FORCES
IN AXIAL TURBO-MACHINERY ROTORS

Shan Fu Shen and Vinod G. Mengle
Cornell University
Ithaca, New York 14853

SUMMARY

The role of fluid-forces acting on the blades of an axial turbo-rotor with regards to whirling is analyzed. The dynamic equations are formulated for the coning mode of an overhung rotor. The exciting forces due to the motion are defined through a set of "rotor stability derivatives" (R.S.D.'s), and analytical expressions of the aerodynamic contributions are found for the case of small mean stream deflection, high-solidity and equivalent flat plate cascade. (Torque-whirl and tip-clearance effects can also be included in the R.S.D.s). For a typical case, only backward whirl is indicated if the phase-shifting of the rotor wake effect is ignored. A parametric study of the dynamic stability boundary reveals that a reduction in blade stagger angle, mass-flow rate, fluid density and an increase in stiffness and external damping are all inducive for improved stability. An optimum overhang distance of the rotor from the bearing-support can also be found. Finally, when two or more opposing whirling mechanisms are present, mutual annihilation is possible by making a certain whirling group "b_0" very small. This concept can be useful in the preliminary design stage or for later improvements.

INTRODUCTION

An increasing number of severe failures in high speed compressors and turbines in recent years are attributable to whirling instability. Ehrich (ref. 1), Shapiro and Colsher (ref. 2) and many others have reviewed the destabilizing mechanisms. To our knowledge, only a few studies have been conducted regarding the fluid-dynamic forces acting on the blades themselves. Alford (ref. 3) dealt only with the periphery of the rotor, namely, the tip-clearance and labyrinth seal forces. Reference 4 includes various other mechanisms acting between the rotor-circumference and its casing. Bousso (ref. 5) and later Vance (ref. 6) analyzed the consequences of the tilting of load-torque, but did not account for other effects produced by the same fluid forces. Trent and Lull (ref. 7) noted the important analogy between turbo-rotor whirl and propeller whirl. Ehrich (ref. 8) considered the fluid reactions based on Euler's turbine equations but his dynamic equation was later found to be in error.

In this paper, we adopt the usual modelling of an overhung rotor in its 'coning mode' to set up the dynamic equations of motion. The forcing terms are from the self-induced aerodynamic forces due to the motion, and the whirling is

267

thus reduced to an eigenvalue problem much like flutter. The analysis follows the basic idea of propeller whirl but the details are carefully reworked for the cascade configuration in turbo-rotor systems. Our emphasis is to lay down a proper framework and outline the methodology, so that only systematic refinements and extensions are needed to yield results of practical significance.

SYMBOLS

a_1, b_1 displacements of shaft-center in y- and z-directions respectively

$\underline{\underline{C}}$ diagonal damping matrix with elements $c_d e^2$

C complex wake function

C_ℓ coefficient of lift

C_{α_β} Rotor Stability Derivative (R.S.D.)

c chord length

$D = 2\zeta K_\theta (e/r_2')^2$

e equivalent overhang shaft length

F real part of wake function C

G imaginary part of wake function C

$H = J/I$, ratio of inertias

$\underline{\underline{I}}$ diagonal inertia matrix with elements I

$I = Mr_2'^2$, moment of inertia of rotor about pivotal axis

$\hat{i}, \hat{j}$ unit vectors in axial flow direction and opposite to rotational speed, respectively

J polar moment of inertia of rotor

$\underline{\underline{K}}$ diagonal stiffness matrix with elements K

K, k_1 equivalent torsional spring

k_o cascade interference factor

$K_\theta = \omega_\theta R/V_a$, reduced structural frequency

k reduced aerodynamic frequency

ℓ elemental lift

M mass of rotor

$M' = \pi R^2 \rho V(1 - \eta_o^2)$, annular mass flow rate

m elemental moment

r radial location

$r_2' = (r_2^2 + e^2)^{1/2}$, radius of gyration of rotor about pivotal axis

R rotor tip radius

s gap between adjacent chords

T kinetic energy

t time

V potential energy

V absolute velocity

W relative velocity

β angle of velocity component with respect to axial direction

γ blade stagger angle

Δ change

δ angle of attack

$\eta = r/R$

η_o hub-to-tip radius ratio

θ_o amplitude of pitch angle

θ_1 coning angle

θ_i azimuthal location of i th blade from horizontal axis

$\kappa = \pi R^5 \rho (1 - \eta_o^2)/I$, ratio of moment of inertia of annular cylinder of air to that of rotor

ρ fluid density

$\sigma = c/s$, solidity ratio

268

ϕ = $V/\Omega R$, tip mass-flow coefficient   comp   compressible

ψ_o amplitude of yaw angle   eff   effective

$\underline{\omega}$ angular velocity vector   inc   incompressible

$\omega_\theta = \sqrt{K/I}$ Im   imaginary part

Subscripts, prefixes, etc.:   Re   real part

o   steady value

1,2   inlet and exit stations   s   inertial reference frame

1,2   forward and backward whirl   x,y,z   in the direction of x,y,z axes

1,2   refers to ($\Omega + \omega$) in context   w   wake contribution
       with reduced frequencies for
       whirl reference value θ tangential direction

a   axial direction $(\bar{\ })$ average value

$(\ )^a$ aerodynamic contribution $(')$ perturbed value

                                       $(\underline{\ })$ matrix notation

THE ROTOR MODEL

A rotor on a flexible shaft is equivalent to a gyroscope tied to a rotating spring. Figure 1 shows the real rotor shaft system and the idealized model considered in this paper. This simplest model focuses on the 'coning mode' and has all the characteristics necessary to produce the phenomenon under study. Some of the implications and further assumptions are:

1. The shaft elastica remains in one plane due to infinite stiffness in torsion.
2. The angular tilt of the rotor axis essential for the coning mode is coupled to the radial deflection of the center of the rotor.
3. The cantilevered shaft is approximated by an equivalent, torsional spring, k_1 and an equivalent, rigid, massless shaft of length, l_1. The notation $K = k_1$ and $e = l_1$ is used in the main text. (See reference 9 for inadequacies in this model.)
4. The bearings are rigid and frictionless.
5. The center of mass of the rigid rotor is at its geometric center, i.e. there is no imbalance or eccentricity.

LAGRANGE'S EQUATIONS OF MOTION

The motion and instantaneous position of the rotor can be completely specified by the Euler angles ψ, θ and Ωt which are, respectively, the yaw, pitch and azimuth angle as shown in figure 2. For small angular deflections ψ, θ and constant rotational speed Ω, we have

$$\omega_x \cong \Omega + \dot{\psi}\theta \ , \quad \omega_y \cong -\dot{\theta} \quad \text{and} \quad \omega_z \cong \dot{\psi} \tag{1}$$

The dynamic equations are derived by using Lagrange's equations:

$$\frac{d}{dt}\left(\frac{\partial L}{\partial \dot{q}_i}\right) - \frac{\partial L}{\partial q_i} + \frac{\partial D}{\partial \dot{q}_i} = Q_i \qquad (2)$$

where,

L = Lagrange function = $T - V = \frac{1}{2}\underline{\omega}^T \cdot \underline{\underline{I}} \cdot \underline{\omega} - \frac{1}{2}\underline{q}^T \cdot \underline{\underline{K}} \cdot \underline{q}$

D = Dissipation function = $\frac{1}{2}\underline{\dot{q}}^T \cdot \underline{\underline{C}} \cdot \underline{\dot{q}}$

Q_i = Generalized force = $\delta W / \delta q_i$

δW = Virtual work

and q_i = Generalized degree of freedom (d.o.f.); ($q_1 = \psi$, $q_2 = \theta$)

After simplifications, the results may be written as:

$$\begin{Bmatrix} I & 0 \\ 0 & I \end{Bmatrix}\begin{Bmatrix} \ddot{\psi} \\ \ddot{\theta} \end{Bmatrix} + \begin{Bmatrix} c_d e^2 & J\Omega \\ -J\Omega & c_d e^2 \end{Bmatrix}\begin{Bmatrix} \dot{\psi} \\ \dot{\theta} \end{Bmatrix} + \begin{Bmatrix} K & 0 \\ 0 & K \end{Bmatrix}\begin{Bmatrix} \psi \\ \theta \end{Bmatrix} = \begin{Bmatrix} Q_1 \\ Q_2 \end{Bmatrix} \qquad (3)$$

In particular, note that I is the moment of inertia of the rotor about the "pivotal axis" and c_d is the "equivalent viscous damping coefficient" to account for the damping effects assumed to be representable by an effective force applied at the tip of the shaft.

According to the principle of virtual work, $\delta W = M_z \delta\psi + M_y \delta\theta$. It follows that $Q_1 = M_z$ and $Q_2 = M_y$, i.e. the generalized forces are the pivotal moments M_z and M_y produced due to the fluid-dynamic forces acting on the rotor. These moments are found in the next section to be functions of both the generalized d.o.f., q_i, and their derivatives. Thus, besides the anti-symmetric gyroscopic coupling due to $\pm J\Omega$ there also exists coupling due to the fluid-dynamic forces. Such external couplings, if anti-symmetric in nature, as is well known, can produce unstable response.

THE ROTOR STABILITY DERIVATIVES (R.S.D.'s)

The generalized forces caused by small perturbations of the d.o.f. will be expressed as a set of 'rotor stability derivatives', abbreviated as R.S.D.'s, in this paper. For a systematic treatment of the aerodynamic terms, the analogy of the present problem to propeller whirl treated in References 10 and 11 is obvious. However, we have to make judicial adjustments for the cascade configurations. As a first approximation, we consider here only the quasi-steady effect of inviscid, potential fluid flow on an axial turbo-compressor.

The quasi-steady lift for an airfoil in cascade depends on the instantaneous angle of attack and is given by

$$\ell = \frac{1}{2}\rho W_{eff}^2 \; C_{\ell_{eff}} \; c \; \Delta r \; . \qquad (4)$$

In order to find the effective reference velocity, W_{eff}, and the coefficient of lift $C_{\ell_{eff}}$, consider the displaced rotor as shown in figure 3a. A circumferential cut AA at any radial location unfolds a cascade of airfoils which can be represented simply by equivalent flat plates as shown in figure 3b (see ref. 12). It is well known that, for a cascade of high solidity, i.e. small gap-to-chord ratio ($s/c \lesssim 0.7$), the angle of the relative outlet velocity with respect to the blade is independent of the relative inlet flow angle and is equal to the equivalent flat plate stagger angle. Hence, assuming that the rotation of the blade due to yaw and pitch is very small as compared to its stagger angle, γ, the perturbed and steady relative outlet velocities, $\vec{W_2}'$ and $\vec{W_2}$, are approximately parallel to each other. Next, assuming constant radius cylindrical stream surfaces, the equation of continuity gives the equivalence of the axial components of the absolute outlet velocity in the steady and perturbed states, i.e. $V_{a2}' = V_{a2} = V_a$. The velocity triangles in figure 3c are shown using these assumptions. The velocity triangles are crucial to the development of the R.S.D.'s. (See ref. 9 for further discussions.)

Defining the reference velocity in cascades by

$$\vec{W}_\infty \equiv \frac{1}{2} (\vec{W}_1 + \vec{W}_2) \tag{5}$$

we get

$$\Delta\vec{W}_\infty \equiv \vec{W}_\infty' - \vec{W}_\infty = v\hat{i} + \frac{1}{2} (u + v\tan\beta_2)\hat{j} \tag{6}$$

where, u and v are the perturbation velocities of the blade in the plane of the rotor disc and normal to it. From kinematical relationships, we can easily write

$$u = - e\dot{\psi} \sin\Omega t + e\dot{\theta} \cos\Omega t$$

$$v = (\psi\Omega - \dot{\theta}) r \sin\Omega t - (\theta\Omega + \dot{\psi}) r \cos\Omega t \tag{7}$$

The angular tilt of the rotor axis and the component of $\Delta\vec{W}_\infty$ normal to $\vec{W}_\infty$ combine to give an effective change in the angle of attack,

$$\Delta\delta = \delta_1 + \delta_2 \tag{8}$$

where,

$$\delta_1 = \psi \sin\Omega t - \theta \cos\Omega t$$

$$\delta_2 = - v (\Omega r + V_a \tan\beta_2 - V_{\theta 1})/2W_\infty^2 + \frac{1}{2} (u + v \tan\beta_2)(V_a/W_\infty^2)$$

Using the coefficient of lift for a flat-plate cascade (ref. 11)

$$C_{\ell_{eff}} = 2\pi k_o \sin\delta_{eff} \tag{9}$$

with

$$\delta_{eff} = \delta_o + \Delta\delta$$

and putting

$$W_{eff} = W_\infty + \Delta W$$

where

$$\Delta W = \text{component of } \Delta\vec{W}_\infty \text{ parallel to } \vec{W}_\infty \text{ ,}$$

we get the perturbed component of lift from equation (4) as follows:

$$\frac{\ell'}{\pi \rho k_o c \, \Delta r} = W_\infty^2 \cos \delta_o \, \Delta \delta + 2 \, W_\infty \sin \delta_o \, \Delta W$$

$$+ 2 W_\infty \cos \delta_o \, \Delta W \, \Delta \delta + \sin \delta_o \, \Delta W^2 + \Delta W^2 \, \Delta \delta. \tag{10}$$

The first term provides the leading contribution and for lifting cascades (i.e. $\delta_o \neq 0$) the second term gives an additional small effect. Equation (10) is a general expression for the perturbed lift component; it can be written for the i th blade by replacing Ωt by $\Omega t + \theta_i$, then summed over all the blades and finally integrated from the hub to the tip radius giving the total perturbed lift.

We now specialize equation (10) for a non-lifting cascade, i.e. $\delta_o = 0$ and uniform axial inlet field with no swirl, i.e. $V_{\theta 1} = 0$. It turns out that even in such a simple case significant forces may be produced.

Using the simple relation for the cascade interference factor, k_o

$$k_o = \frac{2}{\pi} \frac{s}{c} \frac{1}{\cos \gamma} \tag{11}$$

for a high solidity cascade with (s/c) $\lesssim$ 0.7, (see ref. 12), the following result for the non-dimensional force components can be obtained:

$$\frac{P_y}{M'V_a} = C_{y_\psi} \psi + C_{y_q} \left(\frac{\dot{\psi} R}{V_a} \right) + C_{y_r} \left(\frac{\dot{\theta} R}{V_a} \right)$$

$$\frac{P_z}{M'V_a} = C_{z_\theta} \theta + C_{z_r} \left(\frac{\dot{\theta} R}{V_a} \right) + C_{z_q} \left(\frac{\dot{\psi} R}{V_a} \right) \tag{12}$$

where

$$C_{y_\psi} = C_{z_\theta} = 1 + (1 + \eta_o^2)/(4\phi^2)$$

$$C_{y_q} = C_{z_r} = - e/2R$$

$$C_{y_r} = -C_{z_q} = (1 + \eta_o^2)/(4\phi^2) . \tag{13}$$

Similarly, integrating the elementary moment components

$$m_y = - r \, \ell_y \tan \beta_\infty$$

and

$$m_z = r \, \ell_z \tan \beta_\infty \tag{14}$$

we get the non-dimensional moment components as

272

$$\frac{M_y^a}{M'V_a R} = C_{m_\psi} \psi + C_{m_q} \left(\frac{\dot{\psi} R}{V_a}\right) + C_{m_r} \left(\frac{\dot{\theta} R}{V_a}\right)$$

$$\frac{M_z^a}{M'V_a R} = C_{n_\theta} \theta + C_{n_r} \left(\frac{\dot{\theta} R}{V_a}\right) + C_{n_q} \left(\frac{\dot{\psi} R}{V_a}\right) \tag{15}$$

where

$$C_{m_\psi} = -C_{n_\theta} = - \left[(1 + \eta_o^2)/2\phi + (1 + \eta_o^2 + \eta_o^4)/6\phi^3 \right]$$

$$C_{m_q} = -C_{n_r} = \frac{1}{4} \frac{e}{R} (1 + \eta_o^2)/\phi$$

$$C_{m_r} = C_{n_q} = - (1 + \eta_o^2 + \eta_o^4)/6\phi^2 . \tag{16}$$

Analogous to the propeller-in-yaw studies, for example, by Ribner (ref. 13) the perturbed axial force and torque about the rotor axis are zero.

The coefficients C_{y_ψ}, C_{y_q}, C_{y_r}, C_{m_ψ}, C_{m_q}, C_{m_r}, etc. as defined by equations (12-16) and which denote increases in forces/moments due to unit increases in the d.o.f. or their derivatives are termed as the 'Rotor Stability Derivatives' in this paper. Note that in this formulation the R.S.D.'s are independent of the number of blades and solidity ratio and remind one of actuator disc type results. In practical applications reliable determination of the R.S.D.'s is, of course, imperative.

APPROXIMATE CORRECTIONS FOR COMPRESSIBILITY AND WAKE EFFECTS

For compressible flows, a first-order correction on the pressure distribution can be obtained by using the expression given in reference 12, page 61. For the case of small lift and low subsonic Mach numbers it reduces to the well-known Prandtl-Glauert Rule:

$$(C_\ell)_{comp} = (C_\ell)_{inc} \left/ \sqrt{1 - M_\eta^2}\right.$$

where M_η is the local Mach number at any radial location η. The concept of an effective Mach number, M_{eff} was used by Ribner (ref. 13) as an overall correction to the R.S.D. So long as M_{eff} is small, we find only small changes in the R.S.D.'s and the stability boundaries are not significantly affected.

The unsteady rotor wake can be taken into account by the use of complex rotor wake functions; see Houbolt and Reed (ref. 10) in the propeller whirl problem. Instead of the well known Theodorsen function for an isolated airfoil, one needs the oscillating cascade wake functions, C, for example, by Whitehead (ref. 14). In cascades the wake function is a parameter of not only the reduced frequency, k, but also of solidity, blade stagger angle and the phase of vibration between adjacent blades, Φ. Hence,

$$F \equiv \text{Re } \{C\} = fn \ (k, s/c, \ \gamma, \Phi)$$

and

$$G \equiv \text{Im } \{C\} = fn \ (k, s/c, \ \gamma, \Phi) \ . \tag{17}$$

Analysis done parallel to reference 10 leads to the following important conclusions for multi-bladed cascaded rotors (see ref. 9):

1. Two reduced frequencies are involved in whirling:

$$k_{1,2} = (\Omega \pm \omega) \ c/2W_{\infty} \tag{18}$$

2. If the whirling frequency ω is much smaller than the rotor frequency Ω, then the effect of wake is to turn the resultant force and moment clockwise by approximately:

$$\delta^* = \tan^{-1} (\overline{G}/\overline{F}) \tag{19}$$

where

$$\overline{F} = \frac{1}{2} \left\{ F(k_1) + F(k_2) \right\}$$

$$\overline{G} = \frac{1}{2} \left\{ G(k_1) + G(k_2) \right\} \tag{20}$$

without much change in the magnitude of the vectors.

3. Two new R.S.D.'s solely attributable to this effect are added, namely,

$$C^W_{y_\theta} = -C^W_{z_\psi} \cong C_{y_\psi} \tan \delta^*$$

$$C^W_{m_\theta} = C^W_{n_\psi} \cong C_{m_\psi} \tan \delta^* \ . \tag{21}$$

Hence, the contribution to the effective tangential force due to the angular tilt of the rotor, which is important for whirl, appears from two sources:

i) C_{m_ψ} : the quasi-steady moment R.S.D.

ii) $C^W_{z_\psi}$: the unsteady rotor wake force R.S.D.

Ehrich's analysis (ref. 8) did not include either of the above two mechanisms.

The above analysis which was for a compressor or a negative work turbo-machine can be repeated for a turbine or a positive work turbo-machine. Though the previously derived R.S.D.'s are not applicable for thick, curved turbine blades with high flow deflection, it can be shown that the direction of the net force and moment does not change.

For lifting rotors, two other important mechanisms discussed in the literature are Alford's tip-clearance effect (ref. 3) and Bousso's torque whirl effect (ref. 5). Both can be represented by an equivalent tangential force due

274

to a radial displacement and contribute thus only to C_{z_ψ} $(= -C_{y_\theta})$. In ref. 9 the conversion to R.S.D. is explicitly given.

DYNAMIC STABILITY ANALYSIS

The generalized forces are related to the fluid-dynamic forces and moments by

$$Q_1 = M_z = eP_y + M_z^a$$

$$Q_2 = M_y = eP_z + M_y^a . \tag{22}$$

It is advantageous to write the equation of motion (eqn. (3)) in non-dimensional form. Defining a new independent variable

$$\tau = V_a t/R \tag{23}$$

and denoting derivatives with respect to τ as superscripted primes,

$$\begin{Bmatrix} 1 & 0 \\ 0 & 1 \end{Bmatrix} \begin{Bmatrix} \psi'' \\ \theta'' \end{Bmatrix} + \begin{Bmatrix} D & H/\phi \\ -H/\phi & D \end{Bmatrix} \begin{Bmatrix} \psi' \\ \theta' \end{Bmatrix} + \begin{Bmatrix} K_\theta^2 & 0 \\ 0 & K_\theta^2 \end{Bmatrix} \begin{Bmatrix} \psi \\ \theta \end{Bmatrix} = \kappa \begin{Bmatrix} f_\psi \\ f_\theta \end{Bmatrix} \tag{24}$$

where the non-dimensional forces are given by

$$f_\psi = a_o \psi + a_1 \psi' + b_o \theta + b_1 \theta'$$

$$f_\theta = a_o \theta + a_1 \theta' - b_o \psi - b_1 \psi' \tag{25}$$

with

$$a_o = \frac{e}{R} C_{y_\psi} + C_{m_\theta}$$

$$a_1 = \frac{e}{R} C_{y_q} + C_{m_r}$$

$$b_o = \frac{e}{R} C_{y_\theta} - C_{m_\psi}$$

$$b_1 = \frac{e}{R} C_{y_r} - C_{m_q} \tag{26}$$

Hence, the homogeneous equation is

$$\begin{Bmatrix} 1 & 0 \\ 0 & 1 \end{Bmatrix} \begin{Bmatrix} \psi'' \\ \theta'' \end{Bmatrix} + \begin{Bmatrix} D-\kappa a_1 & H/\phi-\kappa b_1 \\ -H/\phi+\kappa b_1 & D-\kappa a_1 \end{Bmatrix} \begin{Bmatrix} \psi' \\ \theta' \end{Bmatrix} + \begin{Bmatrix} K_\theta^2-\kappa a_o & -\kappa b_o \\ \kappa b_o & K_\theta^2-\kappa a_o \end{Bmatrix} \begin{Bmatrix} \psi \\ \theta \end{Bmatrix} = \begin{Bmatrix} 0 \\ 0 \end{Bmatrix}$$

$$\tag{27}$$

The anti-symmetric off-diagonal terms $(H/\phi - \kappa b_1)$ and $(-\kappa b_o)$ are important to the self-excited whirl phenomenon as noted earlier.

In order to find the conditions for which the system becomes neutrally stable, sinusoidal motion for ψ and θ is specified:

$$\psi = \psi_o \, e^{i\omega t} \quad , \quad \theta = \theta_o \, e^{i\omega t} \tag{28}$$

where ω, the whirling frequency is assumed positive.

To avoid a frontal attack of the eigenvalue problem with a large number of parameters, the following approach has proved to be more fruitful. Let D in equation (27) be replaced by $\overline{D}$ which denotes the damping required for neutral stability. Then the substitution of equation (28) in equation (27) gives rise to two algebraic equations in terms of the two unknowns ω and $\overline{D}$. Equating the real and imaginary parts to zero gives

$$\lambda^2 = \frac{1}{2K_\theta^2} \left(b \pm \sqrt{b^2 - 4d} \right) \tag{29}$$

and

$$\overline{\zeta} = \frac{\overline{D}}{2K_\theta (e/r_2')^2} = \frac{1}{2K_\theta (e/r_2')^2} \left\{ \kappa a_1 + \frac{(H/\phi - \kappa b_1)\kappa b_o}{K_\theta^2 (1-\lambda^2) - \kappa a_o} \right\} \tag{30}$$

where

$\lambda = \omega/\omega_\theta$, non-dimensional whirling frequency

$\overline{\zeta} = c_d/2M\omega_\theta$, fraction of critical damping required for neutral stability

$b = (H/\phi)^2 + 2K_\theta^2 - 2\kappa \, (a_o + Hb_1/\phi) + \kappa^2(a_1^2 + b_1^2) - 2\overline{D}\kappa a_1 + \overline{D}^2$

$d = (K_\theta^2 - \kappa a_o)^2 + (\kappa b_o)^2 \; . \tag{31}$

It is necessary for neutral stability that $\lambda^2 \geq 0$. Further, only the positive root for λ is taken and $(b^2 - 4d) \geq 0$ should be satisfied.

The equations (29) and (30) are non-linear in λ and $\overline{\zeta}$; but for the κ- and $\overline{\zeta}$-values of interest, the second order appearance of $\overline{\zeta}$ or $\overline{D}$ in λ^2 can be usually neglected. Letting b* denote the value of b with $\overline{D} = 0$, a very good estimate of λ can be obtained, namely,

$$\lambda_{1,2}^2 = \frac{1}{2K_\theta^2} \left(b* \pm \sqrt{b*^2 - 4d} \right) \tag{32}$$

Substitution of these λ_1, λ_2 into equation (30) gives the corresponding $\overline{\zeta}_1$ or $\overline{\zeta}_2$. If the actual damping ζ is larger than the damping required for neutral stability, $\overline{\zeta}$, we conclude the system must be stable. Otherwise, the system is unstable and the amplitude increases unless limited by non-linearities. Examination of $\overline{\zeta}$ (eqn. (30)) reveals that since κa_1, occurring due to aero-dynamic damping, is always negative, a 'conservative estimate' of $\overline{\zeta}$ can be obtained by dropping κa_1 term. Further analysis shows that generally the term $(1 - \lambda^2)$ changes sign for the two roots of equation (32). A conservative estimate of the needed $\overline{\zeta}$ is thus proportional to b_o, the whirling group. Hence, the larger the magnitude of b_o the larger is the value of damping required to prevent whirling.

276

NUMERICAL RESULTS FOR AN EXAMPLE AND DISCUSSION

Table I gives typical values of design parameters used for numerical analysis. They are believed to be representative of small, high-speed turbo-rotors. The high value of the hub-to-tip radius ratio is tailored to approximate our assumption of constant radius cylindrical stream-surfaces.

The R.S.D.'s are shown in figure 4 as functions of the tip-mass flow coefficient, ϕ. Since $\phi = \cos \gamma$, we notice that R.S.D.'s increase with the blade stagger angle. The whirling R.S.D.'s C_{m_ψ} and $C_{y_\theta}^W$ (which is proportional to C_{y_ψ}) are relatively larger as compared to the remaining R.S.D.'s. Note that $C_{y_\theta}^W$ also depends on tan δ^*, where δ^* is the wake angle given by equation (19). The numerous simplified assumptions under which these R.S.D.'s were formulated constrain them to only a small range of blade stagger angles.

It is instructive to examine the effect of only the gyroscopic coupling $\pm J\Omega$. Thus, neglecting all the external aerodynamic forces and the viscous damping, a plot of λ versus the non-dimensionless rotating speed, Ω / ω_θ, as given by equation (29) is shown in figure 5. At any given rotor speed, the two whirling frequencies λ_1 and λ_2, corresponding to forward and backward whirl, respectively, drift further apart from each other as the parameter H, the ratio of moments of inertias of the rotor is increased. Also, at higher rotor-speeds the backward whirling frequency is very small as compared to the forward one or the rotor speed itself. When a slight damping is present both these modes die out. However, without the fluid-dynamic forces, the gyroscopic action cannot in itself lead to a divergent type whirl instability because the net energy input to the system is zero.

The inclusion of the R.S.D.'s through κ in the whirling frequency expression has an imperceptible effect on λ itself. Hence, the forced whirling frequencies are approximately the same as the natural whirling frequencies. Figure 6 shows λ vs. $1/K_\theta$ with ϕ as parameter. K_θ is the reduced structural frequency and is a convenient independent variable. A tendency to converge to the natural frequency ω_θ is observed as the mass-flow coefficient is increased.

The stability boundary plots $\bar{\zeta}$ vs. $1/K_\theta$ are shown in figure 7 for various parameters. In figure 7a where ϕ is a parameter and wake effects are not included the damping required for forward whirl is negative, i.e. $\bar{\zeta}_1 < 0$. Hence, the quasi-steady analysis predicts no forward whirl. On the other hand, backward whirl can occur and rotors with small ϕ and large $1/K_\theta$ values are more susceptible to whirl. Other studies in ref. 9 indicate that increasing the fluid density or Mach number should decrease stability in general; whereas increasing the rotor-to-bearing distance has a stabilizing effect as in figure 7c. This is attributable to the increase in aerodynamic damping term, κa_1, and also due to the form of the fractional damping ζ assumed. The effect of unsteady rotor wake in terms of the wake angle δ^* is shown in figure 7b. In isolated airfoils the calculation of δ^*, say, from Theodorsen's function always gives negative δ^* for all values of the reduced frequency $0 \leqslant k < \infty$, and, hence, has a stabilizing effect (ref. 10). In cascades, the cascade Theodorsen function C may give positive values of δ^*; moreover, since C is itself a function of the whirling frequency a more involved iterative procedure is needed to

solve for λ and $\overline{\zeta}$. In figure 7b only arbitrary values of $\delta*$ are used to bring out the effect of the sign of $\delta*$. In the actual calculation of $\delta*$ if $\omega_2 << \Omega$ is indicated, then $k \cong \Omega c/2W_\infty$ can be used for $\overline{F}$ and $\overline{G}$.

Finally, the importance of other competing mechanisms can be assessed. For example, the equivalent tangential force contributions to represent the effects of tip-clearance and load-input torque misalignment were added to $C_{y\theta}$. Both these mechanisms being absent for a non-lifting cascade, in reference 9 we have recalculated the R.S.D.'s and the torque coefficient for an assumed case of $\delta_0 = 5°$. The resultant stability plot is shown in figure 7d with e/R as parameter. This plot demonstrates the possibility of forward whirl for certain values of e/R and also shows that backward whirl can be suppressed. According to refs. (3) and (5) both these load-dependent mechanisms give rise to forward whirl for aft-pivoted compressors. In our example, unless modified by the wake effect, only backward whirl is possible. The unsteady rotor wake effect depends on the sign of $\delta*$ and no conclusion is possible pending additional investigation. The direction of whirling which is observed in a practical turbo-rotor is the resultant of all the mechanisms. Since $\overline{\zeta} \propto |b_0|$, it seems evident that an astute aerodynamic design should aim at making b_0 small, thus leading to the total elimination of any undesirable whirl.

CONCLUSIONS

1. The propeller-whirl analogy can be directly applied to the whirl of axial turbo-machinery rotors with modifications for the cascade configuration. The basic driving mechanism of orthogonal moments is seen to remain the same.

2. A set of rotor stability derivatives (R.S.D.'s) for turbo-machinery rotors has been suggested. They are fundamental to the dynamic behavior. Expressions specifically derived for the coning mode of an aft-pivoted compressor with equivalent flat-plate, high solidity cascade are given. For practical applications, experimental verification of the expressions would be invaluable.

3. Quick survey of the dynamic stability as affected by various parameters is made possible by introducing artificial damping for neutral stability.

4. Considerations based on the R.S.D.'s suggest only backward whirl of compressors and turbines. The role of unsteady rotor wake is outlined but the net effect awaits more analysis.

5. The dynamic stability boundary plots reveal that stability can be increased by reducing the blade stagger, mass flow rate, density and increasing the stiffness of the shaft and external damping. Though an increase in over-hang-to-tip radius ratio increases stability, the effective stiffness is decreased. Hence, an optimum e/R can be found.

6. Various mechanisms can be mutually annihilated by making the whirling group b_0 as small as possible. This goal may be achievable at the preliminary design stage or later by modification of the rotor geometry, flow distribution or the structural properties.

278

REFERENCES

1. Ehrich, F. F.: Self-Excited Vibration. Shock and Vibration Handbook, McGraw-Hill, 1976, Chapter 5.

2. Shapiro, W. and Colsher, R.: Rotor Whirl in Turbo-machinery: Mechanisms, Analysis and Solution Approaches. ASME Winter Annual Meeting, Turbo-machinery developments in steam and gas turbines, N.Y., 1977, pp. 89-98.

3. Alford, J. S.: Protecting Turbo-machinery from Self-excited Rotor Whirl. J. Eng'g. for Power, ASME Trans., October 1965, pp. 333-344.

4. Pollman, E., Schwerdtfeger, H., and Termuehlen, H.: Flow-excited Vibration in High Pressure Turbines (steam-whirl). ASME Winter Annual Meeting, N.Y., 1977, pp. 75-87.

5. Bousso, D.: A stability criterion for rotating shafts. Israel J. of Technology, Vol. 10.6, 1972, pp. 409-423.

6. Vance, J. M.: Torque-whirl — A Theory to Explain Non-synchronous Whirling Failures of Rotors with High Speed and Load Torque. J. Eng'g. for Power, ASME, Vol. 100, April 1978, pp. 235-240.

7. Trent, R. and Lull, W. R.: Design and Control of Dynamic Behavior of Rotating Machinery. ASME Paper No. 72-DE-39, May 1972.

8. Ehrich, F. F.: An Aeroelastic Whirl Phenomenon in Turbo-machinery Rotors. ASME Paper No. 73-DET-97, 1973.

9. Mengle, V. G.: Non-synchronous Whirl in Axial Turbo-machinery Rotors Due to Fluid Dynamic Excitation. M.S. Thesis, Cornell University, August 1979.

10. Houbolt, J. C. and Reed, W. H.,III: Propeller Nacelle Whirl Flutter. J. Aero. Sc., Vol. 29. March 1962, pp. 333-346.

11. Reed, W. H., III and Bland, S. R.: An Analytical Treatment of Aircraft Propeller Precession Instability. N.A.S.A. Technical Note, TN D-659, Jan. 1961.
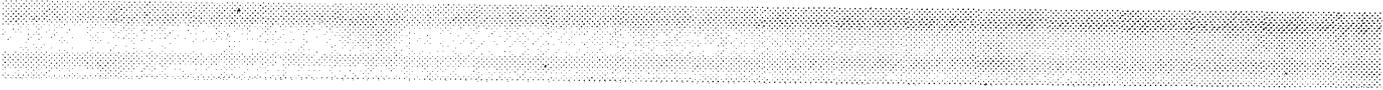
12. Hawthorne, W. R. (editor): Aerodynamics of Turbines and Compressors, High Speed Aerodynamics and Jet Propulsion. Vol. X, Princeton University Press, New Jersey, 1964, Section B.

13. Ribner, H. S.: Propeller in Yaw. N.A.C.A. Report No. 820, 1945.

14. Whitehead, D. S.: Force and Moment Coefficients for Vibrating Airfoils in Cascade. ARC, R & M No. 3254, London, 1962.

TABLE I.- TYPICAL VALUES USED FOR NUMERICAL ANALYSIS

Mass of the rotor . . . . M = 21.89 kg (1.5 slugs)

Radius of tip of the rotor . . . . R = 0.305 m (1 foot)

Hub-to-tip radius ratio . . . . η_o = 0.75

Polar radius of gyration-to-tip radius ratio of the rotor . . . . . r_1/R = 0.6

Radius of gyration of the diametrical moment of inertia-
   to-tip radius ratio . . . . r_2/R = 0.55

Standard density of air . . . . ρ_o = 1.225 kg/m^3 (0.002378 slugs/ft^3)

Shaft overhang-to-tip radius ratio* . . . . e/R = 0.3

---

*In figures 7c and 7d, e/R is a parameter.
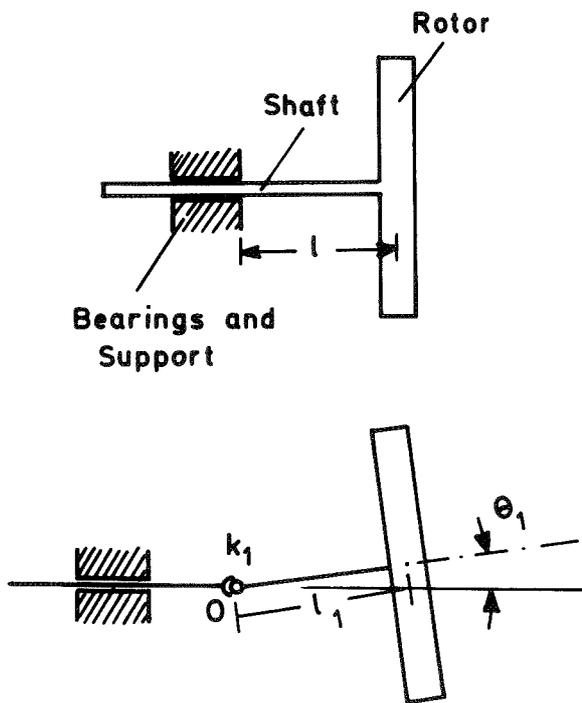
Figure 1. The rotor model.
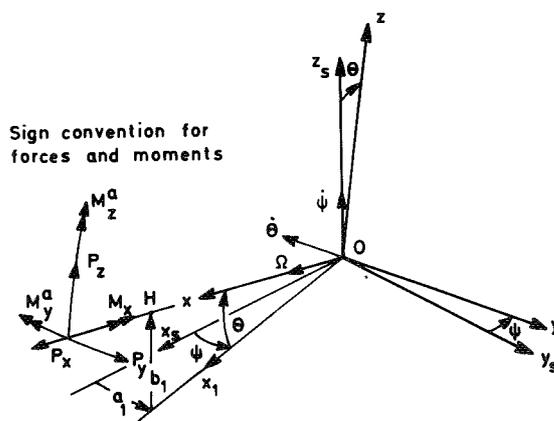
Figure 2. The reference frames and generalized coordinates.
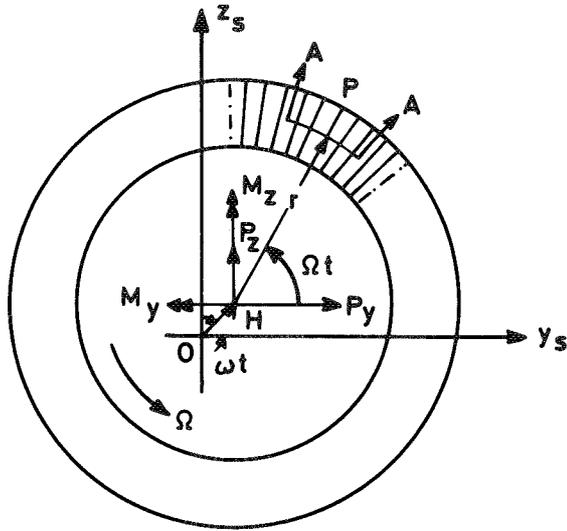
Figure 3a.   The displaced rotor (front-view).
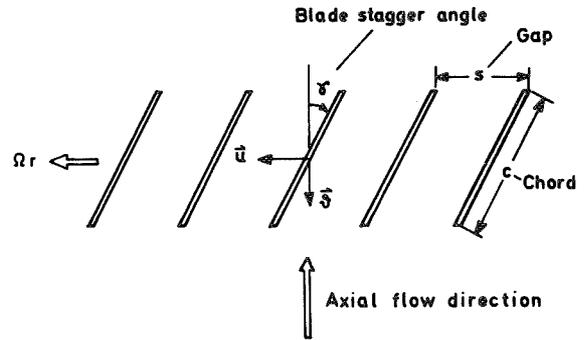
Figure 3b.   The cascade nomenclature.
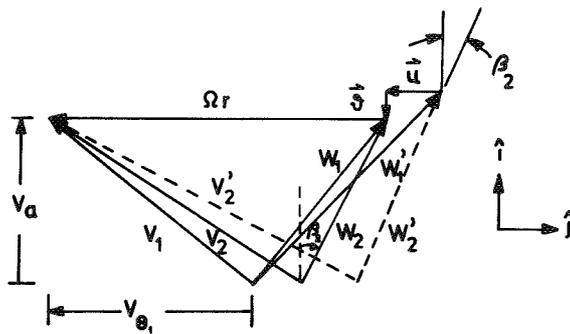
Figure 3c.   The velocity triangles.
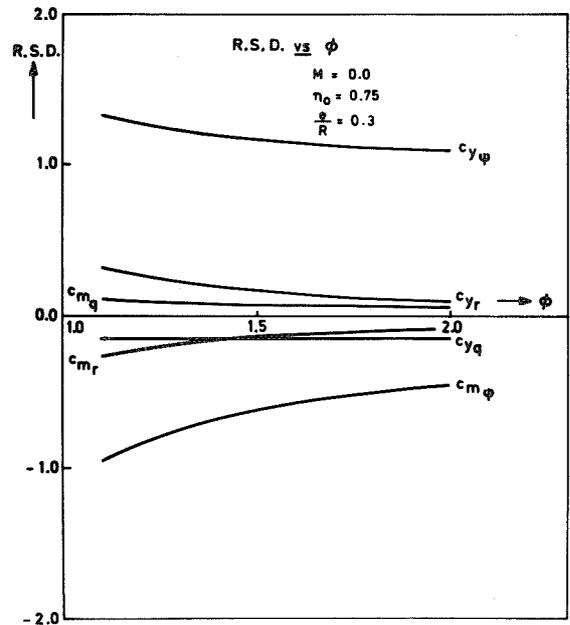
Figure 4.   The rotor stability derivatives as functions of the mass-flow coefficient.

282
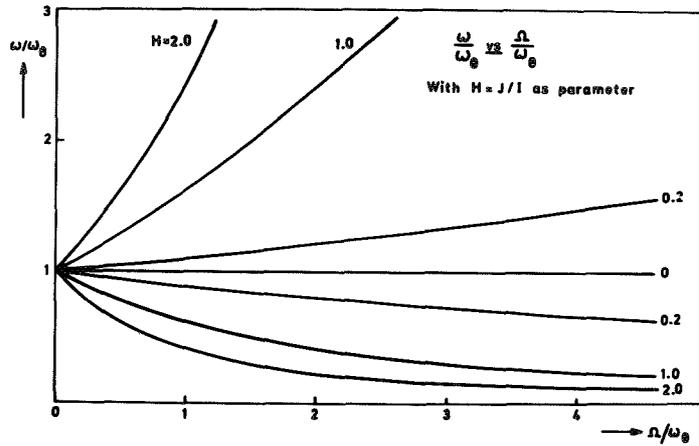
Figure 5. The natural whirling frequencies.
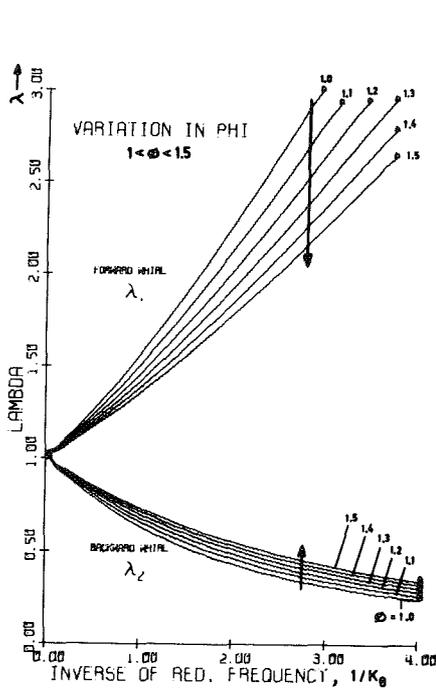
Figure 6. The forced whirling
frequencies with
mass-flow coefficient
as parameter.
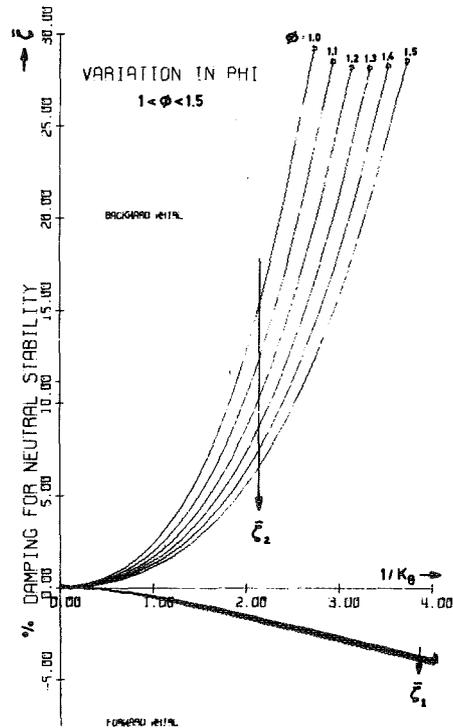
Figure 7a. Stability boundaries with
mass-flow coefficient as
parameter.

283
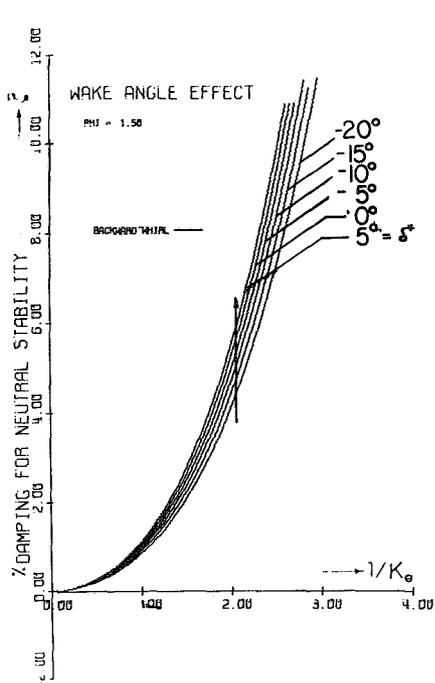
Figure 7b. Effect of wake-angle on the stability boundary.
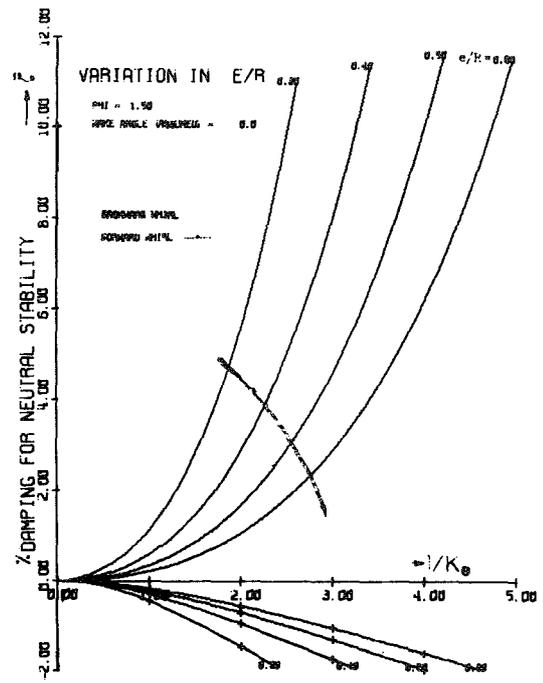
Figure 7c. Effect of shaft-overhang length on the stability boundary.
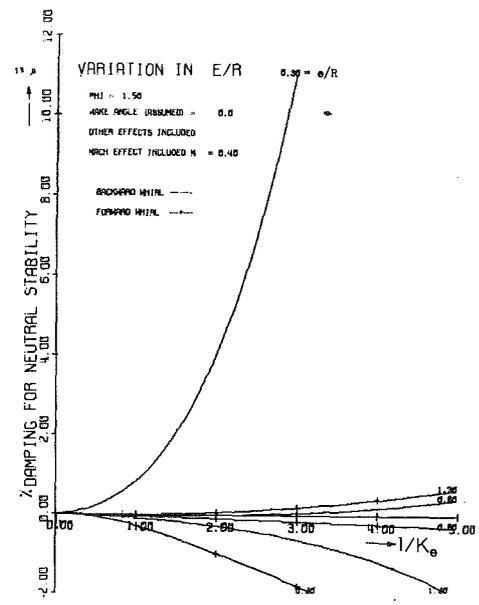
Figure 7d. Inclusion of other effects on the stability boundary with overhang shaft length as parameter.

284

VIBRATION EXCITING MECHANISMS INDUCED

BY FLOW IN TURBOMACHINE STAGES

William E. Thompson[*]
Turbo Research, Inc.
Lionville, Pennsylvania 19353

SUMMARY

The working fluid in a turbomachine stage can excite vibration of the rotor and must be included as an energy source for the system. The system then comprises both fluid and rotor structure, and in stating a stability criterion the damping of both must be considered: $\delta_{total} = \delta_{fluid} + \delta_{mech} > 0$.

Mechanical vibration perturbs the passage flow conditions which then excites or dampens the inducing vibration. Positive excitation (negative damping) results from the positive cross-coupled components of an unbalance force induced by the vibratory displacement as well as the orbital velocity of the rotor.

The equation of motion of flow in a turbomachine shows that unsteady flow is necessary for work transformation. The amplitude, frequency and phase angle of the unsteady flow phenomena must then be found to compare with the structural dynamics of the turbomachine.

Unsteady flow is identified by frequency and size of participating fluid ensemble. There occurs at blade passing frequency axial compressor and turbine blade flutter, and response to blade wakes and condensation shock wave oscillations. Near shaft rotational speed inlet distortion, gusts, rotating stall as well as self-excited shaft displacement and orbital velocity dependent forces are imposed upon the rotor. Surge occurs at system resonance frequency.

The quasi-steady computer analysis of the perturbed centrifugal impeller passage flow is reviewed. The fluid damping coefficient δ_{fluid}, linear in the orbital velocity, is defined and based on 115 stage calculations, the average total damping coefficient per stage needed for stability is $\delta_{total} > 1.85$.

---

[*] Currently with Borg-Warner Research Center, Des Plaines, Illinois.

THE SYSTEM STABILITY CRITERION

There is a growing awareness of the fact that the flow of the working fluid in a turbomachine stage can interact with the structure of the turbomachine rotor in such a way that the distribution of the working fluid pressure over the passage surfaces is perturbed by the lateral vibration of the rotor due, for example, to residual mass unbalance. As a function of both flow conditions and passage geometry, the pressure perturbations, when summed over the surfaces, may result in unbalanced forces which introduce energy into the rotor and enhance the vibration. Such a vibration is deemed self-excited. On the other hand, the flow and geometry conditions may result in a net reduction of energy in the rotor and thus exert a vibration damping influence on the rotor.

Self-excited vibration phenomena are characterized by an available supply of energy and by a zero or negatively damped system. Here

System $\equiv$ Mechanical structure *plus* Working fluid

Energy source $\equiv$ Mechanical sources *plus* Working fluid

The rotor/bearing/pedestal subsystem, including the hydrodynamic bearing film, is generally positively damped. But the ability of bearings to dissipate energy is a function both of their design (style, dimensions, operating conditions, etc.) and their location along the rotor axis. Thus, positive damping of the subsystem cannot be assured a priori. Including the working fluid will either further increase or decrease the system damping. If overall damping capacity exceeds excitation, energy will flow out of the system and stability of the rotor will follow or be assured. But if excitation exceeds the capacity of the system to dissipate the energy, the net influx or accumulation of energy will rapidly produce rotor instability.

It is probably desirable to reduce the concept of energy flux with respect to each component of the system to a damping coefficient δ appropriate to each component. The *system* stability criterion may then be expressed as

$$\delta_{total} = \delta_{fluid} + \delta_{mech} > 0 \qquad (1)$$

Use of an energy criterion for evaluating turbomachinery system stability was suggested by Carta (1967, ref. 1) and further explained by him (ref. 2). A description of its application in a design procedure for axial flow compressor blading was given by Mikolajczak (1975, ref. 3) and a similar application in England was outlined by Halliwell (1977, ref. 4). In 1978, Thompson (ref. 5) introduced the stability increment for multistage centrifugal compressors which, upon comparison, proves to be identical to the criterion of eq. (1).

NATURE OF EXCITATION

The unbalanced force which arises from the perturbed pressure and which is applied to the rotor and leads either to excitation or damping of

its vibration, can be resolved into direct and cross-coupled components. For rotor shaft *displacement* dependent forces, such as developed in shaft end or blade shroud labyrinth seals, the resolution is conveniently taken along and perpendicular, respectively, to the line between the bearing and journal centers. For rotor shaft orbital *velocity* dependent forces, such as developed by the working fluid in a turbomachine stage, the resolution is taken along and perpendicular, respectively, to a virtual radius to which the orbital velocity is perpendicular. The vector diagram of these forces is shown in fig. 1.

In each case, the component of the unbalanced force acting along the line of centers or along the virtual radius is denoted the direct component. If it is in the direction of n_2 or n_2', it has small stiffening effect on the system, somewhat raising the critical speeds and improving the stability. If the direct component acts in a negative n_2 or n_2' direction, it has a slight softening effect, reducing critical speeds and stability margin.

In comparison, the components of the unbalanced force acting perpendicular to the line of centers or to the virtual radius are the cross-coupled components and directly affect the flux of energy to or from the rotor. If the cross-coupled component is in the n_1 or n_1' direction, it adds energy, excites the rotor, and is a destabilizing influence. If it acts in a negative n_1 or n_1' direction, is removes energy from the rotor and is a stabilizing influence. The conception of the effect on rotor system stability of the cross-coupled force components was first introduced by Kapitza (1939, ref. 6).

The unbalanced force, which affects both rotor vibration amplitude and system stability, has been attributed to perturbations of the pressure on the turbomachine stage passage surfaces. In particular in a reaction turbine stage, the effect in the rotor blade passage is comprised of the effect of the rotor orbital velocity and the influence of the seal leakage flow in modifying the throughflow velocity conditions. In addition there is the effect of the nonuniform circumferential static pressure due to nonuniform seal leakage around the periphery of the rotor blade shroud. Both passage and seal leakage effects are induced by rotor vibratory motion. The conception of the effect on rotordynamic stability of the seal leakage as it affects both blade performance and generates an unbalanced force was first introduced by Thomas (1958, ref. 7)

In more recent times, some valuable expositions have been made of the concepts given above. Ehrich (1972, ref. 8; 1973, ref. 9) identified an aeroelastic tip-clearance effect and presented the associated destabilizing force vector diagram. Alford (1965, ref. 10) in an oft-cited paper, identified two aerodynamic disturbing forces, the circumferential pressure variation in the seals and the variation of local efficiency in the rotor blade flow processes, where both were attributed to blade tip clearance. Based on very astute interpretation of the experimental test results of four gas turbine engines, Alford also concluded that rotor whirl resulting from fluid dynamic excitation was in the direction of rotor rotation, that whirl amplitude increased both with increased power output (i.e., in large

287

part with an increase in mass flow rate) and with decreased inlet temperature (i.e., with increased inlet density). These observations seem to be confirmed by experience accumulated up to the present time.

Pollman, Schwerdtfeger, and Termuehlen (1978, ref. 11) provided an extensive account of excitation mechanisms investigated by a European steam turbine manufacturer. Excitation of a fluid dynamic nature was comprised of the effects of seal leakage flow and load dependent influences, so-called "steam whirl." The latter were clearly defined as modification of local rotor blade passage efficiency caused by steam leakage flow and resulting in a local variation in torque developed in the blading. An unbalanced force in the direction of rotor rotation follows from the torque variation.

In Russia, work in this area is carried out at two research institutes, the Moscow Energetics Institute (MEI) and the Central Boiler-Turbine Institute (TsKTI) in support of steam turbine manufacturing. Kostyuk, et al. (1974, ref. 12) identified three nonconservative forces leading to self-excited vibrations. These were oil film bearing forces, seal leakage forces, and circumferentially varying blade forces due to seal leakage. Further Kostyuk, et al. (1975, ref. 13) reported work on two additional and important effects, that of the influence on the blading of passing through the wakes of upstream blades and that of unsteady separation on the blade surfaces due to condensation shock wave/boundary layer interaction which occurs at transonic and mildly supersonic velocities when the steam condition is supersaturated. These latter two effects clearly excite blade vibration, while the former induce rotor vibration. In a later report Kostyuk, et al. (1978, ref. 14) presented experimental results of labyrinth seal force measurements. Olimpiev (1978, ref. 15) presented alternative work on varying blade forces, on shroud band seal leakage forces, and on labyrinth seal forces. He also mentioned that seal configurations could be devised to convert the influence from excitation to damping and that the circumferentially varying blade forces taken proportional to the rotor displacement producing them lead to an effective rotor stiffness coefficient.

NECESSITY OF UNSTEADY FLOW

Dean (1959, ref. 16) has explained the paradox encountered in applying Euler's equation (the equation of motion) to the problem of describing the change of state of the working fluid as work is transferred in a turbomachine. Consider a frictionless, reversible, adiabatic process in an idealized machine. This is simply an inviscid fluid subject to an isentropic process, which assumptions do not, in the present argument, invalidate the conclusions. The energy equation is simply and correctly given as

$$-w_s = h_{02} - h_{01} \tag{2}$$

For a compressor, $h_{02} > h_{01}$ but for a turbine $h_{02} < h_{01}$ and the sign of the result is entirely consistent with the conventions of thermodynamics.

However, Euler's equation (the differential form of the equations of motion) and Bernoulli's equation (integral form of the equations of motion)

are not applicable in describing the process in detail whereby the shaft work changes the state of the working fluid as it passes through blading of turbomachines. Instead, as Dean shows in detail for compressible flow, the equations of motion become

$$Dh_0/Dt = (1/\rho)\, \partial p/\partial t \tag{3}$$

and for incompressible flow

$$Dp_0/Dt = \partial p/\partial t \tag{4}$$

where the material derivative is the operator having unsteady and convective parts:

$$D/Dt = \partial/\partial t + (\bar{c}.\nabla)$$

Thus, while the energy equation (2) demonstrates that stagnation enthalpy (or stagnation pressure) is changed as a consequence of shaft work, eq. (3) or eq. (4) shows, first, that the changes are with respect both to time and to changing location in the fluid field and, second, that both are a function of the time-varying or *unsteady* pressure fluctuations. Therefore, work transfer in a turbomachine *requires* an unsteady flow process. Spannhake (1930, ref. 17) perhaps was the first to point this out to turbomachine designers and analysts.

Three excellent reviews of unsteady flow phenomena can be identified, where in turn a large body of literature is cited. Mikolajczak (1976, ref. 18) pointed out that unsteady effects affect aerodynamic performance, aeroelastic and rotordynamic performance, and the generation of noise. Platzer (1978, ref. 19) provided an exhaustive account of unsteady phenomena in turbomachinery including the unsteady effects in machines exposed to uniform flow, the response to distorted inlet flow, surge and rotating stall conditions, as well as blade flutter. He categorized various prediction methods for these phenomena and described experimental studies. McCroskey (1977, ref. 20) included unsteady turbomachinery flow effects in a general review of unsteady fluid dynamics. Even so, he was able to make critical comments about flutter, inlet distortion, unsteady transonic flow, rotating stall, transitory diffusor stall, surge, vortex shedding from bluff bodies, and the definition of an unsteady Kutta-Joukowski condition. Finally, he included a projection of research needs and future developments.

Two time scales occur in the description of unsteady flow phenomena, the particle transport time:

$$\text{Characteristic length/Fluid velocity} = L/w \text{ [time]}$$

and the period of the pressure fluctuation:

$$1/\text{Fluctuation frequency} = 1/\nu \text{ [time]}$$

Their ratio becomes

$$(L\nu)/w \equiv k, \text{ the reduced frequency} \tag{5}$$

When the particle transport time is short with respect to the fluctuation period, $k \to 0$ and the flow is said to be quasi-steady. Practically, for $k \sim 0.1$, the approximation of steady-flow analysis is often acceptable.

Lastly, unsteady phenomena may be transient or periodic. While a single transient event may have catastrophic consequences for a turbomachine, such events occur over a relatively long period of time and are usually under the control of the process control system. On the other hand, periodic events characterize self-excited vibrations and are of concern here. Such periodic events fall into three categories as a function of both their frequency and a characteristic length of the participating fluid ensemble. For a characteristic length of the order of the blade thickness, the blade passing frequency is appropriate. Frequencies of the order of the shaft rotational speed are associated with phenomena of the size of the stage passages, while phenomena of the size of the bearing span occur at frequencies of the order of the overall duct system resonance. Vibration exciting mechanisms in each of the categories will be described in the next section.

SIZE/FREQUENCY CLASSIFICATION OF PHENOMENA

Three classifications according to size and frequency of the unsteady flow phenomena have been noted above. In each classification one finds a number of phenomena each one of which inherently possesses a mechanism for exciting vibration of the associated structural element. At the order of the blade passing frequency there occur axial compressor and axial turbine blade flutter together with blade vibration due to cutting upstream blade wakes as well as condensation shock wave oscillations. The last condition occurs in steam turbines where the expansion crosses the saturation line and the flow is at transonic speed in order to accommodate the large steam volume within a reasonable passage size. The frequency of the shock wave oscillations is below the blade passing frequency but much above the shaft rotational speed so it is included in this category.

At the order of the shaft rotational speed, inlet flow distortion, gusts in the flow and rotating stall in the rotor blading or the stationary interstage passages are external influences imposed on the rotor. In addition rotor vibration due to, say, residual mass unbalance is capable of inducing both displacement dependent and orbital velocity dependent excitation of the rotor. Finally at the order of the system resonance frequency, surge can occur.

All of these topics are listed in table 1 together with a group of references for each phenomena. The references have been chosen from among a very large number because each in turn identifies and to a great extent evaluates the contributions of a subsequent set of references. In connection with table 1, the writer is indebted to William G. Steltz, Power Generation Divisions, Westinghouse Electric Corp. for the references on condensation shock wave phenomena.

Consistent with the present workshop on rotordynamic instability, phenomena at the order of the shaft synchronous frequency will be emphasized and blade vibration and system surge will not be considered further. Further we understand that from the unsteady flow phenomena there needs to be derived the amplitude, frequency and phase angle of a forcing function which, for analytical purposes, can then be imposed on the rotor system.

290

But it cannot be expected that all topics in table 1 are so well developed fluid dynamically that clear, realistic and practical forcing functions will be available for our use.

ORBITAL VELOCITY-DEPENDENT EXCITATION

The orbital velocity induces the unbalanced fluid dynamic force which is imposed on the rotor of a turbomachine. In both figures 2 and 3, the rotor centerline describes a trajectory or orbit during lateral vibratory motion. The instantaneous tangential velocity of the shaft center along the trajectory is the rotor orbital velocity.

The angular velocity of the rotor results in a tangential velocity at each location on the rotor proportional to its radius from the shaft center. Then for the leading edges of the blades as shown in figures 2 and 3, when the velocity due to rotation and the orbital velocity are in the same sense, they add and when in opposite sense, they subtract. The effect is as if the rotor rotation took place instantaneously about a virtual center displaced from the geometric shaft center as shown in the figures. Those flow passages at the greater radii from the virtual center handle a somewhat greater mass flow and exchange a somewhat greater angular momentum with the fluid than do those at the smaller radii. Blade surface pressure distributions in the flow passages will now vary with the virtual radii, not the geometric radii, and will be nonuniform from passage to passage. Summation of the pressure distributions in all passages at an axial location on the rotor will thus result in an unbalanced force on the rotor.

In the case of the radial compressor in fig. 2, the rotor orbital motion causes the blade leading edges to move in and out radially and, as the orbital velocity first adds then subtracts from the rotational velocity, to accelerate then decelerate tangentially with respect to a steady fluid flow into the passages. Thus, relative to the rotor, the blade appears to be moving through a gust having both lateral and longitudinal components of perturbed velocity and pressure. Such perturbations move in a series of waves over the length of the blade with a frequency equal to the rotor lateral vibratory frequency. In practice this frequency is the subsynchronous frequency of the rotor/bearing/pedestal system. Isay (1958, ref. 69) appears to offer the only known analysis of such unsteady flow.

In much the same way, orbital motion induces velocity perturbations, modified incidence angles, etc. in an axial compressor rotor as shown in fig. 3. In addition the same orbital motion produces varying blade tip clearance or blade shroud band clearance about the periphery at a given rotor axial location yielding varying leakage. The local variation of the leakage modifies the local pressure rise in an axial compressor stage and modifies the local pressure drop in a turbine stage. Thus the velocity perturbation from the orbital motion and the pressure perturbation from the rotor orbital displacement combine to perturb the passage flow non-uniformly from passage to passage resulting in an unbalanced force on the rotor. In the case of the axial flow steam turbine, the combined influence of leakage and orbital motion is called steam whirl.

291

EXAMPLE: THE CENTRIFUGAL COMPRESSOR STAGE

At the outset of this work, ref. 69 was unknown to the writer and circumstances did not permit developing the unsteady flow analysis. Invoking quasi-steady conditions, a "snap shot" was made encompassing the flow in every impeller channel where each is perturbed differently by the shaft orbit velocity. When the blade or channel length is a sufficiently small portion of the disturbance wave length, the flow conditions imposed for an instant on the blade can be considered approximately steady. Expressed in terms of the reduced frequency introduced above, $k < 0.2$ will usually be adequate for the approximation to hold. The fluctuation frequency is given by the shaft subsynchronous frequency.

A computer program was organized to analyze each and every impeller passage under perturbed, quasi-steady conditions; to resolve the summation of the pressure distribution into components of F_1 and F_2 contributed by each passage; and finally to sum the contributions to F_1 and F_2. Practical considerations showed that typical orbital velocities are 0.05 to 0.20 m/s (2 to 8 in./s) in comparison to the passage relative fluid velocity of 46 to 185 m/s (150 to 600 ft/sec). The unbalanced force resulting from such a small perturbation of the velocity proved, upon calculation, to be linear in the orbital velocity. Thus $F_1 = b_1 u_t$, $F_2 = b_2 u_t$, and the contribution of the working fluid to the system stability criterion becomes

$$\delta_{fluid} = -b_1 = -F_1/u_t \qquad (6)$$

The negative sign is needed because a positive excitation corresponds to a negative damping. For an extended explanation of these ideas as well as numerical results for a compressor comprising fourteen stages in two casings, the reader is referred to ref. 5.

CONCLUDING REMARKS

The system stability criterion given in ref. 3 is shown in eq. 1. For the relatively simple blade structural system considered in ref. 3, use of the ideal, zero boundary between stability and instability is evidently justified. Such is not the case in the much more complex rotor/bearing/pedestal/working fluid system. As a result of analyzing 115 individual centrifugal compressor stages which were contained in 20 multistage bodies, the average coefficient per stage needed to assure stability may be suggested as $\delta_{total} = 1.85$. Referring again to eq. 1, only δ_{fluid} is the subject of this paper while δ_{mech} must be determined by other rotodynamic analysis.

Each length/frequency classification of excitation phenomena, once analyzed, will admit suggestions for designing in additional damping of a fluid dynamic nature. Regarding blade flutter, ref. 3 suggests that an entire blade fluid and structural design system has been organized and can yield optimized results. Regarding distorted inlet flow to axial compressors, criteria are emerging (refs. 70, 71) which will lead to configurations which are insensitive to such external influences. Work in this direction for radial turbomachines lags that of axial machines. Finally overall system design ignores completely the opportunity to add damping to minimize

292

the effects of surge.

Regrettably the limitation on scope of this paper due to both preparation time and space has precluded including examples of other phenomena in table 1, an evaluation of the numerical fluid mechanical methods which are used to obtain quantitative predictions of the damping coefficients and evaluation of various experimental techniques for observing unsteady flow and deriving the force and damping coefficients from such observations.

SYMBOLS

a_1, a_2	displacement dependent fluid force coefficient, N/m (lbf/in.)
$\bar{a}_1$, $\bar{a}_2$	stator-fixed coordinates system, m (ft)
b_1, b_2	orbital velocity dependent fluid force coefficient, N-s/m (lbf-s/in.)
c	fluid absolute velocity, m/s (ft/s)
$F_1 = F_{b1}$	cross-coupled force component due to fluid dynamic excitation, N (lbf)
$F_2 = F_{b2}$	direct force component due to fluid dynamic excitation, N(lbf)
h	static enthalpy, m-N/kg(ft-lbf/slug)
h_0	stagnation enthalpy, m-N/kg (ft-lbf/slug)
k	reduced frequency
L	characteristic length, m(ft)
$\bar{n}_1$, $\bar{n}_2$, $\bar{n}_3$	rotor-fixed coordinate system, m(ft)
p	static pressure, kPa(psia)
p_0	stagnation pressure, kPa(psia)
r	radial coordinate, m(ft)
u	blade peripheral velocity, m/s (ft/s)
$\bar{u}_t$	rotor orbital velocity, m/s (in./s)
w	fluid relative velocity, m/s (ft/s)

w_s shaft work, m-N/kg(ft-lbf/slug)

δ damping coefficient, N-s/m (lbf-s/in.)

$\bar{\delta}$ rotor displacement, m(in.)

ν fluctuation frequency (rotor subsynchronous frequency), 1/s

ρ density, kg/m^3 (slugs/ft)

ω angular velocity, rad/s

REFERENCES

1.   F. O. Carta, "Coupled Blade-Disk-Shroud Flutter Instabilities in Turbojet Engine Rotors", *Journal of Engineering for Power, ASME Transactions,* Vol. 89, No. 3, 419-426, July 1967.

2.   F. O. Carta, "Turbomachinery Flutter: Introductory Concepts", *Industrial Compressors,* Vol. 1, Lecture Series 91, von Karman Institute, Belgium, May 1976.

3.   A. A. Mikolajczak, R. A. Arnoldi, L. E. Snyder, H. Stargardter, "Advances in Fan and Compressor Blade Flutter Analysis and Predictions", *Journal of Aircraft,* Vol. 12, No. 4, 325-332,April 1975.

4.   D. G. Halliwell, "The Characteristics, Prediction and Test Analysis of Supersonic Flutter in Turbofan Engines", *Vibration in Rotating Machinery,* Institution of Mechanical Engineers Conference Publication 1976=9, 181-185, 1977.

5.   W. E. Thompson, "Fluid Dynamic Excitation of Centrifugal Compressor Rotor Vibrations", *Journal of Fluids Engineering, ASME Transactions,* Vol. 100, No,. 1, 73-78, March 1978.

6.   P. L. Kapitza, "Stability and Passage through the Critical Speeds of High Speed Rotors in the Presence of Friction" (in Russian), *Zhurnal Tekhnicheskoi Fiziki,* Vol. 9, No. 2, 124-127, 1939.

7.   H. J. Thomas, "Unstable Oscillations of Turbine Rotors Due to Steam Leakage in the Clearances of the Sealing Glands and Buckets" (in German), *Bulletin Scientifique, A.I.M.,* Vol. 71, 1039-1063, 1958.

8.   F. F. Ehrich, "Identification and Avoidance of Instabilities and Self-Excited Vibrations in Rotating Machinery", Paper No. 72-DE-21, ASME, May 1972.

9.   F. F. Ehrich, "An Aeroelastic Whirl Phenomena in Turbomachinery Rotors", Paper No. 73-DET-97, ASME, September 1973.

10. J. S. Alford, "Protecting Turbomachinery from Self-Excited Rotor Whirl", *Journal of Engineering for Power, ASME Transactions*, Vol. 87A, No. 4, 333-344, October 1965.

11. E. Pollman, H. Schwerdtfeger, H. Termuehlen, "Flow Excited Vibrations in High Pressure Turbines (Steam Whirl)", *Journal of Engineering for Power, ASME Transactions*, Vol. 100, No. 2, 219-228, April 1978.

12. A. G. Kostyuk, V. F. Shatokhin, N. M. Ivanov, "Calculation of the Threshold Capacity of Large Turbine Generators" (English Translation), *Thermal Engineering*, Vo. 21, No. 3, 19-25, 1974.

13. A. G. Kostyuk, M. E. Deich, G. S. Samoilovich, G. M. Troyanovskii, G. A. Filippov, A. E. Bulkin, "Some Problems of Increasing the Efficiency and Reliability of High Capacity Turbines" (English Translation), *Thermal Engineering*, Vol. 22, No. 12, 5-12, 1975.

14. A. G. Kostyuk, A. V. Kiryukhin, "Autoscillations and Stability of Turbine Rotors in Sleeve Bearings with Allowance for Nonconservative Aerodynamic Forces" (In Russian), *Teploenergetika*, Vol. 25, No. 9, 14-19, September 1978; (German Translation) *Archiv fur Energiewirtschaft*, Vol. 32, No. 12, 996-1005, 1978; (English Abstract) *Thermal Engineering*, Vol. 25, No. 9, p 71, 1978.

15. V. N. Olimpiev, "Problems of Preventing Low-frequency Vibrations of Shafts of High Capacity Steam Turbine Units" (English Translation), *Thermal Engineering*, Vol. 25, No. 9, 8-14, September 1978.

16. R. C. Dean, "On the Necessity of Unsteady Flow in Fluid Machines", *Journal of Basic Engineering, ASME Transactions*, Vol. 81D, No. 1, 24-28, March 1959.

17. W. Spannhake, "A Fluid Mechanics Problem in Turbomachine Research and an Essay on Its Solution" (In German), Mitteilungen der Instituts für Strömungsmachinen, T. H. Karlsruhe, Vol. 1, 1930.

18. A. A. Mikolajczak, "The Practical Importance of Unsteady Flow", *Unsteady Phenomena in Turbomachinery*, Conference Proceedings 177, AGARD, Paris, April 1976.

19. M. F. Platzer, "Unsteady Flows in Turbomachines – Review of Current Developments", *Unsteady Aerodynamics*, Conference Proceedings 227, AGARD, Paris, February 1978.

20. W. J. McCorskey, "Some Current Research in Unsteady Fluid Dynamics", *Journal of Fluids Engineering, ASME Transactions*, Vol. 99I, No. 1, 8-39, March 1977.

21. F. Sisto, "A Review of the Fluid Mechanics of Aeroelasticity in Turbomachines", *Journal of Fluids Engineering, ASME Transactions*, Vol. 99I, No. 1, 40-44, March 1977.

22. R. Pigott, "Forced and Self-excited Vibrations of Transonic Turbine Cascades", Ph. D. Thesis, University of Pennsylvania, 1975.

23. J. H. Horlock, "Fluctuating Lift Forces on Aerofoils Moving Through Transverse and Chordwise Gusts", *Journal of Basic Engineering, ASME Transactions,* Vol. 90D, No. 4, 495-500, December 1968.

24. H. Yeh, H. Naumann, "Unsteady Induced Velocities in a Cascade", 2nd JSME Symposium *Fluid Machinery and Fluidics,* 201-207, September, 1972.

25. R. Mani, "Compressibility Effect in the Sears-Kemp Problem", *Fluid Mechanics Acoustics, and Design of Turbomachinery,* SP-304, Pt II, 513-533, NASA, 1974.

26. B. Lakshminarayana, "The Nature of Flow Distortion Caused by Rotor Blade Wakes", *Unsteady Phenomena in Turbomachines,* Conference Proceeding 177, AGARD, Paris, April 1976.

27. S. Fleeter, R. L. Jay, W. A. Bennett, "Wake Induced Time-variant Aerodynamics Including Rotor-Stator Axial Spacing Effects", *Nonsteady Fluid Dynamics,* ASME Special Publication, 147-163, December 1978.

28. H. G. Stever, "Condensation Phenomena in High Speed Flow", Section F. *Fundamentals of Gas Dynamics,* Vol. III, Jet Propulsion Series, Princeton University Press, 1958.

29. G. A. Saltanov, "Nonstationary Flows of Superheated and Condensing Steam" (in Russian), *Prave Instytutu Maszyn Przeplywowych,* Vol. 70-72, 433-451, 1976.

30. G.E.A. Meier, "Shock-induced Flow Oscillations in a Laval Nozzle", IUTAM Symposium Transonicum II, Göttingen, September 1975.

31. M. E. Deich, A. G. Kostyuk, G. A. Saltanov, G. A. Filippov, A. N. Kukushkin, G. P. Simanovskii, "Analysis of Tranient Processes in the Flow Sections of Wet Steam Turbines" (English Translation), *Thermal Engineering,* Vol. 24, No. 2, 28-34, February 1977.

32. B. N. Troyanoskii, E. V. Majorskii, V. V. Lakin, B. A. Garagulya, "Supersonic Cascades in the Last Stages of High-Capacity Steam Turbines" (English Translation). *Thermal Engineering,* Vol. 24, No. 10, 7-12, 1977.

33. Y. V. Rzheznikov, E. A. Boitsova, O. A. Kuzinenko, "Determination on a Static Model of the Stiffness Factor of the Transverse Circulation Force in Steam Turbines" (English Translation), *Thermal Engineering,* Vol. 24, No. 2, 48-53, February 1977.

34. B. Lakshminarayana, "Methods of Predicting the Tip Clearance Effects in Axial Flow Turbomachinery", *Journal Basic Engineering, ASME Transactions,* Vol. 92D, No. 3, 467-482, September 1970.

35. F. Sisto, "Aeromechanical Response", *Distortion Induced Engine Instability*, Lecture Series 72, AGARD, Paris, November 1974.

36. H. Mokelke, "Prediction Techniques", *Distortion Induced Engine Instability*, Lecture Series 72, AGARD, Paris, November 1974.

37. B. Lakshminarayana, "Effects of Inlet Temperature Gradients on Turbomachinery Performance", *Journal Engineering for Power, ASME Trans.* Vol. 97A, No. 1, 64-74, January 1975.

38. E. P. Bruce, R. E. Henderson, "Axial Flow Rotor Unsteady Response to Circumferential Inflow Distortions", *Unsteady Phenomena in Turbomachinery*, Conference Proceedings 177, AGARD, Paris, April 1976.

39. R. S. Mazzawy, "Multiple Segment Parallel Compressor Model for Circumferential Flow Distortion", *Journal Engineering for Power, ASME Trans.* Vol. 99A, No. 2, 288-296, April 1977.

40. J. Fabri, "Growth of a Perturbation in an Axial Flow Compressor", *Journal Engineering for Power, ASME Trans.* Vol. 101, No. 1, 87-94, January 1979.

41. R. E. Henderson, "Unsteady Response of a Blade Row from Measurements of the Time-mean Total Pressure", Paper No. 73GT-94, ASME, April 1973.

42. B. Satyanarayana, "Some Aspects of Unsteady Flow Past Airfoils and Cascades", *Unsteady Phenomena in Turbomachinery*, Conference Proceeding 177, AGARD, Paris, April 1976.

43. R. E. Henderson, J. H. Horlock, "An Approximate Analysis of the Unsteady Lift on Airfoils in Cascade", *Journal Engineering for Power, ASME Trans.*, Vol. 94A, No. 4, 233-240, October 1972.

44. B. Satyanarayana, R. E. Henderson, J. P. Gostelow, "Comparison Between Experimental and Theoretical Fluctuating Lift on Cascades at Low Frequency Parameters", Paper No. 74GT-78, ASME, March 1974.

45. J. H. Horlock, E. M. Greitzer, R. E. Henderson, "The Response of Turbomachine Blades to Low Frequency Inlet Distortions", *Journal Engineering for Power, ASME Trans.*, Vol. 99A, No. 2, 195-203, April 1977.

46. H. Takata, S. Nagano, "Nonlinear Analysis of Rotating Stall", *Journal Engineering for Power, ASME Trans.*, Vol. 94A, No. 4, 279-293, October 1972.

47. E. M. Greitzer, "Surge and Rotating Stall in Axial Flow Compressors: I, II", *Journal Engineering for Power, ASME Trans.*, Vol. 98A, No. 2, 19-217, March 1975.

48. I. J. Day, N. A. Cumpsty, "Measurement Interpretation of Flow Within Rotating Stall Cells in Axial Compressors", *Journal Mechanical Engineering Science*, Vol. 20, No. 2, 101-114, April 1978.

49. P. Hergt, P. Krieger, "Radial Forces in Centrifugal Pumps with Guide Vanes", *Advance-Class Boiler Feed Pumps, Proceedings Inst. of Mechanical Engineers*, Vol. 184, No. 3N, 101-107, 1969-1970.

50. U. Domm, P. Hergt, "Radial Forces on Impellers of Volute Casing Pumps", *Flow Research on Blading*, Editor L. S. Dzung, 305-321, Elsevier Pub. Co. 1970.

51. H. F. Black, "Calculation of Forced Whirling and Stability of Centri- fugal Pump Rotor Systems", *Journal Engineering for Industry, ASME Trans.*, Vol. 96I, No. 3, 1076-1081, August 1974.

52. H. F. Black, "Lateral Stability and Vibrations of High Speed Centri- fugal Pump Rotors", *Dynamics of Rotors*, 56-74, Springer Verlag, New York, 1975.

53. S. Mizuki, Y. Kawashima, I. Ariga, "Investigation Concerning Rotating Stall and Surge Phenomena within Centrifugal Compressor channels", Paper No. 78GT-9, ASME, April 1978.

54. Y. Senoo, Y. Kinoshita, "Limits of Rotating Stall and Stall in Vane- less Diffuser of Centrifugal Compressors", Paper No. 78GT-19, ASME, April 1978.

55. C. Rodgers, "A Diffusion Factor Correlation for Centrifugal Impeller Stalling", *Journal Engineering for Power, ASME Trans.* Vol. 100, No. 4, 592-603, October 1978.

56. A. N. Abdelhamid, W. H. Colwill, J. F. Barrows, "Experimental In- vestigation of Unsteady Phenomena in Vaneless Radial Diffusers", *Journal Engineering for Power, ASME Trans.*, Vol. 101, No.1, 52-60, January 1979.

57. H. W. Emmons, "Introduction", *Compressor Stall, Surge and System Response*, Special Publication, ASME, 1960.

58. E. J. Taylor, "The Centrifugal Compressor", Section J, *Aerodynamics of Turbines and Compressors*, Vol. X, Jet Propulsion Series, Princeton University Press, 1964.

59. J. L. Dussourd, "An Investigation of Pulsations in the Boiler Feed System of a Central Power Station", *Journal Basic Engineering, ASME Trans.*, Vol. 90D, No. 4, 607-619, December 1968.

60. P. H. Rothe, P. W. Runstadler, "First-order Pump Surge Behavior", *Journal Fluids Engineering, ASME Trans.* Vol. 100, No. 4, 459-466, December 1978.

61. P. H. Rothe, P. W. Runstadler, F. X. Dolan, "Pump Surge Due to Two-phase Flow", *Polyphase Flow in Turbomachinery*, 121-137, Special Publication, ASME, December 1978.

62. H. M. Schultz, R. K. Miyasaki, T. B. Liem, R. A. Stanley, "Analog Simulation of Compressor Systems, A Straightforward Approach", CPD 74106, Instrument Society of America, 1974.

63. K. Toyama, P. W. Runstadler, R. C. Dean, "Experimental Study of Surge in Centrifugal Compressors", *Journal Fluids Engineering*, ASME *Trans.*, Vol. 99I, No. 1, 115-131, March 1977.

64. D. H. McQueen, "On the Dynamics of Compressor Surge", *Journal Mechanical Engineering Science*, Vol. 18, No. 5, 234-238, 1976.

65. J. L. Dussourd, G. W. Pfannebecker, S. K. Singhania, "Experimental Investigation of the Control of Surge in Radial Compressors Using Close Coupled Resistances", *Journal Fluids Engineering*, ASME *Trans.*, Vol. 99I, No. 1, 64-75, March 1977,

66. G. Gyarmathy, "Nonlinear Analysis of Surge Cycles", *Journal Fluids Engineering*, ASME *Trans.*, Vol. 99I, No. 1, 258-259, March 1977.

67. A. Kolnsberg, "Reasons for Centrifugal Compressor Surging and Surge Control", *Journal Engineering for Power*, ASME *Trans.*, Vol. 101, No. 1, 79-86, January 1979.

68. R. S. Mazzawy, "Surge-induced Structural Loads in Gas Turbines", Paper No. 79GT-91, March 1979.

69. W. H. Isay, "The Flow Through a Vibrating and Rotating Radial Cascade" (In German), *Zeitschrift fur Flugwissenschaft*, Vol. 6, No. 11, 319-328, 1958.

70. R. E. Henderson, "The Unsteady Design of Axial-flow Turbomachines", *Proceedings Joint Symposium on Design and Operation of Fluid Machinery*, Vol. II, 91-108, Colorado State University, June 1978.

71. E. P. Bruce, "Axial Flow Rotor Unsteady Performance", TM79-149, Applied Research Laboratory, Penn State University, August 14, 1979.

Table 1 Size-frequency Classification of Vibration Excitation Mechanisms

Topics	References
Blade thickness/blade passing phenomena	
Axial compressor blade flutter	19, 3, 2, 21
Axial turbine blade flutter	22
Wake flow excitation	23, 24, 25, 26, 27
Condensation shock wave excitation	28, 29, 30, 31, 32
Passage dimension/shaft synchronous phenomena	
Axial configuration:	
Rotor displacement dependent	7, 10, 33, 34
Orbital velocity dependent	
Inlet distortion	35, 36, 37, 38, 39, 40
Gusts	41, 42, 43, 44, 45
Rotating stall	46, 47, 48
Radial configuration:	
Rotor displacement dependent	49, 50, 51, 52
*Orbital velocity dependent	5
Rotating stall	53, 54, 55, 56
Bearing span/systems resonance	
Surge: General	57, 58
Pump	59, 60, 61
Compressor	62, 63, 64, 65, 66, 67, 68

* An example will be presented in the text.
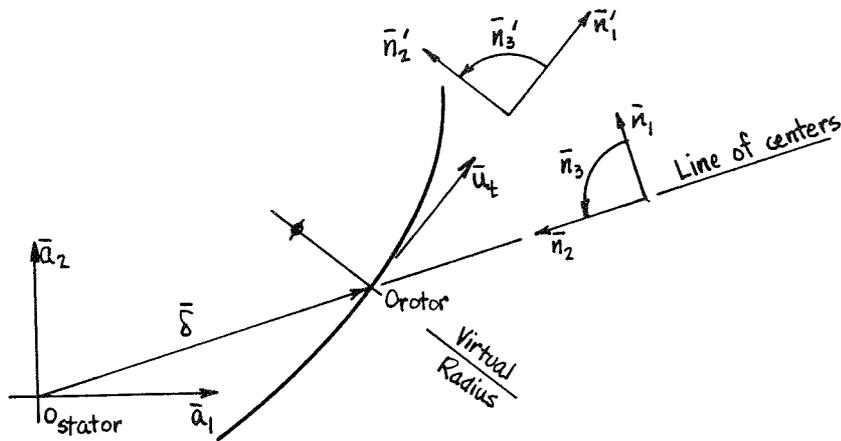
$\bar{n}_1$, $\bar{n}_1'$ cross-coupled component unit vectors

$\bar{n}_2$, $\bar{n}_2'$ direct component unit vectors

$$\bar{F} = \bar{F}_a + \bar{F}_b$$

Where $\bar{F}_a$ is the displacement dependent force,

$$\bar{F}_a = F_{a1}\bar{n}_1 - F_{a2}\bar{n}_2$$

and $\bar{F}_b$ is the velocity dependent force,

$$\bar{F}_b = F_{b1}\bar{n}_1' - F_{b2}\bar{n}_2'$$

Further the rotor displacement vector $\bar{\delta}$

$$\bar{\delta} = \delta(-\bar{n}_2)$$

and the orbital velocity vector $\bar{u}_t$ is

$$\bar{u}_t = u_t\bar{n}_1'$$

Since $\bar{F}_a$ and $\bar{F}_b$ are linear in $\bar{\delta}$ and $\bar{u}_t$ respectively

$$F_{a1} = a_1\delta, \qquad F_{a2} = a_2\delta$$

$$F_{b1} = b_1 u_t, \qquad F_{b2} = b_2 u_t$$

(Note: $F_1 = F_{b1}$, $F_2 = F_{b2}$ in text)

Figure 1   Description of Fluid Dynamic Forces
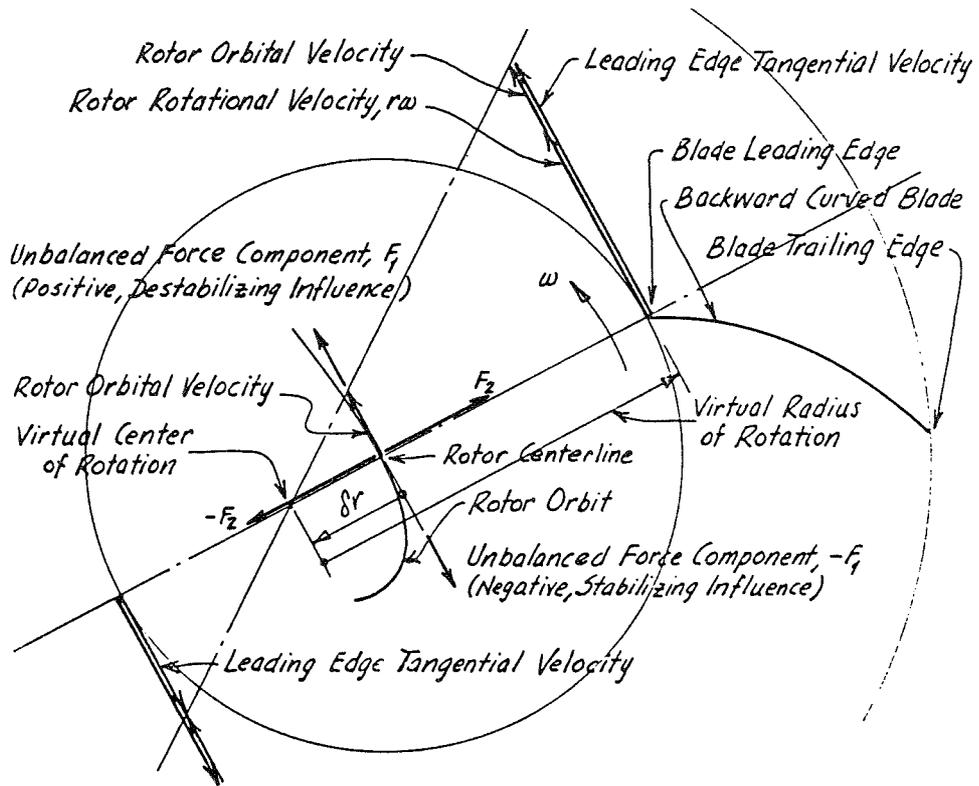
Figure 2 – Fluid Dynamic Excitation Force of a Radial Compressor Impeller
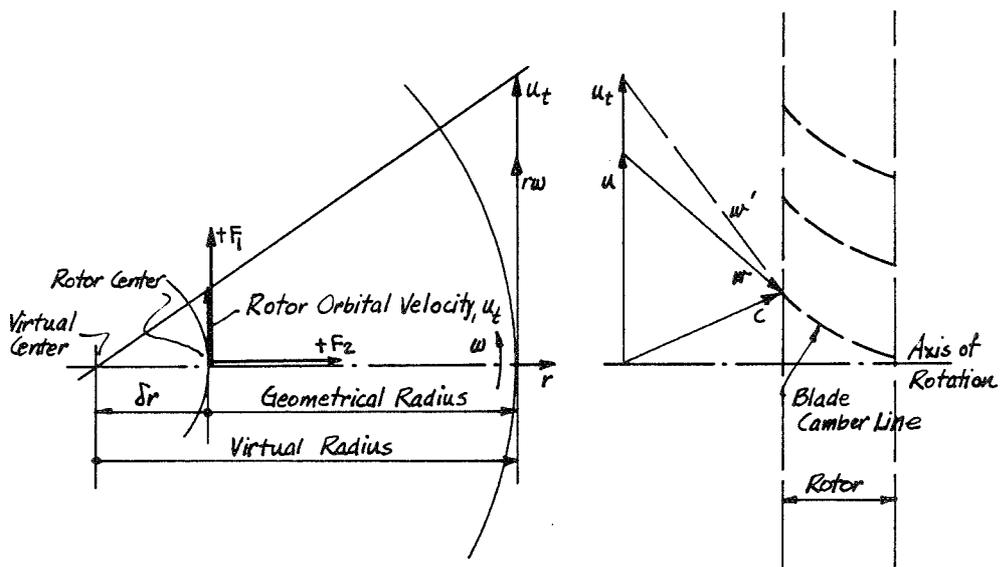
Figure 3   Fluid Dynamic Excitation Force of an Axial Compressor Rotor

SELF-EXCITED ROTOR WHIRL DUE TO TIP-SEAL LEAKAGE FORCES

B. Leie and H.-J. Thomas
Institut für Thermische Kraftanlagen
Technische Universität München, Germany

SUMMARY

Self-excited vibrations may cause severe limitation of the performance of turbomachines. Bearing forces, elastic hysteresis and forces from the fluid flow through clearances are known as origin. Forces from the leakage flow became important with increasing performance because they increase with it. Theoretical approaches and extensive experiments were made to determine the dependence of the forces from the leakage losses and from rotating flow in the radial gaps. Therefore evaluation of the exciting forces for the investigated types of turbine stages should be possible.

Former investigations of the vibration system set the mixed damping coefficients of the bearings to zero, the calculation model was partly extremly simplified. A comparison with a symmetrical rotor without negligence of the mixed damping coefficients shows the limits of the way to do so and presents all important parameters for stability. In certain respect the stiffness and damping coefficients itself are not important, only the relation of them to each other. With a given bearing and its coefficients as a function of the so-called Sommerfeld-number the relation between running and critical speed as well as the ratio bearing/rotor stiffness are the determining parameters for stability. Uncertainties in the bearing coefficients, which may result from differences between ideal test bearing and real rotor bearing are able to change the result in stability calculation in a wide range.

INTRODUCTION

Self-excited rotor bending vibrations are of great importance for turbomachinery. While it is possible to reduce vibrations caused by the unbalance of the rotor to a sufficient degree by balancing, the self-excited rotor whirl is only to be eliminated by design corrections. In thermal turbomachinery it seems there are three origins for self-excited rotor whirl. The first kind is the internal damping or elastic hysteresis, the second arises from the lubricating oil-film in the journal bearing (oil whip) and the third is the so called clearance excitation, induced by fluid flow in radial gaps. The two first causes depend on the running speed of the rotor, the vibrations appear quite suddenly at a certain speed limit. The clearance-excitation increases with increasing power of the turbomachine, therefore the vibrations appear suddenly at a certain threshold power. The frequency of these vibrations generally corresponds to the lowest critical speed of the rotor. The following considerations ignore the rarely important influence of elastic hysteresis.

303

VIBRATION EXCITING FORCES AT THE ROTOR

Bearing- and clearance excitation forces are instationary external forces at the rotor. With x_B and y_B as the displacement in two rectangular coordinates the bearing force follows with

$$B = \begin{bmatrix} B_x \\ B_y \end{bmatrix} = - \begin{bmatrix} c_{xx} & c_{xy} \\ c_{yx} & c_{yy} \end{bmatrix} \begin{bmatrix} x_B \\ y_B \end{bmatrix} - \begin{bmatrix} d_{xx} & d_{xy} \\ c_{yx} & d_{yy} \end{bmatrix} \begin{bmatrix} \dot{x}_B \\ \dot{y}_B \end{bmatrix} \tag{1}$$

The spring- and damping coefficients c and d are defined as functions of the so called Sommerfeld-number. If the coupling values - that are the coefficients with mixed indices - are not zero, a displacement of the journal leads to a force rectangular to the displacement. That force is the cause for self-excited vibrations (oil whip) after reaching a certain running speed (ref. 1 and 2).

The clearance excitation forces do not act on the journal but on the sur- face of the rotor which is in contact with the working fluid. They result from the unsymmetrical fluid flow through the radial clearances at rotor and blading which appears according to the eccentricity between rotor and casing. Thereby cross forces as well as moments are able to act on the rotor. Some theoretical and experimental investigations however show - with respect to the actual pos- sible accuracy of recording these effects - that it is sufficient to have only regard to the cross force as the essential factor in clearance excitation

$$Q = \begin{bmatrix} Q_x \\ Q_y \end{bmatrix} = \begin{bmatrix} 0 & -q \\ q & 0 \end{bmatrix} \begin{bmatrix} x \\ y \end{bmatrix} \tag{2}$$

where x and y are the coordinates of rotor displacement.

Primary this effect was explained and calculated based on the leakage losses of blade tips or labyrinths. From eccentric position in the casing non uniform tangential forces result at the turbine wheel, figure 1. The resultant of these forces - the clearance excitation force Q - acts rectangular to the displacement direction. In case of a compatible circumpolar vibration of the rotor the force Q anticipates 90° to the displacement. Is the loss of energy from damping less than the work done by the exciting force Q, then amplitudes will increase. At compressors Q acts in the opposite direction and is therefore able to excite countermoving vibrations. As tangential forces and power of the turbomachine are proportional vibrations begin at a certain threshold power (ref. 3 and 4).

Tests with shrouded turbine wheels showed considerable larger cross forces than explicable from leakage losses. The cause therefor is a non uniform pres- sure distribution above the shroudings as a result of the unsymmetrical fluid flow through the sealing gap. Such cross forces arise at shaft glands too (ref. 5). By this means generally for the coefficient q in equation (2) must be put up

$$q = q_S + q_D \tag{3}$$

with q_S as the part from clearance losses and q_D as the part from pressure distribution. With U for the tangential force, p the pressure, φ the circumference angle and e the displacement of the shaft you get according to figure 1

$$q_S = \frac{1}{e} \int_{\varphi=0}^{2\pi} \cos\varphi \; dU; \quad q_D = \frac{1}{e} \int_{z=0}^{b} \int_{\varphi=0}^{2\pi} \sin\varphi \; p \; r \; d\varphi \; dz \tag{4}$$

where r is the radius of the shrouding, z the coordinate in axial direction and b the width of the shrouding. q_S in equation (4) can be developed furthermore by known linear statements on clearance losses. Signifies $U_{is} = \dot{m} \cdot \Delta h_{is}/u$ the isentropic tangential force of the turbine stage with $\dot{m}$ the mass flow, Δh_{is} the isentropic enthalpy difference and u the average circumferential speed you can put up

$$q_S = \frac{U_{is}}{1''} \; K_S \tag{5}$$

1" is the length of the rotor blade and K_S a factor which takes into account all essential parameters (ref. 4). For the part q_D several numerical procedures were investigated. You can put up (ref. 6)

$$q_D = \frac{\pi}{4s} \; r \; b \; \Delta p_B \; K_D \tag{6}$$

where s is the radial clearance, Δp_B the pressure difference at the shrouding and K_D a factor which depends essential – in case of given design of the sealing – only on the kinetic energy of the flow in circumferential direction divided by Δp_B

$$C_E^* = \frac{\rho \; c_{1u}^2}{2\Delta p_B} \tag{7}$$

ρ is the density and c_{1u} the tangential component of the absolute outlet velocity of the stator blade flow. Figure 2 e.g. shows the theoretical functional relation between K_D and C_E^* for two shrouding designs.

EXPERIMENTAL INVESTIGATION OF EXCITING FORCES

To obtain data as reliable as possible, applicable for design of turbomachines and to state theoretical assumptions, numerous tests at different turbine stage types (impulse and reaction type) were untertaken (ref. 7). Figure 3 shows three investigated stage types. It was possible to measure the cross force Q directly dependent from the adjustable eccentricity, partly the pressure distribution above the shrouding too. Such "nearly-static" force measurement was sometimes completed by real vibration tests. Measurements at shroudless

blading confirm, that the exciting force is calculable using the part q_S. On the other hand tests with shroudings have shown the important influence of q_D for that stage types. Because pressure distribution measurements were not possible for all test series, the results were pointed out according to equation (5) as dimensionless "clearance-excitation-coefficient"

$$K_2 = \frac{Q/e}{U_{is}/1''} = \frac{q \cdot 1''}{U_{is}} \tag{8}$$

K_2 of course combines the effects from leakage losses and pressure distribution. Figure 4 shows results of a 1-stage and 3-stage test rotor with 50 % reaction-blading and a stepped 3-chamber labyrinth at stator and rotor shroudings. K_2 is plotted over the load factor $\psi = 2\Delta h_{is}/u^2$. In figure 5 the results of a chamber-stage with low reaction is plotted. In both cases the part from leakage losses (corresponding K_S) is drawn in for comparison.

The part of pressure distribution at the exciting force is particularly high for impulse- and low-reaction-stages because of the heavy swirl-flow in the gap between stator and rotor wheel. That shows figure 5 and is possible to deduce from figure 2. For that reason further tests were made measuring the pressure distribution too (ref. 8). The large influence of swirl flow suggests to reduce the exciting force by disturbing the circumferential component of flow. Therefore three labyrinth designs were investigated according to figure 6. For disturbing the swirl-flow axial sheet strips were mounted in chamber one (design B) and chamber one to three (design C). In figure 7 the testing results are plotted. As shown it was possible to reduce the exciting force essentially by help of swirl-disturbing-sheets respectively to eliminate it. Anyway it is important to choose an optimal layout; obviously design B leads to considerable exciting forces with changed sign which may excite countermoving vibrations. For the rest at this stage the part of pressure distribution is exceeding; the part from leakage losses does not correspond with theory or is vectorial compensated – which is more probable – by the resultant force from pressure distributions, in case B even over-compensated.

THE STRUCTURE OF THE VIBRATION SYSTEM

For investigation of rotor stability in the first instance a symmetrical laval-rotor with journal bearings may be suitable because of the large quantity of parameters. Thereby the following questions are to take into consideration:

1. Simplification limits of the rotor model.

2. Influences coming from the bearing properties, especially from data faults or manufacturing tolerances.

Figure 8 presents the vibration system with mass m, rotor-stiffness c_R; both bearings are equal. With equations (1) and (2) as well as the mass forces it is easy to put up the differential equation system for translational motion of the rotor-disk derived from the balance of the forces (ref. 8).

306

$$a_0\ddot{y} + a_1\ddot{x} + a_2\ddot{x} + a_3\dot{y} + a_4\dot{x} + a_5\dot{y} + a_6x + a_7y = 0$$

$$b_0\ddot{x} + b_1\ddot{y} + b_2\ddot{y} + b_3\ddot{x} + b_4\dot{y} + b_5\dot{x} + b_6y + b_7x = 0$$

<div align="right">(9)</div>

The coefficients a and b are combinations of mass, exciting parameter as well as spring- and damping coefficients of the system. The usual starting solution leads to a characteristic equation of 6th degree for the complex natural frequencies which are imaginary at the stability threshold. By iterative solution the maximum of excitation is computed. It at least depends on the relation of stiffness rotor/bearing, to the type of bearing, the Sommerfeld-number and the relation between running speed and ciritical speed of the rigid supported rotor (tuning of system).

A more simplified model (ref. 9) ignores the coupling coefficients of bearing damping. The components of bearing force coming from the coupling coefficients of stiffness are transposed to the centre of mass, the force from damping too. Stiffness of bearings and rotor shaft are considered as spring series. In that way we get the differential equations

$$m\ddot{x} + d_x\dot{x} + c_x x = -(\bar{c}_{xy} + q)\, y$$

$$m\ddot{y} + d_y\dot{y} + c_y y = -(\bar{c}_{yx} - q)\, x$$

<div align="right">(10)</div>

The spring coefficients c respectively $\bar{c}$ and damping coefficients d represent the effect of the parameters of rotor and bearings together. Coupling between x- and y-axis is pointed out by the coupling coefficients of bearings and clearance exciting force alone. For the stability threshold there is a closed solution. Also here the result only depends on relations between the parameters of the system. For sufficient stability it seems to be important - besides the damping - to choose the anisotropy of springs as great as possible.

The more simplified system (10) compared with the exact system (9) shows the usability of the simplified system for qualitative conclusions; on the other hand - dependent on the given conditions - for quantitative investigations large differences may occur. Obvious the simplified calculation is only exact for an inelastic rotor. For real bearings the use of the solution according equation (9) is advisable because of the sensitivity of bearing coefficients as a function of bearing geometry and manufacturing tolerance. Thereby all parameters can change their value the same time, and depending on bearing type and rotor stiffness this might result in very large changes of stability threshold. Unfortunately these changes are small for the not so interesting (because more unstable) cylindrical journal bearing while they are larger for other types of bearings. A clear prediction of the sign of the change is not possible.

Exact calculation from equation (9) using coupling coefficients of bearing damping too gave following results: A larger stiffness ratio rotor/bearing leads to increase or decrease of stability threshold, increasing bearing load acts in the same unpredictable way. With increasing of the ratio running speed/critical speed you will nearly always get a deterioration of the stability threshold. The omission of the coupling coefficients of damping influences the results in different amount and direction, therefore an omission of that bearing

influence is not recommendable; the fault can reach in same case a very large amount, see figure 9, wherein the ordinate S means the ratio of clearance excitation/rotor stiffness: $S = q/c_R$.

The results relating to the influence of Sommerfeld-number and stiffness ratio show that increasing bearing load can improve stability but it must not. In order to answer the question about the reliability of the calculation results dependent on the bearing data systematically only one spring- or damping coefficient was changed by 10 % and the relative change of result was computed. Depending on the ratio of running speed/critical speed and ratio of stiffness for elliptical and three-wedge bearings we got differences up to 300 % to 400 % in stability threshold. These results can be amplified or moderated by taking into account all data faults, see table 1. A good prediction depends essentially on exact geometric bearing conditions – as used at the test bearings – that means exact manufacturing and mounting; on the other hand it is uncertain wether the exactness of bearing data is sufficient. Based on the knowledge of today the calculation looks pretty uncertain. But it is possible to use the tendencies of the results as criteria for design changes at the bearings, as was already stated by experience.

CONCLUSIONS

Clearance excitation forces originate from non uniform leakage losses and from non uniform pressure distribution above shroudings or shaft glands as function of the eccentricity of the rotor. Theroretical investigation of these effects was assisted by numerous experiments, so the clearance excitation coefficients should be reliable for the tested stage types. Swirl preventing sheets at shrouded bladings are able to reduce or eliminate the excitation forces.

Considering the structure of the vibration system the great influence of journal bearings on the stability of the rotor is shown. For stability especially the anisotropy of stiffness is essential. The calculation model should be extended for multiple cased turbomachinery respectively shafts with more than two bearings, methods therefor are known. The strong dependence of the stability on bearing parameters leads to the idea to try to obtain the anisotropy not by help of the bearing geometry but by suitable design of the bearing pedestal.

REFERENCES

1. Kollmann, K.; Someya, T.: Lagerinstabilität eines Turborotors. MTZ 25 (1964) pp. 97-102

2. Glienicke, J.: Experimentelle Ermittlung der statischen und dynamischen Eigenschaften von Gleitlagern für schnellaufende Wellen. Fortschr.Ber. VDI-Z. Reihe 1, Nr. 22 (1976)

3. Thomas, H.-J.: Instabile Eigenschwingungen von Turbinenläufern, angefacht durch die Spaltströmung in Stopfbuchsen und Beschauflungen. Bull. de l'AIM 71 (1958) pp. 1039-1063

4. Thomas, H.-J.: Thermische Kraftanlagen. Berlin, Heidelberg, New York: Springer-Verlag 1975

5. Alford, J. S.: Protecting turbomachinery from self-excited rotor whirl. Trans. ASME J. of Engng. for Power 87 (1965) pp. 333-344

6. Urlichs, K.: Durch Spaltströmungen hervorgerufene Querkräfte an den Läufern thermischer Turbomaschinen. Diss. TU München 1975, s.a. Ing.-Arch. 45 (1976) pp. 193-208

7. Wohlrab, R.: Experimentelle Ermittlung spaltströmungsbedingter Kräfte an Turbinenstufen und deren Einfluß auf die Laufstabilität einfacher Rotoren. Diss. TU München 1975

8. Leie, B. R.: Querkräfte an Turbinenstufen und deren Einfluß auf die Laufstabilität einfacher gleitgelagerter Rotoren. Diss. TU München 1979

9. Thomas, H.-J.: Zur Laufstabilität einfacher Turborotoren, besonders bei Spalterregung. Konstruktion 30 (1978) 9, pp. 339-344

Table 1. CHANGE OF MAX. SYSTEM EXCITATION (ΔS) IN PERCENT BY CHANGING ONE COEFFICIENT 10 %

width/diameter W/D = 0.8
ratio running/critical speed ω_B/ω_k

$c_R/2c_{yy}$		ELLIPTICAL BEARING				THREE WEDGE BEARING			
		o.2		o.6		o.2		o.6	
Δc_{ik}, Δd_{ik}		+1o%	−1o%	+1o%	−1o%	+1o%	−1o%	+1o%	−1o%
	ω_B/ω_k								
c_{xx}	o.8	−4	5	−3	3	−5	6	−5	6
	1.6	−11	11	−14	13	−37	54	−61	315
c_{xy}	o.8	3	−3	−27	28	−2	2	−5	5
	1.6	−74	187	−8o	413	−67	63	−84	455
c_{yx}	o.8	−5	4	−2o	22	−3	3	−6	6
	1.6	−69	168	−84	384	−68	69	−81	459
c_{yy}	o.8	4	−6	2o	−27	−6	7	7	−8
	1.6	173	−99	6o4	−93	57	−41	6o7	−87
d_{xx}	o.8	−7	8	34	−37	4	−5	8	−9
	1.6	145	−72	313	−78	62	−67	375	−7o
d_{xy}	o.8	−3	2	−9	8	1	−1	−1	1
	1.6	11	−11	−2o	16	1	−1	62	−62
d_{yx}	o.8	2	−2	−6	5	2	−2	−1	1
	1.6	−2o	16	−23	21	2	−2	−1o	413
d_{yy}	o.8	5	−6	16	−14	7	−7	1o	−11
	1.6	23	−16	−51	123	69	−65	334	−49

310

FOR EXPLANATION OF THE CLEARANCE EXCITATION
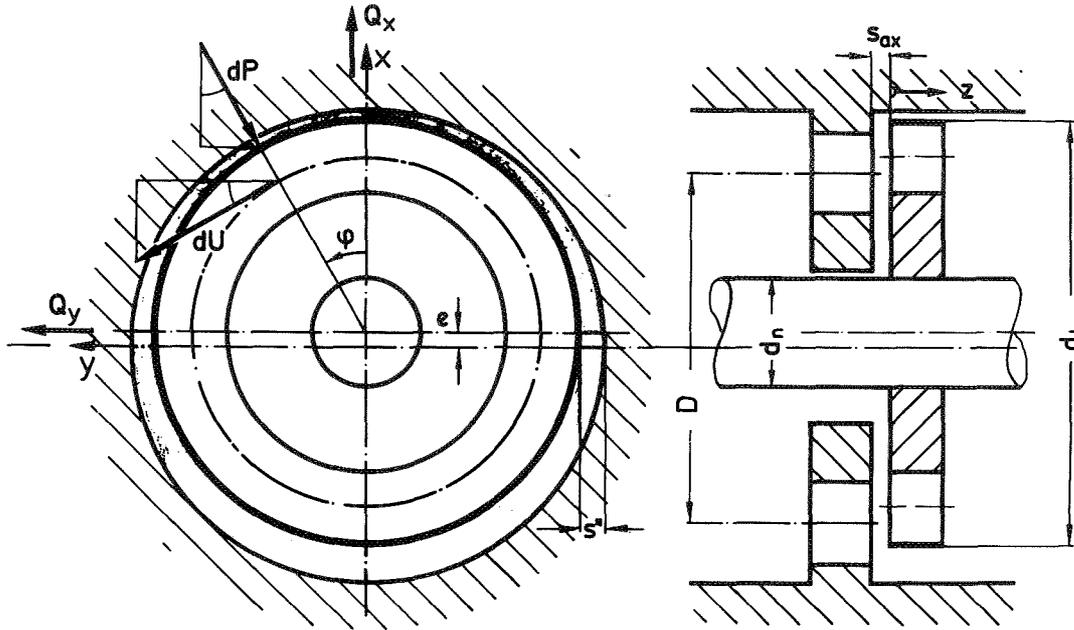
Figure 1.

CALCULATED COEFFICIENT K_D OF CLEARANCE EXCITATION FORCE
RESULTING FROM PRESSURE DISTRIBUTION

a   flat shrouding;   b   stepped shrouding with 3 sealing tips

RELATED FLOW ENERGY C_E^*
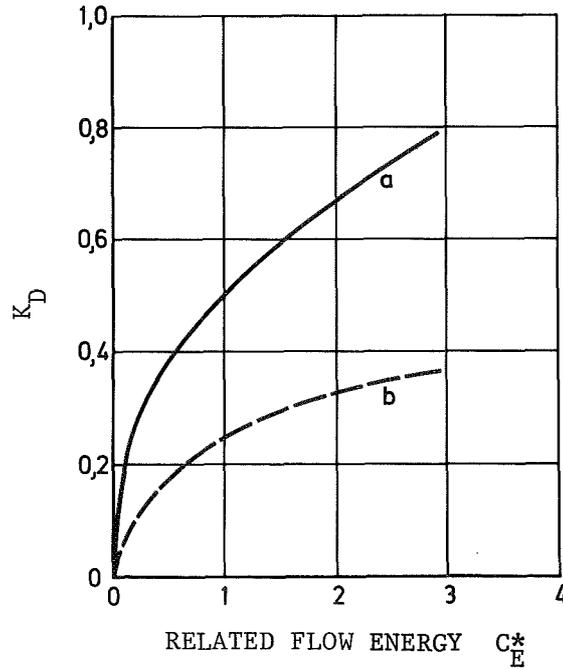
Figure 2.

INVESTIGATED STAGE TYPES
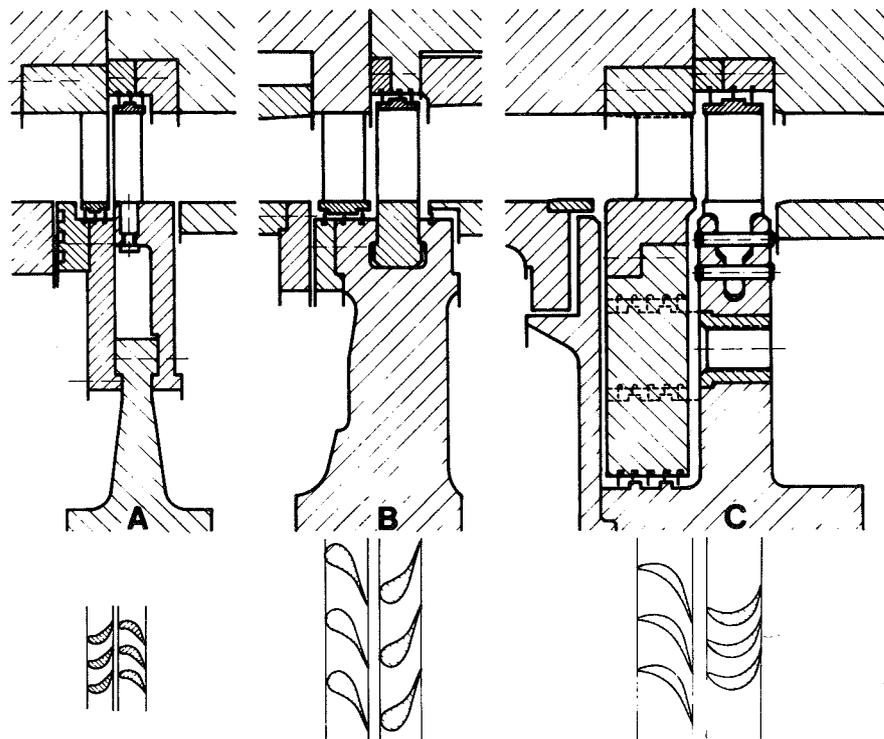
Figure 3.

CLEARANCE EXCITATION COEFFICIENT FOR STAGE B (50 % REACTION)

axial clearance s_{ax} = 3.3 mm

O, △   stage displacement   ◇ ⎫   calculated
  □   rotor displacement   ● ⎬   from
  ✕   stator displacement   ✕ ⎭ leakage losses
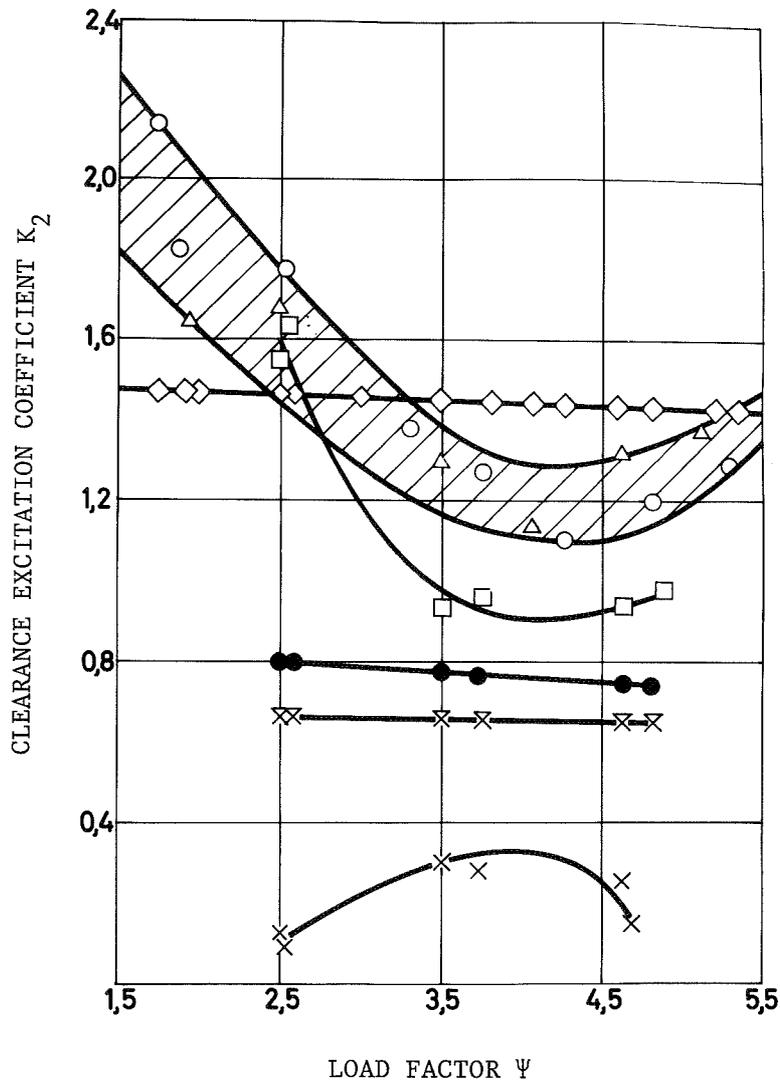
Figure 4.

CLEARANCE EXCITATION COEFFICIENT FOR STAGE C (LOW REACTION TYPE)

axial clearance
- △ 2.2 mm
- ▢ 2.5 mm
- ✕ 3.9 mm
- ◇ 4.2 mm

○ calculated from leakage losses
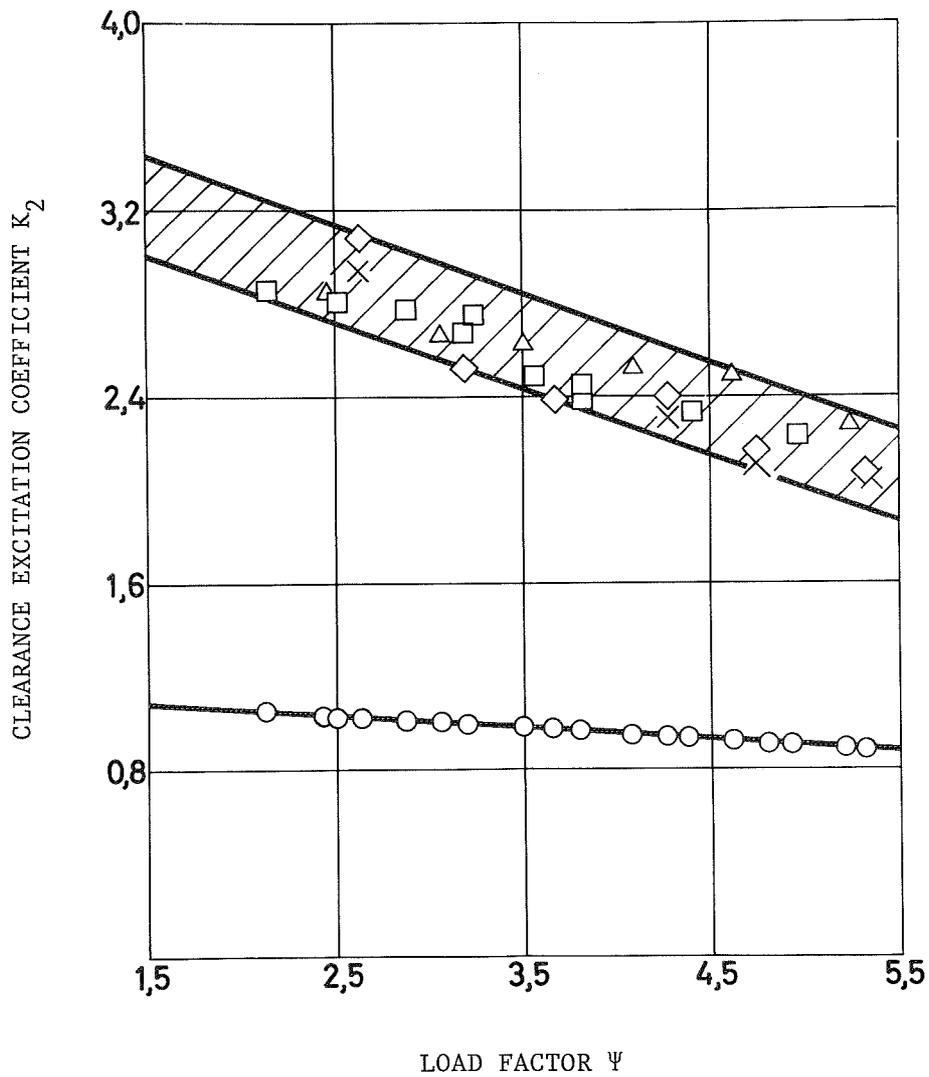
Figure 5.

INVESTIGATED LABYRINTH DESIGNS
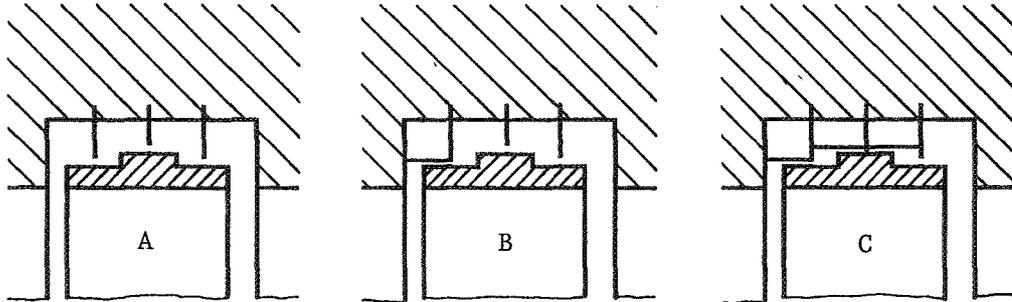
Figure 6.

TESTING RESULTS FOR 3 LABYRINTH DESIGNS (A,B,C)

K_2 clearance excitation coefficient
Ψ load factor
C_E^* related flow energie

□ ———— from force measuring
△ —·— integration of pressure distribution
— — — calculation from leakage losses
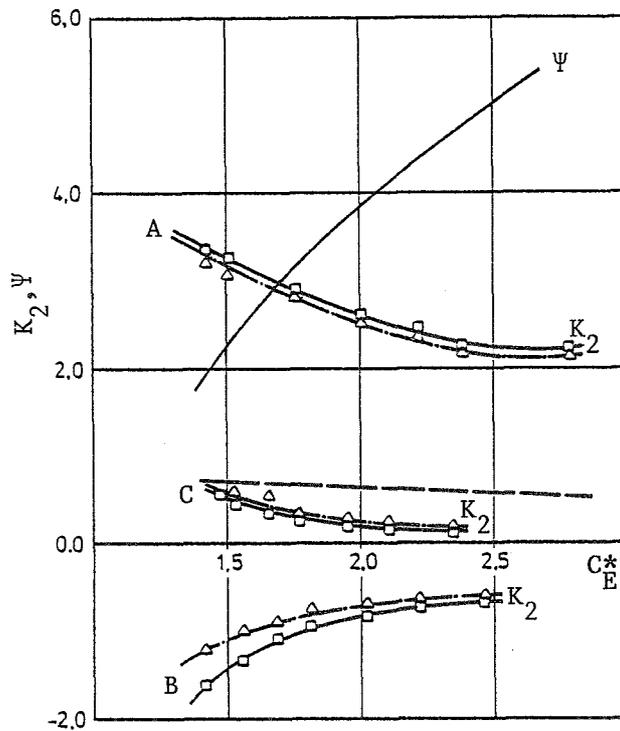
Figure 7.

SIMPLIFIED ROTOR MODEL
(coupling springs and dampers not drawn)
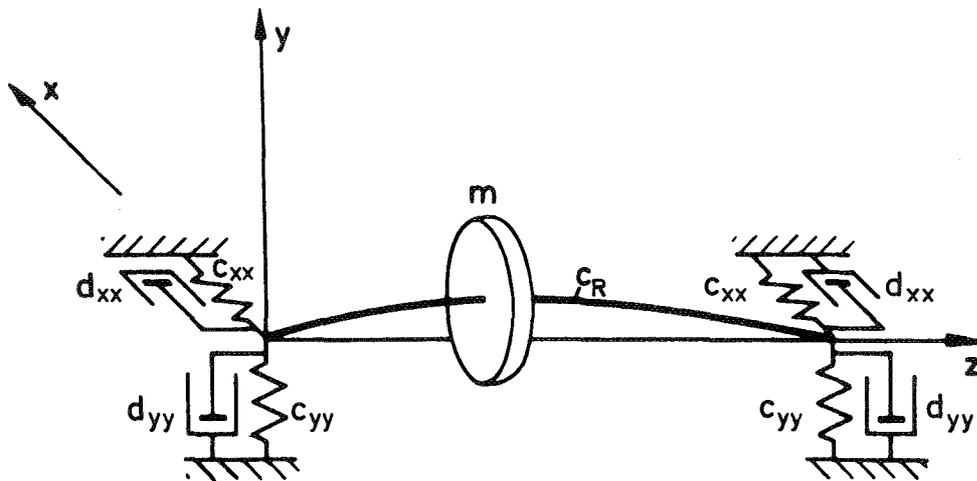
Figure 8.

MAX. SYSTEM EXCITATION FOR 4 BEARING TYPES
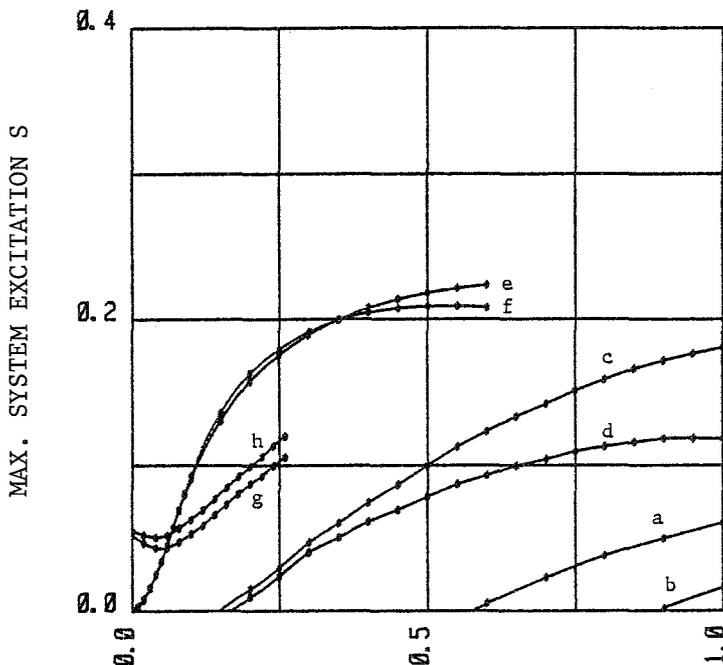
SOMMERFELD-NUMBER So

					$d_{xy}=d_{yx}=0$	$d_{xy}\neq d_{yx}\neq0$
width/diameter	W/D	= 0.8	cylindrical journal			
stiffness ratio	$c_R/2c_{yy}$	= 0.6		bearing	a	b
running/			elliptical bearing		c	d
critical speed	ω_B/ω_k	= 1.6	three-wedge bearing		e	f
			tilting pad bearing		g	h

Figure 9.

FLUID FORCES ON ROTATING CENTRIFUGAL IMPELLER

WITH WHIRLING MOTION*

Hidenobu Shoji and Hideo Ohashi
University of Tokyo
Tokyo, Japan

SUMMARY

Fluid forces on a centrifugal impeller, whose rotating axis whirls with a constant speed, have been calculated by using unsteady potential theory. To simplify the problem, it is assumed that the flow is incompressible and two dimensional, the impeller is surrounded by vaneless diffuser and the eccentricity is constant and small. Calculations are performed for various values of whirl speed, number of impeller blades and angle of blades. Some typical examples of results are shown in vector diagrams. Although the results of this paper are obtained for simplified geometries under idealized assumptions, they will suggest us the nature of fluid forces acting on whirling impeller.

INTRODUCTION

Recent advances in rotor dynamics made it possible to analyse very complicated rotor system like multi-stage pump rotor and multi-bearing turbogenerator shafting. In these analyses the largest weakness seems still to lie in the assumption of radial fluid forces acting on rotor elements such as seal rings, balance pistons and impellers. Many studies have been made and are being carried on this subject; just to mention a few, contribution of Black to pressure seal and centrifugal impeller (ref. 1,2) and of Acosta to centrifugal impeller (ref. 3).

As to radial forces acting on centrifugal impellers, numerous studies and informations have been accumulated on their steady part caused mainly by asymmetric configuration of volute casings. To the contrary limited studies (ref. 2,3) have been published on the unsteady part of radial forces, which is caused by the whirling motion of rotating impeller. This is the very information sought for the improvement of rotor analysis. Most of them are, however, quasi-steady analyses, in which the effect of shed vortices is disregarded.

In this paper, the radial force of a rotating impeller with arbitrary whirling motion is reduced from the flow fields in and outside of the impeller, applying familiar singularity method for the calculation of unsteady potential flow. Though the flow in a real centrifugal turbomachine is very complex because of asymmetric geometry of casing and strong viscous effect in impeller passage for example, following simplifications and assumptions are introduced in the present theory.

---

*Not presented at workshop.

(1)   The fluid is incompressible and inviscid, and the flow is two dimentional and irrotational in the absolute coordinate system.

(2)   The region outside of the rotor is unbounded and free of vanes.

(3)   The ratio of whirl eccentricity to the radius of the impeller is so small that its square can be neglected.

(4)   The flow rate, the prerotation of suction flow, the rotational speed of the impeller and the whirling speed of the shaft center are constant.

(5)   Blades of impeller have no thickness and have the shape of logarithmic spiral.

(6)   Steady part of the flow satisfies the condition of shockless entry at the leading edges of the blades and Kutta's condition at the trailing edges is assumed.

(7)   Free vortices are shed from the trailing edges and are carried downstream along steady streamlines with steady velocities.

After having derived formulations of radial forces for given parameters of whirl to rotational speed ratio, number of impeller vanes and blade angle, typical numerical results are demonstrated in vector diagrams.

SYMBOLS

N	number of blades	β	angle between radius and blades
r_1	inside radius of impeller	r_2	outside radius of impeller
ω	angular speed of impeller, positive clockwise		
Ω	angular speed of whirling motion, positive clockwise		
ε	eccentric radius	Q	flow rate
Γ_p	prerotation	ρ	density of fluid
γ	strength of vortices	$\bar{z}$	complex conjugate of z
i	complex unit with respect to coordinate		
j	complex unit with respect to time		

Subscripts

n	component normal to blade	t	component tangential to blade
s	steady component	0	quasi-steady component
w	component caused by free vortices		
ω	component caused by rotation effect		

318

ANALYSIS

Basic Consideration

The centrifugal impeller shown in figure 1 is considered. It rotates with a constant angular speed ω and its center whirls with a constant eccentric radius ε and a constant angular speed Ω. The boundary condition to the velocity field is in this case unsteady, and the flow around the impeller should be determined by unsteady analysis.

Let an arbitrary point on a reference blade be A. Then the geometry of the points A, O and O' are shown in figure 2, where point O and O' are the center of impeller and whirling motion, respectively. From the viewpoint of flow field, we interpret that the inlet flow to the impeller is unaffected by the whirling motion of the impeller, that is, the location of source Q (representing flow rate) and circulation Γ_p (representing prerotation) is fixed on point O'. Defining the angles β, θ_1 and θ_2 as shown in figure 2, and introducing the lengths AO'=ℓ, AO=r and OO'=ε, ℓ is expressed as

$$\ell = [r^2 + 2 r \cos(\theta_2 - \theta_1) + \varepsilon^2]^{1/2} \doteqdot r [1 + \varepsilon/r \cos(\theta_2 - \theta_1)]$$

The velocity v_Q at A induced by source Q in the direction of O'A is

$$v_Q = \frac{Q}{2\pi\ell} \doteqdot \frac{Q}{2\pi r} [1 - \frac{\varepsilon}{r} \cos(\theta_2 - \theta_1)] \tag{1}$$

Similarly, the velocity v_Γ at A induced by circulation Γ_p is

$$v_\Gamma \doteqdot \frac{\Gamma_p}{2\pi r} [1 - \frac{\varepsilon}{r} \cos(\theta_2 - \theta_1)] \tag{2}$$

where its direction is normal to the line O'A (positive clockwise).

The velocities v_Q and v_Γ are divided into two components respectively. They are v_{Qn} and $v_{\Gamma n}$ which are normal to blade, and v_{Qt} and $v_{\Gamma t}$ which are tangential to blade. As the reference blade intersects the line OA at angle β, the intersection angle between blade and line O'A is given approximately by $\beta + (\varepsilon/r) \sin(\theta_2 - \theta_1)$. Using the above relations, v_{Qn}, $v_{\Gamma n}$, v_{Qt} and $v_{\Gamma t}$ can be expressed as

$$v_{Qn} \doteqdot \frac{Q}{2\pi r} [\sin\beta + \frac{\varepsilon}{r} \sin(\theta_2 - \theta_1 - \beta)] \tag{3}$$

$$v_{\Gamma n} \doteqdot \frac{\Gamma_p}{2\pi r} [\cos\beta - \frac{\varepsilon}{r} \cos(\theta_2 - \theta_1 - \beta)] \tag{4}$$

$$v_{Qt} \doteqdot \frac{Q}{2\pi r} [\cos\beta - \frac{\varepsilon}{r} \cos(\theta_2 - \theta_1 - \beta)] \tag{5}$$

$$v_{\Gamma t} \doteqdot - \frac{\Gamma_p}{2\pi r} [\sin\beta + \frac{\varepsilon}{r} \sin(\theta_2 - \theta_1 - \beta)] \tag{6}$$

When point A on the blade is observed from a fixed coordinate system, A is moving in the normal direction to OA with velocity $r\omega$, and also in the normal direction to OO' with velocity $\varepsilon\Omega$. Both velocities are considered positive clockwise. On the other hand, when observed from the relative coordinate system fixed to the rotating impeller, absolutely still field is considered to have velocities $-r\omega$ and $-\varepsilon\Omega$ in the corresponding directions. These are divided into two components in the same way as v_Q and v_Γ. Using the relations

$d\theta_1/dt=-\Omega$ and $d\theta_2/dt=-\omega$, normal and tangential components $v_{\omega n}$ and $v_{\omega t}$ are

$$v_{\omega n} = -r\,\omega\,\cos\beta - \varepsilon\,\Omega\,\cos(\theta_2 - \theta_1 + \beta) \qquad (7)$$

$$v_{\omega t} = r\,\omega\,\sin\beta + \varepsilon\,\Omega\,\sin(\theta_2 - \theta_1 + \beta) \qquad (8)$$

Hereafter only relative coordinate system fixed to the impeller will be used. Every vector quantity such as location vector OA, force and velocity is indicated in this coordinate system by a complex number, whose real and imaginary (with imaginary unit i) part represents its component in two orthogonal axes.

Imaginary unit with respect to time, j, is also introduced to indicate the phase difference of oscillating quantities. Since two complex units i and j have completely different meanings, they should be distinguished carefully in the reduction of equations.

Let the location of A be z in the complex plane, normal component v_{Qn}, $v_{\Gamma n}$ and $v_{\omega n}$ of equations (3), (5) and (7) can be written as

$$v_{Qn} = \frac{Q}{2\pi|z|}\left[\sin\beta + j\frac{\varepsilon\,\bar{z}}{|z|^2}e^{j\beta}e^{j(\omega-\Omega)t}\right]_j = v_{Qn1} + v_{Qn2} \qquad (9)$$

$$v_{\Gamma n} = \frac{\Gamma_p}{2\pi|z|}\left[\cos\beta - \frac{\varepsilon\,\bar{z}}{|z|^2}e^{j\beta}e^{j(\omega-\Omega)t}\right]_j = v_{\Gamma n1} + v_{\Gamma n2} \qquad (10)$$

$$v_{\omega n} = \left[-|z|\,\omega\,\cos\beta - \frac{\varepsilon\,\bar{z}}{|z|}\Omega\,e^{-j\beta}e^{j(\omega-\Omega)t}\right]_j = v_{\omega n1} + v_{\omega n2} \qquad (11)$$

Since only absolute values of above three quantities are of interest, they are expressed as a complex with respect only to j. Further, tangential component v_{Qt}, $v_{\Gamma t}$ and $v_{\omega t}$ of equations (4), (6) and (8) are written as

$$v_{Qt} = \frac{Q}{2\pi|z|}\left[\cos\beta - \frac{\varepsilon\,\bar{z}}{|z|^2}e^{j\beta}e^{j(\omega-\Omega)t}\right]_j \cdot \left[\frac{z}{|z|}e^{i\beta}\right]_i$$

$$= v_{Qt1} + v_{Qt2} \qquad (12)$$

$$v_{\Gamma t} = -\frac{\Gamma_p}{2\pi|z|}\left[\sin\beta + j\frac{\varepsilon\,\bar{z}}{|z|^2}e^{j\beta}e^{j(\omega-\Omega)t}\right]_j \cdot \left[\frac{z}{|z|}e^{i\beta}\right]_i$$

$$= v_{\Gamma t1} + v_{\Gamma t2} \qquad (13)$$

$$v_{\omega t} = \left[|z|\,\omega\,\sin\beta + \varepsilon\,\Omega\,j\frac{\bar{z}}{|z|}e^{-j\beta}e^{j(\omega-\Omega)t}\right]_j \cdot \left[\frac{z}{|z|}e^{i\beta}\right]_i$$

$$= v_{\omega t1} + v_{\omega t2} \qquad (14)$$

All of the equations from (9) to (14) consist of the steady term indicated by subscript 1, and the unsteady term by subscript 2. Unsteady components are first order quantities in comparison with the steady component.

Since all the unsteady terms contain $e^{j(\omega-\Omega)t}$, this problem can be thought to be the periodic phenomenon with angular speed $(\omega-\Omega)$. All quantities within $[\ ]_j$ are complex with respect to j, and therefore their argument corresponds to the phase of sinusoidally oscillating phenomenon.

Steady Flow

As thickness of blades is disregarded, blades can be replaced by the distribution of vortices. The distribution of steady vortices γ_s has to satisfy the boundary condition that there is no crossing flow through blades. This leads to

$$\int_{z_L}^{z_T} \gamma_s(z') \ Re\left(\frac{N}{2\pi} \ \frac{z^N}{z^N - z'^N} \ \frac{e^{i\beta}}{|z|} \right) \ dz' + v_{Qn1} + v_{\Gamma n1} + v_{\omega n1} = 0 \qquad (15)$$

where z_L and z_T are the complex coordinates at leading and trailing edges of the blade. The integral should be carried out along the blade. For the calculation of the integrand of the above integral, the following relation is also used

$$\sum_{k=1}^{N} \frac{1}{z - z' e^{i2\pi k/N}} = \frac{N z^{N-1}}{z^N - z'^N} \qquad (16)$$

Combining equation (15) and the Kutta's condition at the trailing edge, γ_s can be determined. As shockless entry at the leading edge is assumed in this analysis, γ_s is restricted to finite value. Once γ_s is obtained, the velocity $v(z)$ at an arbitrary point z can be calculated by

$$v(z) = \int_{z_L}^{z_T} \gamma_s(z') \frac{N}{2\pi} \left(\overline{\frac{z^{N-1}}{z^N - z'^N}} \right) dz' + \frac{z(Q - i\Gamma_p)}{2\pi |z|^2} + i z \omega \qquad (17)$$

Unsteady Flow

First we consider the flow field shown in figure 3, in which N discrete vortices with phase difference $2\pi/N$ are ranged on a circumference with equal distance. Let the location of a reference vortex be z', the complex conjugate velocity at an arbitrary point z is given as

$$f(z,z') = u - iv = \frac{i\Gamma}{2\pi} \sum_{k=1}^{N} \frac{e^{-j2\pi k/N}}{z - z' e^{i2\pi k/N}}$$

$$=\frac{i N \Gamma}{4 \pi z}[\frac{(z/z')^{N/2-1}+(z'/z)^{N/2-1}}{(z/z')^{N/2}-(z'/z)^{N/2}}-i \cdot j\frac{(z/z')^{N/2-1}-(z'/z)^{N/2-1}}{(z/z')^{N/2}-(z'/z)^{N/2}}] \tag{18}$$

The above function $f(z,z')$ is very useful for determing unsteady velocity, because the unsteady distribution of vortices γ_u has also the phase difference $2\pi/N$ at the corresponding points on the blades.

Unsteady distribution of vortices γ_u consists of quasi-steady term γ_0 and wake effect term γ_w,
$$\gamma_u = \gamma_0 + \gamma_w \tag{19}$$

The induced velocity by γ_0 has to cancel v_{Qn2}, $v_{\Gamma n2}$ and $v_{\omega n2}$ of equation (9), (10) and (11) on each blade. This relation is expressed by a integral equation as
$$\int_{z_L}^{z_T}\gamma_0(z')\ Im[f(z,z')\ e^{i\beta}z/|z|]\ dz' + v_{Qn2}+ v_{\Gamma n2}+ v_{\omega n2}= 0 \tag{20}$$

Introducing the Kutta's condition at the trailing edge, γ_0 can be finally determined.

The free vortices γ_1 are assumed to be carried downstream along the steady streamline starting from the trailing edge, which can be calculated by equation (17). All wake streamlines have the same geometry, but free vortices on them have also $2\pi/N$ phase difference with one another. Considering the fact that the strength of free vorticies is inversely proportional to the velocity, the distribution of free vortices γ_1 of the reference blade can be written as

$$\gamma_1 = C\left|\frac{v(z_T)}{v(z)}\right| e^{j(\omega-\Omega)t}\ e^{-j\ h(s)} \tag{21}$$

Here, C is a complex constant with respect to j, $|v(z)|$ the absolute velocity on wake streamline, s the length of the streamline measured from the trailing edge z_T. The function $h(s)$ in the above equation is defined further as

$$h(s) = (\omega-\Omega)\int_0^s ds'/|v(z')| \tag{22}$$

Assuming C=1 provisionally, the velocities on the blade induced by free vortices, v_{wn} are written as

$$v_{wn}(z) = Im[\int_{z_T}^{\infty}\left|\frac{v(z_T)}{v(z')}\right| e^{-j\ h(s)}f(z,z')dz'\ e^{i\beta}z/|z|] \tag{23}$$

To cancel this normal component on the blade, the unsteady distribution of vortices γ_{w1} ($\gamma_{w1}=\gamma_w/C$) is to satisfy the following integral equation

$$\int_{z_L}^{z_T}\gamma_{w1}(z')Im[f(z,z')\ e^{i\beta}z/|z|]dz' + v_{wn}(z) = 0 \tag{24}$$

The above equation should be solved under the additional condition that the vortex strength is continuous at the trailing edge.

322

Introducing the circulations Γ_s, Γ_0 and Γ_{w1}, which are caused by γ_s, γ_0 and γ_{w1}, the total circutation Γ is

$$\Gamma = \Gamma_s + \Gamma_0 + C \Gamma_{w1} \qquad (25)$$

Differentiating both sides of the equation (25) with respect to time and using $d/dt = j(\omega-\Omega)$,

$$d\Gamma/dt = j(\omega-\Omega)(\Gamma_0 + C \Gamma_{w1}) \qquad (26)$$

is obtained. Further, Kelvin's law for the conservation of vortices leads to the relation that the rate of total circulation change is equal to the total shed vortices from the trailing edge within unit time. This is expressed by

$$-d\Gamma/dt = C|v(z_T)| e^{-j\,h(0)} \qquad (27)$$

where $|v(z_T)|$ is the steady velocity at the trailing edge. Substitution of equation (27) into equation (26) yields,

$$C = \frac{-j(\omega-\Omega)\Gamma_0}{j(\omega-\Omega)\Gamma_{w1} + |v(z_T)|} \qquad (28)$$

Once C is determined in the above, whole unsteady flow field can be solved completely.

Forces Acting on the Impeller

Forces acting on the impeller can be determined by integrating the pressure distribution on the blades. The assumption of infinitely thin blades makes this calculation comparatively simple. Let A and B be upper and lower surface of a blade point, the pressure difference between these points is expressed as

$$P_B/\rho - P_A/\rho = (v_A^2 - v_B^2)/2 + \partial(\phi_A - \phi_B)/\partial t$$

$$= (v_A + v_B)\gamma/2 + j(\omega-\Omega)\int_{z_L}^{z_A}(\gamma_0 + \gamma_w)dz \qquad (29)$$

where v_A and v_B are the local velocities, and ϕ_A and ϕ_B are the velocity potentials. Here $(v_A+v_B)/2$, the mean velocity of the both sides, is denoted by U_m and is separated further into steady component U_{m1} and unsteady component U_{m2}. U_{m1} can be obtained from equation (17),

$$U_{m1}(z_A) = v(z_A) \qquad (30)$$

Now U_{m2} can be obtained by adding $v_{Qt2}(z_A)$, $v_{\Gamma t2}(z_A)$ and $v_{\omega t2}(z_A)$ from equation (12), (13) and (14) to the tangential component of the velocities induced by γ_0, γ_w and γ_1.

$$U_{m2}(z_A) = \left[\left[\int_{z_L}^{z_T} (\gamma_0(z') + \gamma_w(z')) \mathrm{Re}[f(z_A, z')\, e^{i\beta} z_A / |z_A|]_i\, dz'\right.\right.$$

$$\left.\left. + \int_{z_T}^{\infty} \gamma_1(z') \mathrm{Re}[f(z_A, z') e^{i\beta} z_A / |z_A|]_i\, dz'\right]\, e^{j(\omega - \Omega)t}\right]_j \cdot [z_A e^{i\beta}/|z_A|]_i$$

$$+ v_{Qt2}(z_A) + v_{\Gamma t2}(z_A) + v_{\omega t2}(z_A) \tag{31}$$

Consequently, the first term of the right side of equation (29) may be written as

$$(v_A + v_B)\gamma/2 = (U_{m1} + U_{m2})(\gamma_s + \gamma_0 + \gamma_w)$$

$$\dot= U_{m1}\gamma_s + U_{m1}(\gamma_0 + \gamma_w) + U_{m2}\gamma_s \tag{32}$$

where $U_{m2}(\gamma_0 + \gamma_w)$, which is second order quantities, is neglected. Integrating the pressure difference along all blades, and adding them up as vector quantities, the total force acting on the impeller is given as

$$F = \rho \sum_{k=0}^{N-1} e^{-j2\pi k/N} e^{i2\pi k/N} \int_{z_L}^{z_T} [U_{m1}(z') \left[\gamma_0(z') + \gamma_w(z')\right]$$

$$+ U_{m2}(z')\gamma_s(z') + j(\omega - \Omega) \int_{z_L}^{z'} \left[\gamma_0(z) + \gamma_w(z)\right]\, dz]_j \cdot [iz' e^{i\beta}/|z'|]_i\, dz' \tag{33}$$

Obviously the total force obtained is purely oscillatory without any steady component. This is because steady component vanishes by adding up for all blades.

It is well known from thin airfoil theory that the direction of lift acting on an airfoil is perpendicular to the inlet flow direction, and the lift cannot be calculated by merely integrating the pressure difference between upper and lower surfaces along the airfoil. It is because the infinite strength of vortex at the leading edge generates a finite force in the chordwise direction. In this analysis, γ_s does not become infinite at the leading edge because shockless entry is assumed throughout. Even in this case, γ_0 and γ_w become infinite at the leading edge. Calculation shows, however, that the effect remains always within second order quantities, and thus can be neglected. From the above considerations, it is evident that the integration of the pressure difference leads to the force acting on the impeller.

Method of Numerical Calculation

In the practical calculation the vortex distrbution on blades and wakes are replaced by finite number of discrete vortices, thus transforming the integral equations to simultaneous equations. In the calculation of unsteady vortices, it is noted that the coefficients of simultaneous equations become complex with respect to j. Numerical integrations should resort to trapezoidal method by separating the integrands into real and imaginary part. The integration of γ_1 in equation (23) and (31) can be terminated at a proper distance from trailing edge, since the effect of free vortices diminishes rapidly as they get away from the impeller.

Numerical Results

Calculations are carried out for blade angle β of 30°, 45° and 60°. Some examples are given in figure 4,5 and 6. Figure 4 is the result for the case of N=6, r_1/r_2=0.5, β=45°, Γ_p=0 and the flow coefficient ψ=0.25. The absolute values and the directions of dimensionless forces acting on the impeller at the moment when OO' is in the direction of x axis are shown for various values of Ω/ω. Though the forces acting on each blade are unsteady, the combined forces become always constant, provided the number of blades is greater than three. Observing from the relative coordinate system, the force changes its direction clockwise with the angular speed $(\Omega-\omega)$. While, observing from the fixed coordinate system, the direction changes clockwise with the angular speed Ω. The angle between force vector and OO' remains constant. Figure 5 is the result for the case of N=6, r_1/r_2=0.5, β=30°, Γ_p=0 and ψ=0.443, while figure 6 for the case of N=6, r_1/r_2=0.5, β=60°, Γ_p=0 and ψ=0.1443.

In the stability analysis of a rotor system, hydrodynamic damping force acting on each element of the rotor plays a predominant role. In the present case damping force corresponds to the component of fluid force on the impeller, which is parallel and is in opposite direction to the whirling velocity of shaft center. When damping force is negative, that is, when the fluid force has such component that pushes the shaft center toward its whirling motion, there exists a danger that the rotor system runs into severe whirling.

In the results shown in figures 4, 5 and 6, damping force corresponds to the fluid forces in +y direction for Ω>0 and in -y direction for Ω<0. As seen from figures, fluid force acts as damping throughout the calculated cases.

When Ω is equal to $\omega(\Omega/\omega=1)$, flow through the impeller becomes steady and no free vortices shed out from the blades. In all other cases $(\Omega/\omega\neq1)$, blades are always under unsteady condition and the influence of $\partial\phi/\partial t$ term in equation (33) cannot be neglected. Quasi-steady treatment seems to be inappropriate especially for centrifugal impeller, because the wake vortices shed from one blade pass in the proximity of the next blade, thus resulting in a substantial interference. This tendency becomes more remarkable when blade angle is large.

Besides the examples shown in figures, calculations were performed for various combinations of parameters. From these results it becomes clear that the number of blades has little influence on the total forces.

CONCLUDING REMARKS

Fluid forces on a centrifugal impeller, whose rotating axis whirls with a constant speed, was solved by the singularity method. Some typical examples of

results were shown in vector diagrams. Although the results of this paper are obtained for simplified geometries under idealized assumptions, they will suggest us the nature of fluid forces acting on whirling impeller.

The present study is expected to be extended to those cases in which the condition of shockless entry is eliminated and the effect of volute or guide vanes is taken into account. Experimental study is also under way by the authors and is expected to furnish data to be compared with the present analysis.

REFERENCE

1. Black, H.F., Effects of Hydraulic Forces in Annular Pressure Seals on the Vibrations of Centrifugal Pump Rotors, Journ. Mech. Eng. Science, Vol. 11, No. 2, 1969, pp. 206-213.
2. Black, H.F., Lateral Stability and Vibrations of High Speed Centrifugal Pump Rotors, Dynamics of Rotor, IUTAM Symposium, Lingby, Denmark, 1974, pp.56-74.
3. Chamieh, D. and Acosta, A.J., Dynamic Forces on a Whirling Centrifugal Rotor, Proc. 6th Conf. on Fluid Machinery, Vol. 1, Budapest, 1979, pp. 210-219.
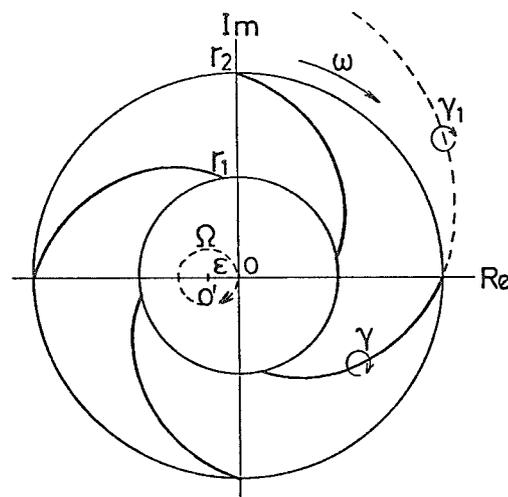
Fig. 1   Schematic geometry of a rotating impeller with whirling motion
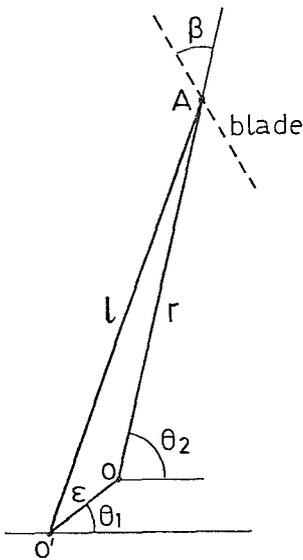
Fig. 2   Relation between center of
  impeller O, center of whirling O'
  and blade point A
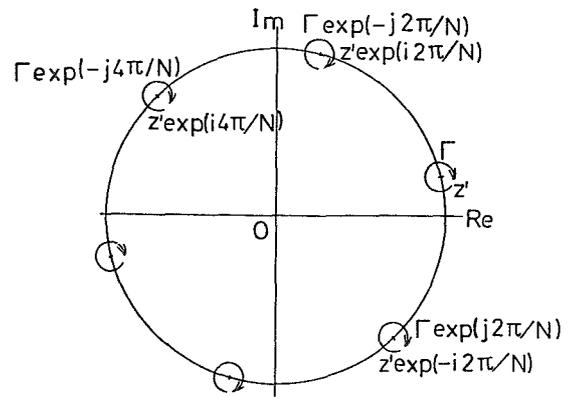
Fig. 3   Discrete vortices with
  phase difference $2\pi/N$ ranged on a
  circumference with equal distance
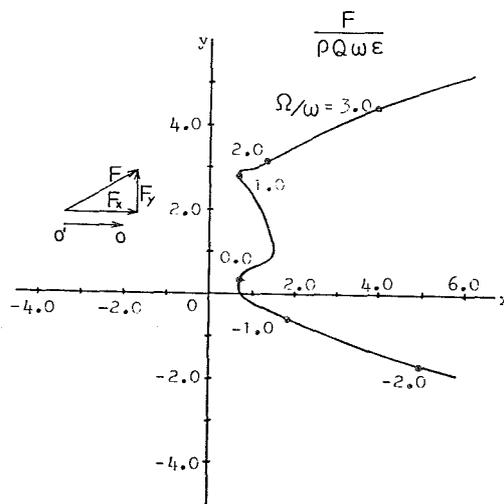
Fig. 4   Vector diagram of radial forces on whirling
  impeller   (N=6, $\beta=45°$, $r_1/r_2=0.5$, $\Gamma_p=0$, $\psi=0.25$)
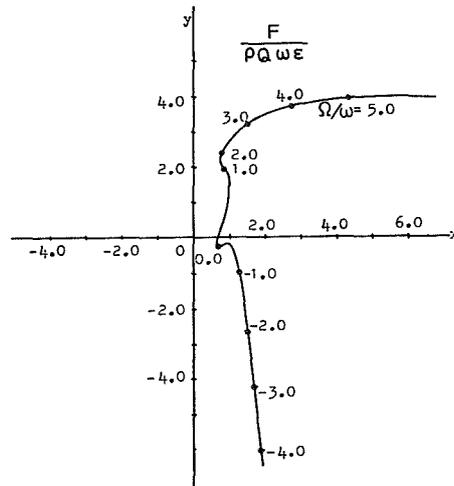
Fig. 5   Vector diagram of radial forces on whirling
         impeller   (N=6, β=30°, r_1/r_2=0.5, Γ_p=0, ψ=0.433)
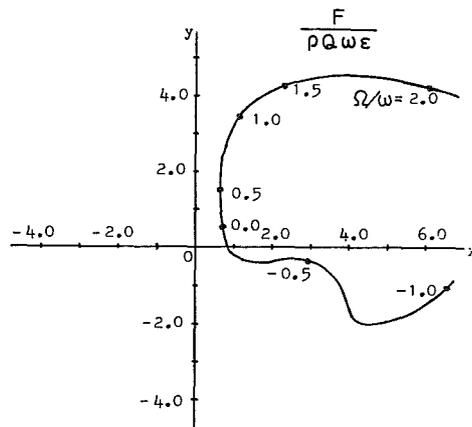
Fig. 6   Vector diagram of radial forces on whirling
         impeller   (N=6, β=60°, r_1/r_2=0.5, Γ_p=0, ψ=0.1443)

SESSION V

UNSTABLE MOTION OF ROTORS IN BEARINGS

John Vance, Texas A&M University
Chairman

Page intentionally left blank

LIMIT CYCLES OF A FLEXIBLE SHAFT

WITH HYDRODYNAMIC JOURNAL BEARINGS IN UNSTABLE REGIMES

R. David Brown and Henry F. Black (deceased)
Mechanical Engineering Department,
Heriot-Watt University, Edinburgh, Scotland, U.K.

SUMMARY

A simple linear stability criterion demonstrates that an
increase in shaft flexibility results in reduced stability. An
examination of the corresponding complex eigenvalues confirms
the stability reduction but also shows that the maximum negative
damping in flexible shafts/bearing systems is very small. Thus
the energy transferred to the shaft whirl through the lubricant
film is also very small.

A non-linear behaviour in these cases can be investigated
if appropriate solutions of Reynolds equation are available. An
approximate but realistic method has been incorporated into a
dynamic simulation. It is demonstrated that in unstable regimes,
flexible shafts have small limit cycle motions.

INTRODUCTION

In the last decade several papers have been published dealing
with the transient response of rotor bearing systems, e.g.
Kirk (ref. 1) and Childs (ref. 2).

McCallion (ref. 3), Myrick and Rylander (ref. 8), used a
finite difference approach to obtain instantaneous bearing forces.
Because of the complexity of the oil film simulation both papers
used a 3 mass symmetrical model and were mainly concerned with
establishing the validity of the method rather than using it in a
systematic way.

The influence of shaft flexibility on instability onset speed
has been examined by Dostal et al. (ref. 5) and Ruhl (ref. 4).
In both these papers a multi-degree of freedom representation of
the shaft was coupled with a short bearing representation of the
oil forces. However it was clearly demonstrated that for a
flexible shaft there was a drastic reduction in the stability
boundary.

An almost universal solution to unstable circular bearings
is to replace them with 4 fixed lobe or tilting pad bearings.
While tilting pad bearings are superior from a linear stability
viewpoint Greathead (ref. 6) has pointed out an increase in
resonant response due to reduced damping. It was also demon-
strated that a subsynchronous vibration due to steam gland forces

increased in severity. Now practical experience with tilting
pad bearings has raised some doubts over mechanical reliability
of the pad pivots. Thus the advantages of tilting pad bearings
may be less than generally assumed.

The work described below deals with a symmetric 3 mass rotor
supported on hydrodynamic bearings. An approximate method of
representing finite bearings is used to calculate bearing forces.
As the method sums forces from a number of independent circular
lobes lemon 3 and 4 lobe bearings can be taken into account.
The calculations in this paper are based on an axial groove
bearing as this is likely to have less stability. Linear
analysis precedes non-linear simulation of some unstable
conditions. The demonstration of small limit cycles suggests
that necessarily flexible rotors e.g. helicopter tail rotors may
be practical without either tilt pad bearings or external
dampers.

<div align="center">SYMBOLS</div>

C $\qquad$ radial clearance

e $\qquad$ journal eccentricity ratio

F $\qquad$ bearing force

H $\qquad$ non-dimensional film gap (1 + e cos θ)

K $\qquad$ half shaft stiffness; bearing stiffness

L $\qquad$ bearing length

M $\qquad$ half central mass

m $\qquad$ bearing mass

P $\qquad$ dimensionless pressure, $\dfrac{P}{\mu\omega}$ $(C/R)^2$

R $\qquad$ bearing radius

X,x $\qquad$ mid-span and bearing horizontal motion

Y,y $\qquad$ midspan and bearing vertical motion

Δ $\qquad$ geometrical eccentricity of masses

ξ $\qquad$ non-dimensionalised bearing axial distance

θ $\qquad$ film co-ordinate

$\dot\phi$ $\qquad$ angular velocity of journal/bearing line of centres

μ   viscosity

ω   angular velocity of journal

HYDRODYNAMIC BEARING FORCES

Reynolds lubrication equation for constant viscosity conditions can be written as

$$\frac{\partial}{\partial\theta}(H^3\frac{\partial P}{\partial\theta}) + \frac{R^2}{L^2}\frac{\partial}{\partial\xi}(H^3\frac{\partial P}{\partial\xi}) = 6e\sin\theta\,(1-2\dot\phi/\omega) + 12\dot e/_\omega\cos\theta \qquad (1)$$

If the axial pressure distribution in an aligned bearing is assumed to be parabolic and symmetric about the mid plane

$$P = 4\,P_{max}\,\xi\,(1-\xi)$$

Reynolds equation can then be written in terms of the mean axial pressure $\overline{P}$

$$\frac{d}{d\theta}(H^3\frac{d\overline{P}}{d\theta}) - 12\frac{R^2}{L^2}H^3\,\overline{P} = 6e\sin\theta\,(1-2\dot\phi/\omega) + 12\dot e/_\omega\cos\theta \qquad (2)$$

An approximate solution can be obtained using the Galerkin technique to minimise the mean square error. In this case only a single approximating function was used, the long bearing solution to equation (1). The approximation is substituted into equation (2) and integrated after multiplication by the long bearing solution. The resulting scaling factor is less than one and can be considered as a leakage correction factor.

The pressure distribution obtained needs to be integrated to obtain the required force components. Traditionally Simpson's rule is used for numerical integration of bearing pressures but a Gaussian method is more efficient.

As the method is recognised to be approximate likely errors in the vector forces need to be assessed. A detailed comparison for static loads and dynamic coefficients for a lemon bore bearing was presented by Black and Brown (ref. 7). Some results for an axial groove bearing are given here (figs. 2,4,5). These comparisons are based on either static conditions or vanishingly small velocity perturbations for the damping coefficients.

Squeeze film effects were calculated and compared for an 180° arc bearing. The comparison between the approximate method and a finite difference method (fig. 3) demonstrates that sufficient accuracy is achieved for dynamic simulation.

SHAFT MODEL AND STABILITY

The simplest model of a realistic shaft (fig. 1) consists of a 3 mass rotor supported in hydrodynamic bearings. By taking advantage of an assumed symmetry, McCallion (ref. 3), the equations of motion can be written in spaced fixed coordinates (fig. 1):

$$[M]\{\ddot{x}\} + [C]\{\dot{x}\} + [K]\{x\} = 0 \text{ for free motion} \qquad (3)$$

where

$$M = \begin{bmatrix} M & 0 & 0 & 0 \\ 0 & M & 0 & 0 \\ 0 & 0 & m & 0 \\ 0 & 0 & 0 & m \end{bmatrix} \qquad K = \begin{bmatrix} K & 0 & -K & 0 \\ 0 & K & 0 & -K \\ -K & 0 & K+K_{xx} & K_{xy} \\ -0 & -K & K_{xy} & K+K_{yy} \end{bmatrix}$$

$$C = \begin{bmatrix} B & 0 & 0 & 0 \\ 0 & B & 0 & 0 \\ 0 & 0 & B_{xx} & B_{xy} \\ 0 & 0 & B_{yx} & B_{yy} \end{bmatrix} \text{ and } x = \begin{Bmatrix} X \\ Y \\ x \\ y \end{Bmatrix}$$

Following Ruhl (ref. 4) equations (1) can be expanded into 8, 1st order equations.

Thus

$$\begin{bmatrix} M & 0 \\ 0 & I \end{bmatrix} \begin{Bmatrix} \ddot{x} \\ \dot{x} \end{Bmatrix} + \begin{bmatrix} C & K \\ -I & 0 \end{bmatrix} \begin{Bmatrix} \dot{x} \\ x \end{Bmatrix} = 0$$

and assuming $x = q\, e^{st}$

$$\lambda \begin{Bmatrix} \dot{x} \\ x \end{Bmatrix} = \begin{bmatrix} -M^{-1}C & -M^{-1}K \\ I & 0 \end{bmatrix} \begin{Bmatrix} \dot{x} \\ x \end{Bmatrix} \qquad (4)$$

where

$$M^{-1}C = \begin{bmatrix} B/M & 0 & 0 & 0 \\ 0 & B/M & 0 & 0 \\ 0 & 0 & B_{xx} & B_{xy}/m \\ 0 & 0 & B_{yx}/m & B_{yy}/m \end{bmatrix}$$

$$M^{-1}K = \begin{bmatrix} K/M & 0 & -K/M & 0 \\ 0 & K/M & 0 & -K/M \\ -K/M & 0 & K+K_{xx}/m & K_{xy}/m \\ 0 & -K/m & K_{xy}/m & K+K_{yy}/m \end{bmatrix}$$

Equation (4) is a standard eigenvalue problem where roots can be obtained using a library sub-routine. The roots will occur in complex conjugate pairs $s_i = \lambda_i \pm j\Omega_i$ or as real roots.

The stability boundary can be established by examining the variation in the real part λ_i of each root as a function of an operating parameter. For stable operation all λ_i must be negative and when any λ_i becomes positive the model becomes unstable.

However the sensitivity of the growth (or decay) factor to operating variables near the stability boundary has not often been investigated in a systematic way. A conventional presentation of the stability for a flexible shaft, Dostal et al. (ref. 5) and Ruhl (ref. 4), has stability parameter plotted against bearing eccentricity for a range of shaft flexibilities. An example of such a stability plot is shown (fig. 6) for the lumped mass model (fig. 1) of Table 1.

Operating lines of constant viscosity are superimposed on the stability plot. These are obtained by noting that eccentricity is a function of Sommerfeld Number, which depends on the product of speed and viscosity for a fixed load and geometry. However, speed is already incorporated into the stability parameter and so operating lines can be presented as lines of constant viscosity.

The variation in the dominant eigenvalue near the stability boundary for a single viscosity (fig. 7) clearly shows the significant effect of shaft flexibility. With shaft flexibility low a small change in bearing eccentricity has a dramatic effect on the rate of decay. However, as the shaft flexibility increases there is a marked convergence of the lines of constant eccentricity. More significantly the region of coalescence moves closer to the stability boundary as flexibility increases.

Replacing the axial groove bearings of the model with lemon bore bearings (ref. 7) produces another stability plot (fig. 8). The stability is clearly much improved compared with axial groove bearings. Indeed for moderate to high flexibility ($C/_\partial < 1$) the shaft is completely stable.

These linear calculations demonstrate that in certain circumstances, unstable flexible shafts have very low negative damping. No external damping was included in these linear calculations so the results are pessimistic if no other destabilizing forces are present.

NON-LINEAR SIMULATION

The equations for free motion (equ. (3)) can be modified for forced vibration

Thus $[M] \{\ddot{x}\} + [C] \{\dot{x}\} + [K] \{x\} = e^{-i\omega t} \{M\Delta\} + \{F\}$

where $\{M\Delta\}$ is the mass eccentricity vector

and $\{F\}$ is bearing force vector

For numerical integration acceleration needs to be implicity defined.

Thus

$$\{\ddot{x}\} = [-M]^{-1} [C] \dot{x} - [M]^{-1} [K] x + \omega^2 \{\Delta\} + [M^{-1}]\{F\}$$

These 4 equations are reformed into a set of 8 first order equations and integrated using a 4th order Runge-Kutta method.

NUMERICAL RESULTS

The 3 mass shaft model (fig. 1) with axial groove bearings was used for non-linear simulation of some unstable cases. Initial vertical deflection of the central mass was set at its static value, all other deflections and velocities zero. For a flexible shaft ($C/_\Delta = 0.1$) with no external damping response, calculations for 12 shaft revolutions shown in figures 9 and 10 for a bearing position indicate limit cycles for zero unbalance and a large central unbalance respectively. However reflection on published work particularly that of Holmes (9) led to closer examination of the calculated results. At the end of the integration the growth rate (log dec) was around 0.0025, graphically insignificant. The calculations were extended with external damping added to the central mass. After some 60 shaft revolutions the undamped model response was increasing while with $\xi = 0.01$ damping maximum excursion at both shaft centre and bearing were reached after 30 revolutions.

Additional calculations were carried out for a stiffer shaft ($C/_\Delta = 0.3$) at a more unstable condition. The results for zero unbalance are summarised in fig. 11. An external damping ratio of 3% is needed before extreme excursion values of mid-span deflection are established after 15 shaft revolutions.

336

DISCUSSION AND CONCLUSIONS

It has been demonstrated that for an unstable flexible shaft the limit cycle motion can be small. These calculations were carried out for axial groove bearings with the addition of a small amount of external damping. The assumed additional damping was less than that used by McCallion (ref. 3). Further work using non-circular bearings for unstable conditions (e.g., fig. 8) is expected to demonstrate that unstable flexible shafts do not develop unacceptable levels of vibration.

TABLE 1.

3 MASS SHAFT WITH AXIAL GROOVE BEARINGS

HALF CENTRAL MASS	7.237 Kg
JOURNAL MASS	4.382 Kg
BEARING LENGTH	25.4 mm
BEARING DIAMETER	50.8 mm
BEARING DIAMETRAL CLEARANCE	50.8 μm

SHAFT FLEXIBILITY $C/_\partial$	0.1	0.3
SHAFT STIFFNESS K $MN/_m$	.279	.837
SPEED R.P.M.	7120	12,470
JOURNAL ECCENTRICITY	.41	0.29
CRITICAL MASS $\omega \frac{C}{g}$	1.2	2.1

REFERENCES

1. Kirk, R.G.; Gunter, E.J.; Transient Response of Rotor-Bearing Systems. ASME Transactions. Journal of Engineering for Industry. May 1974 pp. 682-693.

2. Childs, D.W.; A Modal Transient Simulation Model for Flexible Asymmetric Rotors. ASME Transactions. Journal of Engineering for Industry 1976.

3. McCallion, H.; Wales, D.R.; The Influence of Oil Lubricated Bearings on the Dynamics of Rotating Systems. I.Mech.E. Proceedings Vol. 190 54/76.

4. Ruhl, R.L.; Booker, J.F.; A Finite Element Model for Distributed Parameter Turborotor Systems. ASME Transactions. Journal of Engineering for Industry. February 1972 pp. 126-132.

5. Dostal, M.; Roberts, J.B.; Holmes, R.; Stability Control of Flexible Shafts Supported on Oil-Film Bearings. Journal of Sound and Vibration 1974. Vol. 35 Pt. 3 pp. 361-377.

6. Greathead, S.H.; Bastow, P.; Investigations into Load Dependant Vibrations on the High Pressure Rotor on Large Turbo-Generators. Vibrations in Rotating Machinery. I.Mech.E. Conference, Cambridge 1976.

7. Black, H.F.; Brown, R.D.; Fast Dynamic Calculations for Non-Circular Bearings. I.Mech.E. Tribology Convention, Durham April 1976.

8. Myrick, S.T.; Rylander, H.G.; Analysis of Flexible Rotor Whirl Using A Realistic Hydrodynamic Journal Bearing. ASME Transactions. Journal of Engineering for Industry. November 1976 pp. 1135-44.

9. Holmes, R.; The Non-Linear Performance Of Turbine Bearings Journal of Mechanical Eng. Sc. Vol. 12 No.6 December 1970.
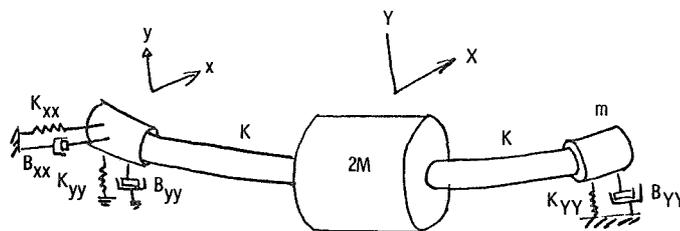
Figure 1. - Three-mass model.
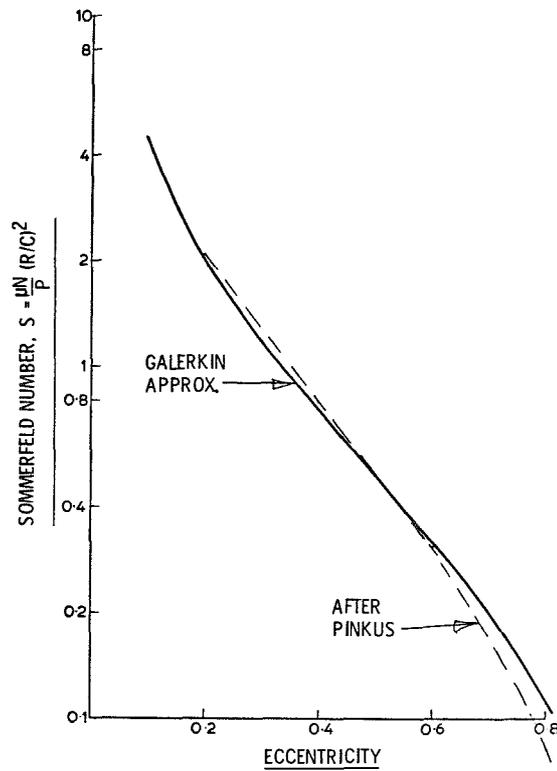
Figure 2. - Two-axial-groove bearing. L/D = 0.5.
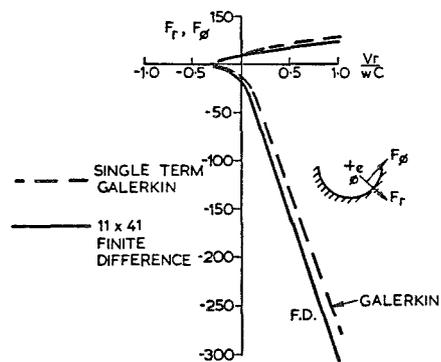
Figure 3. - Comparison of finite difference with an
approximate method. Squeeze forces; L/D = 1;
180^0 arc; ϕ = 45^0; ε = 0.9.
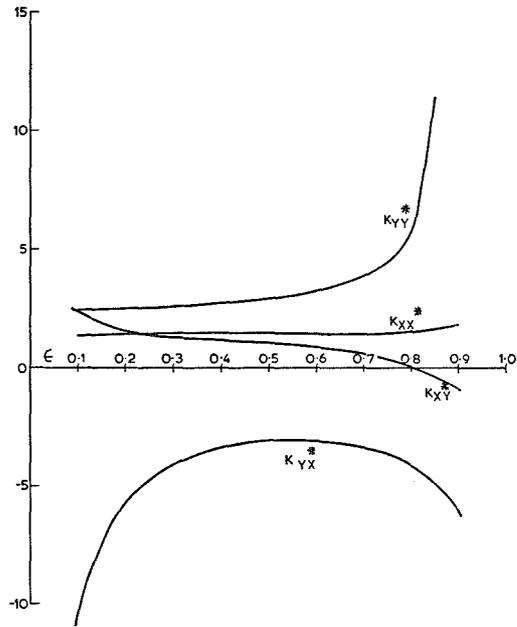
Figure 4. - Axial-groove bearing. L/D = 0.5; nondimensionalized stiffness.
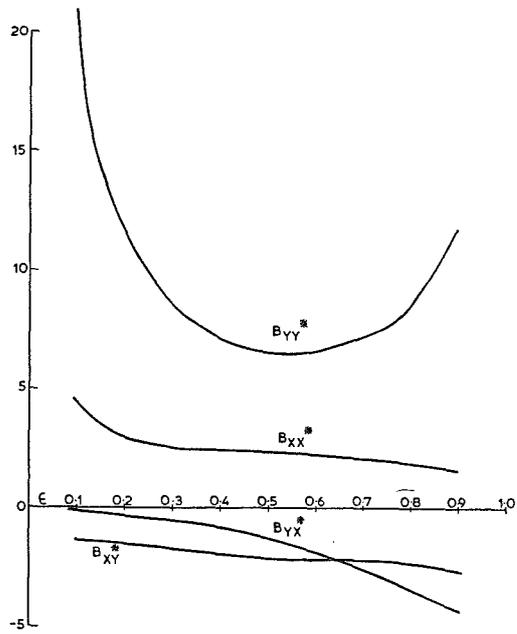
Figure 5. - Axial-groove bearing. L/D = 0.5; nondimensionalized damping.

340
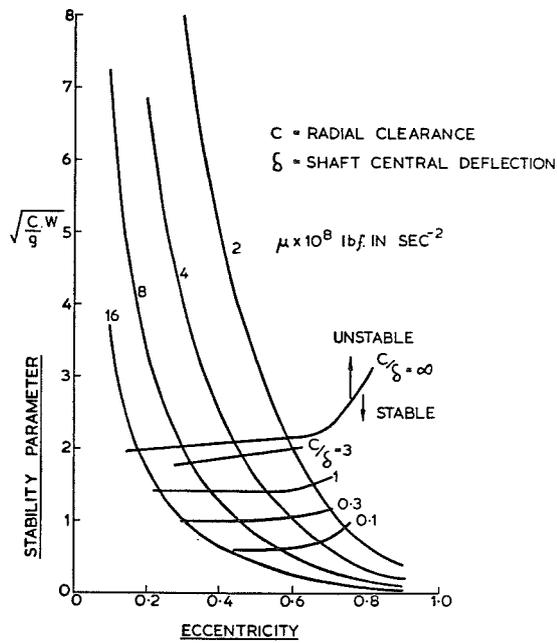
Figure 6. - Effect of stiffness on stability.
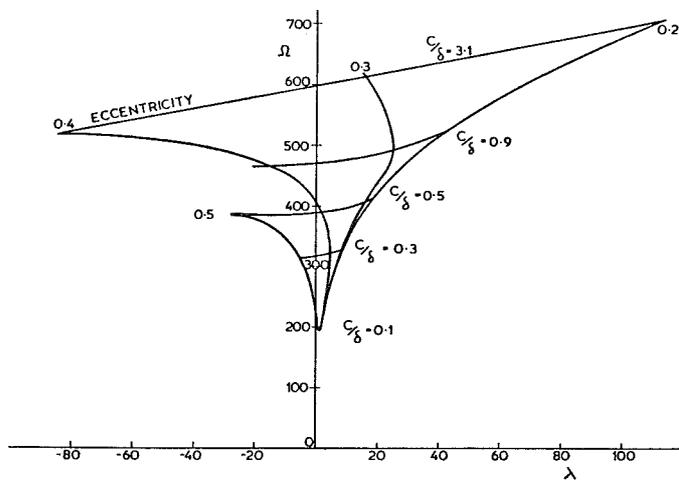
Figure 7. - Complex-plane dominant eigenvalue. Three-mass shift; $\mu = 8\times10^{-8}$ lbf in sec^{-2}; $x = Xe^{\lambda+i\Omega}$.

X-DISPLACEMENT

2 AXIAL GROOVES   C/DELTA=0.1, EC=.41, MC=1.2, U/C=0.0
STATION 3   SCALE 1/1.000000

Y-DISPLACEMENT

2 AXIAL GROOVES   C/DELTA=0.1, EC=.41, MC=1.2, U/C=0.0
STATION 3   SCALE 1/1.000000

2 AXIAL GROOVES   C/DELTA=0.1, EC=.41, MC=1.2, U/C=0.0
STATION 3   SCALE 1/1.000000
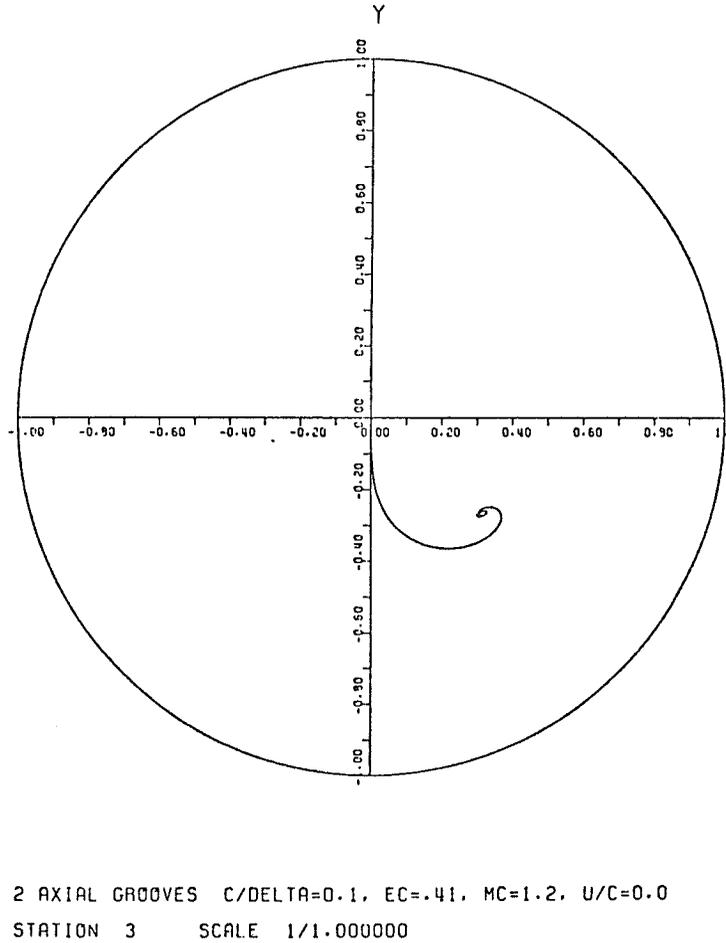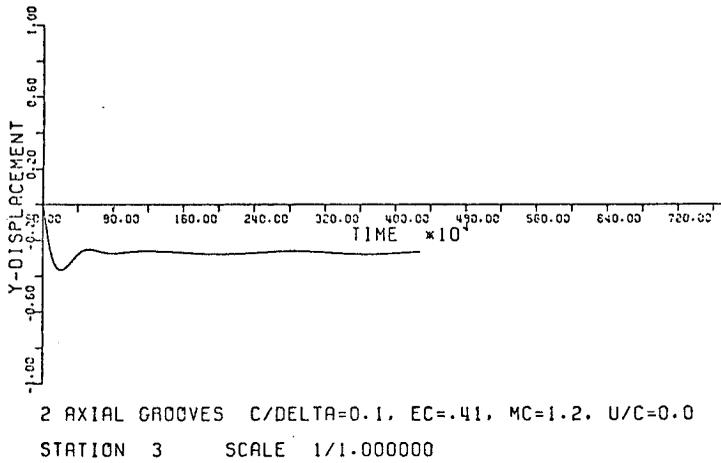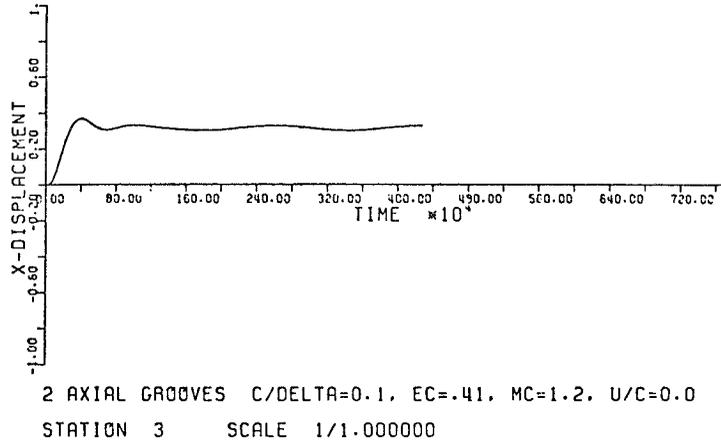
Figure 8. – Example of a flexible shaft.
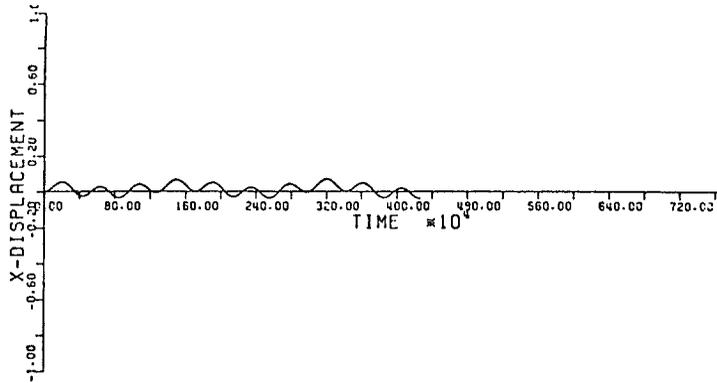
2 AXIAL GROOVES C/DELTA=0.1. EC=.41. MC=1.2. U/C=0.6
STATION 2   SCALE 1/1.000000
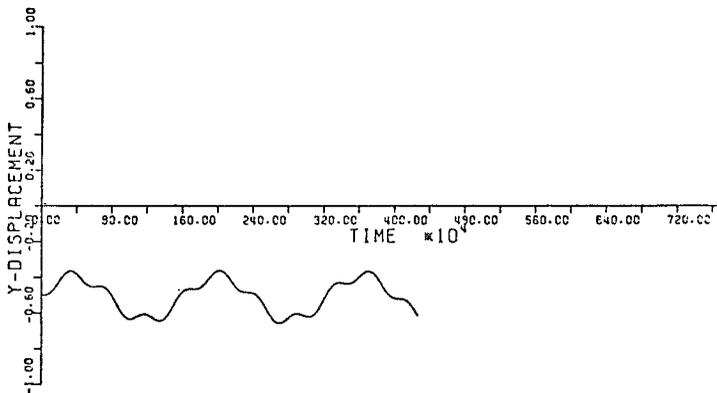
2 AXIAL GROOVES C/DELTA=0.1. EC=.41. MC=1.2. U/C=0.6
STATION 2   SCALE 1/1.000000
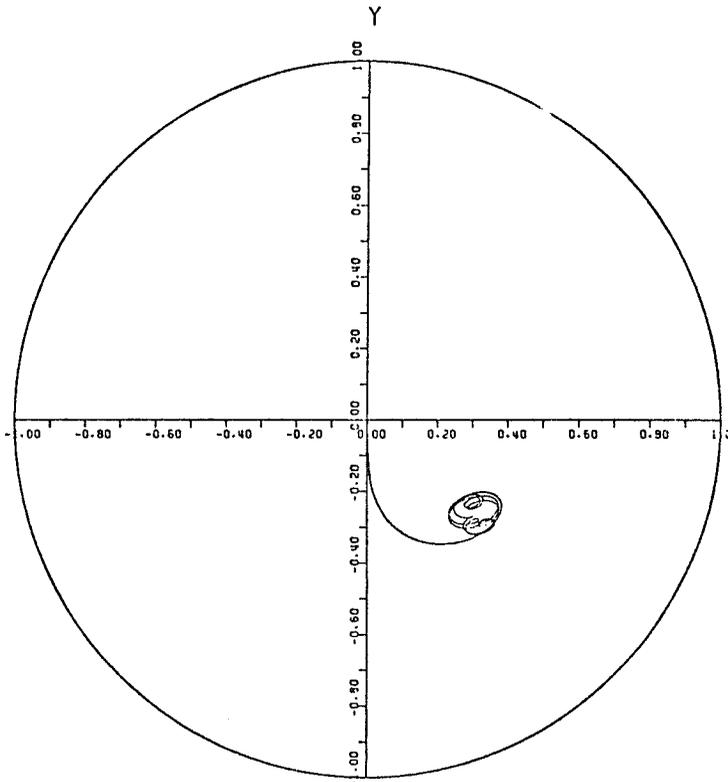
2 AXIAL GROOVES C/DELTA=0.1. EC=.41. MC=1.2. U/C=0.6
STATION 3   SCALE 1/1.000000

Figure 9. – Example of a flexible shaft with large unbalance.

Page intentionally left blank

ON THE ROLE OF OIL-FILM BEARINGS IN PROMOTING SHAFT INSTABILITY: SOME EXPERIMENTAL OBSERVATIONS

R.Holmes
School of Engineering and Applied Sciences
University of Sussex,
Falmer, Brighton, Sussex,
U.K.   BN1,9QT

SUMMARY

An insight into the mechanism of oil whirl instability is obtained by investigating theoretically and experimentally its occurrence in rigid and flexible rotor systems. Means of damping against such instability are applied in the latter case and their effectiveness discussed.

INTRODUCTION

For a rotating shaft supported in oil-film bearings the instability onset speed depends,to a large extent, on the nature of the hydrodynamic forces produced in the bearings. Oil whirl instability is characterized by shaft vibration frequency and amplitude and the purpose of this paper is to report the effect of various bearing parameters on the oil-whirl frequency and amplitude of rigid and flexible shafts supported on fluid-film bearings.

In order to provide a qualitative understanding of such instability the particular extreme cases of a very short bearing and a very long bearing are considered.

A physical insight into the mechanism of oil-whirl instability can be obtained by considering Fig.1. As a result of the application of an external load the journal deflects on the oil film rather as it would on a spring. Consequently, a converging wedge is formed in the region of contracting film thickness into which oil is dragged by journal rotation, ω. Pressure is thus generated in the oil by hydrodynamic action to counteract the external load. The average angular velocity of this oil is about half rotational speed and, should any disturbance to the journal centre cause the line of centres to rotate at this angular velocity, then the wedge into which the oil is dragged will move away from the oil at the same velocity, with the result that no hydrodynamic pressure will be generated. The journal thus loses its load-carrying capacity and may become unstable in a whirling motion, the energy for the instability being fed by its own rotation.
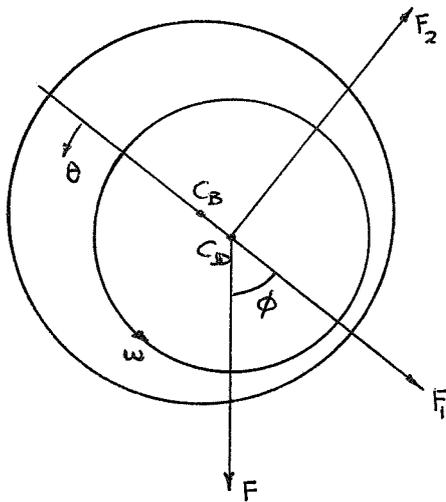
Fig. 1: Forces on journal
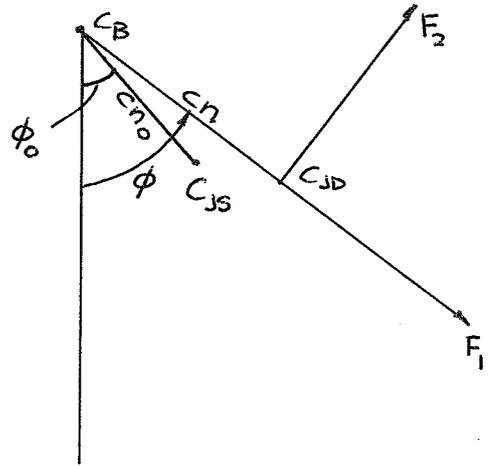
Fig.2: Magnified portion of Fig. 1

NOTATION

a	Damper location	P	$F/mc\omega^2$
b	Damping coefficient	R	$= D/2$ Journal radius
c	Radial clearance	t	Time
c_1	Constant	z	Axial co-ordinate
D	Diameter	α	Constant
F	Static external load per land	β	Constant
F_1,F_2	Oil film forces	ε	Eccentricity of journal at instant considered
g	Gravitational constant	μ	Lubricant viscosity
h	Film thickness at angular co-ordinate $\theta = c(1 + n \cos \theta)$.	ϕ	Angle between static load line and line of centres of journal and bearing
inHg	Inches of mercury	ϕ_0	Attitude angle under static conditions
ℓ	Journal length		
ℓ_s	Shaft span	ω	Journal angular velocity, forcing frequency
m	Rotor mass per bearing land		
n	Eccentricity ratio $= \varepsilon/c$	Ω	Angular velocity of whirl
n_o	Static eccentricity ratio	Ω_1	Lowest pinned critical speed of shaft
p	Hydrodynamic pressure		

$$\nu_{D,I} = \frac{b_{D,I}}{m} \left(\frac{c}{g}\right)^{\frac{1}{2}} \quad \text{where } b_{D,I} \text{ is external or internal damping}$$

$(')$ $d/d(\omega t)$

346

Centres

C_B Bearing centre

C_{JD} Centre of dynamic journal at in-
stant considered

C_{JS} Centre of journal under static load
only

Load numbers

$L_{2\pi}$ Load number for long 360° film
$= Fc^2/2\ell\mu\omega R^3$.

$S_{2\pi}$ Load number for short 360° film
$= 4\pi Fc^2/\mu R\ell^3\omega$

THEORETICAL TREATMENT

In the region of diverging film boundaries the hydrodynamic pressure becomes negative and, should the supply pressure be insufficient to maintain a net pressure in the oil of greater than absolute zero then cavitation will usually result. However, in some cases of lightly loaded bearings a full 360° film of oil is maintained. Not unexpectedly, the spring-like and damping properties of the oil film depend to a large extent on the degree of cavitation present. The equation which governs the generation of hydrodynamic pressure is due to Osborne Reynolds and cannot be solved analytically for the journal bearing situation. However, if one of two approximations is made then a analytical solution is obtainable. These approximations are based on the assumptions that the oil film length in relation to its diameter is (1) very short and (2) very long. These solutions give a good insight into the characteristics of journal bearing oil films. The hydrodynamic forces generated by the short uncavitated oil film (Fig.1) are (Ref.1)

$$F_1 = \frac{-R\ell^3}{c^3}\, \mu c \dot{n} \cdot \frac{\pi(1 + 2n^2)}{(1 - n^2)^{5/2}}$$

$$F_2 = R\ell^3\, \pi c n \mu (\omega - 2\dot{\phi})/2c^3(1 - n^2)^{3/2}$$

Under conditions of static load,

$\dfrac{dn}{dt}$ and $\dot{\phi}$ are zero, $n = n_o$ and thus

$$F_1 = 0$$

$$F_2 = R\ell^3\pi c n_o\mu\omega/2c^3(1 - n_o^2)^{3/2}$$

Also, $F_2 = F$ and $\phi = \pi/2$ (Fig.1).

Therefore $2\pi^2 n_o/(1 - n_o^2)^{3/2} = 4\pi Fc^2/\mu R\ell^3\omega$

Let $4\pi Fc^2/\mu R\ell^3\omega$ be called the 'short 2π' load number, given the symbol $S_{2\pi}$.

In terms of static eccentricity ratio, n_o and static load,F, F_1 and F_2 (Fig.2) become

$$F_1 = -2F(1 - n_o^2)^{3/2}(1 + 2n^2)\dot{n}/\omega n_o(1 - n^2)^{5/2}$$

and

$$F_2 = F(\omega - 2\dot{\phi})(1 - n_o^2)^{3/2}n/\omega n_o(1 - n^2)^{3/2}$$

347

the corresponding expressions for the long bearing are as follows:

$$
\left\{ \begin{array}{c} F_1 \\[2ex] F_2 \end{array} \right\} = \frac{36\pi^2 n_o F}{(2+n_o^2)(1-n_o^2)^{\frac{1}{2}}} \left\{ \begin{array}{c} -\dfrac{\dot{n}}{\omega} \cdot \dfrac{1}{(1-n^2)^{3/2}} \\[3ex] (1-\dfrac{2\dot{\phi}}{\omega}) \cdot \dfrac{n}{(2+n^2)(1-n^2)^{\frac{1}{2}}} \end{array} \right\}
$$

and a 'long 2π' load number may be defined having the value

$$
L_{2\pi} = \frac{Fc^2}{2\mu R^3 \ell \omega} = \frac{6\pi n_o}{(2+n_o^2)(1-n_o^2)^{\frac{1}{2}}} = \frac{S_{2\pi}}{2\pi} \cdot \left(\frac{\ell}{D}\right)^2
$$

NON-LINEAR EQUATIONS OF RIGID ROTOR MOTION

Consider a symmetrical rigid rotor of mass 2m symmetrically supported on two similar, full-film bearings. From Fig. 1 the equations of motion are

$$
F_1 + F \cos \phi = mc(\ddot{n} - n\dot{\phi}^2)
$$

$$
F_2 - F \sin \phi = mc(n\ddot{\phi} + 2\dot{n}\dot{\phi})
$$

These equations become, in non-dimensional form,

$$
\frac{F_1}{mc\omega^2} + P \cos \phi = n'' - n\phi'^2
$$

$$
\frac{F_2}{mc\omega^2} - P \sin \phi = n\phi'' + 2n'\phi'
$$

(1)

where $P = F/mc\omega^2$ and $n' = dn/d(\omega t)$ etc.

The following general conclusions may be made from the numerical solutions of equations (1), which result in unstable transient spirals (Fig.3):

(1) The number of loops within a given radius of the static equilibrium position is governed to a large extent by the value of P, the number of loops increasing with rising values of P. A similar less pronounced effect is noted as n_o decreases. Roughly similar numbers of loops are produced by either theory until the bearing centre is enclosed. After this point, the orbits tend to close up and the short bearing solution does so much more rapidly.

348

The shape of the initial loops is largely dictated by the value of n_o. In general, as n_o is increased, these loops become elongated in the direction of the external load and ultimately may assume a crescent form. Although not restricted to the short bearing solution this distortion is far more pronounced for the case of the short bearing solution than for the long.

Another general conclusion of some interest is that for both the long and short bearing theories the whirl frequency approaches half rotational speed as the eccentricity ratio approaches unity, this approach being at an ever-decreasing rate.

(2) The magnitude of the initial displacement used to commence the solutions has a pronounced effect on the position of loops for solutions having few loops, for example, for low values of P. This effect becomes less apparent as the value of P is increased.

Some general considerations of the equations of motion

One of the main interests attached to the non-linear equations of motion is whether they predict the possibility of a closed orbital motion of the journal centre within the clearance circle. A closed circular orbit concentric with the bearing centre is not possible except for the hypothetical case of a mass-less rotor, since $\ddot{n}$ and hence F_1 and F_2 would be zero, giving no force to counteract the centrifugal force of this postulated whirl. From digital computation with a wide range of parameters it appears that if any other form of closed orbit exists it will occur as $n \to 1$, $n' \to 0$ and $\phi' \to 0.5$. As an approximation these trends were placed in the equations of motion (1).

Experiment

Short bearing
theory
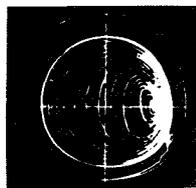
Long bearing
theory

Fig.3: Experimental and theoretical transients.
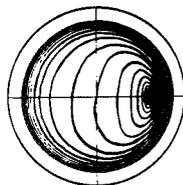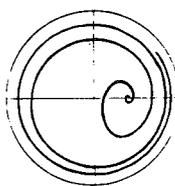
Left-hand column
P = 0.2, n_o = 0.4

Right-hand column
P = 2.5, n_o = 0.6
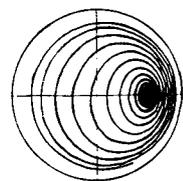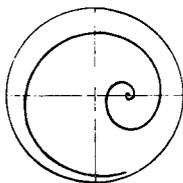
These give on integration

$$n \simeq 1 - \cfrac{1}{\left\{c_1 + \alpha(\beta-1)\left[\dfrac{\omega t}{4P} + 2\sin\dfrac{\omega t}{2}\right]\right\}^{1/(\beta-1)}}$$

c_1 being a constant of integration and $\beta = 2.5$ (short) and 1.5 (long).

Thus n asymptotically approaches unity and it appears that, in general, closed orbits are not possible for $t < \infty$, with the exception of the particular case of $P = \infty$ when the integral oscillates between fixed limits. This corresponds to the massless rotor of Swift (ref.3). It may be seen that dn/dt is curbed more rapidly as n increases, since the exponent β is greater than unity. Further, since β is larger for the short bearing than for the long bearing the curbing for the former is the more pronounced.

Experimental rotor

The motion of an experimental rotor was monitored by pick-ups mounted in the horizontal and vertical planes of the rotor axis and located midway between the bearings. This motion was displayed on a storage oscilloscope and the stored trace was photographed directly when required. This technique allowed the clearance circle to be conveniently displayed by rolling the rotor within the bearing shells. On increasing the rotor speed from zero, an eccentricity locus was traced out on the oscilloscope until the attitude angle ϕ_0 reached 90°, when the rotor became unstable. In view of the low supply pressure in relation to the load pressure this suggested the presence of an oil film supporting sub-atmospheric pressures. In order that different values of P could be inspected, oils of different viscosities were used. This ensured different whirl-onset speeds. When it was required that values of P should be small (high whirl-onset speeds), then the rotor was run up to the required speeds with the supply pressure at approximately 0.5 inHg, being suddenly increased to 6 inHg to give a 90° attitude angle and to initiate whirl. Some comparisons of experimental results with the equivalent short and long bearing solutions are shown in Fig. 3. For the case of low P, it may be observed that the photograph shows a small white area corresponding to an attitude angle between 0° and 90°. This represents a running condition which occurred due to starving the bearings of oil prior to imposing the full supply pressure of 6 inHg. In both the photographs the outer circle denotes the clearance circle. Pick-up non-linearities and the necessary pedestal clamping forces probably contribute to the non-circularity of this clearance circle.

In this experimental work, not only are the initial conditions unknown but they may correspond to an appreciable disturbance for low values of P. Hence although qualitative behaviour may be determined using such values, those likely to show some quantitative agreement with theory are for higher values of P, these being largely unaffected by the initial conditions. Such a case is that corresponding to $P = 2.5$, $n_0 = 0.6$.

Bearing these comments in mind, the experimental results support the theoretical solutions in the following respects:

350

(1) The number of loops increases as P is increased for a given value of n_o. A similar less pronounced effect is obtained on reduction of n_o for a given P.

(2) As n_o is increased, the loops become elongated in the external load direction and can even assume a crescent form.

(3) As the whirl develops the loops become roughly circular in form around the bearing centre.

There is also a general tendency to support the short bearing theory for the initial growth pattern and final decay pattern while the intermediate loops, particularly in distribution, approximate more closely to the long bearing solutions.

One important difference between the computed and experimental spirals is that the former tend to have slightly fewer loops and proceed to bearing contact as time tends to infinity. In the experimental work, bearing contact was never experienced, a closed orbit within the clearance circle always being established. The reasons for this are not clear, though the supply pressure and groove geometry were found to be important factors and it was noted that the size of the final orbit could be reduced by increasing the supply pressure.

As the eccentricity ratio approaches unity, its first derivative approaches zero and the frequency ratio approaches 0.5, then the peak negative pressure is reduced in magnitude. Thus a reduction below the whirl onset speed and/or onset supply pressure is required to cause cavitation and thus quell any already-existing whirl. This probably accounts for the frequently observed 'hysteresis effect'.

Some interesting conclusions can be drawn from the application of a linearising technique to the oil-film forces F_1 and F_2, and using these forces to establish a frequency equation for the rigid test rotor. From this equation the frequency ratios of incipient oil-whirl instability were found and plotted in Figs. 4 and 5. The corresponding experimental plots relating to the observed limit cycles are shown in Fig.6 and show good qualitative agreement.

Whilst an uncavitated oil film promotes instability, this is not always the case for a cavitated film. Instead instability for small (ref.2) and large (ref.4) perturbations is predicted in a region defined by eccentricity ratio and P.
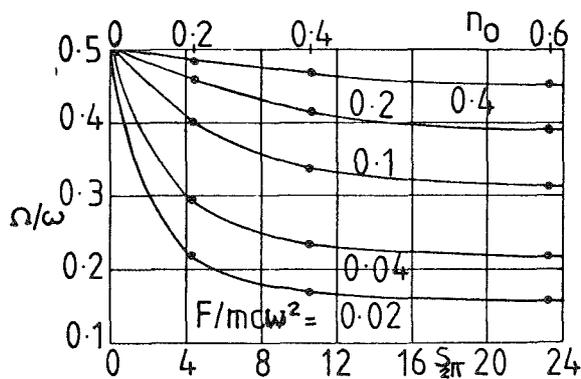
Fig.4: Short bearing
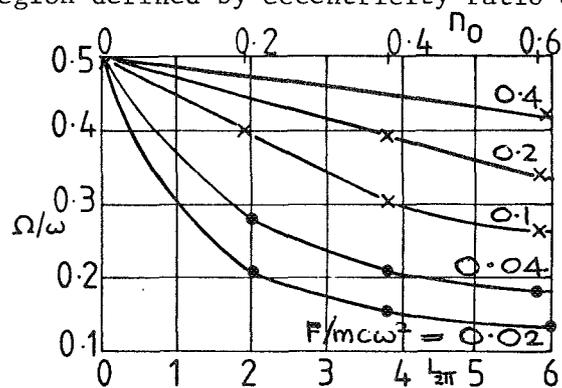
Fig. 5:Long bearing
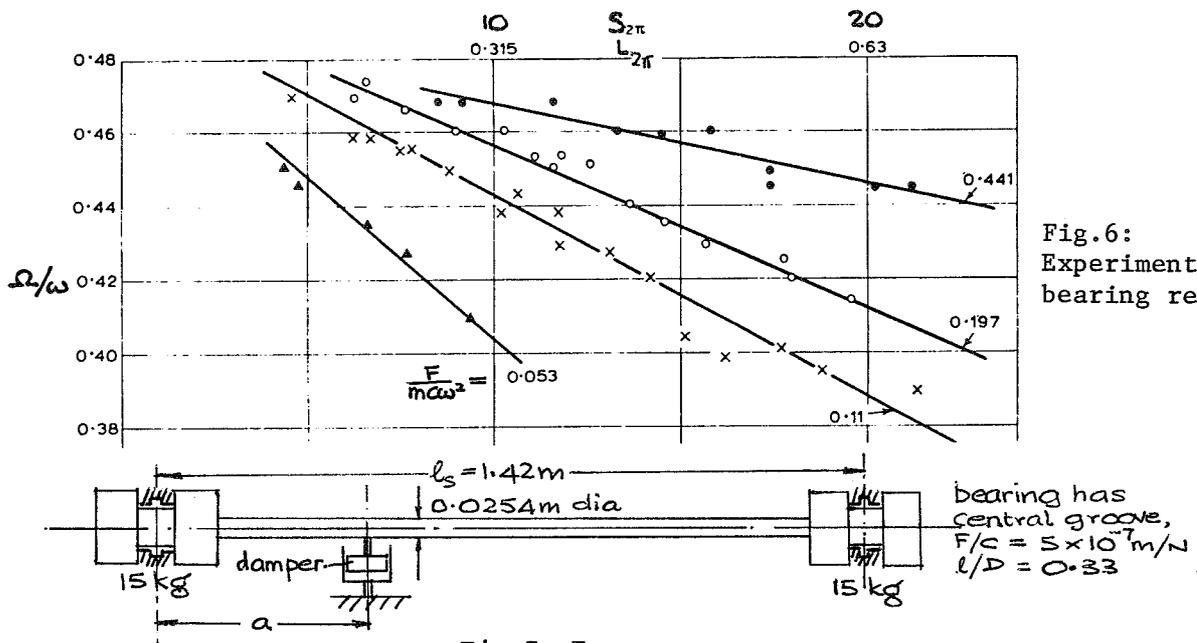
Fig.6:
Experimental
bearing result

Fig.7: Test rotor

FLEXIBLE ROTOR INSTABILITY AND THE EFFECT OF EXTERNAL DAMPING

The vibrational behaviour of a flexible rotor-bearing system may be controlled by the application of external damping either directly to the rotor or by mounting the bearings on flexible, damped supports. The first option is restricted to special types of shafting, such as transmission shafts where sufficient space is available for the damping application, whereas the second option is the more attractive solution in applications such as turbomachinery where the entire length of the shaft is already occupied by discs, seals, bearings, etc.

Firstly, the effect of various parameters on the instability onset speed of the system shown in Fig.7 was examined, where external damping was included in the form of two identical viscous dampers applied at the same axial position on the shaft, one horizontally and one vertically. Later the feasibility of controlling the response and the stability of a rotor-bearing system with flexible, damped bearing supports was investigated both theoretically and experimentally.

For the first system it was found that

(a) at all values of eccentricity ratio, an increase in external damping increased the instability onset speed;

(b) at low values of eccentricity ratio ($n_0 < 0.3$) the effect of external damping was fairly small;

(c) the instability onset speed increased as the damper was moved towards the centre of the span; the effect of damper location was relatively small.

An experimental rotor was built as illustrated in Fig. 7, and to minimize

external damping, the bearings had no seals and there were no axial thrust bearings. A pair of variable external dampers were mounted in the horizontal and vertical planes at one adjustable point on the shaft.
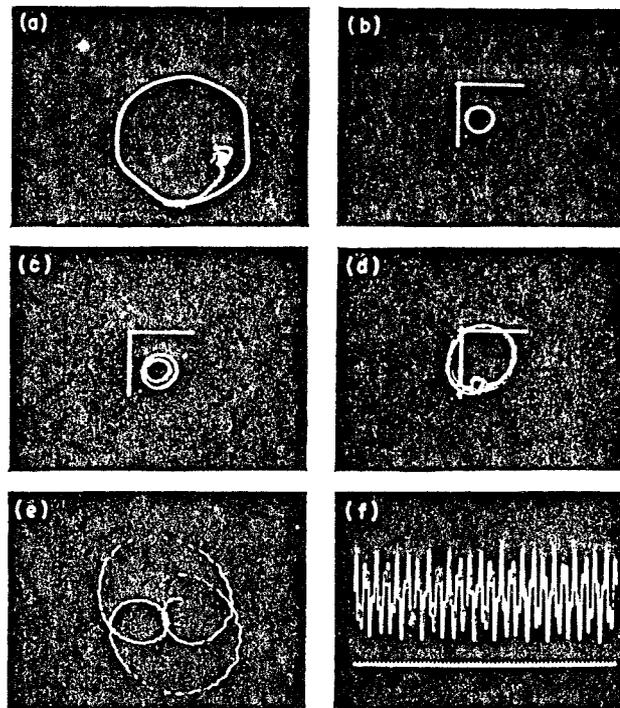
Fig.8: Experimental recordings

For running speeds below the transition range the shaft vibration was linear and harmonic, with no trace of non-synchronous vibration. Fig. 8a shows a typical motion of the journal centre, within its clearance circle, when the shaft speed was increased from zero to 250 rev/min. From its lowest position, corresponding to an eccentricity ratio of unity and a zero attitude angle, the journal acquired a stable operating position, characteristic of a cavitated oil film. Fig. 8b shows a typical journal orbit for a much higher running speed, still well below the transition range. Here the journal is performing a very small, almost circular, synchronous orbit, due to slight mass unbalance and lack of straightness of the shaft. In this figure (and in Fig. 8c and d), the horizontal and vertical lines are radius lines of the clearance circle.

For running speeds within the transition range the shaft exhibited a combination of synchronous and non-synchronous vibration, which showed no tendency to either build-up or decay with time. The non-synchronous vibration had a frequency equal to the first critical speed of the shaft (i.e. its first pinned natural frequency). Fig. 8c and d show typical journal orbits encountered when running in the upper part of the transition range. Here the bearing conditions were such that the ratio of synchronous to non-synchronous frequencies was about 2:1, which accounts for the double-loop character of the journal orbits. Another

353

example of a shaft orbit occurring in the transition range is shown in Fig. 8e. Here bearing conditions are such that the synchronous frequency is about three times the non-synchronous frequency. In all the cases observed it was found that, in the transition range, the journal orbits always centred on a position characteristic of a cavitated oil film, i.e. at a position well below the horizontal line through the centre of the clearance circle. This was an important observation since it showed that oil whirl did not commence as a result of the bearing oil films acquiring a full 360° extent. The complex character of the vibration in the transition range is clearly illustrated by Fig. 8f, which shows a typical variation of the horizontal component of the shaft motion with time.
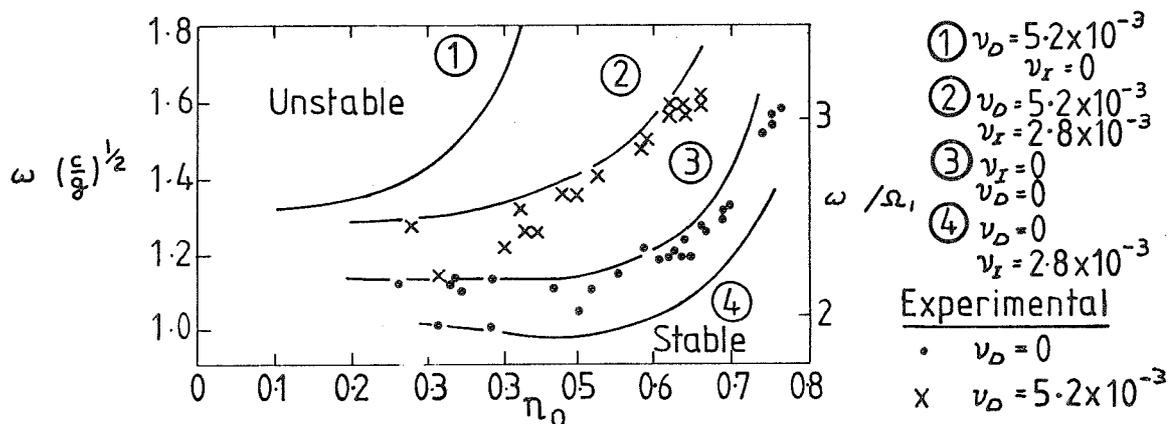
Fig.9: Instability onset speeds

For $v_D = 0$, that is no external damping, the experimentally determined non-dimensional instability onset speed ratios, $\omega \, (c/g)^{\frac{1}{2}}$ and ω / Ω_1 were plotted against n_0 in Fig. 9. At high n_0 it is seen that the experiments yield consistent results and the experimental scatter is small. At low n_0 the scatter of the results is much greater. Also shown in Fig. 9 is the theoretically predicted variation of $\omega \, (c/g)^{\frac{1}{2}}$ with n_0 (3). It is seen that, with the assumption that the internal damping is zero, a predicted curve is obtained which is in close agreement with the experimental results, shown as dots.

When the shaft is running such as to give a high eccentricity ratio ($n_0 = 0.75$) in the bearings the threshold speed is about three times the first critical speed, Ω_1, and indeed is close to the second critical speed. Just below this threshold speed the shaft vibrates synchronously in its second bending mode. The shaft motion was measured at two locations in the horizontal plane (quarter span and three-quarter span) which corresponded to the peaks of the second mode shape. Fig. 10a shows the vibration at these points, for ω = 3300 rev/min. When the threshold speed is reached the shaft becomes unstable with a precession frequency and shape corresponding to the first mode. This is illustrated in the experimental results shown in Fig. 10b for which the same locations have been used and ω = 3350 rev/min.

It was found experimentally that even a small amount of external damping had a considerable stabilizing effect on the shaft. For example, as shown

in Fig. 9 dampers with a ν_D value of 5.2×10^{-3}, applied to the shaft (Fig. 7) at $a/\ell_s = 0.2$, had the effect of substantially extending the range of experimental stable operating speeds. The onset of non-synchronous vibration was found to be more gradual than in the case of no external damping and it sometimes took several minutes for the vibration to build up. In the vicinity of the transition range the shaft was observed to be sensitive to any external disturbances, coming either from the drive unit or intentionally applied by a striker device. It was sometimes possible to create complete instability, when running in the transition range, by applying an external impulse to the shaft. However, in some cases, mainly at high eccentricity ratios, an external impulse had no tendency to promote instability.

As shown in Fig. 9 the predicted instability onset speed of the shaft, with the measured value of external damping but no internal damping is much higher than than experimentally observed, particularly at high eccentricity ratios. As the character of the internal damping and its distribution along the shaft were unknown, the simplest theoretical model was chosen, consisting of uniformly distributed, rotating viscous damping. Computations revealed that internal damping reduced the instability onset speed of the system throughout a wide range of eccentricity ratio, particularly when external damping was present. Such damping, due to shaft hysteresis and shrink fits, of the type employed in the test rig, would probably amount to a damping ratio, ν_I, between about 1 and 10×10^{-3}. In the present case this amounts to an internal damping coefficient between 1 and 10 Ns/m. Theoretical results obtained with an internal damping ratio of $\nu_I = 2.8 \times 10^{-3}$ are shown in Fig. 9, both for the case of zero external damping and for the case of an external damper with $\nu_D = 5.2 \times 10^{-3}$. It will be observed that the inclusion of internal damping in the analysis enables the agreement between theory and experiment to be considerably improved. It is recognized, however, that other factors may help to account for the discrepancy between the experimental results and the theoretical results for no internal damping.

The second rotor-bearing system used in experiments is shown in Fig. 11. It consisted of a flexible, symmetric rotor supported by two identical plain fluid-film bearings surrounded by squeeze-film isolators.
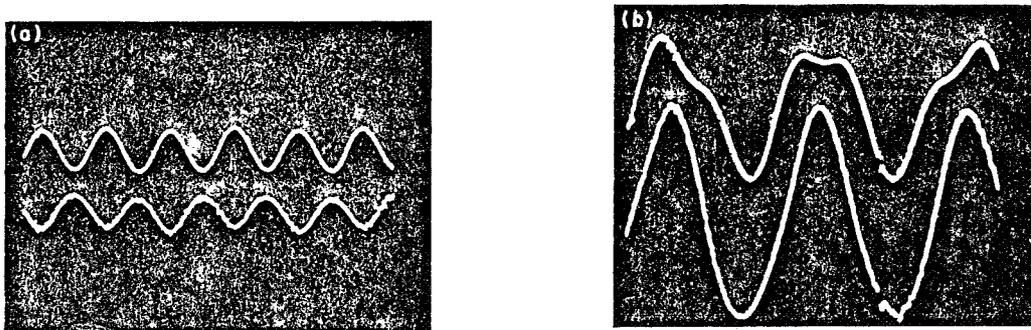
Fig. 10: Experimental recordings

Well-defined instability threshold speeds, as predicted by linear theory, were observed for large values of squeeze-film damping, while for low squeeze-film damping (below 5×10^3 N s/m), the system was stable and well damped in the entire operating speed range 0-4000 rev/min. However, in the damping

range 6 x 10^3 - 3 x 10^4 N s/m, steady non-synchronous whirling commenced at a rotational speed in the region of 1740-2250 rev/min, i.e. between twice and three times the first critical speed, with the exact onset speed depending on the damping value. The non-synchronous whirl amplitude would increase with speed up to about 2400 rev/min, i.e. about three times the first critical speed, whereafter the non-synchronous whirl component amplitude would decrease rapidly and vanish at about 2400-2740 rev/min. The response would then remain synchronous up to about 2870-3230 rev/min, still depending on the particular squeeze-film damping value, where non-synchronous whirling would reappear. In some instances, again depending on the damping, the whirl amplitudes at this speed would continue to grow, indicating conventional system instability, while in other cases the amplitude grew to a maximum with increasing speed and disappeared at about 3690-3800 rev/min. Thereafter,the system would remain stable up to and including the maximum operating speed of 4000 rev/min.

With an increase in oil temperature, it was possible to eliminate the second non-synchronous whirl region, and a further temperature increase would result in the disappearance of the first whirl region also, making the system inherently stable by not allowing the journal bearing oil films to exert their full influence. However, the system remained very sensitive to random transient excitation, such as tapping of the foundation with a rubber hammer, particularly near the first whirl region, and generally appeared to be very lightly damped at all speeds above twice the first critical speed. Variations in oil supply pressure had relatively little effect. The non-synchronous whirling exhibited the well-known hysteresis effect of persisting over a wider speed range once initiated.

Fig. 12 shows examples of the non-synchronous whirl orbits in the two whirl regions. The steady-state double and triple loops indicate whirl speeds of exactly 1/3 and 1/4 of the respective rotational speeds. Only at speeds of 2430 and 3323 rev/min (corresponding to roughly three times and four times the first critical speed) were the orbits stationary. Non-synchronous whirling was never found to reappear, either experimentally or theoretically, as a result of reduction in the bearing support damping from about 1 x 10^4 N s/m down to the minimum value of about 200 N s/m. Both the experimental and the predicted effects of bearing support stiffness were almost negligible within the covered stiffness range of 7 x 10^5 down to 8.85 x 10^4 N/m.

CONCLUSIONS

The main conclusions of the work described in this paper can be summarised as follows.

1) For a rigid rotor running in uncavitated journal bearings a good qualitative understanding of oil-whirl instability can be obtained by utilising in turn the short and long bearing assumptions in numerical computations.

2) For a flexible rotor-bearing system it was revealed that small amounts of external damping at a position in the shaft span increase the instability onset speed and that this effect is most pronounced when the eccentricity ratio for the bearings is high. External point damping is thus a useful method

for achieving stability control.

3) Experimental work has verified the theoretical assumption that the oil films in the bearings remain cavitated, even at the threshold of instability.

4) Instability onset speeds from two up to three times the first critical speed have been achieved experimentally, by varying the bearing operating conditions.

5) Good agreement between theoretically and experimentally determined instability onset speeds has been obtained in the case of no external point damping.

6) In the case of externally applied point damping, it has been shown that the inclusion of internal damping in the analysis enables the agreement between theoretically and experimentally determined instability onset speeds to be considerably improved. Internal damping had relatively little effect when no external point damping was applied.

7) The feasibility of controlling the vibration of a rotor-bearing system by mounting the bearings on squeeze-film isolators has also been demonstrated. Both numerical predictions and experimental results show a great improvement in stability when suitable external damping is employed. Inherent stability could be obtained within a large range of isolator stiffness and damping values, while for other values nonlinear behaviour was observed over distinct speed ranges where subharmonic steady-state vibrations of orders up to four occurred.
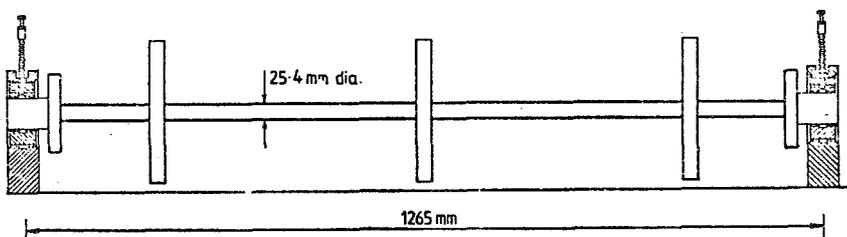
Fig. 11: Experimental system
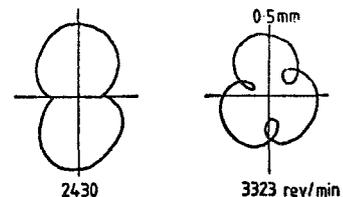
Fig.12: Non-synchronous orbits

REFERENCES

1) Holmes, R. 'Oil whirl characteristics of a rigid rotor in 360° journal bearings'., Proc. Instn Mech.Engrs. 1963, 177, (No.11), 291.

2) Holmes, R. 'The vibration of a rigid shaft on short sleeve-bearings'. Journ. of Mech. Engng Sci.,1960, 2, 337-341.

3) Swift, H.W. 'Fluctuating loads in sleeve bearings'. J. Instn. Civ.Engrs 1937, 5, 161.

4) Capriz ,G. 'Sulle vibrazioni della aste rotanti', 1963, Ann Scuola Normale Superiore, 17, 31.45.

Page intentionally left blank

SESSION VI

OTHER MECHANISMS FOR ROTOR INSTABILITIES

John Glease, NASA Marshall Space Flight Center
Chairman

EXPERIMENTAL RESULTS CONCERNING CENTRIFUGAL IMPELLER EXCITATIONS

J. M. Vance and F. J. Laudadio
Department of Mechanical Engineering
Texas A&M University
College Station, Texas 77840

INTRODUCTION

Based on what the authors have seen, the modern high performance centrifugal compressor is more likely to have problems with nonsynchronous rotordynamic instability than any other single class of machine. When designed for industrial application, these machines are typically multistage, with a rotor designed to operate at supercritical speeds, and supported on oil film bearings.

When such a compressor exhibits nonsynchronous whirl, the first troubleshooting efforts are usually aimed at modifying the oil film bearings. For example, a machine with cylindrical journal bearings may be modified to accept tilt-pad bearings, which have smaller cross-coupling coefficients (but also less damping).

The frequency with which these efforts fail suggests to the authors the existence of rotordynamic destabilizing excitations which are unique to centrifugal-type machines and which are not associated with the bearings.

EXPERIMENTAL OBSERVATIONS FROM A SIMPLE TEST RIG

To begin verification of this intuitive hypothesis, a simple test rig was set up in the Rotor Dynamics and Machinery Vibrations Laboratory at Texas A&M University. The objective was to observe the effect of working fluid, swirling in a housing, on the dynamics of an impeller with radial vanes.

Figure 1 shows the impeller and shaft removed from the rig, and figure 2 shows the impeller installed in the rig but without the fluid container. The impeller is supported vertically from a very flexible quill shaft in order to produce a low critical speed, and to allow the fluid dynamic effects on the impeller to predominate.

The shaft is supported from ball bearings, so that there is no possibility of "oil whip" from fluid film bearings as a destabilizing influence.

The impeller has been run both in the atmosphere (as in Figure 2), and submerged in working fluids contained in a cylindrical housing, open at the top. Variable speed is obtained with a DC gearmotor drive unit. The speed is measured with a proximity probe pulse tachometer and electronic digital counter.

361

The natural frequency of free vibrations was measured with a Selspot optical tracker, with the shaft displacement signal fed into a Nicolet 446 A frequency spectrum analyzer. The frequency spectrum shows the natural frequency in air to be 45 CPM, and the time trace digital memory feature of the Nicolet allowed a calculation of the logarithmic decrement which yielded δ = 0.0198, or 0.315% of critical damping, a very lightly damped rotor. The damping comes from atmospheric drag, and from internal hysteresis in the shaft assembly. The latter is known to be destabilizing on forward whirl, if the internal damping is large enough relative to the external damping.

The first test observations from this rig were reported in reference [1]. Since that time, additional tests have been run with working fluids having different viscosity values, in order to investigate a hypothesis that viscous shear is the exciting force which drives the instability in this rig.

It was found that the threshold speeds of instability are sensitive to the fluid level in the container, so this was held constant for all tests reported here.

Rotating tests in the atmosphere (fluid container removed) showed the impeller to be stable up to a maximum speed allowed by the motor, except that the impeller executes a small backward triangular orbit (bounded) at speeds above 112 rpm. This shows that internal friction is not a significant destabilizing force in this rotor.

To investigate viscosity effects, two working fluids were used: (1) kerosene ($\mu \approx 1 \times 10^{-6}$ lb-sec/in^2) and (2) SAE 40 motor oil ($\mu \approx 100 \times 10^{-6}$ lb-sec/in^2).

With the impeller running in kerosene, the threshold speed of instability for forward whirl is 89 rpm, or twice the critical speed. Above this speed, the impeller executes forward whirl at its natural frequency with an amplitude that grows with time (until contact with the fluid container is made).

At speeds near the threshold speed, the whirling grows to a small amplitude and then dies out repetitively.

With SAE 40 oil, the threshold speed of instability for forward whirl is raised to at least 174 rpm (3.9 times the critical speed), which is the highest speed allowed by the greater horsepower requirements of the high viscosity fluid. (At this speed, with this fluid, the gearmotor draws over 100 amperes).

THEORETICAL CONSIDERATIONS

The test reported above shows that viscous forces are stabilizing rather than destabilizing in this apparatus. This rules out a model based on Reynolds' theory, such as treating the impeller as a large journal bearing or as a large thrust bearing.

362

It seems likely that an inviscid fluid analysis based on Bernoulli's theory would yield useful results if applied correctly. Visual observations indicate that the fluid swirls in a vortex centered around the container's geometric axis, regardless of impeller whirling.

There are several characteristics of centrifugal compressors which are not present in this test apparatus. Notably, they are: (1) high fluid pressures in the volute surrounding the impeller, (2) radial flow of the fluid, proportional to delivery rate, and (3) compressibility.

The last characteristic is minimal in some of the very high pressure machines which seem to be most subject to rotordynamic instability, since the fluids are practically incompressible at the working pressures encountered.

For an imcompressible fluid, variations in radial velocity can produce Coriolis forces on the impeller. Figure 3 shows a case in which radial velocity $\dot{r}$ of the impeller will slow down the fluid in the direction of $\dot{r}$, and allow an increase in fluid radial velocity on the opposite side of the impeller. The variation in fluid radial velocity around the impeller can be expressed as

$$\Delta V_R = \dot{r} \cos \theta \tag{1}$$

At each θ location there is a difference in tangential Coriolis force as compared to the $\theta + \pi$ location, due to ΔV_R. This force difference is

$$d(F_2 - F_1) = 4\rho\omega\Delta V_R \ (R_o - R_i)(\frac{R_o + R_i}{2})ab \ d\theta \tag{2}$$

where ρ = fluid mass density

   ω = rotational speed

   R_o = impeller outside radius

   R_i = impeller inside radius

   a = impeller axial thickness

   b = width between vanes

Substitution of equation (1) into equation (2) gives

$$d(F_2 - F_1) = 2\rho\omega(R_o^2 - R_i^2)b \ \dot{r} \cos \theta \ d\theta$$

which is normal to the vane located at θ, acting opposite to the direction of the vanes' tangential velocity for $-\pi/2 < \theta < \pi/2$, and in the same direction

for $\pi/2 < \theta < 3\pi/2$.

The component normal to the whirl vector r, which is potentially destabilizing, is

$$dF_\phi = \cos\theta \; d(F_2 - F_1) \tag{3}$$

or

$$dF_\phi = 2\rho\omega(R_o^2 - R_i^2)ab \; \dot{r} \cos^2\theta \; d\theta$$

Integration around the impeller yields

$$F_\phi = 2\rho\omega(R_o^2 - R_i^2)ab \; \dot{r} \int_0^{2\pi} \cos^2\theta \; d\theta$$

or

$$F_\phi = 2\pi\rho\omega(R_o^2 - R_i^2)ab \; \dot{r}$$

which indicates a negative cross-coupled damping coefficient

$$C_{\phi r} = -2\pi\rho\omega(R_o^2 - R_i^2)ab \tag{4}$$

so that

$$F_\phi = -C_{\phi r}\dot{r} \; .$$

The effect of this coefficient should be to excite forward whirl, with an amplitude which would tend to grow and decay in a cyclic manner.

THE EFFECT OF LOAD

Many of the rotordynamic instabilities reported for centrifugal compressors are load dependent, or fluid pressure dependent. References [1] and [2] describe specific cases reported in the literature and/or observed by the authors.

364

Reference [3] defines a load-dependent cross-coupled stiffness coefficient which is currently used almost universally by rotordynamics consulting engineers for computerized stability analysis of all types of machines. A study of reference [3] reveals that the coefficient has real meaning only for axial flow machines.

References [2] and [4] describe a theory for load-dependent excitation in machines with very high torque loadings, and is applicable to centrifugal, as well as axial flow, compressors.

All of these theories are yet to be verified by experimental research or controlled tests in real machines.

CONCLUSIONS

The experimental observations reported here point strongly to the probability that centrifugal impellers produce rotordynamic destabilizing forces which are independent of the type of bearing used for rotor support.

A comprehensive and verified theory to explain and predict these forces is yet to be developed.

REFERENCES

1. Vance, J. M., and Laudadio, F. J.: Rotordynamic Instability in Centrifugal Compressors - Are All The Excitations Understood? ASME Paper No. 80-GT-149, presented at the Gas Turbine Conference, New Orleans, LA., March 10-13, 1980.

2. Vance, J. M., and Tison, J. D.: Analysis and Interpretation of Nonsynchronous Whirling in Turbomachinery. ASME Paper No. 78-Pet-26, presented at the Energy Technology Conference, Houston, TX., Nov. 5-9, 1978.

3. Alford, J. S.: Protecting Turbomachinery From Self-Excited Rotor Whirl. ASME Journal of Engineering for Power, Oct. 1965, pp. 333-344.

4. Vance, J. M.: Torquewhirl - A Theory To Explain Nonsynchronous Whirling Failures of Rotors With High Load Torque. ASME Journal of Engineering for Power, April, 1978, pp. 235-240.
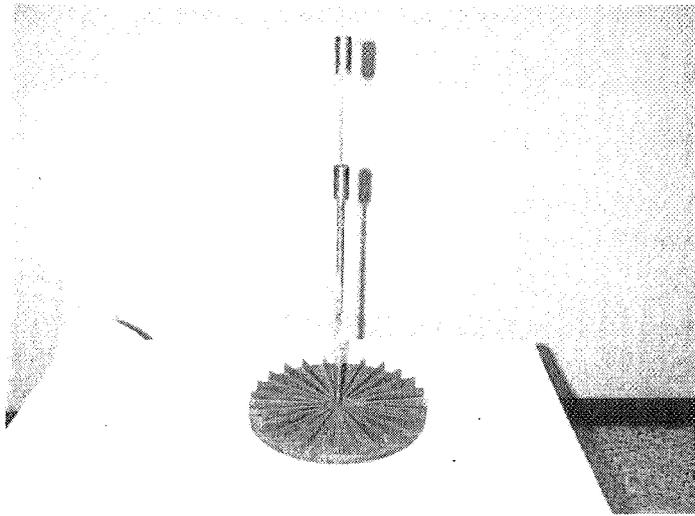
Figure 1. Test Rig Impeller and Shaft
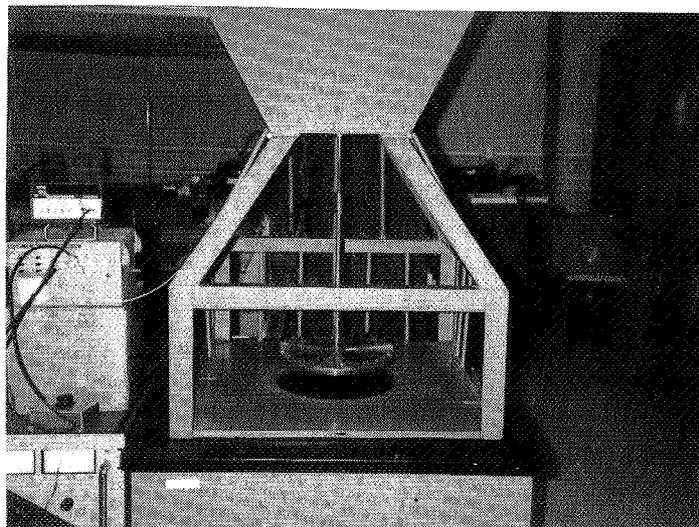
Figure 2. Assembled Test Rig Without Fluid Container
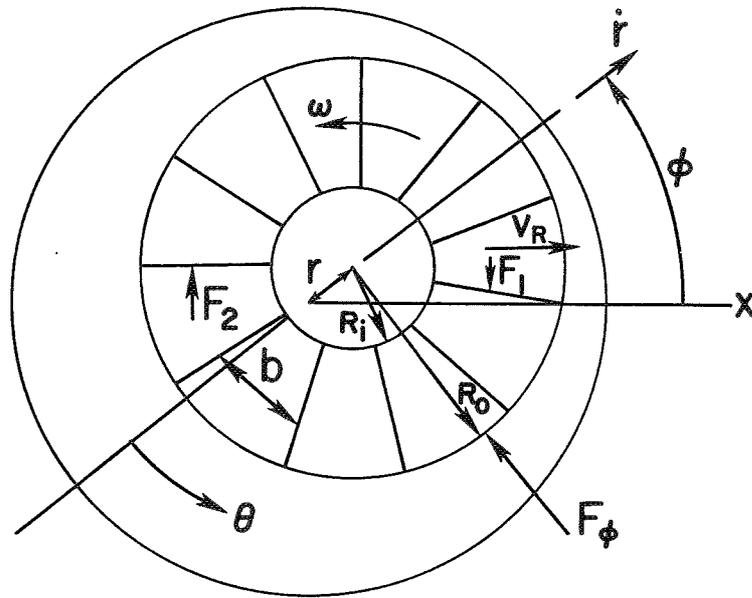
Figure 3. Coriolis forces generated by radial motion of impeller

Page intentionally left blank

PHYSICAL EXPLANATIONS OF THE DESTABILIZING
EFFECT OF DAMPING IN ROTATING PARTS

Stephen H. Crandall
Massachusetts Institute of Technology
Cambridge, Massachusetts 02139

SUMMARY

The original explanation of shaft whipping due to internal friction by
A. L. Kimball in 1923 employed a physical argument based on hysteresis in the
flexural stress-strain relation. Ten years later an even simpler physical
explanation of the destabilizing nature of rotating damping was briefly de-
scribed by D. M. Smith. Subsequently, there have been many discussions of the
effects of rotating damping on rotor stability. In most cases, the emphasis
has been on the mathematical aspects of the stability analysis rather than on
physical explanations. The present note provides an elaboration of Smith's
physical argument. It gives a clear insight into the destabilizing mechanism
and permits an elementary physical determination of the stability limit.

INTRODUCTION

The fundamental critical speed of an elastic rotor is a kind of natural
barrier for rotational speed much like the velocity of sound is for an airplane.
In both cases, there were historical periods when some engineers were of the
opinion that safe operation would not be possible beyond the barrier. Today
both barriers are routinely broken but not without careful engineering to
ensure safety in the supercritical or supersonic regimes.

The first analytical treatments of supercritical rotor whirling were given
by Föppl in 1895, for an undamped model, (ref. 1) and by Jeffcoat in 1919, for
a model with damping, (ref. 2). In this case, art preceded science, for in
1895 some commercial centrifuges and steam turbines were already running super-
critically (ref. 1). These early analyses indicated that, if anything, super-
critical operation should be smoother than subcritical. Since then, many
instability mechanisms (ref. 3) have been encountered, each of which poses a
potential threat to the hoped-for smoothness of supercritical operation. The
first of these to be diagnosed was the mechanism of internal friction or damping
of relative motion with respect to the rotating system. The theory was initially
described in 1923 (ref. 4) by A. L. Kimball, Jr. A fuller account is given in
reference 5. This is a simple physical argument to show that damping forces in
the fibers of the bending shaft have a resultant action which builds up a
whirling motion when the rotation is supercritical. The argument is independent
of the specific type of damping: viscous, hysteretic, or otherwise. Essentially,
the same argument appears in references 3 and 6. In 1933, Baker included the
damping action due to linear frequency-independent hysteresis in the equations of

motion and determined the growth rate of the unstable whirl (ref. 7). An extended presentation of the same analysis appears in reference 8.

In 1933, there also appeared the remarkable paper of D. M. Smith (ref. 9). Many modern investigations in rotor dynamics were anticipated in this paper. In particular, instabilities due to unsymmetrical rotating stiffness and unsymmetrical rotating inertia are described for the first time. Instability due to rotating damping is analyzed for a symmetrical system and the threshold frequency for viscous damping obtained for the first time. An analytical explanation for the ameliorating action of anisotropic support stiffness is also given for the first time. The basic idea of the physical explanation of de-stabilization due to rotating damping which is described in the present note is squeezed into a single sentence of Smith's paper at the conclusion of his analysis for the threshold frequency marking the transition from stability to instability. He also used the idea to give a simple physical explanation for the reason why anisotropic support stiffness raises the onset frequency for instability due to rotating damping.

Smith also made a number of shrewd predictions about rotor systems with several critical speeds, many of which have been verified. In the case of rotating damping, the situation has subsequently been shown (refs. 10,11) to be somewhat more complicated than he envisaged. Later investigators have also extended the theory of rotating damping to include damping mechanisms with arbitrary frequency dependence and nonlinear amplitude dependence (ref. 12).

At present, almost every engineer dealing with rotor dynamics is aware that rotating damping is destabilizing although to many it still is something of a mystery that a mechanism of energy dissipation can cause instability. Kimball's explanation, while physical and easy to follow step by step, is sufficiently intricate because of the awkward geometry of bending during simultaneous rotation and whirling that the argument as a whole is not as compelling as it might be. Smith's explanation is much simpler and persuasive but is not widely known in America. In 1970, the present author independently developed an explanation similar to Smith's which he presented several times in invited lectures based on reference 13. For nearly ten years, he believed his explanation was original until on reviewing A. B. Pippard's recent book (ref. 14) for the Journal of Applied Mechanics (ref. 15) he discovered that the explanation was, in fact, well known in England and was led back to Smith's work.

PLANAR ROTOR MODEL

Consider the planar model of a rotor mounted on a flexible shaft shown in Fig. 1. The rigid ring is forced to turn at the angular rate Ω by an external source. A mass particle m is suspended elastically from the ring by four mass-less linear springs. The mass particle represents the central rotor of the classical Föppl-Jeffcoat model and the springs represent the flexible shaft. Gravity in the plane of the diagram is neglected. The elastic force system for small displacements is circularly isotropic. The equilibrium position is with the mass at the origin and when the mass has a radial displacement r, in any direction within the plane, the elastic restoring force is kr directed back

370
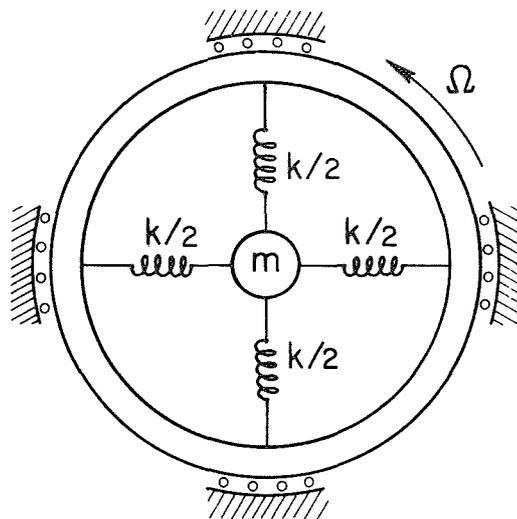
Fig. 1 Planar model of ideal balanced rotor with no damping.

toward the origin. Furthermore, this characteristic of the elastic system is independent of the rotational speed Ω. The equations of motion for the mass particle in Fig. 1 in terms of the stationary coordinates x,y of Fig. 2 are

$$m \begin{Bmatrix} \ddot{x} \\ \ddot{y} \end{Bmatrix} + k \begin{Bmatrix} x \\ y \end{Bmatrix} = 0 \qquad (1)$$

independently of Ω. All natural motions are linear combinations of two independent modes which have the same natural frequency $\omega_n = \sqrt{k/m}$. The two independent modes may be taken as rectilinear oscillations along two diameters or as a pair of circular whirling modes, one counter-clockwise and the other clockwise. The resulting orbit, in the general case, is an elliptical path which is periodically circumnavigated with the period $2\pi/\omega_n$. Due to the isotropy of the system, it is always possible, without loss of generality, to choose the orientation of the x,y axes and the starting phase so that the general free motion has the representation

$$x = a \cos \omega_n t$$
$$(2)$$
$$y = b \sin \omega_n t$$

where $|a|$ and $|b|$ are the major and minor semiaxes of the ellipse. It is sometimes convenient to consider the x,y plane as the locus of the complex variable

$$z = x + iy \qquad (3)$$

In such a setting a counter-clockwise whirl of unit amplitude and angular rate ω is represented by

371
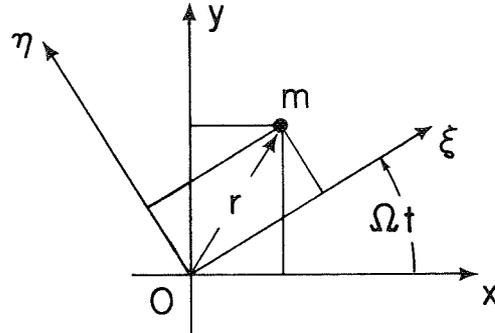
Fig. 2   Stationary coordinates x,y and rotating coordinates ξ,η for the mass particle in Fig. 1.

$$e^{i\omega t} = \cos \omega t + i \sin \omega t \tag{4}$$

The elliptical motion (2) can be represented as a superposition of counter-clockwise and clockwise whirls by inserting (2) into (3) and expressing the trigonometric functions in terms of exponentials of imaginary argument. The result is

$$z = a \cos \omega_n t + ib \sin \omega_n t$$
$$= A\, e^{i\omega_n t} + B e^{-i\omega_n t} \tag{5}$$

where

$$A = 1/2(a + b) \qquad a = A + B$$
$$B = 1/2(a - b) \qquad b = A - B \tag{6}$$

While not necessary for the physical explanation which follows, the equations of free motion with respect to the rotating axes ξ,η of Fig. 2 are given here for completeness

$$m \begin{Bmatrix} \ddot{\xi} \\ \ddot{\eta} \end{Bmatrix} - m\Omega^2 \begin{Bmatrix} \xi \\ \eta \end{Bmatrix} + 2m\Omega \begin{bmatrix} 0 & -1 \\ 1 & 0 \end{bmatrix} \begin{Bmatrix} \dot{\xi} \\ \dot{\eta} \end{Bmatrix} + k \begin{Bmatrix} \xi \\ \eta \end{Bmatrix} = 0 \tag{7}$$

In the elliptical orbit (2), the instantaneous kinetic energy is

$$T = m\omega_n^2 \left(\frac{a^2 + b^2}{4} - \frac{a^2 - b^2}{4} \cos 2\omega_n t \right) \tag{8}$$

and the intantaneous potential energy is

$$V = k \left(\frac{a^2 + b^2}{4} + \frac{a^2 - b^2}{4} \cos 2\omega_n t \right) \tag{9}$$

These energies oscillate about the same mean value with opposite phase so that the total energy E in the rotor orbit remains constant

$$E = T + V = 1/2k(a^2 + b^2) = k(A^2 + B^2) \qquad (10)$$

QUALITATIVE EFFECTS OF DAMPING

Consider now the introduction of isotropic linear damping to the rotor model of Fig. 1. In the following section, arbitrary frequency dependent linear damping mechanisms will be treated. For the present, it is sufficient to consider classical viscous damping. The damping of the motion of m may be with respect to the stationary axes x,y or the rotating axes ξ,η in Fig. 2. Damping with respect to the stationary axes is represented in Fig. 3 by the four dashpots whose outer extremities are fixed in the stationary reference frame. For small motions of m, the system of dashpots develops a circularly isotropic damping force. If the absolute velocity of m is v in any direction within the plane of motion, the resultant dashpot force is $c_s v$ in the opposite direction. In particular, if m is forced to travel in a circular orbit of radius A with counter-clockwise angular rate ω_n, the damping force $c_s A \omega_n$ acts tangent to the circle in a clockwise sense.

Damping of relative motion with respect to the rotating system is represented in Fig. 4 by the four dashpots whose outer extremities are fixed in the rotating ring. For small motions of m, this set of dashpots develops a circularly isotropic damping force which acts in opposition to the velocity of m relative to the rotating system. In particular, if m is forced to travel in a circular orbit of radius A with counter-clockwise angular rate ω_n as viewed from the
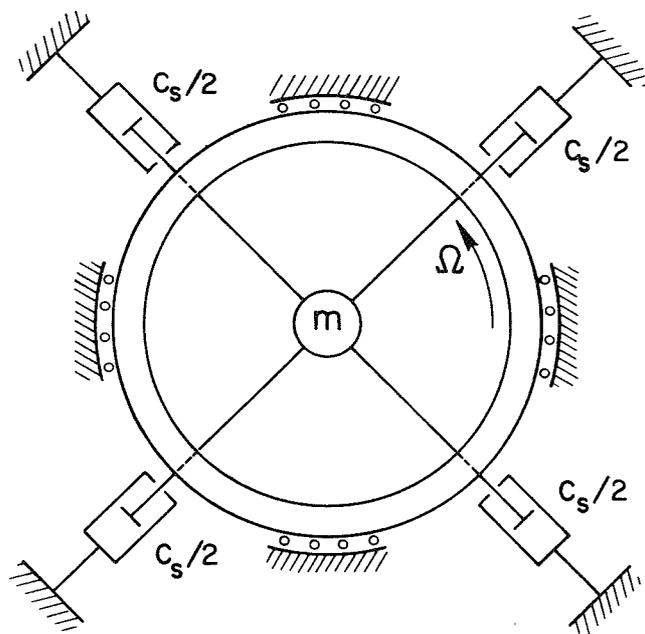
Fig. 3 Damping of motion with respect to stationary axes is represented by four symmetrically oriented dashpots.

stationary axes, it will appear to have a counter-clockwise angular rate $\omega_n - \Omega$ in the rotating frame. The damping force generated by the rotating dashpots is $c_r A(\omega_n - \Omega)$ acting tangentially to the circle in a clockwise sense.

The effects of these damping mechanisms on the free motion of the rotor can be argued qualitatively as follows. Suppose that the damping forces are very small in comparison with the spring forces. This implies that a free orbit will undergo only a small change during one period $2\pi/\omega_n$ as a result of the damping. If initially the orbit is a counter-clockwise circle of radius A, the preceding discussion shows that when the rotor rotation rate Ω is subcritical; i.e., less than the natural frequency of the free motion ω_n, both the stationary and rotating dashpots act to retard the motion of m. The rotor does work on the dashpots and the total energy E of the rotor orbit is diminished. If initially the orbit is a superposition of a counter-clockwise whirl of radius A and a clockwise whirl of radius B as in (5) a similar argument shows that when $\Omega < \omega_n$ the rotor does work on the dashpots in both whirls and that both A and B are diminished after a period $2\pi/\omega_n$. Any rotor orbit generated by an accidental disturbance will thus be damped out and the system is stable.

When the system rotates supercritically, the rotating dashpots do work on the rotor and add energy to the rotor orbit. This destabilizing action can be seen by returning to Fig. 4 and considering the case of a counter-clockwise whirl of radius A at absolute angular rate ω_n when $\Omega > \omega_n$. The relative motion now is
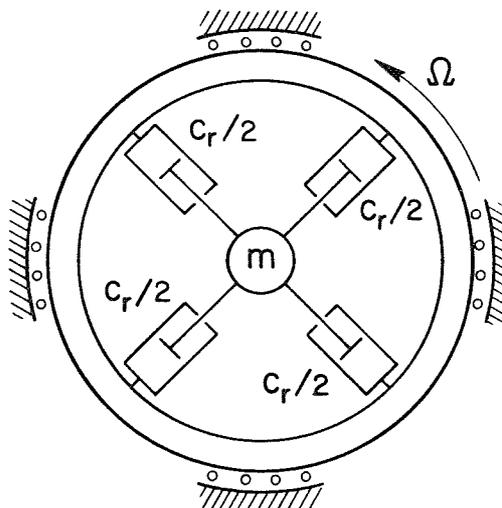
Fig. 4   Damping of relative motion with respect to rotating axes is represented by four symmetrically oriented dashpots.

a backward (i.e., clockwise) whirl with rate $\Omega - \omega_n$. The resultant dashpot force acts tangentially to the circular path in a forward (i.e., counter-clockwise) sense with magnitude $c_r A(\Omega - \omega_n)$. The supercritical rotation of the system thus acts to drag the rotor forward around its orbit through the rotating dashpots.

This action may be seen in an even clearer fashion if, instead of the four dashpots in Fig. 4, it is imagined that the interior of the ring is filled with a massless viscous fluid which rotates with the ring and acts to retard the relative motion of the mass m with respect to the ring. When the mass has a circular orbit in the same absolute sense as the ring rotation, but at a slower rate, the viscous drag pulls the mass forward and adds energy to its orbit.

The model described by Pippard (ref. 14) is essentially equivalent. The rotor is modelled by a conical pendulum with a heavy bob suspended in the gravity field by a string of length L. The natural modes are forward and backward conical whirls with the same natural frequency $\omega_n = \sqrt{g/L}$ (for small cone angles). Damping is modelled by allowing the pendulum bob to dip into a glass of water. If the glass is on a variable speed turntable, damping with respect to a rotating frame can be demonstrated. "If the fluid is caused to rotate more slowly than the pendulum bob in its circular orbit, the bob experiences a retarding force and sinks toward the vertical. But if the fluid rotates faster than the bob, it urges the bob onwards and causes its orbit radius to increase"--- (ref. 14). See Fig. 6 below.

Returning to the planar rotor model with both stationary damping, Fig. 3, and rotating damping, Fig. 4, a forward whirl at absolute angular rate ω_n will be retarded by the stationary damping force and will be urged on by the rotating damping force when the rotation is supercritical, $\Omega > \omega_n$. Whether the net effect is to remove or to add energy to the whirl orbit, depends on which force is larger. Neutral stability occurs when the forces are equal. There is then no change in the orbit energy and the free motion persits indefinitely. The quantitative determination of the stability borderline is discussed in the following section, taking account of the frequency dependence of the damping mechanisms.

In the case of a backward whirl, both the rotating dashpots and the stationary dashpots act to retard the whirl. The orbit energy of a backward whirl is always decreased by either rotating or stationary damping. For completeness, the equations of motion for the planar rotor model of Fig. 2 with the damping elements of Figs. 3 and 4 are given here. In the stationary coordinates, the equations for the damped system are

$$m \begin{Bmatrix} \ddot{x} \\ \ddot{y} \end{Bmatrix} + (c_s + c_r) \begin{Bmatrix} \dot{x} \\ \dot{y} \end{Bmatrix} + k \begin{Bmatrix} x \\ y \end{Bmatrix} + c_r \Omega \begin{bmatrix} 0 & 1 \\ -1 & 0 \end{bmatrix} \begin{Bmatrix} x \\ y \end{Bmatrix} = 0 \qquad (11)$$

in place of (1) for the undamped system. In the rotating coordinates used in (7), the equations for the same damped system are

$$m \begin{Bmatrix} \ddot{\xi} \\ \ddot{\eta} \end{Bmatrix} + (c_s + c_r) \begin{Bmatrix} \dot{\xi} \\ \dot{\eta} \end{Bmatrix} + (k - m\Omega^2) \begin{Bmatrix} \xi \\ \eta \end{Bmatrix} + 2m\Omega \begin{bmatrix} 0 & -1 \\ 1 & 0 \end{bmatrix} \begin{Bmatrix} \dot{\xi} \\ \dot{\eta} \end{Bmatrix} + c_s \Omega \begin{bmatrix} 0 & -1 \\ 1 & 0 \end{bmatrix} \begin{Bmatrix} \xi \\ \eta \end{Bmatrix} = 0 \quad (12)$$

Note that in the stationary coordinates of (11), the rotating damping is represented by both a normal damping term and by a quasi-gyroscopic term. In the rotating coordinates of (12), the stationary damping is represented in like fashion.

375

QUANTITATIVE EFFECTS OF DAMPING

In the preceding section, it was shown that at the stability borderline for a forward whirl the resultant forward drag force of the supercritically rotating damping balances the backward drag of the stationary damping. To give a quantitative expression of this we introduce the concept of <u>loss factor</u>. When a material or mechanical element undergoing harmonic deformation at frequency ω has both elastic and damping behavior, the ratio of the amplitude of the damping force to the amplitude of the elastic force is called the loss tangent, or loss factor, η. In general, η depends on both the amplitude and frequency of the deformation. For linear damping mechanisms, η is independent of amplitude. There are many real damping mechanisms that can be satisfactorily modeled as linear frequency-dependent processes; e.g., polymers, and metals when the dominant damping is due to transverse thermal currents (refs. 13,16). For the planar rotor model of Fig. 1, we can define a stationary loss factor $\eta_s(\omega)$ by taking the ratio of the tangential drag force, due to stationary damping, to the radial spring force when the mass particle executes a circular orbit with radius A at frequency ω. When $\omega = \omega_n$, the backward drag force D_s due to the stationary damping is

$$D_s = \eta_s(\omega_n) \, kA \qquad (13)$$

Similarly, a rotating loss factor $\eta_r(\omega)$ is defined as the ratio of the tangential drag force, due to rotating damping, to the radial spring force when the mass particle executes a circular orbit with radius A at a circular frequency ω, <u>with respect to the rotating system</u>. In a forward whirl at absolue rate ω_n, the circular frequency with respect to the system rotating at rate Ω is $\omega_n - \Omega$. Thus when the system rotates supercritically, the drag force D_r due to the rotating damping is forward and has the magnitude

$$D_r = \eta_r(\Omega - \omega_n) \, kA \qquad (14)$$

for an orbit of radius A. If $D_r = D_s$, we have a steady orbit of fixed radius A. If $D_r < D_s$, there is net retardation and the orbit energy decreases. If $D_r > D_s$, there is net acceleration and the orbit energy increases. Alternatively the stability is decided by the relative magnitudes of the rotating and stationary loss factors as indicated in Fig. 5. The stability borderline condition occurs when the loss factors are equal

$$\eta_r(\Omega - \omega_n) = \eta_s(\omega_n) \qquad (15)$$

The running speeds Ω which satisfy (15) depend crucially on the frequency dependence of the rotating damping mechanism and on the magnitude of the stationa damping.

The planar rotor model also provides a clear insight into the energy relatio ships during whirling of a rotor with stationary and rotating damping mechanisms. Consider a forward whirl with radius A and angular rate ω_n. If the system is rotating supercritically at rate Ω, the external agent responsible for maintaining the rotation rate Ω delivers energy to the system. This power input is mostly dissipated in the stationary and rotating damping mechanisms. If there is excess

input power, energy will be added to the whirl orbit, if the input power is inadequate, energy will be removed from the whirl orbit. Quantitatively, we have the following powers, when $\Omega > \omega_n$

$$P_{input} = D_r A\Omega = kA^2\Omega\eta_r$$

$$P_{diss,rot} = D_r A(\Omega - \omega_n) = kA^2(\Omega - \omega_n)\eta_r$$

$$P_{diss,sta} = D_s A\omega_n = kA^2\omega_n\eta_s$$

(16)

$$P_{orbit} = (D_r - D_s)A\omega_n = kA^2\omega_n(\eta_r - \eta_s)$$
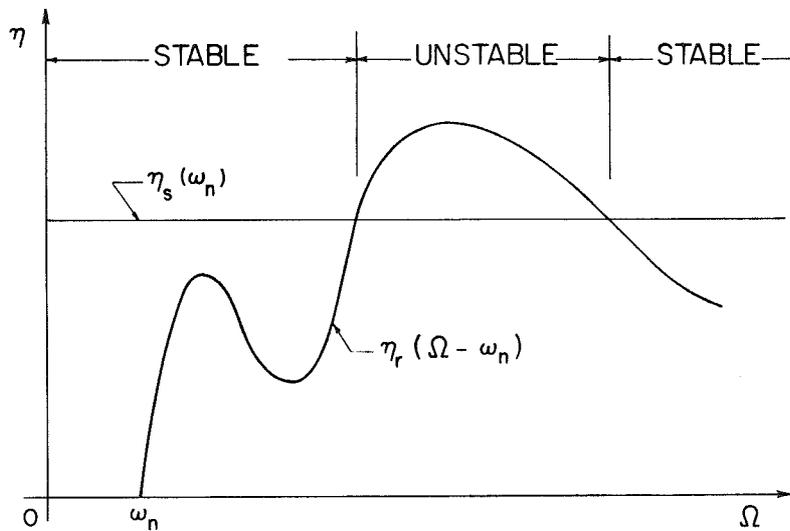
Fig. 5   Forward whirl is unstable for supercritical rotation speeds Ω at which the loss factor of rotating damping is greater than the loss factor of stationary damping.

Note that these satisfy the requirement of energy conservation

$$P_{input} = P_{diss,rot} + P_{diss,sta} + P_{orbit}$$

(17)

At a stability borderline, we have no power flow into, or out of, the orbit which leads back to the requirement (15). Note also that if the frequency dependence of $\eta_r(\omega)$ is such that the instability onset rotation Ω is very close to ω_n then the relative amount of energy dissipated in the rotating damping mechanism will be very small in comparison to the energy dissipated in the stationary damping mechanism even though it is the rotating damping force which is responsible for the instability.

The power flow into the orbit in (16) can be used to estimate the growth rate of the orbit in the unstable regime. Assuming exponential growth of orbit radius

$$A = A_o e^{\alpha t} \tag{18}$$

with small growth rate α, the energy added to an orbit with initial radius A_o and angular rate ω_n would be approximately

$$P_{orbit} \cdot \frac{2\pi}{\omega_n} = 2\pi k A_o^2 (\eta_r - \eta_s) \tag{19}$$

During this period, the radius increases from A_o to $A_o \exp\{2\pi\alpha/\omega_n\}$ and the increase in orbit energy as given by (10) is

$$\Delta E = k A_o^2 (e^{\frac{4\pi\alpha}{\omega_n}} - 1) \approx 4\pi k A_o^2 \frac{\alpha}{\omega_n} \tag{20}$$

Equating (19) and (20), we find

$$\alpha = 1/2 \omega_n (\eta_r - \eta_s) \tag{21}$$

as the estimated growth rate. In (21), $\eta_r(\omega)$ is to be evaluated at $\omega = \Omega - \omega_s$ and $\eta_s(\omega)$ is to be evaluated at $\omega = \omega_n$.

The proceding results can, of course, also be derived by solving (11) or (12). If in (11), for example, we set $z = x + iy$ and $\omega_n^2 = k/m$ the complex variable $z(t)$ must satisfy the equation

$$\ddot{z} + \frac{c_s + c_r}{m} \dot{z} + (\omega_n^2 - i\frac{c_r}{m}\Omega)z = 0 \tag{22}$$

Exponential terms of the form

$$z = A \exp\{(\alpha + i\beta)t\} \tag{23}$$

satisfy (22) if

$$\beta^2 = \omega_n^2 - \alpha^2 - \alpha\frac{c_s + c_r}{m}$$

$$\alpha = \frac{(\Omega - \beta)c_r - \beta c_s}{2\beta} \tag{24}$$

These relations apply with constant c_s and c_r if the damping is viscous. For other linear frequency-dependent damping mechanisms with loss factors $\eta_s(\omega)$ and $\eta_r(\omega)$ we can use the relations (see ref. 13)

$$c_s = \frac{k\eta_s(\beta)}{|\beta|} \qquad c_r = \frac{k\eta_r(\Omega - \beta)}{|\Omega - \beta|} \tag{25}$$

on the assumption that $\alpha << \beta$. This assumption is verified _a posteriori_ for light damping. Then, correct to first order in the loss factors, we have from (24)

$$\beta_1 = \omega_n \qquad\qquad\qquad \beta_2 = -\omega_n$$

$$\alpha_1 = 1/2\omega_n[\eta_r(\Omega - \omega_n) \text{ sgn } (\Omega - \omega_n) - \eta_s(\omega_n)] \quad \alpha_2 = -1/2\omega_n[\eta_r(\Omega + \omega_n) + \eta_s(\omega_n)] \quad (26)$$

To this order of accuracy, the general solution to (11) is

$$z(t) = A_1 \exp\{(\alpha_1 + i\omega_n t)\} + A_2 \exp\{(\alpha_2 - i\omega_n t)\} \tag{27}$$

This is a superposition of Archimedean spirals. The forward spiral has a growth rate α_1 which is positive if $\Omega > \omega_n$ and $\eta_r(\Omega - \omega_n) > \eta_s(\omega_n)$. The magnitude of α_1 in this case agrees with the estimate (21). If $\Omega < \omega_n$ then α_1 is negative and the forward spiral decays. The growth rate α_2 of the backward spiral is always negative.

CONCLUSIONS

Visualization of damping as a drag force on the orbit provides a clear explanation of the destabilizing effect of rotating damping. When the rotation is faster than the whirl, rotating damping drags the orbiting particle forward. When stationary damping is also present, the stability borderline is readily determined by balancing the backward and forward drags. A key notion here is that a forward whirl at rate ω_n with respect to stationary axes appears to be a backward whirl at rate $\Omega - \omega_n$ with respect to a system rotating supercritically at rate Ω. The growth rate of unstable whirls (or the decay rate of stable whirls) is readily estimated by a simple energy balance.

As a final note, we call attention to D. M. Smith's extension of the previous argument to rotor systems with anisotropic non-rotating support elasticity. If the bearings in Fig. 1 are not rigidly supported, but are elastically supported so that the compliance in the x – direction is greater (say) than that in the y – direction, the free motion of the undamped system becomes a super-position of a horizontal oscillation at frequency ω_1 and a vertical oscillation at frequency $\omega_2 > \omega_1$. The more anisotropic the supports, the greater the separation between ω_1 and ω_2. The resultant free orbits no longer whirl with a fixed sense and ---"there is no tendency to set up a whirl of the type which can be dragged forward by rotary damping until the rotary damping forces have been so far increased by rising speed that they are commensurate with the difference between elastic restoring forces in the two principal directions "---(ref. 9). Thus, anisotropic bearing supports should raise the onset speed Ω for instability due to rotating damping. Smith (ref. 9) and others (ref. 17) have verified this by applying Routh's criterion to the equation of motion.

APPENDIX

The description of the destabilizing action of rotating drag forces given above can be extended to give a heuristic explanation of the destabilizing tendency of fluid filled journal bearings when the rotational speed exceeds <u>twice</u> the natural frequency of the rotor. Here, instead of modelling the rotor as a particle travelling in an orbit within a fluid bath whose drag either retards or advances the particle, we model the rotor as a cylindrical journal of radius r rotating within a cylindrical bearing with a small radial clearance $h(h << r)$. When the journal is centered and rotating at angular rate Ω, the incompressible viscous fluid in the gap is pumped circumferentially (longitudinal flow is neglected). The fluid velocity varies linearly across the channel of thickness h, from $v = r\Omega$ at the journal to $v = 0$ at the bearing. This flow can be decomposed into a mean flow with uniform velocity $v = r\Omega/2$ and no vorticity and a residual flow with no mean flow and large vorticity.

Next, consider a small circular whirl of the rotor with amplitude $A(A << h)$ and angular rate ω_n where as before ω_n is the rotor natural frequency. As the center of the journal traverses a circle of radius A, a wave of thickness variation moves around the channel between the journal and the bearing. At the thinnest point, the thickness is $h - A$ and at the thickest point the thickness is $h + A$. If we follow the position of, say, the thinnest point, we note that it appears to whirl at the rate ω_n; i.e., the circumferential velocity of the wave of thickness variation is $r\omega_n$.

Finally, we conclude that such a natural whirling motion will be retarded or aided by the mean flow of the pumped fluid depending on whether the mean fluid velocity $r\Omega_n/2$ is less or greater than the circumferential velocity of the wave of thickness variation $r\omega_n$. Neglecting other mechanisms, the stability borderline is determined by a balance between the destablizing tendency of the mean flow and the stabilizing tendencies of the residual high-vorticity flow. A necessary condition for the onset of instability is $\Omega > 2\omega_n$.

The action of the mean fluid flow in a fluid-filled bearing, in dragging around a wave of thickness variation when $\Omega > 2\omega_n$ is thus proposed as a heuristic physical explanation for the classical oil-whip phenomenon.

380
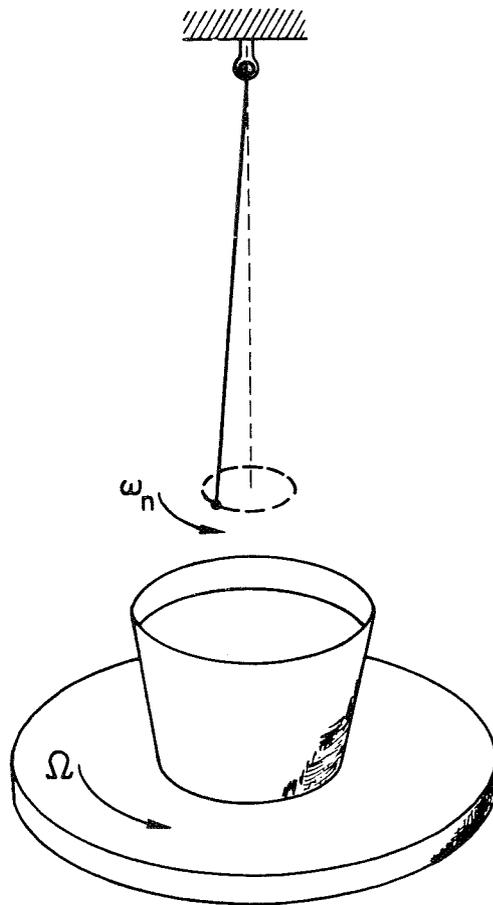
Fig. 6   When $\Omega < \omega_n$, fluid drag retards pendulum bob and
radius of orbit decreases; when $\Omega > \omega_n$, fluid drag
pulls bob around orbit and radius of orbit increases.

REFERENCES

1. A. Föppl. Das Problem der Laval'schen Turbinewelle, <u>Civilingenieur</u> 41, 332-342 (1895).

2. H. H. Jeffcoat. The lateral vibration of loaded shafts in the neighborhood of a whirling speed. - The effect of want of balance, <u>Phil. Mag.</u> [6]37,304-314 (1919).

3. F. F. Ehrich. Identification and avoidance of instabilities and self-excited vibrations in rotating machinery, ASME Paper 72-DE-21 (1972).

4. A. L. Kimball, Jr. Internal friction theory of shaft whirling, <u>Phys. Rev.</u> [2]21,703 (1923).

5. A. L. Kimball, Jr. Internal friction as a cause of shaft whirling, <u>Phil. Mag.</u> [6]49,724-727 (1925).

6. J. P. Den Hartog. <u>Mechanical Vibrations</u>, 4th Ed., McGraw-Hill Book Co., N.Y., 1956, pp. 295-297.

7. J. G. Baker. Self-induced vibrations, <u>J. Appl. Mechs.</u> 1, 5-12 (1933).

8. S. Timoshenko. <u>Vibration Problems in Engineering</u>, 3rd Ed., D. Van Nostrand Co., Princeton, N.J., 1961, pp. 227-232.

9. D. M. Smith. The motion of a rotor carried by a flexible shaft in flexible bearings, Proc. Roy. Soc. (London) A 142, 92-118 (1933).

10. W. Kellenberger. Die Stabilität rotierenden Wellen infolge inner und ausser Dämpfung, <u>Ing. Arch.</u> 32, 323-340 (1963).

11. F. F. Ehrich. Shaft whirl induced by rotor internal damping, <u>J. Appl. Mechs</u> 31, 279-282 (1964).

12. V. V. Bolotin. <u>Non-conservative problems of the theory of elastic stability</u>, Macmillan Co., N.Y., 1963, pp. 155-198.

13. S. H. Crandall. The role of damping in vibration theory, <u>J. Sound Vib.</u> 11, 3-18 (1970).

14. A. B. Pippard. <u>The Physics of Vibration</u> Vol. 1, Cambridge University Press, Cambridge, 1978, pp. 212-216.

15. S. H. Crandall. Review of Reference 14, J. Appl. Mech. 46, 966 (1979).

16. B. J. Lazan. <u>Damping of Materials and Members in Structural Mechanics</u>, Pergamon Press, Oxford, 1968.

17. E. J. Gunter and P. R. Trumpler. Influence of internal friction on the stability of high speed rotors with anisotropic supports, <u>J. Engrg. Indus. Trans. ASME</u> 91, 1105-1113 (1969).

PARAMETRIC INSTABILITIES OF ROTOR-SUPPORT SYSTEMS
WITH APPLICATION TO INDUSTRIAL VENTILATORS

Zdzisław Parszewski, Janusz Krodkiewski,
and Krzysztof Marynowski
Politechnika Łodzka
Łodz, Poland 90245

SUMMARY

Rotor-support systems interaction with parametric excitation is considered for both unequal principal shaft stiffnesses (generators) and off-set disc rotors (ventilators). Instability regions and types of instability are computed in the first case, and parametric resonances in the second case. Computed and experimental results are compared for laboratory machine models. A field case study of parametric vibrations in industrial ventilators is reported. Computed parametric resonances are confirmed in field measurements, and some industrial failures are explained. Also the dynamic influence and gyroscopic effect of supporting structures are shown and computed.

INTRODUCTION

With growing rotor speeds or machine capacities the influence of supporting structures on stability and critical speeds is of increasing importance, specially when some rotor parameters are variable. This is often the case in machines used in mining and power generating industries, for example, large generators, industrial ventilators, and turbopumps. The unequal rotor principal stiffnesses in the first instance and unequal principal moments of inertia of the ventilator disc in the second instance, with the flexible anisotropic support interaction, cause the parametric effect.

A 120-MW generator of Dolmel-Wrocław production is shown in figure 1. Its rotor is of 9.157 m length, with a span of 6.858 m between bearings. The wiring slots distribution gives rise to small unequality of the rotor principal stiffnesses k_x, k_y. Two types of mine ventilators are shown in figure 2: large ventilator No. I of the type SLM (fig. 2(a)) of nominal output of 320 m/min, and universal ventilator No. II of type FKD-30 (fig. 2(b)). The first has an overhang shaft of full length 0.908 m. The disc is between bearings in the second ventilator with a shaft of 0.773 m length. Production errors cause the unequality of principal moments of inertia of the disc.

GENERAL THEORY

The rotor-support system can be considered as two connected and dynamically interacting subsystems. One (rotor) is a discrete parametric system (fig. 3, bold lines). The second is nonparametric, contains the whole supporting structure, and is usually very complicated. A receptance (impedance) matrix is hence used for description of its dynamic behavior. Its elements can then be measured if not calculated. All (usually infinity) but the connecting coordinates

of the supporting structure can be eliminated (ref. 6) from the equations of
motion of the systems, giving their general matrix form

$$\underset{\mathcal{H}\times\mathcal{H}}{M(t)}\ddot{\underset{\mathcal{H}}{x}}+\left[\underset{\mathcal{H}\times\mathcal{H}}{C(t)}+\frac{1}{\beta}\underset{u}{\gamma}_{u}(\beta)\right]\dot{\underset{\mathcal{H}}{x}}+\left[\underset{-\mathcal{H}\times\mathcal{H}}{K(t)}+\underset{\mathcal{H}\times\mathcal{H}}{\gamma_{r}(\beta)}\right]\underset{\mathcal{H}}{x}=\underset{\mathcal{H}}{G}+\underset{\mathcal{H}}{P}\sin\omega t+\underset{\mathcal{H}}{Q}\cos\omega t \qquad (1)$$

Here all the matrices are of the order equal to the sum of the number of de-
grees of freedom of the parametric subsystem (rotor) and the number of connect-
ing coordinates. In the cases considered, for instance, the last number is
four (fig. 2); γ_r and γ_u are, respectively, real and imaginary parts of the
dynamic impedances of the supporting structure along the connecting coordinates;
G, P, and Q are force vectors. For an offset disc mounted flexibly (fig. 4)
or for a rotor of different principal stiffnesses (the two cases are here con-
nected only formally), the equations are

For a rotor of different principal stiffnesses

$$M(t)=M ; \quad C(t)=C; \quad K(t)=K+\varepsilon(E\cos\vartheta t+F\sin\vartheta t) \qquad (2a)$$

For an offset disc and circular shaft

$$M(t)=M+d(t); \quad C(t)=C+Z+c(t); \quad K(t)=K+d(t) \qquad (2b)$$

where

$$M=\begin{bmatrix} m & -S_{\xi\eta} & 0 & 0 & 0 \\ -S_{\xi\eta} & -B-B_{\xi\eta} & 0 & 0 & 0 \\ 0 & 0 & -m & S_{\xi\eta} & 0 \\ 0 & 0 & S_{\xi\eta} & -B-B_{\xi\eta} & 0 \\ 0 & 0 & 0 & 0 & -m \end{bmatrix} \quad Z=\begin{bmatrix} 0 & 0 & 0 & 0 & 0 \\ 0 & 0 & 0 & 2\omega B & 0 \\ 0 & 0 & 0 & 0 & 0 \\ 0 & -2\omega B & 0 & 0 & 0 \\ 0 & 0 & 0 & 0 & 0 \end{bmatrix} \quad \gamma_r=\begin{bmatrix} \gamma_{xR_x} & \gamma_{xM_y} & 0 & 0 & 0 \\ \gamma_{\Psi_y R_x} & \gamma_{\Psi_y M_y} & 0 & 0 & 0 \\ 0 & 0 & \gamma_{yR_y} & \gamma_{yM_x} & 0 \\ 0 & 0 & \gamma_{\Psi_x R_y} & \gamma_{\Psi_x M_x} & 0 \\ 0 & 0 & 0 & 0 & \gamma_{zR_z} \end{bmatrix}$$
$$(3)$$

$$b=\begin{bmatrix} 0 & 0 & & 0 & 0 & & 0 \\ 0 & -\Delta B\cos 2\omega t+D_\xi\sin 2\omega t & & 0 & \Delta B\sin 2\omega t+D_\xi\cos 2\omega t & S_{\eta\xi}\cos\omega t-S_{\xi\xi}\sin\omega t \\ 0 & 0 & & 0 & 0 & & 0 \\ 0 & \Delta B\sin 2\omega t+D_\xi\cos 2\omega t & & 0 & \Delta B\cos 2\omega t-D_\xi\sin 2\omega t & -S_{\eta\xi}\sin\omega t-S_{\xi\xi}\cos\omega t \\ 0 & S_{\eta\xi}\cos\omega t-S_{\xi\xi}\sin\omega t & & 0 & -S_{\eta\xi}\sin\omega t-S_{\xi\xi}\cos\omega t & 0 \end{bmatrix} \quad X=\begin{bmatrix} x \\ \Psi_y \\ y \\ \Psi_x \\ z \end{bmatrix} \qquad (4)$$

$$C=\begin{bmatrix} 0 & 0 & & 0 & 0 & & 0 \\ 0 & 2\Delta B\omega\sin 2\omega t+2D_\xi\omega\cos 2\omega t & & 0 & 2\Delta B\omega\cos 2\omega t-2D_\xi\omega\sin 2\omega t & 0 \\ 0 & 0 & & 0 & 0 & & 0 \\ 0 & 2\Delta B\omega\sin 2\omega t+2D_\xi\sin 2\omega t & & 0 & -2\Delta B\omega\sin 2\omega t-2D_\xi\omega\cos 2\omega t & 0 \\ 0 & -2\omega(S_{\eta\xi}\sin\omega t+S_{\xi\xi}\cos\omega t) & & 0 & -2\omega(S_{\eta\xi}\cos\omega t-S_{\xi\xi}\sin\omega t) & 0 \end{bmatrix} \quad (5) \qquad P=\begin{bmatrix} -\omega^2 S_{\xi\xi} \\ -D_\xi \\ \omega^2 S_{\eta\xi} \\ -D_\eta \\ \omega^2(\Psi_{ys}S_{\xi\xi}+\Psi_{xs}S_{\eta\xi}) \end{bmatrix}$$

384

$$\mathbf{d} = \begin{bmatrix} 0 & 0 & & 0 & 0 & & 0 \\ 0 & 0 & & 0 & 0 & & 0 \\ 0 & 0 & & 0 & 0 & & 0 \\ 0 & 0 & & 0 & 0 & & 0 \\ 0 & -\omega^2(S_{\eta\zeta}\cos\omega t - S_{\xi\zeta}\sin\omega t) & 0 & \omega^2(S_{\eta\zeta}\sin\omega t + S_{\xi\zeta}\cos\omega t) & 0 \end{bmatrix} \quad (6)$$

$$\overset{(7)}{\mathbf{Q}} = \begin{bmatrix} \omega^2 S_{\eta\zeta} \\ D_{\eta} \\ \omega^2 S_{\xi\zeta} \\ -D_{\zeta} \\ -\omega^2(\gamma_{y3}S_{\eta\zeta} - \gamma_{x3}S_{\xi\zeta}) \end{bmatrix}$$

where $S_{\xi\eta}, \ldots B_{\eta\zeta}$ are the first and second moments of the rotor mass with respect to the coordinate planes $\xi\eta\zeta$ connected with the rotor; D_ξ, D_η, D_ζ are corresponding deviation moments; and

$$B = \tfrac{1}{2}\left(B_{\eta\zeta} + B_{\xi\zeta}\right) \qquad \Delta B = \tfrac{1}{2}\left(B_{\eta\zeta} - B_{\xi\zeta}\right) \qquad (8)$$

Finally

$$\beta_i^{(t)} = \frac{i\vartheta \pm 2\mu}{2} \qquad (9)$$

where μ and θ are the arguments of the solutions

$$\mathbf{X} = e^{j\mu t}\sum_{i=0}^{\infty}\left(\mathbf{a}_i \sin\frac{i\vartheta}{2}t + \mathbf{b}_i \cos\frac{i\vartheta}{2}t\right) \qquad (10)$$

of the homogenous part of equation (1) at stability limits.

Instability

The conditions of existence of steady solutions (10), giving the boundary equations in the stability region, in the equivalent forms for odd or even numerals i, are

 $= 0 \qquad (11)$

Consecutive approximations are shown with broken lines in equation (11). The first approximation is

$$g_{jj} = \begin{vmatrix} -\beta_-^2 M + K + \Upsilon_r(\beta_-) & -\tfrac{1}{2}\varepsilon E & -\beta_- C + \Upsilon_u(\beta_-) & \tfrac{1}{2}\varepsilon F \\ -\tfrac{1}{2}\varepsilon E & -(\beta_+)^2 M + K + \Upsilon_r(\beta_+) & \tfrac{1}{2}\varepsilon F & -\beta_+ C + \Upsilon_u(\beta_+) \\ \beta_+ C + \Upsilon_u(\beta_+) & \tfrac{1}{2}\varepsilon F & -(\beta_-^2) M + K + \Upsilon_r(\beta_-) & \tfrac{1}{2}\varepsilon E \\ \tfrac{1}{2}\varepsilon F & \beta_+ C + \Upsilon_u(\beta_+) & \tfrac{1}{2}\varepsilon E & -(\beta_+^2) M + K + \Upsilon_r(\beta_+) \end{vmatrix} = 0 \qquad (12)$$

The instabilities occur in the vicinity of circular frequencies

$$\theta_{jk} = \frac{\lambda_j + \lambda_k}{n} \qquad n = 1, 2, 3, \ldots \qquad (13)$$

The width of the instability region depends on ε and damping C. Here λ_j are the natural frequencies of the system, being the roots of equation (12) at zero parametric excitation ($\varepsilon = 0$) and no damping ($C = 0$, $\Upsilon_u = 0$).

Resonance Speeds

Forced vibrations analysis gives for the resonance speeds ω_{cr} (refs. 3 and 6)

and

$$\left.\begin{array}{c} (2n - 1)\omega_{cr} = \lambda_i(\omega_{cr}) \\ \\ 2n\,\omega_{cr} = \lambda_z(\omega_{cr}) \end{array}\right\} \qquad (14)$$

Here λ_z is the axial natural circular frequency of the system.

LABORATORY MODEL TESTS AND COMPUTATIONS

Computations were done for a laboratory model (fig. 5) and compared with the tests results.

Generator Model - Instabilities

The instability regions were computed for the model with the shaft of different principal stiffnesses k_x, k_y and rotor block between bearing (no disc 5 in fig. 5). The determinants (12) give equations of instability region boundaries in the form $|W(\mu,\theta)| = 0$. Their roots μ_i, θ_i define the stability limits. An example of computed results is given in figure 6. This diagram corresponds to the second-order combined instability region $0.5(\theta_{x1} + \theta_{y1})$ around point N (fig. 6). The solutions of the equation

$$|W(\mu,\theta)| = 0$$

386

for zero parametric excitation ($\varepsilon = 0$) and no damping ($C = 0$, $\gamma_u = 0$) are straight lines

$$\beta^{(\pm)} = \frac{i\Theta \pm 2\mu}{2} = \lambda_j$$

intersecting at point N (fig. 6). For finite parametric excitation the lines curve and do not intersect, separating in the direction Θ for frequencies sums $1/n(\lambda_j + \lambda_k)$ or in the direction μ for their differences $1/n(\lambda_j - \lambda_k)$. Hence there are no instabilities (also with no damping) corresponding to the frequency differences. The curves in figure 6 correspond to constant values of the determinant, and its zero values (denoted with the crosses) give the instability region. They approach each other with increasing damping and, over its limiting value, instability disappears. This was traced with changing shaft length ΔL, and computed and experimental results are compared in figure 7. Corresponding oscillograms for the x and y directions are given in figure 8. The instability region discussed here is denoted by 1 in the instability regions diagram (fig. 9). There are computed instability regions (with the type of instability) shown in figure 9 and against them the observed experimental instabilities shown with the crosses.

Ventilator Model – Resonance Speeds

Analysis of forced vibrations was done for the model with circular shaft and the disc 5 (fig. 5) slightly offset. Hence $B_{\eta\zeta}$ and $B_{\xi\zeta}$ are not equal and $S_{\eta\zeta}, \ldots, D_\zeta$ as well as disbalance forces P and Q are not zero, but $\varepsilon = 0$. Graphical solution of equation (1) for the laboratory model is given in figure 10. The continuous curved lines are the computed natural frequency curves. Abscissas of their points of intersection with the straight lines $\lambda = \omega$ (principal), $\lambda = 2\omega$, $\lambda = 3\omega\ldots$ give the parametric resonance speeds, with one, two, three, $\ldots$ vibration cycles per one revolution. Computed values of 10 resonance speeds (taken from diagram, fig. 10) in s^{-1} are

$$\omega_{cr1} = 20, \; \omega_{cr2} = 36, \; \omega_{cr3} = 46, \; \omega_{cr4} = 58, \; \omega_{cr5} = 82,$$

$$\omega_{cr6} = 99, \; \omega_{cr7} = 108, \; \omega_{cr8} = 112, \; \omega_{cr9} = 140, \; \omega_{cr10} = 175$$

Experimental resonance diagrams measured for the right support (fig. 5) are given in figure 11 as continuous broken and dotted lines for the directions y, x, z, respectively. They compare well with the computed values from figure 10. The vibrations recorded for speeds close to resonance, numbered in the diagrams (figs. 10 and 11) are shown in figure 12. It can be seen that close to resonance speed of the type $n\omega_{cr} = \lambda_i(\omega_{cr})$ vibrations of frequency $n\omega$ dominate. Comparison of figures 10, 11, and 12 shows good consistency of theoretical and experimental results.

FIELD CASE STUDY

The above results were applied in field studies of vibrations of industrial ventilators that developed repeated failures (shaft breakages). These were ventilators No. II of the type FKD-30 (fig. 2(b)) mentioned in the INTRODUCTION.

Analysis

The model of the ventilator consists of two subsystems: the discretized rotor (fig. 13) described in table 1 and the supporting structure containing the ventilator body with bearings and foundation (fig. 14). The supporting structure, for its dynamic interaction with the rotor, was dynamically defined with its receptance matrix along the connecting coordinates x_1, y_1, x_2, y_2

$$\begin{bmatrix} c_{x1x1} & c_{x1x2} & c_{x1y1} & c_{x1y2} \\ c_{x2x1} & c_{x2x2} & c_{x2y1} & c_{x2y2} \\ c_{y1x1} & c_{y1x2} & c_{y1y1} & c_{y1y2} \\ c_{y2x1} & c_{y2x2} & c_{y2y1} & c_{y2y2} \end{bmatrix} = [c_{ik}] \tag{15}$$

The receptances c_{ik} were measured on site. The measuring scheme is given in figure 15. The notations in figure 15 are 1 - ventilator type II, 2 - electro-dynamic exciter, 3 - displacement pickup, 4 - generator, 5 - vibration measuring apparatus, 6 - two-ray cathode oscilloscope, 7 - frequency meter, 8 - phase meter, 9 - ammeter.

The exciting force was measured indirectly (by current measurement). Receptance diagrams are given in figure 16. Because of symmetry all the cross receptances for the perpendicular directions are zero. The other equal pairs are denoted c_{iix}, c_{iiy}, c_{ijx}, c_{ijy}, where $i = 1, 2$. On the basis of the receptance matrix (15) the impedance (dynamic stiffness) matrix

$$[\gamma_{ik}] = [c_{ik}]^{-1}$$

was calculated and introducted in the computing program. Forced vibrations were found as partial solutions of equation (1) for the case of equal rotor stiffnesses by application of the small-parameter method. Their analysis gives the formulas (14) for the resonance speeds. Graphical solution is given in figure 17. The frequency lines are the solutions of the homogenous part of equation (1). With the approximation used, there are computed two principal resonance speeds (in s^{-1}), 344 and 280; two subharmonic ones of second order (of two cycles of vibration per revolution), 172 and 142; and two of third order, 114 and 94.

Experimental Measurement on Site

An experimental resonance test was made on site (in the mine) in the ventilator II in working condition. The measuring arrangement is shown in figure 18. Here 1 denotes the ventilator tested; 2 denotes the dc motor; 3 denotes the transformer displacement transducer; 4 denotes the vibration measuring apparatus; 5 the cathode ray oscilloscope; and 6 the frequency meter.

The resonance diagram for the supports for the practically allowed speed range from approximately 1200 to 2100 rpm is given in figure 19. The two observed subharmonic resonances, 138 and 174 s^{-1}, are in this speed range; both of second order are very close to the corresponding computed values, 142 and 172 s^{-1}.

CONCLUSIONS

The second-order subharmonic of frequency 142 s^{-1} coincided with the nominal working speed of ventilator II, which was below 1500 rpm. Hence it was the second-order parametric resonance that was responsible for the shaft breakages. Supporting structure appreciably lowers critical speeds. The gyroscopic effect was also considered and computed. It is specially visible in the ventilators with the overhang rotor. The frequency diagram for that type of ventilator, designated No. I in the INTRODUCTION, is given in figure 20. Important gyroscopic-effect influence is visible. It was the principal resonance at 144 s^{-1} that was responsible for the failures in those ventilators with nominal working speed below 1500 rpm.

REFERENCES

1. Bolotin, W. W.: Dinamiczeskaja ustoicivost uprugich sistem. GIT-TL, Moskva, 1956.

2. Szemplińska-Stupnicka, W.: Przyblizone metody analityczne badania niestateczności parametrycznej. Ossolineum, PAN, Warszawa, 1976.

3. Parszewski, Z.; Krodkiewski, J.: Stability and Critical Speeds of Non-Circular Shafts on Flexible Anisotropic Supports. Archiwum Budowy Maszyn No. 2, 1975.

4. Krodkiewski, J.: Proc. V. World Congress TMM, Montreal, 1979.

5. Krodkiewski, J.: Habilitation thesis, Politechnika Łódzka, Łódź, 1980.

6. Krodkiewski, J.; Marynowski, K.; Parszewski, Z.: Instabilities of Parametric Rotor-Support Systems. Proc. Conf. Vibrations in Rotating Machinery, Cambridge, 1980, I. Mech. Eng.
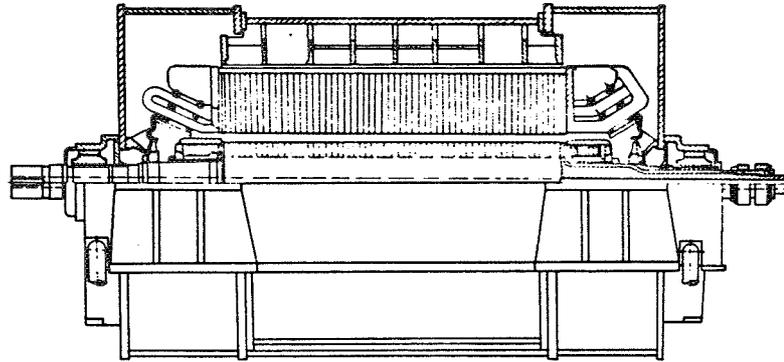
Fig.1
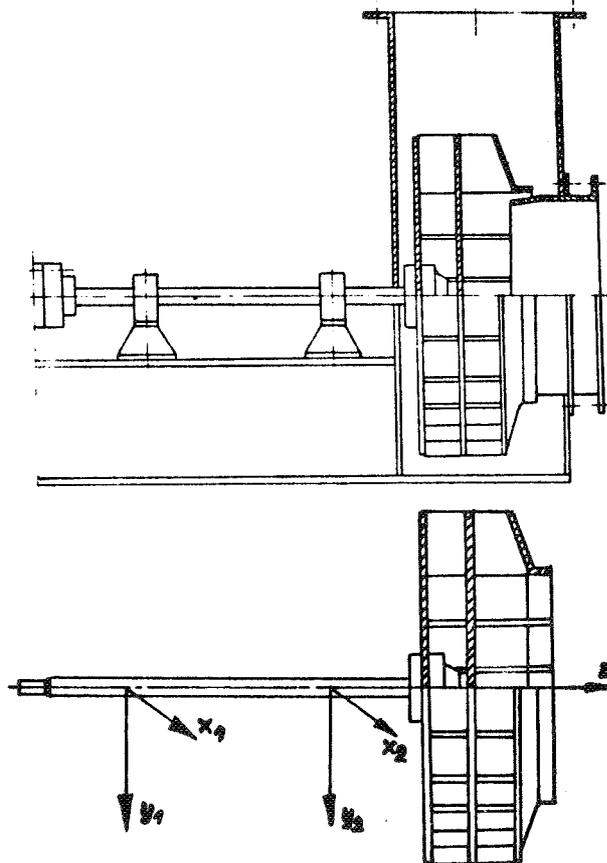
Fig.2a
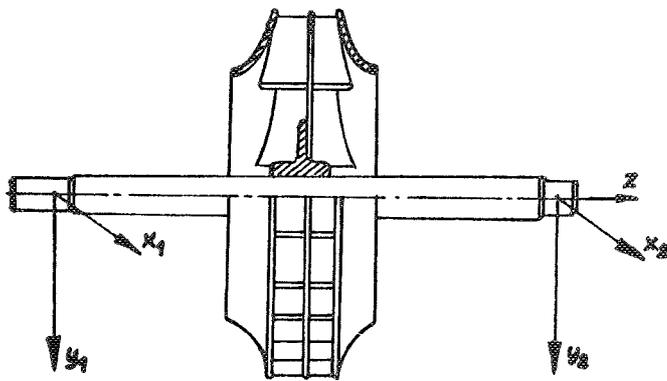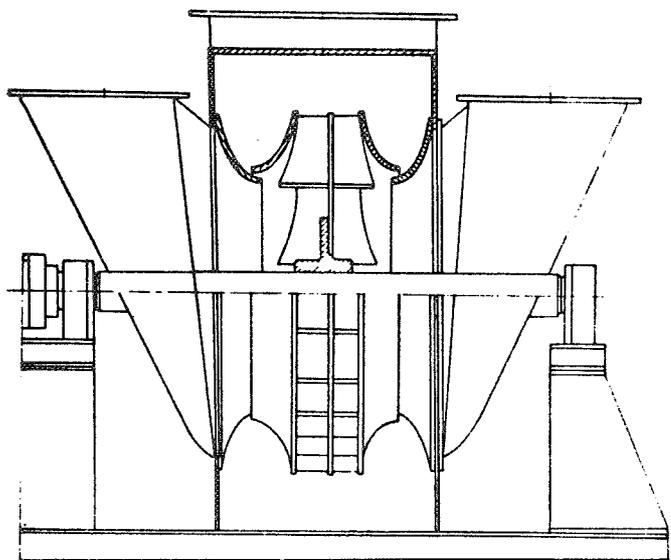
Fig.2b
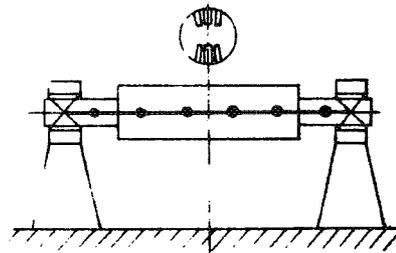
Fig.3a
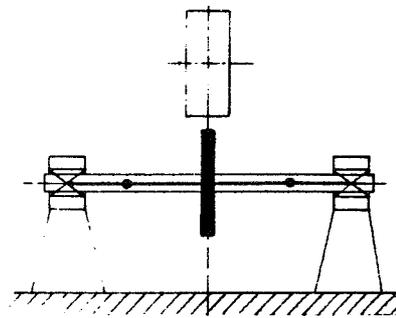
Fig.3b
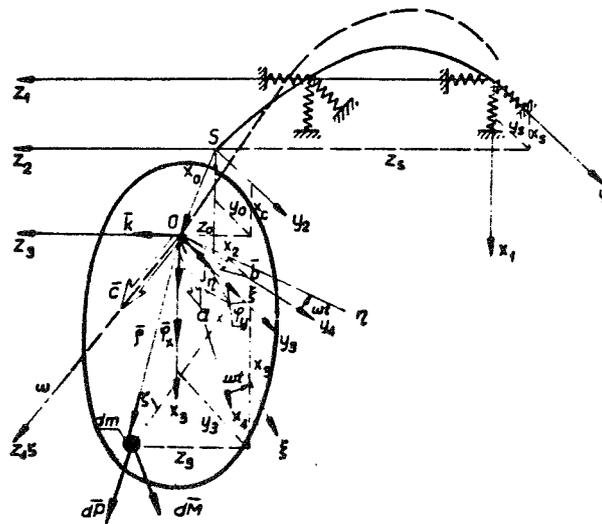
Fig.4
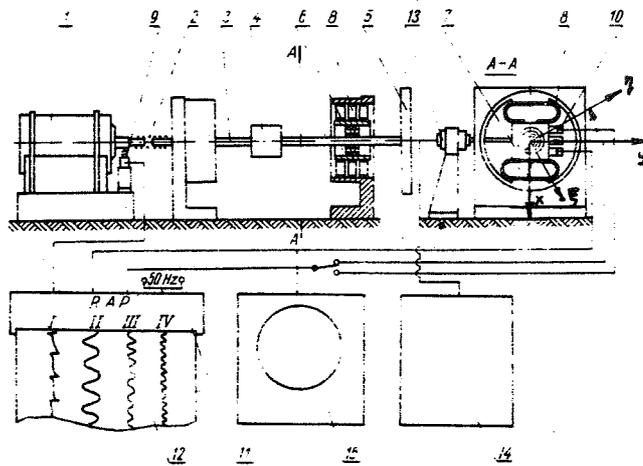
Fig.5 Scheme of model stand
1-DC motor,2-elastic coupling,
3-shaft,4-rotor mass,5-disc,6-ball
bearing,7-anisotropic bearing,
8-flat springs,9-inductive sensor,
10-piezo-electric sensors,11-re-
corder,12-recorder tape,13-ele-
ctrodynamic exciter,14-generator
of harmonic vibration,15-cathode
oscilloscope.
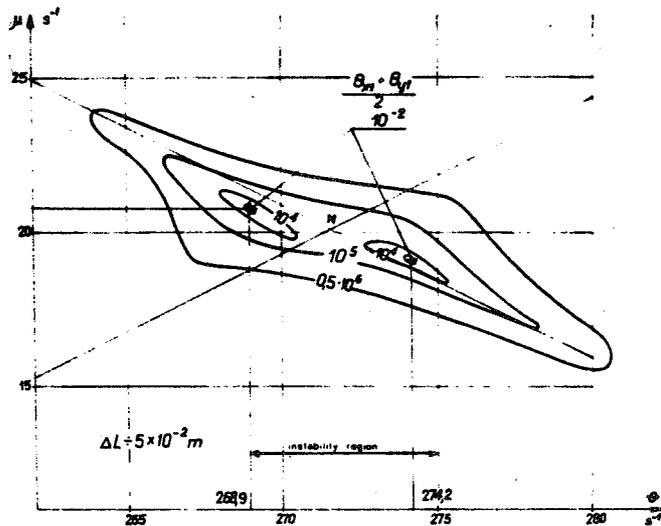
Fig.6
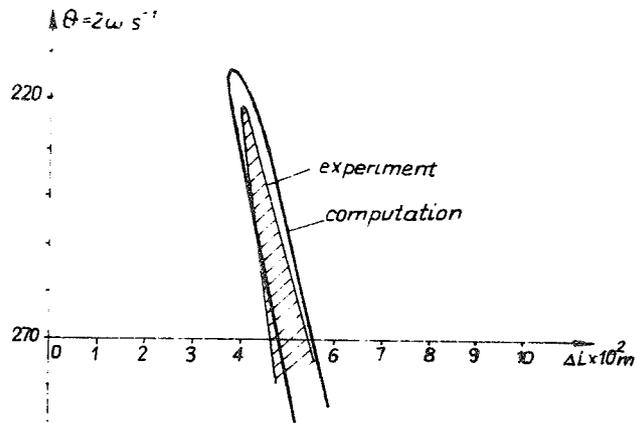
Fig. 7
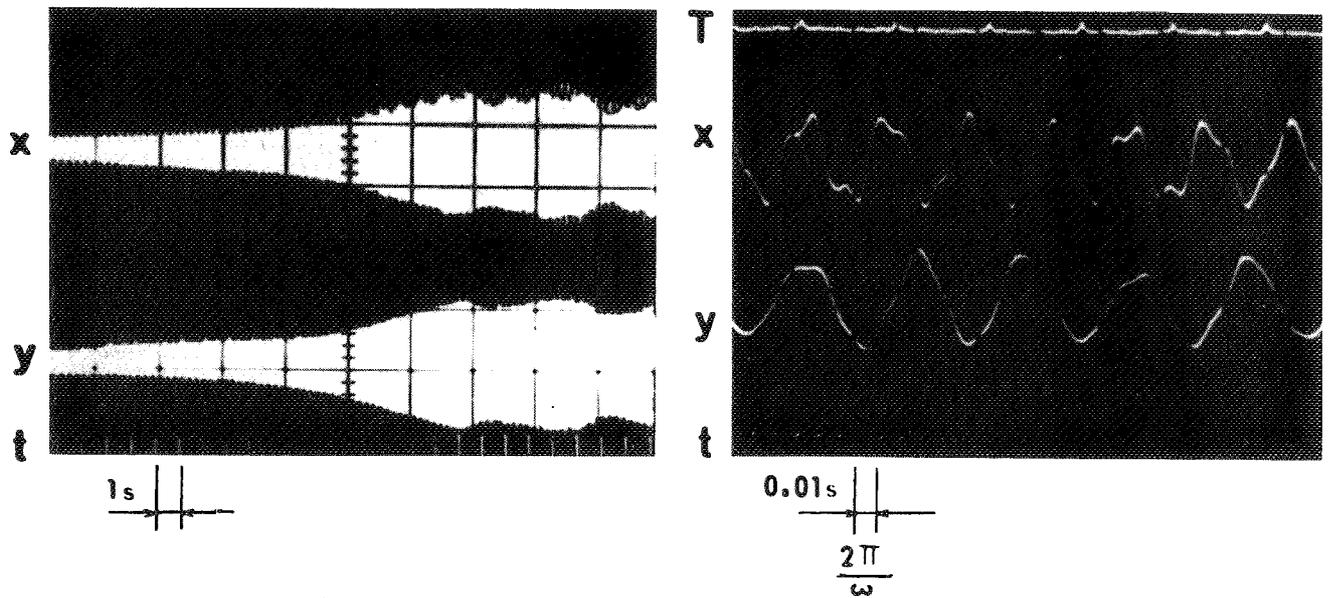
Fig. 8
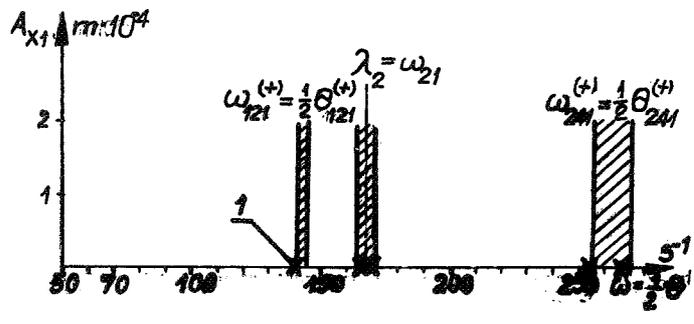
Fig. 9
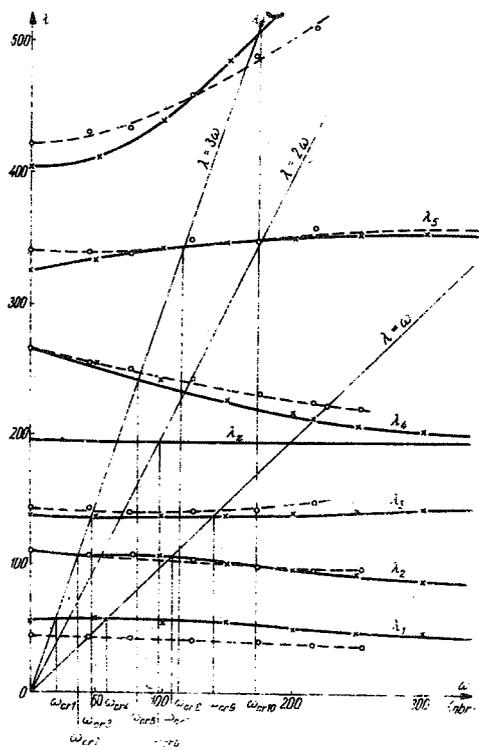
Fig. 10
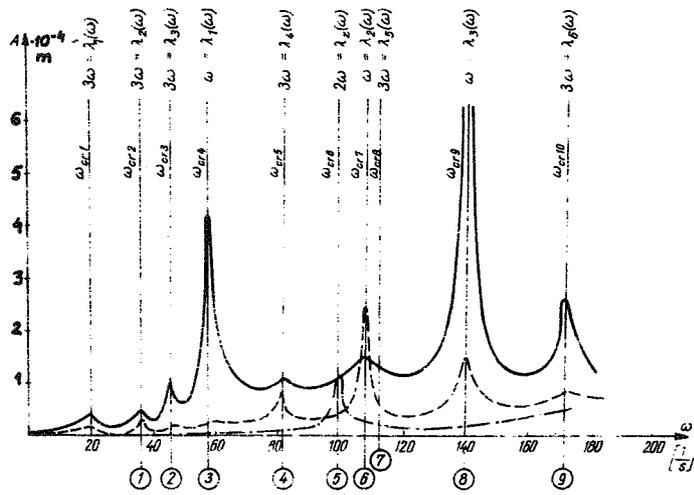
Fig. 11 Resonance diagram of right
support vibration of model stand.

Fig.12

396
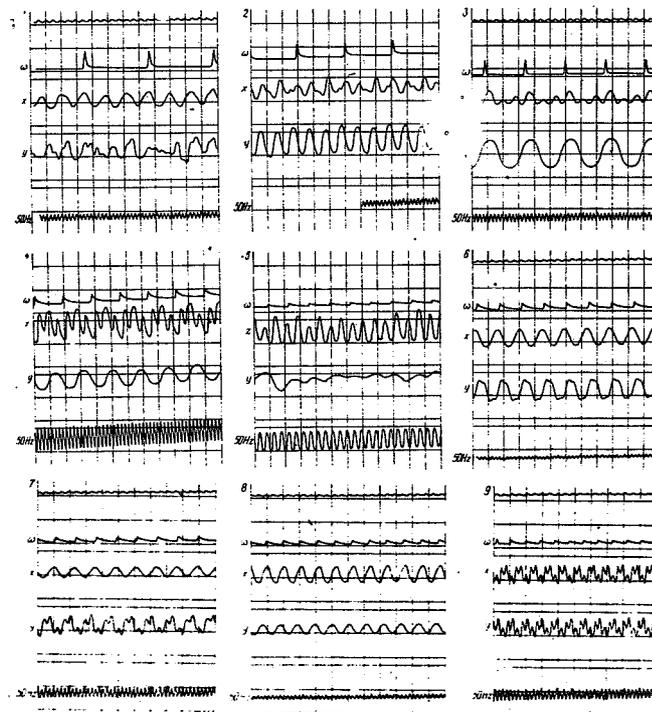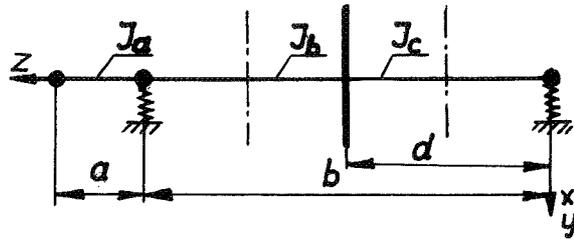
Fig.13

Fig.14

Fig.15

Fig.16

398
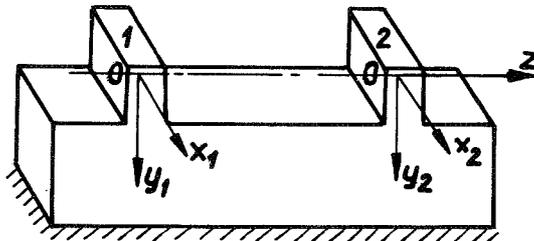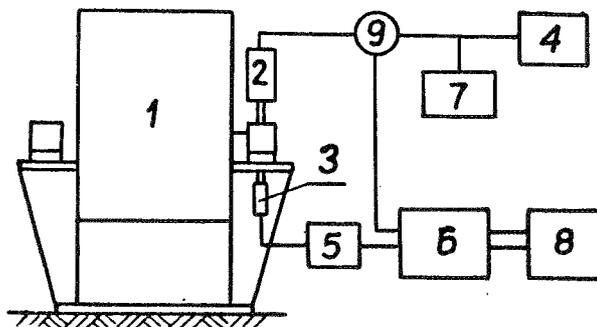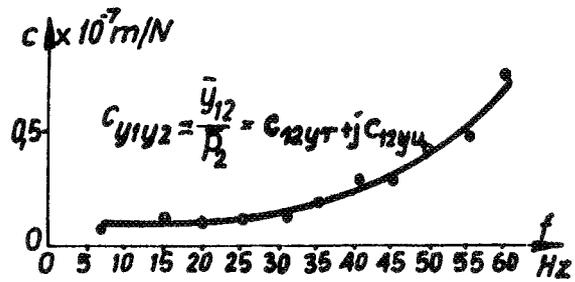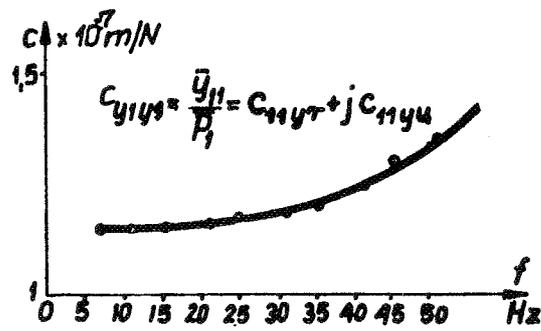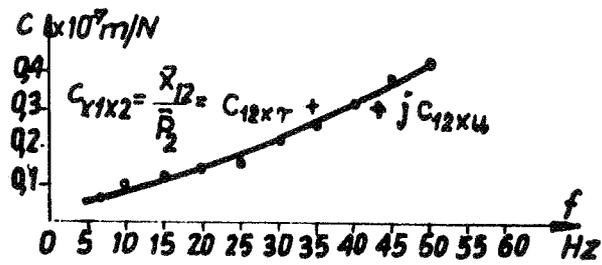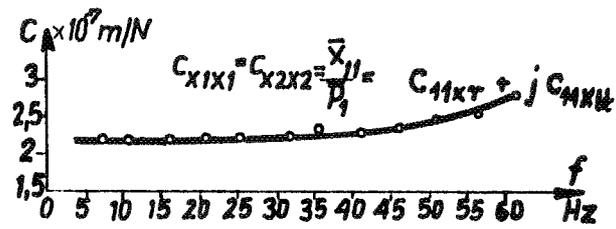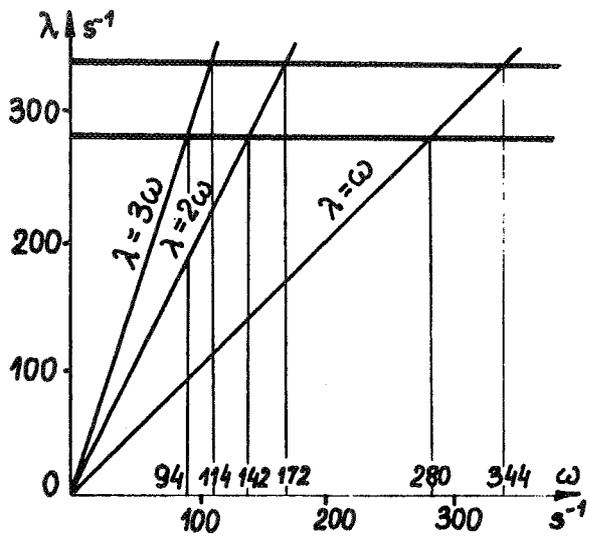
Fig.17
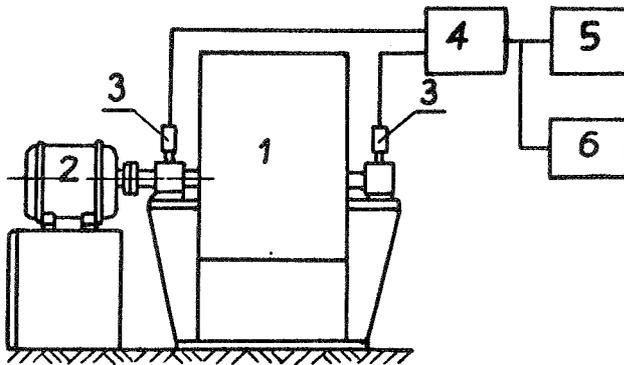
Fig.18
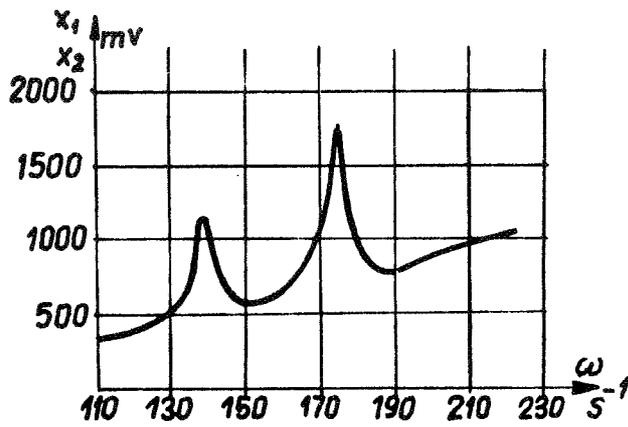
Fig.19
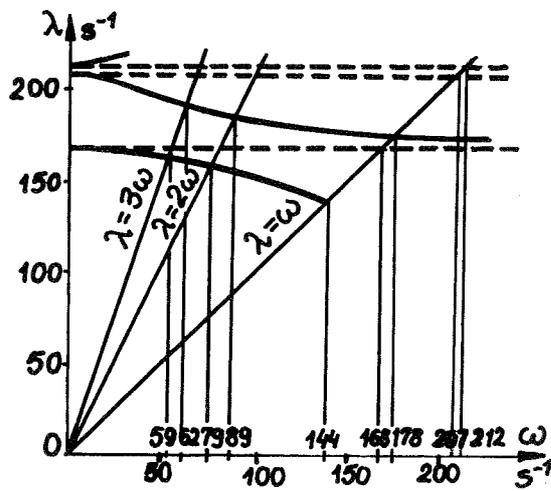
Fig.20

Tabl. 1

m_0	4,0221 kg	$\theta_{1,2}$	0,1995 kgm²	J_b	12,56·10⁻⁸ m⁴
m_1	2,3544 kg	$\theta_{0,2}$	0,3167 kgm²	J_c	10⁻⁸ m⁴
m_2	21,4839 kg	a	0,096 m	μ_0	0
m_3	0	b	0,677 m	μ_2	0,01 m
m_4	2,0601 kg	c	0	E	20,6·10¹⁰ N/m²
θ_1	0	d	0,3385 m		
$\theta_{0,0}$	0	J_a	6,55·10⁻⁸ m⁴		

SESSION VII

CONTROL OF ROTOR INSTABILITIES

Capt. J. Walton, Wright-Patterson Air Force Base
Chairman

Page intentionally left blank

INSTABILITY THRESHOLDS FOR
FLEXIBLE ROTORS IN HYDRODYNAMIC BEARINGS

Paul E. Allaire and Ronald D. Flack
Department of Mechanical and Aerospace Engineering
University of Virginia
Charlottesville, Virginia 22903

ABSTRACT

Turbomachinery supported on hydrodynamic bearings may be either driven unstable or be stabilized by the bearing design. The purpose of this paper is to consider some designs for multilobe and pressure dam bearings in a flexible rotor. For non-optimized bearings, the correlation between theory and experiment is fairly good while for optimum designs it is not. A summary chart giving some of the advantages and disadvantages of various bearing types is also included.

NOMENCLATURE

Dimensional Quantities

c, c_1, c_2	= Bearing radial clearance, number one bearing, number two bearing (L)
c_b	= Minimum film thickness for a centered shaft (L)
c_d	= Step height (L)
c_p	= Lobe clearance (L)
C_{xx}, C_{xy}, C_{yx}, C_{yy}	= Bearing damping coefficients (FTL^{-1})
D	= Bearing diameter (L)
e	= Bearing eccentricity (L)
F_x, F_y	= Bearing forces in the x and y directions (F)
g	= Gravitational acceleration (L/T^2)
h_1, h_2	= Film thickness before, after step, centered bearing ($h_2 = c$) (L)
K_{xx}, K_{xy}, K_{yx}, K_{yy}	= Bearing stiffness coefficients (FL^{-1})

K' $\quad = \dfrac{h_1}{h_2} = \dfrac{h_1}{c}$, Film thickness ratio

L $\quad =$ Bearing length (L)

L_d, L_t $\quad =$ Step bearing axial dam length, relief track axial length (L)

m, m' $\quad =$ Rotor mass (M)

N, N_s $\quad =$ Shaft rotational speed (RPM), (RPS)

O_b, O_j, O_p $\quad =$ Bearing, journal, pad center

R $\quad =$ Radius of shaft (journal) (L)

R_p $\quad =$ Lobe radius (L)

W, W_T $\quad =$ Static bearing load (F)

x, y $\quad =$ Journal position in the x and y coordinates (L)

$\dot{x}, \dot{y}$ $\quad =$ Journal velocity in the x and y coordinates (L/T)

$\ddot{x}, \ddot{y}$ $\quad =$ Journal acceleration in the x and y coordinates (L/T^2)

γ_g $\quad =$ Groove location, (degrees)

δ $\quad =$ Pad tilt angle (degrees)

μ $\quad =$ Fluid viscosity (FT/L^2)

ω_d $\quad =$ Rotor whirl frequency (1/T)

ω_j $\quad =$ Journal rotational speed (1/T)

ω_r $\quad =$ Rotor critical speed on rigid support (1/T)

θ_g $\quad =$ Groove location, (degrees)

θ_s $\quad =$ Location of step measured with rotation from positive x-axis (degrees)

χ $\quad =$ Lobe arc length

Non-Dimensional Quantities

$\bar{L}_d, \bar{L}_t$ $\quad =$ L_d/L, L_t/L, Step bearing axial dam length ratio, relief track axial length ratio

m_1, m_2 $\quad =$ Preload in multilobe bearings

404

$\bar{M}$ = Rotor mass, $\omega_j^2 cm/W$

Re_2 = Reynolds number for step bearing

S = $\dfrac{\mu N_s LD}{W_T} \left(\dfrac{R}{c}\right)^2$, Sommerfeld number

$S^{\prime}$ = $\dfrac{\mu N_s LD}{W_T} \left(\dfrac{R}{c_b}\right)^2$, Sommerfeld number

η = Bearing parameter $\dfrac{S}{\bar{\omega}_j} \mu LD \left(\dfrac{D}{c}\right)^2 \left(\dfrac{W}{cm}\right)^{1/2} /8\pi W$

$\bar{\omega}_d$ = Whirl frequency ratio, ω_d/ω_j

$\bar{\omega}_j$ = Rotor speed parameter, $\omega_j \sqrt{mc/W}$

ω_s = $\omega_j \sqrt{c/g}$, Rotor speed parameter, horizontal rotor

ω_s = $\omega_j \sqrt{\dfrac{mc}{W_T}}$, Rotor speed parameter

$\bar{\omega}_s$ = Rigid rotor stability threshold

$\bar{\bar{\omega}}_s$ = Flexible rotor stability threshold

α = Offset factor

ϵ = e/c_b, Bearing eccentricity ratio

Subscripts

b = Bearing

d = Dam

g = Groove

j = Journal

max = Maximum magnitude

p = Pad or lobe

r = Relative to equilibrium position

s = Step

t = Track

x,y = Horizontal and vertical directions

1,2 = Bearings 1 and 2 in experimental rotor

INTRODUCTION

Many of the bearings which are discussed in this paper have been developed principally to combat one or another of the causes of vibration. It is fortunate for designers of rotating machinery that a bearing which has good stiffness and damping properties such that it will suppress one of the causes of vibration will usually moderate one of the others as well. It should be noted, however, that the range of bearing properties due to the different geometric effects is so large that one must be relatively careful to choose the bearing with the proper characteristics for the particular causes of vibration for a given machine. In other words, there is no one bearing which will fix every machine.

It is often the case in industry that rotating machinery is primarily designed from the point of view of the pressure to be delivered, the flow rate to be delivered, the torque required of an electric motor, and other factors which are independent of machine vibration characteristics. Near the end of the design process, a vibration analysis is conducted on the rotor bearing system. If vibration problems are suggested by the analytical work, changes can be made in the rotor length or diameter, but this is relatively difficult since the designs are usually relatively fixed. Various bearing designs can be considered at this stage with the point of view of changing the rotor bearing critical speeds or reducing the rotor tendency toward instability. Currently, it is the design practice not to conduct a full rotor dynamics analysis considering critical speeds, unbalance response, and stability analysis for every machine which is produced. Thus, a machine may reach the test stand before a particular rotor dynamics problem is encountered. At this point, it is very difficult to redesign many aspects of the rotor besides the bearing. For these reasons, the designer and user of rotating machinery should be well acquainted with the fundamentals of vibration suppression characteristics on a number of different fluid film bearings.

A number of causes of large vibrations in rotating machinery exist. Machine unbalances normally produce large amplitudes of vibration which occur at the rotational frequency. Thus, this vibration is called a synchronous vibration because it is synchronous with the shaft speed. Machine instabilities due to hydrodynamic journal bearings themselves, interaction with the working fluid in a machine, seals in rotating machines, friction rubs, and internal friction due to stress reversals in shrunk on parts - all may produce vibrations which occur at a speed which is normally below that of the shaft rotational frequency. Thus, they are called subsynchronous vibrations. Additional machine vibrations may be caused by effects such as misalignment which normally creates a response at two times running speed (supersynchronous vibration pattern). Often, more than one cause of vibration occurs within a given operating machine so that the overall vibration pattern is quite complex. More than one change needs to be made in order to make the machine run with acceptable vibration characteristics.

It is important to have design information on optimum bearing configurations before entering into the design process. This is because there are so many geometrical choices for bearings that one cannot try all options in the

normal time frame. Also, a designer should have some idea as to how much machine stability can be increased by bearing changes. Stability increases are discussed both in this paper and in another by L. E. Barrett and E. J. Gunter elsewhere in this symposium. A critical question is "how well does current theory predict stability when compared to experiment?"

MULTILOBE BEARINGS

In this section some typical theoretical and experimental studies, which demonstrate the operating characteristics of multilobe bearings, are presented.

Linearized Stability Analysis for Multilobe Bearings

This section [1,2] investigates the problem of the linear stability and the nonlinear behavior of a single mass rigid rotor in four multilobe bearing configurations shown in Fig. 1: (a) an elliptical "lemon" shaped bearing (b) an offset elliptical bearing (c) a three-lobe bearing (d) a four-lobe bearing. All of the bearings have a length to diameter ratio of 0.5, preload factor and offset factor of 0.5 except the offset bearing for which the offset is 1.0. Stiffness and damping coefficients are given elsewhere and do not give much of a basis for comparing various bearing designs with one another. The linearized stability threshold is often used for this purpose. It should be emphasized that the linearized stability threshold assumes that the rotor is rigid, which is usually not correct. A full rotor stability analysis with both rotor and bearing properties must be conducted for any machine.

Since multilobe bearings do exhibit self-excited whirl vibration under certain speed and loading conditions, the designers are faced with the problem of selecting the bearing which will be the most stable or have the lowest force levels for a given application. Sometimes, bearings are classified as more stable simply because they are stiffer. A typical instability takes the form of half-frequency whirl occurring at shaft rotational speed of approximately two times the resonant frequency of a rotor system. The stiffer bearing is designated "more stable" because bearing stiffness increases the natural frequency which effectively raises the stability threshold speed at which bearing induced whirl will occur. In this study, all the bearings are oriented with the weight of the journal directly on the center of the bottom lobe. The ambient and cavitation pressures are taken to be zero. Film rupture is assumed to occur for negative pressures (the half Sommerfeld condition). The Reynolds equation is solved with the pressure at the leading and trailing edge of each bearing sector as well as on the sides assumed to be zero. The hydrodynamic pressure is integrated only over the region in which the pressure is positive.

The equations that lead to the determination of the bearing linearized stability for a rigid rotor are presented in [1]. Figure 2 shows the stability threshold speed ω_s plotted against Sommerfeld number for the four bearing types shown in Fig. 1. Each of the 45° straight lines with positive slope and constant η across the figures gives the locus of the operation of a bearing with a fixed geometry as it is brought up or down in speed. The bearing parameter η is defined as
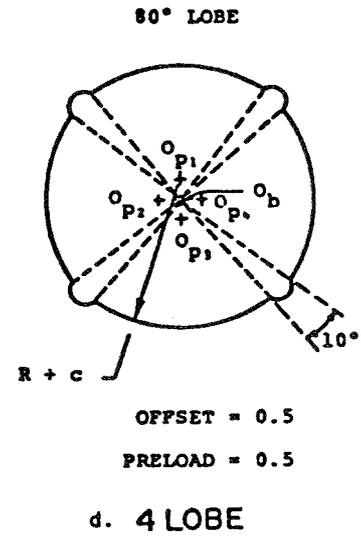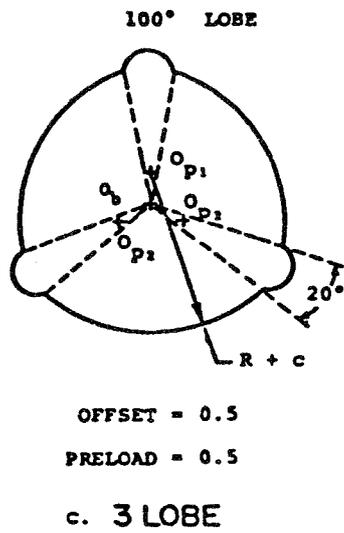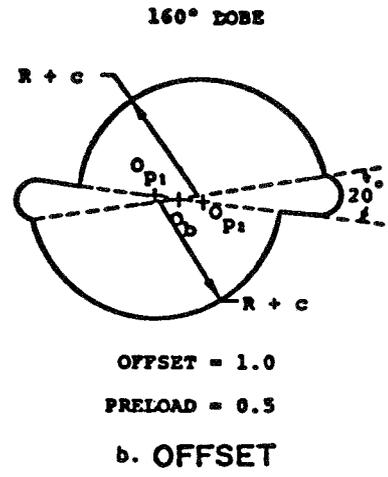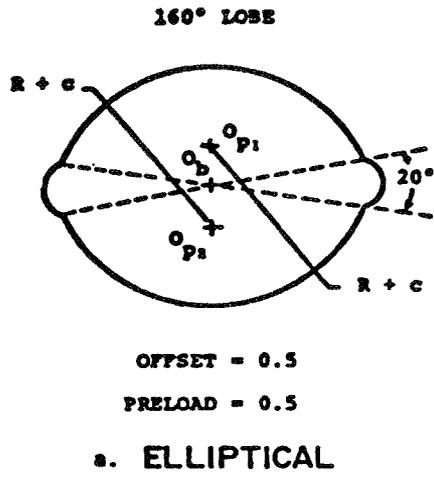
Figure 1   Multilobe Bearing Geometry
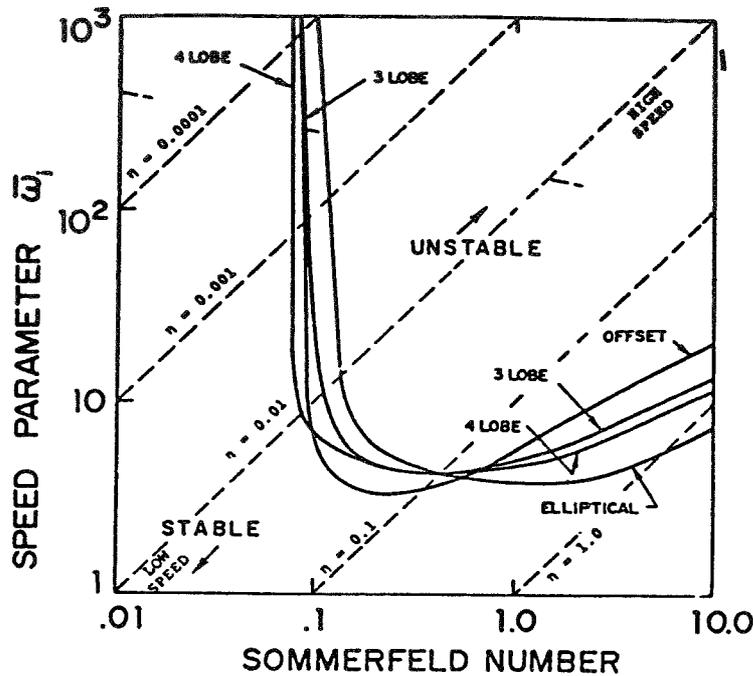
Figure 2   Linearized Bearing Stability for a Rigid Rotor

$$\eta = \frac{S}{\bar{\omega}_j} \frac{\mu LD}{8\pi W} \left(\frac{D}{c}\right)^2 \left(\frac{W}{cm}\right)^{1/2}$$

It should be noted that η is independent of the rotor speed and is in itself
sufficient for the description of a certain bearing geometry on a stability
graph. As a bearing increases in speed, it will proceed along a line of con-
stant η and become unstable as it enters the unstable region by crossing the
stability curve from below.

Figure 2 may be separated roughly into three regions: light load and/or
close clearance (η = 0.1 to 1.0), moderate load and/or moderate clearance (η =
0.01 to 0.1) and heavy load and/or open clearance (η = 0.001 to 0.01). It is
observed that under all operating conditions, the three-lobe bearing is con-
sistently more stable than the four-lobe bearing except at η = 0.1 where the
bearings have about the same stability threshold. All the other stability
curves also appear to intersect roughly at this same point indicating little
difference between the stability characteristics of the bearings in this area
of operation.

At light load and/or close clearance operations, the offset bearing is the
most stable. The three-lobe bearing is better than the four-lobe bearing by a
small margin, while the elliptical "lemon" bearing is the least desirable.
Within this region, the stability may be much improved by reducing the lobe
clearance or effectively increasing the bearing parameter η.

409

Under moderate load conditions, the offset half bearing loses its superiority completely. The most stable bearing in this region is the elliptical bearings; followed by the three-lobe, the four-lobe, and the offset cylindrical bearing. Improvement in the stability performance by increasing lobe clearance or decreasing η is insubstantial on the high η side within this regio

At heavy load and/or open clearance operations, the order of increasing stability is: the four-lobe bearing, the offset bearing, the three-lobe bearings, and the elliptical bearing. Increasing lobe clearance or decreasing η will drastically improve the stability threshold for all of the bearings.

While the offset bearing is superior in stability for light load operation, the elliptical bearing appears to be most stable for a wide range from heavy loaded to relatively lightly loaded applications.

Although the three-lobe bearing does not have the best stability, it offers good overall performance under all load conditions. It is second only to the most stable bearing in each region.

Using a single mass flexible rotor, it can be shown that the flexible rotor stability threshold is given by [1]

$$\bar{\bar{\omega}}_s = \frac{\bar{\omega}_s}{\left[1 + \bar{\omega}_s^{\,2}\, \bar{\omega}_d^{\,2} \left(\frac{g}{c\omega_r^2} \right) \right]^{1/2}}$$

where ω_r is the rotor critical speed on rigid bearings. Because the stability threshold for a flexible rotor is always lower than that for a rigid rotor, Fig 2 should be viewed as the highest possible stability that can be achieved in these bearings.

One of the major concerns in this investigation is the stability of the multi-lobe bearings in light load applications. The non-linear characteristic of the bearings examined in this section are to have the bearing parameter η = 0.3. Insofar as possible, generalization of the results throughout this paper is provided by the use of dimensionless parameters instead of particular bearing specifications and operating conditions. An example bearing with η = 0.3 i

L = 38.1 mm (1.5 in.)
D = 76.2 mm (3.0 in.)
c = 0.152 mm (0.006 in.)
W = 168.3 N (37.8 lb)
μ = 6.89 x 10^{-3} N-s/m^2 (1.0 x 10^{-6} lb-s/in.^{2})

For comparison to the transient analysis, the linear stability thresholds corresponding Sommerfeld numbers, and whirl speed ratios for the four bearing types at η = 0.3 are tabulated in Table 1. The journal speeds for each of the four bearing types are at the threshold speeds of instability are also shown. The order of increasing stability is: the elliptical bearing, the four-lobe bearing, the three-lobe bearing and the offset bearing.

Bearing Type	Sommerfeld Number S	Whirl Ratio $\bar{\omega}_d$	Stability Threshold $\bar{\omega}_s$	Bearing ω_s(RPM)
Elliptical	1.15	.495	3.82	9,252
4-Lobe	1.52	.475	5.08	12,304
3-Lobe	1.86	.470	6.21	15,041
Offset	3.62	.361	12.07	29,234

Table 1　Stability Thresholds and Whirl Ratios for Various Bearing Types with Bearing Parameter η = 0.3

Four Lobe Bearings in a Single Mass Flexible Rotor

In this section, a flexible rotor was mounted in a set of four-lobe bearings. Dynamic behavior and the instability threshold was investigated for several configurations (for more details see Ref. [3]). All parameters were held constant for all tests with the exception of the value of the load angle θ_g. For a four lobe bearing $\theta_s = \gamma_g$. Small changes in this parameter were seen to change the dynamic response considerably. The specifications of the two bearings are summarized in Table 2. The same two bearings were used for all of the tests in this section.

	Bearing 1	Bearing 2
Shaft Diameter D (mm) $\pm$ 0.003	25.377	25.342
Radial Clearance, c_r (mm) $\pm$ 0.003	0.041	0.058
Lobe Clearance, c_ℓ (mm) $\pm$ 0.003	0.178	0.193
Preload Factor, m $\pm$ .025	0.77	0.70
Pad Angle, χ	63°	63°
Bearing Length, L (mm) $\pm$ .05	14.22	14.22
L/D Ratio $\pm$ .003	0.559	0.559
Offset Factor, α	0.50	0.50

Table 2　Four-Lobe Bearing Specifications

411

The first orientation to be discussed is $\theta_g = -15°$. Figure 3 shows the synchronous motion, total motion, and phase angle responses for rotor run-up for the X2 probe. In this figure, the two most important features are the responses at the rotor first critical speed and at high speeds. First, the rotor is seen to remain stable for all speeds. The maximum speed that the rotor was run at approximately 12,500 RPM and neither the total nor synchronous motion of the rotor displayed any large limit cycle vibration. The overall motion did, however, gradually tend to increase as the speed increased above 6000 RPM. Second, the motion of the rotor at the critical speed is seen to increase.
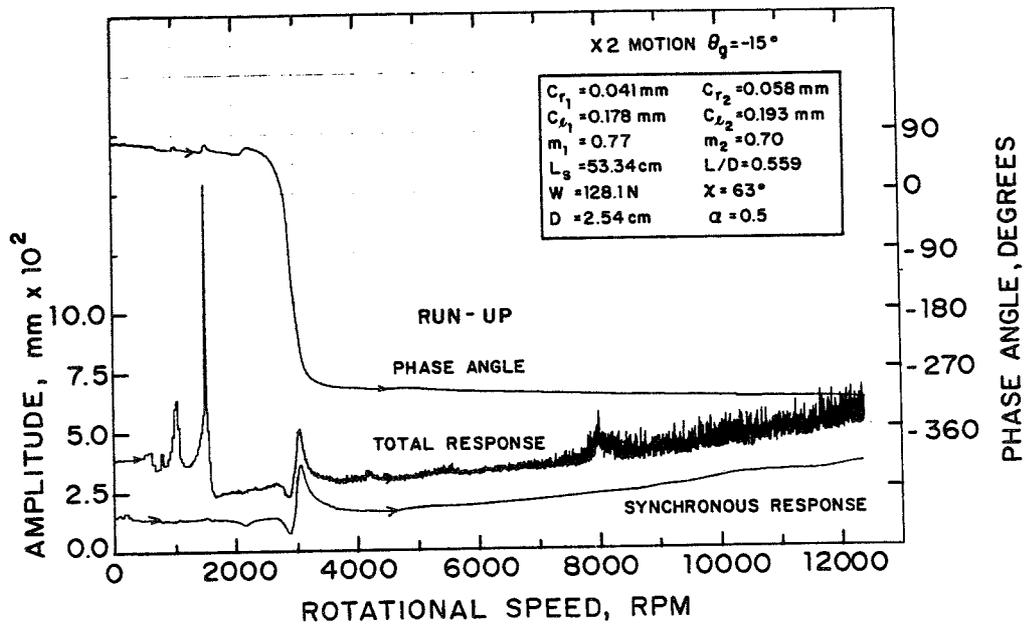
Figure 3   Total and Synchronous X2 Motion (Run-up) for $\theta g = -15°$
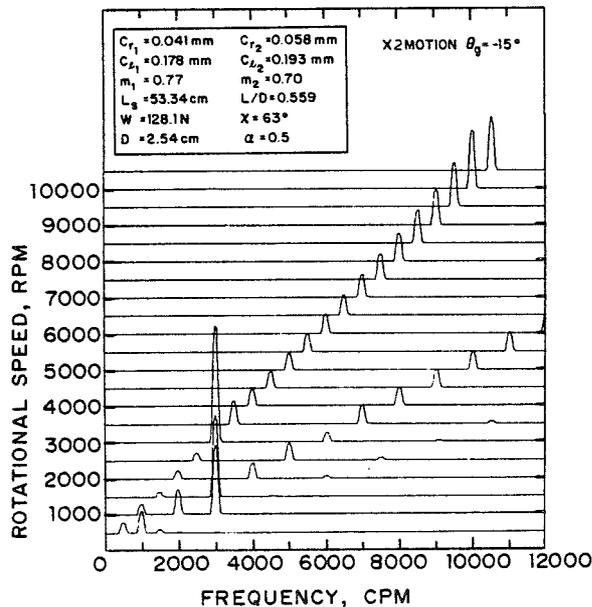
Figure 4   Waterfall Frequency Spectrum X2 Motion for $\theta g = -15°$

412

The waterfall frequency spectrums are presented for the X2 motion in Fig. 4. Such a figure complements the synchronous response plots well. For example, the supersynchronous excitation of the rotor critical speed can easily be seen. Also, the 2x and 3x components that contribute to the total observed motion can easily be seen. Lastly, no subsynchronous motion was seen at any time in the operation range. This rotor-bearing system was thus very stable throughout this test.

The second configuration discussed is θ_g = 30°. The X2 total and synchronous motion and phase angle responses are presented for rotor run-up in Fig. 5. The rotor went unstable very rapidly at 6600 RPM, as indicated by the total motion. Thus, rotating the bearings 45° from the initial position reduced the stability threshold by more than 5900 RPM. On run-down the rotor was locked in an unstable condition has also been observed for pressure dam bearings but has not been observed for axial groove bearings with no preload.

The waterfall frequency spectrum for θ_g = 30° (X2 motion, run-up) is presented in Fig. 6. This figure is presented to demonstrate the frequency at which the rotor was vibrating during the unstable condition. This frequency is the same as the critical speed of the rotor (approximately 3000 CPM). Other configurations which became unstable also oscillated at this same frequency and the rotor was never seen to demonstrate any half frequency oil whirl. Thus, when this rotor-bearing system demonstrated any instabilities, the condition was whip as opposed to whirl.

Using the results presented above and the results from other tests, the instability threshold speed was correlated with the angular position of the groove (θ_g). This plot is presented in Fig. 7. Also plotted in Fig. 7 is the end of the hysteretic effect of whip run-down. As can be seen from this figure, the optimum location of the grooves is for a value of θ_g from -15° to 0°, or from 75° to 90°. The worst case is when θ_g = 30°. On the other hand, the end of whip on run-down is not seen to be a strong function of θ_g. This level remained between 5800 RPM and 7400 RPM for all cases when the system went unstable. This implies that the higher the rotor instability threshold, the longer the rotor will demonstrate whip during run-down. This observation was also made for pressure dam bearings.

The experimental data is next correlated with theoretical predictions. For this section, finite elements were utilized to calculate the bearing coefficients for the four-lobe bearings used here. Also, the flexible rotor was modeled using lumped rotor masses [4]. This model was then used with the bearing coefficients to predict the stability of the rotor-bearing system. This stability threshold was calculated for various values of θ_g and the theoretical predictions are presented in Fig. 7. As can be seen, significant differences exist between the experimental data and theoretical predictions for the instability threshold ranging from 400 RPM at θ_g = 30° to over 4900 RPM at θ_g = 0°. Two reasons may account for these discrepancies. First, the theoretical method, which was used, was based on the half-Sommerfeld boundary condition with isoviscous theory. Using the Reynolds boundary condition and the effect of viscosity in the solution of the differential equations is probably more realistic. Second, small inaccuracies in the dimensions of the shaft and bearings will certainly affect the rotor-bearing stability. Nonetheless, the experimental and theoretical results are in

413

semi-quantitative agreement since the optimum value of θ_g is the same for both $(\theta_g = -15°$ or $75°)$. This value of γ_g (or θ_g for this case) is the same as for the three lobe bearings in a rigid rotor.
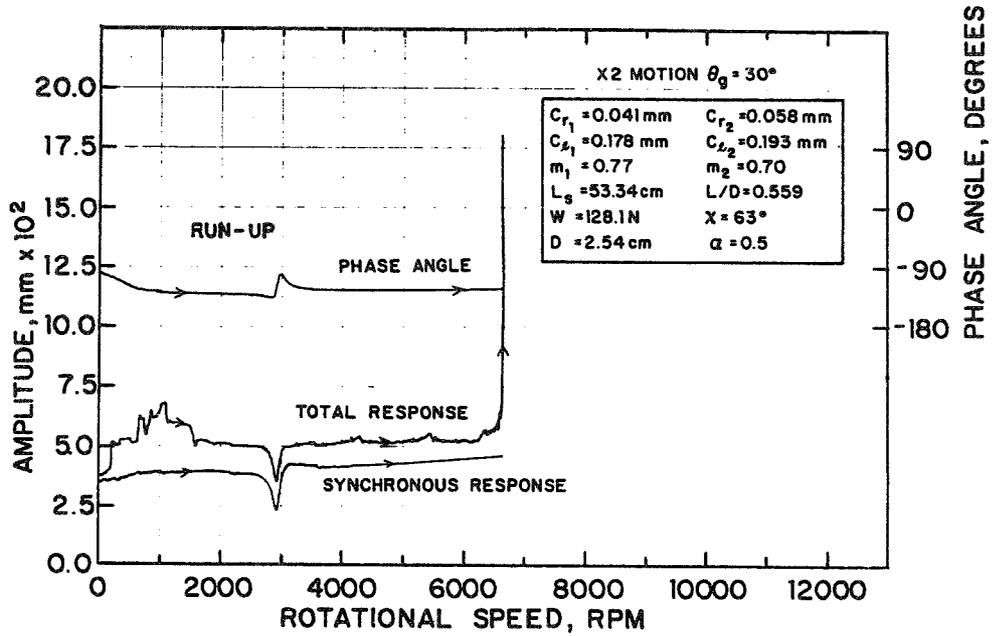
Figure 5   Total and Synchronous X2 Motion (Run-up) for $\theta_g = 30°$
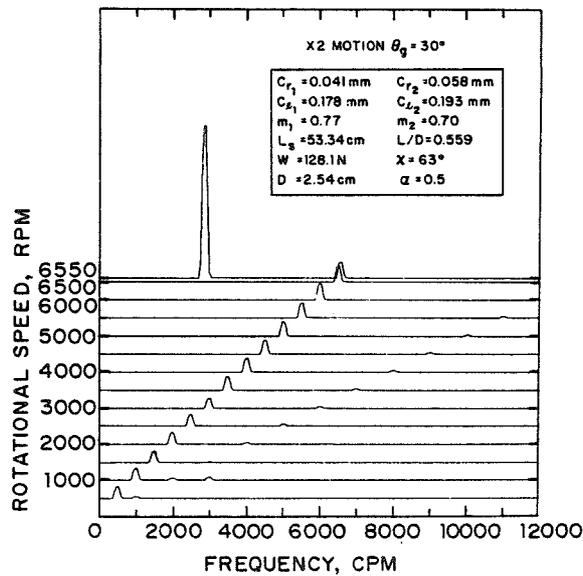
Figure 6   Waterfall Frequency Spectrum for X2 Motion for $\theta_g = 30°$
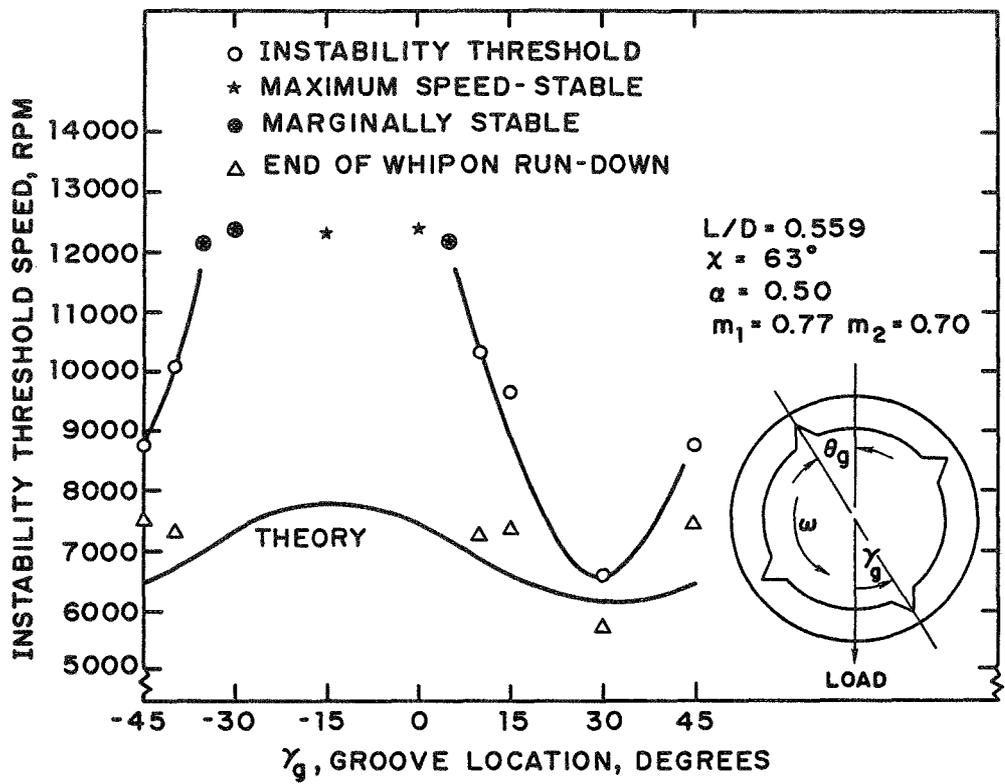
Figure 7   Summary of Correlation of Instability Threshold Speed with γ_g
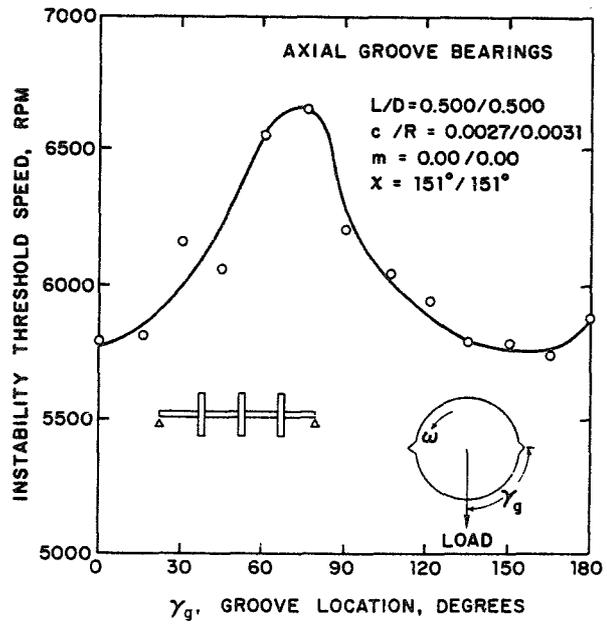
Figure 8   Summary of Correlation of Instability Threshold Speed with γ_g

415

2 Axial Groove Bearings in a 3 Mass Flexible Rotor

Axial groove bearings have been tested in a 3 mass flexible rotor in a similar manner to the studies done in the previous subsection. The apparatus is similar to the single mass flexible rotor. The specifications of the bearings are presented in Table 3. For brevity only, the summary graph is present here (Fig. 8). As can be seen, the instability threshold is considerably lowe for these bearings than for the four lobe bearings in the single mass rotor. There are two reasons for this. First and most importantly, the preload for these bearings is zero. Second, this apparatus is more flexible due to the smaller shaft diameter. The instability threshold does vary with the load angle and the optimum value of γ_g is once again approximately 75°.

Table 3 Two Axial Groove Bearings

	Bearing 1	Bearing 2
Shaft Diameter, D (mm)	25.397	25.387
Clearance, c (mm)	0.037	0.042
Pad Angle, χ	151°	151°
Length, L (mm)	12.70	12.70
Preload, m	0.00	0.00

PRESSURE DAM BEARINGS

Linearized Stability Analysis for Step Bearings

Pressure dam or step journal bearings have long been used to improve the stability of rotating machinery. They can replace plain journal or axial groove bearings in machines operating at high speeds and increase the stabilit threshold. A step or dam is cut in the upper half surface of the bearing producing a pressure rise near the step and a hydrodynamic load on the journal.

At high speeds and/or light loads, the step creates a loading that maintai a minimum operating eccentricity. That is, as speed is increased, the bearin eccentricity does not approach zero as it would for plain journal or two axia groove bearings. The eccentricity approaches some minimum value or may even increase with increasing speed due to the step loading. Thus, a properly designed step bearing would operate at a moderate eccentricity even at high Sommerfeld numbers [5,6].

Consider a finite length step bearing as shown in Figs. 9 and 10. Many industrial bearings have two oil supply grooves in the horizontal plane and a step located in the second quadrant with counterclockwise shaft rotation. A rectangular dam is usually used. A circumferential relief groove or track is sometimes grooved in the bottom half of the bearing. Both of these effects (dam and relief track) combine to increase the operating eccentricity of the bearing when compared to a plain journal or two axial groove bearing.

Many geometric variables affect the performance of pressure dam bearings. For all of the step journal bearings analysis in this paper, two 20° oil inle grooves are located at $\theta = 0°$ and $\theta = 180°$. Also, the dam axial length ratio

is held constant at $\bar{L}_d = 0.75$ for all cases. To study the effects of the remaining variables, only one is changed while the others remain the same. The base line design is

$$L/D = 1.0$$
$$Re_2 = 210$$

$$K' = h_1/h_2$$
$$h_2 = c$$
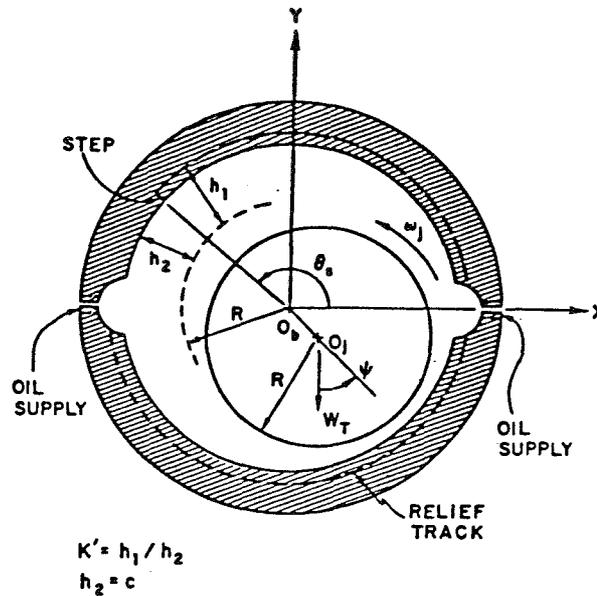
Figure 9   Pressure Dam Bearing Schematic, Side View
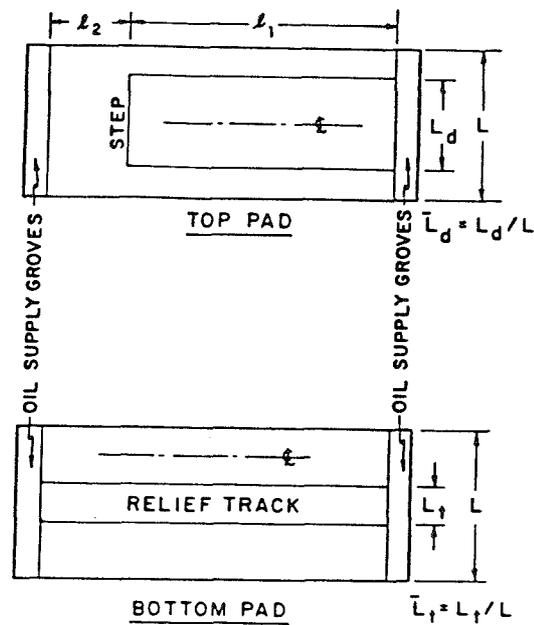
Figure 10   Pressure Dam Bearing Schematic, Top and Bottom Pads

$\theta_s = 125°$
$\overline{K}^s = 3.0$
$\overline{L}_t = 0.25$

This section analyzes the finite pressure dam bearing neglecting step inertia effects, but including the effects of turbulence over the entire bearing surface. Bearing stability threshold curves for vairous pressure dam bearing geometries are compared to plain journal, two axial groove and grooved lower half bearings. The effects on stability threshold of film thickness ratio, dam location, and other geometric parameters are considered. Optimum bearing designs are suggested to provide favorable stability characteristics.

Figure 11 compares the stability characteristics of the plain journal, two axial groove and grooved lower half bearings to two types of pressure dam bearings. The stability threshold speed ω_s is plotted against the Sommerfeld number, S. Also indicated at the top is the bearing eccentricity ratio ε_b for all five bearings. Bearing numbers 1 and 2 are the plain journal and two axial groove bearings, respectively. Note that at high Sommerfeld numbers the stability curves for each approach asymptotic values of $\omega_s = 2.3$ (plain journal) and $\omega_s = 2.05$ (2 axial groove).

Bearing number 3 is the grooved lower half bearing. This bearing is simply a two axial groove bearing with a circumferential relief track or groove cut in the lower half. In this case, the relief track axial length ratio (see Fig. 18) is $\overline{L}_t = 0.25$ (the relief track is 25% of the bottom pad). A considerable increase in the infinite stability region is evident. That is, the plain journal bearing is theoretically stable at all speeds below a Sommerfeld number of 0.48, while the grooved lower half bearing increases this range of infinite stability by a factor of 3 to $S \leq 0.17$. The relief track removes part of the bearing load carrying surface for the bottom pad thereby allowing bearing number 3 to reach 0.8 eccentricity at a higher Sommerfeld number than the plain journal bearing. Around $\varepsilon_b = 0.8$, $\overline{K}_{xy}$ changes sign providing the favorable stability characteristics. Essentially no increase in stability is seen at high Sommerfeld numbers.

Bearing number 4 is a pressure dam bearing with $\overline{K}' = 3.0$ (dam clearance 3 times as large as the bearing clearance) and $\overline{L}_t = 0.0$ (no relief track). For this case, the stability is increased compared to the journal bearing at high Sommerfeld numbers while the region of infinite stability is less. As discussed earlier, at high Sommerfeld numbers the step forces the journal to operate at a moderate eccentricity. From the top of Fig. 21, bearing number 4 operates at an eccentricity ratio of $\varepsilon_b = .25$ at S = 5.5. This moderate eccentricity provides the favorable stability characteristics at high Sommerfeld numbers for this step journal bearing.

Combining the two effects of a relief groove in the lower half and a step in the upper half, bearing number 5 is a dam bearing with $\overline{K}' = 3.0$ and $\overline{L}_t = 0.25$. For this case, the stability is increased for the entire range of Sommerfeld numbers compared to the journal bearing. The two separate effects of a pressure dam bearing are shown clearly in Fig. 21. The relief track forces the bearing to operate at higher eccentricities thereby increasing the region of

418

infinite stability. The dam loads up the journal at high Sommerfeld numbers providing a moderate operating eccentricity and higher stability threshold.

The effect of varying the film thickness ratio K' on stability was carried out but is not shown here. Reference [6] concludes that the optimum (as far as load capacity is concerned) is approximately $K' = 3.0$. A bearing with a film thickness ratio of $K' = 6.0$ is only slightly less superior (a 10% decrease at $S = 10.0$). A 40% decrease in stability is evident for a step bearing with $K' = 12.0$ when compared to the $K' = 3.0$ bearings at $S = 10.0$.
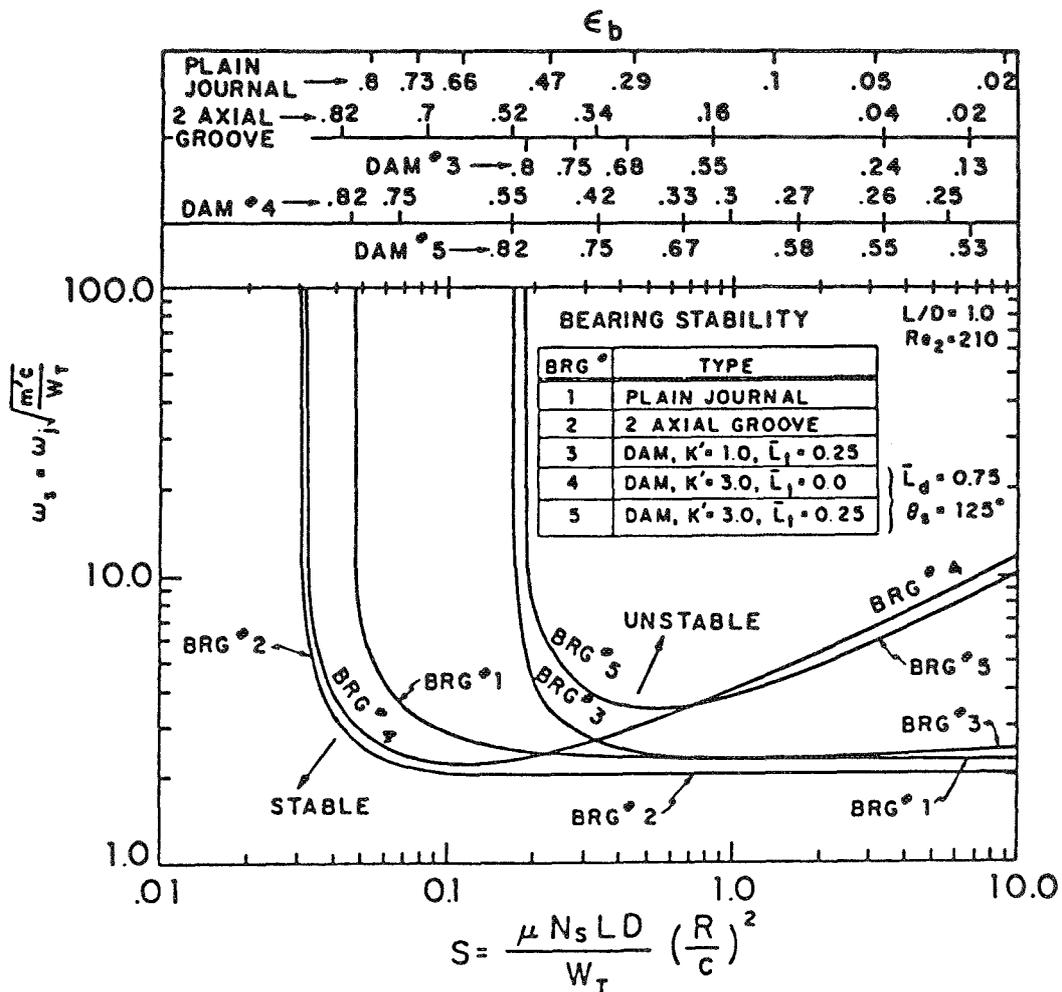
Figure 11   Stability Map Comparing Pressure Dam Bearings to Plain Journal and Two Axial Groove Bearings

The important geometric parameters in pressure dam bearing design are the film thickness ratio, K' and the dam location, θ_s. Steps should be located at around $\theta_s = 145°$ or $150°$, while K' values of between 3.0 and 6.0 are recommended.

From Sommerfeld numbers above $S = 2.0$, step journal bearings designated with near optimum step location and size can increase the rigid rotor stability parameter ω_s by a factor of 10 or more over a plain journal bearing. Additionally, the pressure dam bearing would operate at a moderate eccentricity ratio (between $\varepsilon_b = 0.25$ and $\varepsilon_b = 0.5$) even though the loading is light and/or speed high. However, for Sommerfeld numbers below $S = 2.0$, a step bearing will increase ω_s only slightly (by a factor of around 1.5) over a plain journal bearing even if the optimum dam height and location were used.

Experimental Step Bearing Stability in a Single Mass Flexible Rotor

Experimental results are given for different step configurations in the same experimental flexible rotor described in [7]. A theoretical-experimental comparison of the instability onset speed for the simple flexible rotor is presented [7,8]. Five different step bearing geometries and a two axial groove bearing are considered. The pressure dam bearings employed have different step heights and locations. Optimum and off-optimum designs are used. Instability onset speeds are determined both theoretically and experimentally and a comparison is made to determine the accuracy of the theoretical analysis.

All six pairs of bearings considered have two axial oil supply grooves located at the horizontal split (Fig. 9). These grooves are 20° in arc length making the arc length of both top and bottom pads 160°. The step bearings do not contain a circumferential relief groove in the bottom pad. The two axial groove bearings are identical to the pressure dam design with $h_1 = h_2$ in Fig. 9. The length to diameter ratio for each bearing is 1.0 with $D = 2.54$ cm.

Ideally, each bearing was to have a 5.08×10^{-3} cm (2.0 mil) radial clearance. However, due to difficulties in manufacturing, the radial clearance ranged from 4.57×10^{-3} to 6.35×10^{-3} cm (1.8 to 2.5 mils). The clearance was measured cold with a dial micrometer. Several readings were taken and the average value used.

The important geometric parameters in step bearing design are the film thickness ratio K' and the dam location θ_s. The ratio of film thicknesses is defined as h_1/h_2 when the shaft is centered in the bearing (Fig. 10). Thus, $K' = h/h$, $K'^{-1} = \bar{h}_1/c$ where $h_1 = $ centered clearance inside pocket. The dam location angle θ_s is measured with rotating from the positive x (horizontal) axis. Optimum values for favorable stability are around $K' = 3.0$ and $\theta_s = 125$ to 150°. Other parameters are the dam axial length ratio $\bar{L}_d = L_d/L$ (Fig. 3) and the reliev groove axial length ratio $\bar{L}_t = L_t/L$. For all cases, $L_t = 0.0$, since the bottom pad does not have a circumferential relief groove.

A summary of these parameters is listed in Table 4 for all six sets of bearings. Note that step bearing sets 1 and 2 represent the near optimum design with film thickness ratios between 2.1 and 2.8. Sets 3 and 5 are off-

optimum designs with larger K' values between 6.6 and 11.7. The off-optimum angular location is represented by set 4 with $\theta_s = 90°$. The dual numbers in the Table refer to the left (motor) and right ends of the test rotor, respectively.

Bearing Set No.	Type	K'	θ_s	c $(cm \times 10^3)$	c $(mils)$	$\bar{L}_d$
A	Two Axial Groove	1.0 1.0	– –	4.57 5.08	1.8 2.0	– –
1	Step	2.1 2.4	145°	5.59 6.35	2.2 2.5	0.75
2	Step	2.8 2.6	140°	6.35 6.35	2.5 2.5	0.75
3	Step	6.6 8.6	150°	6.10 6.35	2.4 2.5	0.75
4	Step	3.3 2.1	90°	6.10 6.10	2.4 2.4	0.75
5	Step	11.7 8.3	140°	5.33 6.10	2.1 2.4	0.50

Common to all bearings: L/D = 1.0, $\bar{L}_t$ = 0.0, χ = 160°

Table 4   Summary of Geometric Parameters for the Six
          Bearing Sets

Table 5 summarizes the experimental results. The near-optimum designs (sets 1 and 2) increase the instability onset speed by 109 and 41 percent, respectively, over the two axial groove bearings. The off-optimum designs (sets 3, 4, and 5) increase the instability speed by 35, 30, and 18 percent, respectively.

Comparing step bearing set number 3 to number 5, increasing the film thickness ratios from 6.6 and 8.6 to 11.7 and 8.3 decreases the instability speed by 12 percent. This trend is somewhat tainted since the dam axial length ratio is smaller for set 5 compared to set 3. Also, the step locations differ by 10°.

To obtain the theoretical instability onset speeds, the stiffness and damping properties of the bearings must be determined. The dynamic properties for all six sets of bearings were calculated using a finite element step bearing computer program that solves the Reynolds equation using finite elements [6]. The speed dependent characteristics are used as input data to a stability program that employs a transfer matrix approach similar to the method presented in Ref. [4].

Bearing Set No.	Type	K'	θ_s	Instability Onset Speed (RPM)		Percent Error
				Theoretical	Experimental	
A	Two Axial Groove	1.0	–	6,000	6,600	9.1%
1	Step	2.1, 2.4	145°	11,100	>13,800	>19.6%
2	Step	2.8, 2.6	140°	11,500	9,300	-23.7%
3*	Step	6.6, 8.6*	150°	8,850	8,900	0.6%
4*	Step	3.3, 2.1	90°*	8,100	8,600	5.8%
5*	Step	11.7, 8.3*	140°	7,800	7,800	0.0%

* Off-optimum

Table 5 Summary of Theoretical Instability Onset Speeds for the Six Bearing Designs

Table 5 summarizes the results of the theoretical stability analysis. Th experimental results are also indicated along with the percent error in the theoretical predictions. The error is under 10 percent for all cases except step bearing sets 1 and 2. Set number 1 has an error greater than 19.6 percen Set number 2 overestimates the onset speed by 23.7 percent. All other cases theoretically underpredict the instability speed.

The near-optimum pressure dam bearing designs increase the instability onset speed of the single mass rotor by around 109 and 41 percent compared to the two axial groove bearings. Increasing the film thickness ratio from the near-optimum cases decreases the onset speed. Decreasing the step location to 90° from the near-optimum locations also decreases the onset speed.

Pressures have also been measured in step bearings [9] and compared to theoretical predictions. Pressure measurements qualitatively agree with the stability measurements. Namely, sets 1 and 2 produce the largest pressures at the steps, which result in large artifical loads and good stabilizing chara teristics.

The theoretical stability analysis predicts the general trends in the experimental data. All step bearing designs increase the onset speed over the two axial groove bearings. The near-optimum designs have the highest onset speeds and the off-optimum designs the lowest.

Side rail construction is important in designing step bearings for optimum stability. Care should be taken to insure uniform pocket depth.

In many field applications, if a rotor system is unstable with simple axial groove bearings, one of the common "fixes" is to simply mill a step in the upper half of the bearing. Present results indicate that such a procedure will not guarantee machine stability, even for optimum values of K^{*}.

CONCLUSIONS

Two types of fixed pad hydrodynamic bearings – multilobe and pressure dam – have been considered here. Optimum and non-optimum geometric configurations were tested. The optimum geometric configurations were determined by using a theoretical analysis and then the bearings were constructed for a flexible rotor test rig. It has been found that optimizing bearings using this technique can produce a 100% or greater increase in rotor stability. It should be noted that this increase in rotor stability was carried out in the absence of certain types of instability mechanisms such as aerodynamic cross-coupling. However, the increase in rotor stability should greatly improve rotating machinery performance in the presence of such forces as well. More work remains to be done in this area.

Very significant differences between the experimentally observed stability threshold for certain bearings and the theoretically predicted stability thresholds have been observed. The theoretical results using an isoviscous standard solution of Reynolds equation predicts an increase of something like 10-40% in the stability threshold. There was, therefore, little reason to suspect that optimization of the bearing design would be very worthwhile to investigate. However, when the bearings were constructed and put in the experimental rig, the increase in stability was often greater than a 100% increase. Thus, the optimum bearing designs would appear to be much more worthwhile investigating than previously suspected.

It is also interesting to note that the experimental result was better than the theoretical prediction in all cases. While only a few of the experimental results actually carried out are presented in this paper, a number of other results not directly reported here show the same tendencies. The higher experimental stability threshold was true for various bearing types, bearing manufacturers, distribution of mass on the shaft, type of oil used to lubricate the bearings, bearing surface type, and a number of other factors. Experimentally observed pressures taken for one bearing type were also significantly higher than the peak pressures predicted by theory.

It is apparent from our research that some of the current theories normally used for bearing designs and rotating machinery may not be adequate. It appears that for bearings where a strongly converging area exists in the bearing, such as in both the multilobe and pressure dam pressures considered in this case, a more careful job must be done on the theoretical analysis. Some increases in stability threshold due to the use of Reynolds boundary conditions, temperature effects in the fluid, and other effects may increase the theoretical stability threshold somewhat. Results available to these authors indicate that these increases are not sufficient to give good agreement to theory and experiment. It appears likely that some detailed pressure measurements should be made for beaings involving a film thickness change of 3 to 6 times over one pad length

as shown by the optimum cases in this work.

Several possible effects could be occurring in these bearings. Turbulence theories may not be adequate although some of these effects have been investigated by the authors and found to be small for these bearings. Other theories which may prove worthwhile to investigate could include visco-elastic effects for the rapid changes in the film thickness. Perhaps some combination of all of the above effects would produce a much better agreement between theory and experiment.

It can be seen from the results in this paper that one cannot yet say that the optimum designs for journal bearings are well known. Based on the experimental results one cannot even say that one knows accurately the upper limit for stability produced by journal bearings of various types. The effect that all of this has in the presence of other forces is yet to be known. One major encouraging factor is that when one looks at an optimum bearing design using the current theoretical analysis, one does always predict the best bearing for the situation involved. One may also expect that in most cases it will perform better than theory would tell one.

ACKNOWLEDGEMENTS

REFERENCES

1. Allaire, P. E., "Design of Journal Bearings for High Speed Rotating Machinery," in Fundamentals of the Design of Fluid Film Bearings, ASME Publication, 1979, pp. 45-84.

2. Li, D. F., Choy, K. C., and Allaire, P. E., "Stability and Transient Characteristics of Four Multilobe Journal Bearing Configurations," accepted for

424

publication in Journal of Lubrication Technology, Trans. ASME, Paper No. 79-Lub-3.

3. Leader, M. E., Flack, R. D., and Lewis, D. W., "An Experimental Determination of the Instability of a Flexible Rotor in Four-Lobe Bearings," Wear, Vol. 58, No. 1, 1980, pp. 35-47.

4. Lund, J. W., "Stability and Damped Critical Speeds of a Flexible Rotor in Fluid-Film Bearings," Journal of Engineering for Industry, Trans. ASME, Vol. 96, No. 2, May 1974, pp. 509-517.

5. Allaire, P. E., Nicholas, J. C., and Barrett, L. E., "Analysis of Step Journal Bearings - Infinite Length, Inertia Effects," Trans. ASLE, Vol. 22, No. 4, October, 1979, pp. 333-341.

6. Nicholas, J. C. and Allaire, P. E., "Analysis of Step Journal Bearings - Finite Length, Stability," to be published in ASLE Trans., No. 78-LC-6B-2.

7. Leader, M. E., Flack, R. D., and Allaire, P. E, "The Experimental Dynamic Response of a Single Mass Flexible Rotor with Three Different Journal Bearings," accepted for publication in ASLE Trans. Preprint No. 79-AM-6D-2.

8. Nicholas, J. C., Barrett, L. E., and Leader, M. E., "Experimental-Theoretical Comparison of Instability Onset Speeds for a Three Mass Rotor Supported by Step Journal Bearings," accepted for publication in ASME Trans., Journal of Mechanical Design, Preprint No. 79-DET-56.

9. Flack, R. D., Leader, M. E., and Allaire, P. E., "Experimental and Theoretical Pressures in Step Journal Bearings," accepted for publication in ASLE Trans.

APPENDIX

Bearing Summary Charts

Table 6 gives some of the advantages and disadvantages of various bearing types in condensed form. The bearing stability or resistance to whirl has been explored in some depth in the earlier sections. Other comments such as "good damping at critical speeds" have come from the authors' experience. The table represents input from many different sources.

In summary, a wide range of bearing designs are available to the designers and users of rotating machinery. These range from very simple plain journal bearings, which are low in cost and easy to make, up to very complex tilting pad bearings which have many components and require very careful design. These can be used to reduce or eliminate vibration problems in many rotating machines. The cost and ease of manufacture must be balanced with the requirements for suppression of non-synchronous vibration in rotating machines.

Table 6a Fixed Pad Non-Preloaded Journal Bearings

Bearing Type	Advantages	Disadvantages	Comments
Plain Journal	1. Easy to make 2. Low cost	1. Very subject to oil whirl	Round bearings are nearly always "crushed" to make elliptical bearings
Partial Arc	1. Easy to make 2. Low cost 3. Low horsepower loss	1. Poor vibration resistance 2. Oil supply not easily contained	Bearing used only on rather old machines
Axial Groove	1. Easy to make 2. Low cost	1. Subject to oil whirl	Round bearings are nearly always "crushed" to make elliptical or multi-lobe
Floating Bush	1. Relatively easy to make 2. Low cost	1. Subject to oil whirl	Used primarily in high speed turbo-chargers for diesel engines in trucks and buses

Table 6b Fixed Pad Preloaded Journal Bearings

Bearing Type	Advantages	Disadvantages	Comments
Elliptical	1. Easy to make 2. Low cost 3. Good damping at critical speeds	1. Subject to oil whirl at high speeds 2. Load direction must be known	Probably most wide-ly used bearing at low or moderate speeds
Offset Half (With Horizontal Split)	1. Excellent sup-pression of whirl at high speeds 2. Low cost 3. Easy to make	1. Fair suppression of whirl at mod-erate speeds 2. Load direction must be known	Has high horizontal stiffness and low vertical stiffness-may become popular-used outside U.S.
Three and Four Lobe	1. Good suppres-sion of whirl 2. Overall good performance 3. Moderate cost	1. Some types can be expensive to make properly 2. Subject to whirl at high speeds 3. Goes unstable with little warn-ing 4. Very high vibra-tion levels during instability	Currently used by some manufacturers as standard bearing design

426

Table 6c Fixed Pad Journal Bearings with Steps, Dams or Pockets

Bearing Type	Advantages	Disadvantages	Comments
Pressure Dam (Single Dam)	1. Good suppression of whirl 2. Low cost 3. Good damping at critical speeds 4. Easy to make	1. Goes unstable with little warning 2. Dam may be subject to wear or build-up over time 3. Load direction must be known 4. Does not suppress whirl for very flexible rotors	Very popular with petro-chemical industry. Easy to convert elliptical over to pressure dam
Multi Dam Axial Groove or Multilobe	1. Dams are relatively easy to place in existing bearings 2. Good suppression of whirl 3. Relatively low cost 4. Good overall performance	1. Complex bearing requiring detailed analysis 2. May not suppress whirl due to non-bearing causes	Used as standard design by some manufacturers
Hydrostatic	1. Wide range of design parameter 2. Moderate cost 3. Good load capacity of low speeds	1. Poor damping at critical speeds 2. Requires careful design 3. Requires high pressure lubricant supply	Generally high stiffness properties used for high precision rotors

Table 6d Nonfixed Pad Journal Bearing

Bearing Type	Advantages	Disadvantages	Comments
Tilting Pad	1. Will not cause whirl (no cross-coupling) 2. Wide range of design parameters 3. Original cost about the same as other bearings	1. High replacement cost 2. Requires careful design 3. Poor damping at critical speeds 4. Hard to determine actual clearances 5. High horsepower loss	Widely used bearing to stabilize machines with subsynchronous non-bearing excitations

427

Page intentionally left blank

STABILIZATION OF AERODYNAMICALLY EXCITED TURBOMACHINERY
WITH HYDRODYNAMIC JOURNAL BEARINGS AND SUPPORTS*

Lloyd E. Barrett and Edgar J. Gunter
Department of Mechanical and Aerospace Engineering
University of Virginia
Charlottesville, Virginia 22903

SUMMARY

A method of analyzing the first mode stability and unbalance response of multimass flexible rotors is presented whereby the multimass system is modeled as an equivalent single mass modal model including the effects of rotor flexibility, general linearized hydrodynamic journal bearings, squeeze film bearing supports and rotor aerodynamic cross coupling. Expressions for optimum bearing and support damping are presented for both stability and unbalance response. The method is intended to be used as a preliminary design tool to quickly ascertain the effects of bearing and support changes on rotor-bearing system performance.

INTRODUCTION

The purpose of this paper is to present a method that is easily applied to a large class of industrial turbomachines which will predict the instability onset speeds including the effects of shaft flexibility, generalized hydrodynamic journal bearings, squeeze film bearing supports and aerodynamic rotor excitation. By restricting the analysis to the class of turbomachines which have their mass centers inboard of the bearings and are relatively symmetric about the mass center, a simplified rotor model is established that allows the equations of motion to be manipulated analytically. The restriction to turbomachines of this class does not severely limit its usefulness or applicability since the majority of industrial machines fall within this class. A major advantage of the method is that it allows machine designers to quickly determine the effects of bearing changes, shaft modifications and bearing support designs to determine appropriate system designs. Those designs deemed appropriate using the method can be further verified and finalized using more general analysis tools. A large time and cost savings should be realized by using the method to eliminate impractical designs without incurring the high computer costs and large amounts of data reduction time required using more general rotor dynamic analysis programs. The method is intended to supplement the more general techniques, not to replace them.

Specifically the method represents the rotor, bearings and supports as a linear dynamical system with the rotor represented by a generalized modal mass and modal stiffness. The inclusion of aerodynamic effects using the Alford model shows that an optimum bearing or support damping exists which will maximize the aerodynamic forces required to produce rotor instability for a given rotor and bearing or support flexibility. Definite expressions for the optimum damping are derived which eliminates the requirement of a parametric variation to find the optimum damping.

A number of instability mechanisms have been identified over the years. Chief among these are hydrodynamic bearings and aerodynamic effects.

(1) Hydrodynamic journal bearings - Most industrial turbomachine rotors are supported in fluid film bearings. Bearings with fixed geometries develop forces within the lubricant film which couple the motion of the rotor in any two orthogonal transverse directions and can produce instability under certain conditions of rotor speed and bearing load. Recent emphasis has been placed on determining the linearized fluid film force coefficients for various bearing geometries which can be used for linear stability analyses (refs. 1-9).

(2) Interaction with working fluid flow (Aerodynamic cross coupling) - The vibratory motion of a rotor within the machine working fluid can produce differential pressures around the rotor which result in destabilizing forces and moments. Because of the very complicated nature of the flows around turbine blades and through centrifugal impeller passages a general analysis describing the working fluid forces as a function of rotor motion has not been developed. The coupling between the working fluid and the rotor is commonly referred to as aerodynamic cross coupling.

The most commonly used approximation for predicting the magnitude of aerodynamic cross coupling assumes that the radial deflection of the rotor produces a variation in the thermodynamic efficiency around the impeller circumference and hence a torque variation (ref. 10). The differential torque produces a force on the impeller proportional to the displacement and perpendicular to it in the direction of impeller rotation and thus tends to drive the rotor in a forward (same direction as rotation) whirl. The cross coupling force on each impeller is a function of stage mean torque, pitch radius of the impeller, blade length and impeller displacement. A damping force is not postulated. The force is also proportional to a generally unknown constant which is a function of fluid mass flow rate, pressure, enthalpy and other fluid properties (ref. 10).

Figure 1 shows the frequency spectra for a 7-stage industrial centrifugal compressor designed to operate at 13500 rpm. Originally mounted in rigidly supported tilting pad bearings, the machine became unstable when the rotor speed exceeded 10500 rpm. The instability was due to aerodynamic cross coupling and seal forces. The spectra in figure 1a illustrates the subsynchronous frequency representing the instability shown by the 4300 cpm component of the spectra. This frequency was identified as the first damped frequency of the system and remained nearly constant as the machine speed was increased. The synchronous unbalance excitation is indicated by the 1N line and is seen to peak at about 4300 rpm. The vibration at the subsynchronous frequency was

430

sufficiently large to pervent sustained operation at 13500 rpm and the machine
operation was restricted to below 10000 rpm for a considerable period of time.
Monetary losses to the user due to reduced production capability were large.

Figure 1b shows the spectra after installation of properly designed
squeeze bearings at the tilting pad bearing locations. The subsynchronous
instability has been entirely eliminated. The unit has been successfully
operated at full production capability for nearly four years with no indication
of instability (ref. 11).

SYMBOLS

a	Constant
c	Bearing radial clearance, L
c_b	Tilting pad bearing assembled radial clearance, L
c_{ij}	Damping coefficient for i^{th} direction due to velocity in j^{th} direction, FTL^{-1}
c_p	Tilting pad bearing pad ground in clearance, L
c_r	Average radial damping coefficient, $(c_{ii} + c_{jj})/2$, FTL^{-1}
c_{ro}	Optimum average radial damping coefficient, FTL^{-1}
C_{ij}	$c_{ij}(2c\omega/W)$, dim.
C_o	$c_o(2c\omega/W)$, dim.
C_r	$c_r(2c\omega/W)$, dim.
C_{ro}	$c_{ro}(2c\omega/W)$, dim.
D	Bearing diameter, L
D_1	Defined by equation (19), dim.
D_2	Defined by equation (20), dim.
k_i	Modal stiffness for i^{th} mode, FL^{-1}
k_{ij}	Stiffness coefficient for force in i^{th} direction due to displacement in j^{th} direction, FL^{-1}
k_r	Average radial bearing stiffness $(k_{ii} + k_{jj})/2$, FL^{-1}
k_{rs}	Squeeze film bearing retainer spring stiffness, FL^{-1}
k_s	Fundamental shaft modal stiffness, FL^{-1}

K	Ratio of total bearing principal stiffness to shaft stiffness, dim.
K_c	Average cross coupled bearing stiffness, dim.
K_{ij}	$k_{ij}(c/W)$, dim.
K_r	$k_r(c/W)$, dim.
m	Mass, FT^2L^{-1}
N	Rotor speed, rpm
N_{cr}	Rigid bearing rotor critical speed, rpm
p	real part of eigenvalue, T^{-1}
P	p/ω_d, dim.
q	Aerodynamic cross coupling, FL^{-1}
Q	$2cq/W$, dim.
Q_m	Maximum value of Q, dim.
R	Bearing radius, L
s	Complex eigenvalue, T^{-1}
t	Time, T^{-1}
T	ωt, dim.
W	Weight, F
W_T	Total rotor weight, F
W_m	Rotor modal weight, F
x	Displacement in x-direction, L
X	x/c, dim.
{x}	Vector of x displacements, L
y	Displacement in y-direction, L
Y	y/c, dim.
$\bar{\delta}$	W/ck_s, dim.
λ	Imaginary part of eigenvalue, ω_d/ω, dim.

ω Rotor speed, T^{-1}

ω_{cr} Rotor rigid bearing critical speed, T^{-1}

ω_d Damped natural frequency, T^{-1}

ω_o Rotor operating speed, T^{-1}

ω_s Rotor instability onset speed, T^{-1}

ω_{sr} Rigid rotor instability onset speed, T^{-1}

Ω $\omega\sqrt{c/g}$, dim.

Ω_o $\omega_o\sqrt{c/g}$, dim.

Ω_s $\omega_s\sqrt{c/g}$, dim.

Ω_{sr} $\omega_{sr}\sqrt{c/g}$, dim.

ANALYSIS

Equations of Motion

Consider the generic rotor-bearing system shown schematically in figure 2. This system is representative of a large class of rotors supported in two bearings with most of the mass between the bearings. These machines generally operate above the first critical speed and the instability that occurs is generally associated with the first mode of the system (ref.12). The homogeneous equations of motion for the system are

$$m \, \ddot{x}_2 + k_s(x_2 - x_1) + q \, y_2 = 0 \qquad (1)$$

$$m \, \ddot{y}_2 + k_s(y_2 - y_1) - q \, x_2 = 0 \qquad (2)$$

$$c_{xx} \, \dot{x}_1 + c_{xy} \, \dot{y}_1 + k_{xx} \, x_1 + k_{xy} \, y_1 + \frac{k_s}{2} (x_1 - x_2) = 0 \qquad (3)$$

$$c_{yx} \, \dot{x}_1 + c_{yy} \, \dot{y}_1 + k_{yx} \, x_1 + k_{yy} \, y_1 + \frac{k_s}{2} (y_1 - y_2) = 0 \qquad (4)$$

433

where q represents a destabilizing cross-coupled aerodynamic force acting at the rotor center.

It is convenient to nondimensionalize the equations of motion using the following variables

$$X_i = x_i/c \quad , \quad i = 1, 2 \qquad \qquad \bar{\delta} = \frac{mg}{ck_s}$$

$$Y_i = y_i/c \quad , \quad i = 1, 2 \qquad \qquad Q = \frac{2cq}{mg}$$

$$K_{ij} = \frac{2c}{mg} k_{ij} \quad , \quad i = x, y \qquad \qquad \Omega^2 = \omega^2 c/g$$

$$C_{ij} = \frac{2c\omega}{mg} c_{ij} \quad , \quad i = x, y \qquad \qquad T = \omega t$$

where c is the bearing radial clearance and ω is the rotor speed. Substitution into equations (1)-(4) yields the following set of nondimensional equations

$$\bar{\delta}\, \Omega^2\, X_2'' + (X_2 - X_1) + \frac{\bar{\delta}Q}{2}\, Y_2 = 0 \tag{5}$$

$$\bar{\delta}\, \Omega^2\, Y_2'' + (Y_2 - Y_1) - \frac{\bar{\delta}Q}{2}\, X_2 = 0 \tag{6}$$

$$C_{xx}\, X_1' + C_{xy}\, Y_1' + K_{xx}\, X_1 + K_{xy}\, Y_1 + \frac{1}{\bar{\delta}}\, (X_1 - X_2) = 0 \tag{7}$$

$$C_{yx}\, X_1' + C_{yy}\, Y_1' + K_{yx}\, X_1 + K_{yy}\, Y_1 + \frac{1}{\bar{\delta}}\, (Y_1 - Y_2) = 0 \tag{8}$$

where the primes denote differentiation with respect to ωt.

This set of linear ordinary differential equations may be solved to determine the stability of the rotor-bearing system subject to the bearing forces and the equivalent aerodynamic force. The solution to these equations has the form

$$X_i = A_i\, e^{sT} \quad , \quad i = 1, 2$$

$$Y_i = B_i\, e^{sT} \quad , \quad i = 1, 2$$

where s represents the system complex eigenvalues,

$$s = P + i\lambda$$

The stability of the system is determined by the sign of P. If P < 0, the system is stable and small motions about the system equilibrium position will decay with time. If P > 0, the system is pronounced unstable and the motions will increase with time. If P = 0, the system is said to be at the onset of instability or instability threshold. It is this condition that will be examined in greater detail. For any given set of conditions, λ represents the rotor whirl ratio, that is, the ratio of the rotating shaft damped natural frequency to the rotor speed.

For any given combination of linearized bearing characteristics and aerodynamic excitation, there is a rotor speed where the real part of the eigenvalue, P, is zero. This rotor speed is the instability onset speed, and the rotor is stable for speeds below this.

Since P = 0, by definition, at the instability onset speed, the solution to the equations of motion becomes

$$X_i = A_i\, e^{i\lambda t} \quad , \quad i = 1, 2 \text{ at } \omega = \omega_s$$

$$Y_i = B_i\, e^{i\lambda t} \quad , \quad i = 1, 2 \text{ at } \omega = \omega_s$$

where ω_s is the instability onset speed for the given bearing and aerodynamic conditions. Substitution into equations (4)-(8) gives

$$(1 - \bar{\delta} \, \Omega^2 \, \lambda^2) \; X_2 + \frac{\bar{\delta}Q}{2} \; Y_2 - X_1 = 0 \tag{9}$$

$$(1 - \bar{\delta} \, \Omega^2 \, \lambda^2) \; Y_2 - \frac{\bar{\delta}Q}{2} \; X_2 - Y_1 = 0 \tag{10}$$

$$(K_{xx} + i \, \lambda \, C_{xx}) \; X_1 + (K_{xy} + i \, \lambda \, C_{xy}) \; Y_1 + \frac{1}{\bar{\delta}} \, (X_1 - X_2) = 0 \tag{11}$$

$$(K_{yx} + i \, \lambda \, C_{yx}) \; X_1 + (K_{yy} + i \, \lambda \, C_{yy}) \; Y_1 + \frac{1}{\bar{\delta}} \, (Y_1 - Y_2) = 0 \tag{12}$$

Since equations (9) and (10) are real, they may easily be solved for X_2 and Y_2 in terms of X_1 and Y_1 giving

$$X_2 = \frac{(1 - \bar{\delta} \, \Omega^2 \, \lambda^2) \; X_1 - (\bar{\delta}Q/2) \; Y_1}{(1 - \bar{\delta} \, \Omega^2 \, \lambda^2)^2 + (\bar{\delta}Q)^2/4} \tag{13}$$

$$Y_2 = \frac{(1 - \bar{\delta} \, \Omega^2 \, \lambda^2) \; Y_1 + (\bar{\delta}Q/2) \; X_1}{(1 - \bar{\delta} \, \Omega^2 \, \lambda^2)^2 + (\bar{\delta}Q)^2/4} \tag{14}$$

Substitution into equations (11) and (12) gives

$$\left[K_{xx} - \left\{ \frac{(\Omega \, \lambda)^2 \, (1 - \bar{\delta} \, \Omega^2 \, \lambda^2) - \bar{\delta}Q^2/4}{(1 - \bar{\delta} \, \Omega^2 \, \lambda^2)^2 + (\bar{\delta}Q)^2/4} \right\} + i \, \lambda \, C_{xx} \right] X_1$$

$$+ \left[K_{xy} + \frac{Q/2}{(1 - \bar{\delta} \, \Omega^2 \, \lambda^2)^2 + (\bar{\delta}Q)^2/4} + i \, \lambda \, C_{xy} \right] Y_1 = 0 \tag{15}$$

436

$$\left[K_{yy} - \left\{ \frac{(\Omega\,\lambda)^2\,(1 - \bar{\delta}\,\Omega^2\,\lambda^2) - \bar{\delta}Q^2/4}{(1 - \bar{\delta}\,\Omega^2\,\lambda^2)^2 + (\bar{\delta}Q)^2/4} \right\} + i\,\lambda\,C_{yy} \right] Y_1$$

$$+ \left[K_{yx} - \frac{Q/2}{(1 - \bar{\delta}\,\Omega^2\,\lambda^2)^2 + (\bar{\delta}Q)^2/4} + i\,\lambda\,C_{yx} \right] X_1 = 0 \qquad (16)$$

A nontrivial solution to this set of equations exists only if the determinant of the matrix of coefficients of X and Y is zero. Since the coefficients are complex, the determinant is also complex. The condition of a zero determinant requires that the real and imaginary parts of the determinant both be zero. Expanding equations (15) and (16) into matrix form and solving for the real and imaginary parts of the determinant results in the following two equations.

$$(K_{xx} - D_1)\,(K_{yy} - D_1) - (K_{xy} + D_2)\,(K_{yx} - D_2)$$

$$- \lambda^2\,(C_{xx}\,C_{yy} - C_{xy}\,C_{yx}) = 0 \qquad (17)$$

$$C_{yy}\,(K_{xx} - D_1) + C_{xx}\,(K_{yy} - D_1) - C_{xy}\,(K_{yx} - D_2)$$

$$- C_{yx}\,(K_{xy} + D_2) = 0 \qquad (18)$$

where

$$D_1 = \frac{(\Omega\,\lambda)^2\,(1 - \bar{\delta}\,\Omega^2\,\lambda^2) - \bar{\delta}Q^2/4}{(1 - \bar{\delta}\,\Omega^2\,\lambda^2)^2 + (\bar{\delta}Q)^2/4} \qquad (19)$$

and

$$D_2 = \frac{Q/2}{(1 - \bar{\delta}\,\Omega^2\,\lambda^2)^2 + (\bar{\delta}Q)^2/4} \qquad (20)$$

Equations (17) and (18) represent two equations in the two unknows $(\Omega\lambda)^2$ and λ^2. Once these variables are known, the instability onset speed for the given conditions can be determined and is

$$\Omega_s = \frac{(\Omega\lambda)}{\lambda} \tag{21}$$

or in dimensional terms

$$\omega_s = \frac{(\Omega\lambda)}{\lambda} \sqrt{\frac{g}{c}} \tag{22}$$

The solution is obtained in the following way. First, write equation (18 as

$$D_1 = \frac{C_{yy} K_{xx} + C_{xx} K_{yy} - C_{xy} K_{yx} - C_{yx} K_{xy} + D_2 (C_{xy} - C_{yx})}{C_{xx} + C_{yy}} \tag{23}$$

For hydrodynamic journal bearings, $C_{xy} = C_{yx}$ (ref. 5) so the last term in equation (23) is zero and D_1 is a function only of the known bearing coefficients,

$$D_1 = \frac{C_{yy} K_{xx} + C_{xx} K_{yy} - C_{xy} K_{yx} - C_{yx} K_{xy}}{C_{xx} + C_{yy}} \tag{24}$$

Once D_1 is known, equation (19) may be solved for $(\Omega\lambda)^2$,

$$(\Omega\lambda)^2 = \frac{(1 + 2\bar{\delta}D_1) \pm \sqrt{(1 + 2\bar{\delta}D_1)^2 - \bar{\delta} (1 + \bar{\delta}D_1) \{\bar{\delta}Q^2 (1 + \bar{\delta}D_1) + 4D_1\}}}{2\bar{\delta} (1 + \bar{\delta}D_1)} \tag{25}$$

Now equation (20) is used to determine D_2 and equation (17) is rearranged to give λ^2.

$$\lambda^2 = \frac{(K_{xx} - D_1) (K_{yy} - D_1) - (K_{xy} + D_2) (K_{yx} - D_2)}{C_{xx} C_{yy} - C_{xy} C_{yx}} \tag{26}$$

Finally, equation (21) or (22) is used to determine the instability onset speed. The proper use of equation (25) requires some explanation. If the entire term within the radical is positive, equation (26) gives two real value for $(\Omega\lambda)^2$ and, hence, two instability onset speeds are predicted. For the giv

bearing and aerodynamic conditions, the rotor will be stable only for rotor speeds between the two predicted onset speed values. This condition occurs only for the case when the aerodynamic excitation is greater than zero. As Q approaches zero, the lower value of ω_s approaches zero and the rotor will be stable for all rotor speeds below the upper value of ω_s.

It is apparent from examination of the radical in equation (25) that for a given level of shaft flexibility, δ, and a given set of bearing coefficients, which uniquely determine D_1, there is an upper bound to the level of aerodynamic excitation, Q, that will allow the terms inside the radical to be positive. Once this value of Q is surpassed, the radical term becomes imaginary. This implies that the rotor will be unstable at any rotor speed. Thus, imposing the condition that the radical term be zero in equation (25) will yield the maximum value of aerodynamic excitation for which a stable operating speed exists. Therefore, the maximum aerodynamic excitation the rotor can withstand occurs when

$$(1 + 2 \bar{\delta} D_1)^2 - \bar{\delta} (1 + \bar{\delta} D_1) \{\bar{\delta} Q_m^2 (1 + \bar{\delta} D_1) + 4D_1\} = 0 \tag{27}$$

Rearranging gives

$$Q_m = \frac{1}{\bar{\delta} (1 + \bar{\delta} D_1)} \tag{28}$$

Bearing Induced Instability

It is of interest to examine in detail the effect of hydrodynamic bearings alone on the stability of flexible rotors. With aerodynamic excitation Q = 0, equation (19) gives

$$(\Omega\lambda)^2 = \frac{D_1}{1 + \bar{\delta}D_1} \tag{29}$$

where D_1 is calculated from the bearing properties using equation (24). The whirl ratio, λ, is given by equation (26) so the onset speed is

$$\Omega_s = \frac{1}{\lambda} \sqrt{\frac{D_1}{1 + \bar{\delta}D_1}} \tag{30}$$

Noting that with Q = 0, the whirl ratio at the instability onset speed is independent of shaft flexibility, $\bar{\delta}$, the rigid rotor onset speed is

$$\Omega_{sr} = \frac{1}{\lambda} \sqrt{D_1} \tag{31}$$

so that

$$D_1 = \Omega_{sr}^2 \lambda^2 \tag{32}$$

Substitution into equation (30) gives the flexible rotor instability onset speed as

$$\Omega_s = \frac{\Omega_{sr}}{\sqrt{1 + \bar{\delta}\lambda^2\Omega_{sr}^2}} \tag{33}$$

which clearly shows the reduction in stability with increasing shaft flexibility. For a given flexibility parameter, $\bar{\delta}$, the rotor instability onset speed can be increased by choosing bearings with a higher bearing instability threshold speed, Ω_{sr}, and lower whirl ratio, λ. As Ω_{sr} becomes very large, the limiting value of instability onset speed becomes

$$\Omega_s = \frac{1}{\lambda\sqrt{\bar{\delta}}} \quad , \quad \Omega_{sr} \gg 1 \tag{34}$$

or in dimensional terms

$$\omega_s = \frac{1}{\lambda} \sqrt{\frac{k_s}{m}} \quad , \quad \Omega_{sr} \gg 1 \tag{35}$$

Hence the instability onset speed of a flexible rotor is proportional to the rigid bearing natural frequency of the rotor. From equations (24) and (26) it is observed that increased bearing principal stiffness and damping and decreased cross-coupled stiffness increase bearing induced instability onset speeds. Further increases may be obtained from asymmetry in the principal stiffness and damping.

Aerodynamically Induced Instability

If aerodynamic cross-coupling is present it was previously noted that a maximum value of Q exists beyond which a particular flexible rotor-bearing system will be unstable at all speeds. That value was shown to be

$$Q_m = \frac{1}{\bar{\delta}(1 + \bar{\delta}D_1)} \tag{36}$$

With $Q = Q_m$, equation (25) becomes

$$(\Omega\lambda)^2 = \frac{1 + 2\bar{\delta}D_1}{2\bar{\delta}(1 + \bar{\delta}D_1)} \tag{37}$$

Substituting into equation (20) gives the effective cross coupling at the bearings due to aerodynamic excitation

440

$$D_2 = \frac{(1 + \bar{\delta} D_1)}{\bar{\delta}} \tag{38}$$

This value of D_2 is then used to calculate λ^2.

The instability onset speed becomes

$$\Omega_{sm} = \frac{1}{\lambda} \sqrt{\frac{1 + 2 \bar{\delta} D_1}{2\bar{\delta}(1 + \bar{\delta} D_1)}} \tag{39}$$

It should be remembered that equation (38) represents the instability onset speed with maximum aerodynamic cross-coupling present. With smaller values of Q the actual onset speed may be higher or lower as will be subsequently shown.

Example 1   Single-Stage Centrifugal Pump in Plain Cylindrical Journal Bearings. A single-stage centrifugal pump has the impeller centrally mounted on the shaft. The rotor has the following characteristics:

    Shaft Length = 107.32 cm
    Shaft Diameter = 10.16 cm
    Impeller Weight = 1800.0 N
    Operating Speed = 4,000 rpm

The rotor is mounted in two identical plain cylindrical journal bearings with the following characteristics:

    Bearing Length = 5.08 cm
    Bearing Diameter = 10.16 cm
    Radial Clearance = 0.0508 mm
    Oil Viscosity = 1.23 N-s/cm^2

The shaft weight is 667.2 N. Hence, the modal weight is approximately half the shaft weight plus the impeller weight, or 2134.5 $\underline{N}$. The effective shaft stiffness is k_s = 420,283 N/cm which corresponds to δ = 1.0. The bearing coefficients are

K_{xx} = 2.55 C_{xx} = 20.0
K_{xy} = 10.0 C_{xy} = -2.55
K_{yx} = -10.0 C_{yx} = -2.55
K_{yy} = 1.27 C_{yy} = 20.0

The operating speed parameter is

$$\Omega_0 = \omega_0 \sqrt{\frac{c}{g}} = 0.953$$

Equations (24), (36), (38), and (39) give the maximum aerodynamic excitation as

$$Q_m = 0.344$$

and the instability onset speed as

$$\Omega_s = 1.57$$

Since $\Omega_s \neq \Omega_0$, the rotor will be unstable with Q_m present. The variation of instability onset speed with Q is shown by the solid curve in figure 3. This figure was obtained by varying Q is equation (25). The allowable aerodynamic excitation is Q = 0.17. The dashed curve in figure 3 shows the effect of changing the bearing length from 5.08 cm to 4.45 cm which increases the allowable aerodynamic excitation from 0.17 to 0.245.

Optimum Damping

The stability analysis presented in the preceding sections show that for a given set of nondimensional bearing coefficients, the permissible aerodynamic rotor excitation is a function of rotor operating speed and a maximum value is indicated.

The fact that a maximum value of allowable aerodynamic excitation exists may be construed as the existence of an optimum damping. This concept may be visualized in the following way.

Since the nondimensional stiffness and damping coefficients are constant for a given operating condition, increasing the nondimensional speed (the ordinate of stability map) is equivalent to decreasing the dimensional damping in the bearings since damping is inversely proportional to speed. The stabilit map may be thought of as the effect of increasing the rotor speed assuming the nondimensional bearing stiffness and damping coefficients are independent of speed. The optimum dimensional damping occurs when $\Omega_s = \Omega_{sm}$ and is

$$c_{xx_0} = \frac{W\ C_{xx}}{2c\ \omega_{sm}} \tag{40}$$

$$c_{yy_0} = \frac{W\ C_{yy}}{2c\ \omega_{sm}} \tag{41}$$

where C_{xx} and C_{yy} are the actual nondimensional damping coefficients for the operating conditions being considered and ω_{sm} is the dimensional speed at Ω_{sm}, i.e.,

$$\omega_{sm} = \Omega_{sm} \sqrt{\frac{g}{c}} \tag{42}$$

This value of Ω_s is obviously chosen as the optimum since the maximum allowable aerodynamic excitation, Q_m, occurs at this value. For values of $\Omega_s < \Omega_{sm}$, the actual dimensional damping is excessive, and for $\Omega_s > \Omega_{sm}$, the damping is insufficient. The optimum nondimensional damping coefficients are, therefore,

442

$$C_{xx_0} = \frac{\omega_0}{\omega_{sm}} C_{xx} \qquad (43)$$

$$C_{yy_0} = \frac{\omega_0}{\omega_{sm}} C_{yy} \qquad (44)$$

If the bearings or supports are assumed symmetric, an explicit expression for optimum damping may be obtained. Letting

$$
\begin{aligned}
K_{xx} &= K_{yy} = K_r \\
K_{xy} &= |K_{yx}| = K_c \\
C_{xx} &= C_{yy} = C_r \\
C_{xy} &= C_{yx} \ll C_r
\end{aligned}
$$

the following relationships are obtained

$$D_1 = K_r$$

$$Q_m = \frac{1}{\bar{\delta}(1 + \bar{\delta}K_r)}$$

$$(\Omega\lambda)^2 = \frac{1 + 2\bar{\delta}K_r}{2\bar{\delta}(1 + \bar{\delta}K_r)}$$

$$\lambda = \frac{1 + \bar{\delta}(K_r + K_c)}{\bar{\delta}C_r}$$

The instability onset speed becomes

$$\Omega_{sm} = \frac{C_r}{1 + \bar{\delta}(K_r + K_c)} \sqrt{\frac{\bar{\delta}(1 + 2\bar{\delta}K_r)}{2(1 + \bar{\delta}K_r)}} \qquad (45)$$

For the system to tolerate the maximum aerodynamic excitation, the operating speed must be the same as Ω_{sm},

$$\Omega_0 = \Omega_{sm}$$

and the optimum damping is

$$C_{ro} = \Omega_0 \ \{1 + \bar{\delta}(K_r + K_c)\} \ \sqrt{\frac{2(1 + \bar{\delta}K_r}{\bar{\delta}(1 + 2\bar{\delta}K_r)}} \tag{46}$$

It may be shown (ref. 13,14,15) that the effective damping acting at the rotor center is

$$C_e = \left(\frac{2a}{1 + a^2)}\right) C_{em} \tag{47}$$

where a is the ratio of actual bearing damping to optimum bearing damping, i.e.

$$a = c_r/c_{ro}$$

and C_{em} is the effective damping with optimum bearing damping. Since the allowable aerodynamic is proportional to the effective damping, an estimate of the permissible aerodynamic excitation with non-optimum damping is

$$Q = \left(\frac{2a}{1 + a^2}\right) Q_m \tag{48}$$

Equation (46) can also be written in terms of the bearing (support) principal stiffness to shaft stiffness ratio

$$C_{ro} = \omega_0 \ \omega_{cr} \ \left(\frac{c}{g}\right) (1 + \bar{\delta}K_c + K) \ \sqrt{\frac{2(1 + K)}{1 + 2K}} \tag{49}$$

where $K = 2 \ k_r/k_s = \bar{\delta}K_r$

Flexible, Damped Bearing Supports

The equations previously presented may also be used to evaluate the effect of squeeze film bearing supports in series with a hydrodynamic bearing. Such a support is shown in figure 4 (ref. 16). In this particular application, the squeeze film is used to support a ball bearing mounted rotor, although any type of shaft bearing may be utilized. The particular values of the squeeze film bearing parameters are, of course, dependent on the rotor-bearing system it will support. The essential features of the squeeze film bearing include an annular clearance between the squeeze film journal and damper housing, lubricant supply grooves or holes, bearing end seals, and journal mechanical retaine springs. Various combinations of these components are used to achieve appropriate stiffness and damping properties for a particular application. Since the squeeze film journal does not rotate, the hydrodynamic squeeze film forces result only from translational motion of the journal which squeezes the lubricant.

Figure 5 schematically illustrates a flexible, damped bearing-support component. The bearing and suppport are represented by general linearized stiff-

ness and damping force coefficients. In many squeeze film bearing applications, the inner bearing mass, m_b, is statically supported in mechanical springs to align and preload the inner bearing within the squeeze film annulus. Therefore, the general support radial stiffness is represented by hydrodynamic stiffness coefficients, k_{0xx} and k_{0yy}, and by the mechanical retainer spring stiffness coefficients, k_{rsx}^0 and k_{rsy}^0. The bearing and support can be combined to give overall effective stiffness and damping properties (refs. 2, 13). However, care must be exercised when doing so. The effective coefficients are functions of the whirl ratio, λ. Therefore, the use of the stability equations requires an iterative process whereby a value of λ is chosen, the effective coefficients are calculated, and the value of λ predicted by equation (26) is compared with the chosen value. The process is repeated until the calculated and assumed values of λ are the same. A judicious first guess for λ can be made since the damped natural frequency will usually lie somewhere between the undamped natural frequency of the rotor-bearing-support system and the undamped rigid bearing, rigid support natural frequency. Also, the whirl ratio dependence will be much less if either the bearings or supports have a large impedance due to high stiffness or damping.

A further consideration is that under some conditions the effective damping matrix will not be symmetric ($c_{1exy} \neq c_{1eyx}$. With this condition, D_1, given by equation (23), is a function of the aerodynamic cross coupling of the system as well as the bearing coefficients. Equations (20), (23), and (26) must be solved iteratively for D_1 and D_2.

Example 2 <u>11-Stage Centrifugal Compressor</u>
An 11-stage centrifugal compressor is shown in figure 6. The rotor physical characteristics are

    Overall Length = 216 cm
    Bearing Span   = 175.3 cm
    Rotor Weight   = 5782.4 N
    Operating Speed = 10,000 rpm

The first rigid bearing critical speed is N_{cr} = 3894 rpm. The second critical speed is above the 10,000 rpm operating speed with the bearings described above. The rotor is very nearly symmetrical about the bearing midspan and gyroscopic effects are negligible. The rotor modal weight is 2891.2 N, and the shaft stiffness is k_s = 490350 N/cm.

The rotor was originally mounted in tilting pad bearings with the following dimensions:

    Length = 5.72 cm
    Diameter = 11.43 cm
    Radial Pad Clearance = 0.1016 mm
    Bearing Radial Clearance = 0.0508 mm
    Number of Pads = 5
    Pad Arc Length = 60°
    Offset Factor = 0.50
    Preload = 0.50

Load Direction = Pad Pivot
Oil Viscosity = 1.38×10^{-6} N-s/cm^2

The bearing stiffness and damping coefficients are shown in figure 7 (ref. 7). At 10000 rpm the bearing coefficients are $K_{xx} = K_{yy} = 36.23$, $C_{xx} = C_{yy} = 43.63$. Field experience indicated that the level of aerodynamic excitation at 10000 rpm was q = 35000 N/cm and rotor instability was observed.

Applying equations (36)-(39) the maximum permissible aerodynamic excitation is $Q_m = 0.078$ ($q_m = 11098$ N/cm). This is considerably less than the anticipated value of q = 35000 N/cm. Since Q_m occurs at $\Omega_{sm} = 1.50$ and the operating speed parameter is $\Omega_0 = 3.37$, even less aerodynamic excitation can occur. The variation of Ω_s with Q is shown in figure 8. For $\Omega_s = \Omega_0 = 3.37$, the allowable aerodynamic excitation is Q = 0.055 (q = 7826 N/cm).

If the bearing clearance and pad clearance are increased and pad clearance are increased to 0.1143 mm and 0.2286 mm respectively, the bearing coefficients at 10,000 rpm are

$$K_{xx} = 8.83 \qquad K_{yy} = 14.86$$
$$C_{xx} = 9.88 \qquad C_{yy} = 13.29$$

For this condition $Q_m = 0.970$ ($q_m = 61340$ N/cm) at $\Omega_{sm} = 1.40$. The operating speed parameter is $\Omega_0 = 5.06$ (the change is due to the change in clearance. The variation of Ω_s with Q for this case is also shown in figure 8. The allowable value of aerodynamic excitation is Q = 0.59 (q = 37310 N/cm). This is slightly larger than the anticipated value. Therefore, it is apparent that large changes in stability can be achieved simply by modifying bearing clearance

CONCLUSIONS

(1) The single mass representation including generalized linearized bearing and aerodynamic excitation yields equations which predict instability onset speeds due to bearing cross coupling and aerodynamic effects.

(2) Expressions for the optimum bearing damping for given bearing stiffness coefficients which will maximize the allowable aerodynamic excitation at a given operating speed and predict the maximum aerodynamic excitation have been developed.

(3) The form of the optimum damping expressions for stability are applicable to first mode synchronous unbalance response and the optimum damping minimizes that response.

(4) Optimum nondimensional bearing damping is a function of the rotr operating speed, rigid bearing undamped critical speed, bearing clearance and ratio of principal bearing stiffness to the fundamental rotor modal.

(5) The effect of flexible, damped bearing supports can be incorporated into the single mass modal representation using equivalent bearing-support linear stiffness and damping coefficients.

446

REFERENCES

1. Abdul-Wahed, Frene, J., and Nicolas, D., "Analysis of Fitted Partial Arc and Tilting Pad Journal Bearings," Trans. ASLE, Paper No. 78-AM-2A-3.

2. Warner, R. E. and Soler, A. I., "Stability of Rotor-Bearing Systems with Generalized Support Flexibility and Damping and Aerodynamic Cross-Coupling," Trans. ASME, Journal of Lubrication Technology, July 1975, pp. 461-471.

3. Lund, J. W., "The Stability of an Elastic Rotor in Journal Bearings with Flexible Damped Supports," Trans. ASME, Journal of Applied Mechanics, Vol. 87, 1965, pp. 911-920.

4. Lund, J. W., "Spring and Damping Coefficients for the Tilting Pad Journal Bearing," Trans. ASLE, Vol. 7, No. 4, 1964, pp. 342-352.

5. Lund, J. W. and Thomsen, K. K., "A Calculation Method and Data for the Dynamic Coefficients of Oil-Lubrication Journal Bearings," Topics in Fluid Film Bearing and Rotor Bearing System Design and Optimization, April 1978, pp. 1-28.

6. Nicholas, J. C., "A Finite Element Analysis of Pressure Dam and Tilting Pad Bearings," Ph.D. Dissertation, University of Virginia, May 1977.

7. Nicholas, J. C., Gunter, E. J., and Allaire, P. E., "Stiffness and Damping Coefficients for the Five-Pad Tilting-Pad Bearing," Trans. ASLE, Paper No. 77-LC-3A-2, 1977.

8. Hagg, A. C. and Sankey, G. O., "Elastic and Damping Properties of Oil-Film Journal Bearings for Applicat to Unbalance Vibration Calculations, Trans. ASME, Journal of Applied Mechanics, March 1958, pp. 141-143.

9. Li, D. F., Allaire, P. E., and Barrett, L. E., "Analytical Dynamics of Partial Journal Bearings with Applications," Trans. ASLE, Paper No. 77-LC-1A-1, 1977.

10. Alford, J. S., "Protecting Turbomachinery from Self-Excited Rotor Whirl," Trans. ASME, Journal of Engineering for Power, Oct. 1965, pp. 333-344.

11. Gunter, E. J., Barrett, L. E., and Allaire, P. E., "Stabilization of Turbomachinery with Squeeze Film Dampers - Theory and Application," I. Mech. E., Proceedings of Conference on Vibrations in Rotating Machinery, Cambridge, England, C233/76, Sept. 1976.

12. Lund, J. W., "Stability and Damped Critical Speeds of a Flexible Rotor in Fluid Film Bearings," Trans. ASME, Journal of Engineering for Industry, Vol. 96, 1974, pp. 509-517.

13. Barrett, L. E., "Stability and Nonlinear Response of Rotor-Bearing Systems with Squeeze Film Bearings," Ph.D. Dissertation, University of Virginia, August 1978.

447

14. Barrett, L. E., Gunter, E. J., and Alliare, P. E., "Optimum Bearing and Support Damping for Unbalance Response and Stability of Turbomachinery," Trans. ASME, Journal of Engineering for Power, Jan. 1978, pp. 89-94.

15. Black, H. F., "Stabilizing Capacity of Bearings for Flexible Rotors with Hysteresis," Trans. ASME, Journal of Engineering for Industry, Feb. 1976, pp. 87-91.

16. Cunningham, R. E., Fleming, D. P., and Gunter, E. J., "Design of a Squeeze Film Damper for a Multimass Flexible Rotor," Trans. ASME, Journal of Engineering for Industry, 1976.

FREQUENCY SPECTRUM VS SPEED-
NONSYNCHRONOUS WHIRL

FREQUENCY SPECTRUM SPEED VS SPEED
WITH SQUEEZE FILM DAMPER-STABILIZED SYSTEM

(a)   (b)
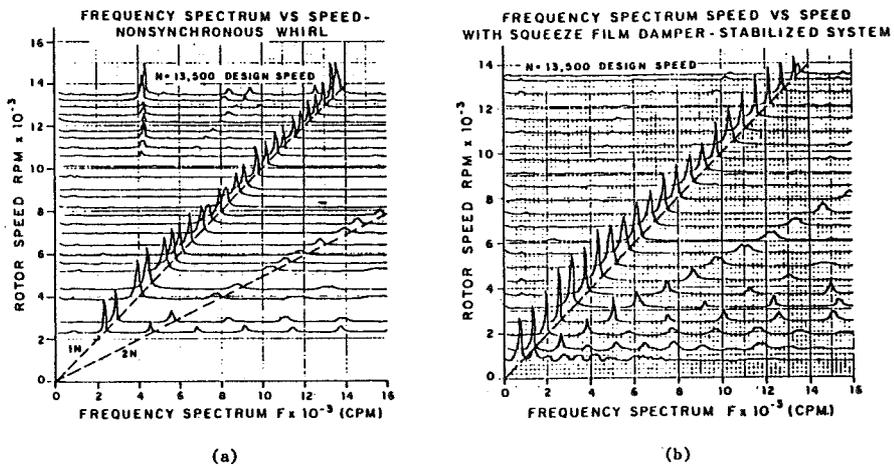
Fig. 1.   Frequency Spectra of 7-Stage Centrifugal Compressor
           (a) Subsynchronous Instability with N > 10500 RPM
           (b) Stabilization with Well Designed Squeeze Film Bearing
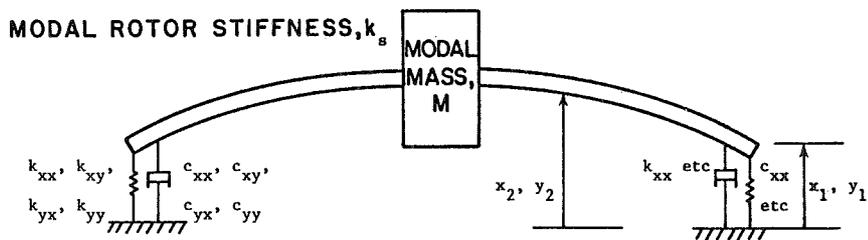
Fig. 2   Schematic of Single Mass Representation
           of Symmetric Multimass Rotors

449
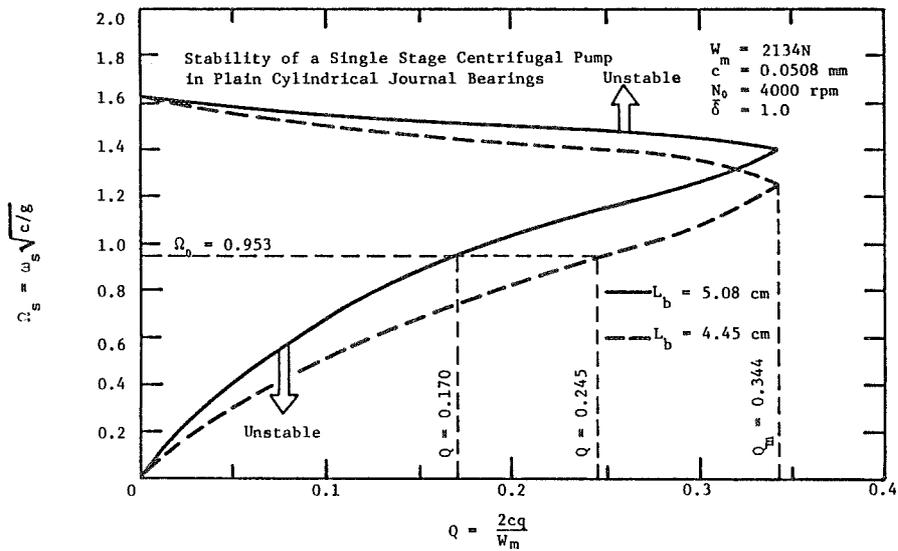
Fig. 3.
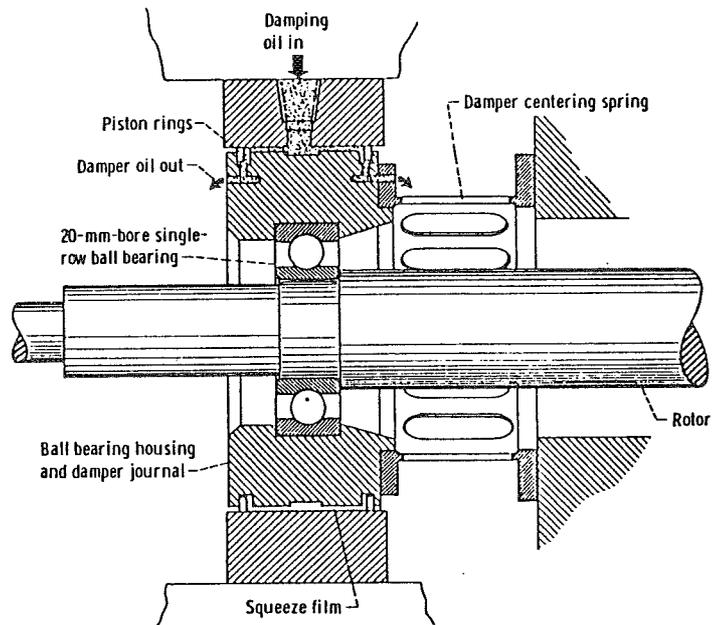
Fig. 4   Axial Cross Section of Squeeze Film Bearing Used in NASA
Experimental Work. Ref (Cunningham, 1977)
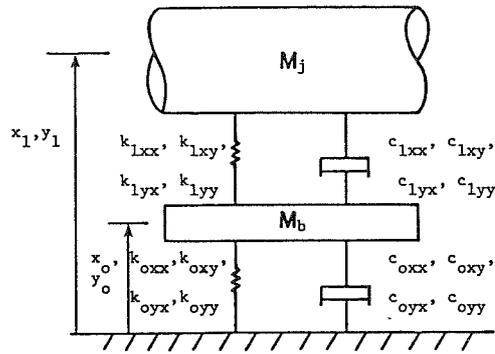
Fig. 5.   Schematic of Bearing in Flexible, Damped Supports
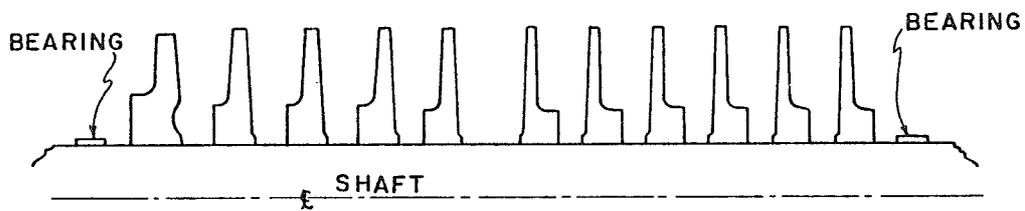
Fig. 6 - Schematic of 11-Stage Centrifugal Compressor

$$S = \frac{\mu N' L D}{W_T} \left(\frac{R}{c_p} \right)^2$$

Fig. 7

$$Q = \frac{2cq}{W_m}$$
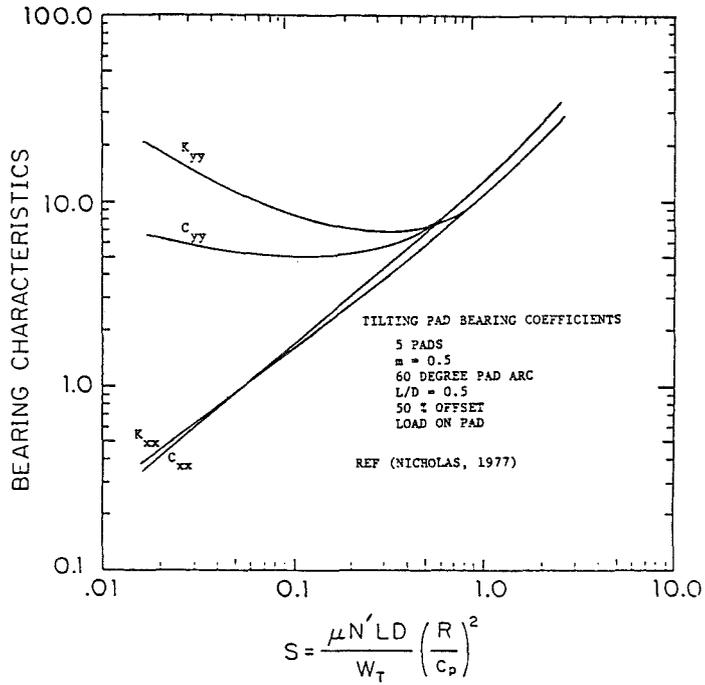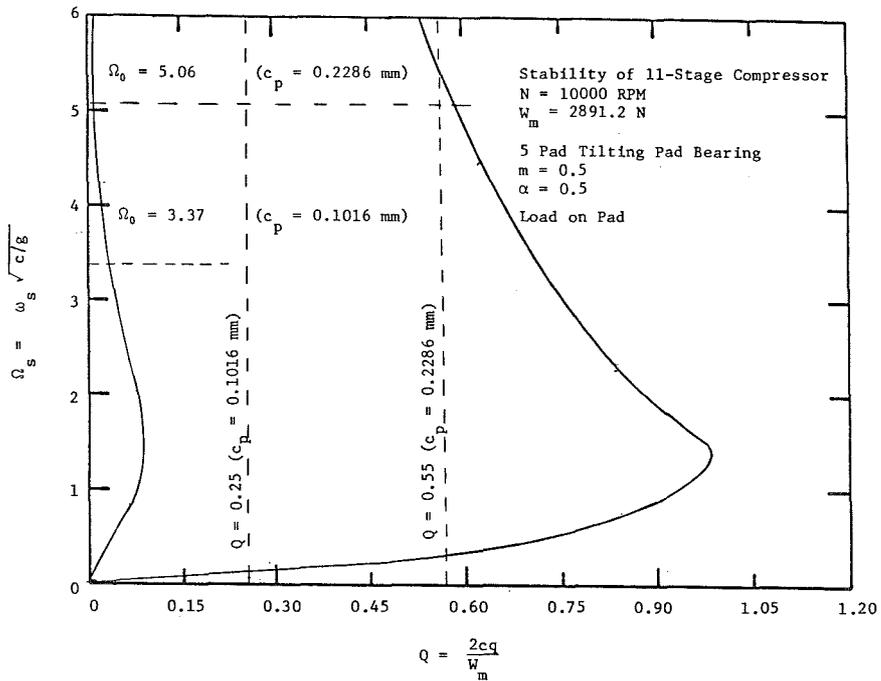
Fig. 8

USE OF ELASTOMERIC ELEMENTS IN CONTROL OF ROTOR INSTABILITY

Anthony J. Smalley
Mechanical Technology Incorporated (MTI)
Latham, New York 12100

SUMMARY

Elastomeric elements are seeing increasing, successful use in control of unstable rotor vibrations. Elastomers are used both as seals for squeeze film dampers and as dissipative elements in their own right. In either application, their success is dependent upon a correct match between rotor and suspension dynamic characteristics. This paper presents information on the dynamic characteristics of elastomeric supports. Stiffness and damping characteristics for elastomers of various geometries including O-rings, buttons loaded in compression, and rectangular elements loaded in shear are presented. The effects of frequency, temperature, and amplitude are illustrated, as well as the effects of material and geometry. The basis for this data is dynamic component testing. Empirical design methods are illustrated, and several examples are presented where elastomers have successfully controlled both synchronous and nonsynchronous vibrations.

INTRODUCTION

In a number of rotating machinery applications, undesirable vibrations, both synchronous and nonsynchronous, can be controlled by simple elastomeric bearing mounts. Belief in this statement has led to a sustained effort at Mechanical Technology Incorporated (MTI), under NASA funding, to provide the necessary elastomer data to develop the means to apply it, and to demonstrate the vibration control capability of elastomers for rotating machinery. The program approach has been empirical and is directed at answering the questions of the rotor dynamicist who must perform analysis and design synthesis to achieve smoothly running rotors.

Some highlights of available data are presented in this paper together with some illustrations of effective vibration control by elastomeric elements. For more extensive data, the reader is referred to the list of references at the end of the paper.

COMPONENT TESTING

Component dynamic data have been generated by the base excitation resonant mass method, whose main features are shown in Figure 1. A high-capacity electromagnetic shaker applies a sinusoidal motion to the base of an elastomeric spring on which a mass is supported, and accelerometers measure the transmissibility and phase difference between base and mass. Near resonance, these measurements are accurately translated into stiffness and damping of the elastomeric spring.

453

Various geometries have been tested, including cylindrical buttons in compression; rectangular elements in shear; ring cartridges under radial loading and O-rings under radial loading. These geometries are illustrated in Figure 2.

In Figure 3, a typical set of test results, covering the frequency range between approximately 100 and 1000 Hz, is presented. These data apply to a rectangular element of Polybutadiene loaded in shear and exhibit small, but acceptable, scatter about a line showing steadily increasing stiffness and damping with frequency. A power law variation of the form $K = A\omega^B$ has been fitted to most data sets.

Shear stiffness of rectangular elements is proportional to sheared area. However, the axial stiffness of cylindrical buttons increases more nearly as the square of the stressed area. Incompressibility of the elastomer causes this effect since any axial deformation of the cylinder must be accompanied by radial deformation to maintain the same volume. Empirical correlations with diameter-to-height ratio for different button sizes are shown in Figure 4.

Stiffness and loss coefficients for O-rings in radial deformation are shown as functions of frequency in Figures 5 and 6. In Figure 5, three differen materials are compared: Viton 70, Viton 90, and Buna-N (70 durometer). The two 70 durometer materials show similar stiffnesses, although Viton 70 has a steeper slope. Viton 90 is approximately four times as stiff as the Viton 70. The loss coefficient for Viton 70, at about 0.9, is highest, compared with 0.5 for Viton 90 and 0.3 for Buna-N. Figure 6 shows the striking effects of increasing temperature on dynamic characteristics of Viton 70. The loss in stiffness is severe, and the decrease in loss coefficient even more pronounced; the excellent room temperature damping characteristics of Viton 70 are not fully maintained at the high temperatures which Viton can withstand.

Another important environmental parameters is the dynamic amplitude to which the elastomeric element is exposed as shown in Figure 7 for cylindrical Polybutadiene elements in compression. Stiffness steadily falls with increasing strain, particularly above 0.003, but loss coefficient steadily increases; properly exploited, strain of this material could result in increasingly effective vibration control!

It has been shown convincingly in several test series that the changes in elastomeric characteristics with strain are not solely the result of self-heatin Even when temperature rise in the elastomer is negligible, strain effects may be pronounced. However, under sufficiently high strains, elastomers do get hot. A 60° temperature increase is possible, as shown by the centerline profiles in Figure 8.

In Figure 9, the effects of strain on Viton 70 are seen to differ slightly from those observed for Polybutadiene. Both stiffness and loss coefficients of Viton 70 fall with increasing strain! Herein lies a further difficulty in dealing with elastomers: generalities are dangerous!

ROTOR DYNAMICS ANALYSIS WITH ELASTOMERIC ELEMENTS

Elastomeric rotor mounts must be matched to the dynamic characteristics of the rotor to give the best possible system dynamic performance. The design analysis and synthesis process are illustrated in Figure 10. Prior to component analysis, the rotor itself is analyzed to determine the optimum support characteristics. Component analysis, within environmental constraints such as temperature and available space, provides either a configuration which meets the desired optimum or a number of compromise configurations which minimize the deviation from optimum. From these alternatives, a final selection of geometry and material is made, and predictions of rotor system performance, with the selected component characteristics, are made. In some cases, the final damper configuration selection may be left to component or system rig test since elastomeric dampers can usually be designed to be readily replaceable.

In Figure 11, typical optimization curves show log decrement for a flexible rotor (a turboshaft engine dynamic simulator) as a function of elastomeric support damping. At first and second critical speeds, 100 lb·sec/in. is a clear optimum for both first and second criticals. The stiffness in this case is 100,000 lb/in., and Table 1 shows the damping which can actually be achieved in a 100,000 lb/in. elastomeric mount at the second critical speed. For Viton 70 and Polybutadiene, the damping will be 38 and 7.2 lb·sec/in., respectively, and the corresponding system log decrements will be 0.31 and 0.075, respectively, compared with the optimum of 0.965. A clear compromise is necessary for either material.

Figure 12 shows how component data are presented in the selection of diameter and height to achieve the desired stiffness of 100,000 lb/in.

APPLICATIONS EXAMPLES

Turboshaft Engine

Figure 13 shows, schematically, a test rotor designed as a dynamic simulator for an advanced, flexible rotor, turboshaft engine. The large disc at one end simulates the power turbine. The rotor runs in ball bearings which are themselves either hard-mounted or mounted in elastomeric dampers. The elastomeric dampers designed for this rig are shown in Figure 14. Around each bearing three groups of three cylindrical buttons support the bearing housing. These individual cartridges could be readily replaced, and several configurations were tested. Variable preload was achieved by means of a preload screw.

Figure 15 shows how elastomer material affects predicted response to unbalance. The higher loss coefficient of the Viton achieves a significantly lower response than Polybutadiene, corresponding to the higher log decrement presented in the previous section. The test data of Figure 16 show how sensitive to unbalance excitation the rotor was when first mounted on rigid metal cartridges. The response at around 20,000 rpm rises sharply to a peak of about nine mils. Figure 17 shows the drastic improvement in dynamic sensitivity when the rotor is flexibly mounted in Viton dampers. The largest response with half a gram of unbalance is less than 3-1/2 mils, and the shape of the response curve is very broad, indicating good system damping. The linear variation in amplitude with

unbalance is also apparent from these curves. It should be noted that the rotor was readily balanced to the lowest vibration curve in Figure 17 with a peak amplitude of only about one-third mil. These results are considered to be strong evidence for the potential benefits of elastomers in controlling flexible rotor vibrations.

Supercritical Power Transmission Shaft

Figure 18 shows, schematically, a test rig designed to evaluate flexible power transmission shafts for helicopter tail rotors. The test shaft was 12 feet long, 3 inches in diameter, with 1/8 inch aluminum walls, and had three critical speeds below 10,000 rpm. The rotor was initially hard-mounted, by means of angularly flexible couplings, from rigid shaft support spindles. Figure 19 shows the sharp response to unbalance at the first critical speed. Limiting amplitudes of about 75 mils peak-to-peak were reached with very small levels of residual unbalance. With great difficulty, the rotor was balanced through this first critical speed, but, as shown in Figure 20, when running at 20 percent above this first critical, the subsynchronous vibration level was almost as high as when negotiating the critical speed and seven or eight times the synchronous amplitude. Violent unstable motion occurred at these and higher speeds and there was no possibility of running the hard-mounted shaft any faster.

A damper was designed for the shaft, and, to ensure motion at the damper, a short extension was added to the test shaft as shown in Figure 21. Initially a squeeze film damper was used with some success, but the present discussion centers on a replacement elastomer damper. This damper consisted of six small elastomeric buttons deployed at 120° intervals in two rings, one of which is shown in Figure 22. The combined stiffness of the elastomer damper was designed to be 4000 lb/in. with a loss factor of 0.75 (selected as a conservative value for Viton 70). Figure 23 shows that this elastomeric damper lets the rotor run to 13,000 rpm without any problem from subsynchronous vibrations. This is about twelve times the speed at which intolerable subsynchronous vibrations were encountered when the power transmission shaft was hard mounted. Figure 24 shows a frequency spectrum at 13,000 rpm where the first critical subsynchronous vibra-tions are still less than 30 percent of the synchronous vibrations. Again, these results are considered impressive evidence of the ability of elastomeric dampers to control undesirable vibrations in flexible rotors.

Gas Bearing Mounted High-Speed Rotor

Striking success was achieved by flexibly mounting the gas bearings used to support a high-speed rotor required to run to over 120,000 rpm. In its hard-mounted configuration, this rotor encountered severe subsynchronous vibrations at about 280 Hz long before it reached its desired running speed. However, by flexibly mounting both gas bearings in O-rings, the rotor could be run all the way to its desired operating speed with only very small amplitude vibrations. The left-hand photograph of Figure 25 shows the 1.4 mil subsynchronous vibration orbit when the hard-mounted rotor was running at 108,600 rpm. The right-hand photograph shows the predominantly synchronous vibration orbit of 0.2 mil when

the O-ring mounted rotor was running at 114,600 rpm. These results are regarded as further strong evidence for the potential benefits of using elastomeric mounts to control instabilities.

CONCLUSIONS

With good material and component data, effective system and component design, and appropriate consideration for the application environment, elastomeric dampers hold considerable promise as simple low-cost devices for controlling undesirable vibrations in rotating machinery, both synchronous and subsynchronous.

REFERENCES

1. Chiang, T., Tessarzik, J.M., and Badgley, R.H., "Development of Procedures for Calculating Stiffness and Damping Properties of Elastomers in Engineering Applications, Part I: Verification of Basic Methods", NASA Report CR-120905, March 1972. Prepared by MTI for NASA-Lewis Research Center under Contract NAS3-15334.

2. Gupta, P.K., Tessarzik, J.M., and Cziglenyi, L., "Development of Procedures for Calculating Stiffness and Damping Properties of Elastomers in Engineering Applications, Part II: Elastomer Characteristics at Constant Temperature", NASA Report CR-134704, April 1974. Prepared by MTI for NASA-Lewis Research Center under Contract NAS3-15334.

3. Smalley, A.J., and Tessarzik, J.M., "Development of Procedures for Calculating Stiffness and Damping Properties of Elastomers in Engineering Applications, Part III: The Effects of Temperature, Dissipation Level and Geometry", NASA Report CR-134939, November 1975. Prepared by MTI for NASA-Lewis Research Center under Contract NAS3-15334, and NAS3-18546.

4. Darlow, M.S., and Smalley, A.J., "Development of Procedures for Calculating Stiffness and Damping Properties of Elastomers in Engineering Applications, Part IV: Testing of Elastomers under a Rotating Load", NASA Report CR-135355, November 1977. Prepared by MTI for NASA-Lewis Research Center under Contract NAS3-18546.

5. Smalley, A.J., Darlow, M.S., and Mehta, R.K., "Stiffness and Damping of Elastomeric O-Ring Bearing Mounts", NASA Report CR-135328, November 1977. Prepared by MTI for NASA-Lewis Research Center under Contract NAS3-19751.

6. Tecza, J.A., Darlow, M.S., Jones, S.W., Smalley, T.J., and Cunningham, R.E., "Elastomer Mounted Rotors an Alternative for Smooth Running Turbomachinery", ASME paper 78-GT-149, presented at the Gas Turbine Conference and Exhibit and Solar Energy Conference in San Diego, CA, March 12-15, 1979.

7. Darlow, M.S., and Smalley, A.J., "The Effects of Strain and Temperature on the Dynamic Properties of Elastomers", ASME paper 79-DET-57.

457

8. Tecza, J.A., Darlow, M.S., Smalley, A.J., and Cunningham, R.E., "Design of Elastomer Dampers for a High-Speed Flexible Rotor", ASME Paper 79DET88.

9. Zorzi, E.S., Burgess, G., and Cunningham, R., "Elastomer Damper Performance A Comparison with a Squeeze Film for A Supercritical Power Transmission Shaft", ASME paper 80-GT-162.

TURBOSHAFT DYNAMIC SIMULATOR COMPARISON OF LOG DECREMENT FOR

POLYBUTADIENE AND VITON-70 WITH OPTIMUM DAMPING

(2nd Critical Speed; Stiffness = 100,000 lb/in.)

	B (lb-sec/in.)	δ
(1) OPTIMUM	100	0.965
(2) POLYBUTADIENE	7.2	0.075
(3) VITON-70	38	0.31

TABLE 1

BASE EXCITATION RESONANT MASS TEST SCHEMATIC
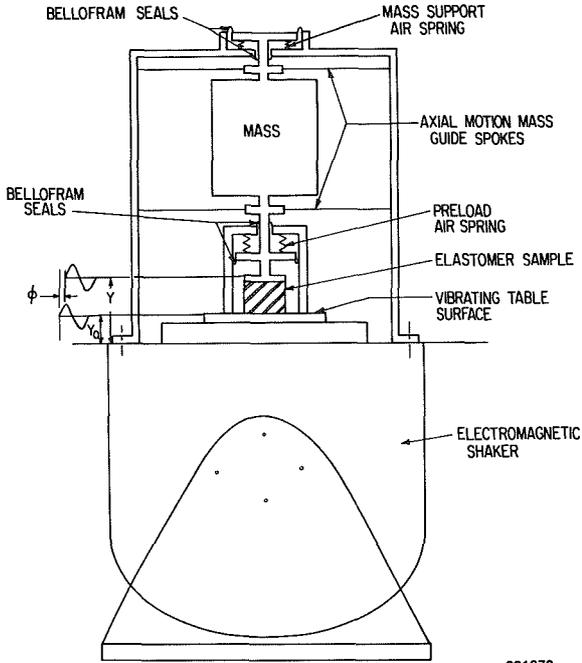
Figure 1

801378

SCHEMATIC OF COMPONENT GEOMETRIES TESTED

A. SHEAR ELEMENT

B. COMPRESSION ELEMENT

C. CARTRIDGE
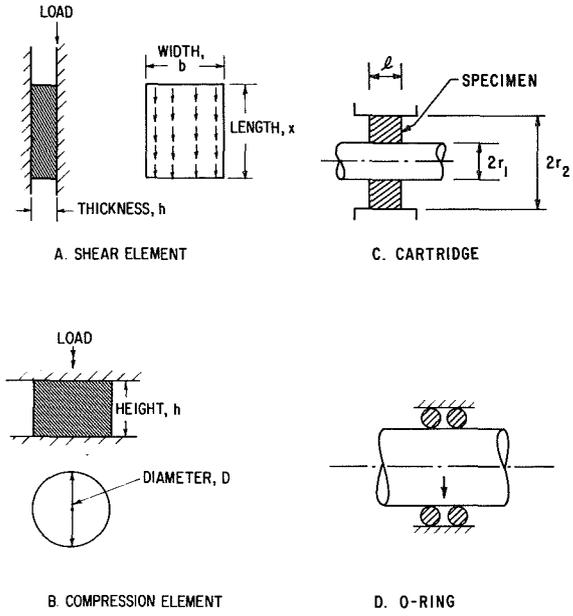
D. O-RING

Figure 2

801393

ILLUSTRATIVE TEST RESULTS: SHEAR SPECIMEN STIFFNESS, DAMPING VERSUS FREQUENCY

$K_1 = 1.355 \times 10^6 \, \omega^{.3009}$

$K_2 = 8.545 \times 10^5 \, \omega^{.1729}$

Figure 3

801423

459
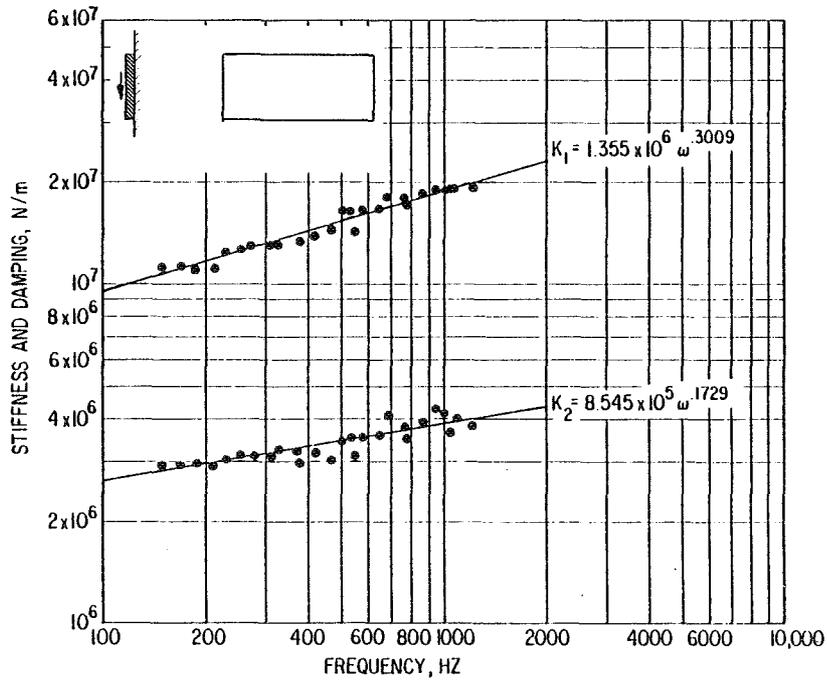
EFFECT OF DIAMETER TO HEIGHT RATIO ON CYLINDRICAL BUTTON STIFFNESS

$$K_2 = \frac{3G''A}{h}\left[1 + 2\left(\frac{d}{4h}\right)^2\right]$$

CORRELATION

$$K_2 = \frac{3G''A}{h}\left[1 + 2.244\left(\frac{d}{4h}\right)^2\right]$$
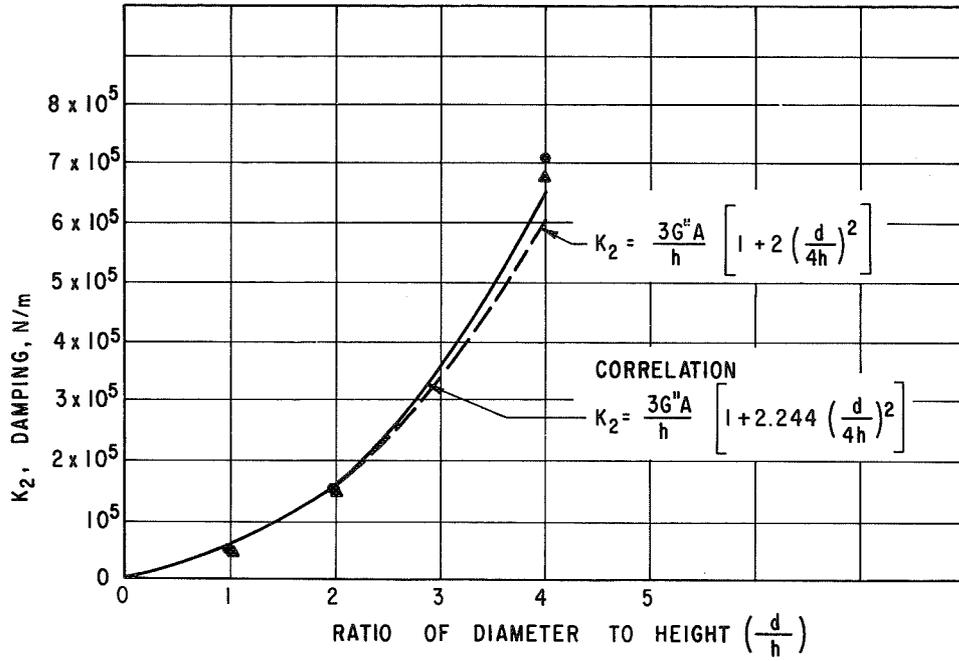
801438

Figure 4

O-RING STIFFNESS AND LOSS COEFFICIENT
FOR DIFFERENT MATERIALS
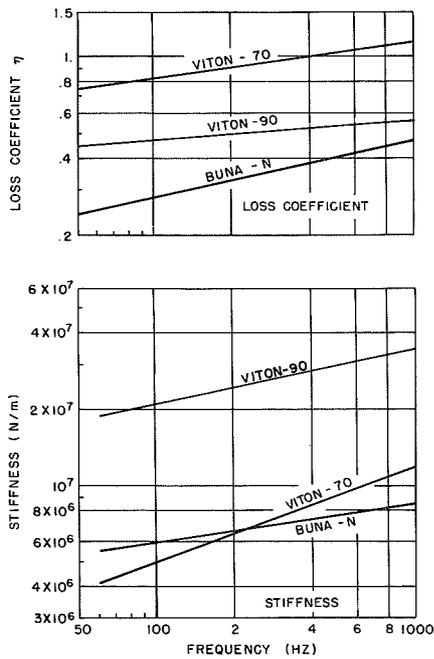
801452

Figure 5

O-RING STIFFNESS AND LOSS COEFFICIENT
FOR VITON-70 AT DIFFERENT TEMPERATURES

801467

Figure 6

460
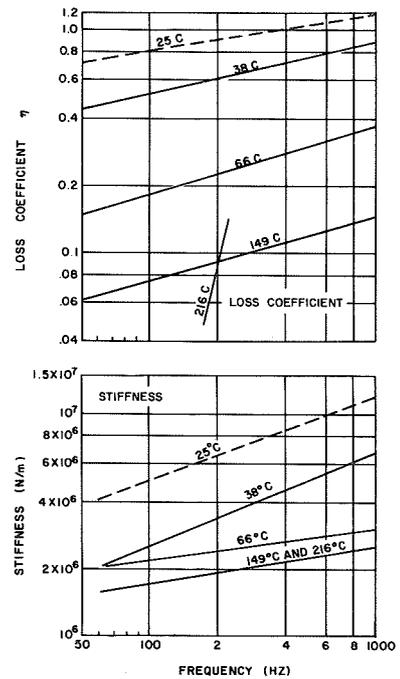
STIFFNESS AND LOSS COEFFICIENT VERSUS STRAIN FOR CYLINDRICAL BUTTONS IN COMPRESSION

Figure 7

792071

O-RING STIFFNESS AND LOSS COEFFICIENT FOR DIFFERENT AMPLITUDES
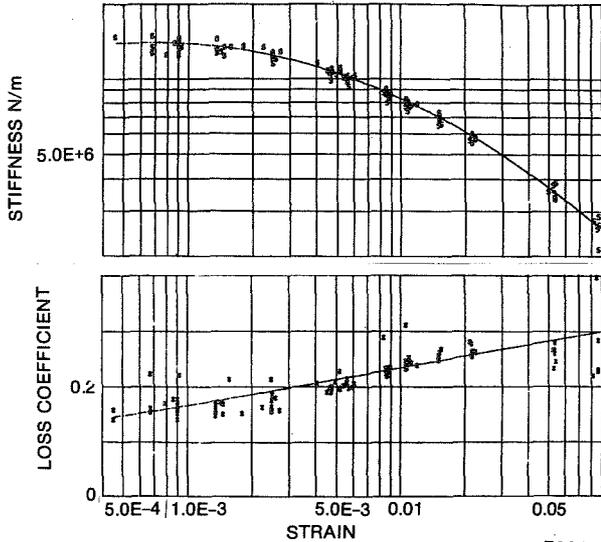
Figure 9

801235

AXIAL TEMPERATURE PROFILE IN CYLINDRICAL BUTTONS FOR COMPRESSION

Figure 8

792072
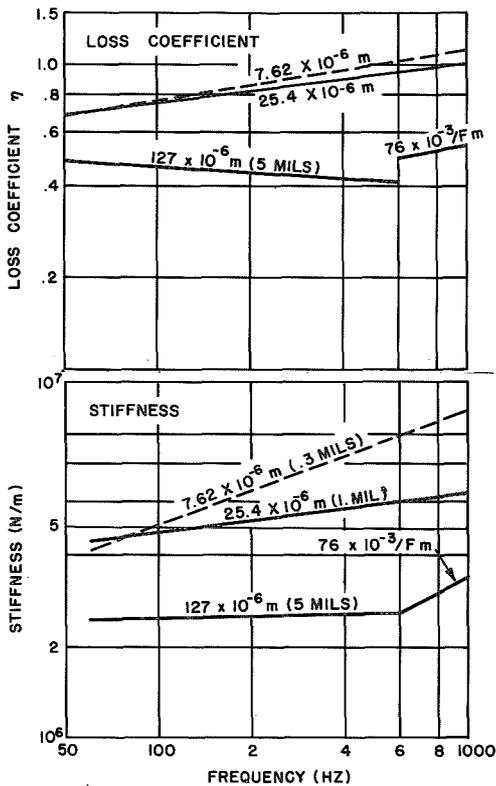
INFORMATION FLOW DIAGRAM FOR ROTORDYNAMICS — COMPONENT INTERACTION

Figure 10

801482

461
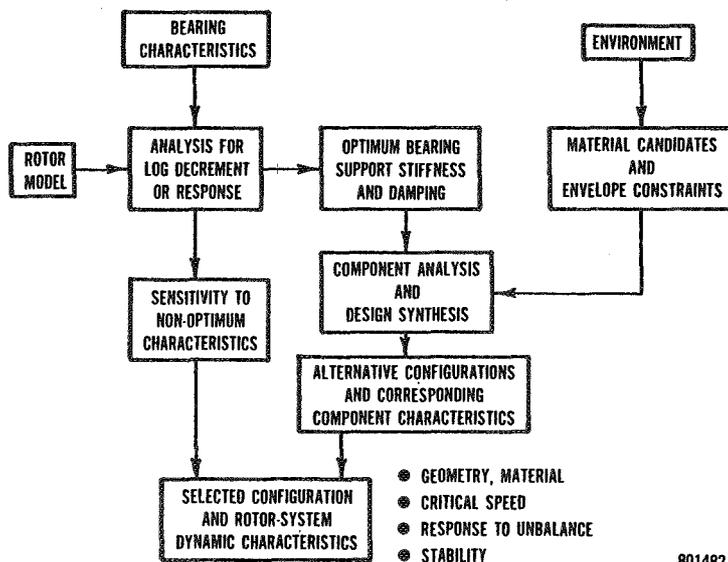
LOG DECREMENT VERSUS DAMPING COEFFICIENT: CYLINDRICAL BUTTONS
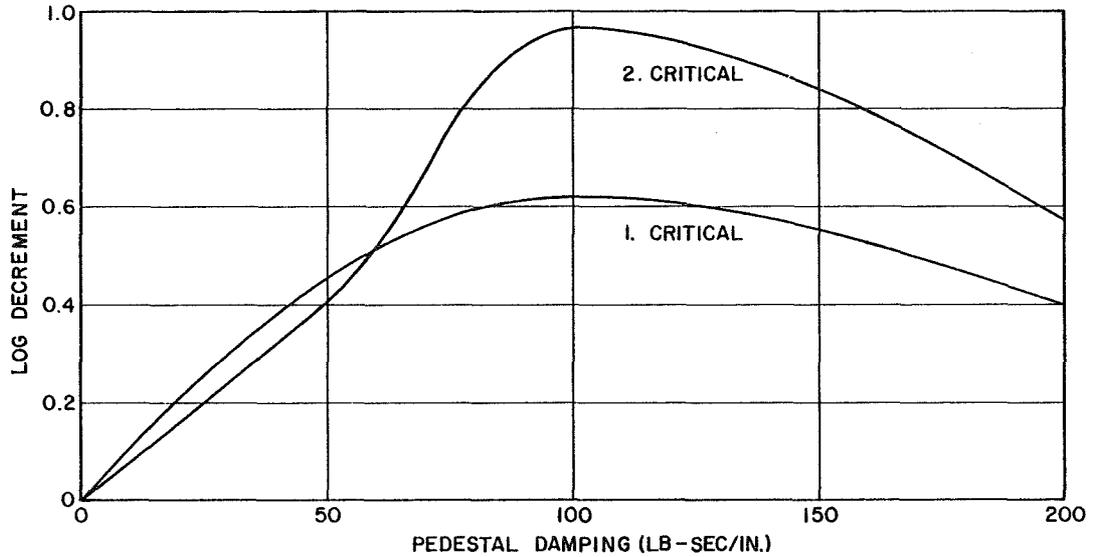
Figure 11

PLOT OF CYLINDRICAL BUTTON STIFFNESS VERSUS DIAMETER FOR DIFFERENT HEIGHTS
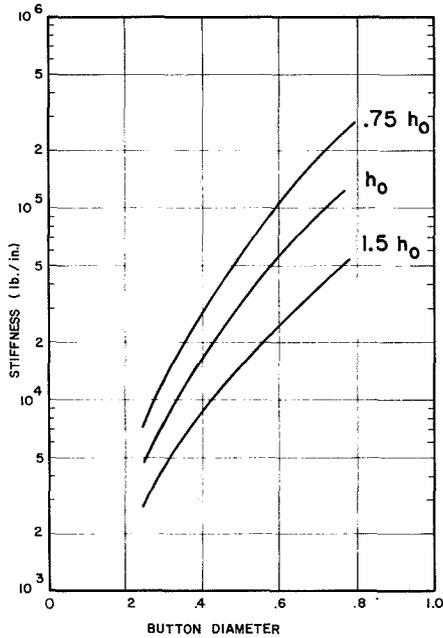
Figure 12

SCHEMATIC OF TURBOSHAFT ENGINE DYNAMIC SIMULATOR RIG

WEIGHT ADDED TO DISC HERE FOR SENSITIVITY RUNS

NONCONTACTING DISPLACEMENT PROBES

1, 2
1, 3 etc.
2, 4 etc.

3, 4 5, 6

7, 8

9, 10 11, 12

13, 14

FRONT VIEW

ELASTOMER BUTTONS

WEIGHT ADDED TO SHAFT HERE FOR SENSITIVITY RUNS

WEIGHT ADDITION PLANES
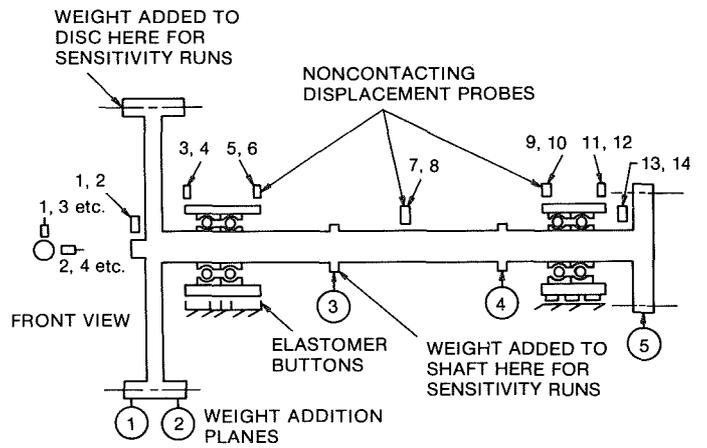
Figure 13

SCHEMATIC OF ELASTOMER DAMPER
CONFIGURATION FOR TURBOSHAFT RIG

A. Arrangement of
   Elastomer Cartridges

B. Cartridge Construction
   with Three Buttons
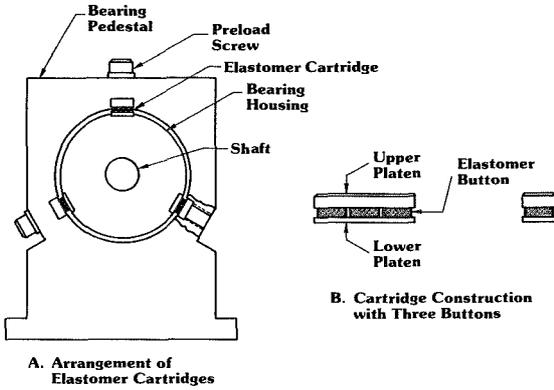
801497

Figure 14

PREDICTED RESPONSE OF TURBOSHAFT RIG
FOR VITON AND POLYBUTADIENE DAMPER
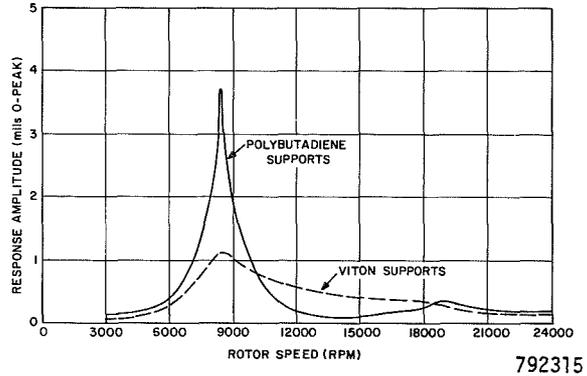
792315

Figure 15

MEASURED RESPONSE
OF TURBOSHAFT DAMPER ON HARD MOUNT
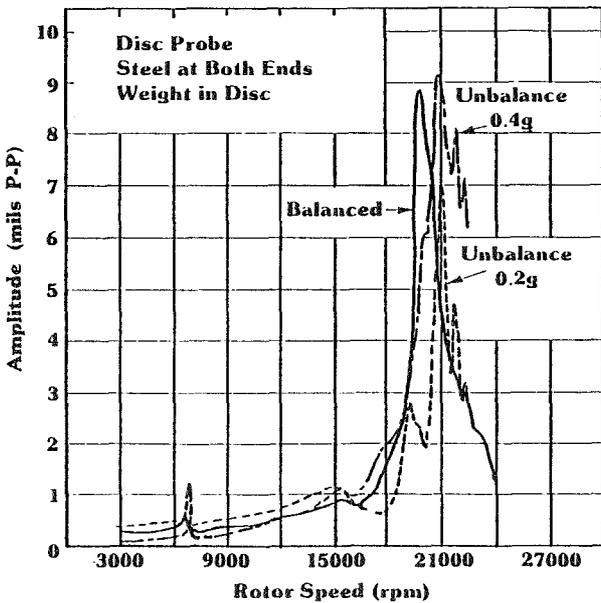
801512

Figure 16

MEASURED RESPONSE
OF TURBOSHAFT RIG ON VITON-70 DAMPER

801527

Figure 17

463
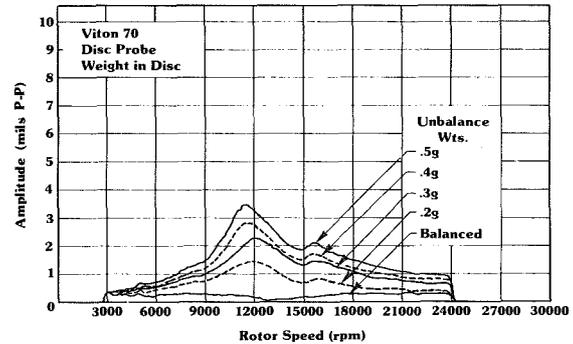
SCHEMATIC OF
SUPERCRITICAL SHAFT TEST RIG
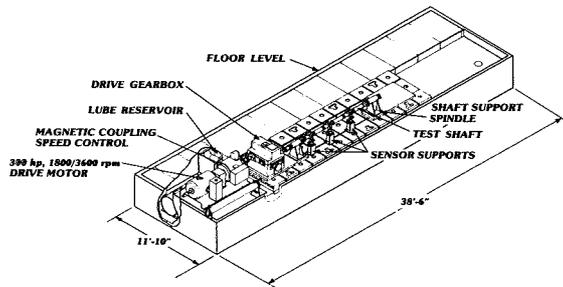
801572

Figure 18

RESPONSE AMPLITUDE VERSUS SPEED;
SUPERCRITICAL SHAFT RIG WITHOUT DAMPER
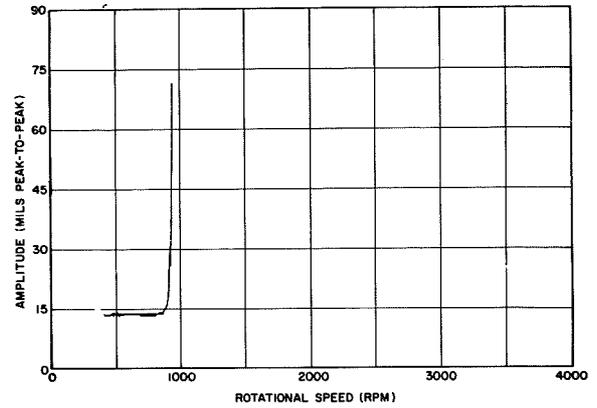
801587

Figure 19

FREQUENCY SPECTRUM;
SUPERCRITICAL SHAFT RUNNING ABOVE
FIRST CRITICAL WITHOUT DAMPER
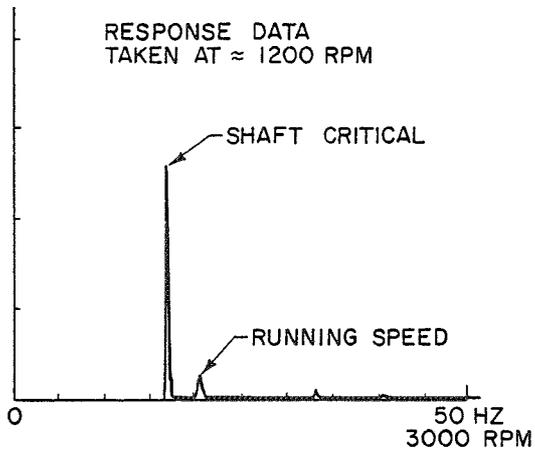
801542

Figure 20

SCHEMATIC SHOWING LOCATION OF
DAMPER ON SUPERCRITICAL SHAFT RIG

801557

Figure 21

464
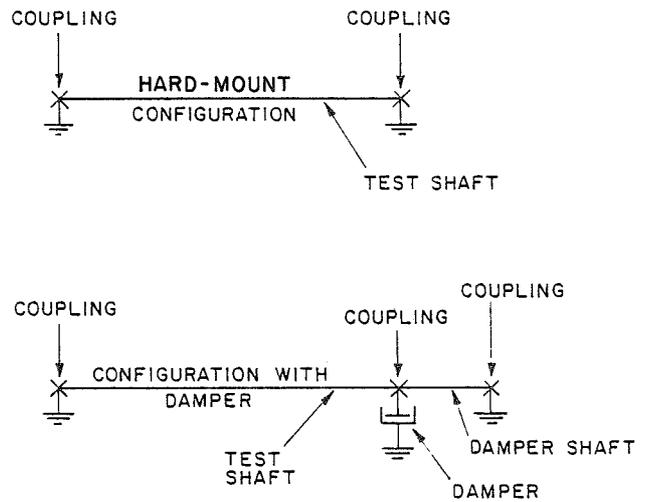
PHOTO OF ELASTOMER DAMPER
FOR SUPERCRITICAL SHAFT

RING ASSEMBLY

ELASTOMER

PLATEN

PRELOAD SCREW
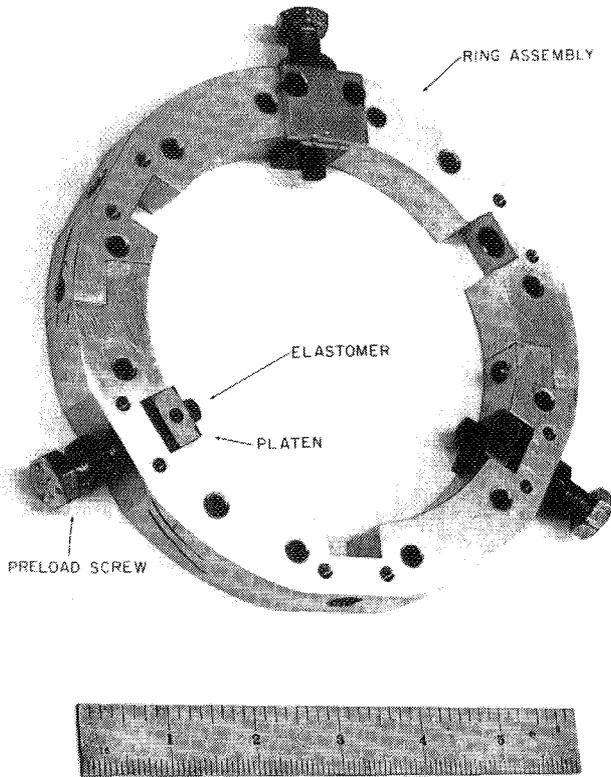
Figure 22

RESPONSE AMPLITUDE VERSUS SPEED;
SUPERCRITICAL SHAFT WITH
ELASTOMER DAMPER

40 MILS

AMPLITUDE

FIRST CRITICAL

THIRD CRITICAL

FOURTH CRITICAL

MAXIMUM SPEED
13,000 rpm

0   Hz   500
                          792379
Figure 23
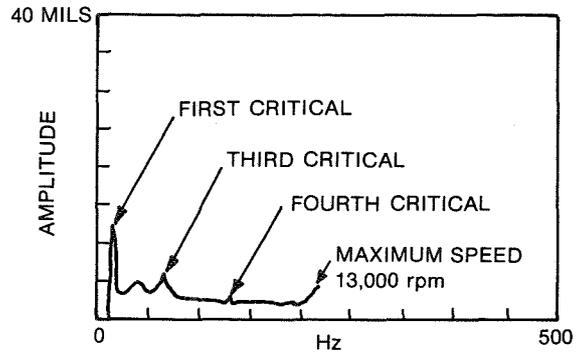
FREQUENCY SPECTRUM;
SUPERCRITICAL SHAFT RUNNING ABOVE
FOURTH CRITICAL WITH ELASTOMER DAMPER

8
MILS

AMPLITUDE

216 Hz ~ 1/REV

16 Hz ~ FIRST
CRITICAL

433 Hz ~ 2/REV
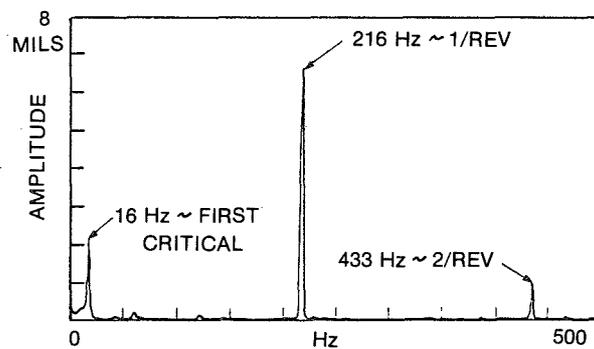
0   Hz   500
Figure 24   792377

COMPARISON OF ORBITS; GAS-BEARING ROTOR HARDMOUNTED AND ON O-RING MOUNTS

1.4
Mils

0.2
Mils

108,600 rpm   114,600 rpm
a. Hard-Mounted   b. O-Ring Mounts

Figure 25

465
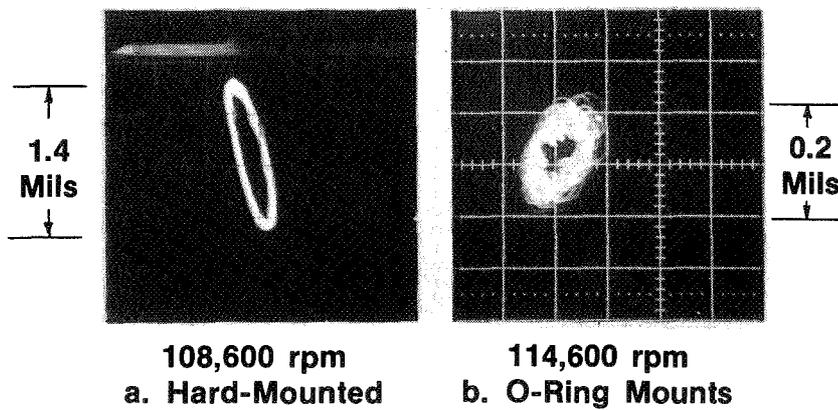
Page intentionally left blank

FEASIBILITY OF ACTIVE FEEDBACK CONTROL
OF ROTORDYNAMIC INSTABILITY*

James W. Moore, David W. Lewis, and John Heinzman
University of Virginia
Charlottesville, Virginia 22903

SUMMARY

This paper discusses some of the considerations involved in the use of
feedback control as a means of eliminating or alleviating rotordynamic instabil-
ity. A simple model of a mass on a flexible shaft is used to illustrate the
application of feedback control concepts. A description is given of a system
now being assembled at the University of Virginia which uses feedback control
to support the shaft bearings.

INTRODUCTION

The feasibility of using active feedback control of rotor dynamics by the
active control of some or all of the forces in the bearing support system is
the subject of research just started at the University of Virginia. If such an
approach is feasible, or even partially so, many benefits could accrue to those
now having problems of rotordynamic instability.

To study this approach a rotor system using control concepts is now being
assembled. It consists of a flexible shaft mounted horizontally in ball bear-
ings at the ends and having provisions for mounting one to three masses. The
bearings are each supported by two high-fidelity speaker motors which have a
linear range in excess of any expected transients. These motors are mounted at
ninety degrees to each other. Induction-type proximity sensors are used to
sense shaft position at the bearings and at the central mass. The position
signals are then input to the control system, which supplies gain and compensa-
tion for the servoamplifiers driving the motors.

The system is designed to use either analog control or computer control of
the individual control loops. Initial efforts will use relatively simple con-
trol algorithms, but ultimately it is expected that the system will have aspects
of pattern recognition and will be adaptive to running speed and to other sys-
tem parameters.

To illustrate some of the potential benefits of using feedback control, a
simple model is analyzed here from the control standpoint. Parameters for the
model are selected to be close to those for a system which was the subject of a
doctoral dissertation by Marvin Taylor at the University of Virginia in 1979.
This work reported on the active feedback control of a rotating cup containing
a steel ball which was free to rotate around the inner periphery of the cup.
The cup was mounted on a slender shaft, positioned vertically and supported at

the upper end only. This study was limited in that motion was sensed and controlled in the plane of unbalance. However, Taylor was able to control not only the vibration amplitude at the critical speed but also the whirl of the ball in the cup.

NOMENCLATURE

$A(s)$	loop gain
a_i	polynomial coefficients
c	shaft damping, N s/cm (lb sec/in)
c_i	support damping, N sec/cm (lb sec/in)
$G(s)$	control transfer function
$G_c(s)$	overall feedback transfer function
j	$(-1)^{1/2}$
K	control gain
k	shaft stiffness, N/cm (lb/in)
k_1	support stiffness, N/cm (lb/in)
L	load disturbance
m	rotor mass, kg (lb sec^2/in)
p_i	control and system poles
r	unbalance position, cm (in.)
s	Laplace variable
u	control signal
Z	displacement of mass center, cm (in.)
Z_1	displacement of bearing center, cm (in.)
z_i	control and system zeros
α	ratio of support stiffness to shaft stiffness
ζ	damping ratio
ϕ_i	phase angles
ω	frequency, rad/sec
ω_r	natural frequency

ILLUSTRATIVE SYSTEM

The system to be modeled and controlled is shown in figure 1. For this study complete symmetry is assumed and the bearings are considered as massless. The springs provide the basic support and the control force is additive at the same point. This allows the system to be considered as being of third order. The equations of motion are

$$c_1 \dot{Z}_1 + k_1 Z_1 + k(Z_1 - Z) = u \qquad (1)$$

$$m\ddot{Z} + c\dot{Z} + k(Z - Z_1) = L \qquad (2)$$

where L represents the loading at the mass due to unbalance and u is the control force to be applied. We take the Laplace transform and solve for transfer functions of Z and Z_1 with input u. The unbalance force we will consider as being a load disturbance.

In addition, the shaft damping is considered as negligible. The transfer functions are

$$Z = \frac{(c_1 s + k + k_1)L + ku}{mc_1\left(s^3 + \dfrac{k + k_1}{mc_1}s^2 + \dfrac{k}{m}s + \dfrac{kk_1}{mc_1}\right)} \qquad (3)$$

$$Z_1 = \frac{(ms^2 + k)u + kL}{mc_1\left(s^3 + \dfrac{k + k_1}{c_1}s^2 + \dfrac{k}{m}s + \dfrac{kk_1}{mc_1}\right)} \qquad (4)$$

The denominator of both equations will have one real root and a pair of complex roots. Using this fact and noting that we need to separate the load and control effects, we can write

$$Z = \frac{(s + z_1)}{m(s + p_1)(s^2 + a_1 s + a_0)}\left[L + \frac{ku}{c_1(s + z_1)}\right] \qquad (5)$$

In this form a block diagram can be drawn. This is shown in figure 2, where control and sensor blocks have also been added. In this instance the sensor is assumed to give position and velocity information.

An actuator, the control motor, is assumed to have the transfer function

$$\frac{p_2}{s + p_2} \qquad (6)$$

and the controller is assumed to have the form of a gain and a lead-lag function. Combining these factors results in the overall control transfer function

$$G_c = \frac{-K(s + z_2)(s + z_1)}{(s + p_3)(s + p_1)} \qquad (7)$$

Combining this with the system transfer function gives a loop gain $A(s)$, which can be used to plot a root locus, which in turn can be used to select the gain and set the control poles and zeros. This function is

$$A = \frac{K_1(s + z_2)(s + z_3)}{(s + p_1)(s + p_2)(s + p_3)(s^2 + a_1 s + a_0)} \tag{8}$$

As mentioned earlier, the parameters for this system were chosen to be approximately equivalent to Taylor's system. This had $k = 20.8$ lb/in and $\omega_n = 85.5$ rad/sec. A number of systems were considered that have second-order parameters close to these. These are listed in table I. Here the entering point is the first column, which is the ratio of support stiffness to shaft stiffness. The second column is the support damping. For each pair of values of these parameters the real pole and zero, the complex poles, and the quadratic coefficients are listed. The parameters chosen for this study are in the row marked with an asterisk.

Root loci of this system for two different values of the control zero are given in figure 3. Also, taking advantage of the vertical symmetry of root locus plots, the lower half plane shows a locus of the system complex poles for a spring rate ratio of 1 and a variable damping factor. The point on the locus for c_1 equals 0.5 is marked with an x, the standard open-loop pole symbol. Its complex conjugate is used in the upper half plane as the starting point for the root loci.

Considering these loci, the solid line is the complex locus with the system motor pole at -200 and a zero at -1. The control compensator pole is at -400 and its zero is at -100.

The dashed line represents the same system except that the compensator zero is moved to -40. The effect is to move the complex locus farther to the left of the imaginary axis. In addition, a new complex locus appears near the real axis.

A root locus is a plot of all possible roots of the closed-loop system with K as the variable parameter. Thus the effect of closing the control loop is very apparent in this case. The principal effect is that the original system poles are eliminated and a new set of poles are established. These poles can be located at any particular points on the branches of the loci by picking a particular value of the control gain K. The poles on the upper complex branch are the ones of particular interest since they will tend to dominate the dynamics of the system. They could be selected for maximum damping or to move them far away from the original system natural frequencies. They represent a quadratic pair in the closed loop system. Considering them only, their damping factor is represented by the arccos ζ, measured from the negative real axis. In figure 3 the maximum ζ lines are shown for both upper branches, and the minimum ζ line is shown for the lower complex branch.

Four values of gain were chosen for calculation of the closed-loop frequency responses of the system. The resulting closed-loop complex poles are re-

presented by the numbered squares on the upper branches. The results are shown in figure 4. Curve 1 is for poles located at point 1 on the solid locus. The resonant peak is about 1.6 at approximately 200 rad/sec. Curve 2 is for the dashed locus with the complex poles having about the same imaginary value as the first case and with the control zero at -40. Curve 3 is from the same locus with the control gain lowered to place the upper complex poles at near maximum ζ. For curve 4 we return to the solid locus and raise the gain to place the complex poles at near the point where the locus crosses the imaginary axis, the point of control loop instability. The response is unbounded for practical purposes at about 270 rad/sec.

EXPERIMENTAL MODEL

The experimental model has already been described and is very similar to the model of figure 1 without the symmetry limitation. Also, the control system almost completely replaces the spring-damper support system and the bearing masses become significant. The analog control system will be of the same form as in the example. All its parameters will be adjustable, and there is provision for making it somewhat adaptive to rotor speed.

The computer control is affected by replacing the control block in figure 2 by a single block Intel 8086 microprocessor and peripherals. Input and output are through appropriate analog-to-digital and digital-to-analog converters. This microprocessor can handle 16-bit words, which allows greater flexibility and precision but which causes it to operate a bit slower than some 8-bit microprocessors. However, preliminary estimates indicate that a computation cycle can be completed about every $10°$ of rotation of a shaft turning at 6000 rpm. The initial programming of the microprocessor will be of a proportional-plus-rate type with adaptivity to rotor speed and potential for adapting to other parameters.

CONCLUSIONS

The example presented illustrates some of the ability of feedback control to modify the basic characteristics of a rotor system. Potential advantages include the possibility of easily negotiating critical speed ranges; lossless electronic damping; and adaptation to changing load conditions, age, lubricant characteristics, and other factors. In addition, computer control offers the potential of parallel, or even on-line, analysis of system characteristics as a means of recognizing potential trouble and of adapting the control system in an optimum manner.

Yet to be considered in detail are a myriad of the problems of real systems. These include all the present problems, which are well known in rotor dynamics, and adds the problems of control systems. These latter include bandwidth limitations of control components; design of control motors; power and force levels; nonlinearities, particularly signal limiting; observability of appropriate system states; selection of optimum control algorithms; computation speed; and many others. Some recommendations with respect to the feasibility of solutions for some of these problems will be made in the near future. An adequate number of problems will remain for several years of research effort.

471

The experimental rotor rig was completed by May 20, 1980. It consists of three rotor disks totaling 10 pounds. They are mounted on a 1/2-inch-diameter shaft with a spring rate of 1040 lb/in. The analog control system was operational on May 21, 1980. Initial testing appears to indicate that the performance exceeds expectations. The system was able to run to 6000 rpm without the rotor having been balanced and with no difficulties in negotiating critical speeds.

Efforts in the immediate future will be on the computer control system and on careful testing and evaluations of the system with either analog or digital control. Experimental work will be under the direction of Dr. Ronald Flack, Assistant Professor, Department of Mechanical and Aerospace Engineering, University of Virginia.

TABLE I. – SYSTEM CHARACTERISTICS

α	c_1	Real	Complex	Quadratic coefficients			Zero
0.5	0.1	−296	−8±50j	1	16	2539	−312
	1	−10.6	−10±84j	1	21	7095	−31
	5	−2	−2±85j	1	4.1	7298	−6
1	0.05	−829	−2±60j	1	4.4	3629	−833
*	.1	−408	−4.4±61j		8.9	3692	−417
	.5	−53	−15±74j		31	5695	−84
	1	−22	−10±82j		20	6871	−42
	5	−4	−2±85j		4	7298	−8
	10	−2	−1±86j		2	7311	−4
	20	−1	−.5±86j		1	7310	−2
2	0.1	−621	−2±70j	1	4	4848	−625
	1	−46	−8±80j	1	17	6549	−63
	5	−8	−2±85j	1	4	7280	−12
5	0.1	−1249	−0.5±78j	1	1	6025	−1250
	.5	−245	−2±78j		5	6138	−250
	1	−117	−4±80j		8	6415	−125
	5	−21	−2±85j		4	7229	−25
	10	−10	−1±85j		2	7294	−12
10	0.1	−2084	−0.2±81j	1	0.4	6503	−2084
	.5	−414	−1±81j		2	6530	−416
	1	−205	−2±81j		3	6613	−208
	5	−38	−2±85j		4	7161	−42
	10	−19	−1±85j		2	7270	−21
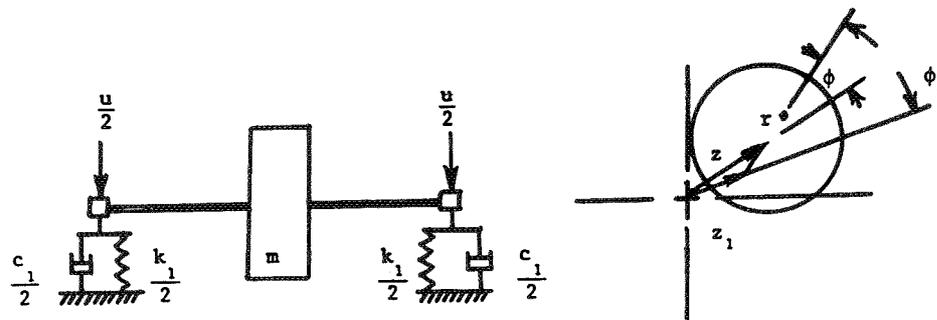
Fig. 1 Physical Model

$$G_c(s) = \frac{-K(s + z_2)(s + z_3)}{(s + p_2)(s + p_3)}$$
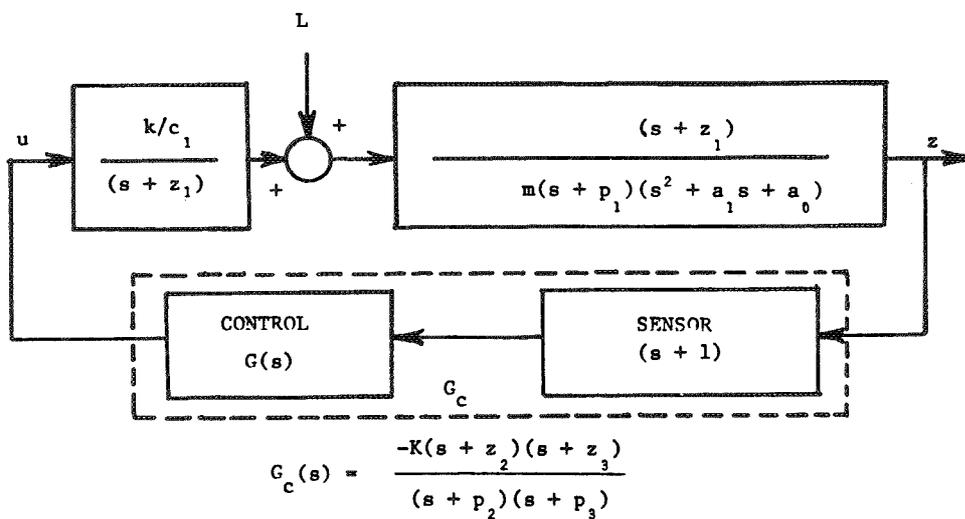
Fig. 2 Control Model

Fig. 3 Root Locus

Solid Line $z_2 = -100$
Dashed Line $z_2 = -40$
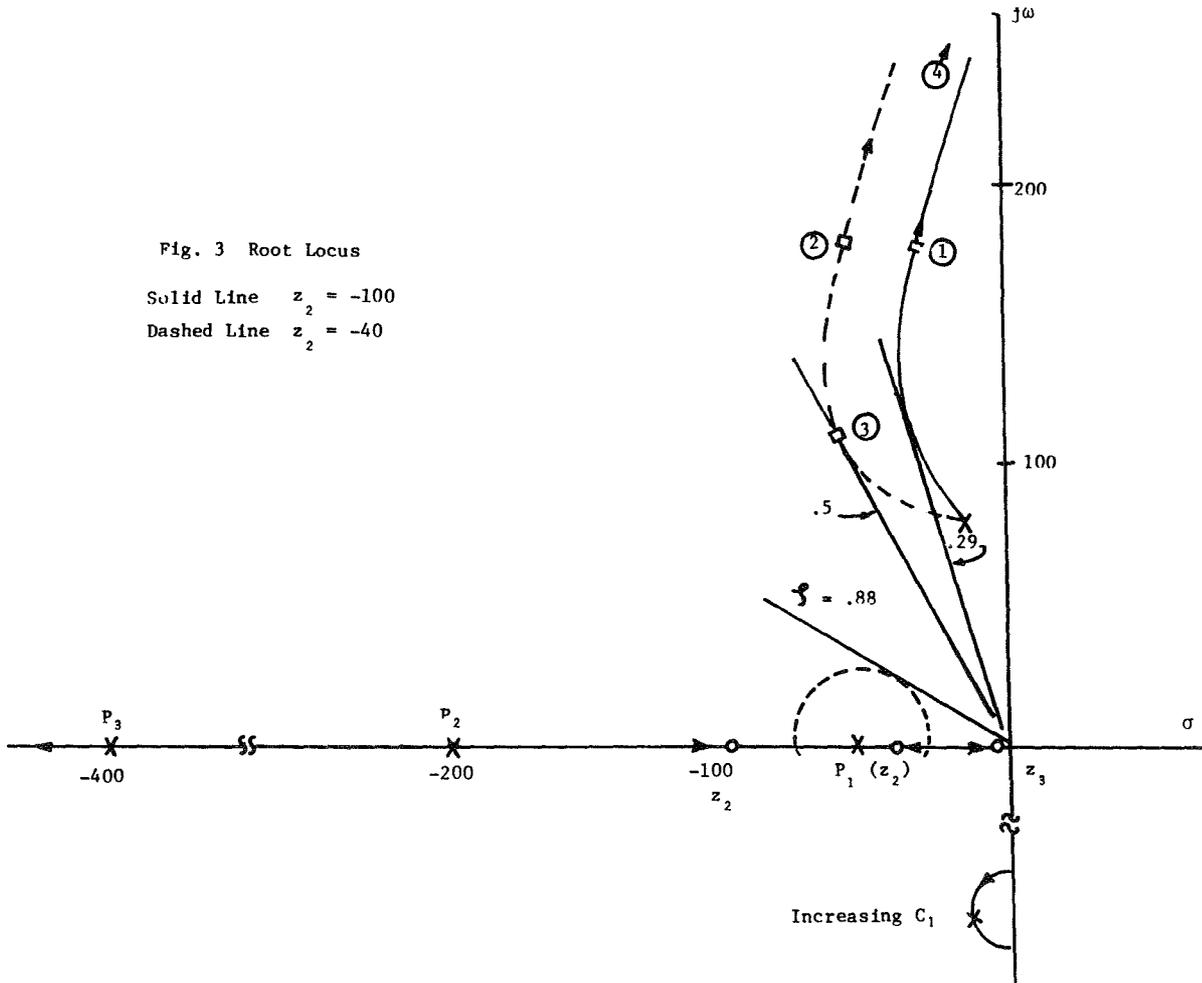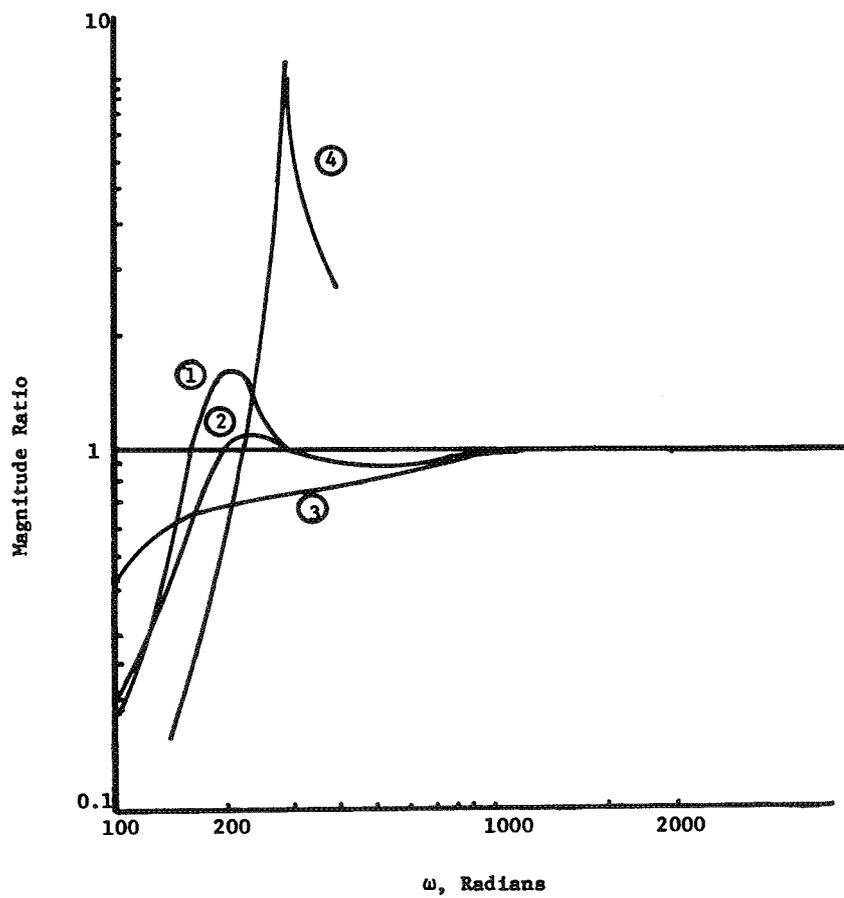
Fig. 4   C. L. Frequency Response

WORKSHOP CLOSURE AND OBSERVATIONS

The opening day presentations relating the experiences of turbomachinery manufacturers and users were particularly welcome and reflected a degree of courage on the part of the presenters in publicly discussing their problems. The detailed discussions of the characteristics of rotordynamic instability incidents presented in these papers certainly stimulated the thought processes of the workshop participants and properly introduced a degree of humility by citing presently inexplicable dynamic behavior (e.g., the 2/3-running-speed whirl cited in the Ingersoll-Rand and Phillips papers).

While most of the opening day papers examined "classical" subsynchronous whirl motion arising from rotordynamic instabilities, the paper by Ferrara rather conclusively implicates pressure fluctuations arising during surge conditions in compressors as an unresolved subsynchronous driving mechanism for rotor motion. The phenomenon of torsional interaction in a lateral rotor instability presented by Wachel has not previously been confirmed by test data although it was anticipated by Lund's 1977 ASME Vibration Conference paper.

The papers presented in the seal-force session on the second day reflect at once that progress has been made in the development and validation of seal models and that a great deal of work remains to be done. It is hoped that the two experimental programs with incompressible seals will yield additional published design data in coming years. The paper by Wachter and Benckert relating their experimental results with labyrinth seals is an outstanding contribution with obvious direct potential for advancing the design of stable turbomachinery. Although illness regrettably prevented Professor Iwatsubo from presenting his analysis of a single-cavity labyrinth seal, his paper, the most complete and comprehensive work presented to date, is included in this proceedings.

The working-fluid destabilizing force presentations of the second day were intriguing. The two papers by Colding-Jorgensen and Shen and Mengle dealing with centrifugal and axial machinery are landmark efforts at defining and quantifying destabilizing forces. They represent a point of departure for more complicated, and perhaps more comprehensive, future analyses. The paper by Thomas and Leie, unfortunately not presented at the workshop, documents many years of test work at the Technical University of Munich aimed at measuring turbine destabilizing forces. The presentation by Brennen of projected work at the California Institute of Technology to measure direct and transverse forces on pump impellers is particularly interesting, holding forth the promise of data to be used in evaluating and stimulating analytical models for impeller-diffuser forces.

Professor Crandall's eloquent presentation of physical explanations for the internal damping mechanism of rotor instability is likely to be retained permanently in the memories of his audience and will certainly find its way into the lecture notes of faculty participants.

The concluding session on control possibilities for rotordynamic instabilities was particularly helpful in documenting the possibilities for stability control by bearing and squeeze-film damper selection. The earlier paper by Malanoski is also notably helpful in this regard. The papers by Smalley and Moore are tantalizing in providing new possibilities for stability control. Although the pioneering work on elastomeric dampers is sufficient to demonstrate their utility and viability in the control of rotordynamic motion, the

477

full potential of this device is certainly far from realization. Professor Moore's proposals for active control are simply too new and novel to assess at this time.

The perceived success of this workshop owes a great deal to the active discussion by its participants. In this regard, the organizers are particularly indebted to Edgar Gunter and Joseph Alford, whose longstanding contributions to an increased understanding and awareness of rotordynamic instability problems are well known. Mr. Alford may properly view this workshop as a vindication of the basic correctness of his vision as enunciated in his frequently quoted 1965 paper.

1. Report No. NASA CP-2133	2. Government Accession No.	3. Recipient's Catalog No.
4. Title and Subtitle ROTORDYNAMIC INSTABILITY PROBLEMS IN HIGH-PERFORMANCE TURBOMACHINERY		5. Report Date August 1980
		6. Performing Organization Code
7. Author(s)		8. Performing Organization Report No. E-413
9. Performing Organization Name and Address NASA Lewis Research Center Cleveland, OH 44135		10. Work Unit No.
		11. Contract or Grant No.
12. Sponsoring Agency Name and Address National Aeronautics and Space Administration Washington, DC 20546		13. Type of Report and Period Covered Conference Publication
		14. Sponsoring Agency Code

15. Supplementary Notes

16. Abstract

Many high-performance turbomachines have experienced severe development and operational problems as a result of subsynchronous instabilities. Although techniques have been developed to cope with units that prove to be unstable, the degree of understanding is completely inadequate to design stable high-performance turbomachinery. This workshop, held at Texas A&M University, May 12-14, 1980, was therefore organized to address the general problem of rotordynamic instability with the intent that the discussions within the workshop and this document will provide an initial catalyst for the systematic resolution of these problems.

17. Key Words (Suggested by Author(s)) Rotordynamics Turbomachinery Instability, rotordynamics	18. Distribution Statement Unclassified — Unlimited Subject Category 34		
19. Security Classif. (of this report) Unclassified	20. Security Classif. (of this page) Unclassified	21. No. of Pages 484	22. Price* A21